NanoScience and Technology

Quan Li *Editor*

Anisotropic Nanomaterials

Preparation, Properties, and Applications

Springer

NanoScience and Technology

The series NanoScience and Technology is focused on the fascinating nano-world, mesoscopic physics, analysis with atomic resolution, nano and quantum-effect devices, nanomechanics and atomic-scale processes. All the basic aspects and technology-oriented developments in this emerging discipline are covered by comprehensive and timely books. The series constitutes a survey of the relevant special topics, which are presented by leading experts in the field. These books will appeal to researchers, engineers, and advanced students.

More information about this series at http://www.springer.com/series/3705

Quan Li
Editor

Anisotropic Nanomaterials

Preparation, Properties, and Applications

Springer

Editor
Quan Li
Liquid Crystal Institute
Kent State University
Kent, OH
USA

ISSN 1434-4904 ISSN 2197-7127 (electronic)
NanoScience and Technology
ISBN 978-3-319-18292-6 ISBN 978-3-319-18293-3 (eBook)
DOI 10.1007/978-3-319-18293-3

Library of Congress Control Number: 2015939641

Springer Cham Heidelberg New York Dordrecht London

Printed on acid-free paper

Springer International Publishing AG Switzerland is part of Springer Science+Business Media (www.springer.com)

Preface

Human civilization, from its beginning to date, has been fondly using wood for building home and furniture, and as a superior construction material. One of the hallmarks of wood's success is its "anisotropy" of strength and hardness in different directions/orientations. Hence wood represents an intrinsically anisotropic material in our natural environment, which candidly manifests the beneficial consequences of anisotropy in its properties. This anisotropy, i.e., the direction-dependency of physical properties, of such natural materials has inspired materials scientists and sparked the quest for anisotropic materials with useful properties. With such an inspiration, the scientists have ventured into the realm of nanometer length-scale and have been curiously exploring the anisotropic nanoscale building blocks such as metallic and nonmetallic particles as well as organic molecular aggregates. It turns out that anisotropic nanoscale building blocks, in addition to direction-dependent properties, exhibit the dimension and morphology dependence of physical properties. Anisotropic nanoparticles in particular display several spectacular unique and unusual properties owing to spatial confinement of electrons, photons, and electric fields around the particles as well as due to their large surface to volume ratio. These promising properties have qualified them as enabling building blocks of twenty-first century materials science, nanoscience, and nanotechnology. There has been tremendous development involving isotropic nanoparticles; however, anisotropic nanoparticles made of metals and metal oxides, etc., are emerging as a burgeoning endeavor because of their superior mechanical, electrical, magnetic, optical and chemical properties. Their applications have been demonstrated in electronics, photonics, biological and chemical sensing, imaging and drug delivery, etc. Owing to their preferred orientation and ordering, anisotropic nanoparticles can be organized into a multitude of well-defined higher-order assembled structures. Moreover, ordered arrays of anisotropic nanoparticles' assemblies furnish novel properties which are often distinctly different from the properties of individual building blocks. Thus unprecedented and synergetic properties are observed in numerous occasions resulting from the mutual cooperative interaction of individual components. On the other hand, anisotropic supramolecular nanostructures of organic molecular and macromolecular components are

known to assemble into functional soft and dynamic architectures with applicable properties. These are easily processable and display greater response to smaller external stimuli thereby expanding their functionalities and controllability toward practical applications.

This book is not an attempt to exhaustively cover all the relevant topics on anisotropic nanomaterials as it is extremely difficult to do so within a single book. Instead, the book focuses on the recent developments of the most fascinating themes on anisotropic nanomaterials: preparation, properties, and applications. The various chapters cover the following contemporary topics: silicon nanowires: fabrication, devices and application (Chap. 1), methods and structures for self-assembly of anisotropic 1D nanocrystals (Chap. 2), anisotropic gold nanoparticles: preparation, properties, and applications (Chap. 3), synthesis and applications of solution-based II–VI and IV–VI semiconducting nanowires (Chap. 4), rare earth-based anisotropic nanomaterials: synthesis, assembly, and applications (Chap. 5), liquid crystalline anisotropic nanoparticles: from metallic and semiconducting nanoparticles to carbon nanomaterials (Chap. 6), self-assembled 1D semiconductors: liquid crystalline columnar phase (Chap. 7), self-organization of metal nanoparticles in two and three dimensions (Chap. 8), self-organized 3D photonic superstructure: liquid crystal blue phase (Chap. 9), interfacial interactions in 1D and 2D nanostructure-based material systems (Chap. 10), mesoporous carbons for energy (Chap. 11), hyperbolic metamaterials: design, fabrication, and applications of ultra-anisotropic nanomaterials (Chap. 12), and printed anisotropic molecular alignments (Chap. 13). In each chapter, the state of the art, along with future potentials in the respective fields, is discussed and highlighted by leading experts.

This book offers up-to-date and accessible coverage of diverse anisotropic materials with emphasis on their preparation, properties, and applications to undergraduate and graduate students, as well as researchers both in academia and industries working in inorganic chemistry, organic chemistry, polymer chemistry, physics, biology, materials science, and engineering, electrical engineering, chemical engineering, photonics, biomedical science, optic-electronics, nanoscience, nanotechnology, and energy. It is hoped that readers will find the book useful and this book may serve as a melting pot of truly multidisciplinary knowledge in the field of anisotropic nanomaterials to stimulate future developments of advanced materials and devices while strengthening our fundamental understanding of these intriguing materials.

Finally, I would like to express my gratitude to Claus Ascheron at Springer for inviting us to bring this fascinating and rapidly emerging field to a wider audience, and to all our distinguished contributors for their dedicated efforts. Also, I am indebted to my wife Changshu, my sons Daniel and Songqiao for their great support and affectionate encouragement.

Kent, USA Quan Li

Contents

Contributors

Ammathnadu S. Achalkumar Department of Chemistry, Indian Institute of Technology, Guwahati, India

Hari Krishna Bisoyi Liquid Crystal Institute and Chemical Physics Interdisciplinary Program, Kent State University, Kent, OH, USA

Chun-Wei Chen Department of Photonics, National Sun Yat-sen University, Kaohsiung, Taiwan

Xiaoming Chen Department of Mechanical Engineering, State University of New York at Binghamton, Binghamton, NY, USA

Sheng Dai Chemical Sciences Division, Oak Ridge National Laboratory, Oak Ridge, TN, USA; Department of Chemistry, University of Tennessee, Knoxville, TN, USA

Antonio De Luca Department of Physics and CNR-NANOTEC UOS di Cosenza, University of Calabria, Rende, Italy

Hao Dong Beijing National Laboratory for Molecular Sciences, State Key Laboratory of Rare Earth Materials Chemistry and Applications, PKU-HKU Joint Laboratory in Rare Earth Materials and Bioinorganic Chemistry, College of Chemistry of Molecular Engineering, Peking University, Beijing, China

S. Holger Eichhorn Department of Chemistry and Biochemistry, University of Windsor, Windsor, ON, Canada

Ming-Yong Han Institute of Materials Research and Engineering, Agency for Science, Engineering and Research, Singapore, Singapore

Chun-Jiang Jia School of Chemistry and Chemical Engineering, Shandong University, Jinan, China

Changhong Ke Department of Mechanical Engineering, State University of New York at Binghamton, Binghamton, NY, USA

Munehiro Kimura Department of Electric Engineering, Nagaoka University of Technology, Nagaoka, Japan

Masaru Kuno Department of Chemistry and Biochemistry, University of Notre Dame, Notre Dame, IN, USA

Lin-Dong Li Beijing National Laboratory for Molecular Sciences, State Key Laboratory of Rare Earth Materials Chemistry and Applications, PKU-HKU Joint Laboratory in Rare Earth Materials and Bioinorganic Chemistry, College of Chemistry of Molecular Engineering, Peking University, Beijing, China

Quan Li Liquid Crystal Institute and Chemical Physics Interdisciplinary Program, Kent State University, Kent, OH, USA

Tsung-Hsien Lin Department of Photonics, National Sun Yat-sen University, Kaohsiung, Taiwan

Guang-Ming Lyu Beijing National Laboratory for Molecular Sciences, State Key Laboratory of Rare Earth Materials Chemistry and Applications, PKU-HKU Joint Laboratory in Rare Earth Materials and Bioinorganic Chemistry, College of Chemistry of Molecular Engineering, Peking University, Beijing, China

Manoj Mathews Post Graduate & Research Department of Chemistry, St. Joseph's College, Devagiri, Calicut, India

Thomas Mikolajick NaMLab GmbH, Dresden, Germany; Institute of Semiconductor and Microsystems, TU Dresden, Dresden, Germany; Center for Advancing Electronics Dresden (CfAED), TU Dresden, Dresden, Germany

Kwok Wei Shah Institute of Materials Research and Engineering, Agency for Science, Engineering and Research, Singapore, Singapore

Shuo Shi Beijing National Laboratory for Molecular Sciences, State Key Laboratory of Rare Earth Materials Chemistry and Applications, PKU-HKU Joint Laboratory in Rare Earth Materials and Bioinorganic Chemistry, College of Chemistry of Molecular Engineering, Peking University, Beijing, China

Kandammathe Valiyaveedu Sreekanth Department of Physics, Case Western Reserve University, Cleveland, OH, USA

Giuseppe Strangi Department of Physics, Case Western Reserve University, Cleveland, OH, USA; Department of Physics and CNR-NANOTEC UOS di Cosenza, University of Calabria, Rende, Italy

Ling-Dong Sun Beijing National Laboratory for Molecular Sciences, State Key Laboratory of Rare Earth Materials Chemistry and Applications, PKU-HKU Joint Laboratory in Rare Earth Materials and Bioinorganic Chemistry, College of Chemistry of Molecular Engineering, Peking University, Beijing, China

Pornthip Tongying Department of Chemistry and Biochemistry, University of Notre Dame, Notre Dame, IN, USA

Yan-Jie Wang Beijing National Laboratory for Molecular Sciences, State Key Laboratory of Rare Earth Materials Chemistry and Applications, PKU-HKU Joint Laboratory in Rare Earth Materials and Bioinorganic Chemistry, College of Chemistry of Molecular Engineering, Peking University, Beijing, China

Walter M. Weber NaMLab GmbH, Dresden, Germany; Center for Advancing Electronics Dresden (CfAED), TU Dresden, Dresden, Germany

Chenming Xue Liquid Crystal Institute and Chemical Physics Interdisciplinary Program, Kent State University, Kent, OH, USA

Chun-Hua Yan Beijing National Laboratory for Molecular Sciences, State Key Laboratory of Rare Earth Materials Chemistry and Applications, PKU-HKU Joint Laboratory in Rare Earth Materials and Bioinorganic Chemistry, College of Chemistry of Molecular Engineering, Peking University, Beijing, China

Jonathan K. Yu Department of Chemistry and Biochemistry, University of Windsor, Windsor, ON, Canada

Chao Zhang Beijing National Laboratory for Molecular Sciences, State Key Laboratory of Rare Earth Materials Chemistry and Applications, PKU-HKU Joint Laboratory in Rare Earth Materials and Bioinorganic Chemistry, College of Chemistry of Molecular Engineering, Peking University, Beijing, China

Pei-Zhi Zhang Beijing National Laboratory for Molecular Sciences, State Key Laboratory of Rare Earth Materials Chemistry and Applications, PKU-HKU Joint Laboratory in Rare Earth Materials and Bioinorganic Chemistry, College of Chemistry of Molecular Engineering, Peking University, Beijing, China

Pengfei Zhang Chemical Sciences Division, Oak Ridge National Laboratory, Oak Ridge, TN, USA

Shuang-Yuan Zhang Institute of Materials Research and Engineering, Agency for Science, Engineering and Research, Singapore, Singapore

Xiao-Yu Zheng Beijing National Laboratory for Molecular Sciences, State Key Laboratory of Rare Earth Materials Chemistry and Applications, PKU-HKU Joint Laboratory in Rare Earth Materials and Bioinorganic Chemistry, College of Chemistry of Molecular Engineering, Peking University, Beijing, China

Maksym Zhukovskyi Department of Chemistry and Biochemistry, University of Notre Dame, Notre Dame, IN, USA

Chapter 1
Silicon Nanowires: Fabrication and Applications

Thomas Mikolajick and Walter M. Weber

Abstract Due to the high surface to volume silicon ratio and unique quasi one-dimensional electronic structure, silicon nanowire based devices have properties that can outperform their traditional counterparts in many ways. To fabricate silicon nanowires, in principle there are a variety of different approaches. These can be classified into top-down and bottom-up methods. The choice of fabrication method is strongly linked to the target application. From an application point of view, electron devices based on silicon nanowires are a natural extension of the downscaling of a silicon metal insulator semiconductor transistor. However, the unique properties also allow implementing new device concepts like the junctionless transistor and new functionalities like reconfigurability on the device level. Sensor devices may benefit from the high surface to volume ratio leading to a very high sensitivity of the device. Also, solar cells and anodes in Li-ion batteries can be improved by exploiting the quasi one-dimensionality. This chapter will give a review on the state-of-the-art of silicon nanowire fabrication and their application in different types of devices.

1.1 Introduction

Silicon nanowires are quasi one-dimensional (1D) structures with a diameter of less than 100 nm. The very small diameter results in a large surface to volume ratio. This can be exploited in many ways in electronic devices [1]. When a gate is wrapped

T. Mikolajick (✉) · W.M. Weber
NaMLab GmbH, Nöthnitzer Strasse 64, 01187 Dresden, Germany
e-mail: thomas.mikolajick@namlab.com

T. Mikolajick
Institute of Semiconductor and Microsystems, TU Dresden,
Nöthnitzer Strasse 64, 01187 Dresden, Germany

T. Mikolajick · W.M. Weber
Center for Advancing Electronics Dresden (CfAED), TU Dresden,
Nöthnitzer Strasse 64, 01062 Dresden, Germany

Q. Li (ed.), *Anisotropic Nanomaterials*, NanoScience and Technology,
DOI 10.1007/978-3-319-18293-3_1

around the nanowire, the optimum control of the nanowire potential by the gate potential is ensured. This makes nanowires an excellent choice for the ultimate silicon metal insulator semiconductor (MIS) devices [2]. However, the same feature also allows implementing device concepts that would have very poor properties in a conventional planar configuration. The junctionless transistor [3] and tunnel field effect transistors [4] are two prominent examples. Additionally, new types of functionalities can be exploited by making the devices reconfigurable [5]. When it comes to sensing devices, the small volume will allow effectively controlling the potential of the nanowire by even a very small input signal, making the approach very sensitive specifically for chemical sensing and bio-sensing [6, 7]. But also the field of energy generation and storage can benefit from the quasi 1D structure. In the solar cells the nanowires allow to more efficiently collect the incoming solar radiation [8] whereby in Li-ion batteries the structure allows for volume expansion [9].

A large number of techniques exist to fabricate silicon nanowires. These can be classified into bottom-up and top-down fabrication techniques. In top-down fabrication, lithography is used to define the fabricated structure that is then transferred from the photo-resist to the substrate by etching or a similar way of structuring the already available material. In the bottom-up approach, the material is added to the substrate in a self-organized way.

This chapter will review the current status of silicon nanowire technology. In the first part the silicon nanowire fabrication techniques will be summarized and there advantages and disadvantages will be discussed. The second part will then review the very important field of silicon nanowire based electron devices. Devices that are targeted to extend the current semiconductor roadmap are discussed together with approaches that are intended to add new functionality to semiconductor devices. The section on silicon nanowire based sensors will then focus on devices that can take full advantage of the know-how from integrated circuit manufacturing and illustrate further concepts. Finally, the possibilities for enhancing solar cells and Li-ion batteries will be discussed. The summary will include the concepts that may also gain importance and that are not covered in the previous sections. In all sections silicon technology is used as the starting point due to the well-established device technologies. However, it has to be considered that one of the advantages of the nanowire approach is the simplicity in which different semiconductor materials can be combined. Therefore, the prospects for even improving the device properties by e.g. using germanium or III–V semiconductors will be discussed where appropriate as well.

1.2 Fabrication Techniques for Silicon Nanowires

Traditionally semiconductor technology is driven by top-down fabrication using photo lithography. This approach has successfully enabled to scale down device dimensions all the way to the 10 nm range [10]. In contrast, bottom-up techniques

have the potential to construct very complex structures without the need of defining them in all details by a mask [11]. Nevertheless, there are still some missing links to make the bottom-up approach a manufactural alternative. When it comes to silicon nanowires, both paths are possible and have their advantages and drawbacks. In the top-down fabrication, a clear path from today's planar and FinFET devices to nanowire devices can be drawn. However, the etching of the nanowire out of the bulk silicon results in non-perfect geometry and requires advanced lithography. The bottom-up approaches, on the other hand, may lead to excellent crystal quality and small diameter using a very simple process. The precise placement and generation of highly complex structures as integrated circuits still remains elusive. Therefore, also combinations of both paradigms are considered. Another alternative is to use a template made from an insulating material like silicon dioxide or aluminium oxide, etch holes into the layer and fill the holes with silicon or the desired semiconductor material. This can be considered as a top-down fabrication process for vertical nanowires. The traditional top-down process, in contrast, will result in horizontal nanowires although etching wires out of a bulk crystal is in principle also possible.

The most prominent nanowire synthesis method is named the vapor liquid solid (VLS) growth mechanism. The VLS growth first described by Wagner and Ellis [12] the growth occurs via phase changes that are mediated through a catalyst particle. That means that the material to be grown, in this case silicon, is delivered in the gas phase, either molecularly or in the form of a gas compound that is introduced into the growth chamber. Figure 1.1 shows a schematic sketch illustrating the widely adopted VLS growth.

In the case of Si, molecular Si precursors can be evaporated either by Si effusion cells, or pulsed vapor deposition. Silicon gas precursors include mono-silane (SiH_4), trichlorosilane ($SiHCl_3$) or higher order silanes. The catalyst particle acts as a collector of silicon. In the case of employing gas precursors, the catalytic nature leads to lowering of the dissociation energies of the gas. Consequently, a high

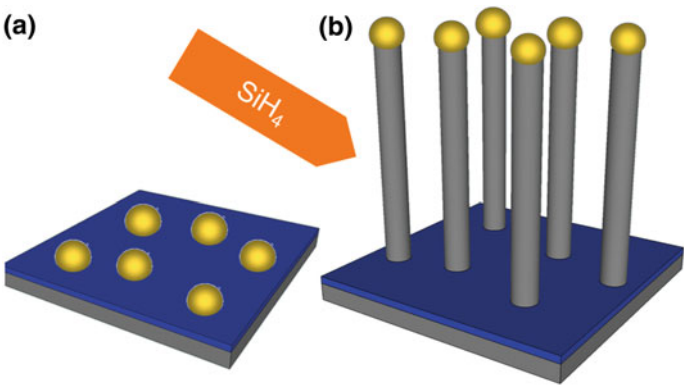

Fig. 1.1 Schematic view of VLS growth of silicon nanowires. **a** Gold particles formed on the growth substrate. **b** VLS growth using silane as silicon precursor

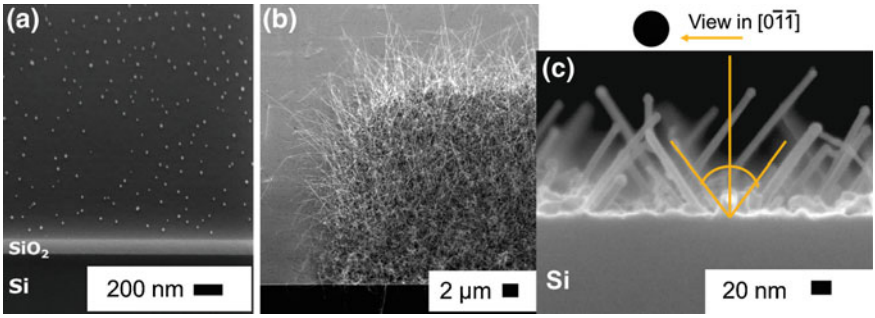

Fig. 1.2 Nanowires grown by the VLS process. **a** Shows the catalytic gold particles formed by sub–nanometer sputter deposition of Gold and a subsequent coalescence with a combination of a thermal anneal in hydrogen atmosphere at 450 °C for 300 s and a subsequent plasma treatment [13]. **b** Shows nanowires grown on an oxidized silicon substrate and **c** shows a close-up of nanowires grown on a (100) oriented single crystalline silicon substrate

concentration of silicon atoms is found at the catalyst particle´s surface, leading to diffusion into the cluster. In the case of employing gold catalyst clusters, the gold-silicon system can become liquid at temperatures above the eutectic point (363 °C), provided that sufficient fraction of Si is present (e.g. 18.6 at.% at the eutectic temperature). In case of a constant silicon flow, silicon atoms will continue to diffuse into the Au–Si melt, although this is thermodynamically unstable. To reduce energies, the super-saturated or excess silicon atoms condense into the solid-phase. Nucleation of Si occurs at the footprint of the Au–Si catalyst layer by layer. Consequently, a silicon monolith or nanowire is formed. Figure 1.2 shows the starting gold catalysts in Fig. 1.2a, silicon nanowires grown on an oxidized silicon wafer in Fig. 1.2b and a close up view of ⟨110⟩ oriented silicon nanowires lattice-matched grown on a crystalline silicon (100) wafer. An important implication of the VLS mechanism is that the size of the Au cluster defines the diameter of the nanowire without the tedious need of further lithographic means. In addition, the catalyst position on the substrate dictates the nanowire placement.

As explained above, in most cases gold particles are used as catalyst that decorates the substrate's surface. This is either done by dispersion of previously synthesized Au particles or by the coalescence of thin Au films. The latter are often done by depositing a very thin sub-nanometer layer of the catalyst film using physical vapor deposition being followed by a coalescence step using thermal annealing or a plasma treatment or the combination of both [13]. However, for compatibility reasons with normal CMOS device fabrication, also gold-free processes have been developed [14–16]. In the 1970's, it was postulated by Givargizov, that due to thermodynamic considerations there is a minimal critical diameter for growth [17]. It lasted until 1998 that Morales and Lieber [18] showed that silicon nanowires with diameters below 20 nm could be grown. A very detailed overview on the growth aspects of nanowires can be found in [11].

One advantage of the VLS method is that the growth can be done on different types of substrates. It has been shown, that thermodynamics dictate the crystal growth direction of the nanowire, even if growth occurs on amorphous substrates, i.e. without pre-defined lattice orientation. In addition, a correlation between crystal direction and nanowire diameter is clearly visible [19, 20]. Schmidt attributed this to the strong contribution of outer silicon atoms on the overall formation energies. When a silicon substrate is used, epitaxial growth can be achieved as well. Moreover, the grown wires can be subsequently transferred to any substrate even if the direct growth on that substrate is not possible. In that case, however, the original vertical nanowire arrangement cannot be maintained.

As alternative to CVD growth a wide variety of other growth methods can be applied using catalysts [9]. Among them are the annealing in a reactive atmosphere like hydrogen to form the nanowires directly from a silicon substrate [21], laser ablation [22] and molecular beam epitaxy [23].

For top-down fabrication of nanowires well-established technologies from silicon VLSI circuit technology can be applied. To form horizontal nanowires that are electrically isolated from the substrate, two approaches are commonly used. In the simplest approach, a SOI substrate is used and the nanowire is etched into the thin active silicon layer using an anisotropic etching process [24]. In the other approach bulk silicon and a deep reactive ion etch (DRIE) process are used together to structure a stack of nanowires [25]. Figure 1.3 shows both approaches schematically. The latter approach has the beauty that the footprint is small and there will be several parallel nanowires to carry the current in a device using nanowires from such a procedure. Figure 1.4 shows examples of nanowires created by both techniques.

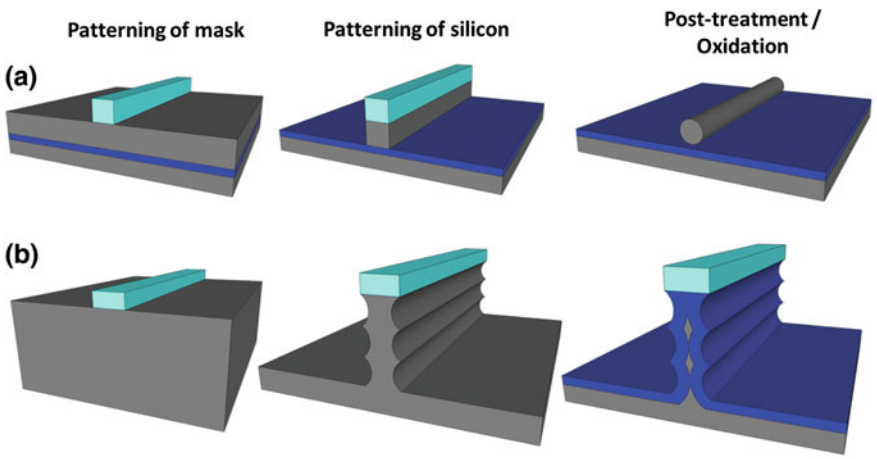

Fig. 1.3 Horizontal silicon nanowires fabricated by top down fabrication. **a** Starting with SOI substrate and etching using anisotropic reactive ion etching. **b** Starting with bulk substrate and etching with deep reactive ion etching and subsequent oxidation.

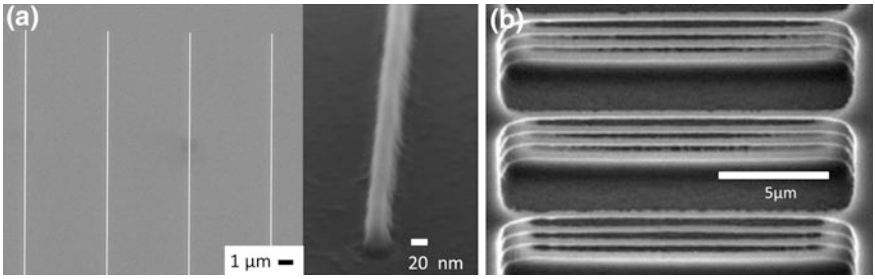

Fig. 1.4 Examples of horizontal silicon nanowires achieved by top-down fabrication. **a** Nanowires with 20 nm height and 25 nm widths produced using an SOI substrate. **b** Close up view of the nanowires form on the SOI substrate. **b** Nanowires formed using the deep reactive ion etch (DRIE) process © 2009 IEEE. Reprinted, with permission, from [25]

According to the above-described procedures the bottom-up fabrication will lead to a vertical arrangement of nanowires and the top-down arrangement will lead to a horizontal arrangement of nanowires. If horizontal nanowires have to be fabricated by the bottom-up technique, the alignment is very critical. In general the nanowires will be dispersed on the receiving substrate. For basic research, it can be sufficient to simply use a direct writing lithography technique to further built the required device. However, for mass fabrication an alignment of the structures will be required. Although some promising approaches have been shown, so far no technique for reliable mass fabrication is available. Therefore, the top-down approach seems to be the approach of choice for the mass fabrication of horizontal silicon wires using a silicon substrate. Also vertical wires can be achieved by using lithography and a subsequent anisotropic etching [26, 27], this technique has the drawback that very high aspect ratios have to be etched and dimensional control is very critical. On the other hand, the bottom-up approach naturally yields vertical devices [28] and the precise positioning can be controlled by a defined positioning of the catalyst particles. As an alternative, a template approach can be used to flexibly define vertical nanowire structures [29]. In that approach first a template layer has to be deposited. In [29] many different bottom-up techniques are described to fabricate such templates. The most popular being anodized aluminum oxidized (AAO) templates. However, also a suitable dielectric may be deposited and holes are etched into the layer using a top-down lithography process to form the template. Then the holes can be filled with the required nanowire material using a chemical vapour deposition process or epitaxial growth process. The drawback is that in case of a semiconducting nanowire like silicon the resulting nanowire will be polycrystalline rather than a single crystal [30]. To achieve single crystals, the technique can be combined with bottom-up nanowire growth using a catalyst. If the holes are generated by a self-organization process, this again can be considered as a true bottom-up fabrication method.

Besides the fabrication of the nanowires themselves, a few critical processing steps have to be available to fabricate electron devices. The most important are: the

previous mentioned alignment of nanowires in case that bottom-up grown nanowires will be used, the doping of nanowires, the formation of contacts to the nanowires and finally the formation of a well-defined dielectric shell.

For alignment, a number of techniques have been proposed [31, 32]. Polar nanowires can be aligned in strong electric fields [33]. Dielectrophoresis has been used successfully for wire alignment [34, 35]. Microfluidic alignment [36], contact printing [37, 38] and Langmuir-Blodgett techniques can also be used [39–41]. Recently a nanoscale combing technique [42] showed encouraging results. However, all methods still face issues with either wire density for high integration or rather low yield of the desired structures or both [31]. Therefore, for high device densities comparable or beyond the state of the art, CMOS top-down approach is still the more preferred choice to define the nanowire location. However, for applications on flexible substrates or in sensors with parallel nanowires [38] some of the available procedures like contact printing could already be sufficient.

Doping of nanowire structures is also a critical issue. In modern CMOS fabrication, most doping steps are done using ion implantation. This, however, is not straightforward due to the geometry of silicon nanowires. Specifically the defined doping in a vertical arrangement is problematic. In bottom-up grown structures different options exist to dope the wires during growth. In case of catalyst-enabled growth, it is an intriguing idea to use the catalyst itself as dopant for the nanowire. In most cases only very low concentrations of the catalyst are actually transferred to the nanowire [10, 14]. Nevertheless, especially p-doping by using aluminum catalysts has recently shown very promising results [16]. In vapor phase processes, the doping can also be supplied by an additional precursor gas [43–45]. Care has to be taken to control the doping distribution both in radial an axial dimension [43].

To contact the nanowires a metal to nanowire contact is required. This can be the limiting factor for the device construction [46]. Using a metal silicide is very favorable method [47, 48]. Specifically intruded nickel silicide contacts offer a very technologically simple method of fabricating the metal to silicon nanowire contacts with sharp interfaces [48–50].

Finally in order to achieve reproducible device properties it is important to passivate the nanowire surface and form a good gate insulator for a field effect transistor (FET). The natural oxide of silicon is one of the main reasons why silicon has considerably outperformed every other semiconductor for high density and high performance circuits and systems [51]. Therefore, it is natural to also use silicon dioxide in silicon nanowire devices and indeed it can deliver excellent properties [52]. However, also here the higher k value of materials like hafnium dioxide (HfO_2), which is established in CMOS technologies today, is of benefit [53]. Atomic layer deposition (ALD) is the technique best suited to deposit dielectrics on nanowires since it can form conformal films on arbitrary geometries. Nanowire devices with aluminum (Al_2O_3), oxide and HfO_2 gate dielectrics have been demonstrated for device [54, 55], sensor [56] and nonvolatile memory applications [57]. Care has to be taken to carefully engineer the silicon/dielectric interface to avoid interface traps and charge trapping in the high-k layer. Another advantage of

deposited dielectrics is the possibility to combine them with different semiconductors like germanium or GaAs and enable their use despite of the absence of a high performance natural oxide like in the case of silicon.

1.3 Electron Devices Based on Silicon Nanowires

Silicon exhibits unique properties when it acquires a 1D shape. Quantum confinement of electrons and holes is predicted to be substantial only at aggressive diameters below of 3 nm [58]. Note that this is in contrast to III–V semiconductors, where confinement is visible already at larger diameters. Therefore, it makes sense to denote the behavior of Si nanowires as quasi 1D. The band structure is strongly modified for Si nanowires with diameters below of $\sim$10 nm. The band gap increases for smaller diameters and a direct band gap can be obtained for sufficiently small diameters [58, 59]. The quasi 1D behavior of silicon nanowires with very small dimensions can be utilized in devices in many different ways. For field effect devices, when the gate electrode is wrapped around the nanowire, the optimum geometric gate coupling can be provided to the active region. In addition to this, if the silicon thickness is small enough to allow a full depletion at low voltages the best scaling behavior of the device can be achieved [60]. A useful parameter to characterize the gate control over the channel is the natural or screening length [61]. It describes the efficiency of bending the energy bands and depends on the gate geometry, gate dielectric, nanowire thickness and doping concentration. Depending on the density of states nanowire field effect devices can be designed to operate either in a classical gate capacitance limited mode or the quantum capacitance limit. In the latter the channel charge remains constant when scaling down the gate oxide thickness leading to an improved power to delay product [62].

Using scaled nanowires, very promising circuit demonstrations have already been shown [63, 64]. Another more conventional approach comes from semiconductor memories, especially NAND Flash. For decades, the dilemma between fast erase and retention is hindering the full success of charge trapping devices [65]. The underlying physical reason is that the field in the tunnel oxide and the top oxide cannot be controlled independently of each other like this can be done in a floating gate device. Generally speaking, it is necessary to enhance the field in the tunnel oxide and possibly at the same time reduce the field in the top oxide. Nanowires and to a lower extent tri-gates [66] offer a unique opportunity here, since the geometry will automatically generate a higher field at the bottom oxide and the extension of the field increase can be controlled by the diameter of the nanowire. Figure 1.5 illustrates that situation. Therefore, nanowire devices have been extensively explored for charge trapping devices. An excellent overview on the literature on that subject can be found in Chap. 3 of [67]. However, up to now the technological hurdle for introducing nanowires to push charge trapping applications is too high, as long as a cheaper scaling can be achieved using floating gates. Since almost ten years intense research has been started to explore the third dimension in NAND

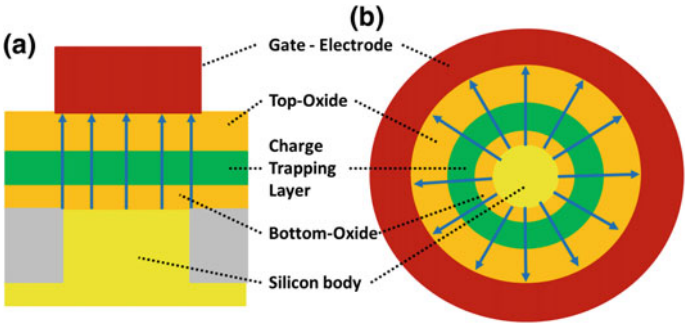

Fig. 1.5 Schematic cut in width direction of a planar (**a**) and a nanowire based (**b**) charge trapping memory cell. The *arrows* indicate the field lines in the device in programing or erase operation. In the nanowire device the field lines are denser in the bottom oxide. Therefore the exchange of carriers between the charge trapping layer and the silicon transistor body is enhanced and the charge exchange between the charge trapping layer and the gate-electrode is reduced

Flash memories, [30, 67] which might turn this cost per function relation. It was shown that by using concepts where many layers can be fabricated and then connected by a single or a few lithography steps is necessary to scale the cost into the desired range.

Many concepts have been proposed to reach that goal [67, 68]. In most of these, a charge-trapping layer is much easier to integrate then a floating gate. Here the nanowire geometry is beneficial. It has further been shown, that for the particular application the small dimensions enable the use of polycrystalline material for the transistor body [69]. This enables a rather simple fabrication technique where holes are etched into the layer stack and the holes are subsequently filled with polysilicon [30, 70]. The basic process is illustrated in Fig. 1.6. One variant of this concept has reached the market recently [71] and more devices are expected in the near future. Besides NAND Flash, the general concept can also be extended to other devices like resistive RAM (RRAM) [72]. Although not all applications can benefit from the nanowire geometry in the same way the charge trapping memory cell does, in most cases a nanowire like structure will be the result of this type of integration scheme.

Also logic devices benefit largely from the excellent gate control when implemented in a nanowire structure. However, for viable applications additional requirements have to be fulfilled. Thus, alternative concepts to the conventional MOSFET have emerged. The most important of these are illustrated in Fig. 1.7. With ever decreasing device dimensions doping becomes more and more problematic. On the one side the doping profiles need to be controlled much more precisely. However, due to diffusion during dopant activation an ideal steplike profile is hard to achieve even if very short millisecond annealing is used. Second, the number of dopants in the active channel region decreases. Since the relative variability will scale with $N^{-1/2}$ [73] doping fluctuations will make the control of the threshold voltage nearly impossible [74]. In addition to these difficulties, it has

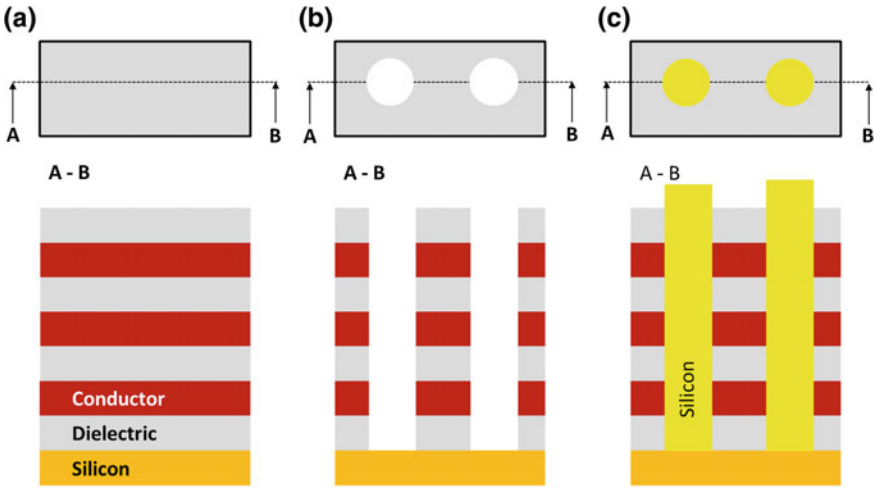

Fig. 1.6 Principle of stacking several layers and connecting them using a single lithography and etching step. The *upper row* shows the top view and the *lower row* shows the cross section according to the cut line A-B as indicated in the top view. The starting layer stack is shown in (**a**). After defining holes by lithography and etching the structure in (**b**) results. Finally the holes are filled again and the filling layer is polished back resulting in a nanowire structure inside the holes (**c**). The flow is strongly simplified to illustrate the basic principle and details like functional layers are omitted

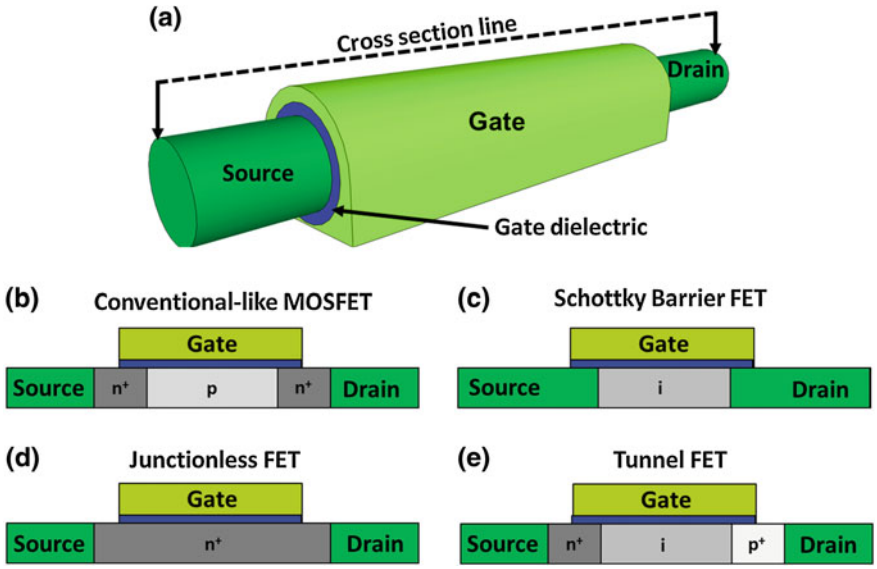

Fig. 1.7 Different options for electron devices using silicon nanowires. The top drawing **a** shows a generic 3-D view of a silicon nanowire device with metallic source/drain regions and the surrounding gate. The cross sections **b**–**e** illustrate different device concepts: **b** Conventional nanowire MOSFET, **c** Schottky Barrier FET, **d** Junctionless FET and **e** Tunnel FET. [1]

been proven by calculations and experiments, that for certain nanowire geometries, the ionization energies of dopants are higher than in bulk [75, 76]. For nanowires without a surrounding gate dopant deactivation takes place, i.e. to achieve the same doping effect, a higher dopant concentration is needed, especially for thin nanowire diameters.

Both the Schottky barrier field effect transistor (SBFET) [77, 78] and the junctionless transistor [3] can help to control these issues. In the SBFET, the highly doped source and drain regions are replaced by metal-semiconductor Schottky junctions, and the silicon body of the transistor can be undoped. The device benefits from the nanowire geometry since very sharp and defined silicide junctions can be used [79]. For charge transport this implies that two energy barriers are introduced along the current path. The thickness of these barriers is efficiently controlled by the gate due to the electric field enhancement at the tip-like metal electrode geometry. The on-state for sufficiently small gate lengths is given by tunneling through the Schottky barriers, while the off-state is controlled by thermionic emission over a high and thick energy barrier. The undoped channel eliminates issues of threshold voltage control caused by doping fluctuations. In the junctionless device, the whole nanowire is highly doped. Thus, the formation of a very sharp junction in the scaled device is elegantly avoided. In contrast to conventional FETs, the on-state is driven in the accumulation mode, and the charge carriers flow throughout the complete nanowire cross-section. Doping fluctuation issues are reduced due to the much higher doping of the channel region.

One of the biggest challenges for further device scaling is the inability to scale the threshold voltage due to the thermal limit of 60 mV/dec for the subthreshold slope [80]. Since lowering the supply voltage is of very high importance both for physical device scaling and reduction of the power consumption it is one of the most pressing issues to find ways in order to reduce the subthreshold slope below this value. One promising option is the tunneling field effect transistor (TFET) [4, 81].

The TFET would also greatly benefit from the nanowire geometry. From an electrostatic point of view, the nanowire geometry with a surrounding gate stack facilitates sufficient band bending for band-to-band tunneling. Furthermore, for sufficiently small diameters the energy distribution of density of states exhibits van Hoove singularities. Hence, a comparatively high amount of states are available for band to band tunneling at the conduction and valence band edges. As the energetic window for band to band tunneling cuts the high energy tail of the Fermi distribution function, the tunnel FET principally enables a switching behaviour with a reduced subthreshold swing below 60 mV/dec at room temperature. However, like in Schottky FETs, the tunneling transmissibility through the energy barriers limits the on-current through the device. Therefore, from today's point of view TFET are alternatives for low operating power. Recently, encouraging results have been shown demonstrating a performance that is coming close to the requirements for an actual implementation [82, 83]. In a recent publication [84] the combination of a junctionless transistor and a tunnel FET is described, combining features of both device types.

There are two more aspects that make the use of nanowires in such devices very attractive. First, it is much easier to combine different semiconductors with

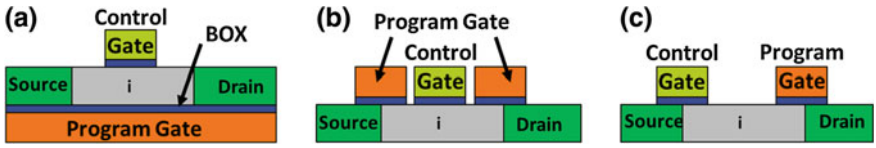

Fig. 1.8 Schematic cross sections of the different concepts for reconfigurable silicon nanowire devices. In the electrostatic doping device (**a**) the back gate is used to adjust the barrier heights and a top gate controls the current trough the device. The simultaneous control of both Schottky barriers (**b**) can also be accomplished by using top gates and an additional control gate in the middle then controls the carrier flow. In the RFET (**c**) approach the program gate above the drain junction and the control gate above the source junction control the polarity and the current flow respectively

considerable lattice mismatch in nanowires [85]. Second, nanowire devices can be constructed both in a horizontal and vertical arrangement. Both features have been exploited in [86, 87] where CMOS compatible nanowire structures using a Si/InAs heterostructure as a building block for TFETs are demonstrated.

All those devices target an improvement of the classical CMOS technology, exploiting the enhanced electrostatic control within the nanowire geometry. However, silicon nanowires also enable a new type of transistor, in which the device polarity can be controlled by an electrical signal [5, 52, 88, 89]. Therefore the same physical device can be used at different times as p-channel or n-channel transistor. These so called reconfigurable field effect transistors (RFET) hold the potential to lower the transistor count needed for the same functionality. The different concepts to build such a device are illustrated in Fig. 1.8 and briefly introduced in the following. Detailed discussions on the different concepts can be found in [1, 5].

In the electrostatic doping approach [88, 90–93], shown in Fig. 1.8a, the back-gate is used as program gate to select electron or hole transport. The program gate bends the silicon bands at both junctions simultaneously. Negative program gate voltages increase the barrier height at the conduction band and thereby block electrons. At the same time the energy barrier height for holes is the natural Schottky barrier height. Albeit, its thickness is diminished and thermal assisted tunneling of holes can take place. Correspondingly, positive program gate voltages block holes and enable electron injection. Once the program gate is set to a specific polarity, the top gate is then used to adjust the amount of current flowing from source to drain. The use of buried and common gates, as employed in Fig. 1.8a, implies having a comparatively weak gate coupling to the active region and therefore a high gate operation voltage. Moreover, the independent operation of neighboring devices, as required in integrated circuitry, can only be solved by substantial technological means leading to a limited scalability of this structure.

In the approach sketched in Fig. 1.8b [89, 94, 95], the two outer top gates are kept at the same potential and provide a similar function as the back gate in Fig. 1.8a. Thus, this concept allows the individual control of different devices in one chip. In the top-down realization a surrounding gate architecture is provided for both control and program gates [94]. Moreover, in a single device numerous

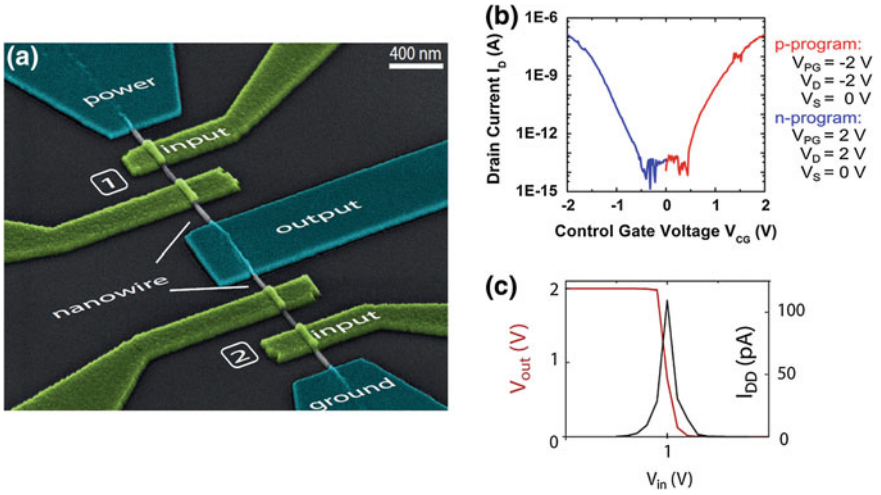

Fig. 1.9 Complementary inverter based on a symmetrical reconfigurable field effect transistor. **a** SEM image of the two identical RFET devices integrated into a single nanowire. In **b** the resulting transfer characteristics of the p-channel and the n-channel programmed devices is shown. In **c** the inverter transfer characteristic is shown together with the current through the inverter demonstrating that a cross current is flowing only during switching

nanowire channels are vertically stacked in parallel to enhance the drive current. The three gates can also be connected independently to allow the control of the threshold voltage of the device [95].

The RFET device shown in Fig. 1.8c uses two independent top gates each overlapping one of the Schottky junctions [52, 96]. One of them is used to control the polarity. The other is used to control the amount of current flowing through the device. In contrast to the other polarity control concepts and to conventional CMOS, the main part of the active region is ungated.

Recently significant progress has been made both in understanding and designing the appropriate transport mechanisms [97–99] and showing the benefit of building circuits out of the reconfigurable devices [100–102]. If CMOS circuits are to be constructed from such devices, it has to be considered, that the geometry cannot be adjusted according to an unbalanced current output of *p*-channel and *n*-channel devices since the same device has to be usable in both configurations. Therefore, the output has to be symmetrical for both carrier types. Using stress engineering this could be demonstrated in the approach with two top gates illustrated in Fig. 1.8c [103]. Figure 1.9 shows an inverter implemented in a single bottom-up fabricated nanowire using this symmetrical RFET device. CMOS functionality can be shown and identical characteristics are achieved if the role of the two devices is interchanged [103]. When comparing the performance of such devices to CMOS there is still a considerable gap due to the Schottky barrier approach. Here, again, the flexibility of integrating different materials into nanowires can be exploited by using germanium nanowires [104].

1.4 Silicon Nanowire Based Sensors

Generally speaking, a sensor device transforms a physical or chemical signal of the environment into an electrical signal [105]. Normally, the sensor device can be split into the active sensing part, which translates the input signal into an intermediate signal and the transducer that translates the intermediate signal into the final electrical signal. In many cases, the two parts are closely linked. The quasi 1-D properties of nanowires can be utilized in transducers and in some cases also for the active sensing part of the chain. Especially chemical and biochemical sensor research has intensively utilized silicon nanowires in the last decade [106]. But also mechanical sensors can benefit especially from the very high piezoresistance effect observed in silicon nanowires [107]. For example, accelerators that utilize the piezoresistance effect for transduction can be significantly improved [108]. Moreover, freestanding nanowires can be very good oscillators. Combined with the high piezoresistance this enables new classes of devices [109, 110].

The research on chemical and biochemical sensors is again strongly driven by the exploitation of the extremely high surface to volume ratio combined with excellent mechanical stability. Having in mind that excellent field effect transistor devices can be constructed, it is a natural consequence to apply the idea which Bergveld first explored in 1971 [111] in the ion sensitive field effect transistor (ISFET) to place the impedance conversion in potentiometric devices in direct vicinity of the measurement. Using classical planar devices, derivatives of this idea have been established as transducers for chemical [112] and biochemical sensors [113]. The transfer of these ideas to nanowire-based devices was therefore already demonstrated more than a decade ago [114]. For biochemical sensors the diameter of the nanowires can be as small as the species to be detected. As illustrated in Fig. 1.10. This enables a very high sensitivity of the sensor device even if parallel

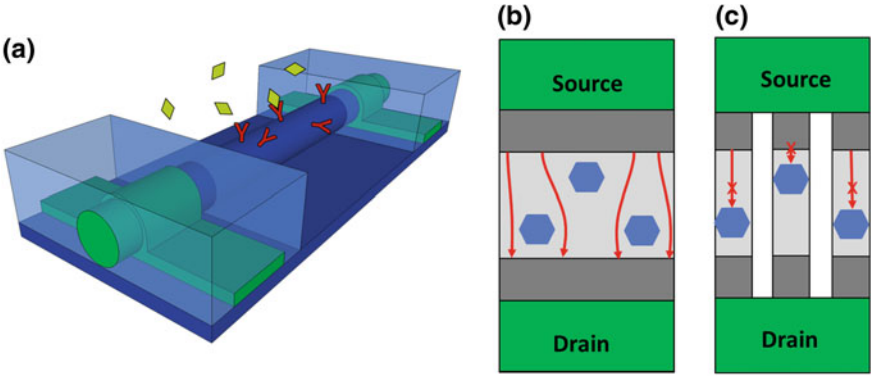

Fig. 1.10 Illustration of a chemical or biochemical sensor based on a nanowire field effect device. **a** Schematic showing the FET transducer receptors immobilized at the surface. **b** Top view of a sensor using conventional planar silicon technology. **c** Top view of nanowire sensor constructed from three parallel nanowires. *Red arrows* indicate current paths

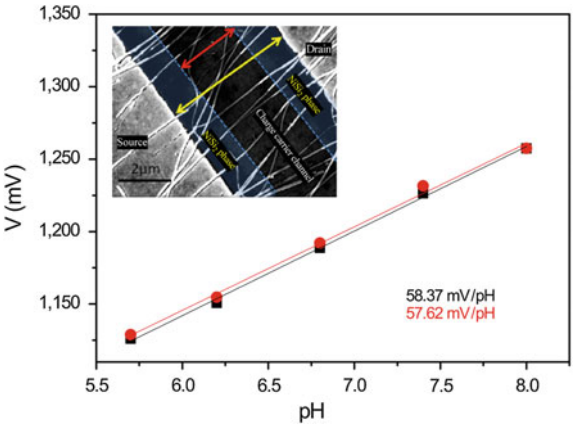

Fig. 1.11 Output voltage of a pH sensor using a parallel nanowire SBFET coated with aluminum oxide as a function of pH. The *red symbols* represent the values for rising pH and the *black symbols* show the values for decreasing pH. The *inset* shows an SEM top view of the used sensor. Reprinted with kind permission from Springer Science+Business Media: [116]

nanowires are used in order to increase the device current, since the current percolation paths are effectively blocked already by a single molecule per nanowire. Looking at a single nanowire this situation paves the way to single molecule detection as demonstrated in [115].

In Fig. 1.11, the response of a pH sensor using a Schottky barrier field effect device with parallel nanowires [38] and an aluminum oxide pH sensitive layer is shown [116]. Nearly Nernstian response is demonstrated for both rising and falling pH. A large number of different biosensors has been demonstrated using nanowire-based transducers, especially FETs [117–121]. The details of the sensing mechanisms and functionalization are beyond the scope of this chapter and the reader is referred to the references given. However, it is important to point out that nanowire based devices have their specific advantage when it comes to a very sensitive detection in small volumes and therefore can enable biosensors that are not possible using a planar transducer.

The small size, flexible fabrication and mechanical properties of nanowires can also be utilized to extend the functionality of biological sensors. Nanoscale FET devices can be integrated at the tip of a kinked silicon nanowire, as it is reported in [122–124]. Here, the nanoscale connections are made by the arms of the kinked nanostructure. However, the spatial resolution of such a device is limited. Therefore, the same group has presented an approach in which a SiO_2 nanotube is synthetically integrated on top of a nanowire FET. This nanotube penetrates the cell membrane, bringing the cell cytosol into contact with the FET, which is then able to record the intracellular trans-membrane potential [123].

1.5 Silicon Nanowire Based Solar Cells and Anodes for Li-Ion Batteries

Energy generation from renewable sources and storage of electrical energy are among the most pressing technical challenges for our society. These fields can benefit from silicon nanowires [9] as well, as they have the potential to increase the optical absorption and collection efficiency in solar cells [8, 125, 126]. Single nanowire solar cells can be used to study the parameters that influence the performance of nanowire based photovoltaics [126–129]. Additionally, they allow a seamless integration with nanowire based electronics and sensors [127, 128]. For doing general purpose solar cells, however, the single wire elements have to be arranged in large arrays [8, 131]. The potential of the single element to enable such a large scale assembly is therefore a strong differentiator for the different concepts. Therefore, the low cost bottom-up growth, which is compatible with different types of substrates, is the fabrication method of choice for such devices. In order to accomplish all the requirements, a coaxial structure is beneficial. First of all, the possibility to fabricate radial pn-junctions has shown promising results [132]. Figure 1.12 shows a schematic view of a silicon nanowire array based solar cell using this concept. Moreover, the flexibility of combining different materials in the nanowire arrangement is utilized as can be seen, for example, in [128]. Also classical heterojunction concepts using crystalline and amorphous silicon can easily be implemented [131].

Li-ion batteries are currently one of the best technical solutions to store electrical energy and retrieve it on a short and flexible timescale [133]. Up to date graphite is the standard anode material used in such batteries. However, theoretical calculations predict that silicon can improve the capacity by almost one order of magnitude.

The increased Li accommodation of up to 3.75 Li atoms per silicon atom comes together with a huge lattice expansion upon lithiation which results in more than 250 % volume expansion [9, 133]. This will lead to the pulverization of the anode during cycling. Figure 1.13a illustrates this for the case of a thin film anode. The

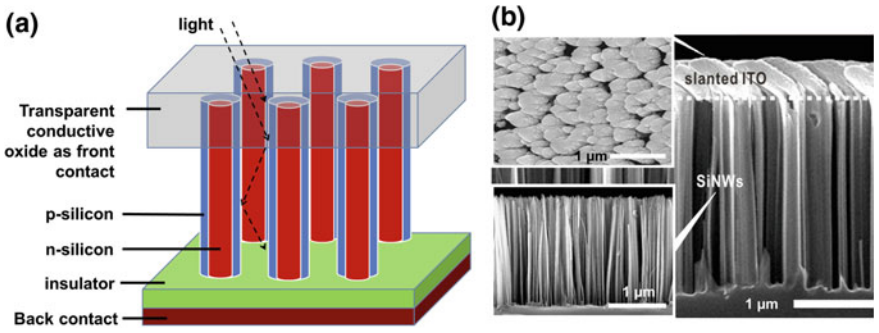

Fig. 1.12 **a** Schematic view of a silicon nanowire based solar cell with a radial pn-junction. **b** SEM micrographs from top view and cross section of the solar cell, as well as from the silicon nanowire array. © Optics Express, reprinted with permission from [130]

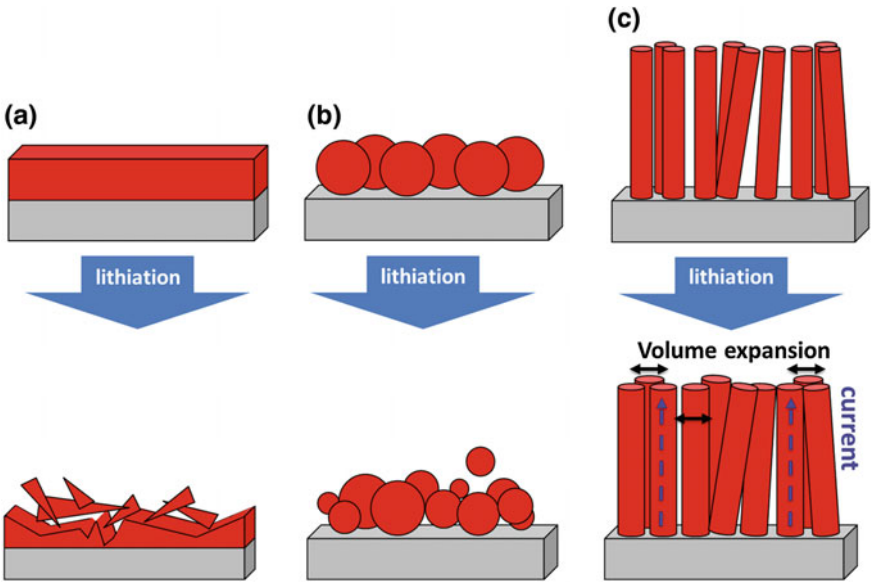

Fig. 1.13 Schematic illustration of the effect of volume expansion during lithiation of silicon [133]. Silicon applied as a thin film (**a**). The massive volume expansion destroys the film. Silicon applied as silicon nanoparticles (**b**). In this case there is room for expansion, but the electrical connection is lost. Silicon applied as silicon nanowires (**c**). For nanowires a radial expansion is possible while maintaining the vertical connection to the underlying substrate

breaking of the structure leads to an interruption of the current flow through the anode. Using silicon nanoparticles (Fig. 1.13b) can improve the cyclability. However, a certain amount of particles is released to the electrolyte and current flow towards the collector is limited. A nanowire on the other side can expand laterally and still maintain the current transport in the vertical direction (Fig. 1.13c) [108]. Excellent research results have been shown in half-cells, but the enhanced cyclability in full cells remains to be shown [9, 134–137]. Promising results with nanowires directly grown on carbon meshes were recently demonstrated [138]. For full cell operation, also the formation of the solid-electrolyte interface (SEI) at the silicon surface needs to be controlled, in order to tune the electrochemical reactions. Again, the flexibility in forming heterostructures including different materials can be utilized to enhance charge storage batteries [139, 140].

1.6 Summary

Silicon nanowires are quasi 1D structures with a diameter below 100 nm. They can be grown with high precision using bottom-up techniques. In addition, today's top down fabrication technology has reached the sub 100 nm nanoelectronic era in

2004 [141]. Therefore also classical lithography techniques can be used to fabricate silicon nanowires. Different devices can strongly benefit from the quasi 1D feature that is reflected by the high surface to volume ratio. The scaling of today's electronics can be enhanced by the ultimate gate control and the possibility to reduce the subthreshold slope below the thermal limit of 60 mV/dec. The vertical NAND Flash device is a first demonstration of nanowire like structures in mass production [71]. Though, in this case the nanowire results from a development coming from top-down microelectronics, but the effect of the nanowires is clearly present. It is expected that we will see more similar examples, where the top-down technologies are developed to a point such that the learning from the bottom-up nanowire research can be exploited in volume manufacturing. Additional, functionalities like reconfigurability can be added to silicon devices as well, based on the precise control of electrical field in such structures. Additionally in nanowire devices different semiconductor and insulator materials can be combined both in a radial and longitudinal fashion much more flexible than in bulk semiconductor technologies. In the framework of electron devices, this feature will allow to implement high mobility materials in a simpler way than in bulk technologies.

The high surface to volume ratio has the potential to design sensors that are much more sensitive than their planar counterparts. Especially biosensors, where very small amounts of analytes have to be detected in very small volumes, can benefit from this feature.

In solar cells, the light trapping is enhanced by forming radial structures, as the pn-junction can be placed much closer to the carrier generating region. In Li-ion batteries the potential of the very high lithium incorporation in silicon cannot be exploited in planar structures. Silicon nanowires also hold a unique opportunity in that field.

Besides the examples given in this chapter, there are many more potential applications like optical devices [142, 143], thermoelectric devices [144], catalysts [145] and even more [146]. It is therefore expected that silicon nanowire technology will evolve as a very versatile supplement to the existing silicon technology.

Acknowledgments The authors want to thank the nanowire team at NaMLab, CfAED and the chairs of "Material Science and Nanotechnology" and "Nanoelectronic Materials" at TU Dresden for the work put into many of the results discussed in the chapter. Special thanks to Jens Trommer for helping with the editing of the chapter and the figures. This work was partly funded by "Deutsche Forschungsgemeinschaft (DFG)" in the framework of the project ReproNano (MI 1247/6-2) and the Cluster of Excellence 'CfAED'.

References

1. T. Mikolajick, A. Heinzig, J. Trommer, S. Pregl, M. Grube, G. Cuniberti, W.M. Weber, Silicon nanowires—a versatile technology platform. Phys. Status Solidi Rapid Res. Lett. **7**, 793–799 (2013)
2. N. Singh, K.D. Buddharaju, A. Agarwal, S.C. Rustagi, C.Q. Lo, N. Balasubramanian, D.L. Kwong, Fully gate-all-around silicon nanowire CMOS devices. Solid State Tech. **51**, 34 (2008)

3. J.-P. Colinge, C.-W. Lee, A. Afzalian, N.D. Akhavan, R. Yan, I. Ferain, P. Razavi, B. O'Neil, A. Blake, M. White, A.-M. Kelleher, B. McCarthy, R. Murphy, Nanowire transistors without junctions. Nat. Nanotechnol. **5**, 225–229 (2010)
4. M.T. Björk, J. Knoch, H. Schmid, H. Riel, W. Riess, Silicon nanowire tunneling field-effect transistors. Appl. Phys. Lett. **92**, 193504 (2008)
5. W.M. Weber, A. Heinzig, J. Trommer, D. Martin, M. Grube, T. Mikolajick, Reconfigurable nanowire electronics—a review. Solid State Electron. **102**, 12–24 (2014)
6. J. Izuan, A. Rashid, J. Abdullah, N.A. Yusof, R. Hajia, The development of silicon nanowire as sensing material and its applications. J. Nanomater. **2013**, 328093–32119 (2013)
7. F. Patolsky, C.M. Lieber, Nanowire nanosensors. Mater. Today **8**, 20–28 (2005)
8. M.D. Kelzenberg, S.W. Boettcher, J.A. Petykiewicz, D.B. Turner-Evans, M.C. Putnam, E.L. Warren, J.M. Spurgeon, R.M. Briggs, N.S. Lewis, H.A. Atwater, Enhanced absorption and carrier collection in Si wire arrays for photovoltaic applications. Nat. Mater. **9**, 239–244 (2010)
9. K.-Q. Peng, X. Wang, L. Li, Y. Hu, S.-T. Lee, Silicon nanowires for advanced energy conversion and storage. Nano Today **8**, 75–97 (2013)
10. C. Mack, The future of semiconductor lithography? Look to flash. J. Micro/Nanolith. MEMS MOEMS **12**, 030101 (2013)
11. V. Schmidt, J.V. Wittemann, S. Senz, U. Goesele, Silicon nanowires: a review on aspects of their growth and their electrical properties. Adv. Mater. **21**, 2681–2702 (2009)
12. R.S. Wagner, W.C. Ellis, Vapor-liquid-solid mechanism of single crystal growth. Appl. Phys. Lett. **4**, 89–90 (1964)
13. W. Weber et al., Silicon nanowires: catalytic growth and electrical characterization. Phys. Stat. Sol. (b) **243**, 3340–33451-6 (2006)
14. F. Iacopi, P.M. Vereecken, M. Schaekers, M. Caymax, N. Moelans, B. Blanpain, O. Richard, C. Detavernier, H. Griffiths, Plasma-enhanced chemical vapour deposition growth of Si nanowires with low melting point metal catalysts: an effective alternative to Au-mediated growth. Nanotechnology **18**, 505307 (2007)
15. I. Zardo, S. Conesa-Boj, S. Estradé, L. Yu, F. Peiro, P. Roca i Cabarrocas, J.R. Morante, J. Arbiol, A. Fontcuberta i Morral, Growth study of indium-catalyzed silicon nanowires by plasma enhanced chemical vapor deposition. Appl. Phys. A **100**, 287–296 (2010)
16. O. Moutanabbir, D. Isheim, H. Blumtritt, S. Senz, E. Pippel, D.N. Seidman, Colossal injection of catalyst atoms into silicon nanowires. Nature **496**, 78–82 (2013)
17. E.I. Givargizov, Fundamental aspects of VLS growth. J. Cryst. Growth **31**, 20 (1975)
18. A.M. Morales, C.M.L. Lieber, A laser ablation method for the synthesis of crystalline semiconductor nanowires. Science **279**, 208–211 (1998)
19. V. Schmidt, S. Senz, U. Gösele, Diameter dependent growth direction of epitaxial silicon nanowires. Nano Lett. **5**, 931–935 (2005)
20. Y. Cui, L.J. Lauhon, M. Gudiksen, J. Wang, C.M. Lieber, Diameter controlled synthesis of single-crystal silicon nanowires. Appl. Phys. Lett. **78**, 2214–2216 (2011)
21. A.V. Sandulova, P.S. Bogoyavlenskii, M.I. Dronyuk, Preparation and some properties of whisker and needle-shaped single crystals of germanium, silicon and their solid solutions. Sov. Phys.-Sol. State **5**, 1883 (1964)
22. Y.F. Zhang, Y.H. Tang, N. Wang, D.P. Yu, C.S. Lee, I. Bello, S.T. Lee, Silicon nanowires prepared by laser ablation at high temperature. Appl. Phys. Lett. **72**, 1835–1837 (1998)
23. P. Werner, N.D. Zakharov, G. Gerth, L. Schubert, U. Gosele, On the formation of Si nanowires by molecular beam epitaxy. Int. J. Mat. Res. **97**, 1008–1015 (2006)
24. F.-L. Yang, D.-H. Lee, H.-Y. Chen, C.-Y. Chang, S.-D Liu, C.-C. Huang, T.-X. Chung, H.-W. Chen, C.-C. Huang, Y.-H. Liu, C.-C. Wu, C.-C. Chen, S.-C. Chen, Y.-T. Chen, Y.-H. Chen, C.-J. Chen, B.-W. Chan, P.-F. Hsu, J.-H. Shieh, H.-J. Tao, Y.-C. Yeo, Y. Li, J.-W. Lee, P. Chen, M.-S. Liang, C. Hu, 5 nm-Gate nanowire FinFET. IEEE Symposium VLSI Technology, pp. 196–197 (2004)
25. D. Sacchetto, M.H. Ben-Jamaa, G. De Micheli, Y. Leblebici, Fabrication and characterization of vertically stacked gate-all-around Si nanowire FET arrays. IEEE

Proceedings European Solid State Device Research Conference ESSDERC, pp. 245–248 (2009)
26. C. Pan, Z. Luo, C. Xu, J. Luo, R. Liang, G. Zhu, W. Wu, W. Guo, X. Yan, J. Xu, Z.L. Wang, J. Zhu, Wafer-scale high-throughput ordered arrays of Si and coaxial Si/Si1–xGex wires: fabrication, characterization, and photovoltaic application. ACS Nano **5**(8), 6629–6636 (2011)
27. J. Nakamura, K. Higuchi, K. Maenaka, Vertical Si nanowire with ultra-high-aspect-ratio by combined top-down processing technique. Microsyst. Tech. **19**, 433–438 (2013)
28. J. Goldberger, A.I. Hochbaum, R. Fan, P. Yang, Silicon vertically integrated nanowire field effect transistors. Nano Lett. **6**, 973–977 (2006)
29. H. Shang, G. Cao, Template-based synthesis of nanorod or nanowire arrays. Handbook of Nanotechnology, pp. 161–178 (Springer, New York, 2007)
30. H. Tanaka, M. Kido, K. Yahashi, M. Oomura, R. Katsumata, M. Kito, Y. Fukuzumi, M. Sato, Y. Nagata, Y. Matsuoka, Y. Iwata, H. Aochi, A. Nitayama, Bit cost scalable technology with punch and plug process for ultra high density flash memory. IEEE Symposium VLSI Technology, pp. 14–15 (2007)
31. R.G. Hobbs, N. Petkov, J.D. Holmes, Semiconductor nanowire fabrication by bottom-up and top-down paradigms. Chem. Mater. **24**, 1975–1991 (2012)
32. M.C.P. Wang, B.D. Gates, Directed assembly of nanowires. Mater. Today **12**, 34–43 (2009)
33. C.H. Lee, D.R. Kim, X. Zheng, Orientation-controlled alignment of axially modulated pn silicon nanowires. Nano Lett. **10**, 5116–5122 (2010)
34. E.M. Freer, O. Grachev, X. Duan, S. Martin, D.P. Stumbo, High-yield self-limiting single-nanowire assembly with dielectrophoresis. Nat. Nanotechnol. **5**, 525–530 (2010)
35. S. Raychaudhuri, S.A. Dayeh, D. Wang, E.T. Yu, Precise semiconductor nanowire placement through dielectrophoresis. Nano Lett. **9**, 2260–2266 (2009)
36. Y. Huang, X. Duan1, Q. Wei, C.M. Lieber. Directed assembly of one-dimensional nanostructures into functional networks. Science **291**, 630–633 (2001)
37. Z. Fan, J.C. Ho, Z.A. Jacobson, R. Yerushalmi, R.L. Alley, H. Razavi, A. Javey, Wafer-scale assembly of highly ordered semiconductor nanowire arrays by contact printing. Nano Lett. **8**, 20–25 (2008)
38. S. Pregl, W.M. Weber, D. Nozaki, J. Kunstmann, L. Baraban, J. Opitz, T. Mikolajick, G. Cuniberti, Parallel arrays of Schottky barrier nanowire field effect transistors: nanoscopic effects for macroscopic current output. Nano Res. **6**, 381–388 (2013)
39. D. Whang, S. Jin, Y. Wu, C.M. Lieber, Nano Lett. **3**, 1255–1259 (2003)
40. A. Tao, F. Kim, C. Hess, J. Goldberger, R. He, Y. Sun, Y. Xia, P. Yang, Nano Lett. **3**, 1229–1233 (2003)
41. S. Acharya, A.B. Panda, N. Belman, S. Efrima, Y. Golan, A semiconductor-nanowire assembly of ultrahigh junction density by the Langmuir-Blodgett technique. Adv. Mater. **18**, 210–213 (2006)
42. J. Yao, C.M. Lieber, A nanoscale combing technique for the large-scale assembly of highly aligned nanowires. Nat. Nanotechnol. **8**, 329–335 (2013)
43. S.T. Picraux, S.A. Dayeh, P. Manandhar, D.E. Perea, S.G. Choi, Silicon and germanium nanowires: growth, properties, and integration. JOM **62**, 35–43 (2010)
44. J. Wallentin, M.T. Borgström, Doping of semiconductor nanowires. J. Mater. Res. **26**, 2142–2156 (2011)
45. V. Robbins, D. Taylor, C. Wanqing, A. Fischer-Colbrie, P. Chungdee, S. Ahmed, D. Stumbo, VLS growth of Si nanowires with in-situ doping for MOS transistors. IEEE-NANO Conference Nanotechnology, pp. 326–329 (2009)
46. H. Park, R. Beresford, R. Ha, H.-J. Choi, H. Shin, J. Xu, Evaluation of metal–nanowire electrical contacts by measuring contact end resistance. Nanotech. **23**, 245201 (2012)
47. Y. Cui, Z. Zhong, D. Wang, W.U. Wang, C.M. Lieber, High performance silicon nanowire field effect transistors. Nano Lett. **3**, 149–152 (2003)

48. W.M. Weber, L. Geelhaar, E. Unger, C. Chèze, F. Kreupl, H. Riechert, P. Lugli, Silicon to nickel-silicide axial nanowire heterostructures for high performance electronics. Phys. Status Solidi (b) **244**, 4170–4175 (2006)
49. W.M. Weber, L. Geelhaar, A.P. Graham, E. Unger, G.S. Duesberg, M. Liebau, W. Pamler, C. Chèze, H. Riechert, P. Lugli, F. Kreupl, Silicon-nanowire transistors with intruded nickel-silicide contacts. Nano Lett. **6**, 2660–2666 (2006)
50. W. Tang, B.M. Nguyen, R. Chen, S.A. Dayeh, Solid-state reaction of nickel silicide and germanide contacts to semiconductor nanochannels. Semicond. Sci. Technol. **29**, 054004 (2014)
51. A.I. Kingon, J.-P. Maria, S.K. Streiffer, Alternative dielectrics to silicon dioxide for memory and logic devices. Nature **406**, 1032–1038 (2000)
52. A. Heinzig, S. Slesazeck, F. Kreupl, T. Mikolajick, W.M. Weber, Nano Lett. **12**, 119–124 (2012)
53. S.T. Chandra, N.B. Balamurugan, Performance analysis of silicon nanowire transistors considering effective oxide thickness of high-k gate dielectric. J. Semicond. **35**, 044001-1 (2014)
54. P. Hashemi, J.T. Teherani, J.L.Hoyt, Investigation of hole mobility in gate-all-around Si nanowire p-MOSFETs with high-κ/metal-gate: effects of hydrogen thermal annealing and nanowire shape. IEEE International Electron Devices Meeting (IEDM), Digest Technology Papers, pp. 34.5.1–34.5.4 (2010)
55. J.W. Sleight, S. Bangsaruntip, G. Cohen, A. Majumdar, Y. Zhang, S. Engelmann, N. Fuller, L. Gignac, S. Mittal, J. Newbury, T. Barwicz, M.M. Frank, M. Guillorn, High performance and highly uniform metal Hi-K gate-all-around silicon nanowire MOSFETs. ECS Trans. **28**, 179–189 (2010)
56. B.R. Dorvel, B. Reddy Jr, J. Go, C.D. Guevara, E. Salm, M.A. Alam, R. Bashir, Silicon nanowires with high-k hafnium oxide dielectrics for sensitive detection of small nucleic acid oligomers. ACS Nano **6**, 6150–6164 (2012)
57. X. Zhu, D. Gu, Q. Li, D.E. Ioannou, H. Baumgart, J.S. Suehle, C.A. Richter, Silicon nanowire NVM with high-k gate dielectric stack. Microelectron. Eng. **8**, 1957–1960 (2009)
58. Y.M. Niquet, A. Lherbier, N.H. Quang, M.V. Fernández-Serra, X. Blase, C. Delerue, Electronic structure of semiconductor nanowires. Phys. Rev. B **73**, 165319 (2006)
59. D.D.D. Ma, C.S. Lee, F.C.K. Au, S.Y. Tong, S.T. Lee, Small-diameter silicon nanowire surfaces. Science **299**, 1874–1877 (2003)
60. K.J. Kuhn, Considerations for ultimate CMOS scaling. IEEE Trans. Electron Devices **59**, 1813–1828 (2012)
61. C.P. Auth, J.D. Plummer, Scaling theory for cylindrical, fully-depleted, surrounding-gate MOSFET's. IEEE Electron Device Lett. **18**, 74 (1997)
62. J. Knoch, M.T. Björk, H. Riel, H. Schmidt, W. Riess, One-dimensional nanoelectronic devices—towards the quantum capacitance limit. IEEE Proceedings Device Research Conference, pp. 173–176 (2008)
63. S. Bangsaruntip, A. Majumdar, G.M. Cohen, S.U. Engelmann, Y. Zhang, M. Guillorn, L.M. Gignac, S. Mittal, W.S. Graham, E.A. Joseph, D.P. Klaus, J. Chang, E.A. Cartier, J.W. Sleight, Gate-all-around silicon nanowire 25-stage CMOS ring oscillators with diameter down to 3 nm. IEEE Symposium VLSI Technology, pp. 21–22 (2010)
64. S.C. Rustagi, N. Singh, W.W. Fang, K.D. Buddharaju, S.R. Omampuliyur, S.H.G. Teo, C.H. Tung, G.Q. Lo, N. Balasubramanian, D.L. Kwong, CMOS inverter based on gate-all-around silicon-nanowire MOSFETs fabricated using top-down approach. Electron Device Lett. **28**, 1021–1024 (2011)
65. T. Mikolajick, M. Specht, N. Nagel, T. Mueller, S. Riedel, F. Beug, T. Melde, K.-H. Küsters, The future of charge trapping memories. Proceedings VLSI-TSA, pp. 130–133 (2007)
66. M. Specht, R. Kömmling, F. Hofmann, V. Klandzievski, L. Dreeskornfeld, W. Weber, J. Kretz, E. Landgraf, T. Schulz, J. Hartwich, W. Rösner, M. Städele, R.J. Luyken, H. Reisinger, A. Graham, E. Hartmann, L. Risch, Novel dual bit tri-gate charge-trapping memory devices. IEEE Electron Device Lett. **25**, 810 (2004)

67. B. Prince, *Vertical 3D Memory Technologies* (Wiley, Chichester, 2014)
68. Forward Insights, How 3D NAND stacks up, Report No. FI-NFL-3DM-0114 2014
69. J. Fu, Y. Jiang, N. Singh, C.X. Zhu, G.Q. Lo, D.L. Kwong, Polycrystalline Si nanowire SONOS nonvolatile memory cell fabricated on a gate-all-around (GAA) channel architecture. IEEE Electron Device Lett. **30**, 246–249 (2009)
70. M. Ishiduki, Y. Fukuzumi, R. Katsumata, M. Kito, M. Kido, H. Tanaka, Optimal device structure for pipe-shaped BiCS flash memory for ultra high density storage device with excellent performance and reliability. IEEE International Electron Devices Meeting (IEDM) Technology Digest, pp. 625–628 (2009)
71. K.-T. Park et al., Three-dimensional 128 Gb MLC vertical NAND flash-memory with 24-WL stacked layers and 50 MB/s high-speed programming. IEEE International Solid-State Circuits Conference (ISSCC) Digest Technology Papers, pp. 334–335 (2014)
72. A. Nitayama, H. Aochi, Bit cost scalable (BiCS) technology for future ultra high density memories. International Symposium VLSI Technology, Systems, and Applications (VLSI-TSA), pp. 1–2 (2013)
73. T. Mikolajick, H. Ryssel, Influence of statistical dopant fluctuations on MOS transistors with deep submicron channel lengths. Microelectron. Eng. **21**, 419–422 (1993)
74. T. Mikolajick, V. Häublein, H. Ryssel, The effect of random dopant fluctuations on the minimum channel length of short-channel MOS transistors. Appl. Phys. A **64**, 555–560 (1997)
75. M. Diarra, Y.-M. Niquet, C. Delerue, G. Allan, Ionization energy of donor and acceptor impurities in semiconductor nanowires; importance of dielectric confinement. Phys. Rev. B **75**, 045301 (2007)
76. M.T. Björk, H. Schmid, J. Knoch, H. Riel, W. Riess, Donor deactivation in silicon nanostructures. Nat. Nanotech. **4**, 103–107 (2009)
77. S.M. Koo, M.D. Edelstein, Q. Li, C.A. Richter, E.M. Vogel, Silicon nanowires as enhancement mode Schottky barrier field effect transistors. Nanotech. **16**, 1482–1485 (2005)
78. J. Knoch, J. Appenzeller, Impact of the channel thickness on the performance of Schottky barrier metal–oxide–semiconductor field-effect transistors. Appl. Phys. Lett. **81**, 3082 (2002)
79. W. Tang, S.A. Dayeh, S.T. Picraux, J.Y. Huang, K.-N. Tu, Ultrashort channel silicon nanowire transistors with nickel silicide source/drain contacts. Nano Lett. **12**, 3979–3985 (2012)
80. M.B. Das, Physical limitations of MOS structures. Solid-State Electron. **12**, 305–336 (1969)
81. A.M. Ionescu, H. Riel, Tunnel field-effect transistors as energy-efficient electronic switches. Nature **479**, 329–337 (2011)
82. L. Knoll, M. Schmidt, Q.T. Zhao, S. Trellenkamp, A. Schäfer, K.K. Bourdelle, S. Mantl, Si tunneling transistors with high on-currents and slopes of 50 mV/dec using segregation doped $NiSi_2$ tunnel junctions. Solid-State Electron. **84**, 211–215 (2013)
83. L. Knoll, Q.-T. Zhao, A. Nichau, S. Trellenkamp, S. Richter, A. Schafer, D. Esseni, L. Selmi, K.K. Bourdelle, S. Mantl, Inverters with strained Si nanowire complementary tunnel field-effect transistors. IEEE Electron Device Lett. **34**, 813–815 (2013)
84. B. Ghosh, M.W. Akram, Junctionless tunnel field effect transistor. IEEE Electron Device Lett. **34**, 584–586 (2013)
85. J.K. Hyun, S. Zhang, L.J. Lauhon, Nanowire heterostructures. Ann. Rev. Mater. Res. **43**, 451–479 (2013)
86. M. Borg, H. Schmid, K.E. Moselund, G. Signorello, L. Gignac, J. Bruley, C. Breslin, P. Das Kanungo, P. Werner, H. Riel, Vertical III–V nanowire device integration on Si(100). Nano Lett. **14**, 1914–1920 (2014)
87. K.E. Moselund, H. Schmid, C. Bessire, M.T. Björk, H. Ghoneim, H. Riel, InAs-Si nanowire heterojunction tunnel FETs. IEEE Electron Device Lett. **33**, 1453–1455 (2012)
88. F. Wessely, T. Krauss, U. Schwalke, CMOS without doping: multi-gate silicon-nanowire field-effect-transistors. Solid State Electron. **70**, 33–38 (2012)

89. M. De Marchi, D. Sacchetto, S. Frache, J. Zhang, P.-E. Gaillardon, Y. Leblebici, G. De Micheli, Polarity control in double-gate, gate-all-around vertically stacked silicon nanowire FETs. IEEE International Electron Devices Meeting (IEDM), pp. 8–4 (2012)
90. U. Schwalke, T. Krauss, F. Wessely, CMOS without Doping on SOI: multi-gate Si-nanowire transistors for logic and memory applications. ECS J. Solid State Sci. Technol. **2**, Q88–Q93 (2013)
91. A. Colli, A. Tahraou, A. Fasoli, J.M. Kivioja, W.I. Milne, A.C. Ferrari, Top-gated silicon nanowire transistors in a single fabrication step. ACS Nano **3**, 1587–1593 (2009)
92. F. Wessely, T. Krauss, U. Schwalke, Reconfigurable CMOS with undoped silicon nanowire midgap Schottky-barrier FETs. Microelectron. J. **44**, 1072–1076 (2013)
93. M. Mongillo, P. Spathis, G. Katsaros, P. Gentile, S. De Franceschi, Multifunctional devices and logic gates with undoped silicon nanowires. Nano Lett. **12**, 3074–3079 (2012)
94. M. De Marchi, D. Sacchetto, J. Zhang, S. Frache, P.-E. Gaillardon, Y. Leblebici, G. De Micheli, Top-down fabrication of gate-all-around vertically-stacked silicon nanowire FETs with controllable polarity. IEEE Trans. Nanotech. **13**, 1029–1038 (2014)
95. J. Zhang, M. De Marchi, D. Sacchetto, P.-E. Gaillardon, Y. Leblebici, G. De Micheli, Polarity-controllable silicon nanowire transistors with dual threshold voltages. IEEE Trans. Electron Devices **61**, 3654–3660 (2014)
96. W.M. Weber, A. Heinzig, J. Trommer, M. Grube, F. Kreupl, T. Mikolajick, Reconfigurable nanowire electronics-enabling a single CMOS circuit technology. IEEE Trans. Nanotech. **13**, 1020–1028 (2014)
97. J. Beister, A. Wachowiak, A. Heinzig, J. Trommer, T. Mikolajick, W.M. Weber, Temperature dependent switching behaviour of nickel silicided undoped silicon nanowire devices. Phys. Status Solidi (c) **11**, 1611–1617 (2014)
98. D. Martin, A. Heinzig, M. Grube, L. Geelhaar, T. Mikolajick, H. Riechert, W.M. Weber, Direct probing of Schottky barriers in Si nanowire Schottky barrier field effect transistors. Phys. Rev. Lett. **107**, 216807 (2011)
99. J. Zhang, M. De Marchi, P.E. Gaillardon, G. De Micheli, A Schottky-barrier silicon FinFET with 6.0 mV/dec subthreshold slope over 5 decades of current. Proceedings International Electron Devices Meeting (IEDM) 2014
100. J. Trommer, A. Heinzig, S. Slesazeck, T. Mikolajick, W.M. Weber, Elementary Aspects for circuit implementation of reconfigurable nanowire transistors. IEEE Electron Device Lett. **35**, 141–143 (2014)
101. M. De Marchi, J. Zhang, S. Frache, D. Sacchetto, P.-E. Gaillardon, Y. Leblebici, G. De Micheli, Configurable logic gates using polarity controlled silicon nanowire gate-all-around FETs. IEEE Electron Device Lett. **35**, 880–882 (2014)
102. P.-E. Gaillardon, L. Amáru, J. Zhang, G. De Micheli, Advanced system on a chip design based on controllable-polarity FETs. Design, Automation Test Europe Conference (DATE) 2014
103. A. Heinzig, T. Mikolajick, J. Trommer, D. Grimm, W.M. Weber, Dually active silicon nanowire transistors and circuits with equal electron and hole transport. Nano Lett. **13**, 4176–4181 (2013)
104. J. Trommer, A. Heinzig, A. Heinrich, P. Jordan, M. Grube, S. Slesazeck, T. Mikolajick, W. M. Weber, Material prospects of reconfigurable transistor (RFETs)—from silicon to germanium nanowires. MRS Proceedings, p. 1659 (2014)
105. W. Göbel, J. Hesse, J.N. Zerne (eds.), *Sensors, a Comprehensive Survey*, vol. 1. Fundamentals (VCH-Verlag, Weinheim, 1989)
106. J.I.A. Rashid, J. Abdullah, N.A. Yusof, R. Hajian, The development of silicon nanowire as sensing material and its applications. J. Nanomater. **3**, 1–16 (2013)
107. R. He, P. Yang, Giant piezoresistance effect in silicon nanowires. Nat. Nanotechnol. **1**, 42–46 (2006)
108. M. Messina, J. Njuguna, Potential of silicon nanowires structures as nanoscale piezoresistors in mechanical sensors. IOP Conference Series Material Science Engineering **40**, 012038 (2012)

109. X.L. Feng, R. He, P. Yang, M.L. Roukes, Very high frequency silicon nanowire electromechanical resonators. Nano Lett. **7**, 1953–1959 (2007)
110. R. He, X.L. Feng, M.L. Roukes, P. Yang, Self-transducing silicon nanowire electromechanical systems at room temperature. Nano Lett. **8**, 1756–1761 (2008)
111. P. Bergveld, Development of an ion-sensitive solid-state device for neurophysiological measurements. IEEE Trans. Biomed. Eng. **17**, 70 (1970)
112. P.-K. Shin, T. Mikolajick, H. Ryssel, pH sensing properties of ISFETs with silicon nitride sensitive-gate. J. Electrical Eng. Inf. Sci. **2**, 82–87 (1997)
113. T. Vering, W. Schuhmann, H.-L. Schmidt, T. Mikolajick, T. Falter, H. Ryssel, J. Janata, Field-effect transistors as transducers in biosensors for substrates of dehydrogenases. Electroanalysis **6**, 953–956 (1995)
114. Y. Cui, Q. Wei, H. Park, C.M. Lieber, Nanowire nanosensors for highly sensitive and selective detection of biological and chemical species. Science **293**, 1289–1292 (2001)
115. F. Patolsky, G. Zheng, O. Hayden, M. Lakadamyali, X. Zhuang, C.M. Lieber, Electrical detection of single viruses. Proc. Natl. Acad. Sci. USA **101**, 14017–14022 (2004)
116. F.M. Zörgiebel, S. Pregl, L. Römhildt, J. Opitz, W. Weber, T. Mikolajick, L. Baraban, G. Cuniberti, Schottky barrier-based silicon nanowire pH sensor with live sensitivity control. Nano Res. **7**, 263–271 (2014)
117. K.-I. Chen, B.-R. Li, Y.-T. Chen, Silicon nanowire field-effect transistor-based biosensors for biomedical diagnosis and cellular recording investigation. Nano Today **6**, 131–154 (2011)
118. G.-J. Zhang, Y. Ning, Silicon nanowire biosensor and its applications in disease diagnostics: a review. Anal. Chim. Acta **749**, 1–15 (2012)
119. B.-R. Li, C.-W. Chen, W.-L. Yang, T.-Y. Lin, C.-Y. Pan, Y.-T. Chen, Biomolecular recognition with a sensitivity-enhanced nanowire transistor biosensor. Biosens. Bioelectron. **45**, 252–259 (2013)
120. T.-S. Pui, A. Agarwal, F. Ye, Y. Huang, P. Chen, Nanoelectronic detection of triggered secretion of pro-inflammatory cytokines using CMOS compatible silicon nanowires. Biosens. Bioelectron. **26**, 2746–2750 (2011)
121. A.K. Wanekaya, W. Chen, N.V. Myung, A. Mulchandan, Nanowire-based electrochemical biosensors. Electroanalysis **18**, 533–550 (2006)
122. B. Tian, T. Cohen-Karni, Q. Qing, X. Duan, P. Xie, C.M. Lieber, Three-dimensional, flexible nanoscale field-effect transistors as localized bioprobes. Science **13**, 830–834 (2010)
123. X. Duan, R. Gao, P. Xie, T. Cohen-Karni, Q. Qing, H.S. Choe, B. Tian, X. Jiang, C.M. Lieber, Intracellular recordings of action potentials by an extracellular nanoscale field-effect transistor. Nat. Nanotech. **7**, 174–179 (2012)
124. Q. Qing, Z. Jiang, L. Xu, R. Gao, L. Mai, C.M. Lieber, Free-standing kinked nanowire transistor probes for targeted intracellular recording in three dimensions. Nat. Nanotech. **9**, 142–147 (2014)
125. L. Tsakalakos, J. Balch, J. Fronheiser, B.A. Korevaar, O. Sulima, J. Rand, Silicon nanowire solar cells. Appl. Phys. Lett. **91**, 233117 (2007)
126. M.D. Kelzenberg, D.B. Turner-Evans, B.M. Kayes, M.A. Filler, M.C. Putnam, N.S. Lewis, H.A. Atwater, Photovoltaic measurements in single-nanowire silicon solar cells. Nano Lett. **8**, 710–714 (2008)
127. B. Tian, X. Zheng, T.J. Kempa, Y. Fang, N. Yu, G. Yu, J. Huang, C.M. Lieber, Coaxial silicon nanowires as solar cells and nanoelectronic power sources. Nature **449**, 885–889 (2007)
128. T.J. Kempa et al., Semiconductor nanowires: a platform for exploring limits and concepts for nano-enabled solar cells. Energy Environ. Sci. **6**, 719–733 (2013)
129. B.Z. Tian, T.J. Kempa, C.M. Lieber, Single nanowire photovoltaics. Chem. Soc. Rev. **38**, 16–24 (2009)
130. Y.-J. Lee, Y.-C. Yao, C.-H. Yang, Direct electrical contact of slanted ITO film on axial p-n junction silicon nanowire solar cells. Opt. Express **21**, A7–A14 (2012)

131. X. Hua, Y. Zeng, W. Wang, W. Shen, Light absorption mechanism of c-Si/a-Si Half-coaxial nanowire arrays for nanostructured heterojunction photovoltaics. IEEE Trans. Electron Devices **61**, 4007–4013 (2014)
132. E.C. Garnett, P. Yang, Silicon nanowire radial p-n junction solar cells. J. Am. Chem. Soc. **130**, 9224–9225 (2008)
133. C.M. Hayner, X. Zhao, H.H. Kung, Materials for rechargeable lithium-ion batteries. Annu. Rev. Chem. Biomol. Eng. **3**, 445–471 (2012)
134. C.K. Chan, H. Peng, G. Liu, K. McIlwrath, X.F. Zhang, R.A. Huggins, Y. Cui, High-performance lithium battery anodes using silicon nanowires. Nat. Nanotech. **3**, 31–35 (2008)
135. R. Szczech, S. Jin, Nanostructured silicon for high capacity lithium battery anodes. Energy Environ. Sci. **4**, 56–72 (2011)
136. V. Etacheri, R. Marom, R. Elazari, G. Salitra, D. Aurbach, Challenges in the development of advanced Li-ion batteries: a review. Energy Environ. Sci. **4**, 3243–3262 (2011)
137. H. Wu, Y. Cui, Designing nanostructured Si anodes for high energy lithium ion batteries. Nano Today **7**, 414–429 (2012)
138. A. Krause, M. Grube, J. Brueckner, H. Althues, T. Mikolajick, W.M. Weber, Stability and performance of heterogeneous anode assemblies of silicon nanowires on carbon meshes for battery applications. MRS Proceedings (2015)
139. T.D. Bogart, D. Oka, X. Lu, M. Gu, C. Wang, B.A. Korgel, Lithium ion battery performance of silicon nanowires with carbon skin. ACS Nano **8**, 915–922 (2014)
140. L.-F. Cui, R. Ruffo, C.K. Chan, H. Peng, Y. Cui, Crystalline-amorphous coreshell silicon nanowires for high capacity and high current battery electrodes. Nano Lett. **9**, 491–4955 (2009)
141. B. Hoefflinger, Chips 2020: a guide to the future of nanoelectronic. Springer Science and Business Media (2012)
142. D. Ramos, E. Gil-Santos, O. Malvar, J.M. Llorens, V. Pini, A. San Paulo, M. Calleja, J. Tamayo, Silicon nanowires: where mechanics and optics meet at the nanoscale, Sci. Rep. **3**, 3445 (2013)
143. E. Baek, S. Pregl, M. Shaygan, L. Römhildt, W.M. Weber, T. Mikolajick, D.A. Ryndyk, L. Baraban, G Cuniberti, Optoelectronic switching of nanowire-based hybrid organic/oxide/semiconductor field-effect transistors. Nano Research (2014)
144. A.I. Boukai, Y. Bunimovich, J. Tahir-Kheli, J.-K. Yu, W.A. Goddard, J.R. Heath, Silicon nanowires as efficient thermoelectric materials. Nature **451**, 168–171 (2008)
145. Y. Liu, G. Ji, J. Wang, X. Liang, Z. Zuo, Y. Shi, Fabrication and photocatalytic properties of silicon nanowires by metal-assisted chemical etching: effect of H_2O_2 concentration. Nanoscale Res. Lett. **7**, 663 (2012)
146. M. Shao, D.D.D. Ma, S.-T. Lee, Silicon nanowires—synthesis, properties, and applications. Eur. J. Inorg. Chem. **27**, 4264–4278 (2010)

Chapter 2
Methods and Structures for Self-assembly of Anisotropic 1D Nanocrystals

Shuang-Yuan Zhang, Kwok Wei Shah and Ming-Yong Han

Abstract In the nanoscience and nanotechnology, the study of nanocrystal self-assembly has been regarded as a key technology in leading future industrial development. The colloidal self-assembly techniques, particularly for one-dimensional (1D) building blocks, have been widely adopted for the systematic fabrication of functional nanocrystals and received an extensive research attention. However, the increase in the building blocks' anisotropy, e.g. from sphere to rod/wire, has dramatically leveled up the difficulty in organizing them into ordered structures. To realize tailored 1D nanocrystal self-assembled structures, a profound understanding and detailed design of self-assembly mechanism and procedures are much needed. Here, a thorough review over 1D nanocrystal self-assembly methods and alignments are present to achieve large-scale functional structures. Through different techniques, such as evaporation, template, electric field, Langmuir-Blodgett film and chemical bonding, nanocrystals with various shapes can be self-assembled on substrates, at interfaces and in solutions. These assembled structures that have been achieved so far, can exhibit different degrees of alignments, such as stripe pattern as non-close-packed structure, horizontal, vertical alignments as close-packed monolayers, nematic, semectic alignments, AB stacking of vertical alignments, three-dimensional (3D) assembly as close-packed multilayers. In general, these self-assembly techniques can reach much small dimension and create microstructures that possess unique properties different from their individual building blocks.

S.-Y. Zhang (✉) · K.W. Shah · M.-Y. Han (✉)
Institute of Materials Research and Engineering, Agency for Science, Engineering and Research, 3 Research Link, 117602 Singapore, Singapore
e-mail: zhangs@imre.a-star.edu.sg

M.-Y. Han
e-mail: my-han@imre.a-star.edu.sg

Q. Li (ed.), *Anisotropic Nanomaterials*, NanoScience and Technology,
DOI 10.1007/978-3-319-18293-3_2

2.1 Introduction

The past few decades have witnessed an enormous explosion in the research efforts in the nanoscience and nanotechnology: from synthesizing new nanomaterials to characterizing [1–9], understanding their unique chemical, physical, biological properties [10–18], and more recently to self-assembling these individual components into larger systems and structures [19–25]. The self-assembly of individual nanocrystals has provided a bottom-up method that reaches much smaller dimension. It is able to align, pattern, integrate nanocrystals into ordered and functional microscale structures that is inaccessible from top-down methods, e.g. lithography, nano imprinting [26–28]. The colloidal route of nanocrystal self-assembly is an alternative means of nanofabrication to develop efficient micro-sized devices in a simple and versatile manner [29]. More importantly, it offers an inexpensive approach to build up large structures with new functions that differ from their initial building blocks. These new collective properties of assembled structures are tunable upon varying size, morphology and composition of these building blocks as well as the packing order [30]. A variety of nanomaterials including metals [31–37], semiconductors [38, 39], oxides [40–42], inorganic salts [28, 43], and polymers [38, 44] have been achieved to be self-assembled into larger, ordered structures with new properties. These assembled structures provide new perspectives for the application in the photonics [45–50], plasmonics [51–53], SERS [54–59], devices and deliver revolutionary solutions for magnetics [16, 41, 60, 61], electronic/photovoltaic devices [62–64], catalysis and energy storage [65]. Many of these applications are based not only on individual nano-objects but also on assemblies in which these nano-objects interact with one another and organize in dedicated ways. Therefore, the ability to self-assemble various nanocrystals into large ordered structures with desired size, shape and orientation has become crucial in solving new challenges and problems in nanoscience and nanotechnology research.

The building blocks for ordered self-assembled structures, which have been achieved so far, are priced restrictive requirements to be mono-dispersed [66, 67]. Individual nanocrystals, often terms as “artificial atoms” can assemble into large, microscale supercrystal or ordered solid structure in a dynamic equilibrium process when prepared with high uniformity. Traditionally, the building blocks of most assemblies are limited to spherical nanoparticles, and are studied extensively using simple drop-casting method [68–73]. The face-centered cubic (*fcc*) or hexagonal close-packed (*hcp*) packing pattern are usually observed when drop-casting and drying the uniform spherical nanoparticle dispersion onto a flat surface. Recent advances put emphasis to improve drop-casting method, with careful control over the evaporation rate and the choice of carrier solution, to enable the near-spherical nanoparticles, e.g. cubic, octahedral to form close-packed assembled structures. However, the increase in the building blocks’ anisotropy is found dramatically level up the difficulties to assemble such nanocrystals into long-ranged ordered structure [74–76], and the conventional drop-casting method face complexities in

self-assembling one-dimensional (1D) high anisotropic nanostructures, such as nanorods, nanowires [74].

In addition, when the self-assembly building blocks become assorted, especially lD anisotropic nanocrystals are used to assemble ordered structures, the crystal orientations (facet orientation) of these nanocrystals within the assembled structure become a prominent issue and of fundamental and practical research interest. Unlike spherical nanocrystals fitting into *fcc* or *hcp* pattern with a random crystal facet orientation, some 1D anisotropic nanocrystals assemble into more complicated packing patterns with both positional and orientational orders that otherwise unattainable using spherical nanocrystals [20, 22, 74–77]. This is particularly significant for certain applications as assemblies consisting of anisotropic nanocrystals possess unique properties due to their anisotropic nature [78]. Therefore, a significant research attention is diverted to this field and different self-assembly approaches, e.g. evaporation-mediated method, electric-field-assisted assembly, and template-assisted assembly [26, 27, 79–85] have been developed to assemble 1D anisotropic nanocrystals into ordered structures.

In this chapter, we focus on self-assemblies using 1D nanoscale building blocks and assess various assembling methods and different packing structures. The recent approaches that achieve self-assemblies on substrates, at interfaces, and in solutions are categorized and illustrated with detailed working mechanisms and actual setups. The different packing structures, such as stripes, monolayers, and multilayers that are fabricated from 1D nanocrystals are listed in the following section, with the emphases on the internal organization and unique properties. The challenges that faced by the current research works are also discussed, hoping to offer an outlook into future development. The ultimate goal is to provide a channel to fine tune 1D nanocrystals self-assembly into desired structures that is both functional and accessible for microscale applications.

2.2 Self-assembly Methods

Monodispersed colloidal nanocrystals with uniform size and shape distribution can self-assemble into large and ordered structures in a dynamic process on substrate or at interface or even in the colloidal solutions via different approaches. The formation of ordered structures depends on the building blocks and assembly approaches. The 1D anisotropic nanocrystals are particularly difficult to self-assemble due to their anisotropic structure properties and therefore require specific techniques and external facilitations. Here we summarize the approaches that have been developed so far to assemble 1D colloidal nanocrystals especially nanorods and nanowires into ordered structures.

2.2.1 Self-assembly on Substrates

2.2.1.1 Evaporation-Mediated Assembly

The controlled evaporation-mediated assembly is derived from simple drop-casting method that has been widely used in self-assembling spherical and non-isotropic colloidal nanocrystals [86, 87] on solid substrates. The formation of ordered self-assembled nanostructures was first observed using TEM by drop-casting the ferrofluid ($Fe_{1-x}C_x$) solution on a TEM grid [88]. In general, when a drop of nanocrystals suspension is withdrawn to deposit onto a flat substrate, as the carrier solvent is slowly evaporated, the nanocrystals self-assembled into ordered structure on the substrate surface to minimize the free energy (Fig. 2.1a) [89]. The relatively weak attraction forces (electrostatic interaction, Van Der Waals force, capping ligands interaction, hydrophobic interaction, capillary force [29] among nanocrystals in the suspension gain importance when the solvent is slowly evaporated, forcing nanocrystals to organize [82]. This aggregation process is also well explained using thermodynamics [90] and phase segregation model [91, 92], where the formation of final ordered structure depends on temperature, concentration, choices of solvent, nanoparticles sizes and thermodynamic state. Therefore, when the simple drop-casting method faces difficulty in self-assembling 1D anisotropic nanocrystals, different approaches that control the evaporation parameters such suspension concentration, choice of carrier solvent, evaporation rate have been proposed and demonstrated in anisotropic nanocrystals assembly.

To self-assemble 1D nanocrystals into ordered structures, the as-prepared nanocrystals are usually first subjected to a post-reaction treatment to narrow the size distribution. Most often, a non-solvent is added into stock solution with stirring until the initially homogeneous solution become turbid [81]. The large nanocrystals aggregate and precipitate at low centrifugation speed while the small sized nanocrystals remain in the supernatant. To further screening nanocrystals, additional non-solvent is added into the supernatant and another size selection can be carried out with a higher centrifugation speed. The above process is repeated until desired size distribution is reached. The size selection can also be carried out using filtration instead of centrifugation.

For the preparation of nanocrystal self-assemblies via controlled evaporation, the resulting uniform nanocrystals are dispersed into appropriate solvent with desired nanocrystal concentration. The concentration and choice of stabilizing surfactant can be adjusted by centrifugation, re-dispersion and ligand-exchange to avoid disordered aggregation [93, 94]. The surfactant concentration in the nanocrystal dispersions has to be larger than a critical value for the formation of ordered superstructures. This critical concentration appears to correspond to the amount of surfactant required to form a bilayer on the nanocrystal surface. Au nanorods without the surfactant bilayer coating tend to aggregate in a disordered manner because of the large van der Waals attraction (Au–Au Hamaker constant $A \approx 1.95$ eV) [95]. A minimum surfactant concentration is therefore required to

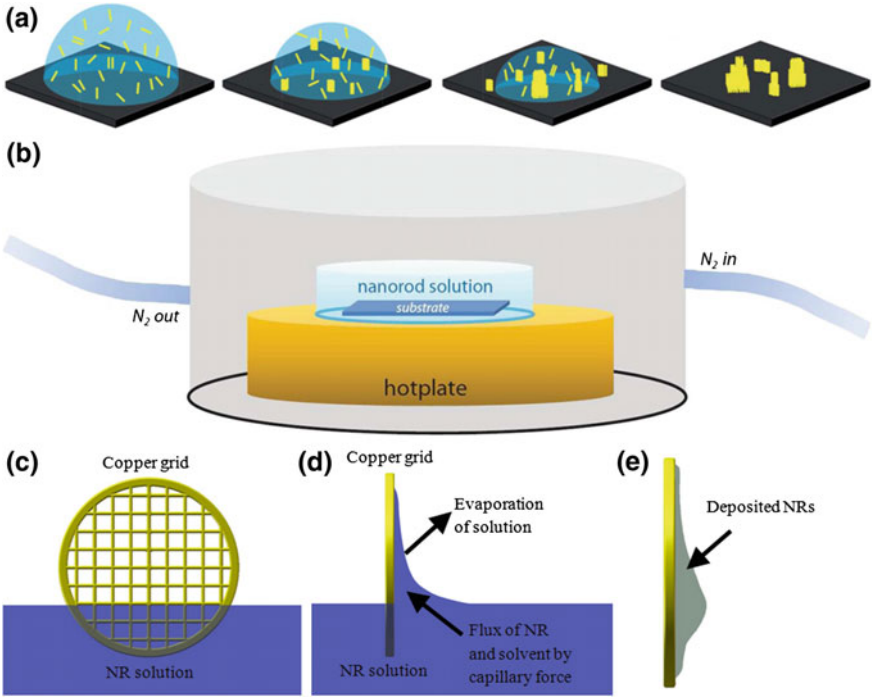

Fig. 2.1 Evaporation-mediated assembly. **a** Schematics showing the progression of evaporation-mediated assembly: the initial random distribution of nanorods, self-assembly during evaporation, formation of small assemblies, and final deposition of large-area assembled structures. Reproduced with permission from [89]. **b** Schematic diagram of an evaporation-mediated assembly setup. The substrate is placed in the *bottom* of a short-walled container, which is filled with 1D nanocrystal solution. This container is set on a hotplate, and placed inside a small Teflon evaporation chamber. A controlled flow rate of dry nitrogen through the small atmosphere of the chamber enables control of solvent evaporation rate. Reproduced with permission from [93]. **c–e** Schematics of the deposition method in evaporation-mediated assembly. **c** A TEM grid is inserted about 1/4 of the diameter into the Au nanorod solution. A thin film of solution is formed due to the capillary action. **d** Evaporation of water from the thin film causes influx of water and nanorods. **e** The accumulation of nanocrystals leads to the formation of self-assembled structures. Reproduced with permission from [96]

maintain the balance between the entropic depletion potential and electrostatic repulsion potential for the formation of nanorod superstructures [94].

A typical setup for controlled evaporation is shown in Fig. 2.1b, in which the solvent was evaporated with a fine control. A drop (5–10 mL) of 1D nanocrystal dispersion was placed onto a clean flat substrate, e.g. silicon, silicon nitride. The droplet was kept undisturbed at a particular temperature (usually 30–60 °C depends on the chosen solvent's boiling point and desired evaporation rate) for a constant evaporation rate. Higher temperature above 60 °C was reported to cause disordered assemblies as the evaporation was too fast for the nanorods to attain their equilibrium positions. The humidity of the evaporation chamber was also under

carefully control for a constant evaporation rate. In often cases, approximately 60 % humidity caused by water or solvent was maintained during the evaporation [94]. Very slow evaporation rate which took several hours was usually adopted in self-assembling 1D nanocrystals and found helpful to increase packing order and assembled structure size. The evaporation chamber could also be supplied with a controlled flow of dry nitrogen either under atmosphere or under reduced pressure. The final assembled structures were shown related to concentration of 1D nanocrystal dispersions. Different nanorod concentrations were tested. The use of relatively concentrated solutions resulted in well-ordered nanorod assemblies, whereas the use of dilute solutions did not favor the formation of ordered assemblies.

The evaporation can also be controlled by capillary action in a much simple setup. The capillary force is able to induce a flow (solvent and nanocrystal) from solution to the substrate and create a thin film on the substrate. The solvent flux compensates the evaporated solvent from the film; while the nanocrystal flux causes nanocrystal accumulation and results in the self-assembled structures. El-Sayed and co-workers [96] have described an immersion method in controlling the evaporation so as to grow self-assembled structures from Au nanorods. In a general scenario, a flat substrate (a carbon-coated copper gird for instance) was vertically inserted partially into Au nanorod solution with the bottom part of gird immersed in the solution (Fig. 2.1c–e). Drying of the colloidal solution over 8 h led to the formation of reproducible self-assembled structures in most regions of the substrate. The immersion of substrate in colloidal solution first created a thin film on the substrate. The gentle evaporation of solvent from the thin film increased the lateral capillary forces between nanorods and built up a pressure gradient. This caused the influx of water and nanorods, and finally led to the packing of nanorods at the contact interface of the solution and substrate. It was shown that the immersion method could produce self-assemblies with high quality and factors such as the rate of water evaporation, the ionic strength, the surfactant concentration, and the particle size and shape distributions were important in this process.

2.2.1.2 Electric-Field-Assisted Assembly

In colloidal system, the external electric field has long been found to induce or strengthen the interactions between the nanocrystals and/or their capping ligands [97]. For 1D nanocrystals (including their capping ligands) carrying free electrons or with strong dipole moment, the electric field is a perfect stimulus in directing their assembly into a desire pattern and orientation [48, 76, 98–104]. These 1D nanocrystals are usually polarized along their longitudinal axes and experienced forces exerted by the electric field in the field streamline direction. When the electric-field-induced interactions are sufficiently strong to overcome Brownian motion, 1D nanocrystals can move along the electric field streamline and form a well-ordered structures with little defects and increased symmetry [102, 105]. A simple model can be established by considering thermal energy to evaluate the energy input in order to align 1D nanocrystals into ordered structures.

The electric-field-induced alignment energy are required to overcome thermal energy at room temperature k_BT = 26 meV (k_B is the Boltzmann constant) that would otherwise randomize the orientation of the 1D nanocrystals [100, 101]. On the basis of this, the minimum external electric field strength, lower bound of free electron density or dipole moment magnitude of nanocrystals can be determined when assembling the 1D nanocrystals.

In general, both direct current (DC) and alternating current (AC) electric field can be used as the external field in assisting 1D nanocrystals assembly. The nanorods or nanowires are able to be aligned uniformly over areas on the scale of several tens of square micrometers by following the electric field streamlines. In the case of DC electric-field-assisted assembly, a non-conducting flat surface, e.g. Si_3N_4, is used as the substrate and a pair of electrodes are placed either on the two sides of the substrate (left-right manner, Fig. 2.2a) or in a top-down manner (Fig. 2.2b). The placement of the electrodes determines the electric field direction and thus decides the assembled 1D nanocrystals orientation: perpendicular (top-down manner) or parallel (left-right manner) to the substrate. A drop of colloidal 1D nanocrystals solution is deposited on the substrate for a slow evaporation over a period of several hours that depends on the solvent vapor pressure and environment. A direct voltage **V** is applied simultaneously during the solvent evaporation, the magnitude of which has to produce alignment energy larger than thermal energy at room temperature (k_BT) as discussed above. The DC electric-field-assisted is a voltage-magnitude-dependent process and forces a high concentration of 1D nanocrystals inside the gap between two electrodes. In fact, the 1D nanocrystals concentration distribution contour strongly resembles that of electric field strength, where the nanocrystals concentration is highest around the electrodes [101].

The AC electric-field-assisted assembly shares a similar setup as that of DC electric field, with the change of alternating voltage applied at the electrodes. An electrically insulated electrode structure that consists of multiple interdigitated fingers pattern can be used to scale-up the assembly ability (Fig. 2.2c–e). The interdigitated electrode structures are fabricated by optical lithography and subsequent metal evaporation onto a Si/SiO_2 substrate with sizes and spacings in the order of a few microns [48, 76, 98]. The use of the AC electric field for the self-assembly avoids charging effect and excessive accumulation of the 1D nanocrystals around the electrodes [48]. Besides, it prevents the interference of electro-osmotic and electro-chemical effects that present in the DC system [82]. Different from the DC electric-field-assisted assembly, in which the applied voltage magnitude is the major parameter in controlling the assembly; in the case of AC circuit, the frequency of the alternating voltage also plays a role in assembling the 1D nanocrystals. In general, as the frequency of the AC circuit increases, the assembling time to form order assembled structure decreases. The high frequency prevents the polar molecules in the solvent to reorient in the rapidly changed electric filed because of their long relaxation times. This results in greater net polarization of the 1D nanocrystals and stronger alignment forces and thus shorter assembling time [106].

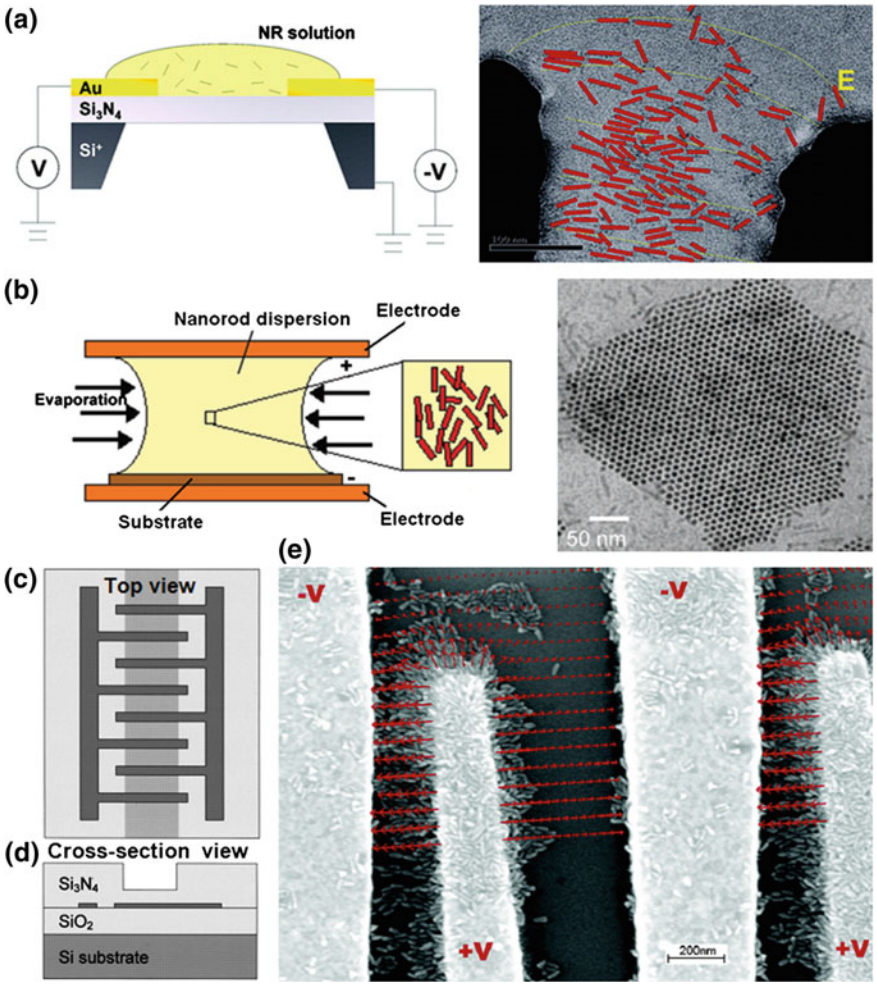

Fig. 2.2 External-field-assisted assembly. **a**, **b** Schematic representations of the experimental set-ups used in the assembly of colloidal cadmium chalcogenide nanorods under DC electric fields. **a** When the parallel electrodes (Au) are arranged in a coplanar manner, the nanorods are aligned in the plane of the substrate. The TEM image shows CdSe nanorods (shown as *red bars*) aligned along the electric field streamlines (shown in *yellow*). Reproduced with permission from [101]. **b** A *top-down* arrangement of the electrodes results in nanorods that are oriented perpendicular to the substrate. The TEM image shows perpendicularly aligned CdS nanorods. Reproduced with permission from [102]. **c** *Top* and **d** cross-sectional views of the multiple electrode structures used in the AC electric-field-assisted assembly. The interdigitated electrode fingers are placed on the SiO_2/Si substrate and covered with Si_3N_4 layer to prevent short circuit. Reproduced with permission from [98]. **e** SEM image showing nanorods accumulate in the region of strongest electric field and aligned along the electric field streamlines. Reproduced with permission from [48]

2.2.1.3 Template-Assisted Assembly

For colloidal nanocrystal self-assembling with a template, the template geometry and surface chemistry play an important role by incorporating active sites for nanocrystal selective deposition [107–111]. Modulating the geometry and surface chemistry of templates therefore offers a convenient tool in assisting 1D nanocrystal assembly. These templates can serve as hosts to accommodate 1D nanocrystals and allow the creation of ordered structures [75, 112–116]. For instance, conventional photo lithography permits patterning a substrate's surface with precise spatial and chemical control. This surface-modified substrate contains geometrically constrained sites and/or chemically active groups that induce the selective deposition of nanocrystals onto substrate with desired pattern. It shall be noted that other than the surface-modified substrates, biological molecules, e.g. DNA, peptides [117–123], microstructures, e.g. carbon nanotubes [124] or block copolymers [125–128], can also be considered as template in a broad sense. These molecules or structures provide a platform onto which nanocrystals are aligned into ordered structures that is complementary to themselves, through the covalent or non-covalent interactions.

The geometrically constrained template is a straightforward method that can create different assembly patterns. The pattern feature size and morphology put strict restrictions on how 1D nanocrystal deposit onto the surface. Due to the anisotropic nature of 1D nanocrystals, only certain orientations are accessible for their deposition (Fig. 2.3a–c). These templates need to be designed in accordance with building blocks. An excessive large feature sizes lead to disordered structures while a small feature sizes prevent the deposition of nanocrystals onto the template. The pattern feature sizes are generally in the same order of building blocks dimensions. For the case shown in Fig. 2.3a–c, to assembly CdSe nanorods with dimension around 35 × 7.5 nm into horizontal line alignment, a channel width of 30 nm can be used to selectively align these nanorods [114].

Other than geometrically constrained template, 1D nanocrystals can also be aligned on chemically active template. For instance, thiol groups tend to form colvent Au–S bonding with Au nanocrystals and deposition of such dispersion results in preferential anchoring of Au nanocrystals onto thiol-patterned surface [109]. However, this type of assembling is applicable only to specific binding combination. A more generic method is making using of the wettability of the template surface. The substrate surface is patterned with hydrophobic and hydrophilic regions (Fig. 2.3d–g). Any 1D nanocrystals that are dispersed in the water are able to remain in the hydrophilic patterns when the excess suspension is withdrawn by pipette. Once the water is evaporated, the 1D nanocrystals are confined within the designed hydrophilic regions [113]. The orientation of 1D nanocrystals inside the hydrophilic regions can be further controlled by narrowing the width of hydrophilic region. When the width of hydrophilic region is less than the length of nanorods or nanowires, these nanocrystals align along the longitudinal axis of hydrophilic region.

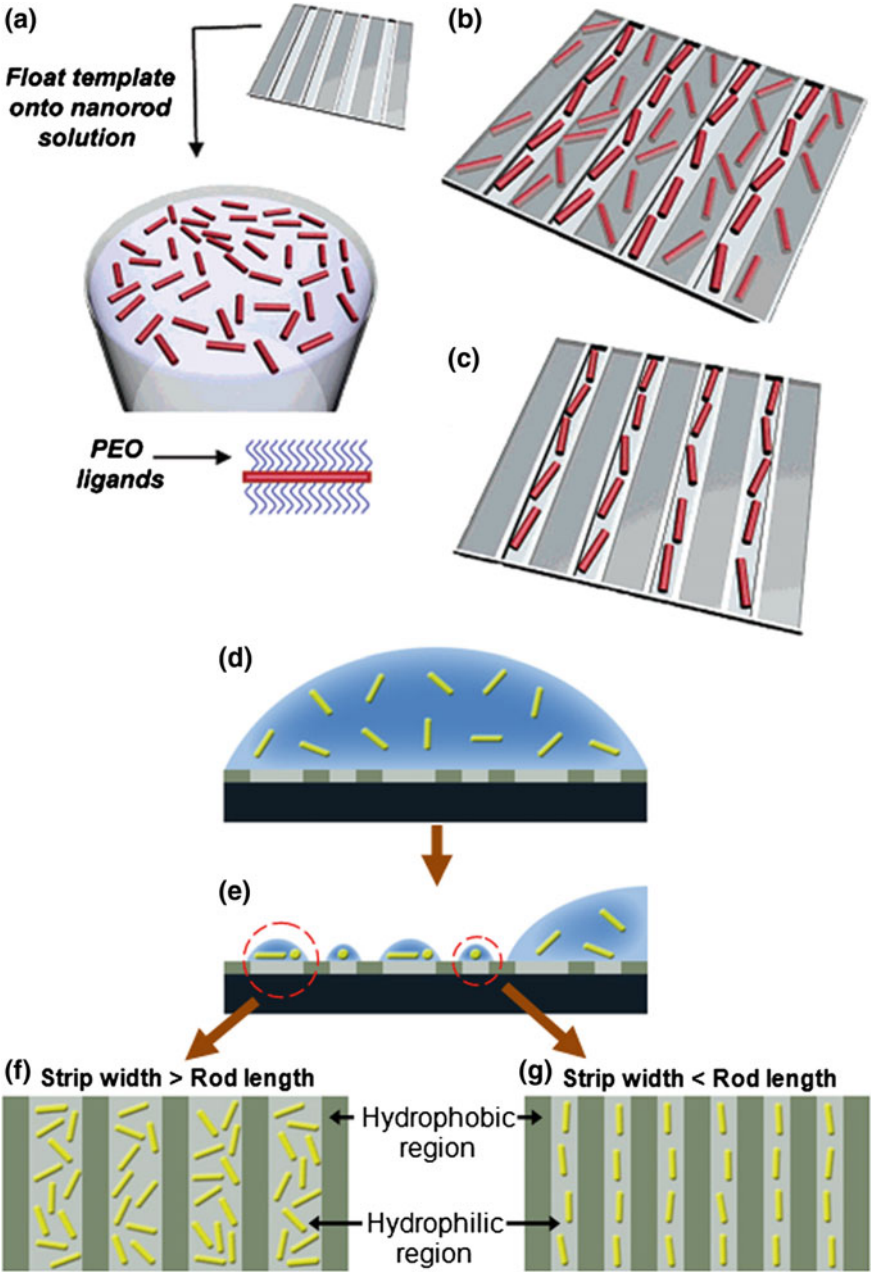
(a)
Float template onto nanorod solution
PEO ligands
(b)
(c)
(d)
(e)
(f) Strip width > Rod length
(g) Strip width < Rod length
Hydrophobic region
Hydrophilic region

◀ **Fig. 2.3** Template-assisted assembly. **a–c** Schematics of template-assisted assembly process via geometric confinement: **a** flotation of template onto aqueous solution of PEO-covered CdSe nanorods; **b** CdSe nanorods within the channels and on the template surface; **c** CdSe nanorods isolated in the channels following rinsing of the template. Reproduced with permission from [114]. **d–g** Schematics of template-assisted assembly process via chemical interaction: **d** a nanowire suspension is drop-casted on substrates with hydrophilic and hydrophobic patterns; **e** settling of nanowires onto substrates; **f** formation of discrete droplets during the removal of the nanowire suspension; **g** patterned nanowires on substrates. Reproduced with permission from [113]

2.2.2 Self-assembly at Interfaces

Self-assembly at the interface has been observed and studied for more than a century. A well-known example is Pickering emulsions, in which solid particles adsorb at the paraffin-water interface to stabilize the emulsion droplets from coalescence [129, 130]. This phenomenon has been extended to self-assemble colloidal micron-sized particles and later on nanocrystals between two immiscible phases. The alignment of particles at the interface can cause a reduction of total interfacial energy and it is the dominant force in driving such self-assembly. If the decrease of the interfacial energy is larger than the thermal energy that causes fluctuations, the colloidal particles can be aligned at the interface. In general, the interfacial energy is related to the particle size by Pieranski's theoretical calculation [131–134]. The total decrease of interfacial energy is smaller for small particles and therefore, interfacial assembly originally only targets micro-sized particles. Nevertheless, recent studies have successfully demonstrated 1D nanocrystals self-assembly at interface, offering a flexible pathway for bottom-up assembly of nanorods or nanowires into organized structures [135–138].

The Langmuir-Blodgett (LB) and Langmuir-Schaefer (LS) techniques are the most widely used and developed methods in achieving 1D nanocrystal assembly at interface. The nanorods or nanowires are required to be protected with hydrophobic capping ligands [54] and spread evenly on the water surface. At the air-water interface, the randomly orientated nanocrystals are compressed slowly using a barrier with the surface pressure monitored (Fig. 2.4a–c). At different stages of compression, a horizontally aligned monolayer or nematic, smectic aligned multilayer nanocrystals assemblies can be observed and collected onto desirable substrate using either vertical (LB technique) or horizontal (LS technique) deposition procedure [62]. The assembled 1D nanocrystals exhibit remarkable alignment parallel to the barrier. Providing suitable surface passivation chemistry, this interface-based method is applicable to various 1D building blocks, and the assembled structure size, packing order and inter-nanocrystal spacing can be controlled independently with engineering precision [135].

Deposition at the oil/water interface is another extensively studied technique in directing self-assembly of 1D nanocrystals. The purified 1D nanocrystals are first dispersed in organic solvent that is immiscible with water and has a low vapor pressure. A small amount of such dispersion is drop-casted carefully onto the water

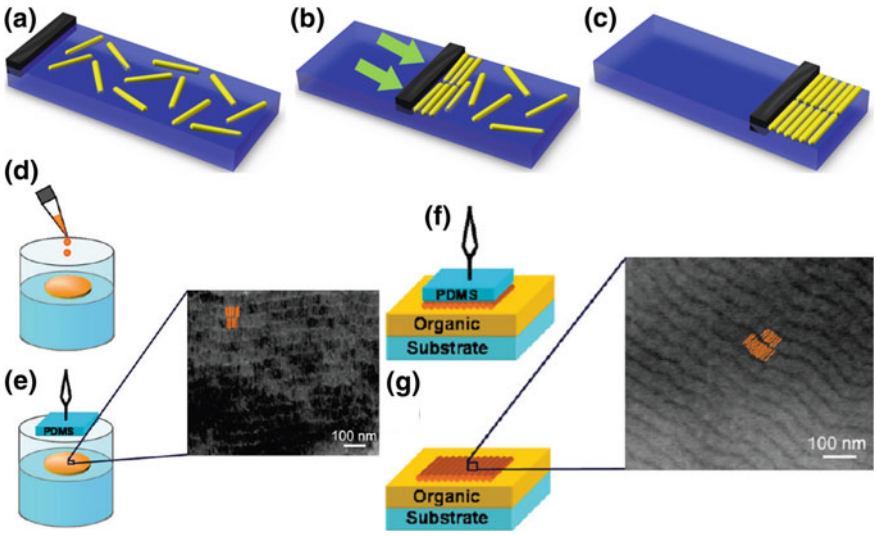

Fig. 2.4 Self-assembly at interfaces. **a–c** Schematics of Langmuir-Blodgett nanorod assembly at the air-water interface. **a** Random distribution of nanorods at air-water interface. **b** Organization of nanorods as the barrier compressing the nanorods. **c** Assembled structures when barrier reaches final compression stage. **d–g** Schematics of nanorod assembly at water-toluene interface. **d** CdSe/CdS nanorods in toluene are spread dropwise on water surface. **e** After the toluene evaporation, the floating film is harvested by liftoff of a PDMS stamp pad. The zoomed image shows a TEM image of self-assembled CdSe/CdS nanorods. **f** The inked PDMS is brought into contact with the organic layer by a gentle pressure. **g** The self-assembled is transferred onto organic surface after PDMS stamp is removed. The zoomed image shows a SEM image of self-assembled CdSe/CdS nanorods. Reproduced with permission from [49]

surface. The 1D nanocrystals are able to aggregate and align at the oil/water interface while the organic solvent is allowed to evaporate slowly over a period of several hours (Fig. 2.4d–g). The in-plane compression, interfacial tension and the capillary force mediate the assembly of 1D nanocrystals. The ordered structures are then harvested by a contact printing technique with a hydrophobic substrate, e.g. polydimethylsiloxane (PDMS) stamp pad and eventually transfer to a device [49]. These individual 1D nanocrystals assembled at the interface maximize the interfacial coverage per nanocrystal and minimize the Helmholtz free energy of the whole system. Due to its anisotropic nature, the 1D nanocrystals aligned parallel to the interface generally cover more surface area and possess much lower interfacial energy than those oriented perpendicular to the interface [132]. However, the nanorods orientated perpendicular to the interface are still observed when the concentration of nanorods reach a critical value [30, 133]. The interfacial energy between liquids and nanocrystals, the aspect ratio and concentration are the major parameters in controlling the orientation and structures of 1D nanocrystals interfacial assembly.

2.2.3 Self-assembly in Solutions

Solution based assembly is perhaps the most simple while complicated method in achieving 1D nanocrystals self-assembly. It is simple as it involves little or no external facilitations (e.g. electric-filed, template), while enables the nanorods or nanowires spontaneously assembled within the solution [58, 137, 139–143]. It is complicated as it engages a variety of chemical interactions, e.g. hydrogen bond, chemical bonding, electrostatic force [144–151], among the whole spectrum of nano-entities inside the solution. Each of the interaction works in a unique way and is very specific towards different combinations of nanocrystals, capping ligands and solvent. In that sense, the solution-based assembly is a complicated method requires dedicated design of the whole solution system.

Although the driving forces vary for different solution based assemblies, this type of assemblies, however, shares a similar process. At first glance, small self-assemblies are formed randomly in the solution due to the chemical interactions and collisions caused by the Brownian motion. These small self-assemblies, serve as nucleation sites, subsequently draw neighboring building blocks together and grow into ordered microscale structures [152–155]. The assembly process is closely related to the concentration and temperature of the stocking solution. In general, as the concentration of 1D nanocrystals and temperature increase, the collisions between the nanocrystals are more frequent and thus the assembling of collided nanocrystals become easier and faster [156]. A selective change of solvent quality can trigger or facilitate the above process, by causing the destabilization of a well-dispersed nanocrystal solution [74, 138, 155, 157].

Making use of the hydrogen bond of capping ligand is one frequently used method in directing solution-based assembly. Bifunctional molecules such as cysteine, glutathione, 3-mercaptopropionic acid, 11-mercaptoundecanoic acid, and α,ω-alkanedithiols which carries thiol group are shown selectively bind to the end or side surface of Au nanorods via hydrogen bonds [145, 148, 156–158]. This hydrogen bonding can be controlled by the variation of the pH value of the solution, which enables the Au nanorods assembled in a side-by-side (Fig. 2.5a) or end-to-end (Fig. 2.5b) pattern or disassembled back to random alignment. The pH value of solvent close to these bifunctional molecules PK_a value favors the assembly while the pH value away from the PK_a value favors the disassembly, which agrees with the hydrogen-bonding theory. Other than hydrogen bond between the capping ligands, the chemical bonding is another useful force in assembling 1D nanocrystals. Zhang et al. have reported chemical bond driven self-assembly of CoP nanowires when aging them in the reaction solution for 120 min [159]. The capping ligands adsorbed/desorbed from CoP nanowires dynamically in the mother reaction solution, and their controlled removal led to direct interaction between adjacent nanowires to form Co-P chemical binding. As shown in Fig. 2.6a, b, this chemical bond was direction-specific, forcing nanowires position in a particular facet, thus

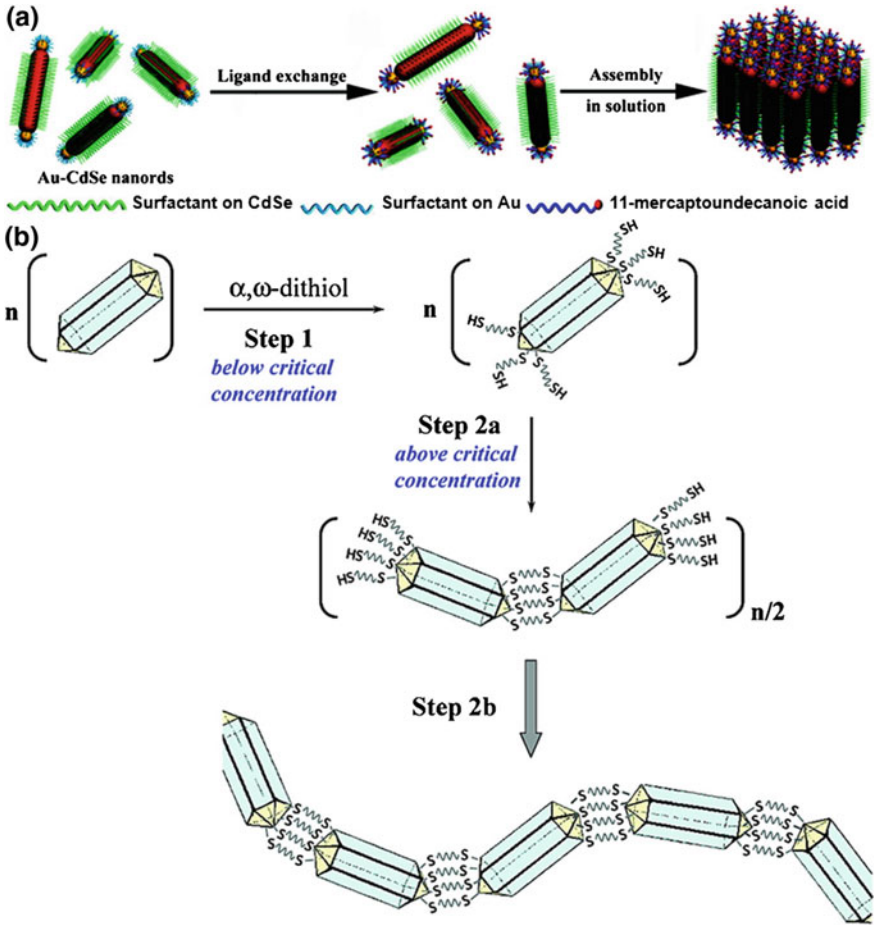

Fig. 2.5 Self-assembly in solutions. **a** Schematics of the side-by-side self-assembly of Au-tipped CdSe nanorods via hydrogen bonds. The Au tips are ligand-exchanged with 11-mercaptoundecanoic acid and cross-linked via hydrogen bonds between their carboxylic groups. Reproduced with permission from [157]. **b** Schematics of the end-to-end self-assembly of Au nanorods via hydrogen bonds. (Step 1) The Au tips are capped with *α*,*ω*-alkanedithiols. (Step 2a) Above a critical concentration of *α*,*ω*-alkanedithiols, nanorods form dimmers and (Step 2b) subsequently chain structure via hydrogen bonds between their thiol groups. Reproduced with permission from [148]

provided both positional and orientational order. In addition, electrostatic force [160], depletion attraction (Fig. 2.6c–f) [161] and avidin-biotin recognition [144, 162] have also been demonstrated successfully in self-assembling nanorods or nanowires at specific locations to form ordered close-packed or non-close-packed structures.

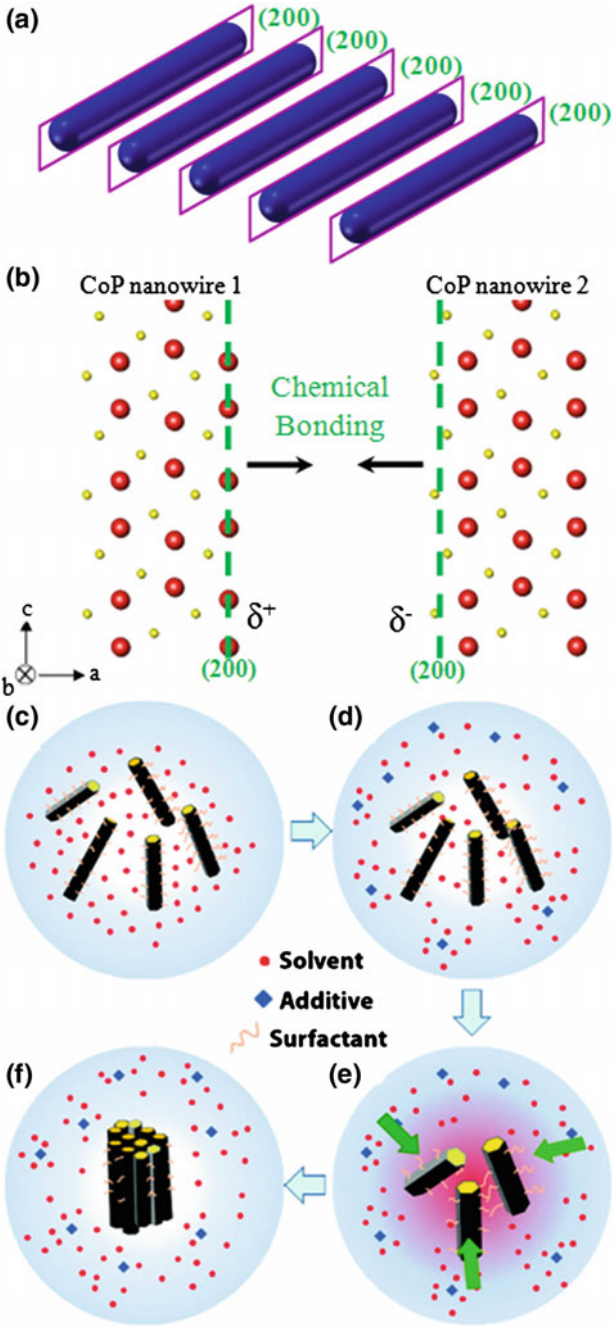
(a)
(200)
(200)
(200)
(200)
(200)
(b)
CoP nanowire 1
CoP nanowire 2
Chemical Bonding
δ+
δ-
(200)
(200)
c
b
a
(c)
(d)
Solvent
Additive
Surfactant
(f)
(e)

◀ **Fig. 2.6** Self-assembly in solutions. **a–b** Schematics of solution-based self-assembly of CoP nanowires via chemical bonds. **a** The CoP nanowires are aligned along (200) facet and **b** allow the irreversible formation of chemical bonds between Co and P atoms from neighboring nanowires. Reproduced with permission from [159]. **c–f** Schematics of solution-based self-assembly of CdS, CdSe, CdS/CdSe nanorods via depletion attraction. **c** Nanorods coated with hydrophobic surfactant are dispersed in organic solvent. **d** Assembly is triggered by introducing additive (macromolecule) into the solvent. **e** An osmotic pressure (depletion attraction) is developed and drive nanorods aligned together when nanorods approach each other and create a volume inaccessible to additive. **f** Final assembled structures. Reproduced with permission from [161]

2.3 Self-assembly Packing Structures

Other than various methods that have been demonstrated to self-assemble 1D nanocrystals, numerous packing orders have also been achieved using these 1D building blocks. Different from the *fcc* or *hcp* pattern that is typically formed by isotropic nanocrystals, the anisotropic nature of 1D nanocrystals renders them great possibility to be arranged into diverse packing orders, such as stripes, horizontal/vertical monolayer, nematic/smectic multilayer, AB stacking of vertical alignments, and 3D assemblies. The assembled structures from 1D nanocrystals usually possess both positional and orientational orders that require precise alignment of building blocks. The collective properties of these assembled structures differ from their individual building blocks and vary upon the change of the packing order. In this section, we review various alignments that have been achieved in self-assembling 1D nanocrystals with the emphasis on the nanorod and nanowire building blocks.

2.3.1 Non-close-Packed Structures

The non-close-packed structures formed by the 1D nanocrystals refer to the self-assembled structures that are not continuously aligned over a large-scale area in at least two directions, e.g. x, y directions in Cartesian coordinates. They are of low surface coverage and generally in the form of networks of stripes pattern (also called ribbons or chains in some literatures) with substantial amount of space in between [163–165]. Each stripe is a single layer structure, which can reach several micrometers long. These stripes are usually placed independently with low level of ordering (Fig. 2.7a–d). However, within the stripes, the building blocks are well organized in two basic alignments: side-by-side or end-to-end. A single stripe pattern can consist of either one of these alignments or a combination of both. In general, the inter-nanorod/nanowire energetic forces such as van der Waals force, dipole-dipole interaction favor side-by-side alignment due to the large contact area when they are aligned along the longitudinal axis. This alignment is widely observed in various stripe patterns. Nevertheless, in certain cases, such as a kinetically limited self-assembly process [166], end-to-end structures can be the dominated form in composing the stripes.

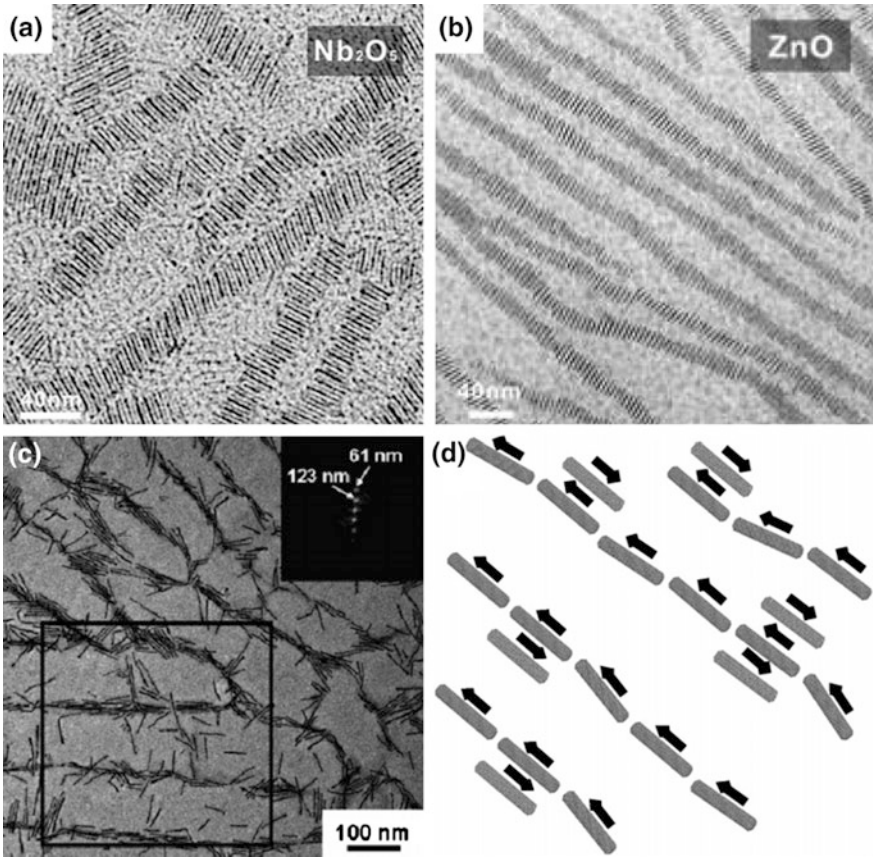

Fig. 2.7 TEM images of side-by-side stripe pattern formed by **a** Nb_2O_5 nanorods, **b** ZnO nanorods. Reproduced with permission from [143]. **c** TEM images of primarily end-to-end stripe pattern formed by CdS nanorods. The *inset* shows an FFT of the region enclosed by an outlined square. **d** Corresponding schematic diagram of primarily end-to-end stripe pattern. Within the stripes, a few nanorods are packed side-by-side, an orientation favored by both antiparallel dipole interactions (represented by the *black arrows*) and van der Waals attraction. Reproduced with permission from [166]

One example of non-close-packed structures that are based on side-by-side alignment is displayed in Fig. 2.7a, b, which has been reported by Yang and his co-workers [143]. Nb_2O_5 nanorods with diameter of 1.3–1.6 nm (Fig. 2.7a) and ZnO nanorods with diameter of 1.1–1.4 nm (Fig. 2.7b) were demonstrated to be self-assembled into well-defined, uniform, stripe structures that could reach 1.6 μm in the length with aspect ratio of ~ 80. The side-by-side arrangements here created the largest contact area for the neighboring nanorods, and thus ensured the formation of stripes through the interactions between surfactants and inorganic species. A range of sub-2 nm (down to one unit cell) transition metal oxide (TiO_2,) and rare earth

oxides (Eu_2O_3, Sm_2O_3, Er_2O_3, Y_2O_3, Tb_2O_3, and Yb_2O_3) were also demonstrated to be self-assembled into arrays of stripes.

The end-to-end alignment in the non-close-packed structures is mostly seen when specific bindings, e.g. hydrogen bonding, exist at the tips of the nanorods/nanowires, as the case we mentioned in solution based assembly (Fig. 2.5b). The contact area of end-to-end alignment is much limited compared with side-by-side configuration, and therefore it is not the preferred structures. Nevertheless, Korgel and his co-workers showed in a kinetically limited self-assembly process, in which the CdS nanorods formed primarily end-to-end alignments (Fig. 2.7c) when evaporating a small amount of CdS colloidal solution at a low surface coverage. The evaporation process promoted a kinetically limited structure (Fig. 2.7d) via the spinodal decomposition. There was also a preferred orientation of the stripes as shown by the fast Fourier transforms (FFT) image in Fig. 2.7c inset. The distances specified by the linear spot positions in FFT corresponded to the distances between stripes (center to center). However, when the FFT was taken at a large scale of multiple domains of stripes, a diffuse ring instead of spots was observed, suggesting the stripe pattern lacked long-range ordering [166].

The non-close-packed structures can also be constructed from a combination of both side-by-side and end-to-end alignments. Each stripe pattern, for instance, is able to consist of a few columns of nanorods that are aligned end-to-end. Meanwhile, within each column, the nanorods are attached to each other via a side-by-side alignment. Such structures require dedicated constrains in directing nanocrystal alignment, and are usually achieved with the aid of external facilitation. The internal organization of stripes such as the number of columns in a single stripe can be further controlled by adjusting external facilitation. The competition between the side-by-side and end-to-end alignments within the stripes is a destabilizing factor that can lead to the disorganization of the self-assembly. Banin and his colleagues have used a copolymer film as a template, to successfully self-assemble polystyrene-coated (PS-coated) CdSe nanorods into non-close-packed structures with both side-by-side and end-to-end alignments (Fig. 2.8a–d) [125]. The copolymer film was casted from polystyrene-block-poly(methyl methacrylate) (PS-b-PMMA) and featured with alternating PS and PMMA domains. The PS-coated CdSe nanorods were therefore selectively bound to the PS domains on the template. By aligning perpendicular with respect to their hosting PS domains, the CdSe nanorods maximized attractive van der Waals interactions from neighboring nanorods, while minimized the repulsive interactions from surrounding PMMA domains (Fig. 2.8b). Via adjusting the ratio between the PS domain width and the nanorod length, the CdSe could form multiple end-to-end aligned rows. However, this orientational preference of nanorods in both side-by-side and end-to-end alignment diminished for decreasing nanorod aspect ratio and gave way for adverse orientational entropy effects [126]. The long nanorods with long copolymers template were preferred for highly organized stripe patterns as short nanorods and/or short copolymers were more prone to morphological defects.

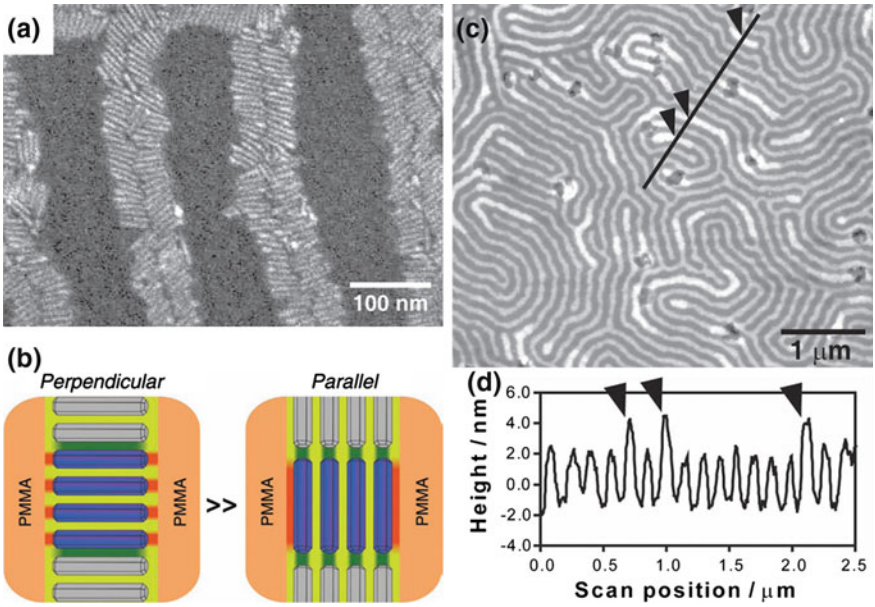

Fig. 2.8 **a** SEM images of non-close-packed structures formed by PS-coated CdSe nanorods on PS-*b*-PMMA coated substrate, showing a coexistence of both side-by-side and end-to-end alignments. **b** Schematic diagram showing the preferential alignment of the perpendicular orientation over the parallel orientation with respect to their hosting PS domain. The attractive and repulsive interactions depicted as *green* and *red* stripes, respectively; while PMMA domains are colored *orange*, and PS domains underneath the nanorods are colored *yellow*. **c** AFM micrograph of non-close-packed structures formed by PS-protected CdSe nanorods on PS-*b*-PMMA coated substrate. *Height scale* 10 nm. **d** AFM height profile corresponds to the *black line*, where *arrowheads* mark crossed nanorod-filled PS domains. Reproduced with permission from [125]

2.3.2 Close-Packed Monolayers

2.3.2.1 Horizontal Alignment

Close-packed monolayers in horizontal alignment from 1D nanocrystals are simple two-dimentional (2D) planar monolayer structures, with all building blocks closely assembled and arranged horizontally with respect to the monolayers. In an ideal scenario, the longitudinal axes of these building blocks are aligned parallel to one common direction to maximize the attractive interactions while maintain the lowest system energy. One typical example of such parallel structures is the Langmuir-Blodgett film (Fig. 2.4a–c); in which all 1D nanocrystals' longitudinal axes are aligned parallel to the barrier when the barrier compresses the air-water interface slowly. The alignment along the 1D nanocrystals' transverse direction, however, enjoys more degrees of freedom. As shown in Fig. 2.9a, the ZnS nanorods in the transverse direction form zigzag staggered rows with neighboring nanorods

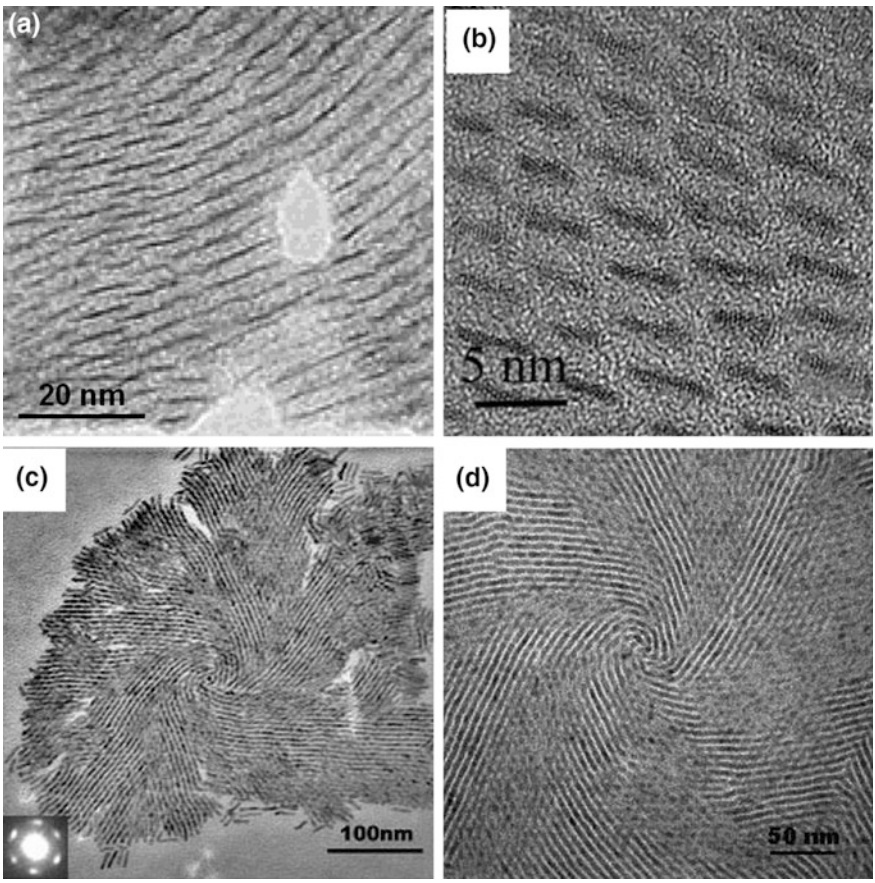

Fig. 2.9 TEM images of horizontally aligned ZnS nanorod monolayer in **a** zigzag staggered structures and **b** layered structures. Reproduced with permission from [137]. **c** TEM and **d** magnified TEM images of horizontally aligned CdSe nanorod monolayer in disclination structures. The *inset* of **c** gives the corresponding SAED pattern. The disclination structure nucleates at the *center* and grows into six branches with angel discontinuity of 60°. Reproduced with permission from [139]

overlapping with each other. This arrangement is sometimes termed as 2D nematic phase (see nematic alignment in 2.3.3 close-packed multilayers for more details). In addition to the zigzag-staggered structures, 1D nanocrystals in the transverse direction can also form ordered rows without overlapping. Showing in Fig. 2.9b, the ends of any ZnS nanorod are evenly spaced with the ends of other nanorods either ahead or behind it [137]. This forms layered structures in the transverse direction and is sometimes termed as 2D smectic phase (see smectic alignment in 2.3.3 close-packed multilayers for more details).

Other than longitudinal axes aligned parallel to one common direction, the self-assembly of 1D nanocrystals in the horizontal alignment can exhibit a disclination structure. It is usually observed as a disruption towards the long-range parallel structures, where the director of individual nanorods/nanowires changes continuously about the center [135]. The disclination structure is initially thought energetically unfavorable and should not occur for the monolayer system. However, Alivisatos's group [139] later observed a disclination structure in a vortex shape with CdSe nanorods. Figure 2.9c showed an isolated vortex-shaped self-assembly, the inset of which gave the corresponding selected area electron diffraction (SAED). The hexagonal spot pattern from SAED indicated a sixfold symmetry of ordering. A magnified image in Fig. 2.9d further revealed CdSe nanorods around the center were separated into six branched, which agreed with SAED pattern. Within each branch, the nanorods were arranged parallel to a common direction and formed a distinct crystalline domain. In-between two adjacent branches, a discontinuity of 60^{o} in nanorod orientation existed. The centers of disclination structures were generally regarded as defects, which served as nucleation sites for the disclination structure to grow.

In the horizontal alignment, the inter-nanocrystal spacing is an important parameter that influences the collective property of the whole assembly. It is shown this spacing affects the coupling between adjacent nanocrystals and therefore coupled plasmon modes that give rise to coherent propagation of energy along the array. When the spacing is well adjusted, the assembled monolayer is able to propagate light along the nanorod–nanorod chain effectively [52, 167]. In general, the inter-nanocrystal spacing remains the same within one horizontally aligned monolayer, even for the 1D nanocrystals aligned differently at the ends. As illustrated in Fig. 2.10a, b [58, 142], two ends of neighboring Au nanorods were either aligned perfectly along the same axis (eclipsed end-to-end, Fig. 2.10a), or had a lateral displacement (staggered end-to-end, Fig. 2.10b). Though these two arrangements were different in organizing the structure, the inter-nanorods spacing between two ends of the Au nanorods were shown to be the same, $\sim$8.5 nm. This spacing also coincided with the distance between two sides of neighboring Au nanorods. The inter-nanocrystal spacing generally remains constant for the same monolayer, but varies for different monolayers. In the case of Langmuir-Blodgett film, the inter-nanocrystal spacing can even be manually controlled through the compression pressure.

Unlike the self-assembly structures from spherical nanocrystals, some horizontally aligned monolayers have exhibited both positional and orientational orders due to their anisotropic building blocks. Zhang et al. have reported a solution-based self-assembly process in which horizontally aligned CoP nanowire monolayers were assembled with the same facet orientation. The CoP nanowires with aspect ratio greater than 40 were self-assembled into monolayers with horizontal alignment. As shown in the Fig. 2.10c, the CoP nanowires were aligned along their longitudinal axes and close-packed with neighboring nanowires. The corresponding FFT in Fig. 2.10d clearly indicated a linear spot diffraction pattern that signified the parallel alignment and same inter-nanowire distance (center to center).

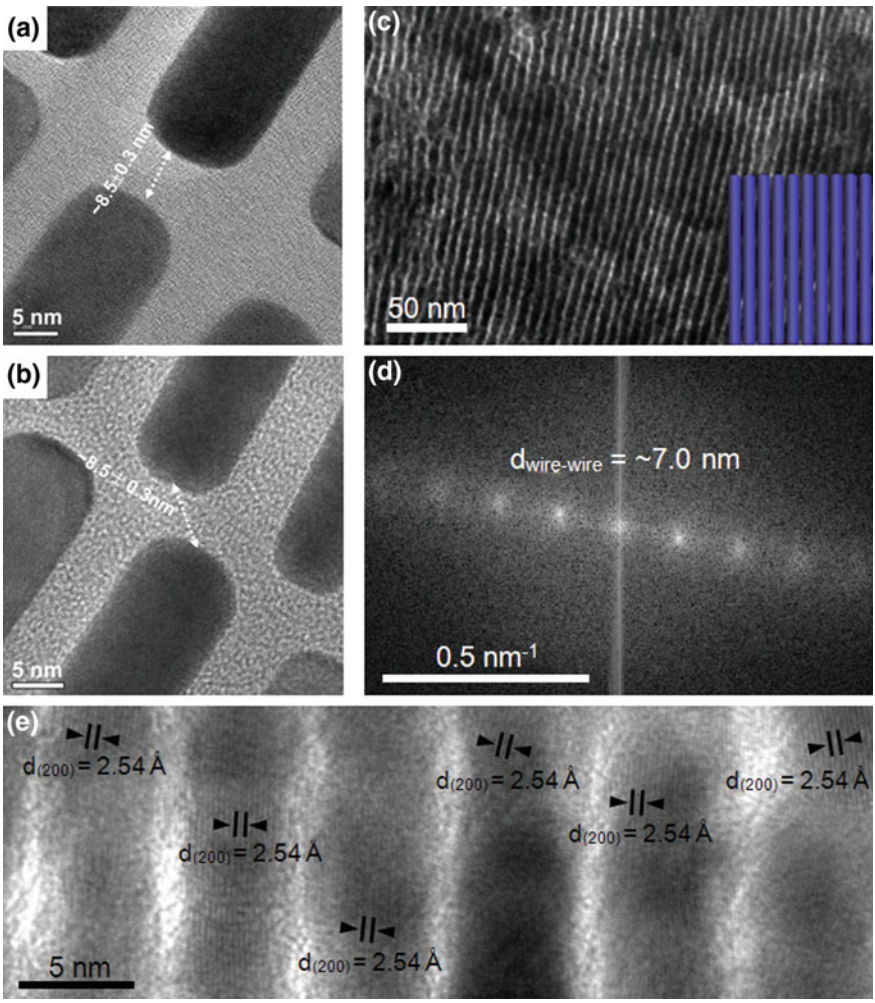

Fig. 2.10 TEM images of horizontally aligned Au nanorod monolayer in **a** eclipsed end-to-end and **b** staggered end-to-end patterns. Reproduced with permission from [142]. **c** TEM and **d** corresponding FFT images of horizontally aligned CoP nanowire monolayer. **e** HRTEM images of six neighboring CoP nanowires, showing uniform lattice orientation from (200) planes. Reproduced with permission from [159]

The HRTEM image revealed that all the (200) planes were parallel in the adjacent CoP nanowires, indicating the oriented attachment of nanowires with the same lattice orientation. This orientational order is particular important for the anisotropic materials, as the collective properties are associated with their anisotropy, e.g. magnetism, can be maintained and even strengthened.

2.3.2.2 Vertical Alignment

Close-packed monolayers in vertical alignment from 1D nanocrystals are three-dimentional (3D) block monolayer structures, with all building blocks closely assembled and arranged vertically with respect to the monolayers. Vertical alignment of nanorods is of special interest because it helps to further minimize the size below the lithographic limit and exhibit single transistor behavior [168]. For a vertically aligned monolayer that perfectly aligned, it possesses a honeycomb structure, as the case in Fig. 2.11a, b. When viewing from top of such monolayer, (Fig. 2.11a), each of the 1D nanocrystals stands perpendicularly to the substrate and is surrounded by six neighboring nanocrystals. These six nanocrystals form a hexagonal pattern, which achieves the highest packing efficiency that is energetically favorable. The lateral arrangement of neighboring nanocrystals is similar to those in horizontally aligned monolayers (Fig. 2.11b), in which the longitudinal axes of these 1D building blocks are aligned parallel to one direction so as to maximize the attractive interactions [157].

Similarly to the horizontally aligned monolayers, some vertically aligned monolayers also possess both positional and orientational orders. Ryan's group [75] has observed the anisotropic CdS nanorods were aligned vertically in the hexagonal shape on a substrate with uniform lattice orientation (Fig. 2.11c–e). The transmission electron diffraction pattern of a single crystal (Fig. 2.11d) revealed its perfect wurtzite crystal structure from [001] zone axis. Close analysis from the HRTEM image in Fig. 2.11e indicated clearly a similar orientation of (100) planes from the vertically aligned nanorods. Only a slight angular variation of ±6 °C was observed for (100) planes from neighboring nanorods that affirmed the orientational ordering. A quantitative assessment of vertically aligned nanocrystals can be further calculated based on the building blocks' orientational ordering. Since the nanocrystals are assembled with uniform lattice orientation, the information of the lattice orientation can be transferred into the information of the nanocrystal orientation. Alivisatos's group has demonstrated an evaluation technique in assessing the percentage of vertically aligned CdS nanorods against entire nanorod population using grazing-incidence wide-angle X-ray diffraction. The longitudinal axes of these wurtzite CdS nanorods coincided with the *c*-axis [001] direction. When the nanorods were aligned vertically as shown in Fig. 2.11f, the diffraction pattern from (002) planes (blue dashed line in Fig. 2.11g) reflected to the top of Bragg ring, which corresponded to the ω direction at 0° (green arrow in Fig. 2.11g). Integrating diffraction intensity of (002) planes as a function of ω gave the orientation distribution, with the ω = 0° refer to the vertically aligned structures. In the case they demonstrated, 75 % nanorods were self-assembled in the vertical alignment [93].

As the vertical and horizontal alignment share similar structure properties, experiment has shown the coexistence of horizontally and vertically aligned structures [30, 169]. A concentration correlation with the packing order has been observed when drying colloidal water droplets containing CdSe nanorods [100, 133]. At a high concentration region (e.g. the center of the droplet), the nanorods are aligned vertically to the substrate. However, at a low concentration

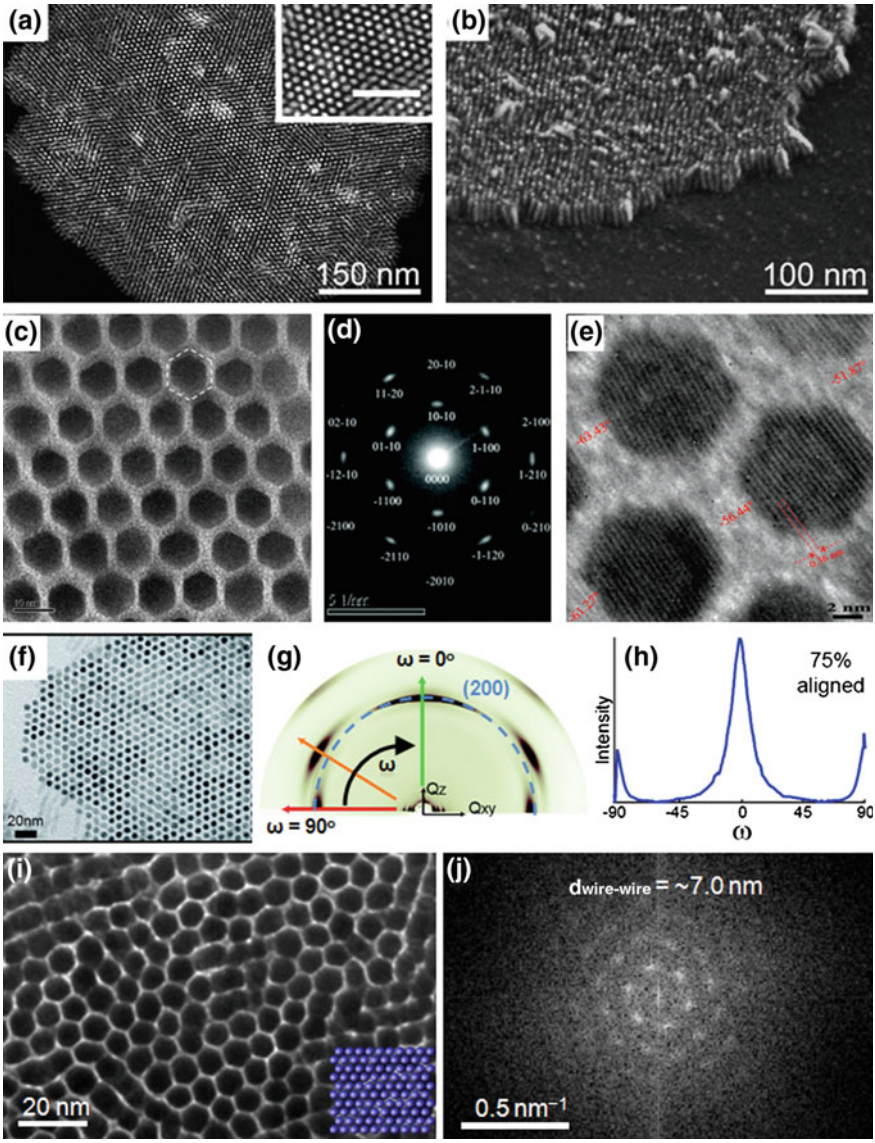

region (e.g. in between the center and periphery of the droplet), the nanorods are aligned horizontally to the substrate. At the lowest concentration region (e.g. the periphery of the droplet), a less-organized structure with nanorods in local ordering is observed. In addition to the coexistence of horizontally and vertically aligned structure, Zhang et al. have demonstrated a selective alignment at different aging temperature. For example, at low aging temperature 0 °C, the CoP nanowires were found to form horizontally aligned monolayers (Fig. 2.10c). While at high aging

◀ **Fig. 2.11** **a** *Dark* field TEM image (*top view*) and **b** SEM image (*side view*) of vertically aligned Au-tipped CdSe nanorod monolayer. The *inset* of **a** shows a magnified image and the *scale bar* represents 50 nm. Reproduced with permission from [157]. **c** TEM image of vertically aligned CdS nanorod monolayer. **d** Single-crystal electron diffraction indexing of one CdS nanorod at [001] zone axis. **e** HRTEM image of three neighboring CdS nanorods, showing uniform lattice orientation from (100) planes. Reproduced with permission from [75]. **f** TEM image and **g** X-ray diffraction pattern of vertically aligned CdS nanorod monolayer. The diffraction from (200) planes is marked by *blue dashed line*. The *green arrow* at $\omega = 0°$ corresponds to vertically aligned nanorods; the *red arrow* at $\omega = 0°$ corresponds to horizontally aligned nanorods. **h** Orientation distribution of vertically aligned CdS nanorods obtained by plotting the diffraction intensity of (002) planes in **g** as a function of ω. Reproduced with permission from [93]. **i** TEM and **j** corresponding FFT images of vertically aligned CoP nanowire monolayer. Reproduced with permission from [159]

temperature, *i.e.* room temperature, the CoP nanowires formed vertically aligned monolayers (Fig. 2.11i). The inter-nanowire distance (center to center) given by the FFT image (Fig. 2.11j) is ~7.0 nm, which was the same as the spacing in the horizontal alignment, suggesting the basic unit of horizontal and vertical alignment was similar.

2.3.3 Close-Packed Multilayers

2.3.3.1 Nematic Alignment

"Nematic" is a common term used primarily in describing the phase of liquid crystals. It refers to the organization of liquid molecules with a long-range orientational order in the longitudinal direction but no translational order. The liquid molecules in nematic liquid crystals are free to flow and randomly distributed as long as they keep the orientational order. Some of close-packed multilayer structures self-assembled from 1D building blocks resemble this ordering; and the term "nematic" has been borrowed to describe such structures. As shown by the SEM image in Fig. 2.12a, a nematic aligned multilayer structure has all longitudinal axes of Au nanorods pointing in the same direction. However, in the transverse direction, there is no periodicity observed for the Au nanorods. The FFT pattern of nematic alignment (Fig. 2.12a inset) also reveals single-direction diffuse streaks, which agrees with the long-range orientational order but no translation order. The nematic alignment can be viewed as the 3D assembly of nanocrystals in two steps. The nanorods/nanowires are first assembled together in an end-to-end pattern to form stripes (chains). These stripes are then packed together, nearly parallel to each other, into a 3D structure [94].

Similar to the liquid crystals, the nematic alignment of 1D nanocrystals is frequently observed in the electric-field-assisted assembly. The anisotropic 1D nanocrystals, especially metal, oxide, sulfide, can be polarized and behave like liquid crystals in the electric filed. When an external electric field is applied to the

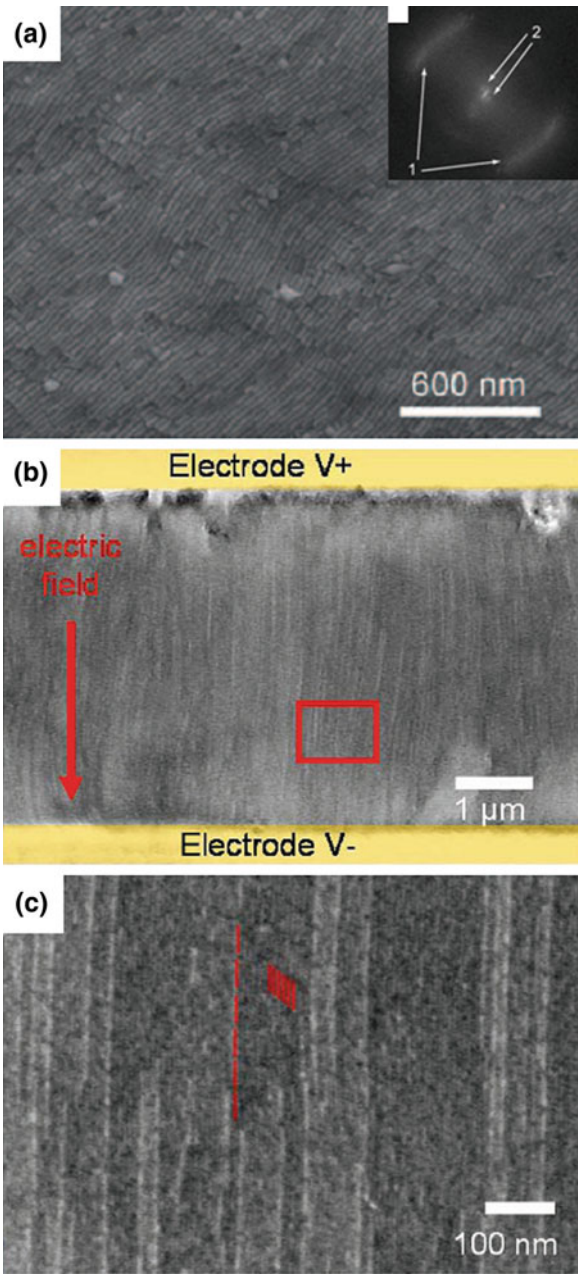

Fig. 2.12 **a** SEM image of Au nanorod multiplayers in nematic alignment. The corresponding FFT pattern in the *inset* shows single-direction diffuse streaks, suggesting only the orientational order but no translational order. Reproduced with permission from [94]. **b**, **c** SEM images of CdSe@CdS nanorod multiplayers in nematic alignment which are self-assembled in the electric field. The *red arrow* in **b** indicates the direction of the electric field, and the *red square* marks the region that is displayed in **c**. Some rods in **b** are highlighted in red as a guide to the eye. Reproduced with permission from [76]

colloidal solution, these polarized 1D nanocrystals tend to orient themselves along the direction of the field and form a nematic aligned structures. An example is illustrated by Manna and his colleagues, where asymmetric core-shell CdSe@CdS

nanorods were self-assembled in the electric field. The nanorods in between the electrodes were aligned uniformly over areas on the scale of tens of micrometers by following the field streamlines (Fig. 2.12b). The magnified view of a selected area (Fig. 2.12c) further indicated the nematic alignment [76]. It has shown that, even with a rather small dipole moment, the presence of sufficient anisotropy in the nanocrystal morphology can induce the ordering in orientation [104].

2.3.3.2 Smectic Alignment

"Smectic" is another term used frequently in liquid crystal field to describing a distinct ordered phase. Molecules in the smectic liquid crystals enjoy a general orientational order in the longitudinal direction like the nematic liquid crystals. In the transverse direction, they tend to organize into well-defined layers and exhibit a translational order. These layers can slide over one another as one entity. However, movement is restricted for molecules to cross the layers. Similar to the term "nematic", "smectic" has also been borrowed to describe some of close-packed multilayer structures from 1D building blocks. The 1D nanocrystals show remarkable similarity to the liquid modules and can be self-assembled into structures resembling smectic liquid crystals. A typical example of smectic aligned nanorods is presented in Fig. 2.13a. The longitudinal axes of Au nanorods are aligned roughly parallel to each other. In the transverse direction, the nanorods form separated layers that positioned to one direction. There is twofold of ordering for the smectic alignment as indicated by two-direction diffuse streaks in the FFT pattern (Fig. 2.13a inset). The parallel alignment of Au nanorods in the longitudinal direction is reflected by two diffuse streaks marked with arrow 3; while the layer-by-layer stacking in the transverse direction is reflected by an orthogonal set of streaks as marked with arrow 4 [94]. Talapin has further elucidated an antiparallel organization for the smectic multilayer structure that based on the attractive dipole interactions. For instance, the CdSe nanorods, which possessed large permanent dipole along the longitudinal axes, were able to be close-packed into smectic multilayers. The attractive dipole interactions were the driving forces and responsible for such alignment. The pairing of dipole moments required an antiparallel organization of neighboring nanorods within a layer and between adjacent layers (Fig. 2.13b) [74]. The Monte Carlo simulations for hard spherocylinders show the antiparallel organization is energetically favorable and can stabilize the smectic alignment. The smectic alignment can also be considered as 3D assembly of nanocrystals in two steps. The nanorods/nanowires are first assembled together in a side-by-side pattern to form layers. These layers are then stacked together, nearly parallel to each other, into a 3D structure.

The smectic alignment shares a lot of similarities with nematic alignment, and often case, both alignments can be achieved with same materials upon a slight change of experiment settings. According to the Onsager's hard-rod model [170, 171], 1D nanocrystals interacting with repulsive forces can display nematic

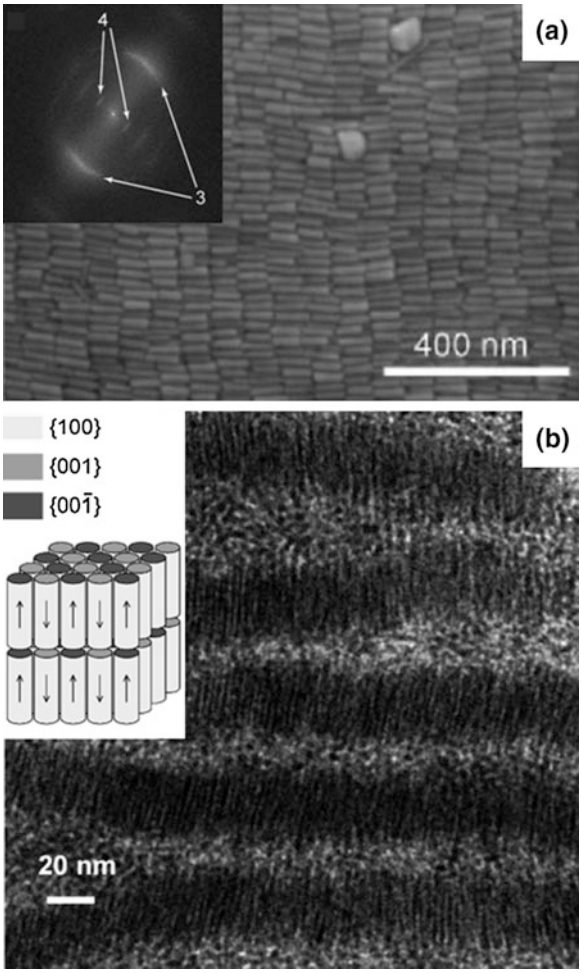

Fig. 2.13 **a** SEM image of Au nanorod multilayers in smectic alignment. The corresponding FFT pattern in the *inset* shows two-direction diffuse streaks, suggesting both orientational and translational order. Reproduced with permission from [94]. **b** TEM image of CdSe nanorod multilayers in smectic alignment. The antiparallel organization of nanorods in the *inset* shows a possible energetically favorable orientation to pair dipole moments both within and across layers. Reproduced with permission from [74]

alignment at low packing density. The anisotropic nanocrystals favor the parallel ordering as it increases the translational entropy by minimizing the excluded volume from the adjacent 1D nanocrystals. The sacrifice of orientational entropy can be compensated by the increase in the translational entropy. Frenkel's later computer simulation has demonstrated upon the increase of packing density, a thermodynamically stable smectic alignment is instead developed in the colloidal system with predominantly repulsive interactions. Apart from the packing density, the formation of nematic or smectic alignment is found experimentally aspect-ratio dependent as well. Long 1D nanocrystals (aspect ratio >7) tend to form nematic alignment while smectic alignment is favorable for short ones [78].

2.3.3.3 AB Stacking of Vertical Alignments

The AB stacking of vertical alignments is a 3D close-packed organization, which is composed of multiple vertically aligned layers that stacked in an end-to-end fashion. The alternating layers in the AB stacking structures have exactly the same organization within layers, however, with a rotational or lateral displacement across layers. The self-assembly of AB stacking structures is considered to start with the formation of individual vertically aligned monolayers. The vertically aligned monolayers are usually in the form of honeycomb structures (see vertical alignment for more details). When depositing such monolayers sequentially, a multilayer is expected which results from the layer-by-layer stacking. The stacking of vertical aligned monolayers maintains their original alignments, but creates diverse 3D arrangements. Typically, 3D stacking of nanorods is routinely observed when the concentration of 1D nanocrystals in solution is high [102]. A four-layer structure is shown in the SEM image in Fig. 2.14. Each layer by itself is an individual continuous 2D planar structure and the rods at the edges are perfectly orthogonal to the substrate, suggesting monolayers are preassembled before the multilayer structures [89]. This is further evidenced in experiments as both monolayers and multilayers are observed at the same time [172]. For AB stacking multilayers TEM images, a typical interference pattern can be observed due to the superimposition from two overlapping vertically aligned honeycomb structures. The AB stacking with a misorientation angle and/or lateral displacement from the two layers is the primary reason in causing such periodic effects when viewing two layers simultaneously in transmission mode. This further manifests a rotational and/or translational movement exist between the AB stacked layers [165].

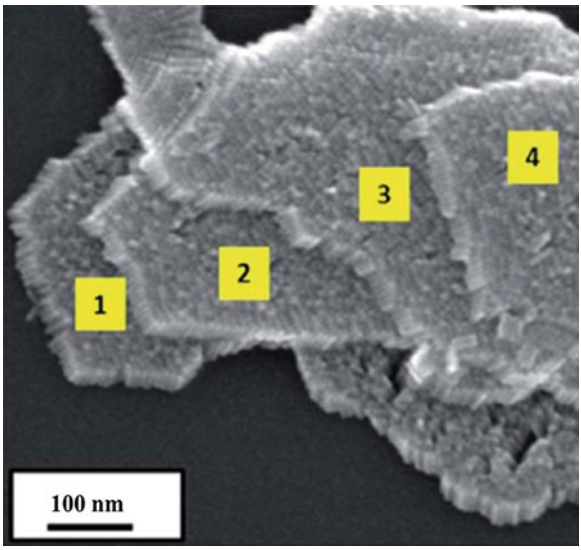

Fig. 2.14 SEM image of a four-layer CdS nanorod structure by AB stacking of vertical alignments. Reproduced with permission from [89]

Many self-assembled multilayer structures are based on a close-packing of building blocks, with the incoming building blocks filling the spaces between the previous assembled ones. For instance, the *fcc* and *hcp* patterns for the spherical nanocrystal self-assemblies are aligned upon one sheet of spheres arranged at the interstices of triangular bases from the underlying sheet. The vertically aligned monolayer, generally, is flat at the top and bottom surfaces and does not have obvious spacing. The 3D stacking pattern of monolayers from 1D nanocrystals therefore possesses more degrees of freedom than spherical building blocks. The incoming layer is less restricted and able to have both rotational and translation movements over the underlying base layer. The actual lateral displacement can be determined from TEM images while the misorientation angle can be obtained with the help from corresponding FFT or SAED patterns. There are generally two sets of spots in the electron diffraction patterns that arise from different orientated layers; and measuring the rotational deviation between them gives the misorientation angle. For honeycomb structures, the hexagonal symmetry in the monolayer means that every 30° rotation is a period. The exact structure of AB stacking of honeycomb structures has been studied comprehensively by Ryan and coworkers using STEM. When there was no offset in the overlapping layers, the TEM image (Fig. 2.15a) remained as a typical honeycomb packing pattern. However, the moiré fringe emerged when a misorientation angle existed between stacked layers (Fig. 2.15b–d). The interference appeared as a repeating hexagonal motif, with the size inversely proportional to the misorientation angle. As the angle offset increased to 29°, near to one period of 30°, a 12-fold ordering was seen (Fig. 2.15d), suggesting the rotational symmetry but no translational symmetry. A different interference pattern occured when a lateral displacement existed between the stacking layers (Fig. 2.15e, f). Only one hexagonal pattern was seen in the FFT pattern (Fig. 2.15e inset), suggesting the hexagonal symmetry of individual monolayer was kept intact, and further confirming the monolayer was preassembled before the stacking [173].

2.3.3.4 3D Assemblies

Other than nematic, smectic and AB stacking of vertical alignments, 1D nanocrystals can be self-assembled into other close-pack multilayer structures, which are termed as 3D assemblies here. 3D assemblies exist in many shapes, such as sphere, cylinder, and are difficult to realize compared with other packing alignments. The studies of complex 3D assemblies started from isotropic building blocks. Han's group has reported an oriented self-assembly of nanoparticles into uniform ellipsoidal structure [174], in which all the building blocks were aligned in the same facet orientation (identical crystallographic directions in all three dimensions). The resultant self-assembly appeared as monocrystalline structure in SEAD and HRTEM investigations. The facile desorption and exchange of capping ligands facilitated direct interactions between nanoparticles and led to orientated attachment of nanoparticle to form ellipsoidal structure.

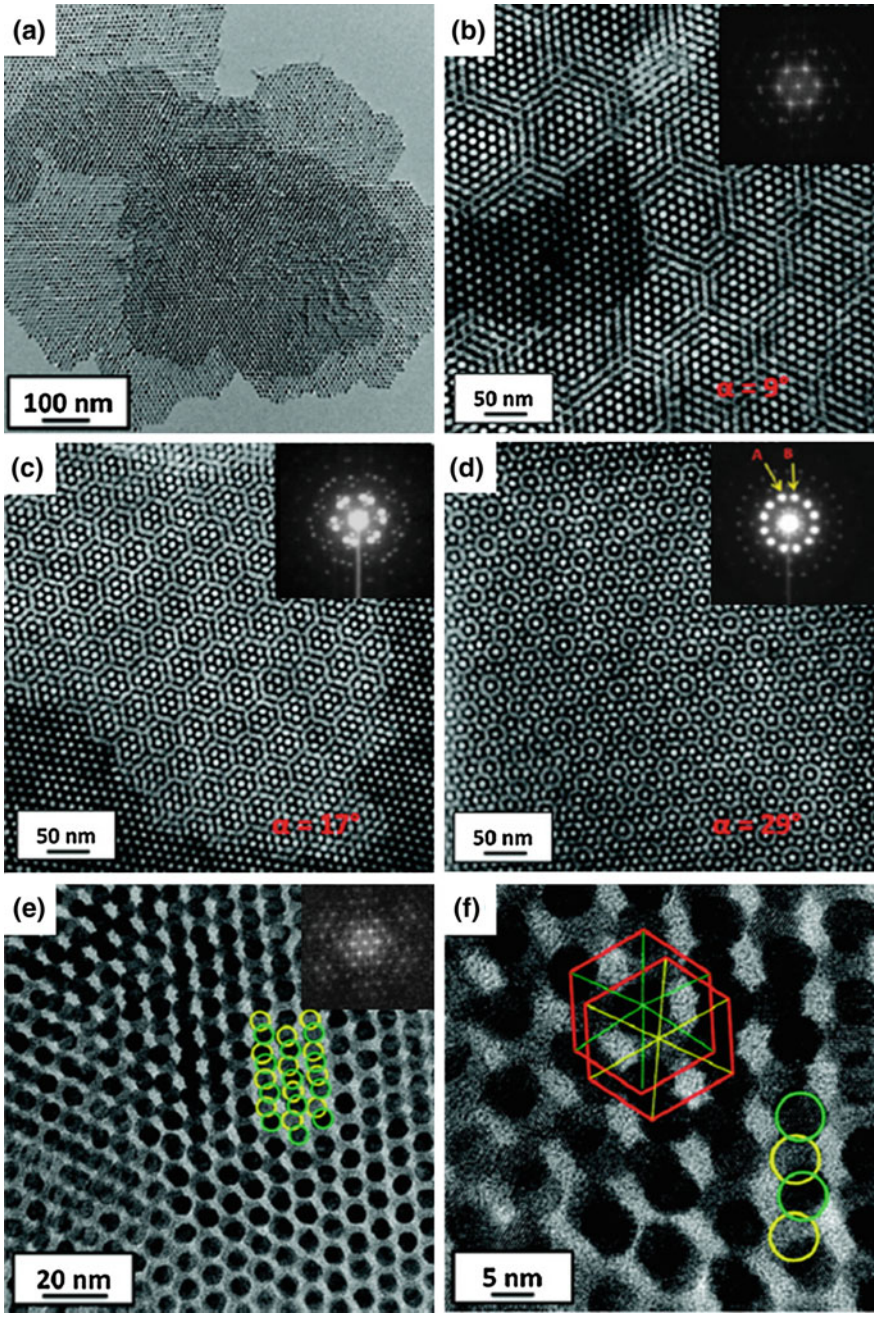
(a)
100 nm
(b)
50 nm
α = 9°
(c)
50 nm
α = 17°
(d)
A
B
50 nm
α = 29°
(e)
20 nm
(f)
5 nm

◀ **Fig. 2.15** TEM images, FFT and SAED patterns of CdS nanorod multiplayers by AB stacking of vertical alignments. **a** TEM images showing honeycomb packing when two layers are stacked perfectly. **b–d** DF-STEM images and corresponding FFT and SAED patterns (*insets*) showing Moiré fringes when two layers are stacked at a misorientation angle: **b** ~9°, **c** ~17°, **d** ~29°. **e**, **f** TEM and HRTEM images showing interference when two layers are stacked with lateral displacement. The FFT in **e** *inset* displays only one set of hexagonal diffraction spots. Reproduced with permission from [173]

Hollow spherical assemblies, such as micelle and vesicle, are one of the common 3D assemblies from 1D building blocks. Kumacheva and coworkers have reported a hollow spherical assembly by using Au nanorods. As shown in Fig. 2.16a, b, the walls of these spheres were composed of a single layer of Au nanorods, and the side-to-side spacing between the nanorods remained approximately at 5.3 nm. The cylindrical surfaces of the Au nanorods were exposed to the surroundings while the two ends were interconnected with neighboring nanorods. Similar to the isotropic building blocks, the surface chemistry played an important role in self-assembling such alignment. Showing in Fig. 2.16a, the cylindrical surfaces of Au nanorods were coated with a double layer of cetyl trimethylammonium bromide (CTAB), while the two ends of nanorods were anchored with thiol-terminated polystyrene molecules. This ligands coating essentially formed a hydrophilic gold nanorod tethered with a hydrophobic homopolymer at both ends. When adding water into the stock solution and incubating, these amphiphilic nanorods tended to interconnect at the ends to reduce the exposure of hydrophobic chain into water. By further assembling into sphere, they could minimize such exposures and interfacial energy, reaching a thermodynamically favored structure [138].

Recently, Cao's group has reported solid self-assembled structures with multiple well-defined supercrystalline domains, which open up new avenues for aligning 1D nanocrystals into more complex structures. These multiple domains structures were self-assembled in solution from highly fluorescent CdSe-CdS nanorods with their configurations and sizes dependent on the total number (N_t) of constituent nanorods

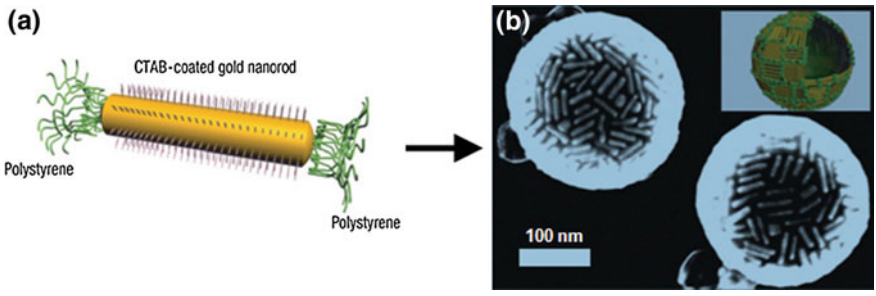

Fig. 2.16 **a** Schematic diagram of polymer-tethered gold nanorods. **b** SEM image of the hollow spherical self-assemblies obtained in the ternary dimethyl formamide/tetrahydrofuran/water mixture. The *inset* shows corresponding schematic diagram of the nanorod assemblies. Reproduced with permission from [138]

inside each self-assembly. For a regular double-domed cylinder structure, N_t needed to be less than ~80,000. Different from above-mentioned self-assembled structures, this double-domed cylinder itself consisted of seven distinct domains: the central cylinder, two domes at the top and bottom of cylinder, and four corners. The cylinder and two domes were comprised of multiple layers in AB stacking of vertical alignments, where the cylinder domain occupied a larger volume than that of corresponding domes. The four corners had their constituent nanorods aligned parallel to the electron beam and therefore these nanorods were seen as dots in the TEM images. In general, the longitudinal axes of nanorods within each domain were aligned parallel to each other, where the longitudinal axes of nanorods from two neighboring domains were aligned perpendicular to each other. The building blocks in this self-assembly possessed certain degrees of freedom (largely due to the rotational freedom around the longitudinal axes) as the corresponding SAED data showing ring or arc patterns. This internal organization of double-domed cylinders was further affirmed by the SAXS data. Two types of peaks were identified and corresponded to: (1) layer-to-layer periodicity from neighboring layers along rod longitudinal direction, (2) rod-to-rod periodicity within the same layer perpendicular to rod longitudinal direction. By varying incubating solvent, Cao's group has also demonstrated the formation of single-domain, needle-like self-assemblies [175, 176].

2.4 Summary and Outlook

In recent years, the self-assembly of 1D nanocrystals have become one of the most prominent fields for the nanoscience research and applications. The ability to organize and integrate small dimensional building blocks into large-area functional assemblies is an indispensible piece in incorporating nanotechnology into practical innovations. The self-assembled structures can possess unique properties that differ from the original building blocks. Different applications based on the optical, electronic, magnetic properties [82] of the self-assemblies are demonstrated. In particular, 1D nanocrystals, due to anisotropic structural properties, exhibit both challenges for self-assembling techniques as well as fascinating properties that appeal broad research interest. 1D nanocrystals, especially nanorods and nanowires, are shown here to be assembled via evaporation-mediated, electric-field-assisted and template-assisted assemblies on substrates. The evaporation-mediated self-assembly can strengthen the relatively weak attraction forces and help 1D nanocrystals aggregate together to minimize the free energy. The electric-field-assisted and template-assisted assembly is able to make use of external facilitations and induce building blocks orientated according to electric fields or template constrains. In the case of self-assembly at interfaces, the alignment of 1D nanocrystals leads to a reduction of total interfacial energy and drives them into ordered structures. The self-assembly in solutions is also demonstrated, which utilizes the chemical interactions in between 1D nanocrystals, capping ligands and solvents. Distinct from

isotropic building blocks, the self-assemblies of 1D nanocrystals display a number of different assembled structures. The 1D nanocrystals can form non-close-packed structures, such as stripes in both end-to-end and side-by-side alignments. The close-packed structures, in the other hand, exist in the form of monolayers or multilayers. A horizontal or vertical alignment is observed for the basic monolayer assemblies; while nematic, smectic, AB stacking of vertical alignments, and 3D assemblies are seen for the organization of 1D nanocrystals into multilayer structures. The self-assembly of 1D nanocrystals has gradually evolved into a versatile tool that could ultimately form tailored structures using specific approaches.

Looking ahead, the self-assembly of 1D nanocrystals will be the next step of nanofabrication for future technological innovations. It is a bottom up approach that is inexpensive and operates at smaller dimensions than current lithography based techniques. However, comparing to the patterned structures that built upon lithography, the self-assembled structures are prone to defects and the sizes of most assemblies are limited to micrometer range. The abilities to create centimeter-scale and defect-free nanocrystals assemblies are crucial for the development of reliable devices and shall be major focus in industrial applications. Meanwhile, the current self-assembly methods require the building blocks to be mono-dispersed. The restriction on the uniformity hinders the assembling of 1D nanocrystals with different sizes and shapes. The early attempts on binary 1D building blocks reported so far, usually find a phase separation of binary mixture instead of blended self-assembled patterns [94, 137, 177]. The fields that self-assemble two or more components with different chemical compositions still remain unexplored. A patterned structure with different chemical compositions now can only be obtained from physical methods, e.g, lithography, nanoimprinting. In addition, self-assembly of 1D nanocrystals utilizing magnetic field has seldom been reported. As a comparison, spherical nanoparticles are often demonstrated to be aligned in the external magnetic field. The 1D nanocrystals, due to the shape anisotropy, actually induce magnetic anisotropy that would open a new window to self-assemble 1D building blocks. In general, the self-assembly of 1D nanocrystals is still at its early stage of research and needs a better understanding towards the assembly mechanisms and structure-property relationships. Further comprehensive studies are required to find out simple and versatile methods that can create complicated, large-scale and defect-free self-assembled functional hierarchical architectures.

References

1. V.F. Puntes, K.M. Krishnan, A.P. Alivisatos, Colloidal nanocrystal shape and size control: the case of cobalt. Science **291**, 2115–2117 (2001)
2. J.J. Li, Y.A. Wang, W. Guo, J.C. Keay, T.D. Mishima, M.B. Johnson, X. Peng, Large-scale synthesis of nearly monodisperse CdSe/CdS core/shell nanocrystals using air-stable reagents via successive ion layer adsorption and reaction. J. Am. Chem. Soc. **125**, 12567–12575 (2003)

3. X. Wang, J. Zhuang, Q. Peng, Y. Li, A general strategy for nanocrystal synthesis. Nature **437**, 121–124 (2005)
4. Y. Yin, A.P. Alivisatos, Colloidal nanocrystal synthesis and the organic-inorganic interface. Nature **437**, 664–670 (2005)
5. Y. Xia, Y. Xiong, B. Lim, S.E. Skrabalak, Shape-controlled synthesis of metal nanocrystals: simple chemistry meets complex physics? Angew. Chem. Int. Ed. **48**, 60–103 (2009)
6. Z. Zhuang, Q. Peng, Y. Li, Controlled synthesis of semiconductor nanostructures in the liquid phase. Chem. Soc. Rev. **40**, 5492–5513 (2011)
7. K. Zhou, Y. Li, Catalysis based on nanocrystals with well-defined facets. Angew. Chem. Int. Ed. **51**, 602–613 (2012)
8. E. Ye, S.-Y. Zhang, S.H. Lim, M. Bosman, Z. Zhang, K.Y. Win, M.-Y. Han, Ternary Cobalt–iron phosphide nanocrystals with controlled compositions, properties, and morphologies from nanorods and nanorice to split nanostructures. Chem. Eur. J. **17**, 5982–5988 (2011)
9. S.-Y. Zhang, M.D. Regulacio, K.W. Shah, T. Sreethawong, Y. Zheng, M.-Y. Han, Colloidal preparation of monodisperse nanocrystals. J. Mol. Eng. Mater. **2**, 1430001 (2014)
10. P. Moriarty, Nanostructured materials. Rep. Prog. Phys. **64**, 297 (2001)
11. C.N.R. Rao, A.K. Cheetham, Science and technology of nanomaterials: current status and future prospects. J. Mater. Chem. **11**, 2887–2894 (2001)
12. M. Law, J. Goldberger, P. Yang, Semiconductor nanowires and nanotubes. Annu. Rev. Mater. Res. **34**, 83–122 (2004)
13. P.D. Cozzoli, T. Pellegrino, L. Manna, Synthesis, properties and perspectives of hybrid nanocrystal structures. Chem. Soc. Rev. **35**, 1195–1208 (2006)
14. Z.W. Seh, S. Liu, S.-Y. Zhang, M.S. Bharathi, H. Ramanarayan, M. Low, K.W. Shah, Y.-W. Zhang, M.-Y. Han, Anisotropic growth of titania onto various gold nanostructures: synthesis, theoretical understanding, and optimization for catalysis. Angew. Chem. Int. Ed. **50**, 10140–10143 (2011)
15. Z.W. Seh, S. Liu, S.-Y. Zhang, K.W. Shah, M.-Y. Han, Synthesis and multiple reuse of eccentric Au@TiO_2 nanostructures as catalysts. Chem. Commun. **47**, 6689–6691 (2011)
16. G. Wang, Q. Peng, Y. Li, Lanthanide-doped nanocrystals: synthesis, optical-magnetic properties, and applications. Acc. Chem. Res. **44**, 322–332 (2011)
17. G. Guan, S.-Y. Zhang, Y. Cai, S. Liu, M.S. Bharathi, M. Low, Y. Yu, J. Xie, Y. Zheng, Y.-W. Zhang, M.-Y. Han, Convenient purification of gold clusters by co-precipitation for improved sensing of hydrogen peroxide, mercury ions and pesticides. Chem. Commun. **50**, 5703–5705 (2014)
18. T. Sreethawong, K.W. Shah, S.-Y. Zhang, E. Ye, S.H. Lim, U. Maheswaran, W.Y. Mao, M.-Y. Han, Optimized production of copper nanostructures with high yields for efficient use as thermal conductivity-enhancing PCM dopant. J. Mater. Chem. A **2**, 3417–3423 (2014)
19. C.L. Choi, A.P. Alivisatos, From artificial atoms to nanocrystal molecules: preparation and properties of more complex nanostructures. Annu. Rev. Phys. Chem. **61**, 369–389 (2010)
20. M. Grzelczak, J. Vermant, E.M. Furst, L.M. Liz-Marzán, Directed self-assembly of nanoparticles. ACS Nano **4**, 3591–3605 (2010)
21. M.P. Pileni, Inorganic nanocrystals self ordered in 2D superlattices: how versatile are the physical and chemical properties? Phys. Chem. Chem. Phys. **12**, 11821–11835 (2010)
22. Z. Quan, J. Fang, Superlattices with non-spherical building blocks. Nano Today **5**, 390–411 (2010)
23. M.R. Jones, K.D. Osberg, R.J. Macfarlane, M.R. Langille, C.A. Mirkin, Templated techniques for the synthesis and assembly of plasmonic nanostructures. Chem. Rev. **111**, 3736–3827 (2011)
24. T. Wang, D. LaMontagne, J. Lynch, J. Zhuang, Y.C. Cao, Colloidal superparticles from nanoparticle assembly. Chem. Soc. Rev. **42**, 2804–2823 (2013)
25. S.-Y. Zhang, M.D. Regulacio, M.-Y. Han, Self-assembly of colloidal one-dimensional nanocrystals. Chem. Soc. Rev. **43**, 2301–2323 (2014)

26. P. Bartlett, R.H. Ottewill, P.N. Pusey, Superlattice formation in binary mixtures of hard-sphere colloids. Phys. Rev. Lett. **68**, 3801–3804 (1992)
27. C.P. Collier, T. Vossmeyer, J.R. Heath, Nanocrystal superlattices. Annu. Rev. Phys. Chem. **49**, 371–404 (1998)
28. C.B. Murray, C.R. Kagan, M.G. Bawendi, Snthesis and characterization of monodisperse nanocrystals and close-packed nanocrystal assemblies. Annu. Rev. Mater. Sci. **30**, 545–610 (2000)
29. T.K. Sau, C.J. Murphy, Self-assembly patterns formed upon solvent evaporation of aqueous cetyltrimethylammonium bromide-coated gold nanoparticles of various shapes. Langmuir **21**, 2923–2929 (2005)
30. K.C. Ng, I.B. Udagedara, I.D. Rukhlenko, Y. Chen, Y. Tang, M. Premaratne, W. Cheng, Free-standing plasmonic-nanorod superlattice sheets. ACS Nano **6**, 925–934 (2012)
31. T.S. Ahmadi, Z.L. Wang, T.C. Green, A. Henglein, M.A. El-Sayed, Shape-controlled synthesis of colloidal platinum nanoparticles. Science **272**, 1924–1925 (1996)
32. M. Brust, M. Walker, D. Bethell, D.J. Schiffrin, R. Whyman, Synthesis of thiol-derivatised gold nanoparticles in a two-phase Liquid-Liquid system. J. Chem. Soc. Chem. Commun. **1994**, 801–802 (1994)
33. M.-C. Daniel, D. Astruc, Gold nanoparticles: Assembly, supramolecular chemistry, quantum-size-related properties, and applications toward biology, catalysis, and nanotechnology. Chem. Rev. **104**, 293–346 (2004)
34. S. Sun, C.B. Murray, D. Weller, L. Folks, A. Moser, Monodisperse FePt nanoparticles and ferromagnetic FePt nanocrystal superlattices. Science **287**, 1989–1992 (2000)
35. Y. Sun, Y. Xia, Shape-controlled synthesis of gold and silver nanoparticles. Science **298**, 2176–2179 (2002)
36. S.-H. Liu, H. Gao, E. Ye, M. Low, S.H. Lim, S.-Y. Zhang, X. Lieu, S. Tripathy, W. Tremel, M.-Y. Han, Graphitically encapsulated cobalt nanocrystal assemblies. Chem. Commun. **46**, 4749–4751 (2010)
37. E. Ye, S.-Y. Zhang, S. Liu, M.-Y. Han, Disproportionation for growing copper nanowires and their controlled self-assembly facilitated by ligand exchange. Chem. Eur. J. **17**, 3074–3077 (2011)
38. M. Bruchez, M. Moronne, P. Gin, S. Weiss, A.P. Alivisatos, Semiconductor nanocrystals as fluorescent biological labels. Science **281**, 2013–2016 (1998)
39. T. Trindade, P. O'Brien, N.L. Pickett, Nanocrystalline semiconductors: synthesis, properties, and perspectives. Chem. Mater. **13**, 3843–3858 (2001)
40. E.A. Meulenkamp, Synthesis and growth of ZnO nanoparticles. J. Phys. Chem. B **102**, 5566–5572 (1998)
41. S. Sun, H. Zeng, Size-controlled synthesis of magnetite nanoparticles. J. Am. Chem. Soc. **124**, 8204–8205 (2002)
42. E. Ye, S.-Y. Zhang, S.H. Lim, S. Liu, M.-Y. Han, Morphological tuning, self-assembly and optical properties of indium oxide nanocrystals. Phys. Chem. Chem. Phys. **12**, 11923–11929 (2010)
43. S. Vaucher, M. Li, S. Mann, Synthesis of prussian blue nanoparticles and nanocrystal superlattices in reverse microemulsions. Angew. Chem. Int. Ed. **39**, 1793–1796 (2000)
44. C.R. Martin, Nanomaterials: a membrane-based synthetic approach. Science **266**, 1961–1966 (1994)
45. A. Stein, R.C. Schroden, Colloidal crystal templating of three-dimensionally ordered macroporous solids: materials for photonics and beyond. Curr. Opin. Solid State Mater. Sci. **5**, 553–564 (2001)
46. B. Amir Parviz, D. Ryan, and G.M. Whitesides, Using self-assembly for the fabrication of nano-scale electronic and photonic devices. IEEE Trans. Adv. Pack. **26**, 233–241 (2003)
47. C.J. Murphy, T.K. Sau, A.M. Gole, C.J. Orendorff, J. Gao, L. Gou, S.E. Hunyadi, T. Li, Anisotropic metal nanoparticles: synthesis, assembly, and optical applications. J. Phys. Chem. B **109**, 13857–13870 (2005)

48. C. Nobile, V.A. Fonoberov, S. Kudera, A. Della Torre, A. Ruffino, G. Chilla, T. Kipp, D. Heitmann, L. Manna, R. Cingolani, A.A. Balandin, R. Krahne, Confined optical phonon modes in aligned nanorod arrays detected by resonant inelastic light scattering. Nano Lett. **7**, 476–479 (2007)
49. A. Rizzo, C. Nobile, M. Mazzeo, M.D. Giorgi, A. Fiore, L. Carbone, R. Cingolani, L. Manna, G. Gigli, Polarized light emitting diode by long-range nanorod self-assembling on a water surface. ACS Nano **3**, 1506–1512 (2009)
50. D. Vennerberg, Z. Lin, Upconversion nanocrystals: synthesis, properties, assembly and applications. Sci. Adv. Mater. **3**, 26–40 (2011)
51. S.A. Maier, M.L. Brongersma, P.G. Kik, S. Meltzer, A.A. G. Requicha, B.E. Koel, H.A. Atwater, Plasmonics—a route to nanoscale optical devices (Adv. Mater. **13**, 1501 (2001)), Adv. Mater. (Weinheim, Ger.) **15**, 562–562 (2003)
52. S.A. Maier, P.G. Kik, H.A. Atwater, S. Meltzer, E. Harel, B.E. Koel, A.A.G. Requicha, Local detection of electromagnetic energy transport below the diffraction limit in metal nanoparticle plasmon waveguides. Nat. Mater. **2**, 229–232 (2003)
53. M. Rycenga, C.M. Cobley, J. Zeng, W. Li, C.H. Moran, Q. Zhang, D. Qin, Y. Xia, Controlling the synthesis and assembly of silver nanostructures for plasmonic applications. Chem. Rev. **111**, 3669–3712 (2011)
54. A. Tao, F. Kim, C. Hess, J. Goldberger, R. He, Y. Sun, Y. Xia, P. Yang, Langmuir–Blodgett silver nanowire monolayers for molecular sensing using surface-enhanced Raman spectroscopy. Nano Lett. **3**, 1229–1233 (2003)
55. J. Fang, S. Du, S. Lebedkin, Z. Li, R. Kruk, M. Kappes, H. Hahn, Gold mesostructures with tailored surface topography and their self-assembly arrays for surface-enhanced Raman spectroscopy. Nano Lett. **10**, 5006–5013 (2010)
56. A. Chen, A.E. DePrince, A. Demortière, A. Joshi-Imre, E.V. Shevchenko, S.K. Gray, U. Welp, V.K. Vlasko-Vlasov, Self-assembled large Au nanoparticle arrays with regular hot spots for SERS. Small **7**, 2365–2371 (2011)
57. X.-Z. Shi, C.-M. Shen, D.-K. Wang, C. Li, Y. Tian, Z.-C. Xu, C.-M. Wang, H.-J. Gao, Surface-enhanced Raman scattering properties of highly ordered self-assemblies of gold nanorods with different aspect ratios. Chin. Phys. B **20**, 076103 (2011)
58. T.S. Sreeprasad, T. Pradeep, Reversible assembly and disassembly of gold nanorods induced by EDTA and its application in SERS tuning. Langmuir **27**, 3381–3390 (2011)
59. Z. Zhu, H. Meng, W. Liu, X. Liu, J. Gong, X. Qiu, L. Jiang, D. Wang, Z. Tang, Superstructures and SERS properties of gold nanocrystals with different shapes. Angew. Chem. Int. Ed. **50**, 1593–1596 (2011)
60. S. Sun, C.B. Murray, Synthesis of monodisperse cobalt nanocrystals and their assembly into magnetic superlattices. J. Appl. Phys. **85**, 4325–4330 (1999)
61. S. Behrens, Preparation of functional magnetic nanocomposites and hybrid materials: recent progress and future directions. Nanoscale **3**, 877–892 (2011)
62. D. Whang, S. Jin, Y. Wu, C.M. Lieber, Large-scale hierarchical organization of nanowire arrays for integrated nanosystems. Nano Lett. **3**, 1255–1259 (2003)
63. D.V. Talapin, J.-S. Lee, M.V. Kovalenko, E.V. Shevchenko, Prospects of colloidal nanocrystals for electronic and optoelectronic applications. Chem. Rev. **110**, 389–458 (2010)
64. I.J. Kramer, E.H. Sargent, Colloidal quantum dot photovoltaics: a path forward. ACS Nano **5**, 8506–8514 (2011)
65. Z.-Y. Zhou, N. Tian, J.-T. Li, I. Broadwell, S.-G. Sun, Nanomaterials of high surface energy with exceptional properties in catalysis and energy storage. Chem. Soc. Rev. **40**, 4167–4185 (2011)
66. W. Lu, J. Fang, K.L. Stokes, J. Lin, Shape evolution and self assembly of monodisperse PbTe nanocrystals. J. Am. Chem. Soc. **126**, 11798–11799 (2004)
67. J. Zhang, A. Kumbhar, J. He, N.C. Das, K. Yang, J.-Q. Wang, H. Wang, K.L. Stokes, J. Fang, Simple cubic super crystals containing PbTe nanocubes and their core–shell building blocks. J. Am. Chem. Soc. **130**, 15203–15209 (2008)

68. L. Motte, F. Billoudet, E. Lacaze, M.-P. Pileni, Self-organization of size-selected, nanoparticles into three-dimensional superlattices. Adv. Mater. **8**, 1018–1020 (1996)
69. T. Mokari, M. Zhang, P. Yang, Shape, size, and assembly control of PbTe nanocrystals. J. Am. Chem. Soc. **129**, 9864–9865 (2007)
70. J. Zhuang, H. Wu, Y. Yang, Y.C. Cao, Supercrystalline colloidal particles from artificial atoms. J. Am. Chem. Soc. **129**, 14166–14167 (2007)
71. A. Demortière, P. Launois, N. Goubet, P.A. Albouy, C. Petit, Shape-controlled platinum nanocubes and their assembly into two-dimensional and three-dimensional superlattices. J. Phys. Chem. B **112**, 14583–14592 (2008)
72. M. Pang, H.C. Zeng, Highly ordered self-assemblies of submicrometer Cu_2O spheres and their hollow chalcogenide derivatives. Langmuir **26**, 5963–5970 (2010)
73. K.X. Yao, X.M. Yin, T.H. Wang, H.C. Zeng, Synthesis, self-assembly, disassembly, and reassembly of two types of Cu_2O nanocrystals unifaceted with 001 or 110 planes. J. Am. Chem. Soc. **132**, 6131–6144 (2010)
74. D.V. Talapin, E.V. Shevchenko, C.B. Murray, A. Kornowski, S. Förster, H. Weller, CdSe and CdSe/CdS nanorod solids. J. Am. Chem. Soc. **126**, 12984–12988 (2004)
75. S. Ahmed, K.M. Ryan, Self-assembly of vertically aligned nanorod supercrystals using highly oriented pyrolytic graphite. Nano Lett. **7**, 2480–2485 (2007)
76. L. Carbone, C. Nobile, M. De Giorgi, F.D. Sala, G. Morello, P. Pompa, M. Hytch, E. Snoeck, A. Fiore, I.R. Franchini, M. Nadasan, A.F. Silvestre, L. Chiodo, S. Kudera, R. Cingolani, R. Krahne, L. Manna, Synthesis and micrometer-scale assembly of colloidal CdSe/CdS nanorods prepared by a seeded growth approach. Nano Lett. **7**, 2942–2950 (2007)
77. W. Lu, Q. Liu, Z. Sun, J. He, C. Ezeolu, J. Fang, Super crystal structures of octahedral c-In_2O_3 nanocrystals. J. Am. Chem. Soc. **130**, 6983–6991 (2008)
78. N.R. Jana, Shape effect in nanoparticle self-assembly. Angew. Chem. Int. Ed. **43**, 1536–1540 (2004)
79. C.B. Murray, S. Sun, W. Gaschler, H. Doyle, T.A. Betley, C.R. Kagan, Colloidal synthesis of nanocrystals and nanocrystal superlattices. IBM J. Res. Dev. **45**, 47–56 (2001)
80. M.P. Pileni, Nanocrystal self-assemblies: fabrication and collective properties. J. Phys. Chem. B **105**, 3358–3371 (2001)
81. A.L. Rogach, D.V. Talapin, E.V. Shevchenko, A. Kornowski, M. Haase, H. Weller, Organization of matter on different size scales: monodisperse nanocrystals and their superstructures. Adv. Funct. Mater. **12**, 653–664 (2002)
82. S. Kinge, M. Crego-Calama, D.N. Reinhoudt, Self-assembling nanoparticles at surfaces and interfaces. ChemPhysChem **9**, 20–42 (2008)
83. Y. Min, M. Akbulut, K. Kristiansen, Y. Golan, J. Israelachvili, The role of interparticle and external forces in nanoparticle assembly. Nat. Mater. **7**, 527–538 (2008)
84. Y. Ofir, B. Samanta, V.M. Rotello, Polymer and biopolymer mediated self-assembly of gold nanoparticles. Chem. Soc. Rev. **37**, 1814–1825 (2008)
85. K.J.M. Bishop, C.E. Wilmer, S. Soh, B.A. Grzybowski, Nanoscale forces and their uses in self-assembly. Small **5**, 1600–1630 (2009)
86. Y. Nagaoka, O. Chen, Z. Wang, Y.C. Cao, Structural control of nanocrystal superlattices using organic guest molecules. J. Am. Chem. Soc. **134**, 2868–2871 (2012)
87. T. Wang, X. Wang, D. LaMontagne, Z. Wang, Z. Wang, Y.C. Cao, Shape-controlled synthesis of colloidal superparticles from nanocubes. J. Am. Chem. Soc. **134**, 18225–18228 (2012)
88. M.D. Bentzon, J. van Wonterghem, S. Mørup, A. Thölén, C.J.W. Koch, Ordered aggregates of ultrafine iron oxide particles: 'super crystals'. Philos. Mag. B **60**, 169–178 (1989)
89. A. Singh, R.D. Gunning, S. Ahmed, C.A. Barrett, N.J. English, J.-A. Garate, K.M. Ryan, Controlled semiconductor nanorod assembly from solution: influence of concentration, charge and solvent nature. J. Mater. Chem. **22**, 1562–1569 (2012)
90. W.M. Gelbart, R.P. Sear, J.R. Heath, S. Chaney, Array formation in nano-colloids: theory and experiment in 2D. Faraday Discuss. **112**, 299–307 (1999)

91. E. Rabani, D.R. Reichman, P.L. Geissler, L.E. Brus, Drying-mediated self-assembly of nanoparticles. Nature **426**, 271–274 (2003)
92. G. Yosef, E. Rabani, Self-assembly of nanoparticles into rings: a lattice-gas model. J. Phys. Chem. B **110**, 20965–20972 (2006)
93. J.L. Baker, A. Widmer-Cooper, M.F. Toney, P.L. Geissler, A.P. Alivisatos, Device-scale perpendicular alignment of colloidal nanorods. Nano Lett. **10**, 195–201 (2010)
94. T. Ming, X. Kou, H. Chen, T. Wang, H.-L. Tam, K.-W. Cheah, J.-Y. Chen, J. Wang, Ordered gold nanostructure assemblies formed by droplet evaporation. Angew. Chem. Int. Ed. **47**, 9685–9690 (2008)
95. D. Bargeman, F. van Voorst Vader, Van der waals forces between immersed particles, J. Electr. Chem. Interf. Electrochem. **37**, 45–52 (1972)
96. B. Nikoobakht, Z.L. Wang, M.A. El-Sayed, Self-assembly of gold nanorods. J. Phys. Chem. B **104**, 8635–8640 (2000)
97. J. Kleinert, S. Kim, O.D. Velev, Electric-field-assisted convective assembly of colloidal crystal coatings. Langmuir **26**, 10380–10385 (2010)
98. P.A. Smith, C.D. Nordquist, T.N. Jackson, T.S. Mayer, B.R. Martin, J. Mbindyo, T.E. Mallouk, Electric-field assisted assembly and alignment of metallic nanowires. Appl. Phys. Lett. **77**, 1399–1401 (2000)
99. O. Harnack, C. Pacholski, H. Weller, A. Yasuda, J.M. Wessels, Rectifying behavior of electrically aligned ZnO nanorods. Nano Lett. **3**, 1097–1101 (2003)
100. S. Gupta, Q. Zhang, T. Emrick, T.P. Russell, "Self-corralling" nanorods under an applied electric field. Nano Lett. **6**, 2066–2069 (2006)
101. Z. Hu, M.D. Fischbein, C. Querner, M. Drndić, Electric-field-driven accumulation and alignment of CdSe and CdTe nanorods in nanoscale devices. Nano Lett. **6**, 2585–2591 (2006)
102. K.M. Ryan, A. Mastroianni, K.A. Stancil, H. Liu, A.P. Alivisatos, Electric-field-assisted assembly of perpendicularly oriented nanorod superlattices. Nano Lett. **6**, 1479–1482 (2006)
103. M. Mittal, E.M. Furst, Electric field-directed convective assembly of ellipsoidal colloidal particles to create optically and mechanically anisotropic thin films. Adv. Funct. Mater. **19**, 3271–3278 (2009)
104. M. Zorn, M.N. Tahir, B. Bergmann, W. Tremel, C. Grigoriadis, G. Floudas, R. Zentel, Orientation and dynamics of ZnO nanorod liquid crystals in electric fields. Macromol. Rapid Commun. **31**, 1101–1107 (2010)
105. G. Michael, H. Michael, The preparation of ordered colloidal magnetic particles by magnetophoretic deposition. J. Phys. D Appl. Phys. **32**, L111 (1999)
106. J.O.M. Bockris, A.K.N. Reddy, M. Gamboa-Aldeco, M.E. Gamboa-Aldeco, *Modern Electrochemistry.* Springer, 2000
107. T. Vossmeyer, E. DeIonno, J.R. Heath, Light-directed assembly of nanoparticles. Angew. Chem. Int. Ed. Engl. **36**, 1080–1083 (1997)
108. T. Vossmeyer, S. Jia, E. DeIonno, M.R. Diehl, S.-H. Kim, X. Peng, A.P. Alivisatos, J.R. Heath, Combinatorial approaches toward patterning nanocrystals. J. Appl. Phys. **84**, 3664–3670 (1998)
109. H.X. He, H. Zhang, Q.G. Li, T. Zhu, S.F.Y. Li, Z.F. Liu, Fabrication of designed architectures of Au nanoparticles on solid substrate with printed self-assembled monolayers as templates. Langmuir **16**, 3846–3851 (2000)
110. F. Fan, K.J. Stebe, Size-selective deposition and sorting of lyophilic colloidal particles on surfaces of patterned wettability. Langmuir **21**, 1149–1152 (2005)
111. A. Akey, C. Lu, L. Yang, I.P. Herman, Formation of thick, large-area nanoparticle superlattices in lithographically defined geometries. Nano Lett. **10**, 1517–1521 (2010)
112. M. Artemyev, B. Möller, U. Woggon, Unidirectional alignment of CdSe nanorods. Nano Lett. **3**, 509–512 (2003)
113. S. Liu, J.B.H. Tok, J. Locklin, Z. Bao, Assembly and alignment of metallic nanorods on surfaces with patterned wettability. Small **2**, 1448–1453 (2006)

114. Q. Zhang, S. Gupta, T. Emrick, T.P. Russell, Surface-functionalized CdSe nanorods for assembly in diblock copolymer templates. J. Am. Chem. Soc. **128**, 3898–3899 (2006)
115. C. Hamon, M. Postic, E. Mazari, T. Bizien, C. Dupuis, P. Even-Hernandez, A. Jimenez, L. Courbin, C. Gosse, F. Artzner, V. Marchi-Artzner, Three-dimensional self-assembling of gold nanorods with controlled macroscopic shape and local smectic B order. ACS Nano **6**, 4137–4146 (2012)
116. C. Kuemin, L. Nowack, L. Bozano, N.D. Spencer, H. Wolf, Oriented assembly of gold nanorods on the single-particle level. Adv. Funct. Mater. **22**, 702–708 (2012)
117. A.P. Alivisatos, K.P. Johnsson, X. Peng, T.E. Wilson, C.J. Loweth, M.P. Bruchez, P.G. Schultz, Organization of 'nanocrystal molecules' using DNA. Nature **382**, 609–611 (1996)
118. E. Dujardin, L.-B. Hsin, C.R.C. Wang, S. Mann, DNA-driven self-assembly of gold nanorods. Chem. Commun. **2001**, 1264–1265 (2001)
119. B. Pan, L. Ao, F. Gao, H. Tian, R. He, D. Cui, End-to-end self-assembly and colorimetric characterization of gold nanorods and nanospheres via oligonucleotide hybridization. Nanotechnology **16**, 1776 (2005)
120. B. Pan, D. Cui, C. Ozkan, P. Xu, T. Huang, Q. Li, H. Chen, F. Liu, F. Gao, R. He, DNA-templated ordered array of gold nanorods in one and two dimensions. J. Phys. Chem. C **111**, 12572–12576 (2007)
121. H.-C. Huang, P. Koria, S.M. Parker, L. Selby, Z. Megeed, K. Rege, Optically responsive gold nanorod–polypeptide assemblies. Langmuir **24**, 14139–14144 (2008)
122. W. Cheng, M.J. Campolongo, J.J. Cha, S.J. Tan, C.C. Umbach, D.A. Muller, D. Luo, Free-standing nanoparticle superlattice sheets controlled by DNA. Nat. Mater. **8**, 519–525 (2009)
123. R. Iwaura, T. Iizawa, H. Minamikawa, M. Ohnishi-Kameyama, T. Shimizu, Diverse morphologies of self-assemblies from homoditopic 1,18-nucleotide-appended bolaamphiphiles: effects of nucleobases and complementary oligonucleotides. Small **6**, 1131–1139 (2010)
124. M.A. Correa-Duarte, J. Pérez-Juste, A. Sánchez-Iglesias, M. Giersig, L.M. Liz-Marzán, Aligning Au nanorods by using carbon nanotubes as templates. Angew. Chem. Int. Ed. **44**, 4375–4378 (2005)
125. E. Ploshnik, A. Salant, U. Banin, R. Shenhar, Hierarchical surface patterns of nanorods obtained by co-assembly with block copolymers in ultrathin films. Adv. Mater. **22**, 2774–2779 (2010)
126. E. Ploshnik, A. Salant, U. Banin, R. Shenhar, Co-assembly of block copolymers and nanorods in ultrathin films: effects of copolymer size and nanorod filling fraction. Phys. Chem. Chem. Phys. **12**, 11885–11893 (2010)
127. M.A. Modestino, E.R. Chan, A. Hexemer, J.J. Urban, R.A. Segalman, Controlling nanorod self-assembly in polymer thin films. Macromolecules **44**, 7364–7371 (2011)
128. K. Thorkelsson, A.J. Mastroianni, P. Ercius, T. Xu, Direct nanorod assembly using block copolymer-based supramolecules. Nano Lett. **12**, 498–504 (2011)
129. S.U. Pickering, CXCVI.-Emulsions. J. Chem. Soc. Trans. **91**, 2001–2021 (1907)
130. W. Ramsden, Separation of solids in the surface-layers of solutions and 'suspensions' (observations on surface-membranes, bubbles, emulsions, and mechanical coagulation).—preliminary account. Proc. R. Soc. Lond. **72**, 156–164 (1903)
131. P. Pieranski, Two-dimensional interfacial colloidal crystals. Phys. Rev. Lett. **45**, 569–572 (1980)
132. A. Boker, J. He, T. Emrick, T.P. Russell, Self-assembly of nanoparticles at interfaces. Soft Matter **3**, 1231–1248 (2007)
133. J. He, Q. Zhang, S. Gupta, T. Emrick, T.P. Russell, P. Thiyagarajan, Drying droplets: a window into the behavior of nanorods at interfaces. Small **3**, 1214–1217 (2007)
134. E.M. Furst, Directing colloidal assembly at fluid interfaces. Proc. Natl. Acad. Sci. U.S.A. **108**, 20853–20854 (2011)
135. F. Kim, S. Kwan, J. Akana, P. Yang, Langmuir–Blodgett nanorod assembly. J. Am. Chem. Soc. **123**, 4360–4361 (2001)

136. P. Yang, F. Kim, Langmuir-Blodgett assembly of one-dimensional nanostructures. ChemPhysChem **3**, 503–506 (2002)
137. N. Pradhan, S. Efrima, Supercrystals of uniform nanorods and nanowires, and the nanorod-to-nanowire oriented transition. J. Phys. Chem. B **108**, 11964–11970 (2004)
138. Z. Nie, D. Fava, E. Kumacheva, S. Zou, G.C. Walker, M. Rubinstein, Self-assembly of metal-polymer analogues of amphiphilic triblock copolymers. Nat. Mater. **6**, 609–614 (2007)
139. L.S. Li, A.P. Alivisatos, Semiconductor nanorod liquid crystals and their assembly on a substrate. Adv. Mater. **15**, 408–411 (2003)
140. K. Soulantica, A. Maisonnat, M.-C. Fromen, M.-J. Casanove, B. Chaudret, Spontaneous formation of ordered 3D superlattices of nanocrystals from polydisperse colloidal solutions. Angew. Chem. Int. Ed. **42**, 1945–1949 (2003)
141. H.-S. Park, A. Agarwal, N.A. Kotov, O.D. Lavrentovich, Controllable side-by-side and end-to-end assembly of Au nanorods by lyotropic chromonic materials. Langmuir **24**, 13833–13837 (2008)
142. T.S. Sreeprasad, A.K. Samal, T. Pradeep, One-, two-, and three-dimensional superstructures of gold nanorods induced by dimercaptosuccinic acid. Langmuir **24**, 4589–4599 (2008)
143. Z. Huo, C.-K. Tsung, W. Huang, M. Fardy, R. Yan, X. Zhang, Y. Li, P. Yang, Self-organized ultrathin oxide nanocrystals. Nano Lett. **9**, 1260–1264 (2009)
144. K.K. Caswell, J.N. Wilson, U.H.F. Bunz, C.J. Murphy, Preferential end-to-end assembly of gold nanorods by Biotin–Streptavidin connectors. J. Am. Chem. Soc. **125**, 13914–13915 (2003)
145. K.G. Thomas, S. Barazzouk, B.I. Ipe, S.T.S. Joseph, P.V. Kamat, Uniaxial plasmon coupling through longitudinal self-assembly of gold nanorods. J. Phys. Chem. B **108**, 13066–13068 (2004)
146. J.-Y. Chang, H. Wu, H. Chen, Y.-C. Ling, W. Tan, Oriented assembly of Au nanorods using biorecognition system. Chem. Commun. **2005**, 1092–1094 (2005)
147. X. Hu, W. Cheng, T. Wang, E. Wang, S. Dong, Well-ordered end-to-end linkage of gold nanorods. Nanotechnology **16**, 2164 (2005)
148. S.T. Shibu Joseph, B.I. Ipe, P. Pramod, K.G. Thomas, Gold nanorods to nanochains: mechanistic investigations on their longitudinal assembly using α,ω-alkanedithiols and interplasmon coupling. J. Phys. Chem. B **110**, 150–157 (2006)
149. P.K. Sudeep, S.T.S. Joseph, K.G. Thomas, Selective detection of cysteine and glutathione using gold nanorods. J. Am. Chem. Soc. **127**, 6516–6517 (2005)
150. M.H. Zareie, X. Xu, M.B. Cortie, In situ organization of gold nanorods on mixed self-assembled-monolayer substrates. Small **3**, 139–145 (2007)
151. S. Zhang, X. Kou, Z. Yang, Q. Shi, G.D. Stucky, L. Sun, J. Wang, C. Yan, Nanonecklaces assembled from gold rods, spheres, and bipyramids. Chem. Commun. **2007**, 1816–1818 (2007)
152. N.D. Denkov, O.D. Velev, P.A. Kralchevsky, I.B. Ivanov, H. Yoshimura, K. Nagayama, Two-dimensional crystallization. Nature **361**, 26–26 (1993)
153. F. Dumestre, B. Chaudret, C. Amiens, M. Respaud, P. Fejes, P. Renaud, P. Zurcher, Unprecedented crystalline super-lattices of monodisperse cobalt nanorods. Angew. Chem. Int. Ed. **42**, 5213–5216 (2003)
154. C.-C. Kang, C.-W. Lai, H.-C. Peng, J.-J. Shyue, P.-T. Chou, 2D self-bundled CdS nanorods with micrometer dimension in the absence of an external directing process. ACS Nano **2**, 750–756 (2008)
155. A.M. Hung, N.A. Konopliv, J.N. Cha, Solvent-based assembly of CdSe nanorods in solution. Langmuir **27**, 12322–12328 (2011)
156. W. Ni, R.A. Mosquera, J. Pérez-Juste, L.M. Liz-Marzán, Evidence for hydrogen-bonding-directed assembly of gold nanorods in aqueous solution. J. Phys. Chem. Lett. **1**, 1181–1185 (2010)
157. N. Zhao, K. Liu, J. Greener, Z. Nie, E. Kumacheva, Close-packed superlattices of side-by-side assembled Au-CdSe nanorods. Nano Lett. **9**, 3077–3081 (2009)

158. Z. Sun, W. Ni, Z. Yang, X. Kou, L. Li, J. Wang, pH-Controlled reversible assembly and disassembly of gold nanorods. Small **4**, 1287–1292 (2008)
159. S.-Y. Zhang, E. Ye, S. Liu, S.H. Lim, S.Y. Tee, Z. Dong, M.-Y. Han, Temperature and chemical bonding-directed self-assembly of cobalt phosphide nanowires in reaction solutions into vertical and horizontal alignments. Adv. Mater. **24**, 4369–4375 (2012)
160. C.J. Orendorff, P.L. Hankins, C.J. Murphy, pH-Triggered assembly of gold nanorods. Langmuir **21**, 2022–2026 (2005)
161. D. Baranov, A. Fiore, M. van Huis, C. Giannini, A. Falqui, U. Lafont, H. Zandbergen, M. Zanella, R. Cingolani, L. Manna, Assembly of colloidal semiconductor nanorods in solution by depletion attraction. Nano Lett. **10**, 743–749 (2010)
162. A. Gole, C.J. Murphy, Biotin–Streptavidin-induced aggregation of gold nanorods: tuning rod–rod orientation. Langmuir **21**, 10756–10762 (2005)
163. K. An, N. Lee, J. Park, S.C. Kim, Y. Hwang, J.-G. Park, J.-Y. Kim, J.-H. Park, M.J. Han, J. Yu, T. Hyeon, Synthesis, characterization, and self-assembly of pencil-shaped CoO nanorods. J. Am. Chem. Soc. **128**, 9753–9760 (2006)
164. B.P. Khanal, E.R. Zubarev, Rings of nanorods. Angew. Chem. Int. Ed. **46**, 2195–2198 (2007)
165. B. Ye, G. Qian, X. Fan, Z. Wang, Self-assembled superlattices from colloidal TiO_2 nanorods. Curr. Nanosci. **6**, 262–268 (2010)
166. A. Ghezelbash, B. Koo, B.A. Korgel, Self-assembled stripe patterns of CdS nanorods. Nano Lett. **6**, 1832–1836 (2006)
167. S.A. Maier, M.L. Brongersma, P.G. Kik, S. Meltzer, A.A.G. Requicha, H.A. Atwater, Plasmonics—a route to nanoscale optical devices. Adv. Mater. **13**, 1501–1505 (2001)
168. M.S. Gudiksen, K.N. Maher, L. Ouyang, H. Park, Electroluminescence from a single-nanocrystal transistor. Nano Lett. **5**, 2257–2261 (2005)
169. K. Mitamura, T. Imae, N. Saito, O. Takai, Fabrication and self-assembly of hydrophobic gold nanorods. J. Phys. Chem. B **111**, 8891–8898 (2007)
170. L. Onsager, The effects of shape on the interaction of colloidal particles. Ann. NY. Acad. Sci. **51**, 627–659 (1949)
171. D. Frenkel, H.N.W. Lekkerkerker, A. Stroobants, Thermodynamic stability of a smectic phase in a system of hard rods. Nature **332**, 822–823 (1988)
172. A. Singh, H. Geaney, F. Laffir, K.M. Ryan, Colloidal synthesis of Wurtzite Cu_2ZnSnS_4 nanorods and their perpendicular assembly. J. Am. Chem. Soc. **134**, 2910–2913 (2012)
173. A. Singh, C. Dickinson, K.M. Ryan, Insight into the 3D architecture and quasicrystal symmetry of multilayer nanorod assemblies from Moiré interference patterns. ACS Nano **6**, 3339–3345 (2012)
174. Z. Zhang, H. Sun, X. Shao, D. Li, H. Yu, M. Han, Three-dimensionally oriented aggregation of a few hundred nanoparticles into monocrystalline architectures. Adv. Mater. **17**, 42–47 (2005)
175. J. Zhuang, A.D. Shaller, J. Lynch, H. Wu, O. Chen, A.D.Q. Li, Y.C. Cao, Cylindrical superparticles from semiconductor nanorods. J. Am. Chem. Soc. **131**, 6084–6085 (2009)
176. T. Wang, J. Zhuang, J. Lynch, O. Chen, Z. Wang, X. Wang, D. LaMontagne, H. Wu, Z. Wang, Y.C. Cao, Self-assembled colloidal superparticles from nanorods. Science **338**, 358–363 (2012)
177. Z.-C. Xu, C.-M. Shen, C.-W. Xiao, T.-Z. Yang, S.-T. Chen, H.-L. Li, H.-J. Gao, Fabrication of gold nanorod self-assemblies from rod and sphere mixtures via shape self-selective behavior. Chem. Phys. Lett. **432**, 222–225 (2006)

Chapter 3
Anisotropic Gold Nanoparticles: Preparation, Properties, and Applications

Chenming Xue and Quan Li

Abstract Anisotropic metal nanoparticles with a catalog of promising anisotropic electronic, optical, and chemical properties have been regarded as enabling building blocks in the bottom-up fabrication of functional materials and devices. Specifically, anisotropic gold nanoparticles are currently emerging as fascinating materials due to their unique shape-, size-, and surface-dependent properties. In this chapter, we present the synthesis, properties and applications of different one-, two- and three-dimensional anisotropic gold nanoparticles (AuNPs). The most widely adopted top-down and bottom-up synthesis approaches have been discussed in addition to some of the recently introduced new methods for the fabrication of differently shaped anisotropic AuNPs. The optical property, photothermal effect, surface enhanced Raman scattering, fluorescence enhancement and quenching, surface modification, toxicology, and supramolecular organizations of anisotropic AuNPs have been highlighted. Various practical and potential applications of anisotropic AuNPs in catalysis, sensing, photothermal therapy, drug and gene delivery, and biological and biomedical areas are briefly outlined.

3.1 Introduction

Since medieval period, gold nanoparticles (AuNPs) have been used to decorate church glasses and Lycurgus cup [1]. However, they were beyond comprehension due to the then scientific limitations. In the early part of 20th century, scientists began to investigate these extremely small particles, and several theories were developed to explain their unusual and unique physical properties compared to the bulk materials. For example, the famous Mie theory [2] of which the most special one is localized surface plasmon resonance (LSPR), e.g. the free electrons trapped

C. Xue · Q. Li (✉)
Liquid Crystal Institute and Chemical Physics Interdisciplinary Program,
Kent State University, Kent, OH 44242, USA
e-mail: qli1@kent.edu

Q. Li (ed.), *Anisotropic Nanomaterials*, NanoScience and Technology,
DOI 10.1007/978-3-319-18293-3_3

in the particle surface show the collective oscillation (Fig. 3.1) frequency, resulting in a plasmon absorption band in the visible to near infrared (NIR) and even to infrared (IR) region. A solution of well-dispersed AuNPs shows a typical deep-red color [3]. In the past decades, the AuNPs were systematically studied, nevertheless sophisticated synthesis methods and attractive applications based on their unusual properties are under intensive investigation. In this context, the spherical (isotropic) AuNPs are so far the most studied class of metal nanoparticles.

In contrast to isotropic AuNPs, anisotropic AuNPs have caught a broad interest due to their appealing and unprecedented properties. The existence of anisotropic AuNPs was noticed in the beginning of the twentieth century by Zsimondy, who discovered colored solutions of anisotropic AuNPs. He also invented the ultramicroscope to visualize the shapes of gold particles, and received the 1925 Nobel Prize for "his demonstration of the heterogeneous nature of colloidal solutions and for the methods he used". It was not until the past decade that anisotropic AuNPs became a research endeavor at its own right and has been drawing great attention because the structural, optical, electronic, and catalytic properties are different from, and most often superior to those of spherical AuNPs. All these fascinating applications are based on their size- and shape-dependent electronic and optical properties that also vary in individual state and self-assembled state. For example, isotropic AuNPs exhibit one relatively simple LSPR, while anisotropic gold nanorods (AuNRs) exhibit two LSPR signals: longitudinal (along the long axis) and transverse (across the long axis) LSPR (Fig. 3.1b). Owing to their unusual properties, anisotropic AuNPs have qualified for broad and interesting applications in different areas such as sensors, biological and biomedical treatments, optical devices and metamaterials.

During the past two decades, the explorations of anisotropic AuNPs including their properties and applications have become accessible and been extensively expanded. The anisotropic AuNPs show interesting light absorption and scattering phenomena, resulting from extraordinary shape dependent collective electronic resonances. According to their anisotropic shape and self-assembled state, they can absorb light from visible to IR region. For example, depending on the AuNRs' tunable aspect ratio (length/diameter), the longitudinal LSPR varies from visible frequency (small aspect ratio) to NIR and even IR frequencies (large aspect ratio). The wavelength region between 800 and 1300 nm, the so-called "biological window" can penetrate tissue and cells without causing cell damage. Moreover, the self-assemblies of AuNRs can further alter LSPR due to plasmon coupling between neighboring AuNRs. Based on these unusual plasmonic effects of anisotropic AuNPs, they show attractive properties such as light absorption and scattering, fluorescence, photothermal effect, and optical tuning, leading to promising applications in medicinal diagnostics and photothermal therapy ("theranostics") [4–7], and optical devices [8].

The fabrications of anisotropic AuNPs are based on two different well-developed methods: top-down physical nanofabrication approach and bottom-up wet chemistry approach. Both approaches have their own pros and cons. The top-down methods are easy to produce AuNPs in a well-organized fashion and with controlled narrow size distribution, but the sizes are usually relatively large. The bottom-up

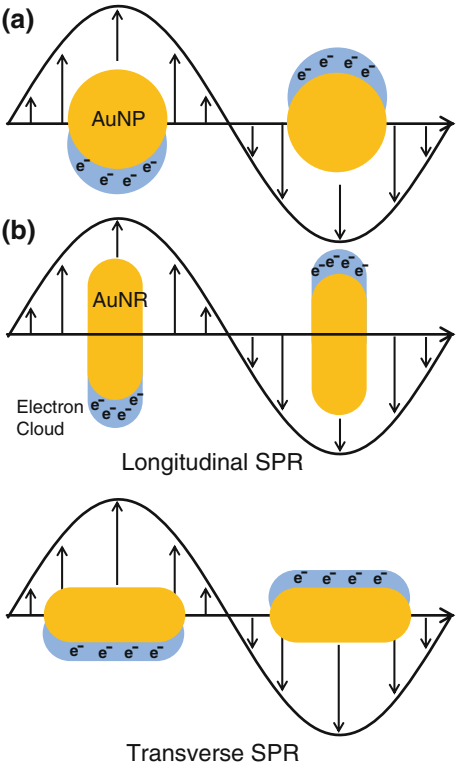

Fig. 3.1 Schematic depictions of the LSPRs of **a** isotropic AuNP and **b** anisotropic AuNR

wet-chemistry methods have advantages in preparing small size colloidal AuNPs with good yields and controllable polydispersity. However, organizing them into well-ordered arrays is challenging. For the chemistry methods, during the past two decades scientists have discovered and improved the seed-mediated growth method to prepare AuNPs with high efficiency and excellent size distribution. This method is very successful in synthesizing AuNRs, the most representative anisotropic AuNPs. There are also other wet-chemistry synthesis methods, e.g. photochemistry, electrochemistry, sonochemistry, templates, galvanic replacement, for anisotropic AuNP synthesis. With these methods, fascinating shapes of anisotropic AuNPs including one-dimensional (1D) (nanowires, nanotubes, and nanobelts), two-dimensional (2D) (stars, pentagons, squares/rectangles, dimpled plates, hexagons, and truncated triangles), and three-dimensional (3D) (nanotadpoles, nano-urchins, nanodentrites, nanocubes and core-shell structures) have been realized.

It is interesting to note that anisotropic AuNPs show special properties according to their different shapes such as optical property, photothermal effect, surface-enhanced Raman scattering (SERS) effect, fluorescence enhancement and quenching phenomena, toxicology, and self-assembly behaviors. Surface coating is an important issue after synthesis, providing stability as well as compatibility. Especially for biological and biomedical applications, it is utmost important to

passivate the surface of nanoparticles with biocompatible groups in order to introduce AuNPs into biosystem for functionalization and to provide necessary intermolecular interactions to combine AuNPs with demanding materials for drug delivery or gene transfer. Furthermore, anisotropic AuNPs have shown other interesting applications in diverse areas such as catalysis, sensing and molecular recognition, nanoelectrodes and optical tuning.

Although anisotropic AuNPs are relatively new building blocks, they have become a rapidly emerging research field due to their promising applications. This chapter covers an overview of this interesting research subject. Various synthesis approaches for preparing and stabilizing anisotropic AuNPs with an emphasis on the representative and most commonly used seed-mediated wet-chemistry approach are introduced. The typical properties of different anisotropic AuNPs are highlighted based on the AuNPs' morphology and supramolecular assemblies. Finally, the functionalization and attractive applications of the anisotropic AuNPs in optics, photonics, catalysis, materials science, biological and biomedical areas are presented.

3.2 Methods and Techniques for Synthesis of Anisotropic Gold Nanoparticles

3.2.1 Top-Down Method

Top-down physical lithography methods are direct ways to produce anisotropic AuNPs, which have typical polycrystalline structures. Among them, the most widely used method is electron-beam lithography (EBL) [9]. In the typical procedure, an electron-sensitive resist is initially coated on the substrate. Followed by the exposure to an electron beam, the area will dissociate into smaller polymer segments that can be selectively removed by washing with a developing agent. Then, gold can be deposited onto the opening patterns written by the electron beam. This lift-off technique can offer anisotropic AuNPs with controllable shapes and sizes in tens of nanometers' length-scale. Focused ion beam (FIB) lithography [10] is another lithography technique which sputters away unwanted portions of a continuous film by a raster ion beam (typically gallium), creating nanostructures of the desired shapes. Anisotropic AuNPs have been produced using both EBL [10] and FIB techniques [11]. FIB produced Au nanodisks [12]. EBL and FIB techniques were also combined to prepare anisotropic AuNPs arrays of Au microholes [13], grooves, nanowire circuits [14], hexagonal arrays of Au triangles [15] and Au nanorings [16]. Mirkin's group has discovered another lithography method called on-wire lithography (OWL) [17, 18], which can make gapped cylindrical structures on a solid support with gaps and segment length controlled on a length scale under 100 nm by the template-based electrochemical process (Fig. 3.2) [19]. Although the top-down lithography techniques can produce AuNPs with controllable size, shape, and alignment, their scaling up is limited and smaller AuNPs with sizes less than 10 nm are not easily accessible.

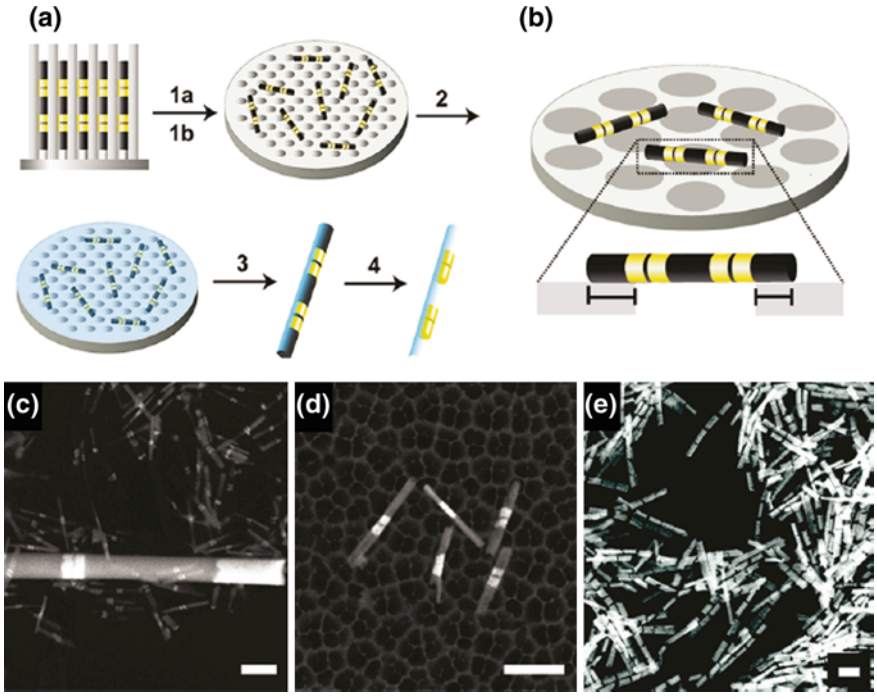

Fig. 3.2 Synthetic strategy for preparing sub-100 nm diameter nanostructure arrays with on-wire lithography (OWL). **a** Schematic depiction of method beginning with (1a) release of template-synthesized multisegmented metal nanowires from anodic aluminum oxide (AAO) membranes into solution by dissolving the membrane and metal backing. (1b) Vacuum filtration of nanowires on to larger pore AAO membranes. (2) Electron beam evaporation of a thin (5–10 nm) SiO_2 backing layer (*blue* coating). (3) Sonication in ethanol to release half-coated wires into solution. (4) Selective etching of sacrificial material (typically Ni, black segments) to produce 1D nanostructure arrays with geometry matching the original nanowire. **b** Schematic showing the decreased interaction area (*solid black lines*) between the nanowires and the porous substrate, decreasing the van der Waals attraction between the surfaces. **c–e** SEM images of 55 nm Au–Ni nanowires after steps 1, 2, and 4 (**c**, **d**, and **e**, respectively). **c** The 55 nm diameter Au–Ni nanowires codeposited with 270 nm Au–Ni nanowires, highlighting the increased resolution available with this new method compared to the previous smallest OWL structure. Scale bar is 350 nm. **d** Au–Ni nanowires filtered on to a porous AAO substrate, depicting the decreased interaction area shown schematically in (**b**). Scale bar is 300 nm. **e** SEM image of 55 nm Au nanorods arrays with varying gap sizes after etching away the Ni segments. Scale bar is 165 nm [19]. Copyright 2011 American Chemical Society

3.2.2 Bottom-Up Method

To prepare anisotropic AuNPs, the bottom-up solution based method has been well developed and widely used. The simplest and most easily accessible 1D anisotropic AuNRs have drawn great attention from scientists. Conditions of seed-mediated growth method, photochemistry, electrochemistry, sonochemistry, templates,

galvanic replacement have been discovered and developed. During the earlier research, different methods have been attempted to produce anisotropic AuNPs. In early 1960s, vapor−liquid−solid (VLS) method has been demonstrated [20]. In 1989, Wiesner and Wokaun reported the first example of AuNRs by adding Au seeds into the solution of $HAuCl_4$. The seeds were created by reduction of $HAuCl_4$ with phosphorus (as in Faraday's synthesis) and these seeds further grew up to AuNRs by reduction of Au^{3+} with H_2O_2 [21]. Until 1990s, seed-mediated growth approach for AuNRs was discovered and after continual improvement, it has become the method of choice [22]. It offered a convenient and versatile wet-chemistry way to synthesize AuNRs with excellent yield, monodispersity and controllable aspect ratio and size, and also reproducibility. A typical procedure is shown in Fig. 3.3. Accompanying the progress of this seed-mediated growth method that provides feasible access to AuNRs, fundamental optical properties were recognized. AuNRs with the sizes of ~150−180 nm × 25 nm (length × width), which exhibit the aspect ratio between 8 and 20, have been synthesized [23]. It is worthwhile to mention that the modifications from the El-Sayed research group improved the yield and polydispersity of the AuNRs by replacing sodium citrate with the stronger cetyltrimethylammoniumbromide (CTAB) stabilizer during the formation of the seeds, as well as using $AgNO_3$ to

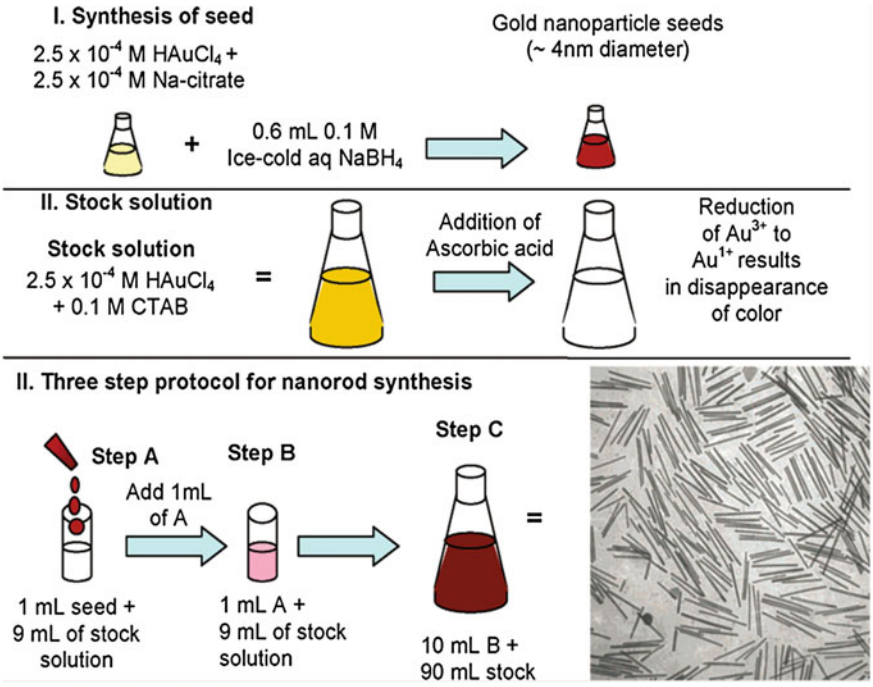

Fig. 3.3 Three-step seed-mediated growth approach for making gold and silver nanorods with a controlled aspect ratio [29]. Copyright 2005 American Chemical Society

direct the formation and to control the aspect ratio of the AuNRs [24]. The role of Ag^+ is also critical in formation of other shapes of AuNPs, for example, high-index concave cubic Au nanocrystals have been synthesized by the reduction of $HAuCl_4$ with ascorbic acid in the presence of a chloride-containing surfactant and small amounts of $AgNO_3$ [25]. The yield of such a procedure is about 99 % with aspect ratios between 1.5 and 4.5. Higher aspect ratios up to 10 or 20 were obtained upon the addition of a cosurfactant (benzylhexadecylammonium chloride (BDAC) [24] or Pluronic F-127 [26]) to the original growth solution and by varying the concentration of $AgNO_3$. The synthesized single crystal AuNRs have a penta-twinned structure with Au {111} lattice at the end-caps and the Au {100} or {110} along the longitudinal faces [27]. Besides, $AgNO_3$ has been found to play a critical role in the formation of long AuNRs [28].

AuNRs with low aspect ratio (aspect ratio: 2–5, size: ~20−60 nm × 12 nm) have been developed by a modified seed-mediated growth protocol [24, 30]. In this method, smaller AuNP seeds (ca. 1.5 nm) stabilized with CTAB are added to the growth solution with the assistance of a small amount of $AgNO_3$ and the mild reducing agent ascorbic acid. $AgNO_3$ used herein is crucial in controlling AuNR shapes. The AuNRs produced by this method display different crystal faces compared to the earlier ones [31]. Later, the seed-mediated growth procedure has been modified as a "seedless" version which uses small organic additives to control AuNR sizes and aspect ratios (between 2 and 5). In such a new way, the standard silver-assisted growth method is employed and seeds are generated in situ by adding a small amount of the strong reducing agent sodium borohydride, instead of using preformed AuNP seeds [32]. The control of aspect ratio is based on the sodium borohydride concentration rather than the $AgNO_3$ concentration. Interestingly, although the size of AuNRs (~25 nm × 6 nm) prepared through this "seedless" method is quite smaller than the formal procedures, the yield is poorer and the size distribution is broader.

Having been developed in the past years, the seed-mediated growth approach and its modified ones have become the most popular for synthesizing anisotropic AuNRs with aspect ratios from 2 to 20 with desirable yield and monodispersity. They have advantages of simple procedure, high yield, scale-up quantity, feasible size/shape control, and flexible for further structural modifications [33]. Similarly, AuNRs themselves can be used as seeds in the synthesis of more complex structures, for instance, Pt nanodots can form on AuNR surface which possesses more complex properties [34]. Based on this method, now commercially available AuNRs have appeared in market. This greatly promotes the research in anisotropic AuNPs and their fascinating applications.

With different additives (e.g. foreign metal ions, iodide ions), the overgrowth of colloidal AuNRs can be tuned affecting their shape, facet, aspect ratio and composition, e.g. forming dumbbell-like AuNR nanostructures [35]. Shape transformation from rod to octahedron is observed under sonication in dimethylformamide (DMF) in the presence of poly(vinylpyrrolidone) (PVP) [36]. Similarly, overgrowth of AuNRs can induce nanopeanut and octahedra structures by glutathione and cysteine [37].

However, the mechanism of AuNR growth during synthesis is one unsolved challenge to date. Even though large efforts have been devoted to this subject, it is still not fully understood. Fixing this can improve the efficiency and versatility of the synthesis of AuNRs in the future [38]. Two AuNR growth mechanisms were brought up and studied [39]. The growth is governed either by binding the head group of a cationic surfactant to the {100} face of the AuNP seed preferentially, instead of the less-favored rod end [29], or by the electric field of the double layer between the positively charged seed and negatively charged $AuCl^{2-}$ on the CTAB micelle. Different from multiply twinned crystalline citrate-capped seeds growing into multiply twinned structures, single-crystalline CTAB-capped seeds lead to single-crystalline AuNRs with {110} faces on the side and {100} faces on the end. Ag deposits on the {110} sides faster than that on the {100} ends, and in this way the seeds grow into rods. A hybrid mechanism involving diffusion of $AuCl^{2-}$ on the CTAB micelles to CTAB-capped seed spheres resulting from electric-field interactions has been proposed by Murphy and co-workers. Silver ions preferentially deposit onto the {110} facets, where CTAB molecules are preferentially bound and providing bromide counter ions forming an AgBr solid layer thereon, which results in particle growth into AuNRs along the {110} direction. There is a critical $[Br^-]/[Au^{3+}]$ ratio around 200 that leads to the maximum aspect ratio of the AuNRs, however beyond such ratio, Br^- acts as a poison.

3.2.3 Other Methods

3.2.3.1 Photochemistry

Photoreduction was an alternative method for generating anisotropic AuNPs. For instance, UV light can reduce $HAuCl_4$ to form AuNRs with the aid of rod shaped cationic micelles. The pioneer work of this method was introduced in 1995 by Esumi et al. [40]. Different from the seed-mediated procedure where the micelle surfactant molecules stabilize a specific crystal face resulting in AuNRs, in the photoreduction procedure, Au^{3+} ions bound to rodlike cationic micelle surfactant molecules to form ion pairs. After excited by UV light with 235 or 300 nm [41], the Au^{3+} ions were reduced to Au^0. This process includes the aggregation of metal nuclei to form primary particles, and these particles assemble to form AuNRs resulting from the stabilization of a specific crystal face by surfactant micelles [42]. One prominent advantage of this photocatalyzed procedure is that high yield of AuNRs can be obtained in a single step [32], rather than the typical two-step seed-mediated growth method. In the presence of poly(vinylpyrrolidone) (PVP) and ethylene glycol [43], or TiO_2 colloids [44], the photochemical method could be used to synthesize other anisotropic AuNPs such as platelet-like shape with an asymmetric five-twinned structure and six-star shape.

3.2.3.2 Electrochemistry

The electrochemical method to produce AuNPs was first reported by Svedberg in 1921. During 1990s chemists modified the electrochemical reduction method using organic surfactant (CTAB) and porous aluminum oxide membrane templates for shape control [45], and arrays of AuNRs with micrometer scale dimensions ($\sim$100 nm by 100–200 μm) were created [46]. Those sizes are too large, but smaller AuNRs (60 nm × 12 nm) can be prepared with modified synthesis approach by using surfactant mixtures as soft templates [47]. In this approach, an Au plate anode and a Pt plate cathode were immersed into an electrolyte containing CTAB and co-surfactant tetradodecylammonium bromide (TOAB). Binding to the CTAB micelle, $Au^{3+}Br_4^-$ first formed from the Au anode due to electrolytic oxidation, and then migrated to the cathode and reduced to Au^0. By the assistance from Ag^+ cations from redox reaction between Au^{3+} and an Ag plate, AuNRs were formed with controllable aspect ratios. These AuNRs were separated from the cathode by sonication [47]. As shown by high-resolution transmission electron microscopy (HRTEM) and diffraction studies, AuNRs produced by this way are single crystals having no stacking faults, twins, or dislocations, with aspect ratios of 3–7 [48]. With the advantages of simplicity, efficiency and applicability, electrochemical method is continually developed for the synthesis of other anisotropic AuNPs, for example dendritic AuNPs [49]. The photochemistry and electrochemistry methods have limitations of expensive synthesis and significant amount of byproducts: spheres, rods, cubes, plate, and prisms AuNP mixtures.

3.2.3.3 Sonochemistry

Ultrasonication is another useful approach for the synthesis of small nanoparticle, which can control both their shapes and sizes by the use of surfactants and alcohols [50]. With this method, single-crystalline flexible Au nanobelts with a width of 30–50 nm and a length of several micrometers have been synthesized [51].

3.2.3.4 Template

One successful well-known template for the synthesis of AuNPs is silica nanospheres. Around such templating cores, Au layers can be coated. This powerful strategy allows the control over the size and thickness of the Au nanoshells by changing the reaction time and the concentration of the plating solution [52]. Anisotropic AuNRs were generated on substrates from colloidal solution using catalytic seed nanospheres to directly grow [53]. However, only 15 % of seeds are converted to rods while the rest seeds promoted a myriad of shapes including spherical, triangular and hexagonal. To improve this method, nanoporous track-etched polycarbonate or anodized alumina membrane was used as the templates where gold atoms are deposited by electrochemical reduction [54]. To tune the

AuNR aspect ratio, the pore diameter (5–200 nm) in the membrane template was adopted to control the width, while the amount of the deposited gold determines the length. Various templates have been used for synthesizing different anisotropic AuNPs: porous membranes [55], mesoporous silica [56], Si(100) wafers [55], pyrolytic graphite [57], polymers [58], nanoparticles [59], carbon nanotubes [60], inorganic clusters (e.g. $LiMo_3Se_3$) [61], surfactants organized in micelles [27, 47] as well as biomolecules (e.g. plant extracts) [62], microorganisms [63], polypeptides, and DNA [64].

3.2.3.5 Galvanic Replacement

Galvanic replacement is another approach for making anisotropic AuNPs. Without external current sources, Au cations in the plating bath are reduced by a metal in a spontaneously thermodynamically and kinetically favorable reaction [65]. The driving force of this reaction is the difference of the redox potential between the reducing metal and the Au^{3+}/Au^0 system. Intensively developed by Xia group, the reduction of Ag nanostructure has been used as a sacrificial template to fabricate hollow Au nanostructures [66, 67]. Starting from Ag nanocubes, anisotropic gold nanocages have been synthesized. These reactions proceed in two steps: formation of seamless hollow structures with the walls made of Au–Ag alloys by galvanic replacement; and subsequent formation of hollow structures with porous walls by dealloying [68]. In addition, aluminium is also used as the metal source since aluminium foil is inexpensive and has a very low oxidation potential which can reduce many transition-metal cations [69]. As fluoride forms stronger bonds than chloride, NaF and NH_4F were used to dissolve the alumina layer to allow the galvanic displacement, resulting in anisotropic Au dendrites [70]. The galvanic technique has some advantages such as no need of template, surfactant, or stabilizer, and can be conducted simply at room temperature, compared to the former methods.

3.2.4 Other Shapes of Anisotropic AuNPs

3.2.4.1 One-Dimensional (1D) AuNPs

Except for the widely investigated 1D anisotropic AuNRs, there are various remarkable shapes of anisotropic AuNPs. Among 1D structures, there are nanowires (NWs), nanotubes (NTs), and nanobelts (NBs). If the AuNRs continually grow to an extremely large aspect ratio, they become AuNWs, which generally show some mechanical flexibility. For example, the AuNRs stabilized by CTAB and pentahedrally twinned were used for preparing AuNWs by the tip-selective growth [71], generating crystalline AuNWs with 12–15 μm in length and 90 ± 10 nm in diameter. UV irradiation, photoreduction, and thermal reduction

were also used to make AuNWs [72]. With other metal elements such as Pt and Cu combining with Au, the bimetallic NWs can be fabricated [73]. Interestingly, the method of fabrication of AuCuNWs can also lead to the formation of AuCu nanotubes (AuCuNTs). Therefore, CuNWs were used as templates, and the AuCuNWs were formed as intermediates that ultimately led to the AuCuNTs [74].

Both AuNWs and AuNTs can be prepared by electroless deposition onto the pore walls of porous polymer membranes working as a template, and long Au deposition time leads to AuNWs while short time leads to AuNTs [75]. 4-(Dimethylamino)pyridine is a powerful auxiliary reagent for the electroless deposition method to yield AuNTs (Fig. 3.4) [76]. In other ways, hollow AuNTs with highly ordered Au arrays were synthesized by the galvanic replacement reaction using an anodized aluminum oxide template [77], a polymer NT as a sacrificial core [78], and thiol-functionalized nanoporous films as a scaffold [79].

Gold nanodumbbells (AuNDs) were synthesized by a modified seed-mediated method [80, 81]. The presence of tiny amounts of iodide stimulated tip growth prominently, resulting in well-defined dumbbell structures. Hybrid AuNDs were attractive according to their multiple functions. The Au/Ag core/shell structures have been created either by silver deposition onto AuNDs [82], or by galvanic replacement and reduction [83]. There are other metals for hybrid AuNDs, including CdSe [84], $CoPt_3$, FePt and Pt [85].

3.2.4.2 Two-Dimensional (2D) AuNPs

Beyond 1D structures, anisotropic AuNPs have 2D structures with well-defined specific shapes, such as stars, pentagons, squares/rectangles, dimpled plates, hexagons, and truncated triangles [86]. One widely used approach is using polymer templates, since the versatile polymers can act as stabilizers, templates, and

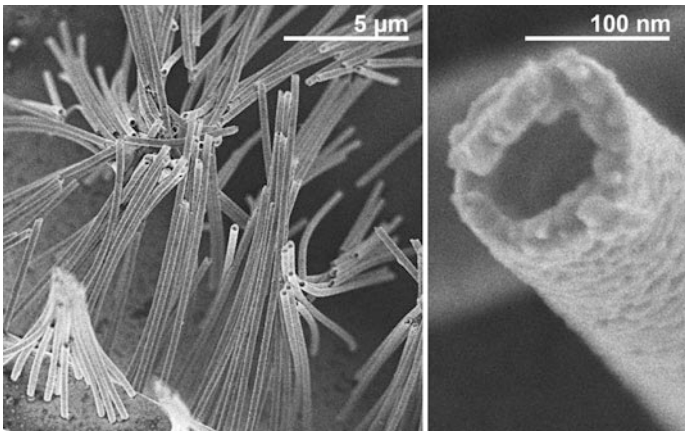

Fig. 3.4 SEM images of free-standing AuNTs [76]. Copyright 2010 American Chemical Society

reductants [72, 87–89]. For example, $PEO_{20}PPO_{70}PEO_{20}$ (PEO = poly(ethylene oxide), PPO = poly(propylene oxide)) was used as both the reductant and stabilizer to prepare large gold nanosheets (10 μm in width and 100 nm in thickness) [72].

The morphology could be finely adjusted through control of the reactant ratio and the reaction conditions. A large-scale synthesis of micrometer sized Au nanoplates was carried out [90]. Triangular and hexagonal gold nanoplates in aqueous solution were synthesized by thermal reduction of $HAuCl_4$ with trisodium citrate and CTAB, yielding gold nanoplates with the width as small as 10 nm to several hundreds of nanometers [91].

A mild and relatively environmental friendly one-pot biomimetic method was developed to fabricate gold nanoplates having hexagonal and truncated triangular structure with a thickness less than 30 nm [92]. The use of a biological reductant such as brown seaweed Sargassum [93], tannic acid [94], serum albumin protein [95], and glycine [96] was explored over the last decade. There is a type of special gold nanoplates having triangular nanoprisms morphology. These nanostructures show three congruent edge lengths in the range from 40 nm to 1 μm and a thickness ranging from 5 to 50 nm [97–99]. They can be prepared in high yields, which exhibit visible and IR LSPR.

3.2.4.3 Three-Dimensional (3D) AuNPs

For 3D anisotropic AuNPs, gold nanotadpoles have an interesting tadpole-like structure. They have special optical and electrical properties leading to unique potential applications in second-order nonlinear optics, nanoelectronics. Gold nanotadpoles were synthesized via a simple chemical procedure, i.e. in aqueous solution reducing chloroauric acid with trisodium citrate in the presence of sodium dodecylsulfonate as a capping agent, and the 3D crystalline structures were characterized by TEM, AFM, and HRTEM (Fig. 3.5) [100]. Tadpole-shaped AuNPs later were synthesized in high yield by a temperature-reducing seeding approach without any additional capping agent or surfactant [101]. The formation mechanism was ascribed to an aggregation-based growth process. A 3D hybrid nanostructure consisting of Au heads and Pd tails has been demonstrated, these 3D nanotadpoles were expected to display properties of both Pd nanorods and AuNPs [102].

Since branched gold nanostructures, such as monopods, bipods, tripods, tetrapods, hexapods, and multipods like nanoflowers, nanostars, and urchins have sharp edges and corresponding high localization of surface plasmon modes [103], they are anticipated for applications in nanocircuits and nanodevices, and in vivo tests, including biosensing [104], imaging [105], targeting [106], and photothermal therapy [107]. The branched AuNPs in aqueous solution was first synthesized by Carroll and co-workers in 2003 [108], using triangular Ag platelets as seeds and reducing Au^{3+} with ascorbic acid in the presence of CTAB leading to anisotropic Au monopods, bipods, tripods, and tetrapods. The dimension and number of branches were varied under combinations of the [seed]/[Au^{3+}] ratio in a seed-mediated synthesis approach [109]. There are other routes to produce branched

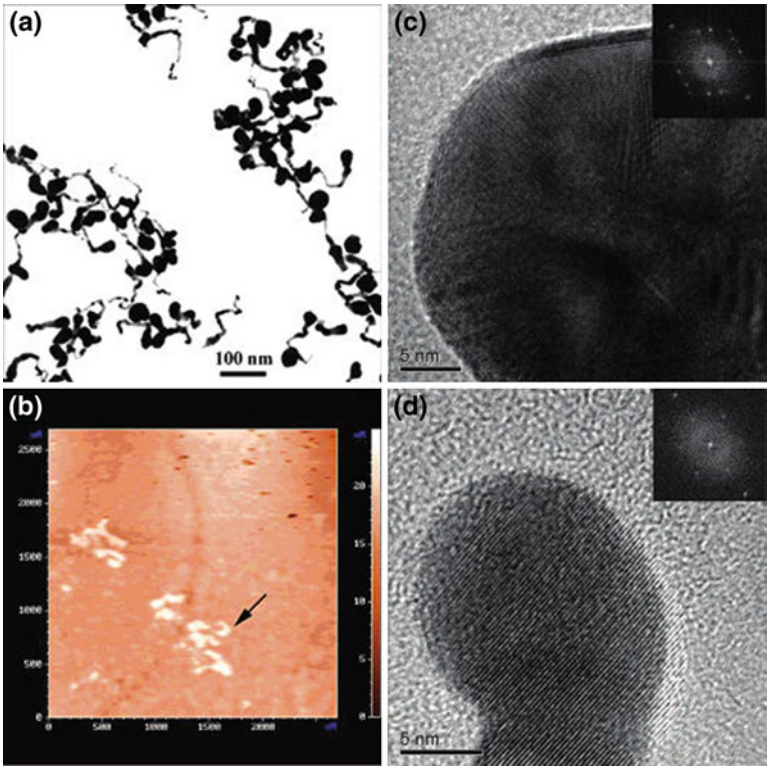

Fig. 3.5 **a** TEM and **b** AFM images of tadpole-shaped AuNPs. **c**, **d** HRTEM images of the **c** head and **d** tail of a gold nanotadpole. *Insets* The corresponding Fourier transform patterns [100]. Copyright 2004 American Chemical Society

AuNPs [110], with a high yield up to 90 % [111]. Generally, the branched AuNPs have poorer monodispersity than other shapes.

For the branched nanoparticles, they have complicated LSPR consisted of multiple sharp peaks in the visible and NIR region. The study showed the resulting LSPR energies can be considered as a hybridization of the core and tip plasmons (Fig. 3.6) [112].

Interestingly, another type of anisotropic AuNP dendrites exhibits the hierarchical tree-type architecture with trunks, branches, and leaf components. With such hyperbranched architectures, they have attracted much attention for their fascinating fractal growth phenomena and their potential applications in functional devices, plasmonics, biosensing, and catalysis [113, 114]. They are mainly synthesized by electrochemical deposition. For example, Au dendrites are synthesized on a glassy carbon electrode by electrodeposition with a square-wave potential from a solution of $HAuCl_4$ containing cysteine as the blocking molecule [113]. Shape-controlled synthesis of Au dendrites was achieved in the presence of supramolecular

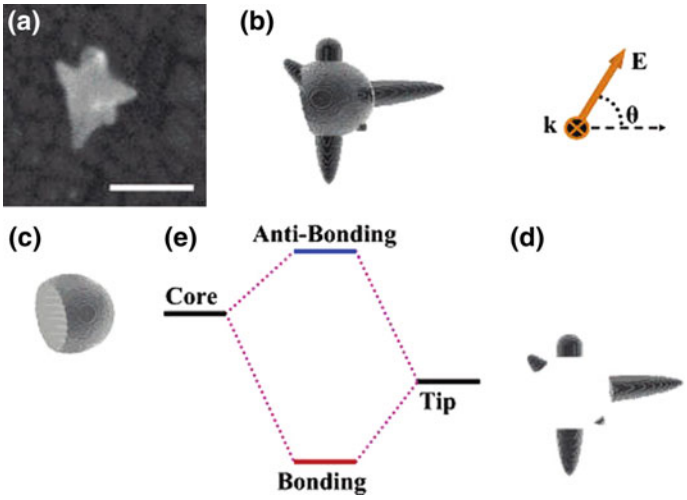

Fig. 3.6 Principle of the plasmon hybridization of the LSPR of a gold nanostar. Panel **a** shows an experimental scanning electron micrograph. The scale bar is 100 nm. Panel **b** shows the theoretical model, consisting of a truncated spherical core, (**c**) and tips, consisting of truncated prolate spheroids (**d**). Panel **e** illustrates the concept of plasmon hybridization in the nanostar. The core plasmons interact with the tip plasmons and form bonding and antibonding nanostar plasmons. The polarization angle is defined in the *upper right corner* [112]. Copyright 2007 American Chemical Society

complexes formed from dodecyltrimethylammonium bromide (DTAB) and β-cyclodextrin (β-CD) (Fig. 3.7) [115].

A typical core/shell nanostructure contains a supporting core and a thin Au nanoshell, for example, SiO_2@Au NPs exhibit a strong plasmon resonance, and core radius and shell thickness dependent SERS effect [116]. The plasmon wavelength could be tuned by varying the relative size of the inner and outer shell layer over a wide range from visible to IR spectrum, of which the NIR region between 700–1100 nm is particularly useful in biomedical applications, such as therapy and diagnostics [117]. There are other metal or metal oxide cores used to replace SiO_2 [118]. For example, Fe_3O_4@Au core/shell NPs modified with antibodies and fluorescent dyes work as contrast probes for the multimodal imaging of tumors [119]. In a more complicated system, covering a magnetic Co@Au core/shell NPs with a pure Co core and an intermediate Au shell, a compact outer cobalt oxide shell was further coated on it [120].

A layer of hard inorganic nanomaterials is used for surface modification of AuNRs, showing advantages of increasing stability, facilitating surface chemistry, and tunable properties. Silver coating on AuNRs is successfully accomplished whose thickness can be controlled through the concentration of silver precursors and reducing agents [121]. The silver coated AuNRs have practical application in enhancing Raman scattering [122]. Silicon coatings can be achieved by simple addition of aqueous sodium silicate to the AuNR solution, which is then mixed with

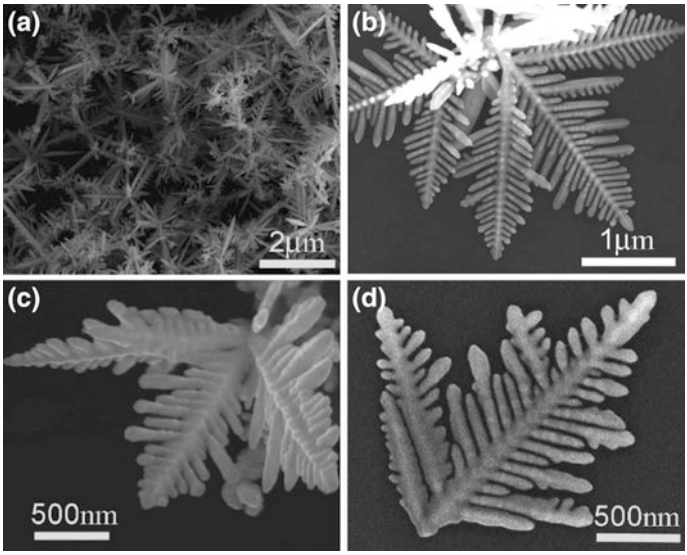

Fig. 3.7 SEM images of Au nanodentrites grown in mixed DTAB/β-CD solution, [DTAB] = 5.0 mM; [β-CD]/[DTAB] = 0.5. From [115]. Copyright 2009 American Chemical Society

3-mercaptopropyl trimethoxysilane (MPTMS) or 3-mercaptopropyl triethoxysilane (MPTES) solution, forming mesoporous silicon shell on AuNR surface resulting in red-shifted longitudinal LSPR [123]. Other hard inorganic coating layers on AuNRs have been explored such as iron oxide coating [124], platinum coating [125], and silver sulfide or selenide [126]. These inorganic layers coated AuNRs have promising applications of magnetic separation, imaging, catalysis, and optical nonlinearities.

Hollow gold nanospheres (HAuNSs) were synthesized by layer-by-layer (LbL) assembly [52, 127]. Through the size-controllable LbL technique, HAuNSs were deposited on a sacrificial template of polyelectrolyte-modified polystyrene (PS) nanospheres. Afterwards, the PS core was removed by either calcination or dissolution [128].

Recently, there is a novel class of remarkable nanostructures gold nanocages (AuNCs) possessing hollow interiors and porous walls synthesized by galvanic replacement [129], which have potential in colorimetric sensing and biomedical applications. During synthesis, $HAuCl_4$ solution was added to a boiling suspension of Ag nanocubes which act as both template and reducing agent in a controlled manner. Due to the difference of electrochemical potential between Au and Ag (the reduction potential of $AuCl^{4-}$/Au: 0.99 V, of AgCl/Ag: 0.22 V versus the standard hydrogen electrode), there happened galvanic replacement and thereby Au deposited on Ag nanocube surface. The resulting hollow, porous cage-like Au nanostructures were characterized by SEM and TEM [129]. For a representative process

and structure (Fig. 3.8), nanoboxes derived from 50 nm Ag nanocubes were first converted into nanocages. Then by increasing the amount of the etchant $Fe(NO_3)_3$ during the dealloying process, only porous cubic nanoframes were left [130].

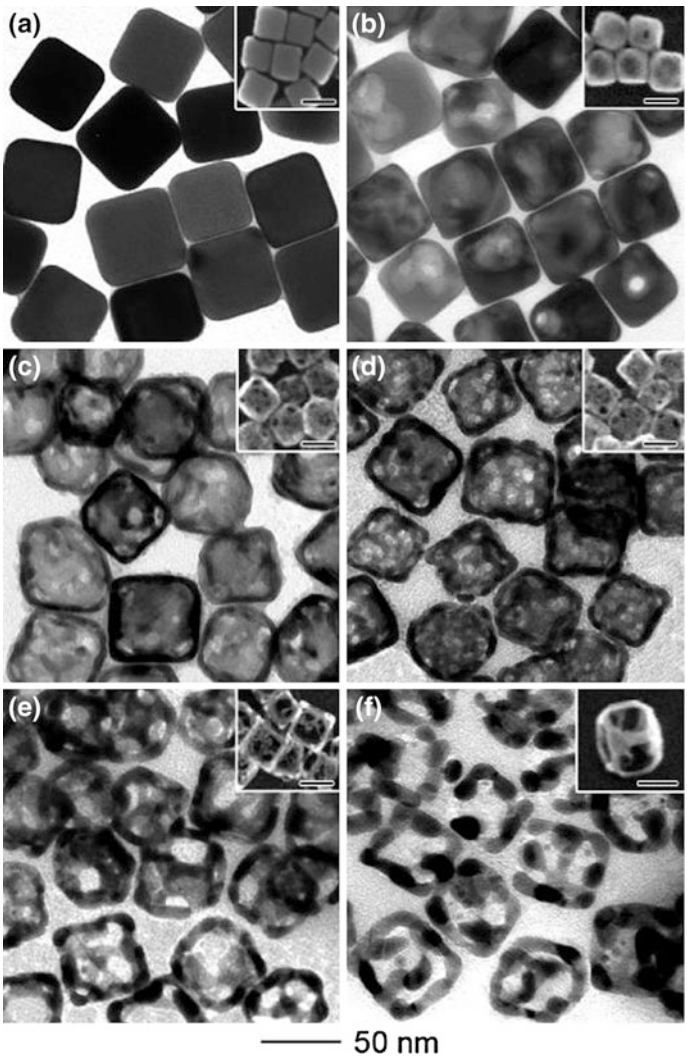

Fig. 3.8 TEM and SEM (*inset*) images of **a** 50-nm Ag nanocubes; **b** Au/Ag alloy nanoboxes obtained by reacting the nanocubes with 4.0 mL of 0.2 mM $HAuCl_4$ aqueous solution; and **c**–**f** nanocages and nanoframes obtained by etching the nanoboxes with 5, 10, 15, and 20 μL of 50 mM aqueous $Fe(NO_3)_3$ solution. The inset in (**f**) was obtained at a tilting angle of 45°, clearly showing the 3D structure of a nanoframe. The scale bars in all insets are 50 nm. EDX analysis indicates the atomic ratio of Au:Ag was 15:85, 30:70, 45:55, 60:40, and 100:0 for the samples in panels b, c, d, e, and f, respectively [130]. Copyright 2007 American Chemical Society

3.3 Properties

3.3.1 Morphology

For the AuNPs synthesized by seed-mediated growth approach [109], AuNPs generally show morphologies of tetrahedron (four triangles) [131], hexahedron (cube, six squares) [132], octahedron (eight triangles) [133], dodecahedron (twelve pentagons) [134], and icosahedron (twenty triangles) [135], which are characterized by low-index facets ({111} for tetrahedron, octahedron, dodecahedron and icosahedron, and {100} for the cube. AuNPs also showed rhombic dodecahedral shape [133], which could further transform into other nonplatonic shapes such as rhombic cuboctahedron and then truncated octahedron in the presence of PVP at a low water content [109].

3.3.2 Optical and Photothermal Property

One characteristic property of AuNPs is that they exhibit LSPR, an optical phenomenon leading to confined resonant photon within the dimensions of the AuNPs when a AuNP interacts with incident photons, which results in an oscillation of the conduction band electrons back and forth on its surface and further induces a charge separation between the free electrons and the ionic metal core, and thereby generates a dipole oscillation [136]. The LSPR oscillation of the colloidal AuNPs usually results in a certain color of the solution that has a strong absorption signal in the visible region. The LSPR is dependent on the particle material, size, shape and the dielectric properties of the surrounding medium [137]. For spherical AuNPs, both light absorption and scattering are enhanced by AuNPs, which cause light extinction [138]. Based on Mie theory and relative Gan theory [139], quantitative description of the cross-sections of absorption (C_{abs}), scattering (C_{sca}), and total extinction (C_{ext}) are derived [140].

Different from those of spherical AuNPs, anisotropic AuNPs have their own particular LSPR. Normally, AuNPs with core diameters between ~3 and 200 nm display a LSPR with a maxima intensity at approximately 520 nm. AuNRs are well known for their characteristic LSPR signals: once the symmetry of the gold core is altered to the anisotropic AuNRs, two distinct LSPR modes corresponding to the different axes across the AuNRs emerged, i.e. a transverse LSPR along the short axis and a longitudinal LSPR along the long axis. Typically, the longitudinal LSPR peak will red shift when the aspect ratio increases, which has been investigated by simulation and demonstrated in experiments [138]. A representative experimental example is displayed in Fig. 3.9 [141]. Quantitatively, it has been discovered that there is a linear relationship between the peak position and aspect ratio [47]:

$$\lambda_{max} = 95R + 420$$

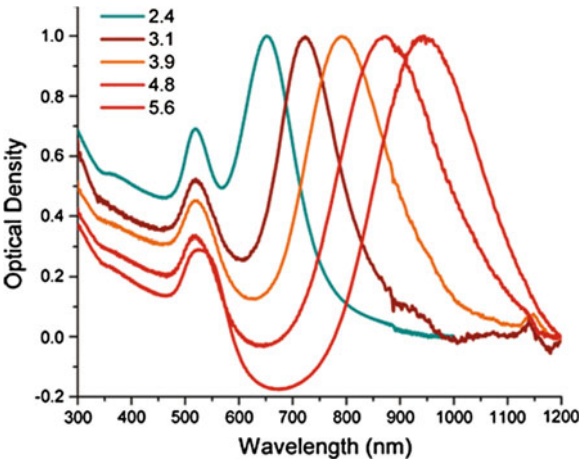

Fig. 3.9 Surface plasmon absorption spectra of AuNRs of different aspect ratios, showing the sensitivity of the strong longitudinal band to the aspect ratios of the AuNRs [141]. Copyright 2006 American Chemical Society

Owing to the interesting photothermal effect of AuNRs, they show promising biological and biomedical applications. When AuNRs are exposed to the laser light resonant with their surface plasmon oscillation, they can strongly absorb the light and rapidly convert it into heat via a series of photophysical processes. The mechanism was investigated and explained by El-Sayed group [142]. When the heating rate is much faster than the cooling rate, heat is accumulated within the lattice causing a temperature rise of the AuNRs in a short time which is sufficient enough to lead to structural changes, such as shape transformation and particle fragmentation. For example, when a colloidal AuNR solution was exposed to femtosecond laser pulses (100 fs, 52 μJ) [143], the shape transformation is observed as shown in Fig. 3.10. The wavelength of the exciting laser (800 nm) coincides with longitudinal plasmon absorption of AuNRs. In Fig. 3.10b, all the AuNRs have transformed into spheres. For the UV-vis spectrum in Fig. 3.10c, only one LSPR band at about 520 nm exists for typical spherical AuNPs and the longitudinal plasmon band has totally disappeared. In Fig. 3.10d, the volume of the resulting spherical particles is similar to the original AuNRs, which concludes that AuNRs melt into spherical AuNPs under the intense laser irradiation based on photothermal effect. From more exploration, it was discovered that the shape transformation of AuNRs depends on laser's energy and pulse-width [143], and the unusual photothermal melting process and its mechanism were investigated [144]. Also there are other related spectral properties such as the aspect ratio dependent fluorescence [145], shape-dependent electron-photon relaxation [146] and LSPR line width (for sensing local environmental changes for biomolecular recognition) [147].

Since AuNRs have important applications in sensing, plasmon-enhanced spectroscopies, biomedical imaging, and photothermal therapy for cancer, controlling the shapes (aspect ratio) and sizes of AuNRs with desired physical and chemical properties are required, which are crucial for their performances [148]. For example, AuNRs with larger aspect ratio have response to NIR light and therefore are

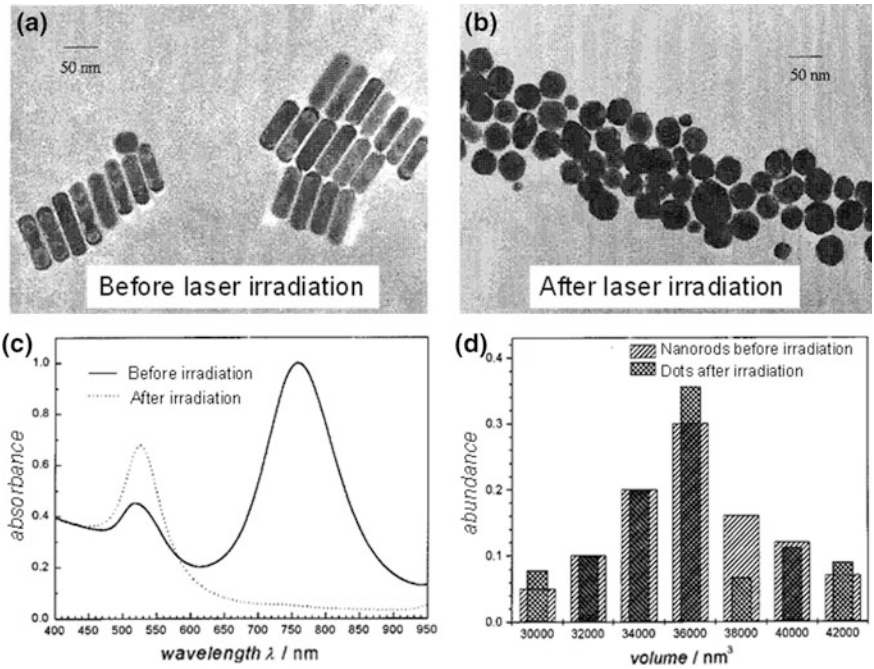

Fig. 3.10 Effect of laser heating on AuNRs, shown in TEM images of a colloidal AuNR solution having a mean aspect ratio 3.8 before (**a**) and after (**b**) irradiation with 100 fs laser pulses centered at 800 nm. **c** UV-vis absorption spectra of this colloidal gold solution before (*solid line*) and after (*dotted line*) irradiation with laser pulses. **d** The volume of the AuNRs before and after this laser irradiation is compared [143]. Copyright 1999 American Chemical Society

excellent candidates for photothermal therapy. At a fixed aspect ratio, larger AuNRs having larger extinction coefficients due to stronger light scattering provide better performance in optical imaging applications, whereas smaller AuNRs provide improved efficiency in photothermal therapy applications due to their higher absorption efficiency [149]. The plasmon bands of other anisotropic AuNPs with different shapes have been also explored [129, 150]. Typically, there are bands from separate parts and ensemble structure. For example, gold nanostars show a plasmon band of the core and variant plasmon bands relating to the tips and core–tip interactions [111].

3.3.3 Surface Enhanced Raman Scattering (SERS)

Because of the plasmon resonance, the Raman signals depending on the power of the local electric field is very high at the AuNP surface. Originating from the dramatic amplification of electromagnetic fields in the AuNP ensembles, AuNPs in

close proximity to each other will result in near-field interparticle interactions, creating a collective extinction response that is quite different from the individual ones [151]. Excitation of the LSPR produces a strong electromagnetic field at the surface of the AuNP that can interact with materials in close proximity to the AuNP surface [22, 152]. The plasmon electromagnetic field can therefore be used to enhance the scattering spectra of chemical species adsorbed on AuNPs, a phenomenon known as surface enhanced Raman scattering (SERS) or to detect changes of specific analytes in the local chemical environment. For anisotropic AuNPs, the Raman scattering signal of molecules is enormously enhanced by contributions from the strong absorptions in the NIR regime and the extremely high electric field intensities at the tip or hollow structures [153]. Therefore, it is necessary to control the size, shape, and structure of anisotropic AuNPs to effectively enhance the sensitivity of effective molecular detection [77, 154]. The most attractive ones are AuNRs because of their easily accessible anisotropic shape and tunable size. There are two coupling fashions for AuNRs: side-by-side and head-to-head configurations which result in different shifts of LSPR signals: the one with side-by-side geometry shows a blue-shift in the longitudinal LSPR and a red-shift in the transverse LSPR, while the other with head-to-head geometry shows a red-shift in the longitudinal LSPR with little change in the transverse LSPR [155]. Such plasmonic coupling effect is an emerging field which is of great interest to SERS applications for molecular detecting as the SERS effect of AuNRs is much higher (e.g. 10^5 times) than spherical AuNPs [156]. On the aspect of biomedicine, AuNRs aligned by oral cancer cells showed excellent sensitivity in detecting the cancer cells [157]. Acidic cancer cells and healthy cells are distinguished by monitoring changes in the Raman spectrum induced by pH changes of carboxy groups in a mercaptobenzoic acid layer on HAuNSs which have activity in NIR region [158].

3.3.4 Fluorescence Enhancement and Quenching

The interaction between AuNPs and a fluorophore results from a change in the electromagnetic field and the intensity of the photonic mode near the fluorophore. For AuNP–fluorophore distances less than 4 nm, the fluorescence is strongly quenched. At larger distances, the fluorescence intensity is increased. For fluorescence quenching, characteristic fluorescence of organic dyes such as perylene and porphyrin attaching on AuNP and AuNR surface via Au–S linkage with distance less than 4 nm were significantly quenched (Fig. 3.11) [159, 160]. In another experiment, the simple inert short *n*-C_{10} alkyl chain protected AuNPs with different size and AuNRs could quench the perylene diimide dyes (PDIs) close to their surface, from which the mechanism of such quenching effect was investigated and ascribed to energy transfer [161]. The fluorescence enhancement originates coupling with far-field scattering. For example, the quantum yield of indocyanine green (ICG), a NIR fluorophore, was increased by up to 80 % near the surface of an Au

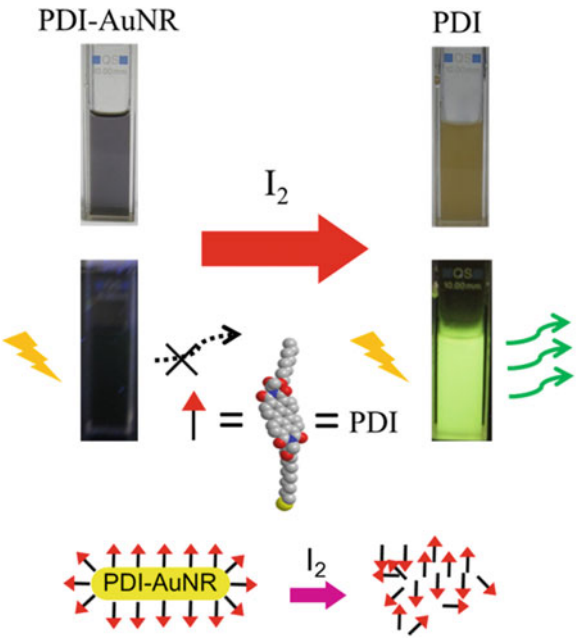

Fig. 3.11 *Left* PDI-AuNR CH_2Cl_2 solution shows no emission under UV lamp (365 nm, 6 W). *Right* free PDI after detaching from PDI-AuNR by adding I_2 in CH_2Cl_2 solution shows strong *yellow −green* fluorescence under UV lamp [160]. Copyright 2012 American Chemical Society

nanoshell. Such conjugates have been used for enhancing sensitivities in fluorescence imaging in vitro and in vivo [162].

3.3.5 Toxicology

In general from in vitro studies, AuNP cores are nontoxic for cells, which are in contrast with other nanoparticles such as carbon nanotubes, asbestos, and metal oxides causing drastic damage to cells. Anisotropic AuNPs have an enormous potential in theranostics and addressing the in vivo nontoxicity of these AuNPs are essential to convince drug administration. In vitro and in vivo toxicology studies have been undertaken to examine the damage of cells, tissues, and organs of animals upon loading AuNPs for biomedical applications [22, 163].

In vitro studies have shown that the toxicity of AuNRs is ascribed to the CTAB ligands, rather than the Au core itself. Researchers successfully found biocompatible materials such as polyacrylic acid or poly(allylamine) hydrochloride to coat AuNPs, resulting in almost no death of cells [164]. For citrate-capped AuNPs, a study in mice by Chen et al. showed that small (3–5 nm) and large AuNPs (30 and 100 nm) were not toxic, but medium-sized AuNPs (8, 12, 17, and 37 nm) provoked severe sickness, loss of weight, change in fur color, and shorter life spans due to injury of the liver, spleen and lungs [165].

For the stability issue of AuNPs in biosystems, it is also an important subject to be investigated, since AgNPs are as intrinsically toxic for their relative easy

oxidation to Ag^+. On contrary, Au^0 is much more difficult to oxidize than Ag^0, which guarantees the safety issue of AuNPs. The AuNP cores of isotropic AuNPs larger than 5 nm are biologically inert [22, 166]. However, for the anisotropic AuNPs with highly exposed AuNP surface areas and defects, more studies are required aiming at the toxicology in biosystems.

3.3.6 Surface Modification

Surface modification not only provides stability to the AuNPs, but also introduces foreign functions. In addition, to introduce AuNPs into biosystems, it requires surface modification for desirable compatibility with the systems.

A number of organic materials are used to functionalize AuNPs and introduce multiple functions. This has been realized by the exchanging process in which the surface grafted surfactant molecules exchange with functional organic molecules, usually a type of organic thiols (RSH) or a mixture of two kinds of organic thiols. Owing to the strong covalent Au–S bondings, this is a relatively simple and effective procedure that can completely remove the original surfactants and replace with organic functional thiols on the entire surface. For the organic thiol monolayer protected anisotropic AuNRs, the solubility, surface chemistry and related properties are dominated by the organic shell. Simple *n*-alkyl thiols [167], and other functional materials such as photoresponsive azo thiols [168], chiral-azo thiols [169], organic dyes (porphyrin, perylene) [159, 160] and polymers terminated with thiols (poly2-(dimethylamino)ethyl methacrylate, poly(acrylic acid), polystyrene) have been used [170].

Different from isotropic AuNPs, AuNRs have unique properties in thiol exchange process and the resulting AuNRs have more shape-dependent properties. For example, the seed-mediated growth approach prepared AuNRs coated by CTAB with open positions on the two heads where there are no CTAB surfactant molecules covering [29]. Therefore, the thiols will first bind on the open tips of these AuNRs and then replace the CTAB surfactants on sides, leading to sequential surface modification of AuNRs which induce more functions such as directed self-assemblies, including side-by-side and head-to-head types [171].

Another effective way to functionalize the surface of AuNR is covering the surfactant layer (e.g. CTAB) with materials having intermolecular interactions such as electrostatic and ionic interaction to CTAB molecules. With the presence of the CTAB layer on the surface imparting a net positive charge, alternate adsorption of anionic and cationic polyelectrolytes on these positively charged AuNRs leads to the formation of polyelectrolyte multilayers around the AuNRs [172, 173]. One representative example of AuNRs coated by polyelectrolytes multilayers [poly acrylic acid sodium salt (PAA) and polyallylamine hydrochloride (PAH)] is displayed in Fig. 3.12, which briefly indicates the process of layer-by-layer coating on AuNRs and encapsulating of functional small Rhodamine 6G molecules.

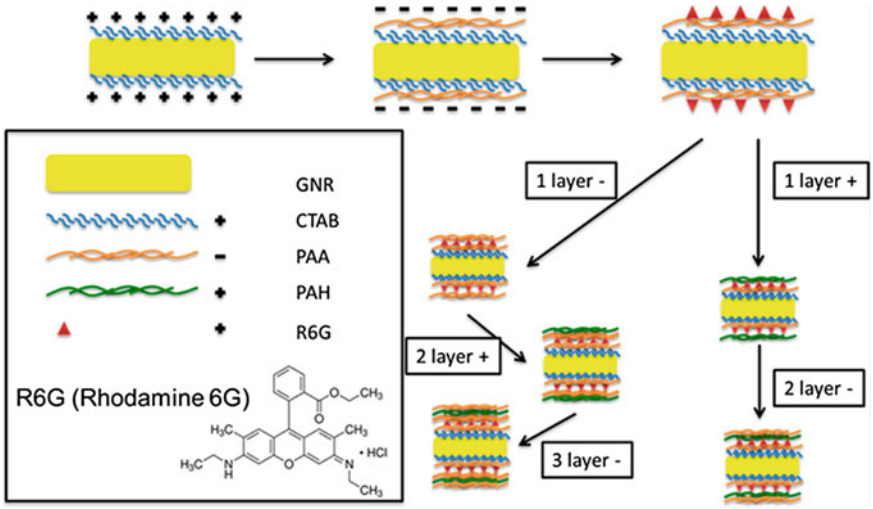

Fig. 3.12 AuNR coated with layer-by-layer polyelectrolytes where and R6G is wrapped in different types of polymer layers [173]. Copyright 2012 American Chemical Society

The critical prerequisite to introduce AuNRs into the biosystem is to functionalize AuNRs with biocompatible materials, because for potential clinical trials, AuNRs should be friendly to human health and the environment. With the widely used seed-mediated synthesis approach, AuNRs are coated by a CTAB layer. Free CTAB molecules are detrimental to human cells but surface bound CTAB molecules are not toxic [174] and AuNRs are supposed to be safe for in vivo and clinical studies. However, although free CTAB molecules can be separated by centrifugation or dialysis membrane, CTAB surfactants could leave AuNR surface because they are dynamically unstable. The charge interactions that adsorb CTAB on AuNR surface are much weaker than Au–S covalent bonds. Therefore, a better way is to modify the AuNR surface that CTAB is either replaced or covered by biocompatible molecules. For example, by coating phosphatidylcholine on AuNRs, there was much lower cytotoxicity than the twice-centrifuged CTAB-AuNRs [175]. Poly (diallyldimethylammonium chloride)-AuNR, poly(4-styrenesulfonic acid)-AuNR even showed no observable toxicity [176]. Another simple approach to prepare biocompatible AuNRs is using polyethylene glycol polymers (PEG), via mixing PEG-SH with the CTAB-AuNR in solution undergoing thiol exchange for hours [177]. More experiments have been carried out to conjugate biomolecules to AuNRs and mainly four different methodologies have been developed: (a) direct ligand exchange, (b) electrostatic adsorption, (c) the use of a biofunctional linker, and (d) surface coating [148].

The thiol exchange reaction is effective for small biofunctional molecules such as 3-mercaptopropionic acid (MPA) [178], but challenging for large molecules such as antibodies and proteins that are too large to reach the AuNR surface because of the densely packed CTAB layer.

3.3.7 Supramolecular Organizations (Self-assembly and Alignment)

The functional molecules providing attractive intermolecular interactions on the surface of AuNPs could work as molecular "glue" to assist anisotropic AuNP assemblies. For anisotropic AuNPs, the LSPR allows them to concentrate and manipulate light depending on their size, shape and proximity and assemblies in specific patterns. For example, AuNRs having head-to-head or side-by-side assembly fashions exhibit distinct collective properties due to plasmon coupling between them, which are different from those of both individual AuNRs and bulk materials [109, 179]. Controlling and tuning anisotropic AuNP self-assemblies are highly interesting and vital. The AuNR self-assembly might potentially contribute to the preparation of metamaterials with unusual electromagnetic properties [180]. To achieve AuNR self-assemblies, intermolecular interactions offered by functional materials on AuNR surface can be exploited. So far, promising AuNR self-assembly nanostructures have been developed. Bifunctional small molecules with a thiol on one end for binding onto AuNRs and another functional group on the other end providing intermolecular interaction are used to promote head-to-head AuNR assemblies. The first chemically driven assembly of AuNRs by DNA was reported by Dujardin et al. who assembled AuNRs in parallel stacks by DNA hybridization [181]. Appropriate choice of the thiolate ligands (e.g. 1,2-dipalmitoyl-sn-glycero-3-phophothioethanol) [182] or mercaptopropylsilane [183]) and solvent evaporation are joint to prepare side-by-side assembly of AuNRs. Recently, prominent results have been found. For example, with hydrophobic favoring effect, AuNRs with PS on AuNR tips resulted in impressive linear chain like head-to-head assemblies (Fig. 3.13) [171]. Functional groups, providing streptavidin bridging, hydrogen bonds and DNA hybridizations, are good candidates. For example, AuNRs are functionalized with thioacetic acid at the ends and further conjugated to anti-mouse IgG [184]. Mouse IgG having two binding sites with the AuNRs is added and initiated AuNR head-to-head assemblies forming linear chains up to 3 mm.

Apart from thiols, Pan et al. [185] showed that the AuNRs can be directly assembled into 1D and 2D architectures via the electrostatic interaction between DNA and AuNRs. Such assemblies via ionic interaction were also demonstrated using adipic acid [186], citrate molecules [187], and dimercaptosuccinic acid [182]. By using Gemini surfactants replacing CTAB during AuNR growth, the resulting AuNRs can self-assemble even into standing superlattices formed during drying [188]. This method has also been applied to inorganic Ag layer coated AuNRs, which form similar 3D super lattices of AuNR side-by-side assemblies, demonstrating highly efficient SERS [189].

Furthermore, inducing AuNR alignment in thin film is of particular importance for their practical applications [190, 191]. In early work, an electric field was tested to induce AuNR alignments in solution [192]. Recently, Lavrentovich group has applied electric field to align colloidal AuNRs in a concentric fashion to

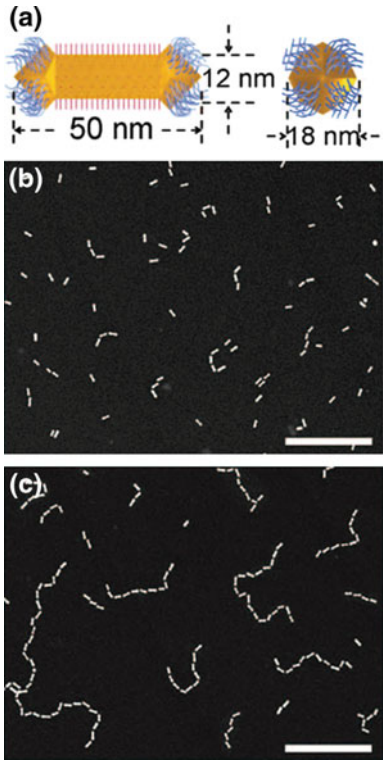

Fig. 3.13 **a** Schematics of the side view of the long face (*left*) and the edge (*right*) of the AuNR carrying CTAB on the long side and thiol-terminated PS molecules on the ends. (**b** and **c**) Darkfield TEM images of the AuNR chains after 2 (**b**) and 24 (**c**) hours assembly. $[M]_0 = 0.84 \times 10^{-9}$ (mol/L). Scale bar, 100 nm (both panels) [171]. Copyright Science 2010

demonstrate cloaking effect, which is similar to the simulated prediction model [193]. LCs provide a long range orientational order to assist AuNR alignments which also respond to external field such as mechanical, electric and magnetic field. Lyotropic LC hosts that form nematic and hexagonal phases can be quite advantageous in aligning a high loading of AuNRs which are functionalized with micelles on surface [194]. Recently, organo-soluble thermotropic LCs were also used for such purpose [195]. In solid medium, polymer engineering is an attractive strategy to assemble AuNRs. AuNRs dispersed poly(2-vinyl pyridine) (P2VP) polymer films exhibit controllable optical properties through AuNR self-assembly and percolations [196]. There are other polymers such as poly(*N*-isopropylacrylamide) and its acrylic acid derivative [197, 198], poly(vinyl alcohol) (PVA) [191, 199], poly (styrene-b-methylacrylate) [200] enable fabrication of anisotropic arrangements of AuNPs. For example, colloid AuNRs were embedded during the polymer preparation. The alignment of AuNRs can be confirmed by polarized light: with the electric field of the incident light parallel or perpendicular to the alignment direction of AuNR, only the longitudinal or the transverse LSPR band can be excited and detected [191]. In another way using patterned channels, translational ordered AuNR arrangements have been fabricated by the synergetic self- and directed-assembly processes and lithography [201].

3.4 Applications

Unlike spherical AuNPs, there are more remarkable plasmonic phenomena of anisotropic AuNPs. Among them, particularly for AuNRs with exceptional optical properties, a variety of applications have emerged including biological and biomedical applications such as biosensing, biomedical imaging, gene and drug delivery, disease detection, diagnosis, plasmon-enhanced spectroscopy, and photothermal cancer therapies [22, 142, 202].

3.4.1 Catalytic Application

The catalytic activity and sensitivity of metal NPs (MNPs) are dependent primarily on their size and shape. As a consequence of the presence of sharp edges and corners, the number of active surface sites in anisotropic AuNPs is very high compared to spherical AuNPs. Therefore nano-engineering is crucial in tailoring NP properties.

A breakthrough in catalysis research that opened up a wide area of AuNP-catalyzed oxidation reactions [203] is carbon monoxide (CO) oxidation by dioxygen at low temperature catalyzed by small (<5 nm) AuNPs on titanium oxide [204]. It is widely accepted that CO molecules are preferentially adsorbed at edges and steps on the surface of AuNPs rather than on the facets. For example, it was shown that the perimeter interfaces around AuNPs are the sites for CO oxidation [205]. Thus, research interests in such catalysts began to focus on anisotropic AuNPs [206], which show higher catalytic efficiency than simple AuNPs due to more edges and steps on anisotropic ones [207]. Some hybrid bimetallic anisotropic AuNPs also exhibit high activities in various catalytic reactions [208–210], e.g. for the tandem reaction of alcohols and nitrobenzenes to generate N-alkyl amines and imines [209].

3.4.2 Sensors and Molecular Recognition

Since the strong affinity between anisotropic AuNPs and heavy metal cations can alter the position of the plasmon band of AuNRs or the fluorescence of targeted ions, it allows detecting heavy metal cations in aqueous solutions with ultrahigh sensitivity without sample pretreatment. Since the LSPR frequency of AuNRs depends on the dielectric constant of the surrounding medium, the shift of LSPR band provides an opportunity to monitor the changes of the local environment, which can be used for sensors [211]. There are many examples of functionalized AuNRs for devices including multiplex colorimetric detection [212, 213]. Heavy metal ions are widely distributed in biological systems that play an important role in

many biological and environmental processes. The analytical determination of toxic metals is an important issue in both environmental monitoring and clinical research [214]. Currently, AuNRs are the most widely used anisotropic AuNPs for detecting heavy metal ions. A multiplex biosensor assay using different responses of AuNRs relating to different targets is developed [215], in which human, rabbit, and mouse immunoglobulin G (IgG) were conjugated to AuNRs with different aspect ratios via a MUDA linker. Variant shifts of the LSPR wavelength of AuNRs were monitored when binding to their respective complements (anti-IgGs). Except for the absorption spectrum shift of AuNRs, the scattering wavelength shift from individual AuNRs was also reported in biomolecular protein sensing [213]. Single molecular DNA detection is achievable by using AuNR sensors linked to F1-ATPase motors in dark field microscopy [216].

In recent years, AuNRs as SERS probes in biological applications were intensively investigated [156, 217]. The reasons are: they have strong SERS enhancement; their LSPR bands can be tuned by the aspect ratio to match with the excitation laser (especially in the harmless red to NIR region); and they have proper size (length scale of 20–100 nm) with optimal enhancement [217]. Although using SERS effect for sensing was first discovered based on spherical AuNPs [218], AuNRs show much stronger SERS enhancement with the factors on the order of 10^4–10^5 due to the lightening-rod effect [156]. One representative example is peptide-conjugated AuNRs for molecular cancer diagnosis [219].

The AuNRs with various functionalized ligands on the surface exhibit the variation in the characteristic longitudinal plasmon absorption when in contact (coordination) with metal ions. Cysteine (Cys) modified AuNRs have been used as colorimetric probes in the titration of Cu^{2+} ions. The strong coordination of Cu^{2+} ions with cysteine results in a stable Cys-Cu-Cys complex and induces the aggregation of the AuNRs along with a rapid color change from blue-green to dark gray [214]. Dithiothreitol (DTT) modified AuNRs were used as a LSPR sensor of Hg^{2+} ions. In this case, the DTT molecules were strongly adsorbed on the surface of the AuNRs through thiol groups and induced the aggregation of AuNRs. The induced aggregation of AuNRs was inhibited in the presence of Hg^{2+} ions, and the aggregation level was dependent on the concentration of Hg^{2+} ions. The degree of aggregation could be determined by the change in the intensity of the longitudinal plasmon absorption in the UV/Vis spectrum [220]. The detection of some other metals such as Cr^{6+} and Pb^{2+} was recently reported by using a similar method [221].

Besides the change of longitudinal plasmon absorption signal, fluorescence is another effective method for ion detection, for example for the detection of Hg^{2+} ions in a homogeneous medium, with AuNRs used as a fluorescence quencher [222]. Nanowires are required for applications such as ultrasensitive and multiplex DNA detection through SERS and other biomedical SERS-based techniques [223]. Bimetallic AuPtNWs are useful electrochemical sensors for glucose with increased selectivity, sensibility, and repeatability compared to monometallic nanowires [73].

Besides AuNRs, other shapes of anisotropic AuNPs also have advantages for biosensors [224]. Au nanopyramids, nanotubes, nanocages, nanowires, nanostars and Au@Ag NRs have been reported as biosensors and bioprobes [225]. These

anisotropic AuNPs functionalized with specific molecules (small molecules, DNA, antibodies, and biotin) can recognize particular nano-objects (protein, DNA, drugs, and streptavidin) based on the change in the plasmon absorption, or the SERS intensity. Conical AuNT/pores can be advantageous to avoid unwanted plugging and are ideally suited to detect protein-type bioanalytes [226]. Au nanoplates exhibit a wide range of unique electrical and optical properties. For example, they show significant SERS [227], tip-enhanced Raman scattering (TERS) [228], and a shape- and size-dependent surface plasmon absorbance in the visible to IR region, which have potential applications in sensors and probes [228]. Dendritic AuNPs exhibited significant catalytic activities, and the good SERS sensitivity for the detection of biomolecules also indicated their potential applications in biosensing and nanodevices. SiO_2@Au NPs were applied to optical imaging [229], biomedical detection [230], and photothermal cancer therapeutic ability [231], and may enable a new class of infrared materials, components, and devices to be developed. AuNCs and Au nanoframes were investigated in catalysis [232] and biosensing in view of their controllable LSPR properties that depend on the size and, most importantly, the thickness of the walls [233].

Similar to biosensors described above, with the same principle of showing LSPR shifts, anisotropic AuNPs are used for molecular recognition. For example, functionalized AuNRs and Au nanoplates have been used for organic solvent recognition, toxin recognition and glucose recognition, respectively [94, 234, 235].

3.4.3 Nanoelectrodes

Anisotropic AuNPs have also been used in electrochemistry applications. Au nanotubes were applied as nanoelectrodes showing a much higher sensitivity (more than twice) than the embedded Au nanoelectrodes, which could be used in applications like molecular detection [236]. The AuNWs and AuNTs synthesized in this way can be used as nanoelectrodes, molecular filters, and chemical switches [75].

3.4.4 Biomedical Applications: Imaging, Diagnostics and Therapy

3.4.4.1 Imaging

AuNRs, HAuNSs, AuNCs, and Au nanostars are remarkable anisotropic AuNPs for biomedical applications because: (1) they have a large absorption in the NIR window for photothermal therapy; (2) they can selectively accumulate at sites of interest through the enhanced permeability and retention (EPR) effect or by surface modification with specific coatings; (3) their simple functionalization (e.g. with PEG) and structural features allow their use as nanocarriers for drugs, DNA, or

RNA; and (4) they have long body circulation times [129, 237]. The emerged term "theranostic" of AuNP nanocomposites combines functionalities of both contrast agent and therapeutic actuators within a single nanoparticle. Au nanoshells were the first AuNPs to be used as efficient theranostic agents that combine imaging and phototherapy functions [162].

The development of new techniques to diagnose cancer early is contributing to increase the cancer survival rate. To detect the cancer cells, AuNPs such as spherical Au nanoshells [162], AuNPs [238], AuNRs, Au nanocages, and Au nanostars are photoresistant and stable, thus offering long-time operation for optical imaging, owing to their unique interaction process with light particles showing efficient contrast in optical imaging. The most important factors in vivo diagnostic techniques include light scattering imaging, two-photon fluorescence imaging, and photothermal/photoacoustic imaging [22]. The Au nanoshells developed by Halas and co-workers that scatter light in the NIR physiological "water window" have been used as contrast agents for dark-field scattering [162, 229], photoacoustic imaging [162], and optical coherence tomography (OCT) [162, 231].

AuNPs strongly scatter light of their plasmon wavelengths. AuNRs having strong scattering in the NIR region are capable of detecting cancer cells under excitation at spectral wavelengths where biological tissues absorb only slightly (Fig. 3.14) [141]. For other imaging techniques, AuNRs can greatly enhance the contrast in the photo acoustic tomography (PAT) technique due to the high

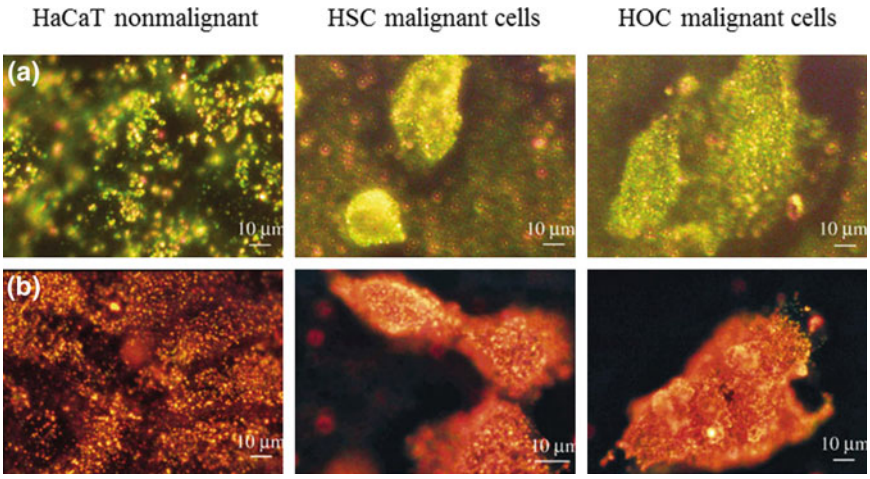

Fig. 3.14 Cancer diagnostics using AuNR-enhanced light scattering. Optical dark-field microscopy of normal HaCaT cells and cancerous HSC and HOC cells incubated with anti-EGFR antibody conjugated gold nanospheres (*top panels*, *left* to *right*). *Bottom*, as above, but with AuNRs. Anti-EGFR-conjugated gold nanoparticles specifically bound to cancer cells, thereby resulting in strong scattering under dark-field microscopy and thus enabling detection of malignant cells. **a** Light scattering images of anti-EGFR/Au nanospheres after incubation with cells for 30 min at room temperature. **b** Light scattering images of anti-EGFR/Au nanorods after incubation with cells for 30 min at room temperature [141]. Copyright 2006 American Chemical Society

efficiency of the surface plasmon absorption in the NIR region for opto-acoustic imaging [239]. For example, Etanercept-conjugated AuNRs were able to show PAT imaging of a rat tail joint [240] and this technique can be used for detecting prostate cancer [241]. Currently, dark-field imaging based on the light-scattering properties of anisotropic AuNPs (shells, spheres, rods, and cages) is widely used for cancer imaging through functionalized nanoparticle–receptor binding to cell-surface biomarkers [22, 242]. Compared with Au nanoshells, the AuNCs appear to be more effective contrast enhancement agents [243].

3.4.4.2 Photothermal Therapy

Using photothermal effect, there are applications of AuNPs for thermal therapy, drug/gene delivery. Thermal therapy involves the destruction of cancer cells by heating. Taking AuNRs as an example, they can release heat during relaxation after irradiated by laser pulse [141, 244]. When activated by a NIR laser which can penetrate cells or tissues without damage, AuNRs with low aspect ratio can be used as therapy agents to treat tumor cells in vitro based on such photothermal effect [141]. Various energy sources have been applied, including radio frequencies, high-intensity focused ultrasound, microwaves, and lasers. The heat energy can be delivered by external or internal manners, through interstitial, intraluminal, or intracavitary approaches. However, because of absorption by normal tissues, the amount of energy delivered to the treatment volume is limited, which reduces the potency of the thermal effect. To improve the efficacy and tumor selectivity, light-absorbing materials (known as photothermal contrast agents) are introduced into tumor cells to mediate the photothermal effect. A temperature increase of 30–35 °C provokes cell death. Various Au nanostructures, including nanoshells [245], NRs, NCs, and nanostars that absorb NIR light (wavelength 700–850 nm), have been shown to be effective in photothermal therapy [246]. The first use of anisotropic AuNPs in targeted photothermal therapy was conducted by the Halas research group by using silica@Au nanoshells functionalized with antibodies such as anti-HER2. The antibodies directed the AuNPs toward the cancer cells because they could conjugate with surface cell markers that were overexpressed by cancer cells. These antibodies were linked to orthopyridyl disulfide-PEG-*n*-hydrosuccinimide (OPSS-PEG-NHS) that was bound to the Au surface through strong Au–S bonds. The advantage of the PEG linker is that it provides an enhanced permeability and retention effect which involves the new blood vessels formed at the tumor site. This photothermal therapy was first demonstrated in mice with subcutaneous tumors of 1 cm size. Analysis showed that photothermal treatment resulted in tissue damage over a similar sized area as that was exposed to laser irradiation. Magnetic resonance thermal imaging (MRTI) revealed an average temperature increase of 37 °C after 5 min irradiation, which is sufficient to induce irreversible tissue damage. Nanoshell-free samples showed an average increase of 9 °C, which was considered to be safe for cell viability [247].

AuNRs have been extensively applied in this research recently. El-Sayed and coworkers pioneered strategies in utilizing AuNRs in photothermal therapy. In an

example of preferential AuNR binding to human oral cancer cells, conjugation of AuNRs to anti-EGFR antibodies could enable selective photothermal therapy [141]. In more-recent studies, they linked macrolide to PEG-functionalized AuNRs, which preferentially delivered AuNRs into inflamed tumor tissues via tumor-associated macrophage cells (TAMs) [248]. AuNRs coated by mPEG-SH 5000 could be activated by 808 nm laser with an energy of 1 W/cm^2 for 10 min and then effectively stopped the growing of mice tumors [249]. The photothermal heat generated by laser irradiated AuNRs in cells can be calculated [250]. In addition, it is noteworthy to point out in the case of pulse laser irradiation, it could induce cell death, while successive irradiation causes reshaping of the nanorods into nanospheres, thereby preventing the cell death [251]. Their promising function in photothermal therapy has the potential to replace conventional surgery and chemotherapy [252].

AuNCs with large absorption cross-sections also show a large photothermal effect. The absorbed photons are converted into phonons (lattice vibrations), which in turn produce a localized temperature increase. Xia and co-workers demonstrated the photothermal destruction of breast cancer cells in vitro through the use of immuno-AuNCs. AuNCs with an edge length of 45 nm were selected because of their predicted large absorption cross-section. SK-BR-3 cells were treated with these immuno-AuNCs, and then irradiated by a laser with a wavelength of 810 nm and a power density of 1.5 Wcm^{-2} for 5 min. The treated cells were stained with calcein-AM and ethidium homodimer-1, so that live cells showed green fluoresce and dead cells showed red fluoresce. This analysis revealed a well-defined zone of cellular death consistent with the size of the laser spot [253]. Au nanostars were successfully conjugated with anti-HER2 nanobodies and demonstrated specific interaction with HER2t and SKOV3 cells and the conjugates resulted in specific photothermal destruction of tumor cells in vitro. Exposing the cells to either only NIR light or nanoparticles did not affect cell viability. Nonspecific NPs conjugated with anti-PSA nanobodies did not result in any cell death upon laser irradiation, thus demonstrating the high specificity of these anti-HER2-conjugated Au nanostars [107]. Hybrid nanomaterials composed of two unique components not only retain the beneficial features of both, but also show synergistic properties. Hybrid AuNCs were also investigated in photothermal therapy. Single-wall carbon nanotubes (SWCNTs) were functionalized and attached to AuNCs through a thiol group. The as-prepared AuNC-decorated SWCNTs were then modified with RNA aptamer A9, which is specific to human prostate cancer cells. The photothermal response for the hybrid nanomaterial is much higher than that for single nanomaterials [254].

3.4.4.3 Drug and Gene Delivery

Anisotropic AuNPs have recently been used as nanocarriers for effective drug or gene delivery systems [255, 256]. Generally, surface functionalized AuNRs work as plasmonic carriers that simultaneously exhibit carrier capabilities, improved colloidal stability, plasmonic properties, and non-cytotoxicity under physiological

conditions. Critically, the surface of AuNRs can adsorb cargos such as DNA oligonucleotides, RNA oligonucleotides, and siRNA [238]. For the mechanism that how this system works, since there is shape transformation of AuNRs under exposure to NIR laser pulses, AuNRs are used to release DNA or drugs [257]. The AuNRs assisted gene delivery approach has caught much attention in recent years because they can replace the conventional virus-mediated gene delivery to avoid the risk of cytotoxicity and immunologic responses. For example, thiolated gene having enhanced green fluorescence protein (EGFP) was covalently conjugated to AuNRs and exposed to Q-switched Nd:YLF laser. The laser induced both of AuNR shape transformation and DNA release due to Au–S bond breakage (Fig. 3.15) [257]. During laser irradiation, the intensity of the longitudinal LSPR absorption peak at 782 nm decreased and the transverse LSPR at 520 nm increased, suggesting the transition from rod shape to spherical shape. The irradiated cells showed strong gene expression after 1–2 days, whereas in nonirradiated cells there was no gene expression. Besides thiols, Plasmid DNA was adsorbed to phosphatidylcholine (PC)-modified AuNRs by electrostatic interaction which was release by Q-switched Nd:YAG laser illumination [258]. For the result, 1 % of the DNA molecules was released and 0.5 % was active [255].

With AuNRs, the remote control of gene expression with an optical switch is accomplished. Drug delivery can also be activated under NIR laser irradiation based on AuNRs functionalized with polymer materials, such as typical poly(*N*-isopropylacrylamide) (PNIPAM) as well as its acrylic acid forms [259], due to their prominent thermal responsive properties. When temperature increases above the lower critical solution temperature (LCST), the polymer layer undergoes shrinkage. Laser irradiation induces the AuNRs to produce heat that affects the surface temperature-responsive polymer materials. By electrostatic interactions, both AuNRs and drug molecules are loaded inside the particles. When irradiated by laser, the heating energy by AuNRs triggers the microgel to deswell and release drug molecules. Further when the laser is turned off, the microgel will swell back to its original volume, thus the drug release can be controlled. Figure 3.16 illustrates the process of such laser irradiation controlled volume phase transition of AuNRs embedded PNIPAAM-hydrogels [260]. In the system, PEG modified AuNRs were first prepared

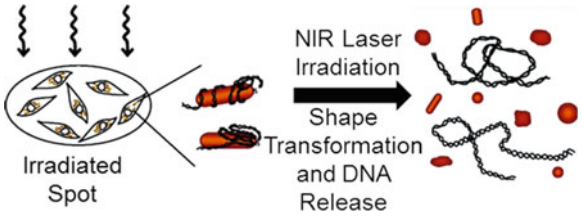

Fig. 3.15 Schematic illustration demonstrating that the cells containing EGFP-AuNR conjugates within a spot (3.5 mm in diameter) are irradiated by NIR laser (*left*). After laser irradiation, the gold nanorods of EGFP-AuNR conjugates undergo shape transformation that resulted in the release of EGFP DNA (*right*) [257]. Copyright 2006 American Chemical Society

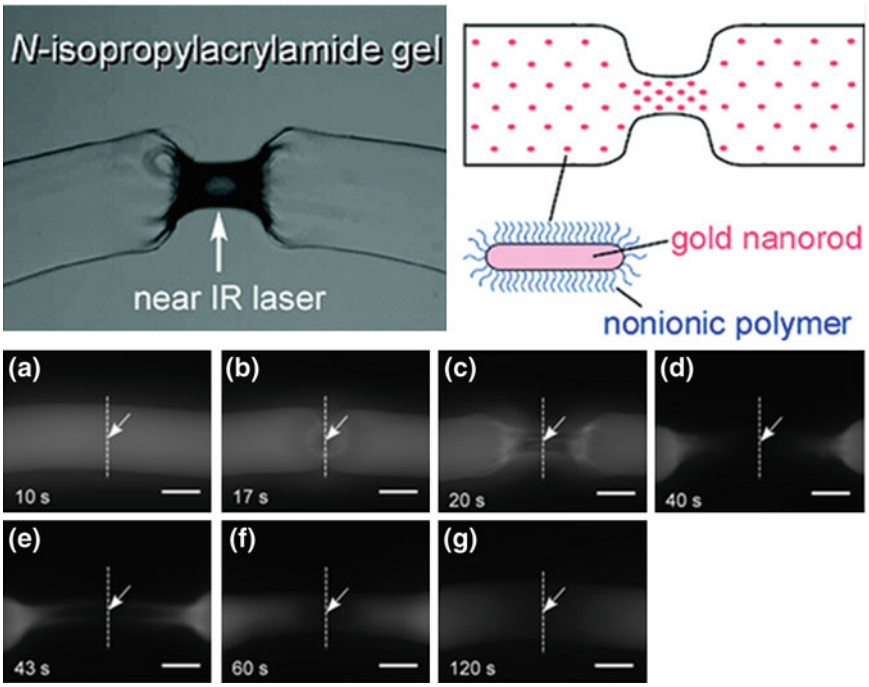

Fig. 3.16 *Top* The collapse of polymer with temperature above its LCST when under IR laser. *Bottom* **a**–**g** Fluorescence microscopic images of the polymer containing AuNRs and R-Dex-1 which has fluorescence during NIR irradiation. *Scale bars* 100 μm [260]. Copyright 2007 American Chemical Society

and then dispersed in PNIPAAM hydrogels, with concentration more than 100 μM. When stimulated by the NIR irradiation with power >490 mW, cylindrical shape gel (original diameter: 140 μm) showed shrinkage at the irradiated spot which further grew along the gel. This induced gel shrinking occurred much more rapidly by NIR irradiation than by temperature increasing. The process was monitored by the fluorescence microscope as the drug molecules (R-Dex-1) showing fluorescence pictured deformation of the gel. With the advantage of the high spatial resolution and rapid release at the irradiated spot, controlled release at the specific point of the drug was successfully achieved [260]. One attractive aspect of functional AuNRs is that they can have these applications simultaneously with proper surface materials. This is also a field for future research. In another example, AuNR/poly(*N*-isoproylacrylamide) core/shell can release norvancomycin under NIR laser irradiation [261].

Halas and co-workers described a SiO_2@Au nanoshell system that released single-stranded DNA from its surface when illuminated with plasmon-resonant light. This system allowed examination of DNA dehybridization induced by excitation of localized surface plasmons on the NPs [262]. In another study, the light-triggered release of the fluorescent molecule DAPI (4,6-diamidino-2-phenylindole) inside living cells was investigated from a host–guest complex with DNA

bound to SiO_2@Au nanoshells [263]. Diagnostic and therapeutic drug delivery based on SiO_2@Au nanoshells was also investigated recently for the treatment of ovarian cancer [264]. With their hollow structures, AuNCs serve as "pockets" that are appropriate for drug release. PEG-coated AuNCs have been used as nanocarriers for doxorubicin and triggered drug release under irradiation with NIR light. This drug delivery system was considered to be a dual-modality cancer therapy that combined both photothermal therapy and chemotherapy. An in vivo study of this delivery system indicated greater antitumor activity than either doxorubicin or AuNCs alone [246]. In another example, AuNCs coated with a thin monolayer of temperature sensitive PNIPAAm and acrylamide (Am) precursors with disulfide groups have been used for triggering release with NIR light. The IR light can be absorbed by the nanocage and converted into heat, triggering the smart polymer to collapse and release the drug payload. When the laser is turned off, the polymer chains will revert to the extended conformation and terminate the release (Fig. 3.17) [265]. The surface of AuNCs was functionalized with thermally responsive polymers to control the release through NIR laser irradiation or high-intensity focused ultrasound. Another system to achieve the controlled release was obtained using a phase-change material (PCM) loaded in the hollow interiors of AuNCs. An increase in temperature uncaps the pores and releases the guest molecules from the AuNCs. The release is controlled by varying the power or duration of the ultrasound treatment [266]. Very recently, Wan and co-workers reported a bioresponsive controlled-release AuNC system. The AuNC was selected as a support and an ATP molecule was used as the target [267].

3.4.5 Optical Tuning

Since AuNRs can provide intensive local electromagnetic fields and large field enhancements [268], there are impressive nonlinear properties leading to applications such as optical devices [269]. AuNRs show important potential in metamaterials, e.g. negative index materials for super lenses and invisible cloaking. For example, the well-organized AuNRs including self-assembly and orientations are demanded [270]. According to the design based on coordinate transformation, AuNRs self-assemble in head-to-head fashion forming continuous strips are good candidate for an optical cloak in visible frequency (Fig. 3.18). The AuNR strips are all perpendicular to the cylinder's inner and outer interfaces. For easier material generation, AuNR spatial position does not have to be periodic and can be random, and for large-scale cloaks the wires can be broken into smaller pieces that are smaller in size than the incoming wavelength. In addition, to accomplish the above materials, the fabrication techniques with controls over spacing, aspect ratio, and orientation are also important [11].

AuNWs have potential applications as nanoscale optical waveguides in the visible and NIR regions [271]. AuNWs are indeed an ideal platform to produce surface plasmon waves by direct illumination of one end of the nanostructure. They

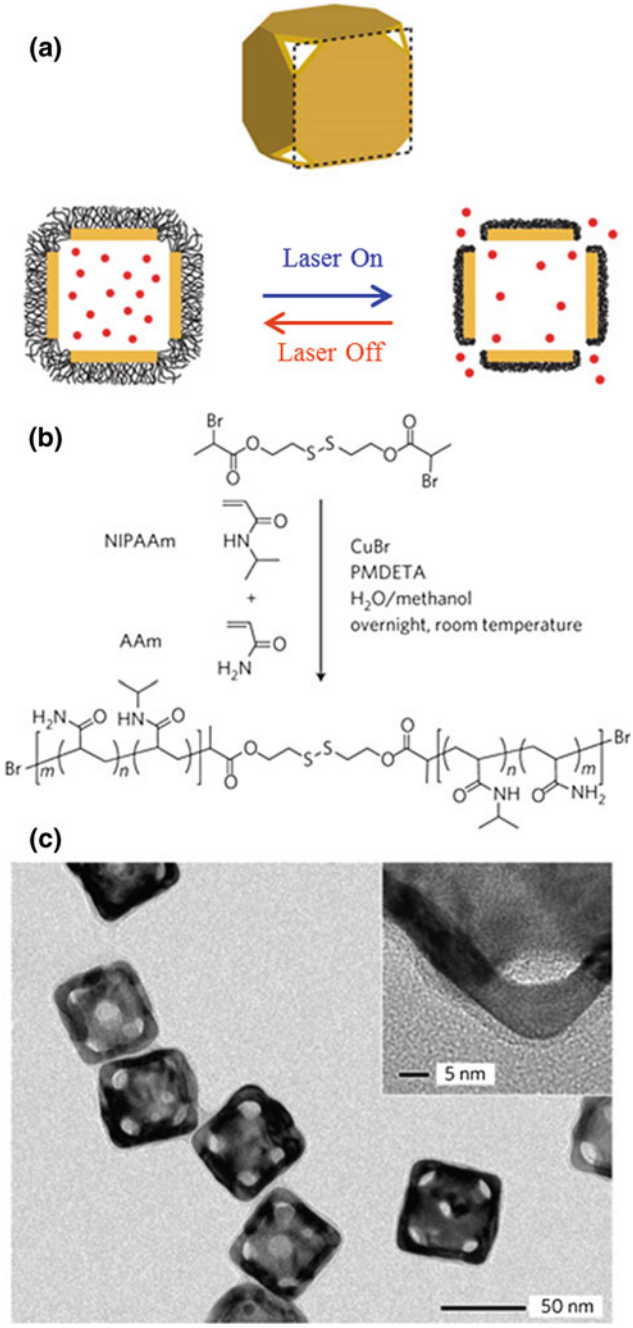
(a)
Laser On
Laser Off
(b)
NIPAAm
AAm
CuBr
PMDETA
H2O/methanol
overnight, room temperature
(c)
5 nm
50 nm

◀ **Fig. 3.17** Schematic illustration and characterization of controlled-release system by AuNCs. **a** How the system works. A side view of the Au nanocage is used for the illustration; **b** atom-transfer radical polymerization of NIPAAm and AAm monomers (at a molar ratio of m = n) as initiated by a disulphide initiator and in the presence of a Cu(I) catalyst; **c** TEM images of Au nanocages for which the surface was covered by a pNIPAAm-co-pAAm copolymer with an LSCT at 39 °C. The *inset* shows a magnified TEM image of the *corner* of such a nanocage [265]. Copyright 2009 Nature group

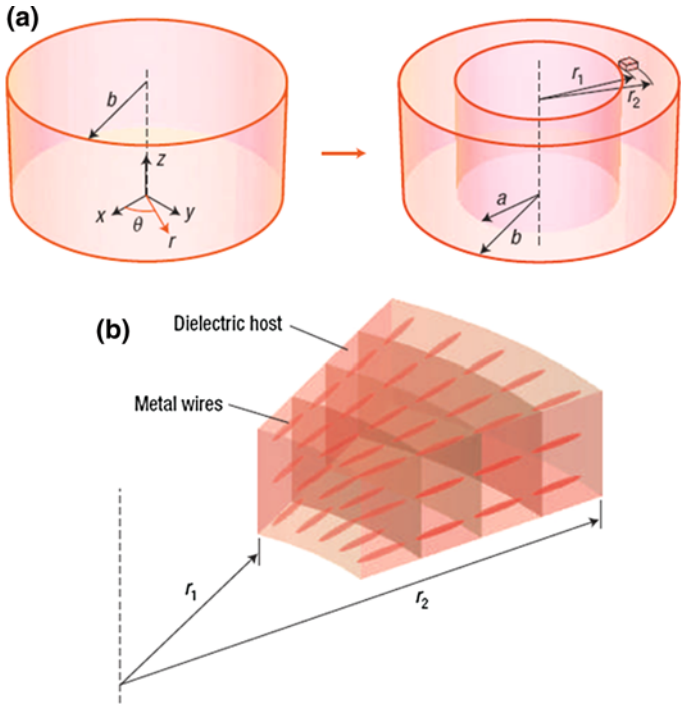

Fig. 3.18 Coordinate transformation and structure of the non-magnetic optical cloak. **a** The coordinate transformation that compresses a cylindrical region r < b into a concentric cylindrical shell a < r < b. r_1 and r_2 define the internal and external radius of a fraction of the cylindrical cloak. There is no variation along the z direction. **b** A small fraction of the cylindrical cloak showing well-organized AuNR wires [270]. Copyright 2007 Nature Group

can thus be used as tools for fundamental studies of subwavelength plasmon-based optics of wave propagation. This strategy was pioneered by Halas and co-workers, who used Ag- and Au-NWs with longitudinal dimensions of more than 10 μm. The addition of an adjacent NWs, substrate, or other symmetry-breaking defect enables direct coupling with the guided waves in a NW. Networks of plasmonic AuNWs can serve as the basis for optical devices such as interferometric logic gates, which can lead to nanorouters and multiplexes, light modulators, and a complete set of Boolean logic functions [272]. For AuNPs with branched structure such as

nanostars, it greatly increases the overall excitation cross-section and field enhancement of the nanostar tips. The antenna effect of the nanostar core may be responsible for the relatively bright and narrow scattering spectra of nanostars in the single particle measurements [273].

3.5 Conclusions and Outlook

After an extensive research in spherical AuNPs in last decades, enabled by versatile synthesis method the anisotropic AuNPs have emerged as a hot topic in recent years showing an impressive potential in applications including catalysis, sensors, biomedical uses (bioimaging, therapy, drug delivery), and optical devices. Bottom-up chemical and top-down physical approaches have been effective to provide anisotropic AuNPs with different shapes and sizes based on the knowledge of the key roles of some stabilizers such as CTAB, Ag^+, and halide ions. However, large-scale reproducible production of AuNPs of specific shapes and sizes remains a crucial challenge although such controllability has been envisioned to open up numerous opportunities for these intriguing anisotropic functional nanoscale building blocks.

Anisotropic AuNPs exhibit superior and unique optical and catalytic properties compared to their isotropic spherical counterparts [206]. They display tunable LSPR depending on their size, shape, the dielectric properties of the surrounding medium, and the self-assembly state. The LSPR band of anisotropic AuNPs can shift to the NIR region (usually 800–1300 nm) while that of spherical isotropic AuNPs position in the visible region. In the NIR region, the absorption by cells and tissues is lower, therefore the biomedical applications, including cell imaging, sensing, cancer diagnosis and treatment, and optical controlled drug and gene delivery become possible. Through suitable surface modifications, anisotropic AuNPs have been rendered biocompatible thus significantly widening their scope. Another important aspect is the emergence of metamaterials that can be fabricated from the assemblies of anisotropic AuNPs. Moreover, the applications of AuNRs and AuNWs have been demonstrated in plasmon waveguides and optical devices. Development of methods toward dynamic ordered assemblies of anisotropic AuNPs could furnish reconfigurable functional materials and devices which exploit their electronic and optical properties. Judging from the research and development progress of the anisotropic AuNPs, it can be optimistically anticipated that they will play a greater role in the nanoscience and nanotechnology of twenty-first century besides their biological and biomedical applications.

Acknowledgments The preparation of this chapter benefited from the support to Quan Li by US Air Force Office of Scientific Research (AFOSR), US Department of Energy (DOE), US Army Research Office (ARO), US Department of Defense Multidisciplinary University Research Initiative (DoD MURI), US National Aeronautics and Space Administration (NASA), and US National Science Foundation (NSF), and Ohio Third Frontier.

References

1. I. Freestone, N. Meeks, M. Sax, C. Higgitt, The lycurgus cup-a roman nanotechnology. Gold Bull. **40**, 270–277 (2007)
2. A.P. Alivisatos, Semiconductor clusters, nanocrystals, and quantum dots. Science **271**, 933–937 (1996)
3. P. Mulvaney, Surface plasmon spectroscopy of nanosized metal particles. Langmuir **12**, 788–800 (1996)
4. S. Lal, S.E. Clare, N.J. Halas, Nanoshell-enabled photothermal cancer therapy: impending clinical impact. Acc. Chem. Res. **41**, 1842–1851 (2008)
5. C.J. Murphy, A.M. Gole, J.W. Stone, P.N. Sisco, A.M. Alkilany, E.C. Goldsmith, S.C. Baxter, Gold nanoparticles in biology: beyond toxicity to cellular imaging. Acc. Chem. Res. **41**, 1721–1730 (2008)
6. C. Burda, X.B. Chen, R. Narayanan, M.A. El-Sayed, Chemistry and properties of nanocrystals of different shapes. Chem. Rev. **105**, 1025–1102 (2005)
7. Y. Yin, A.P. Alivisatos, Colloidal nanocrystal synthesis and the organic-inorganic interface. Nature **437**, 664–670 (2005)
8. N.J. Halas, S. Lal, W.S. Chang, S. Link, P. Nordlander, Plasmons in strongly coupled metallic nanostructures. Chem. Rev. **111**, 3913–3961 (2011)
9. L. Billot, M.L. de la Chapelle, A.S. Grimault, A. Vial, D. Barchiesi, J.L. Bijeon, P.M. Adam, P. Royer, Surface enhanced Raman scattering on gold nanowire arrays: evidence of strong multipolar surface plasmon resonance enhancement. Chem. Phys. Lett. **422**, 303–307 (2006)
10. E.J. Smythe, E. Cubukcu, F. Capasso, Optical properties of surface plasmon resonances of coupled metallic nanorods. Opt. Express **15**, 7439–7447 (2007)
11. E. Cubukcu, E.A. Kort, K.B. Crozier, F. Capasso, Plasmonic laser antenna. Appl. Phys. Lett. **89**, 093120 (2006)
12. A.N. Grigorenko, N.W. Roberts, M.R. Dickinson, Y. Zhang, Nanometric optical tweezers based on nanostructured substrates. Nat. Photon. **2**, 365–370 (2008)
13. E. Devaux, T.W. Ebbesen, J.C. Weeber, A. Dereux, Launching and decoupling surface plasmons via micro-gratings. Appl. Phys. Lett. **83**, 4936–4938 (2003)
14. W.L. Barnes, A. Dereux, T.W. Ebbesen, Surface plasmon subwavelength optics. Nature **424**, 824–830 (2003)
15. B.J.Y. Tan, C.H. Sow, T.S. Koh, K.C. Chin, A.T.S. Wee, C.K. Ong, Fabrication of size-tunable gold nanoparticles array with nanosphere lithography, reactive ion etching, and thermal annealing. J. Phys. Chem. B **109**, 11100–11109 (2005)
16. D.D. Jia, A. Goonewardene, Two-dimensional nanotriangle and nanoring arrays on silicon wafer. Appl. Phys. Lett. **88**, 053105 (2006)
17. L.D. Qin, S. Park, L. Huang, C.A. Mirkin, On-wire lithography. Science **309**, 113–115 (2005)
18. L. Qin, S. Zou, C. Xue, A. Atkinson, G.C. Schatz, C.A. Mirkin, Designing, fabricating, and imaging Raman hot spots. Proc. Natl. Acad. Sci. USA **103**, 13300–13303 (2006)
19. K.D. Osberg, A.L. Schmucker, A.J. Senesi, C.A. Mirkin, One-dimensional nanorod arrays: independent control of composition, length, and interparticle spacing with nanometer precision. Nano Lett. **11**, 820–824 (2011)
20. R.S. Wagner, W.C. Ellis, Vapor-liquid-solid mechanism of single crystal growth. Appl. Phys. Lett. **4**, 89–90 (1964)
21. J. Wiesner, A. Wokaun, Anisometric gold colloids-preparation, characterization, and optical-properties. Chem. Phys. Lett. **157**, 569–575 (1989)
22. E.C. Dreaden, A.M. Alkilany, X. Huang, C.J. Murphy, M.A. El-Sayed, The golden age: gold nanoparticles for biomedicine. Chem. Soc. Rev. **41**, 2740–2779 (2012)
23. C.J. Murphy, A.M. Gole, S.E. Hunyadi, C.J. Orendorff, One-dimensional colloidal gold and silver nanostructures. Inorg. Chem. **45**, 7544–7554 (2006)

24. B. Nikoobakht, M.A. El-Sayed, Preparation and growth mechanism of gold nanorods (NRs) using seed-mediated growth method. Chem. Mater. **15**, 1957–1962 (2003)
25. J. Zhang, M.R. Langille, M.L. Personick, K. Zhang, S. Li, C.A. Mirkin, Concave cubic gold nanocrystals with high-index facets. J. Am. Chem. Soc. **132**, 14012–14014 (2010)
26. M. Iqbal, Y.I. Chung, G. Tae, An enhanced synthesis of gold nanorods by the addition of Pluronic (F-127) via a seed mediated growth process. J. Mater. Chem. **17**, 335–342 (2007)
27. B.D. Busbee, S.O. Obare, C.J. Murphy, An improved synthesis of high-aspect-ratio gold nanorods. Adv. Mater. **15**, 414–416 (2003)
28. N.R. Jana, L. Gearheart, C.J. Murphy, Wet chemical synthesis of high aspect ratio cylindrical gold nanorods. J. Phys. Chem. B **105**, 4065–4067 (2001)
29. C.J. Murphy, T.K. San, A.M. Gole, C.J. Orendorff, J.X. Gao, L. Gou, S.E. Hunyadi, T. Li, Anisotropic metal nanoparticles: synthesis, assembly, and optical applications. J. Phys. Chem. B **109**, 13857–13870 (2005)
30. T.K. Sau, C.J. Murphy, Seeded high yield synthesis of short Au nanorods in aqueous solution. Langmuir **20**, 6414–6420 (2004)
31. N. Garg, C. Scholl, A. Mohanty, R. Jin, The role of bromide ions in seeding growth of au nanorods. Langmuir **26**, 10271–10276 (2010)
32. N.R. Jana, Gram-scale synthesis of soluble, near-monodisperse gold nanorods and other anisotropic nanoparticles. Small **1**, 875–882 (2005)
33. R.A. Alvarez-Puebla, A. Agarwal, P. Manna, B.P. Khanal, P. Aldeanueva-Potel, E. Carbo-Argibay, N. Pazos-Perez, L. Vigderman, E.R. Zubarev, N.A. Kotov, L.M. Liz-Marzan, Gold nanorods 3D-supercrystals as surface enhanced Raman scattering spectroscopy substrates for the rapid detection of scrambled prions. Proc. Natl. Acad. Sci. USA **108**, 8157–8161 (2011)
34. L.L. Feng, X.C. Wu, L.R. Ren, Y.J. Xiang, W.W. He, K. Zhang, W.Y. Zhou, S.S. Xie, Well-controlled synthesis of Au@Pt nanostructures by gold-nanorod-seeded growth. Chem. Eur. J. **14**, 9764–9771 (2008)
35. J.H. Song, F. Kim, D. Kim, P.D. Yang, Crystal overgrowth on gold nanorods: tuning the shape, facet, aspect ratio, and composition of the nanorods. Chem. Eur. J. **11**, 910–916 (2005)
36. E. Carbo-Argibay, B. Rodriguez-Gonzalez, J. Pacifico, I. Pastoriza-Santos, J. Perez-Juste, L. M. Liz-Marzan, Chemical sharpening of gold nanorods: the rod-to-octahedron transition. Angew. Chem. Int. Ed. **46**, 8983–8987 (2007)
37. X.S. Kou, S.Z. Zhang, Z. Yang, C.K. Tsung, G.D. Stucky, L.D. Sun, J.F. Wang, C.H. Yan, Glutathione- and cysteine-induced transverse overgrowth on gold nanorods. J. Am. Chem. Soc. **129**, 6402–6404 (2007)
38. S.E. Lohse, C.J. Murphy, The quest for shape control: a history of gold nanorod synthesis. Chem. Mater. **25**, 1250–1261 (2013)
39. N. Li, P.X. Zhao, D. Astruc, Anisotropic gold nanoparticles: synthesis, properties, applications, and toxicity. Angew. Chem. Int. Ed. **53**, 1756–1789 (2014)
40. K. Esumi, K. Matsuhisa, K. Torigoe, Preparation of rodlike gold particles by uv irradiation using cationic micelles as a template. Langmuir **11**, 3285–3287 (1995)
41. F. Kim, J.H. Song, P.D. Yang, Photochemical synthesis of gold nanorods. J. Am. Chem. Soc. **124**, 14316–14317 (2002)
42. E. Leontidis, K. Kleitou, T. Kyprianidou-Leodidou, V. Bekiari, P. Lianos, Gold colloids from cationic surfactant solutions. 1. Mechanisms that control particle morphology. Langmuir **18**, 3659–3668 (2002)
43. S. Eustis, H.Y. Hsu, M.A. El-Sayed, Gold nanoparticle formation from photochemical reduction of Au^{3+} by continuous excitation in colloidal solutions. A proposed molecular mechanism. J. Phys. Chem. B **109**, 4811–4815 (2005)
44. C.Y. Wang, C. Y. Liu, X. Zheng, J. Chen, T. Shen, The surface chemistry of hybrid nanometer-sized particles-I. Photochemical deposition of gold on ultrafine TiO_2 particles. Colloids Surf. A **131**, 271–280 (1998)

45. G.L. Hornyak, C.J. Patrissi, C.R. Martin, Fabrication, characterization, and optical properties of gold nanoparticle/porous alumina composites: the nonscattering Maxwell-Garnett limit. J. Phys. Chem. B **101**, 1548–1555 (1997)
46. J.C. Hulteen, C.R. Martin, A general template-based method for the preparation of nanomaterials. J. Mater. Chem. **7**, 1075–1087 (1997)
47. Y.Y. Yu, S.S. Chang, C.L. Lee, C.R.C. Wang, Gold nanorods: electrochemical synthesis and optical properties. J. Phys. Chem. B **101**, 6661–6664 (1997)
48. Z.L. Wang, R.P. Gao, B. Nikoobakht, M.A. El-Sayed, Surface reconstruction of the unstable 110 surface in gold nanorods. J. Phys. Chem. B **104**, 5417–5420 (2000)
49. W. Ye, J. Yan, Q. Ye, F. Zhou, Template-free and direct electrochemical deposition of hierarchical dendritic gold microstructures: growth and their multiple applications. J. Phys. Chem. C **114**, 15617–15624 (2010)
50. K. Barbour, M. Ashokkumar, R.A. Caruso, F. Grieser, Sonochemistry and sonoluminescence in aqueous $AuCl_4^-$ solutions in the presence of surface-active solutes. J. Phys. Chem. B **103**, 9231–9236 (1999)
51. J.L. Zhang, J.M. Du, B.X. Han, Z.M. Liu, T. Jiang, Z.F. Zhang, Sonochemical formation of single-crystalline gold nanobelts. Angew. Chem. Int. Ed. **45**, 1116–1119 (2006)
52. T. Pham, J.B. Jackson, N.J. Halas, T.R. Lee, Preparation and characterization of gold nanoshells coated with self-assembled monolayers. Langmuir **18**, 4915–4920 (2002)
53. N. Taub, O. Krichevski, G. Markovich, Growth of gold nanorods on surfaces. J. Phys. Chem. B **107**, 11579–11582 (2003)
54. A.J. Mieszawska, F.P. Zamborini, Gold nanorods grown directly on surfaces from microscale patterns of gold seeds. Chem. Mater. **17**, 3415–3420 (2005)
55. J. Henzie, E.S. Kwak, T.W. Odom, Mesoscale metallic pyramids with nanoscale tips. Nano Lett. **5**, 1199–1202 (2005)
56. G.M. Lu, R. Zhao, G. Qian, Y.X. Qi, X.L. Wang, J.S. Suo, A highly efficient catalyst Au/MCM-41 for selective oxidation cyclohexane using oxygen. Catal. Lett. **97**, 115–118 (2004)
57. R.M. Penner, Mesoscopic metal particles and wires by electrodeposition. J. Phys. Chem. B **106**, 3339–3353 (2002)
58. V.M. Cepak, C.R. Martin, Preparation and stability of template-synthesized metal nanorod sols in organic solvents. J. Phys. Chem. B **102**, 9985–9990 (1998)
59. S.E. Skrabalak, J. Chen, L. Au, X. Lu, X. Li, Y. Xia, Gold nanocages for biomedical applications. Adv. Mater. **19**, 3177–3184 (2007)
60. Y. Zhang, H.J. Dai, Formation of metal nanowires on suspended single-walled carbon nanotubes. Appl. Phys. Lett. **77**, 3015–3017 (2000)
61. J.H. Song, Y.Y. Wu, B. Messer, H. Kind, P.D. Yang, Metal nanowire formation using Mo_3Se^{3-} as reducing and sacrificing templates. J. Am. Chem. Soc. **123**, 10397–10398 (2001)
62. J.L. Gardea-Torresdey, J.G. Parsons, E. Gomez, J. Peralta-Videa, H.E. Troiani, P. Santiago, M.J. Yacaman, Formation and growth of Au nanoparticles inside live alfalfa plants. Nano Lett. **2**, 397–401 (2002)
63. S. He, Y. Zhang, Z. Guo, N. Go, Biological synthesis of gold nanowires using extract of Rhodopseudomonas capsulata. Biotechnol. Prog. **24**, 476–480 (2008)
64. S. Brown, M. Sarikaya, E. Johnson, A genetic analysis of crystal growth. J. Mol. Biol. **299**, 725–735 (2000)
65. M.Q. Zhao, R.M. Crooks, Intradendrimer exchange of metal nanoparticles. Chem. Mater. **11**, 3379–3385 (1999)
66. M.F. Mrozek, Y. Xie, M.J. Weaver, Surface-enhanced Raman scattering on uniform platinum-group overlayers: preparation by redox replacement of underpotential-deposited metals on gold. Anal. Chem. **73**, 5953–5960 (2001)
67. L. Au, X. Lu, Y. Xia, A comparative study of galvanic replacement reactions involving Ag nanocubes and $AuCl_2^-$ or $AuCl_4^-$. Adv. Mater. **20**, 2517–2522 (2008)

68. Y.G. Sun, Y. Xia, Mechanistic study on the replacement reaction between silver nanostructures and chloroauric acid in aqueous medium. J. Am. Chem. Soc. **126**, 3892–3901 (2004)
69. Q. Xu, G. Meng, X. Wu, Q. Wei, M. Kong, X. Zhu, Z. Chu, A generic approach to desired metallic nanowires inside native porous alumina template via redox reaction. Chem. Mater. **21**, 2397–2402 (2009)
70. W. Ye, Y. Chen, F. Zhou, C. Wang, Y. Li, Fluoride-assisted galvanic replacement synthesis of Ag and Au dentrites on aluminum foil with enhanced SERS and catalytic activities. J. Mater. Chem. **22**, 18327–18334 (2012)
71. A. Paul, D. Solis Jr, K. Bao, W.-S. Chang, S. Nauert, L. Vidgerman, E.R. Zubarev, P. Nordlander, S. Link, Identification of higher order long-propagation-length surface plasmon polariton modes in chemically prepared gold nanowires. ACS Nano **6**, 8105–8113 (2012)
72. J.U. Kim, S.H. Cha, K. Shin, J.Y. Jho, J.C. Lee, Preparation of gold nanowires and nanosheets in bulk block copolymer phases under mild conditions. Adv. Mater. **16**, 459–464 (2004)
73. C.C. Mayorga-Martinez, M. Guix, R.E. Madrid, A. Merkoci, Bimetallic nanowires as electrocatalysts for nonenzymatic real-time impedancimetric detection of glucose. Chem. Commun. **48**, 1686–1688 (2012)
74. Z. Jiang, Q. Zhang, C. Zong, B.-J. Liu, B. Ren, Z. Xie, L. Zheng, Cu-Au alloy nanotubes with five-fold twinned structure and their application in surface-enhanced Raman scattering. J. Mater. Chem. **22**, 18192–18197 (2012)
75. M. Wirtz, C.R. Martin, Template-fabricated gold nanowires and nanotubes. Adv. Mater. **15**, 455–458 (2003)
76. F. Muench, U. Kunz, C. Neetzel, S. Lauterbach, H.-J. Kleebe, W. Ensinger, 4-(Dimethylamino)pyridine as a powerful auxiliary reagent in the electroless synthesis of gold nanotubes. Langmuir **27**, 430–435 (2011)
77. N.R. Sieb, N.-C. Wu, E. Majidi, R. Kukreja, N.R. Branda, B.D. Gates, Hollow metal nanorods with tunable dimensions, porosity, and photonic properties. ACS Nano **3**, 1365–1372 (2009)
78. C.R. Bridges, P.M. DiCarmine, D.S. Seferos, Gold nanotubes as sensitive, solution-suspendable refractive index reporters. Chem. Mater. **24**, 963–965 (2012)
79. J.-H. Ryu, S. Park, B. Kim, A. Klaikherd, T.P. Russell, S. Thayumanavan, Highly ordered gold nanotubes using thiols at a cleavable block copolymer interface. J. Am. Chem. Soc. **131**, 9870–9871 (2009)
80. M. Grzelczak, A. Sanchez-Iglesias, H.H. Mezerji, S. Bals, J. Perez-Juste, L.M. Liz-Marzan, Steric hindrance induces crosslike self-assembly of gold nanodumbbells. Nano Lett. **12**, 4380–4384 (2012)
81. M. Grzelczak, A. Sanchez-Iglesias, B. Rodriguez-Gonzalez, R. Alvarez-Puebla, J. Perez-Juste, L.M. Liz-Marzan, Influence of iodide ions on the growth of gold nanorods: tuning tip curvature and surface plasmon resonance. Adv. Funct. Mater. **18**, 3780–3786 (2008)
82. M.F. Cardinal, B. Rodriguez-Gonzalez, R.A. Alvarez-Puebla, J. Perez-Juste, L.M. Liz-Marzan, Modulation of localized surface plasmons and SERS response in gold dumbbells through silver coating. J. Phys. Chem. C **114**, 10417–10423 (2010)
83. W. Xie, L. Su, P. Donfack, A. Shen, X. Zhou, M. Sackmann, A. Materny, J. Hu, Synthesis of gold nanopeanuts by citrate reduction of gold chloride on gold-silver core-shell nanoparticles. Chem. Commun. **35**, 5263–5265 (2009)
84. E. Shaviv, U. Banin, Synergistic effects on second harmonic generation of hybrid CdSe-Au nanoparticles. ACS Nano **4**, 1529–1538 (2010)
85. G. Krylova, L.J. Giovanetti, F.G. Requejo, N.M. Dimitrijevic, A. Prakapenka, E.V. Shevchenko, Study of nucleation and growth mechanism of the metallic nanodumbbells. J. Am. Chem. Soc. **134**, 4384–4392 (2012)

86. Y. Kuroda, Y. Sakamoto, K. Kuroda, Selective cleavage of periodic mesoscale structures: two-dimensional replication of binary colloidal crystals into dimpled gold nanoplates. J. Am. Chem. Soc. **134**, 8684–8692 (2012)
87. S. Porel, S. Singh, T.P. Radhakrishnan, Polygonal gold nanoplates in a polymer matrix. Chem. Commun. **14**, 2387–2389 (2005)
88. X.P. Sun, S.J. Dong, E.K. Wang, High-yield synthesis of large single-crystalline gold nanoplates through a polyamine process. Langmuir **21**, 4710–4712 (2005)
89. B. Lim, P.H.C. Camargo, Y. Xia, Mechanistic study of the synthesis of an nanotadpoles, nanokites, and microplates by reducing aqueous $HAuCl_4$ with poly(vinyl pyrrolidone). Langmuir **24**, 10437–10442 (2008)
90. X.P. Sun, S.J. Dong, E. Wang, Large-scale synthesis of micrometer-scale single-crystalline Au plates of nanometer thickness by a wet-chemical route. Angew. Chem. Int. Ed. **43**, 6360–6363 (2004)
91. H.C. Chu, C.H. Kuo, M.H. Huang, Thermal aqueous solution approach for the synthesis of triangular and hexagonal gold nanoplates with three different size ranges. Inorg. Chem. **45**, 808–813 (2006)
92. Y. Shao, Y.D. Jin, S.J. Dong, Synthesis of gold nanoplates by aspartate reduction of gold chloride. Chem. Commun. **9**, 1104–1105 (2004)
93. B. Liu, J. Xie, J.Y. Lee, Y.P. Ting, J.P. Chen, Optimization of high-yield biological synthesis of single-crystalline gold nanoplates. J. Phys. Chem. B **109**, 15256–15263 (2005)
94. Y. Zhang, G. Chang, S. Liu, W. Lu, J. Tian, X. Sun, A new preparation of Au nanoplates and their application for glucose sensing. Biosens. Bioelectron. **28**, 344–348 (2011)
95. J. Xie, J.Y. Lee, D.I.C. Wang, Synthesis of single-crystalline gold nanoplates in aqueous solutions through biomineralization by serum albumin protein. J. Phys. Chem. C **111**, 10226–10232 (2007)
96. L. Wang, X. Wu, X. Li, L. Wang, M. Pei, X. Tao, Facile synthesis of concave gold nanoplates in hexagonal liquid crystal made of SDS/water system. Chem. Commun. **46**, 8422–8423 (2010)
97. J.E. Millstone, S.J. Hurst, G.S. Metraux, J.I. Cutler, C.A. Mirkin, Colloidal gold and silver triangular nanoprisms. Small **5**, 646–664 (2009)
98. M.R. Jones, R.J. Macfarlane, A.E. Prigodich, P.C. Patel, C.A. Mirkin, Nanoparticle shape anisotropy dictates the collective behavior of surface-bound ligands. J. Am. Chem. Soc. **133**, 18865–18869 (2011)
99. M.J. Banholzer, N. Harris, J.E. Millstone, G.C. Schatz, C.A. Mirkin, Abnormally large plasmonic shifts in silica-protected gold triangular nanoprisms. J. Phys. Chem. C **114**, 7521–7526 (2010)
100. J.Q. Hu, Y. Zhang, B. Liu, J.X. Liu, H.H. Zhou, Y.F. Xu, Y.X. Jiang, Z.L. Yang, Z.Q. Tian, Synthesis and properties of tadpole-shaped gold nanoparticles. J. Am. Chem. Soc. **126**, 9470–9471 (2004)
101. L. Huang, M. Wang, Y. Zhang, Z. Guo, J. Sun, N. Gu, Synthesis of gold nanotadpoles by a temperature-reducing seed approach and the dielectrophoretic manipulation. J. Phys. Chem. C **111**, 16154–16160 (2007)
102. P.H.C. Camargo, Y. Xiong, L. Ji, J.M. Zuo, Y. Xia, Facile synthesis of tadpole-like nanostructures consisting of Au heads and Pd tails. J. Am. Chem. Soc. **129**, 15452–15453 (2007)
103. D.Y. Kim, T. Yu, E.C. Cho, Y. Ma, O.O. Park, Y. Xia, Synthesis of gold nano-hexapods with controllable arm lengths and their tunable optical properties. Angew. Chem. Int. Ed. **50**, 6328–6331 (2011)
104. S.K. Dondapati, T.K. Sau, C. Hrelescu, T.A. Klar, F.D. Stefani, J. Feldmann, Label-free biosensing based on single gold nanostars as plasmonic transducers. ACS Nano **4**, 6318–6322 (2010)
105. H. Yuan, C.G. Khoury, H. Hwang, C.M. Wilson, G.A. Grant, V.-D. Tuan, Gold nanostars: surfactant-free synthesis, 3D modelling, and two-photon photoluminescence imaging. Nanotechnology **23**, 075102 (2012)

106. J. Xie, Q. Zhang, J.Y. Lee, D.I.C. Wang, The synthesis of SERS-active gold nanoflower tags for in vivo applications. ACS Nano **2**, 2473–2480 (2008)
107. B. Van de Broek, N. Devoogdt, A. D'Hollander, H.-L. Gijs, K. Jans, L. Lagae, S. Muyldermans, G. Maes, G. Borghs, Specific cell targeting with nanobody conjugated branched gold nanoparticles for photothermal therapy. ACS Nano **5**, 4319–4328 (2011)
108. S.H. Chen, Z.L. Wang, J. Ballato, S.H. Foulger, D.L. Carroll, Monopod, bipod, tripod, and tetrapod gold nanocrystals. J. Am. Chem. Soc. **125**, 16186–16187 (2003)
109. T.K. Sau, C.J. Murphy, Room temperature, high-yield synthesis of multiple shapes of gold nanoparticles in aqueous solution. J. Am. Chem. Soc. **126**, 8648–8649 (2004)
110. Z. Li, W. Li, P.H.C. Camargo, Y. Xia, Facile synthesis of branched an nanostructures by templating against a self-destructive lattice of magnetic fe nanoparticles. Angew. Chem. Int. Ed. **47**, 9653–9656 (2008)
111. E. Hao, R.C. Bailey, G.C. Schatz, J.T. Hupp, S.Y. Li, Synthesis and optical properties of "branched" gold nanocrystals. Nano Lett. **4**, 327–330 (2004)
112. F. Hao, C.L. Nehl, J.H. Hafner, P. Nordlander, Plasmon resonances of a gold nanostar. Nano Lett. **7**, 729–732 (2007)
113. T.H. Lin, C.W. Lin, H.H. Liu, J.T. Sheu, W.H. Hung, Potential-controlled electrodeposition of gold dentrites in the presence of cysteine. Chem. Commun. **47**, 2044–2046 (2011)
114. D. Huang, X. Bai, L. Zheng, Ultrafast preparation of three-dimensional dendritic gold nanostructures in aqueous solution and their applications in catalysis and SERS. J. Phys. Chem. C **115**, 14641–14647 (2011)
115. T. Huang, F. Meng, L. Qi, Controlled synthesis of dendritic gold nanostructures assisted by supramolecular complexes of surfactant with cyclodextrin. Langmuir **26**, 7582–7589 (2010)
116. C. Radloff, N.J. Halas, Nano Lett. **4**, 1323 (2004)
117. S.J. Oldenburg, J.B. Jackson, S.L. Westcott, N.J. Halas, Infrared extinction properties of gold nanoshells. Appl. Phys. Lett. **75**, 2897–2899 (1999)
118. L.R. Hirsch, A.M. Gobin, A.R. Lowery, F. Tam, R.A. Drezek, N.J. Halas, J.L. West, Metal nanoshells. Ann. Biomed. Eng. **34**, 15–22 (2006)
119. T. Zhou, B. Wu, D. Xing, Bio-modified Fe_3O_4 core/Au shell nanoparticles for targeting and multimodal imaging of cancer cells. J. Mater. Chem. **22**, 470–477 (2012)
120. D. Llamosa Perez, A. Espinosa, L. Martinez, E. Roman, C. Ballesteros, A. Mayoral, M. Garcia-Hernandez, Y. Huttel, Thermal diffusion at nanoscale: from CoAu alloy nanoparticles to Co@Au core/shell structures. J. Phys. Chem. C **117**, 3101–3108 (2013)
121. M.Z. Liu, P. Guyot-Sionnest, Synthesis and optical characterization of Au/Ag core/shell nanorods. J. Phys. Chem. B **108**, 5882–5888 (2004)
122. L.H. Lu, H.S. Wang, Y.H. Zhou, S.Q. Xi, H.J. Zhang, H.B.W. Jiawen, B. Zhao, Seed-mediated growth of large, monodisperse core-shell gold-silver nanoparticles with Ag-like optical properties. Chem. Commun. **21**, 144–145 (2002)
123. S.O. Obare, N.R. Jana, C.J. Murphy, Preparation of polystyrene- and silica-coated gold nanorods and their use as templates for the synthesis of hollow nanotubes. Nano Lett. **1**, 601–603 (2001)
124. A. Gole, J.W. Stone, W.R. Gemmill, H.C. zur Loye, C.J. Murphy, Iron oxide coated gold nanorods: synthesis, characterization, and magnetic manipulation. Langmuir **24**, 6232–6237 (2008)
125. M. Grzelczak, J. Perez-Juste, B. Rodriguez-Gonzalez, L.M. Liz-Marzan, Influence of silver ions on the growth mode of platinum on gold nanorods. J. Mater. Chem. **16**, 3946–3951 (2006)
126. M. Liu, P. Guyot-Sionnest, Preparation and optical properties of silver chalcogenide coated gold nanorods. J. Mater. Chem. **16**, 3942–3945 (2006)
127. F. Caruso, M. Spasova, V. Saigueirino-Maceira, L.M. Liz-Marzan, Multilayer assemblies of silica-encapsulated gold nanoparticles on decomposable colloid templates. Adv. Mater. **13**, 1090–1094 (2001)
128. Z.J. Liang, A. Susha, F. Caruso, Gold nanoparticle-based core-shell and hollow spheres and ordered assemblies thereof. Chem. Mater. **15**, 3176–3183 (2003)

129. S.E. Skrabalak, J. Chen, Y. Sun, X. Lu, L. Au, C.M. Cobley, Y. Xia, Gold nanocages: synthesis, properties, and applications. Acc. Chem. Res. **41**, 1587–1595 (2008)
130. X. Lu, L. Au, J. McLellan, Z.-Y. Li, M. Marquez, Y. Xia, Fabrication of cubic nanocages and nanoframes by dealloying Au/Ag alloy nanoboxes with an aqueous etchant based on Fe $(NO_3)_3$ or NH_4OH. Nano Lett. **7**, 1764–1769 (2007)
131. F. Kim, S. Connor, H. Song, T. Kuykendall, P.D. Yang, Platonic gold nanocrystals. Angew. Chem. Int. Ed. **43**, 3673–3677 (2004)
132. Y.G. Sun, Y.N. Xia, Shape-controlled synthesis of gold and silver nanoparticles. Science **298**, 2176–2179 (2002)
133. C. Li, K.L. Shuford, Q.H. Park, W. Cai, Y. Li, E.J. Lee, S.O. Cho, High-yield synthesis of single-crystalline gold nano-octahedra. Angew. Chem. Int. Ed. **46**, 3264–3286 (2007)
134. T.W. Hamann, N. Srivatsan, H. van Willigen, Time-resolved EPR study of the photophysics and photochemistry of 1-(3-(methoxycarbonyl)propyl)-1-phenyl[6.6]C61. J. Phys. Chem. A **109**, 11665–11672 (2005)
135. K. Kwon, K.Y. Lee, Y.W. Lee, M. Kim, J. Heo, S.J. Ahn, S.W. Han, Controlled synthesis of icosahedral gold nanoparticles and their surface-enhanced Raman scattering property. J. Phys. Chem. C **111**, 1161–1165 (2007)
136. U. Kreibig, M. Vollmer, *Optical properties of metal clusters* (Springer, Berlin, 1995)
137. S. Link, M.A. El-Sayed, Shape and size dependence of radiative, non-radiative and photothermal properties of gold nanocrystals. Int. Rev. Phys. Chem. **19**, 409–453 (2000)
138. P.K. Jain, K.S. Lee, I.H. El-Sayed, M.A. El-Sayed, Calculated absorption and scattering properties of gold nanoparticles of different size, shape, and composition: applications in biological imaging and biomedicine. J. Phys. Chem. B **110**, 7238–7248 (2006)
139. G.C. Papavassiliou, Optical-properties of small inorganic and organic metal particles. Prog. Solid State Ch. **12**, 185–271 (1979)
140. L. Qiu, T.A. Larson, D.K. Smith, E. Vitkin, S. Zhang, M.D. Modell, I. Itzkan, E.B. Hanlon, B.A. Korgel, K.V. Sokolov, L.T. Perelman, Single gold nanorod detection using confocal light absorption and scattering spectroscopy. IEEE J. Sel. Top. Quantum Electron. **13**, 1730–1738 (2007)
141. X.H. Huang, I.H. El-Sayed, W. Qian, M.A. El-Sayed, Cancer cell imaging and photothermal therapy in the near-infrared region by using gold nanorods. J. Am. Chem. Soc. **128**, 2115–2120 (2006)
142. S. Link, M.A. Ei-Sayed, Optical properties and ultrafast dynamics of metallic nanocrystals. Annu. Rev. Phys. Chem. **54**, 331–366 (2003)
143. S. Link, C. Burda, M.B. Mohamed, B. Nikoobakht, M.A. El-Sayed, Laser photothermal melting and fragmentation of gold nanorods: energy and laser pulse-width dependence. J. Phys. Chem. A **103**, 1165–1170 (1999)
144. S. Link, Z.L. Wang, M.A. El-Sayed, How does a gold nanorod melt? J. Phys. Chem. B **104**, 7867–7870 (2000)
145. M.B. Mohamed, V. Volkov, S. Link, M.A. El-Sayed, The 'lightning' gold nanorods: fluorescence enhancement of over a million compared to the gold metal. Chem. Phys. Lett. **317**, 517–523 (2000)
146. S. Link, M.A. El-Sayed, Spectral properties and relaxation dynamics of surface plasmon electronic oscillations in gold and silver nanodots and nanorods. J. Phys. Chem. B **103**, 8410–8426 (1999)
147. G. Raschke, S. Kowarik, T. Franzl, C. Sonnichsen, T.A. Klar, J. Feldmann, A. Nichtl, K. Kurzinger, Biomolecular recognition based on single gold nanoparticle light scattering. Nano Lett. **3**, 935–938 (2003)
148. X.H. Huang, S. Neretina, M.A. El-Sayed, Gold nanorods: from synthesis and properties to biological and biomedical applications. Adv. Mater. **21**, 4880–4910 (2009)
149. K.S. Lee, M.A. El-Sayed, Dependence of the enhanced optical scattering efficiency relative to that of absorption for gold metal nanorods on aspect ratio, size, end-cap shape, and medium refractive index. J. Phys. Chem. B **109**, 20331–20338 (2005)

150. L.J.E. Anderson, C.M. Payne, Y.-R. Zhen, P. Nordlander, J.H. Hafner, A tunable plasmon resonance in gold nanobelts. Nano Lett. **11**, 5034–5037 (2011)
151. P.K. Jain, W.Y. Huang, M.A. El-Sayed, On the universal scaling behavior of the distance decay of plasmon coupling in metal nanoparticle pairs: a plasmon ruler equation. Nano Lett. **7**, 2080–2088 (2007)
152. P.K. Jain, X. Huang, I.H. El-Sayed, M.A. El-Sayed, Noble metals on the nanoscale: optical and photothermal properties and some applications in imaging, sensing, biology, and medicine. Acc. Chem. Res. **41**, 1578–1586 (2008)
153. L. Xu, H. Kuang, L. Wang, C. Xu, Gold nanorod ensembles as artificial molecules for applications in sensors. J. Mater. Chem. **21**, 16759–16782 (2011)
154. H. Ko, S. Singamaneni, V.V. Tsukruk, Nanostructured surfaces and assemblies as SERS media. Small **4**, 1576–1599 (2008)
155. M. Gluodenis, C.A. Foss, The effect of mutual orientation on the spectra of metal nanoparticle rod-rod and rod-sphere pairs. J. Phys. Chem. B **106**, 9484–9489 (2002)
156. B. Nikoobakht, J.P. Wang, M.A. El-Sayed, Surface-enhanced Raman scattering of molecules adsorbed on gold nanorods: off-surface plasmon resonance condition. Chem. Phys. Lett. **366**, 17–23 (2002)
157. X. Huang, I.H. El-Sayed, W. Qian, M.A. El-Sayed, Cancer cells assemble and align gold nanorods conjugated to antibodies to produce highly enhanced, sharp, and polarized surface Raman spectra: a potential cancer diagnostic marker. Nano Lett. **7**, 1591–1597 (2007)
158. S.W. Bishnoi, C.J. Rozell, C.S. Levin, M.K. Gheith, B.R. Johnson, D.H. Johnson, N. J. Halas, All-optical nanoscale pH meter. Nano Lett. **6**, 1687–1692 (2006)
159. C.M. Xue, Y.Q. Xu, Y. Pang, D.S. Yu, L.M. Dai, M. Gao, A. Urbas, Q. Li, Organo-soluble porphyrin mixed monolayer-protected gold nanorods with intercalated fullerenes. Langmuir **28**, 5956–5963 (2012)
160. C.M. Xue, O. Birel, M. Gao, S. Zhang, L.M. Dai, A. Urbas, Q. Li, Perylene monolayer protected gold nanorods: unique optical, electronic properties and self-assemblies. J. Phys. Chem. C **116**, 10396–10404 (2012)
161. C.M. Xue, Y.H. Xue, L.M. Dai, A. Urbas, Q. Li, Size- and shape-dependent fluorescence quenching of gold nanoparticles on perylene dye. Adv. Opt. Mater. **1**, 581–587 (2013)
162. R. Bardhan, S. Lal, A. Joshi, N.J. Halas, Theranostic nanoshells: from probe design to imaging and treatment of cancer. Acc. Chem. Res. **44**, 936–946 (2011)
163. E. Boisselier, D. Astruc, Gold nanoparticles in nanomedicine: preparations, imaging, diagnostics, therapies and toxicity. Chem. Soc. Rev. **38**, 1759–1782 (2009)
164. A.M. Alkilany, P.K. Nagaria, C.R. Hexel, T.J. Shaw, C.J. Murphy, M.D. Wyatt, Cellular uptake and cytotoxicity of gold nanorods: molecular origin of cytotoxicity and surface effects. Small **5**, 701–708 (2009)
165. Y.-S. Chen, Y.-C. Hung, I. Liau, G.S. Huang, Assessment of the in vivo toxicity of gold nanoparticles. Nanoscale Res. Lett. **4**, 858–864 (2009)
166. A.M. Alkilany, C.J. Murphy, Toxicity and cellular uptake of gold nanoparticles: what we have learned so far? J. Nanopart. Res. **12**, 2313–2333 (2010)
167. X.L. Zhou, J.M. El Khoury, L.T. Qu, L.M. Dai, Q. Li, A facile synthesis of aliphatic thiol surfactant with tunable length as a stabilizer of gold nanoparticles in organic solvents. J. Colloid Interface Sci. **308**, 381–384 (2007)
168. J.M. El Khoury, X.L. Zhou, L.T. Qu, L.M. Dai, A. Urbas, Q. Li, Organo-soluble photoresponsive azo thiol monolayer-protected gold nanorods. Chem. Commun. **16**, 2109–2111 (2009)
169. Y. Li, D. Yu, L. Dai, A. Urbas, Q. Li, Organo-soluble chiral thiol-monolayer-protected gold nanorods. Langmuir **27**, 98–103 (2011)
170. J.W. Hotchkiss, A.B. Lowe, S.G. Boyes, Surface modification of gold nanorods with polymers synthesized by reversible addition-fragmentation chain transfer polymerization. Chem. Mater. **19**, 6–13 (2007)
171. K. Liu, Z.H. Nie, N.N. Zhao, W. Li, M. Rubinstein, E. Kumacheva, Step-growth polymerization of inorganic nanoparticles. Science **329**, 197–200 (2010)

172. A. Gole, C.J. Murphy, Polyelectrolyte-coated gold nanorods: synthesis, characterization and immobilization. Chem. Mater. **17**, 1325–1330 (2005)
173. J.Y. Huang, K.S. Jackson, C.J. Murphy, Polyelectrolyte wrapping layers control rates of photothermal molecular release from gold nanorods. Nano Lett. **12**, 2982–2987 (2012)
174. E.E. Connor, J. Mwamuka, A. Gole, C.J. Murphy, M.D. Wyatt, Gold nanoparticles are taken up by human cells but do not cause acute cytotoxicity. Small **1**, 325–327 (2005)
175. H. Takahashi, Y. Niidome, T. Niidome, K. Kaneko, H. Kawasaki, S. Yamada, Modification of gold nanorods using phospatidylcholine to reduce cytotoxicity. Langmuir **22**, 2–5 (2006)
176. T.S. Hauck, A.A. Ghazani, W.C.W. Chan, Assessing the effect of surface chemistry on gold nanorod uptake, toxicity, and gene expression in mammalian cells. Small **4**, 153–159 (2008)
177. T. Niidome, M. Yamagata, Y. Okamoto, Y. Akiyama, H. Takahashi, T. Kawano, Y. Katayama, Y. Niidome, PEG-modified gold nanorods with a stealth character for in vivo applications. J. Control. Release **114**, 343–347 (2006)
178. Q. Dai, J. Coutts, J.H. Zou, Q. Huo, Surface modification of gold nanorods through a place exchange reaction inside an ionic exchange resin. Chem. Commun. **25**, 2858–2860 (2008)
179. Z.Y. Tang, Z.L. Zhang, Y. Wang, S.C. Glotzer, N.A. Kotov, Self-assembly of CdTe nanocrystals into free-floating sheets. Science **314**, 274–278 (2006)
180. K.J. Stebe, E. Lewandowski, M. Ghosh, Oriented assembly of metamaterials. Science **325**, 159–160 (2009)
181. E. Dujardin, L.B. Hsin, C.R.C. Wang, S. Mann, DNA-driven self-assembly of gold nanorods. Chem. Commun. **14**, 1264–1265 (2001)
182. T.S. Sreeprasad, A.K. Samal, T. Pradeep, One-, two-, and three-dimensional superstructures of gold nanorods induced by dimercaptosuccinic acid. Langmuir **24**, 4589–4599 (2008)
183. K. Mitamura, T. Imae, N. Saito, O. Takai, Fabrication and self-assembly of hydrophobic gold nanorods. J. Phys. Chem. B **111**, 8891–8898 (2007)
184. J.Y. Chang, H.M. Wu, H. Chen, Y.C. Ling, W.H. Tan, Oriented assembly of Au nanorods using biorecognition system. Chem. Commun. **8**, 1092–1094 (2005)
185. B. Pan, D. Cui, C. Ozkan, P. Xu, T. Huang, Q. Li, H. Chen, F. Liu, F. Gao, R. He, DNA-Templated ordered array of gold nanorods in one and two dimensions. J. Phys. Chem. C **111**, 12572–12576 (2007)
186. C.J. Orendorff, P.L. Hankins, C.J. Murphy, pH-triggered assembly of gold nanorods. Langmuir **21**, 2022–2026 (2005)
187. P.K. Jain, S. Eustis, M.A. El-Sayed, Plasmon coupling in nanorod assemblies: optical absorption, discrete dipole approximation simulation, and exciton-coupling model. J. Phys. Chem. B **110**, 18243–18253 (2006)
188. A. Guerrero-Martinez, J. Perez-Juste, E. Carbo-Argibay, G. Tardajos, L.M. Liz-Marzan, Gemini-surfactant-directed self-assembly of monodisperse gold nanorods into standing superlattices. Angew. Chem. Int. Ed. **48**, 9484–9488 (2009)
189. S. Gomez-Grana, J. Perez-Juste, R.A. Alvarez-Puebla, A. Guerrero-Martinez, L.M. Liz-Marzan, Self-assembly of Au@Ag nanorods mediated by gemini surfactants for highly efficient SERS-active supercrystals. Adv. Opt. Mater. **1**, 477–481 (2013)
190. M.J.A. Hore, R.J. Composto, Nanorod self-assembly for tuning optical absorption. ACS Nano **4**, 6941–6949 (2010)
191. J. Perez-Juste, B. Rodriguez-Gonzalez, P. Mulvaney, L.M. Liz-Marzan, Optical control and patterning of gold-nanorod-poly(vinyl alcohol) nanocomposite films. Adv. Funct. Mater. **15**, 1065–1071 (2005)
192. B.M.I. van der Zande, G.J.M. Koper, H.N.W. Lekkerkerker, Alignment of rod-shaped gold particles by electric fields. J. Phys. Chem. B **103**, 5754–5760 (1999)
193. A.B. Golovin, O.D. Lavrentovich, Electrically reconfigurable optical metamaterial based on colloidal dispersion of metal nanorods in dielectric fluid. Appl. Phys. Lett. **95**, 254104 (2009)
194. Q. Liu, Y. Cui, D. Gardner, X. Li, S. He, I.I. Smalyukh, Self-alignment of plasmonic gold nanorods in reconfigurable anisotropic fluids for tunable bulk metamaterial applications. Nano Lett. **10**, 1347–1353 (2010)

195. C. Xue, K. Gutierrez-Cuevas, M. Gao, A. Urbas, Q. Li, Photomodulated self-assembly of hydrophobic thiol monolayer-protected gold nanorods and their alignment in thermotropic liquid crystal. J. Phys. Chem. C **117**, 21603–21608 (2013)
196. G.Q. Jiang, M.J.A. Hore, S. Gam, R.J. Composto, Gold nanorods dispersed in homopolymer films: optical properties controlled by self-assembly and percolation of nanorods. ACS Nano **6**, 1578–1588 (2012)
197. M. Das, N. Sanson, D. Fava, E. Kumacheva, Microgels loaded with gold nanorods: photothermally triggered volume transitions under physiological conditions. Langmuir **23**, 196–201 (2007)
198. M. Karg, I. Pastoriza-Santos, J. Perez-Juste, T. Hellweg, L.M. Liz-Marzan, Nanorod coated PNIPAM microgels: thermoresponsive optical properties. Small **3**, 1222–1229 (2007)
199. C.L. Murphy, C.J. Orendorff, Alignment of gold nanorods in polymer composites and on polymer surfaces. Adv. Mater. **17**, 2173–2177 (2005)
200. R.D. Deshmukh, Y. Liu, R.J. Composto, Two-dimensional confinement of nanorods in block copolymer domains. Nano Lett. **7**, 3662–3668 (2007)
201. D. Nepal, M.S. Onses, K. Park, M. Jespersen, C.J. Thode, P.F. Nealey, R.A. Vaia, Control over position, orientation, and spacing of arrays of gold nanorods using chemically nanopatterned surfaces and tailored particle-particle-surface interactions. ACS Nano **6**, 5693–5701 (2012)
202. L. Vigderman, B.P. Khanal, E.R. Zubarev, Functional gold nanorods: synthesis, self-assembly, and sensing applications. Adv. Mater. **24**, 4811–4841 (2012)
203. G. Schmid, Large clusters and colloids-metals in the embryonic state. Chem. Rev. **92**, 1709–1727 (1992)
204. M. Haruta, N. Yamada, T. Kobayashi, S. Iijima, Gold catalysts prepared by coprecipitation for low-temperature oxidation of hydrogen and of carbon-monoxide. J. Catal. **115**, 301–309 (1989)
205. Y. Kuwauchi, H. Yoshida, T. Akita, M. Haruta, S. Takeda, Intrinsic catalytic structure of gold nanoparticles supported on TiO_2. Angew. Chem. Int. Ed. **51**, 7729–7733 (2012)
206. R. Narayanan, M.A. El-Sayed, Catalysis with transition metal nanoparticles in colloidal solution: nanoparticle shape dependence and stability. J. Phys. Chem. B **109**, 12663–12676 (2005)
207. M.A. Sanchez-Castillo, C. Couto, W.B. Kim, J.A. Dumesic, Gold-nanotube membranes for the oxidation of CO at gas-water interfaces. Angew. Chem. Int. Ed. **43**, 1140–1142 (2004)
208. P. Li, Z. Wei, T. Wu, Q. Peng, Y. Li, Au-ZnO hybrid nanopyramids and their photocatalytic properties. J. Am. Chem. Soc. **133**, 5660–5663 (2011)
209. X. Cui, C. Zhang, F. Shi, Y. Deng, Au/Ag-Mo nano-rods catalyzed reductive coupling of nitrobenzenes and alcohols using glycerol as the hydrogen source. Chem. Commun. **48**, 9391–9393 (2012)
210. M. Stratakis, H. Garcia, Catalysis by supported gold nanoparticles: beyond aerobic oxidative processes. Chem. Rev. **112**, 4469–4506 (2012)
211. K. Aslan, J.R. Lakowicz, C.D. Geddes, Plasmon light scattering in biology and medicine: new sensing approaches, visions and perspectives. Curr. Opin. Chem. Biol. **9**, 538–544 (2005)
212. C. Novo, A.M. Funston, P. Mulvaney, Direct observation of chemical reactions on single gold nanocrystals using surface plasmon spectroscopy. Nat. Nanotechnol. **3**, 598–602 (2008)
213. G.J. Nusz, S.M. Marinakos, A.C. Curry, A. Dahlin, F. Hook, A. Wax, A. Chilkoti, Label-free plasmonic detection of biomolecular binding by a single gold nanorod. Anal. Chem. **80**, 984–989 (2008)
214. C.J. Murphy, A.M. Gole, S.E. Hunyadi, J.W. Stone, P.N. Sisco, A. Alkilany, B.E. Kinard, P. Hankins, Chemical sensing and imaging with metallic nanorods. Chem. Commun. **5**, 544–557 (2008)
215. C. Yu, J. Irudayaraj, Quantitative evaluation of sensitivity and selectivity of multiplex nanoSPR biosensor assays. Biophys. J. **93**, 3684–3692 (2007)

216. J. York, D. Spetzler, F.S. Xiong, W.D. Frasch, Single-molecule detection of DNA via sequence-specific links between F-1-ATPase motors and gold nanorod sensors. Lab Chip **8**, 415–419 (2008)
217. N.R. Jana, T. Pal, Anisotropic metal nanoparticles for use as surface-enhanced Raman substrates. Adv. Mater. **19**, 1761–1765 (2007)
218. X.M. Qian, X.H. Peng, D.O. Ansari, Q. Yin-Goen, G.Z. Chen, D.M. Shin, L. Yang, A.N. Young, M.D. Wang, S.M. Nie, In vivo tumor targeting and spectroscopic detection with surface-enhanced Raman nanoparticle tags. Nat. Biotechnol. **26**, 83–90 (2008)
219. A.K. Oyelere, P.C. Chen, X.H. Huang, I.H. El-Sayed, M.A. El-Sayed, Peptide-conjugated gold nanorods for nuclear targeting. Bioconjugate Chem. **18**, 1490–1497 (2007)
220. N. Bi, Y. Chen, H. Qi, X. Zheng, Y. Chen, X. Liao, H. Zhang, Y. Tian, Spectrophotometric determination of mercury(II) ion using gold nanorod as probe. Sensor. Actuat. B-Chem. **166**, 766–771 (2012)
221. F.-M. Li, J.-M. Liu, X.-X. Wang, L.-P. Lin, W.-L. Cai, X. Lin, Y.-N. Zeng, Z.-M. Li, S.-Q. Lin, Non-aggregation based label free colorimetric sensor for the detection of Cr (VI) based on selective etching of gold nanorods. Sensor. Actuat. B-Chem. **155**, 817–822 (2011)
222. G. Chen, Y. Jin, L. Wang, J. Deng, C. Zhang, Gold nanorods-based FRET assay for ultrasensitive detection of Hg^{2+}. Chem. Commun. **47**, 12500–12502 (2011)
223. S.M. Yoo, T. Kang, H. Kang, H. Lee, M. Kang, S.Y. Lee, B. Kim, Combining a nanowire SERS sensor and a target recycling reaction for ultrasensitive and multiplex identification of pathogenic fungi. Small **7**, 3371–3376 (2011)
224. E.C. Dreaden, M.A. El-Sayed, Detecting and destroying cancer cells in more than one way with noble metals and different confinement properties on the nanoscale. Acc. Chem. Res. **45**, 1854–1865 (2012)
225. L. Wu, Z. Wang, S. Zong, Z. Huang, P. Zhang, Y. Cui, A SERS-based immunoassay with highly increased sensitivity using gold/silver core-shell nanorods. Biosens. Bioelectron. **38**, 94–99 (2012)
226. Z. Siwy, L. Trofin, P. Kohli, L.A. Baker, C. Trautmann, C.R. Martin, Protein biosensors based on biofunctionalized conical gold nanotubes. J. Am. Chem. Soc. **127**, 5000–5001 (2005)
227. G. Lin, W. Lu, W. Cui, L. Jiang, A simple synthesis method for gold nano- and microplate fabrication using a tree-type multiple-amine head surfactant. Cryst. Growth Des. **10**, 1118–1123 (2010)
228. P. Pienpinijtham, X.X. Han, T. Suzuki, C. Thammacharoen, S. Ekgasit, Y. Ozaki, Micrometer-sized gold nanoplates: starch-mediated photochemical reduction synthesis and possibility of application to tip-enhanced Raman scattering (TERS). Phys. Chem. Chem. Phys. **14**, 9636–9641 (2012)
229. C. Loo, A. Lowery, N.J. Halas, J. West, R. Drezek, Immunotargeted nanoshells for integrated cancer imaging and therapy. Nano Lett. **5**, 709–711 (2005)
230. L.R. Hirsch, J.B. Jackson, A. Lee, N.J. Halas, J. West, A whole blood immunoassay using gold nanoshells. Anal. Chem. **75**, 2377–2381 (2003)
231. A.M. Gobin, M.H. Lee, N.J. Halas, W.D. James, R.A. Drezek, J.L. West, Near-infrared resonant nanoshells for combined optical imaging and photothermal cancer therapy. Nano Lett. **7**, 1929–1934 (2007)
232. M.A. Mahmoud, M.A. El-Sayed, Time dependence and signs of the shift of the surface plasmon resonance frequency in nanocages elucidate the nanocatalysis mechanism in hollow nanoparticles. Nano Lett. **11**, 946–953 (2011)
233. S.A. Khan, R. Kanchanapally, Z. Fan, L. Beqa, A.K. Singh, D. Senapati, P.C. Ray, A gold nanocage-CNT hybrid for targeted imaging and photothermal destruction of cancer cells. Chem. Commun. **48**, 6711–6713 (2012)
234. M.H. Rashid, R.R. Bhattacharjee, T.K. Mandal, Organic ligand-mediated synthesis of shape-tunable gold nanoparticles: an application of their thin film as refractive index sensors. J. Phys. Chem. C **111**, 9684–9693 (2007)

235. Y. Zhu, H. Kuang, L. Xu, W. Ma, C. Peng, Y. Hua, L. Wang, C. Xu, Gold nanorod assembly based approach to toxin detection by SERS. J. Mater. Chem. **22**, 2387–2391 (2012)
236. Y.B. Mollamahalle, M. Ghorbani, A. Dolati, Electrodeposition of long gold nanotubes in polycarbonate templates as highly sensitive 3D nanoelectrode ensembles. Electrochim. Acta **75**, 157–163 (2012)
237. R. Mout, D.F. Moyano, S. Rana, V.M. Rotello, Surface functionalization of nanoparticles for nanomedicine. Chem. Soc. Rev. **41**, 2539–2544 (2012)
238. S.E. Lee, D.Y. Sasaki, T.D. Perroud, D. Yoo, K.D. Patel, L.P. Lee, Biologically functional cationic phospholipid-gold nanoplasmonic carriers of RNA. J. Am. Chem. Soc. **131**, 14066–14074 (2009)
239. K. Kim, S.-W. Huang, S. Ashkenazi, M. O'Donnell, A. Agarwal, N.A. Kotov, M.F. Denny, M.J. Kaplan, Photoacoustic imaging of early inflammatory response using gold nanorods. Appl. Phys. Lett. **90**, 223901 (2007)
240. D.L. Chamberland, A. Agarwal, N. Kotov, J.B. Fowlkes, P.L. Carson, X. Wang, Photoacoustic tomography of joints aided by an Etanercept-conjugated gold nanoparticle contrast agent—an ex vivo preliminary rat study. Nanotechnology **19**, 095101 (2008)
241. A. Agarwal, S.W. Huang, M. O'Donnell, K.C. Day, M. Day, N. Kotov, S. Ashkenazi, Targeted gold nanorod contrast agent for prostate cancer detection by photoacoustic imaging. Appl. Phys. Lett. **102**, 064701 (2007)
242. C. Loo, L. Hirsch, M.H. Lee, E. Chang, J. West, N.J. Halas, R. Drezek, Gold nanoshell bioconjugates for molecular imaging in living cells. Opt. Lett. **30**, 1012–1014 (2005)
243. X. Yang, S.E. Skrabalak, Z.-Y. Li, Y. Xia, L.V. Wang, Photoacoustic tomography of a rat cerebral cortex in vivo with au nanocages as an optical contrast agent. Nano Lett. **7**, 3798–3802 (2007)
244. R. Huschka, J. Zuloaga, M.W. Knight, L.V. Brown, P. Nordlander, N.J. Halas, Light-induced release of DNA from gold nanoparticles: nanoshells and nanorods. J. Am. Chem. Soc. **133**, 12247–12255 (2011)
245. C. Loo, A. Lin, L. Hirsch, M.H. Lee, J. Barton, N.J. Halas, J. West, R. Drezek, Nanoshell-enabled photonics-based imaging and therapy of cancer. Tech. Canc. Res. Treat. **3**, 33–40 (2004)
246. J. You, R. Zhang, G. Zhang, M. Zhong, Y. Liu, C.S. Van Pelt, D. Liang, W. Wei, A.K. Sood, C. Li, Photothermal-chemotherapy with doxorubicin-loaded hollow gold nanospheres: a platform for near-infrared light-trigged drug release. J. Control. Release **158**, 319–328 (2012)
247. L.R. Hirsch, R.J. Stafford, J.A. Bankson, S.R. Sershen, B. Rivera, R.E. Price, J.D. Hazle, N. J. Halas, J.L. West, Nanoshell-mediated near-infrared thermal therapy of tumors under magnetic resonance guidance. Proc. Natl. Acad. Sci. USA **100**, 13549–13554 (2003)
248. E.C. Dreaden, S.C. Mwakwari, L.A. Austin, M.J. Kieffer, A.K. Oyelere, M.A. El-Sayed, Small molecule-gold nanorod conjugates selectively target and induce macrophage cytotoxicity towards breast cancer cells. Small **8**, 2819–2822 (2012)
249. E.B. Dickerson, E.C. Dreaden, X.H. Huang, I.H. El-Sayed, H.H. Chu, S. Pushpanketh, J.F. McDonald, M.A. El-Sayed, Gold nanorod assisted near-infrared plasmonic photothermal therapy (PPTT) of squamous cell carcinoma in mice. Cancer Lett. **269**, 57–66 (2008)
250. D. Pissuwan, S.M. Valenzuela, M.C. Killingsworth, X.D. Xu, M.B. Cortie, Targeted destruction of murine macrophage cells with bioconjugated gold nanorods. J. Nanopart. Res. **9**, 1109–1124 (2007)
251. H. Takahashi, T. Niidome, A. Nariai, Y. Niidome, S. Yamada, Photothermal reshaping of gold nanorods prevents further cell death. Nanotechnology **17**, 4431–4435 (2006)
252. L.C. Kennedy, L.R. Bickford, N.A. Lewinski, A.J. Coughlin, Y. Hu, E.S. Day, J.L. West, R. A. Drezek, A new era for cancer treatment: gold-nanoparticle-mediated thermal therapies. Small **7**, 169–183 (2011)
253. J. Chen, D. Wang, J. Xi, L. Au, A. Siekkinen, A. Warsen, Z.-Y. Li, H. Zhang, Y. Xia, X. Li, Immuno gold nanocages with tailored optical properties for targeted photothermal destruction of cancer cells. Nano Lett. **7**, 1318–1322 (2007)

254. F. Tielens, J. Andres, Prediction of gold zigzag nanotube-like structure based on Au_{32} units: a quantum chemical study. J. Phys. Chem. C **111**, 10342–10346 (2007)
255. Y. Horiguchi, T. Niidome, S. Yamada, N. Nakashima, Y. Niidome, Expression of plasmid DNA released from DNA conjugates of gold nanorods. Chem. Lett. **36**, 952–953 (2007)
256. L. Dykman, N. Khlebtsov, Gold nanoparticles in biomedical applications: recent advances and perspectives. Chem. Soc. Rev. **41**, 2256–2282 (2012)
257. C.C. Chen, Y.P. Lin, C.W. Wang, H.C. Tzeng, C.H. Wu, Y.C. Chen, C.P. Chen, L.C. Chen, Y.C. Wu, DNA-gold nanorod conjugates for remote control of localized gene expression by near infrared irradiation. J. Am. Chem. Soc. **128**, 3709–3715 (2006)
258. H. Takahashi, Y. Niidome, S. Yamada, Controlled release of plasmid DNA from gold nanorods induced by pulsed near-infrared light. Chem. Commun. **17**, 2247–2249 (2005)
259. I. Gorelikov, L.M. Field, E. Kumacheva, Hybrid microgels photoresponsive in the near-infrared spectral range. J. Am. Chem. Soc. **126**, 15938–15939 (2004)
260. A. Shiotani, T. Mori, T. Niidome, Y. Niidome, Y. Katayama, Stable incorporation of gold nanorods into N-isopropylacrylamide hydrogels and their rapid shrinkage induced by near-infrared laser irradiation. Langmuir **23**, 4012–4018 (2007)
261. Q. Wei, J. Ji, J. Shen, Synthesis of near-infrared responsive gold nanorod/PNIPAAm core/shell nanohybrids via surface initiated ATRP for smart drug delivery. Macromol. Rapid Commun. **29**, 645–650 (2008)
262. A. Barhoumi, R. Huschka, R. Bardhan, M.W. Knight, N.J. Halas, Light-induced release of DNA from plasmon-resonant nanoparticles: Towards light-controlled gene therapy. Chem. Phys. Lett. **482**, 171–179 (2009)
263. R. Huschka, O. Neumann, A. Barhoumi, N.J. Halas, Visualizing light-triggered release of molecules inside living cells. Nano Lett. **10**, 4117–4122 (2010)
264. W. Chen, R. Bardhan, M. Bartels, C. Perez-Torres, R.G. Pautler, N.J. Halas, A. Joshi, A molecularly targeted theranostic probe for ovarian cancer. Mol. Cancer Ther. **9**, 1028–1038 (2010)
265. M.S. Yavuz, Y.Y. Cheng, J.Y. Chen, C.M. Cobley, Q. Zhang, M. Rycenga, J.W. Xie, C. Kim, K.H. Song, A.G. Schwartz, L.H.V. Wang, Y.N. Xia, Gold nanocages covered by smart polymers for controlled release with near-infrared light. Nat. Mater. **8**, 935–939 (2009)
266. W. Li, X. Cai, C. Kim, G. Sun, Y. Zhang, R. Deng, M. Yang, J. Chen, S. Achilefu, L.V. Wang, Y. Xia, Gold nanocages covered with thermally-responsive polymers for controlled release by high-intensity focused ultrasound. Nanoscale **3**, 1724–1730 (2011)
267. W. Wang, T. Yan, S. Cui, J. Wan, A bioresponsive controlled-release biosensor using Au nanocages capped with an aptamer-based molecular gate and its application in living cells. Chem. Commun. **48**, 10228–10230 (2012)
268. E. Hao, G.C. Schatz, Electromagnetic fields around silver nanoparticles and dimers. J. Chem. Phys. **120**, 357–366 (2004)
269. J.-M. Lamarre, F. Billard, C.H. Kerboua, M. Lequime, S. Roorda, L. Martinu, Anisotropic nonlinear optical absorption of gold nanorods in a silica matrix. Opt. Commun. **281**, 331–340 (2008)
270. W. Cai, U.K. Chettiar, A.V. Kildishev, V.M. Shalaev, Optical cloaking with metamaterials. Nat. Photon. **1**, 224–227 (2007)
271. S. Nah, L. Li, R. Liu, J. Hao, S.B. Lee, J.T. Fourkas, Metal-enhanced multiphoton absorption polymerization with gold nanowires. J. Phys. Chem. C **114**, 7774–7779 (2010)
272. S. Lal, J.H. Hafner, N.J. Halas, S. Link, P. Nordlander, Noble metal nanowires: from plasmon waveguides to passive and active devices. Acc. Chem. Res. **45**, 1887–1895 (2012)
273. C.L. Nehl, J.H. Hafner, Shape-dependent plasmon resonances of gold nanoparticles. J. Mater. Chem. **18**, 2415–2419 (2008)

Chapter 4
Synthesis and Application of Solution-Based II–VI and IV–VI Semiconductor Nanowires

Pornthip Tongying, Maksym Zhukovskyi and Masaru Kuno

Abstract Semiconductor nanowires (NWs) possess unique optical and electrical properties due to their anisotropic shape as well as their size-tunable electronic structure. In this chapter, we discuss the solution phase synthesis of II–VI and IV–VI semiconductor nanowires (e.g. ZnSe, CdS, CdSe, CdTe, PbS, PbSe, and $PbSe_xS_{1-x}$) as well as NW-based heterostructures involving core/shell and metal nanoparticle-decorated morphologies. We subsequently discuss the application of these materials within the context of nanowire yarns, nanowire-functionalized cotton textiles, and renewable energy applications involving nanostructured solar cells and photocatalytic hydrogen generation.

4.1 Introduction

One-dimensional (1D) II–VI and IV–VI semiconductor nanowires possess distinct optical and electrical properties due to their two-dimensional (2D) confinement and anisotropic shape. These features make them desirable for use in various applications. As illustrations, II–VI NWs have been used in photodetectors [1–4], solar cells [5–9] and in photocatalytic applications [10, 11]. Likewise, IV–VI NWs, especially the lead chalcogenides, have been used in infrared photodetectors [12], thermoelectric devices [13, 14] and in field effect transistors (FETs) [15–17]. NWs can also serve as the foundation for heterostructures having specifically engineered properties. This high degree of applicability, possessed by NWs, has thus made them one of the most studied nanosystems to date.

P. Tongying · M. Zhukovskyi (✉) · M. Kuno (✉)
Department of Chemistry and Biochemistry, University of Notre Dame,
251 Nieuwland Science Hall, Notre Dame, IN 46556, USA
e-mail: mzhukovs@nd.edu

M. Kuno
e-mail: mkuno@nd.edu

Q. Li (ed.), *Anisotropic Nanomaterials*, NanoScience and Technology,
DOI 10.1007/978-3-319-18293-3_4

Numerous approaches exist for creating NWs. Well established techniques include Vapor-Liquid-Solid (VLS) [18], oriented attachment [19], Supercritical-Fluid-Liquid-Solid (SFLS) [20] and Solution-Liquid-Solid (SLS) growth [21]. In this chapter, we focus on the SLS growth of group II–VI and IV–VI semiconductor NWs and their core/shell and metal nanoparticle-decorated counterparts. We then describe their potential uses in various applications.

4.2 Synthesis of II–VI and IV–VI Nanowires (NWs)

4.2.1 Solution-Liquid-Solid (SLS) Growth

SLS growth was first developed by Trentler et al. in 1995 [21] and is the liquid phase analogue of traditional VLS growth. In Trentler's original study, crystalline InP, InAs and GaAs nanowhiskers were synthesized using In and Ga/In nanoparticle (NP) catalysts formed in situ by the decomposition of tri-*tert*-butylindane and gallane. Resulting whiskers possessed widths of 10–150 nm with complementary lengths up to several micrometers. Metallic In (or Ga/In) droplets were found at the tips of these fibers suggesting their seeded growth.

SLS, like VLS growth, employs molten metal nanoparticles to solubilize elements derived from the thermolysis of molecular precursors. Semiconductor nucleation occurs within "catalyst" NPs once they become supersaturated. This eventually leads to self-segregation of the semiconductor at the droplet/solvent interface and, in turn, initiates seeded NW growth. The deposition of additional material at the semiconductor/droplet interface extends the NW length with continued growth occurring until the droplet becomes depleted of precursors. NW diameter control is established through the choice of catalyst nanoparticle size. Consequently, when narrow diameter NPs are used, growth of NWs with radii within the confinement regime of a number of systems is possible. Unwanted radial growth is additionally suppressed by using surfactants in solution that bind to exposed NW surfaces. Figure 4.1 summarizes this general SLS growth scheme.

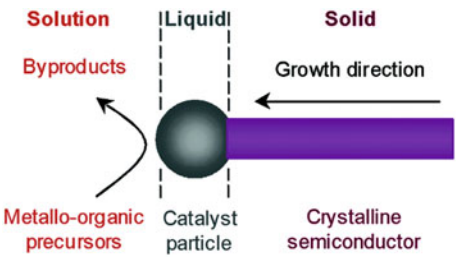

Fig. 4.1 Qualitative SLS growth mechanism for semiconductor NWs using low melting metal nanoparticle catalysts. Reprinted with permission from [34]. Copyright 2006 American Chemical Society

Although Trentler's early report showed proof-of-concept, resulting whiskers exhibited irregular morphologies as well as broad diameter and length distributions. This could be attributed, in part, to the uncontrolled size of employed metal NP catalysts. Consequently, the next stage in the development of SLS growth was the controlled synthesis of high quality metal NP catalysts with well-defined sizes and with narrow size distributions. Empirically, Bi has proven to be the best metal catalyst for producing high quality SLS NWs. This has motivated the various syntheses for size controlled Bi NPs described below.

In 2001, Yu et al. reported the formation of nearly monodisperse Bi, Sn and In NPs with controlled diameters using a heterogeneous seeded growth mechanism [22]. Specifically, NPs were formed by decomposing $Bi[N(SiMe_3)_2]_3$, $Sn(NMe_2)_2$, or $In(C_5H_5)$, in a solution containing Au NP seeds (diameter $\sim$1.5 nm) stabilized by a polymer [poly(styrene$_{0.86}$-co-vinyl-pyrrolidinone$_{0.14}$)]. Resulting NP diameters ranged from 7 to 25 nm. This work was followed by the development of a similar synthesis for d = 3–115 nm (d = 5–17 nm) Bi NPs involving the decomposition of $Bi[N(SiMe_3)_2]_3$ (or $BiCl_3$) in the presence of $Na[N(SiMe_3)_2]$ and poly(1-hexadecene)$_{0.67}$-co-(1-vinylpyrrolidinone)$_{0.33}$] [23]. Resulting NPs from these studies were subsequently used to grow InP and GaAs NWs with diameters in the range of 3.5–11 nm [24] and 6.0–17 nm [25]. Corresponding Bi NPs were used to demonstrate the growth of CdSe NWs with mean diameters ranging from 5 to 20 nm [26].

Grebinski et al. similarly reported the synthesis of Au/Bi core/shell NPs. This entailed coating small 1.5 nm diameter Au NPs with Bi through the decompositions of $Bi(Et)_3$ or $Bi(Bu)_3$ at low temperatures ($\sim$100 °C) in diphenyl ether [27]. The size of resulting NPs (d = 1.5–2.5 nm) was controlled through the amount of Bi precursor introduced. Using these particles, Grebinski subsequently demonstrated SLS-induced CdSe NW growth with diameters below 10 nm [27].

Later, Fanfair et al. reported the synthesis of Bi NPs through the $NaBH_4$ induced reduction of Bi(III) 2-ethylhexanoate in the presence of tri-*n*-octylphosphine (TOP) and dioctyl ether [28]. Resulting Bi NPs possessed an average diameter of 20 nm. This was followed by Li et al. who demonstrated a simple room temperature synthesis for Bi NPs involving the reduction of $Bi[N(SiMe_3)_2]_3$ or $BiCl_3$ with TOP in dioctyl ether [29]. Resulting Bi NPs were stabilized with amines such as oleylamine and had a mean diameter of $\sim$3.3 nm. These Bi NPs were subsequently used to demonstrate the growth of d = 7.9 and d = 22.3 nm CdSe NWs.

Finally, Puthussery et al. found that Bi NPs could be produced in situ through the exposure of $BiCl_3$ to chalcogen precursors being introduced into NW reaction mixtures [30]. Resulting Bi NP diameters were found to scale with $BiCl_3$ concentration and ultimately resulted in the development of facile "one pot" syntheses for CdS, CdSe and CdTe NWs.

In what follows, we describe details about the Bi-NP seeded growth of II–VI and IV–VI NWs.

4.2.1.1 Synthesis of Group II–VI NWs [CdE (E = S, Se, Te) and ZnE (E = Se, Te)]

The first synthesis of straight (d = 5–20 nm) CdSe NWs using Bi and Au/Bi NP seeded SLS growth was reported by Yu et al. in 2003 [26]. This was soon followed by Grebinski et al. who demonstrated the growth of d < 10 nm CdSe NWs using Au/Bi core/shell NPs [27]. The same group later reported the Au/Bi NP seeded growth of both straight and branched (d = 8–10 nm) CdSe and CdTe NWs [31, 32] as well as (d = 10.4 nm) CdS NWs [30]. Later, Li et al. reported the Bi NP seeded growth of straight CdSe NWs where a systematic variation of the reaction parameters (e.g. reaction temperature, precursor concentration and reaction time) led to wires with diameters ranging from d = 6 to 33 nm and with corresponding lengths up to tens of micrometers [33].

In the case of zinc chalcogenide NWs, Wang et al. first synthesized ZnTe NWs using Bi NPs in the presence of $Zn(stearate)_2$ (or diethylzinc, $ZnEt_2$) and tributylphosphine telluride (TBPTe) [34]. This was followed by the work of Dong et al. who produced $ZnSe_xTe_{1-x}$ NWs using Bi NPs in the presence of $Zn(stearate)_2$ and trioctylphosphine selenide (TOPSe)/TBPTe [35]. Resulting diameters were on the order of 10 nm with accompanying lengths of $\sim$1 μm. Fanfair et al. likewise showed the Bi NP seeded growth of branched ZnSe NWs using ZnO and TOPSe as precursors [36]. Resulting diameters were on the order of $\sim$10–40 nm with lengths on the micrometer scale. Finally, Petchsang et al. demonstrated the growth of ZnSe NWs using $Zn(stearate)_2$, TOPSe and $BiCl_3$ in tri-*n*-octylphosphine oxide (TOPO) [37]. The mean NW diameter was $\sim$22 nm with lengths on the order of 10 μm.

Chemicals involved in the synthesis of II–VI NWs generally include a group II metal source, a chalcogen precursor, a high boiling coordinating/non-coordinating solvent and a low melting metal NP catalyst. Furthermore, Bi is often the preferred catalyst since it empirically produces high quality wires. We now provide more details about the SLS growth of CdSe NWs since it has been the most extensively studied and developed SLS system to date.

4.2.1.2 Synthesis of CdSe NWs

For CdSe NWs, the group II precursor is often a metal salt [e.g. cadmium acetate ($CdAc_2$)] or a metal oxide [e.g. cadmium oxide (CdO)]. These metal salts/oxides, however, are not used directly. Instead, they are converted into intermediate species through exposure to long chain fatty acids such as octanoic, myristic or stearic acid. What results are species such as cadmium octanoate, cadmium myristate and cadmium stearate which are the actual cadmium precursors used in reactions and whose decomposition kinetics are controlled through the compound's corresponding ligand stability constant. This enables kinetic control of subsequent NW reactions and leads to the production of high quality wires.

Next, TOPSe, trioctylphosphine sulfide (TOPS) and trioctylphosphine telluride (TOPTe) are often employed as convenient chalcogen sources. They originate from

the work first done by Steigerwald [38] to find chemical routes for synthesizing bulk solid state materials. These convenient precursors are easily prepared by dissolving S, Se or Te powder in neat TOP, yielding TOPS, TOPSe or TOPTe stock solutions with concentrations in the ~1 M range. Such TOPX (X = S, Se, Te) precursors have since been used extensively in the chemical synthesis of analogous colloidal quantum dots [39].

Both coordinating (e.g. TOPO) and non-coordinating [e.g. octadecene (ODE)] growth solvents have been used in the SLS growth of CdSe NWs. These solvents serve two roles. First, they act as high boiling media that can sustain NW growth at elevated temperatures to improve their crystallinity. Common growth temperatures range from 240 to 360 °C. Next, coordinating solvents act as surface passivating agents during growth. This helps maintain optimal growth kinetics, prevents radial NW growth, and, in the case of surfactants such as TOPO, passivates surface-related NW defect states.

The experimental setup, which incorporates all of these elements, is shown in Fig. 4.2. In brief, growth solvents and precursors are combined in a three-neck flask. The flask is then connected to a Schlenk line. This allows the reaction vessel to be evacuated and backfilled with an inert gas such as nitrogen. A resistive heating mantle heats the precursors. Temperatures are controlled via a thermocouple connected to a temperature controller [40].

A more detailed description about the synthesis of CdSe NWs follows. First, CdO, TOPO and octanoic acid are mixed in a three neck flask. The mixture is then

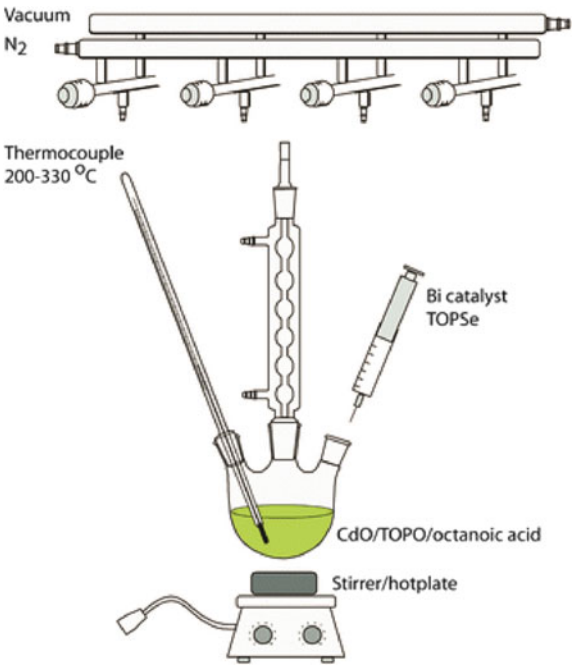

Fig. 4.2 Cartoon illustrating the reaction apparatus used for SLS NW growth. Chemicals and conditions represent those used in the synthesis of CdSe NWs [40]. Reproduced by permission of the PCCP Owner Societies

heated to melt the TOPO and is simultaneously degassed under vacuum to remove any water. Once complete, the temperature of the reaction mixture is raised to 320 °C under nitrogen. During this heating process, CdO reacts with octanoic acid to produce Cd(octanoate)$_2$. A color change of the solution from red to clear occurs highlighting this. Afterwards, the temperature is adjusted to the final growth temperature that typically ranges from 240 to 360 °C.

Once the reaction mixture temperature has stabilized, an injection solution consisting of TOPSe and Bi NPs (or $BiCl_3$) is introduced. An immediate color change from clear to brown occurs, indicating the nucleation and growth of CdSe NWs. The reaction mixture is then left heated at the growth temperature for several minutes whereafter it is cooled to room temperature. While still warm, the reaction mixture is diluted with toluene to prevent TOPO from solidifying. Produced NWs are recovered by centrifuging the resulting suspension. Subsequent washings steps are carried out to remove any excess surfactant where washing is done by exposing the wires to neat toluene and then centrifuging the suspension to recover the NWs. The obtained product is ultimately stored as a concentrated toluene suspension and remains stable for several years. Representative transmission electron microscopy (TEM) images of straight CdSe, CdTe and CdS NWs are shown in Fig. 4.3.

4.2.1.3 NW Diameter Control

In the SLS growth of CdSe and other NWs, diameter control is primarily achieved by preselecting the starting catalyst NP size. In this regard, a link between catalyst size and NW diameter has previously been established by Yu et al. who showed that in the case of CdSe NWs synthesized with Au/Bi (d = 8.72 nm) and Bi (d = 21 and 24 nm) NPs, resulting NWs had near identical diameters of 5–11 and 16–20 nm respectively [26]. A later study by Grebinski et al. showed that CdSe NWs made using d = 1.5–3.0 nm Au/Bi NPs had corresponding mean diameters which ranged from 7 to 10 nm and which increased with increasing Au/Bi NP size [31].

When $BiCl_3$ is used to produce NWs, diameter control is achieved by varying its concentration in the reaction mixture. Empirically, increasing $BiCl_3$ concentrations result in larger diameter Bi NPs as seen through increases in corresponding NW diameters. In the case of CdSe NWs, diameters have been tuned from d = 5 to 10.6 nm using a ten-fold increase in the amount of $BiCl_3$ added to reaction mixtures [30].

Apart from catalyst size, indirect ways exist for tuning NW diameters. In particular, varying the metal to chalcogen ratio of preparations influences NW diameters. Namely, larger NW diameters are obtained by increasing the Cd:Se ratio of SLS preparations [31]. Analogously, using more reactive metal/chalcogen precursors results in narrower diameter NWs. As an example, in the growth of ZnTe NWs, narrower wires were obtained when $ZnEt_2$ was used as a precursor over less reactive Zn(stearate)$_2$ under the same conditions [$ZnEt_2$: d = 3.7–5.0 nm; Zn (stearate)$_2$ d = 5–12 nm] [34].

Figure 4.4 shows resulting ensemble absorption and photoluminescence (PL) spectra of SLS grown CdSe NWs with varying mean diameters between 5 and

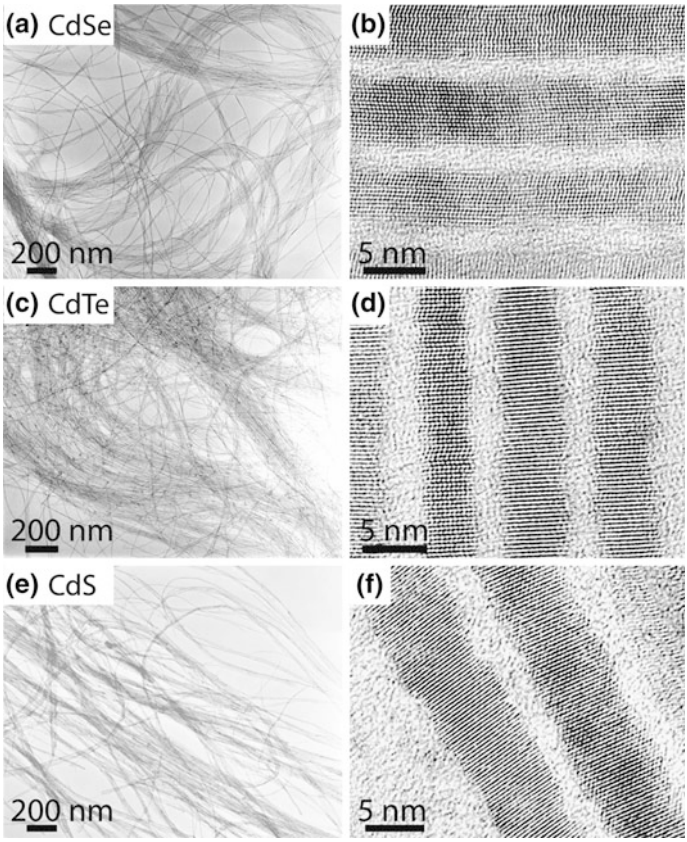

Fig. 4.3 Low and high magnification TEM images of straight **a**, **b** CdSe, **c**, **d** CdTe, and **e**, **f** CdS NWs. (Facile synthesis of II–VI nanowires using bismuth salts [30]. Copyright 2010 WILEY-VCH Verlag GmbH & Co. KGaA, Weinheim)

10.5 nm [30]. The spectra show that CdSe's band edge absorption and PL energies blueshift in tandem with decreasing NW diameter. This demonstrates the existence of carrier confinement effects and more broadly, highlights the ability of SLS growth to produce nanowires within the confinement regime of a number of important systems.

4.2.1.4 NW Branching

Next, despite the relatively low growth temperatures used in SLS growth, resulting wires are highly crystalline. However, many SLS-produced CdSe NWs exhibit mixtures of zincblende (ZB) and wurtzite (W) phases as well as twin boundaries [30, 31]. Interestingly, ZB/W phase admixtures have also been seen in VLS grown

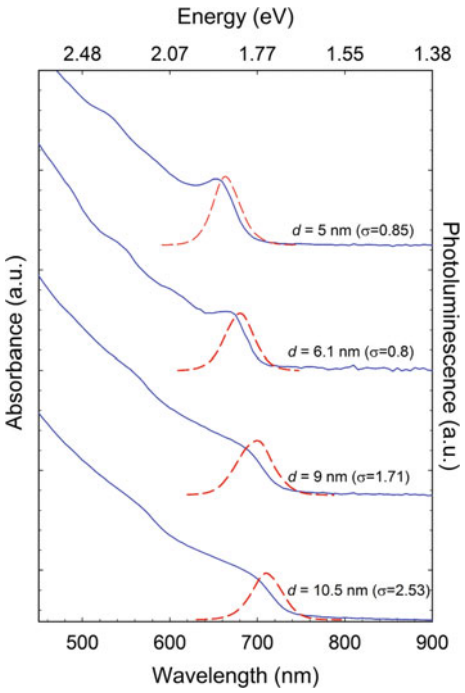

Fig. 4.4 Ensemble absorption (*solid blue line*) and PL (*dashed red line*) spectra of CdSe NWs with various diameters. (Facile synthesis of II–VI nanowires using bismuth salts [30]. Copyright 2010 WILEY-VCH Verlag GmbH & Co. KGaA, Weinheim)

GaAs, InAs and ZnSe NWs and occur when two crystal phases of similar energy exist [41, 42].

While such phase admixtures are not optimal for transport applications, other opportunities arise. Namely, phase admixtures can be used to control NW morphologies. This, in turn, enables the production of branched NWs. In the case of CdSe and CdTe NWs, what results are tripod, V-shaped and Y-shaped wires [31, 32]. Representative TEM images of branched CdSe NWs can be seen in Fig. 4.5.

The underlying origin of these branched morphologies results from the presence of a central ZB core at branching points of the wire. Exposed {111} faces then enable NW growth in different directions. This results in characteristic tripod, V-shape and Y-shape NW morphologies for II–VI NWs, first seen in Fig. 4.5 and outlined schematically in Fig. 4.6.

Branching is not unique to CdSe and CdTe NWs. It has also been seen in ZnSe [36] and PbSe NWs (discussed in the next section) [43]. Consequently, a general branching mechanism that rationalizes this phenomenon is discussed in detail in [40]. In brief, the simultaneous nucleation and growth of *two* NWs on a single catalyst NP (a geminate nucleation event) explains the various morphologies. Specifically, having two nucleated wires on a molten catalyst enables a common crystalline core to develop between the two wires. This core can subsequently lock the two arms into place along its unique crystallographic directions. For II–VI NWs such as CdSe and CdTe, a ZB core can thus unite two wires with orientations along

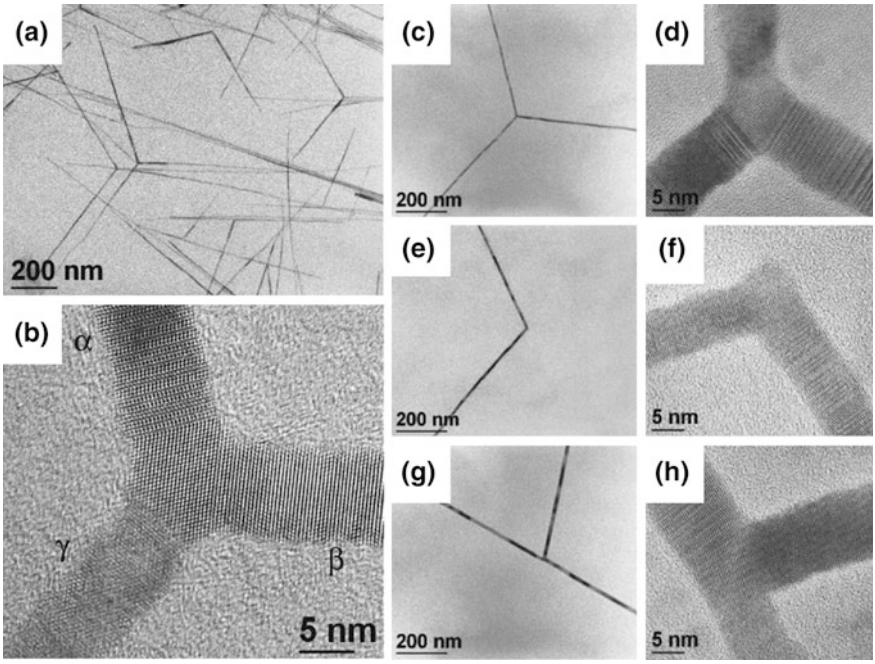

Fig. 4.5 **a** Low magnification TEM image of branched CdSe NWs. **b** High magnification TEM image of a tripod NW. Additional low and high magnification TEM images of **c**, **d** tripod, **e**, **f** V-shaped and **g**, **h** Y-shaped NWs. Adapted with permission from [31]. Copyright 2004 American Chemical Society

different ⟨111⟩ directions. At this point, if growth stops, a V-shaped NW results with a characteristic 109.5° angle. If growth continues through addition of material along a new {111} face of the ZB core, a tripod NW results. Alternatively, if growth continues through addition of material along an existing ⟨111⟩ direction, identical to that of one of the two arms, a Y-shaped NW results. In this manner, the appearance of tripod, V-shaped, Y-shaped and other branched CdSe/CdTe NW morphologies can be rationalized. An identical mechanism can be invoked to explain branching in lead chalcogenide wires described in the next section.

4.2.1.5 Synthesis of Group IV–VI NWs (PbS, PbSe, and $PbSe_xS_{1-x}$)

The flexibility of SLS growth enables not only II–VI but also IV–VI NWs to be synthesized [43–46]. Specifically, crystalline PbS and PbSe NWs have been made using Bi and Au/Bi NP seeded growth in tandem with lead oleate/TOPS [44] and lead acetate/TOPSe [43] precursor pairs. Specifically, PbSe NWs have been made by injecting a solution of TOPSe and Au/Bi NPs into TOP containing lead acetate and octanoic acid at 175 °C [43]. Resulting NWs possess mean diameters between

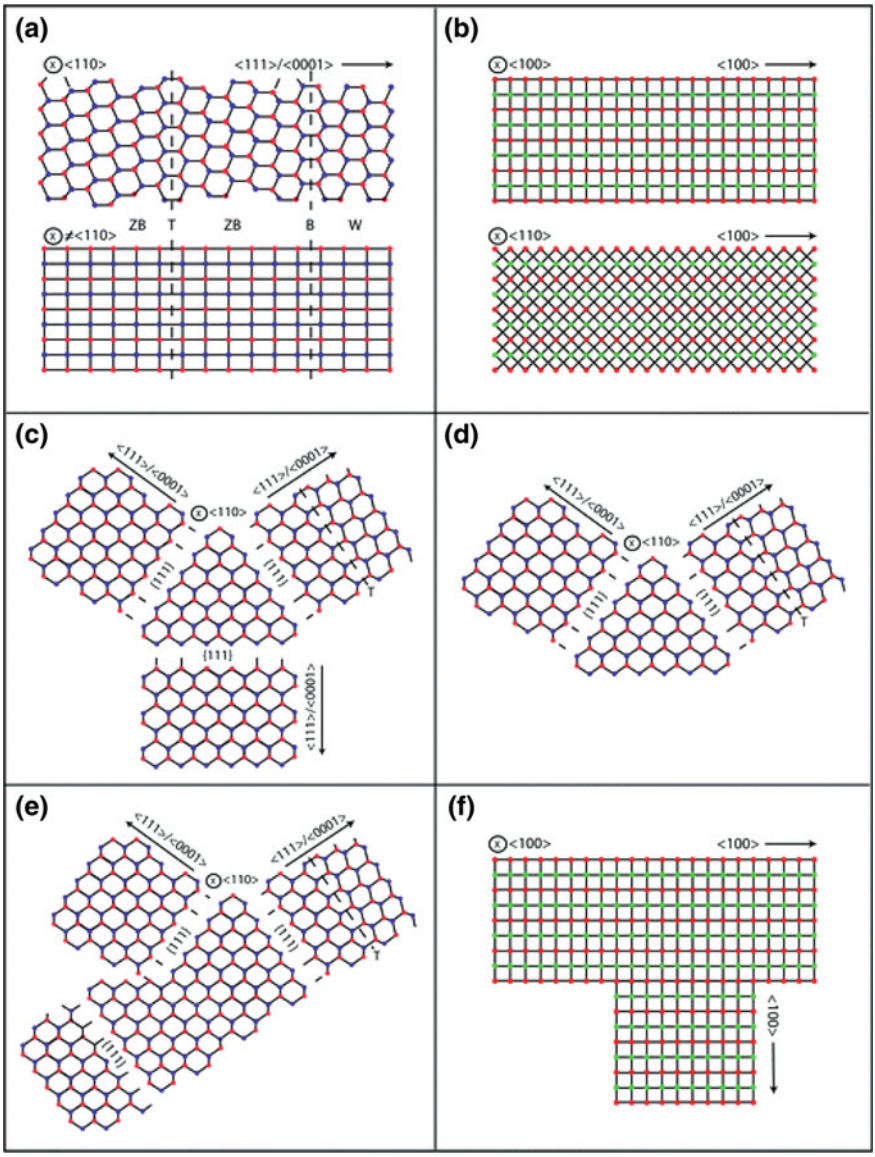

Fig. 4.6 Cartoon schematic of straight **a** CdSe or CdTe and **b** PbSe NWs. **c–e** Cartoon schematic of branched CdSe and CdTe NWs. **f** Cartoon schematic of T-shaped PbSe NWs [40]. Reproduced by permission of the PCCP Owner Societies

5 and 10 nm and have lengths ranging from 1 to 5 μm. In all cases, as with II–VI NWs, lead chalcogenide NW diameters are controlled by the size of the starting catalyst NP.

Branching has also been demonstrated with PbSe NWs despite the absence of a ZB/W phase admixture in this system [43]. In this regard, given that the rock salt crystal structure of PbSe is its only low energy crystallographic phase, only rock salt NWs are obtained. At first glance, this would not seem amenable to inducing branching. However, in practice, branched PbSe NWs with characteristic right angle and T-shapes have been produced [43]. The existence of these morphologies can again be rationalized using the above mentioned geminate NW nucleation mechanism described in the NW branching section of this chapter.

4.2.1.6 Use of Single Source Precursors

Due to the differing decomposition kinetics and/or reactivity of individual precursors, the use of metal/chalcogen precursor pairs has occasionally failed to produce highly crystalline and diameter controlled lead chalcogenide NWs [45]. Thus, to overcome this problem, single source precursors, where both metal and chalcogen exist within the same compound, have been employed. Specifically, Sun et al. have reported the synthesis of straight, diameter controlled PbS NWs using lead(II) diethyldithiocarbamate [$Pb(S_2CNEt_2)_2$] [45]. Binary PbS and PbSe as well as ternary $PbSe_xS_{1-x}$ NWs have also been made using lead(II) diethyldithiocarbamate [$Pb(S_2CNEt_2)_2$] or lead(II) imido(selenodiisopropylphosphinate) [$Pb((SeP^iPr_2)_2N)_2$] in the presence of $BiCl_3$ and TOPO [46]. In the latter study, resulting PbS and PbSe NWs possess a mean diameter of 9 nm with lengths exceeding 10 µm. Representative low and high magnification TEM images of these wires are shown in Fig. 4.7a–d.

The use of single source precursors simultaneously enables the growth of ternary alloy $PbSe_xS_{1-x}$ NWs. They are synthesized in an analogous manner to binary PbS and PbSe NWs through the decomposition of both $Pb((SeP^iPr_2)_2N)_2$ and $(Pb(S_2CNEt_2)_2$ in the presence of $BiCl_3$ [46]. Of note is that the NW composition can readily be tuned by varying the mole ratio of these two precursors. Specifically, $Pb((SeP^iPr_2)_2N)_2/Pb(S_2CNEt_2)_2$ mole ratios of 4:1, 1.5:1, 1:1, 1:1.5 and 1:4 yield ternary $PbSe_xS_{1-x}$ NWs where x = 0.8, 0.6, 0.5, 0.4 and 0.2, respectively. Resulting $PbSe_xS_{1-x}$ NW diameters range from d = 9 to 11 nm with corresponding lengths between 4 and 10 µm. The wires are fully alloyed with no apparent compositional gradients along their length. Representative low and high magnification TEM images of $PbSe_xS_{1-x}$ NWs are shown in Fig. 4.7e, f.

4.2.2 Synthesis of Core/Shell Semiconductor NWs

We now transition to a discussion about the growth of NW heterostructures, specifically, core/shell semiconductor NWs which possess a number of potentially useful properties given the presence of nanoscale heterojunctions [47]. In this section, we therefore describe how such core/shell morphologies can be synthesized, starting with the wires described in Sect. 4.2.1. In practice, this entails

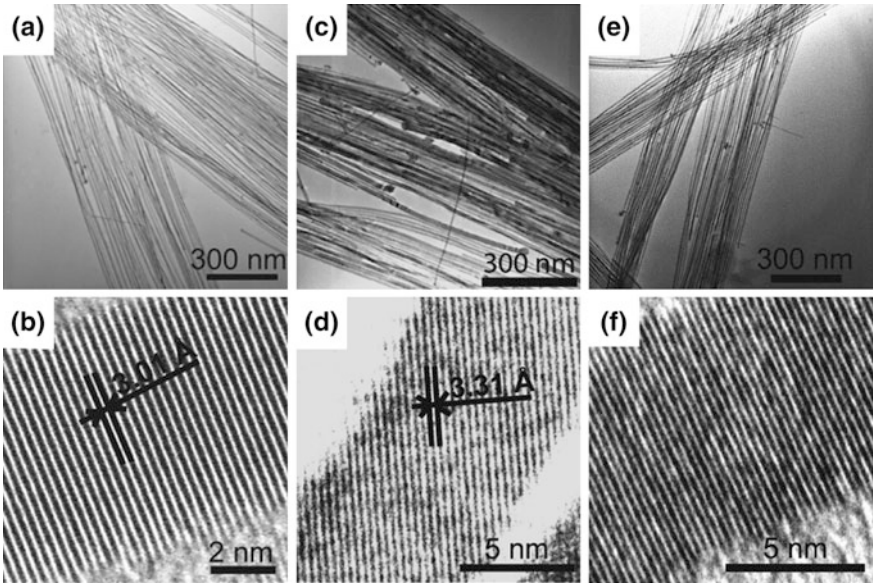

Fig. 4.7 Low and high magnification TEM images of binary **a**, **b** PbSe, **c**, **d** PbS and ternary **e**, **f** $PbSe_xS_{1-x}$ NWs. Adapted with permission from [46]. Copyright 2012 American Chemical Society

coating SLS-produced NWs with a second species through the slow introduction and thermolysis of molecular precursors.

Such core/shell structures generally involve Type I or Type II band offsets. In the former case, a Type I offset is created when the shell possesses a larger band gap than the NW core and when its conduction and valence bands simultaneously enclose those of the core. Consequently, upon photoexcitation of the core/shell structure, resulting carriers find themselves confined to the core. In principle, this leads to improved NW emission quantum yields (QYs), which stems from suppressed carrier access to surface states. For example, CdSe NWs coated with 6 and 10 monolayers CdS exhibit PL quantum which increase from 0.14 % (uncoated) to 0.25 and 0.46 %, respectively [48]. As will be discussed later in this chapter, photocatalytic hydrogen generation efficiencies also increase due to enhanced carrier lifetimes [10].

By contrast, Type II heterostructures possess staggered band offsets between core and shell conduction/valence bands. This means that one of the bands of the shell is higher in energy than that of the corresponding core. At the same time, the opposite is true of the other band. Representative systems include CdSe/ZnTe and CdS/ZnTe core/shell NWs.

The potential usefulness of such Type II heterostructures stems from their improved charge separation efficiencies upon photoexcitation [49, 50]. Specifically, because of the nature of the band offsets, carriers of one type are forced to stay in

the core while carriers of the other type experience favorable charge transfer into the shell. Consequently, Type-II heterostructures exhibit charge separation tendencies suitable for solar cell applications. Furthermore, these band offsets mean that tunable emission wavelengths in the red as well as infrared are possible if spatially indirect transitions in these materials can be realized [51]. Figure 4.8 shows SEM images of the various Type I and II core/shell NWs systems that have been made. Insets illustrate corresponding bulk core/shell band offsets.

The synthesis of these heterostructured NWs remains challenging due to the large parameter space that must be explored. This includes a consideration of the lattice mismatch between materials, the thermal stability of the parent NWs, the

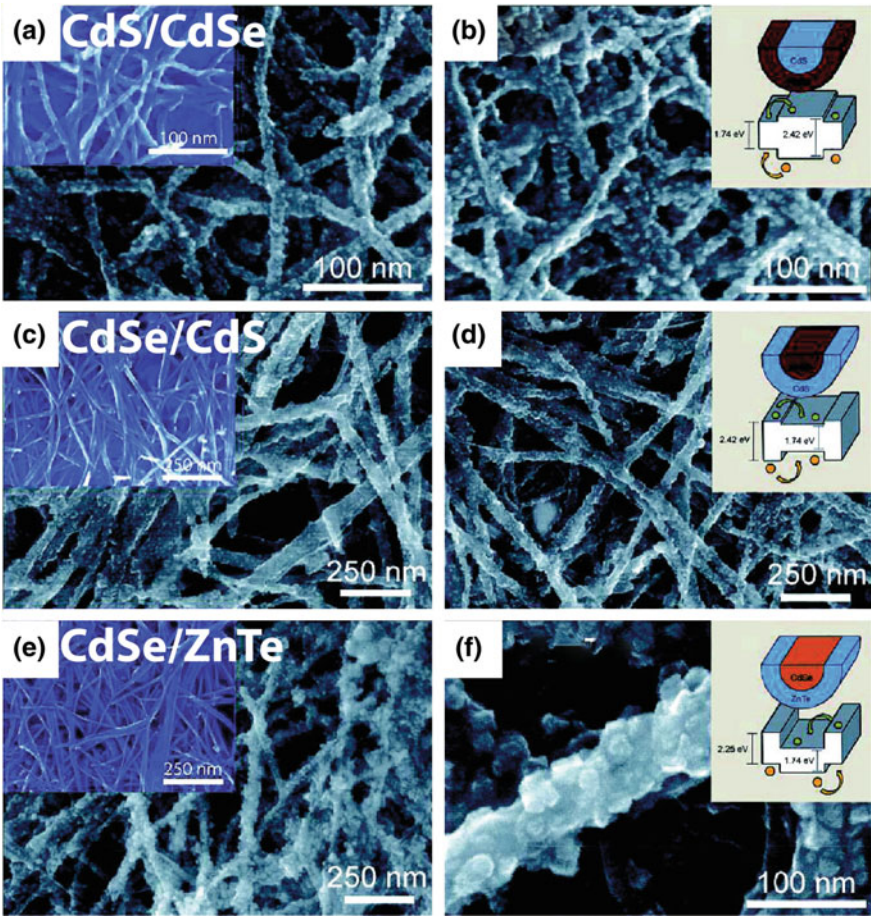

Fig. 4.8 SEM images of **a**, **b** CdS/CdSe, **c**, **d** CdSe/CdS and **e**, **f** CdSe/ZnTe core/shell NW heterostructures. *Insets* on the *right* illustrate bulk band offsets between the core and shell in each system. Reprinted with permission from [49]. Copyright 2008 American Chemical Society

selection of appropriate metal/chalcogen precursors for the shell, and the choice of a suitable growth solvent.

Having a small lattice mismatch between the NW and the shell makes more favorable the formation of core/shell structures. As an illustration, the 3.9 % lattice mismatch between CdSe and CdS makes the creation of CdSe/CdS or CdS/CdSe core/shell morphologies possible, as first demonstrated with colloidal CdSe quantum dots (QDs) [52]. Analogous CdSe/CdS NW heterostructures have since been realized [48, 49]. Similarly, CdSe/ZnTe NWs have been made by taking advantage of the 0.8 % lattice mismatch between CdSe and ZnTe [49]. Although a small lattice mismatch between the core and shell is generally preferred, a tolerance for larger mismatches exists. In the case of colloidal nanocrystals, CdSe/ZnS QDs have been made where the bulk lattice mismatch between CdSe and ZnS is 12 % [53, 54]. Likewise, in the case of NWs, ZnSe/CdSe NWs have been made with a 6.3 % lattice mismatch between materials [37].

At the same time, core NWs must remain stable at the elevated temperatures needed to thermalize shell precursors. Hence, the thermal stability of core NWs is important and is often tested by suspending them in a growth solvent and heating the suspension to temperatures compatible with the decomposition of the shell precursors. This has been discussed by Goebl et al. for CdSe and CdS NWs [49].

Optimal shell deposition temperatures, in turn, depend on the reactivity of the molecular precursors. For example, reactive precursor pairs such as dimethylcadmium ($CdMe_2$) and bis(trimethylsilyl)sulfide $(TMS)_2S$ [or bis(trimethylsilyl)selenide, $(TMS)_2Se$] thermalize at temperatures as low as 215 °C and lead to acceptable shell growth for CdSe (CdS) NWs. Replacing $(TMS)_2S$ [or $(TMS)_2Se$] with TOPS (or TOPSe), however, requires an increase in the deposition temperature in order to achieve suitable shell growth. This is due to the lesser reactivity of TOP-based precursors [49].

Finally, precursor introduction rates play an important role in determining the quality of resulting core/shell NWs. Specifically, slower injection rates result in smoother, more uniform coatings [49]. By contrast, rapidly introducing shell precursors often leads to uneven or patchy coatings.

4.2.2.1 Examples of Core/Shell NWs

Some examples of core/shell NWs include CdSe/CdS and CdSe/ZnS wires produced by Li et al. [48]. In this study, cadmium hexadecyl xanthate (Cd-HDX) and Zn-HDX single source precursors were used to achieve shell growth as well as different shell morphologies. Shell growth begins with the nucleation of CdS (or ZnS) on core CdSe NWs via the decomposition of Cd-HDX (or Zn-HDX) in TOP at 90 °C. This is then followed by a ripening process which ultimately results in ribbon formation along the core NW length, as illustrated in Fig. 4.9a [48].

CdSe/CdS NWs have likewise been made by decomposing $CdMe_2/(TMS)_2S$ [49] or $CdMe_2$/S powder [10] precursor pairs in a noncoordinating solvent such as squalane. Resulting shells appear rough and exhibit islanding (Fig. 4.8). Initial shell

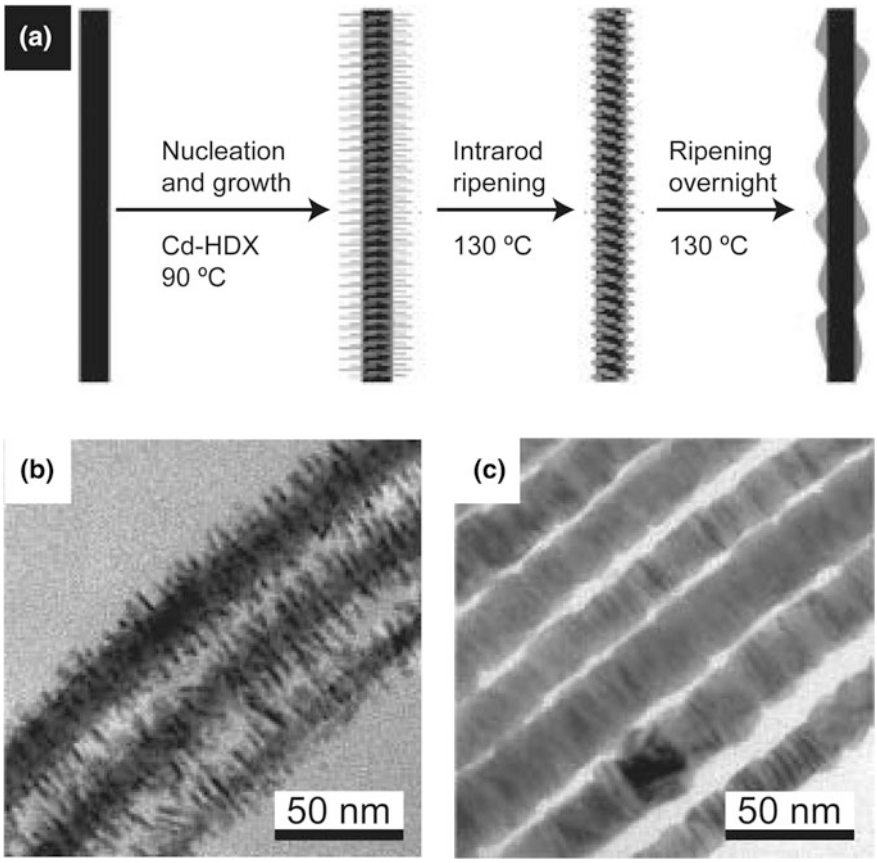

Fig. 4.9 **a** Schematic showing the growth of CdSe/CdS NWs. TEM images of **b** initial CdS nanorod formation on the surface of CdSe NWs and **c** the subsequent appearance of the shell after ripening. (Synthesis and characterization of colloidal core–shell semiconductor nanowires [48]. Copyright 2010 WILEY-VCH Verlag GmbH & Co. KGaA, Weinheim)

growth occurs through a Stranski-Krastanov growth mechanism, involving monolayer formation prior to island growth. This has also been observed for CdSe/ZnTe core/shell NWs. In the case of CdS/CdSe NWs, Volmer-Weber growth is observed where three-dimensional island growth is preferred from the beginning due to the unfavorable wetting of CdS with CdSe. In all cases, beyond these initial differences in shell growth, what results are thick polycrystalline shells, composed of randomly oriented nanocrystalline domains.

ZnSe/CdSe NWs have likewise been made by exposing ZnSe wires to $CdAc_2$ in TOPO at moderate temperature. TOPSe is subsequently introduced to initiate shell growth [37]. The procedure yields uniform shells where thicknesses can be varied by altering the reaction time after injection of the Se precursor. Representative TEM images of these core/shell NWs have been provided in Fig. 4.10.

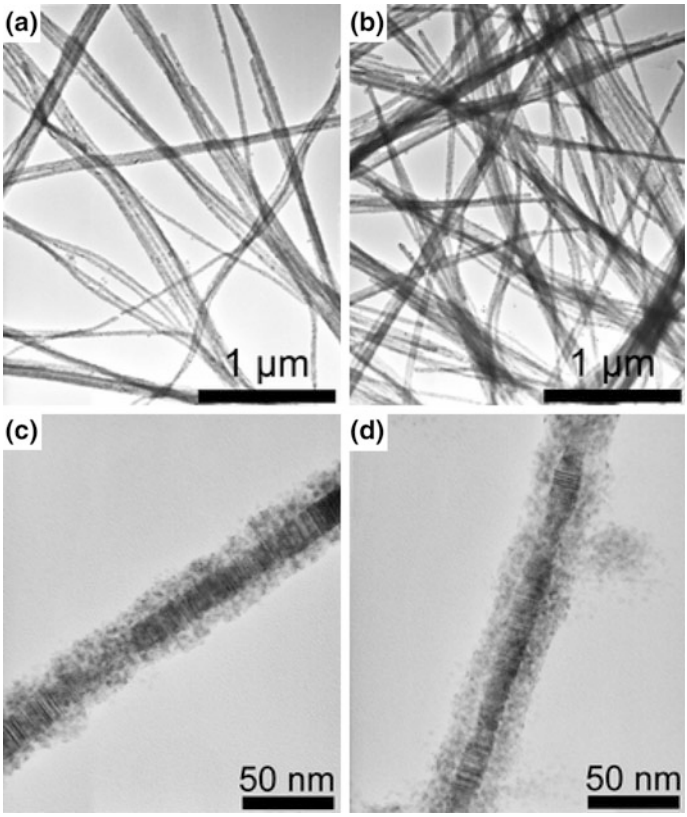

Fig. 4.10 Low and high magnification TEM images of ZnSe/CdSe NWs [37]. Reproduced by permission of The Royal Society of Chemistry

4.2.3 Hybrid Metal Nanoparticle Decorated NWs

Hybrid metal-semiconductor nanostructures result from combining two or more disparate metal and semiconductors into one system. Such heterostructures are multifunctional, making them useful in optoelectronic and photocatalytic applications [55–57]. As examples, decorating semiconductor nanostructures with metal nanoparticles has led to improved semiconductor charge separation efficiencies. This stems from photogenerated electrons preferentially migrating into metal nanoparticles, leaving behind holes in the semiconductor. Such enhanced charge transfer has been observed in CdSe NWs decorated with surface adsorbed Pt NPs [11]. Additionally, NW optical properties can be influenced by the presence of these particles. As an example, the presence of metal NP plasmon resonances has led to the observation of emission enhancement in Au NP decorated CdS NWs [58].

In what follows, we discuss the synthesis and growth of such hybrid metal-semiconductor NWs. This task of combining two or more dissimilar materials into

one nanostructured system is challenging. As described in Sect. 4.2.2 on the synthesis of core/shell nanowires, a numbers of parameters must be considered simultaneously in order to carry out such syntheses successfully. This includes a consideration of lattice constant mismatches between materials, the interfacial energy among materials, the presence of surface defects, and the accessibility/reactivity of the surface.

The energetics of the reaction also play a crucial factor in determining the growth of metal NPs onto NW surfaces. Fortunately, spontaneous nucleation of metal nanoparticles in the absence of elevated temperature or reducing agents is suppressed by the large barrier for homogeneous nucleation. Correspondingly, the deposition of metal NPs onto NW surfaces is aided by the lower barrier for heterogeneous nucleation [59, 60].

4.2.3.1 Examples of Hybrid Metal Nanoparticle Decorated Semiconductor NWs

We now illustrate several examples where metal NPs have been deposited onto the surfaces of solution-grown NWs. An initial example comes from Talapin et al. where Au NPs have been preferentially deposited onto the edges of zig-zag PbSe NWs by exposing them to $HAuCl_4$ in the presence of oleic acid and oleylamine at 35 °C (Fig. 4.11e) [61]. The decoration density is variable and can be further increased by

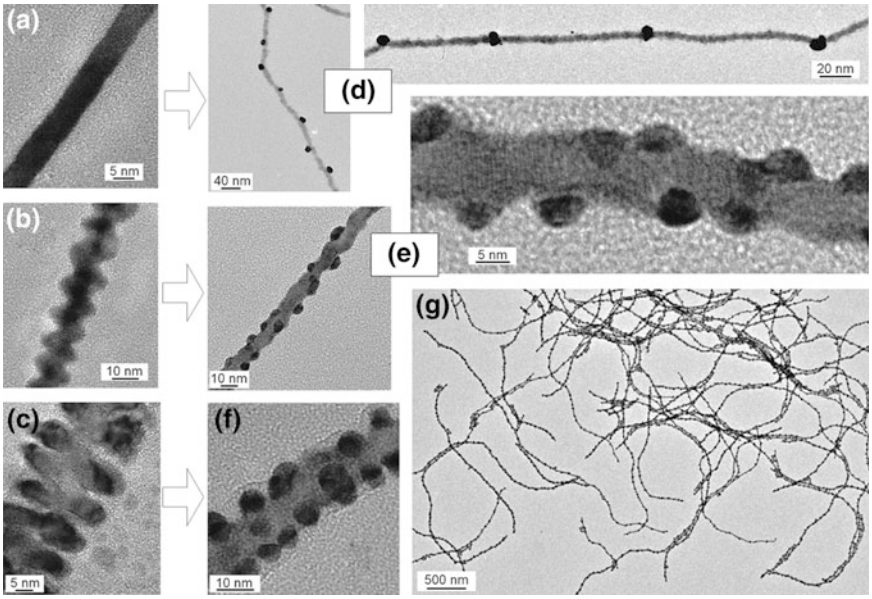

Fig. 4.11 TEM images of PbSe NWs with **a** straight, **b** zig-zag and **c** branched morphologies. TEM images of Au NP decorated **d** straight, **e** zig-zag and **f** branched PbSe NWs. **g** low magnification TEM images of Au NP decorated PbSe NWs. Reprinted with permission from [61]. Copyright 2007 American Chemical Society

using PbSe NWs with branched morphologies. This results in NW surfaces that are almost entirely covered with 5 nm Au NPs (Fig. 4.11f). Notably, NPs preferentially nucleate at the edges and branches of wires due to their higher surface energies.

Talapin et al. have similarly demonstrated the deposition of Au NPs onto straight PbSe NWs [61]. Resulting NWs show nearly equidistant Au NPs across the NW surface with a mean inter-particle spacing of 40–60 nm (Fig. 4.11d). Nucleation and growth in this case is non-selective given that straight NWs lack topological features that can serve as distinct nucleation sites.

Jen-La Plante et al. have likewise reported decorating straight CdSe NWs with Au NPs by adding a solution of gold chloride ($AuCl_3$), didodecyldimethylammonium bromide (DDAB, a phase transfer agent) and dodecylamine (DDA, a reducing agent) to a suspension of NWs. This results in Au NP nucleation and growth along the NW length [62]. Finally, Tongying et al. have successfully decorated CdSe and CdSe/CdS core/shell NWs with nanometer-sized Au NPs [10] using a procedure adapted from Menagen et al. [63]. In this study, a solution of $AuCl_3$ was added to a suspension of CdSe and CdSe/CdS core/shell NWs under vigorous stirring and under simultaneous UV illumination. Subsequent deposition of uniform d = 3–5 nm Au NPs was observed along the NW length within an extremely short period of time ($\sim$30 s). Images of these Au NP decorated wires are shown in Fig. 4.12.

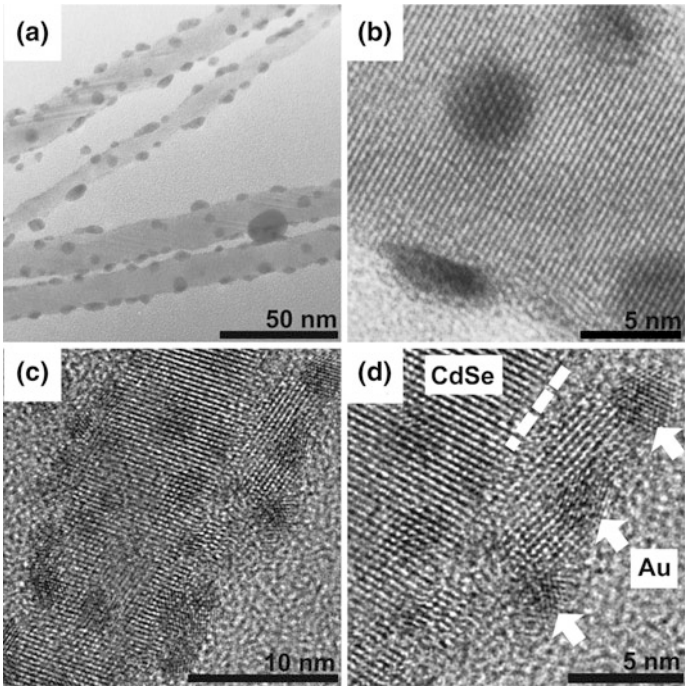

Fig. 4.12 Low and high magnification TEM images of Au NP decorated **a**, **b** CdSe **c**, **d** CdSe/CdS core/shell NWs. Reprinted with permission from [10]. Copyright 2012 American Chemical Society

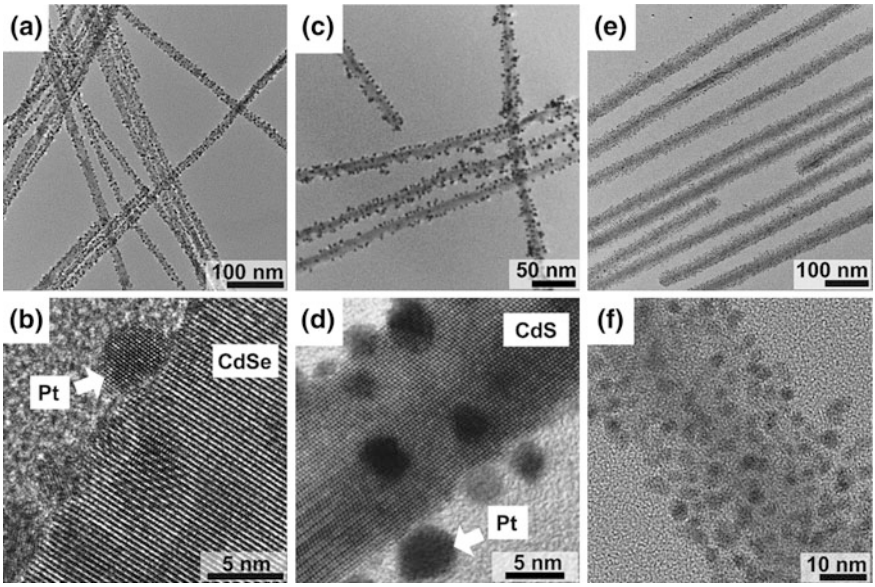

Fig. 4.13 Low and high magnification TEM images of Pt NP decorated **a**, **b** CdSe, **c**, **d** CdS and **e**, **f** CdSe/CdS core/shell NWs [11]. Adapted by permission of The Royal Society of Chemistry

In addition to Au, NWs can be functionalized with Pt NPs. This has been shown by Jen-La Plante et al. [62] for CdSe NWs as well as by Tongying et al. for CdSe and CdSe/CdS NWs [11]. In the latter case, CdSe and CdSe/CdS core/shell NWs were decorated with Pt NPs by modifying a procedure first developed for CdS NRs [64]. The synthesis entails exposing a suspension of NWs to platinum acetylacetonate in 1,2 dichlorobenzene. The mixture is then injected into a solution of oleic acid, oleylamine, and diphenyl ether at 200 °C to initiate NP growth. Pt NPs subsequently form along the NW length with resulting Pt NP sizes (diameter: 3–5 nm) controlled by the overall reaction time (5–7 min). Representative TEM images of these wires are shown in Fig. 4.13.

4.3 Applications of Semiconductor Nanowires

In Sect. 4.2 of this chapter we have discussed the SLS growth of NWs. We have also shown how NW morphologies can be altered by varying parameters such as the nature and concentration of precursors as well as the NP catalyst size. In addition, we have seen how NWs can be further modified by creating NW-based heterostructures. This includes core/shell morphologies as well as metal-semiconductor hybrid structures. In this section, we describe the assembly of solution-based NWs and their use in renewable energy application such as in photocatalytic hydrogen generation.

4.3.1 NW Assembly

The large carrier mobility, strong light absorbing nature, mechanical flexibility and high aspect ratio of semiconductor NWs make them suitable for a variety of electronic applications. Successful integration of NWs into devices, however, requires their assembly into mesoscopic structures. Towards this end, there have been many techniques which have been developed, including microfluidics [65], electrospinning [66], Langmuir–Blodgett [67], and magnetic/electric field alignment [68]. Unfortunately, many of these methods possess disadvantages including not being applicable to a wide range of semiconductors, not being scalable, and potentially resulting in the original nanostructure being affected through the use of additional chemicals (e.g. polymers, epoxides, amines etc.). The development of scalable NW assembly techniques is thus an important, ongoing research topic.

Manipulating NWs using electric fields represents one promising approach for their large-scale assembly. As an illustration, CdSe NWs have recently been aligned using AC dielectrophoresis (DEP) [1]. The approach entails depositing a suspension of NWs between two electrodes followed by the application of an AC electric field to align the wires. Figure 4.14a, b show bright field and PL images of resulting aligned CdSe NWs. Specifically, wires are seen to deposit onto both electrodes, orienting themselves along the field lines.

The origin of the AC DEP alignment effect stems from the interaction between induced dipoles in the wires and field gradients that exist at the electrode edges. Consequently, the DEP force and alignment velocity depend strongly on the

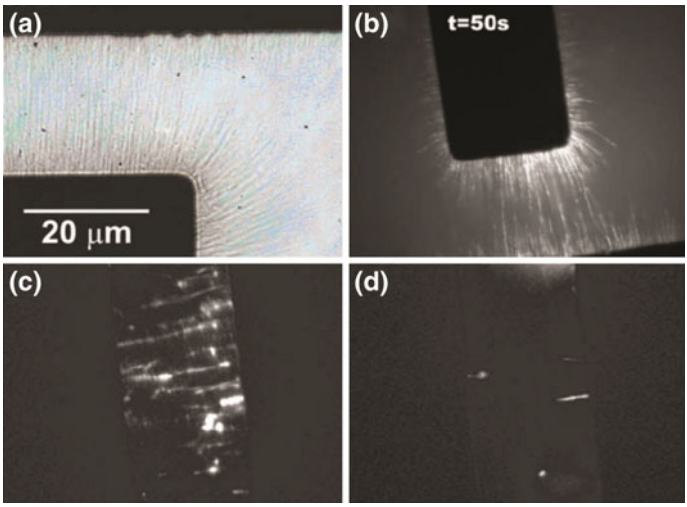

Fig. 4.14 AC DEP aligned CdSe NWs. **a** Bright field image after alignment. **b** Epifluorescence image taken at a given time during the alignment process. Emission images of CdSe NWs aligned **c** under illumination and **d** in the dark. Reprinted with permission from [1]. Copyright 2007, AIP Publishing LLC

magnitude of the induced dipoles in the wires. In this regard, an interesting observation made during these measurements was the enhancement of DEP alignment efficiency when CdSe NWs were illuminated with light. A hypothesis developed to explain this effect invoked the presence of mobile charges in the wires generated through above band gap illumination. Consequently, larger induced dipoles could result in the wires, leading to better overall NW alignment. Representative PL images comparing AC DEP aligned NWs under illumination and in the dark are shown in Fig. 4.14c, d.

The linear alignment of CdSe NWs results in a high degree of PL polarization anisotropy in both their absorption and emission. Figure 4.15a, b show representative photoluminescence images of aligned CdSe NW ensembles, which clearly demonstrate differences in the emission intensity with polarization angle. Furthermore, by defining an absorption/emission polarization anisotropy $\rho = (I_{\parallel} - I_{\perp})/(I_{\parallel} + I_{\perp})$ [$I_{\parallel}$ ($I_{\perp}$) is the observed emission intensity under parallel (perpendicular) polarized excitation relative to the aligned NW ensemble long axis] the degree of NW alignment can be quantified. These experiments reveal ρ-values of $\rho_{abs} = 0.24$ ($\rho_{em} = 0.27$) for aligned NW ensembles as well as $\rho_{abs} = 0.74$ ($\rho_{em} = 0.60$) for small NW bundles. When compared to ρ-values measured in individual NWs [$\rho_{abs} = 0.77$ ($\rho_{em} = 0.76$)], these ensemble ρ-values reveal the high degree of NW alignment achieved using AC DEP.

An analogous technique for organizing NWs into macroscopic yarns involves Light Induced Nanowire Assembly (LINA) [2]. The method entails slowly depositing a concentrated NW solution with a glass pipette onto the surface of a

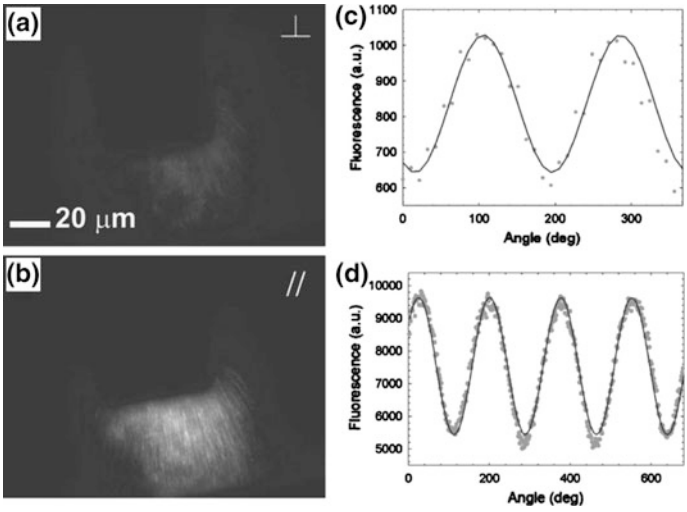

Fig. 4.15 **a** Perpendicular and **b** parallel polarized photoluminescence images of AC DEP aligned CdSe NW ensembles. Corresponding **c** absorption and **d** emission polarization anisotropy plots from an aligned ensemble. Reprinted with permission from [1]. Copyright 2007, AIP Publishing LLC

triboelectrically charged glass substrate under visible light illumination. A Van de Graaff generator (VDGG) charges the substrate prior to deposition. Experimentally, what results are NW fibers that spontaneously form, oriented normal to the substrate.

As with AC DEP, the approach exploits the interaction between induced dipoles in the wires and externally applied electric fields, in this case, stemming from charges on the substrate. Of note is that deliberately illuminating the sample with above band gap light creates many photogenerated carriers in the wires. This is aided by their large absorption cross sections [CdSe: $\sigma_{abs} \approx 6.93 \times 10^{-13}$ to $\sigma_{abs} \approx 3.91 \times 10^{-11}$ cm^2 μm^{-1} (d = 6–42 nm); CdTe: $\sigma_{abs} \approx 4.32 \times 10^{-13}$ to $\sigma_{abs} \approx 5.10 \times 10^{-12}$ cm^2 μm^{-1} (d = 7.5–11.5 nm)] [69–71] and leads to corresponding induced dipole moments of $\approx 10^5$ D assuming complete charge separation along the NW length [1]. Dipole-dipole interactions in solution then lead to end-to-end as well as side-to-side NW bundling and result in macroscopic NW bundles that consist of many wires aligned along the same direction. Figure 4.16 illustrates LINA conducted in toluene for three dilute CdSe, PbS and $PbSe_{0.5}S_{0.5}$ NW suspensions.

Next, Fig. 4.17a–e illustrates CdSe and CdTe NW yarns made using LINA. In this case, concentrated suspensions of the wires are slowly deposited onto a triboelectrically charged substrate under visible light illumination. Macroscopic NW alignment occurs whereupon subsequent solvent evaporation results in a NW yarn. Typical lengths are on the order of centimeters but yarns as long as 25 cm have been made. Corresponding diameters range from 10 to 20 μm and can be altered by changing the pulling rate from the NW suspension or by changing its concentration. In particular, increasing the pulling rate or alternatively, decreasing the NW stock concentration yields thinner yarns. Most importantly, LINA can be automated and enables the scalable formation of various NW yarns (Fig. 4.17f).

At the same time, LINA allows the creation of heterostructured yarns. For example, using a homogeneously mixed solution of CdSe and CdTe NWs results in a yarn made of both CdSe and CdTe NWs. Longitudinally segmented yarns made of different materials are also possible when LINA is carried out in a sequential fashion. This entails starting a yarn of one material followed by positioning the end of this yarn over a second charged substrate supporting a separate concentrated NW suspension. The second NW type subsequently adds to the end of the first yarn and extends it. Moving the resulting yarn back over the original substrate and repeating LINA then creates a segmented yarn of the form CdSe/CdTe/CdSe/CdTe etc.

In all cases, NW yarns show sizable optical polarization anisotropies. Specifically, CdSe NW yarns exhibit absorption polarization anisotropies of $\rho_{abs} \sim 0.2$ while homogenously mixed CdSe/CdTe yarns possess corresponding ρ-values of $\rho_{abs} \sim 0.13$. As with the earlier AC DEP results, this indicates that NWs in the yarns exhibit a relatively high degree of overall alignment. This opens up the possibility of using NW yarns in applications such as polarization-sensitive photodetectors [1, 2], a topic that will be discussed later in this chapter.

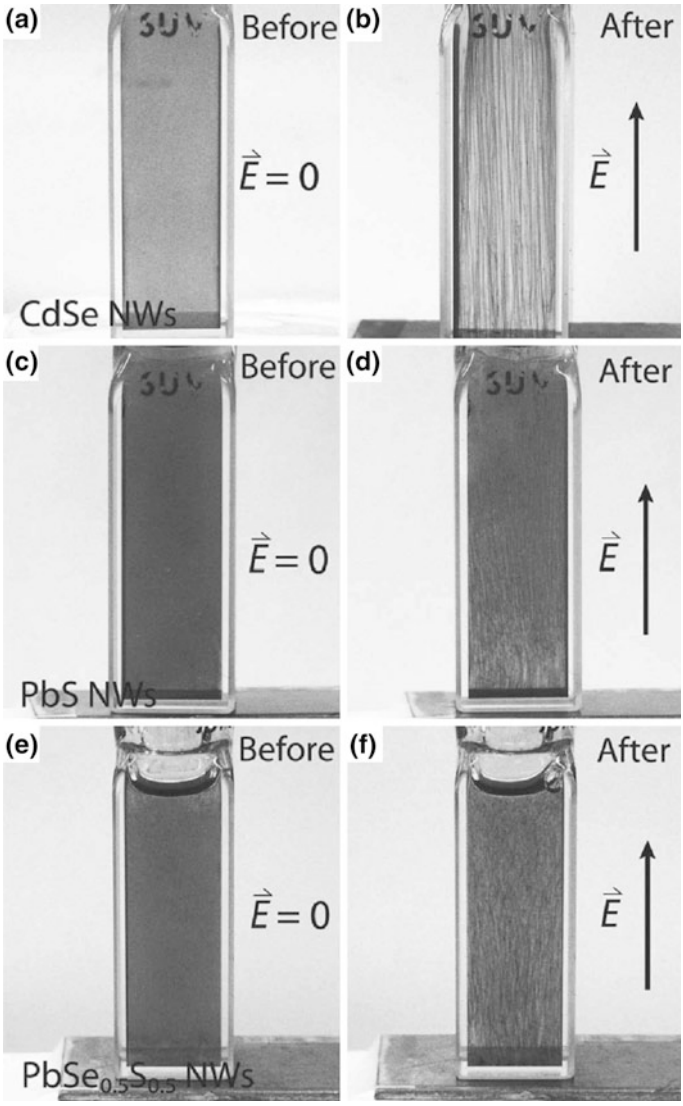

Fig. 4.16 **a**, **b** CdSe, **c**, **d** PbS, and **e**, **f** $PbSe_{0.5}S_{0.5}$ NW suspensions in toluene before and after LINA. (Light induced nanowire assembly: The electrostatic alignment of semiconductor nanowires into functional macroscopic yarns [2]. Copyright 2013 WILEY-VCH Verlag GmbH & Co. KGaA, Weinheim)

Finally, NWs can be used to functionalize natural fibers. In particular, cotton can be decorated with SLS grown NWs using the light or electrostatically-induced attraction of NWs [3]. What results are cotton fibers and textiles that retain their original mechanical properties while inheriting new chemical and optical properties from the deposited wires.

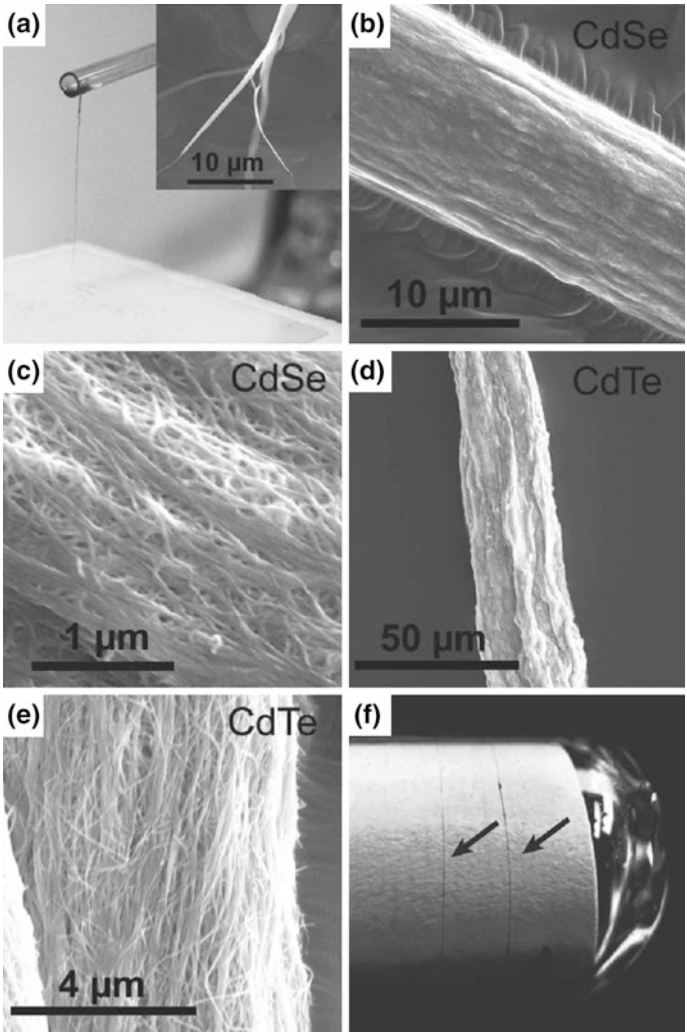

Fig. 4.17 **a** Image depicting NW yarn formation. SEM images of resulting **b**, **c** CdSe and **d**, **e** CdTe NW yarns. **f** 8 cm long CdSe NW yarn formed by automated pulling. (Light induced nanowire assembly: The electrostatic alignment of semiconductor nanowires into functional macroscopic yarns [2]. Copyright 2013 WILEY-VCH Verlag GmbH & Co. KGaA, Weinheim)

NW functionalization of cotton is carried out by dip-coating cotton fibers and textiles into NW suspensions under illumination with above band gap light. Alternatively, the cotton is charged with a VDGG prior to dip coating. The deposited NWs subsequently form an interlinked network that encapsulates individual cotton fibers in a conformal fashion (Fig. 4.18).

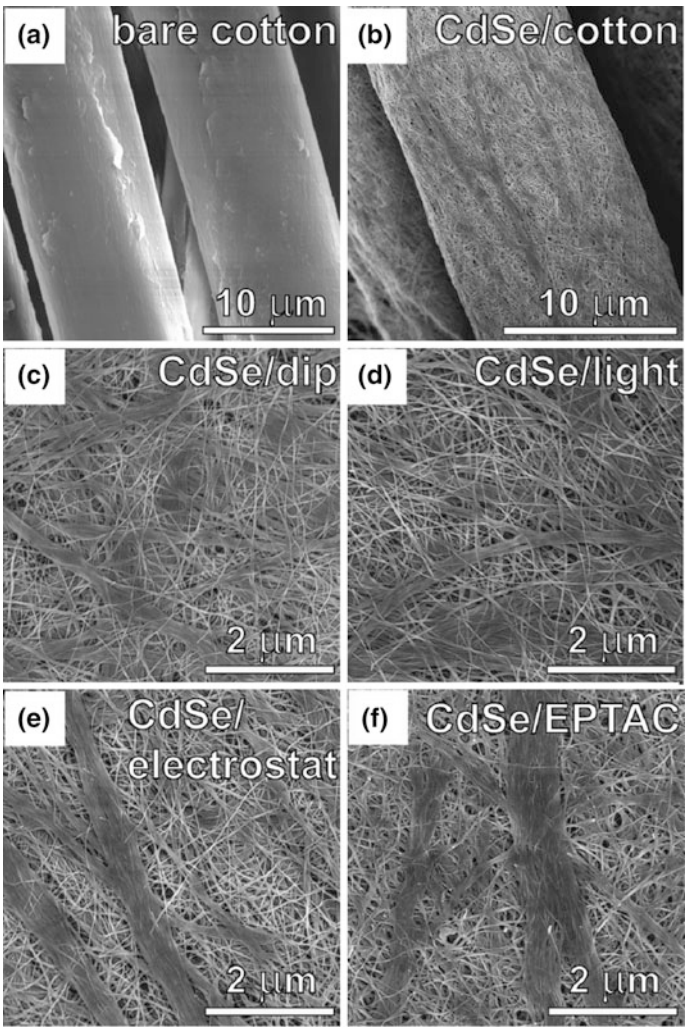

Fig. 4.18 SEM images of **a** bare cotton, and cotton functionalized with CdSe NWs after **b**, **c** simple dip-coating, **d** light-enhanced dip-coating, **e** VDGG-enhanced dip-coating and **f** dip-coating onto cationized cotton. Reprinted with permission from [3]. Copyright 2014 American Chemical Society

Illuminating NW suspensions with light during cotton functionalization results in an increased proclivity for depositing macroscopic NW bundles. As seen with LINA, the bundling phenomenon originates from the light-induced dipole-dipole interaction between individual wires. A bundling tendency is also observed when cotton is chemically cationized with 2,3-epoxypropyltrimethylammonium chloride (EPTAC) prior to dip-coating (Fig. 4.18f).

4.3.2 NW Barcodes

The ability to functionalize cotton with a wide variety of NWs as well as with binary combinations of NWs, enables the barcoding of textiles for identification purposes [3]. As shown in Fig. 4.19, the cotton/NW fabrics exhibit characteristic Raman spectra of component NWs. For illustration purposes, three NW combinations on cotton (i.e. CdTe/CdS, CdSe/CdS, CdTe/CdSe) have been tested. Consequently, combinations of NW types can lead to unique Raman signatures with potential uses in anti-counterfeiting and in other applications.

4.3.3 NW-Based Photodetectors

SLS-grown NWs have also been used to fabricate NW-based photodetectors [1–3]. In a first example, devices have been made using NW functionalized cotton fibers/textiles. Specifically, cotton/CdSe, cotton/CdTe and cotton/CdSe/CdTe threads were placed over two Au electrodes 60 μm apart. Under bias (−150 to 150 V) and

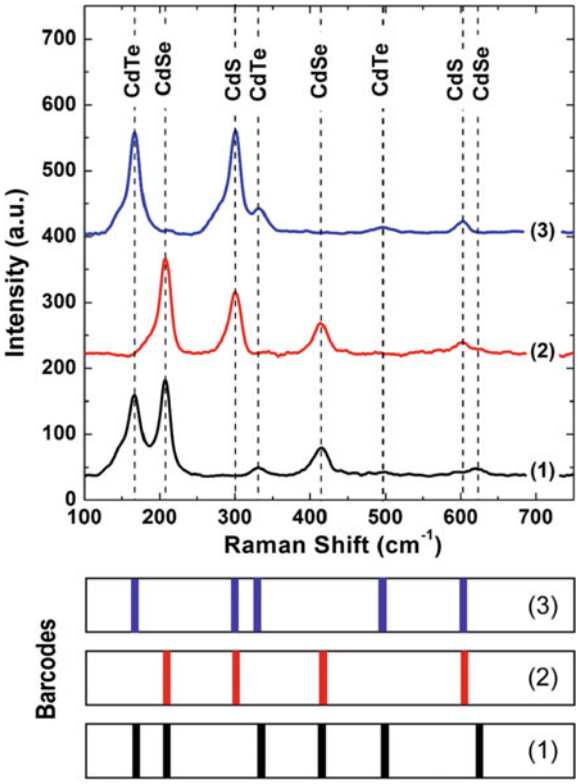

Fig. 4.19 Raman spectra of homogeneously mixed (*1*) cotton/CdSe/CdTe, (*2*) cotton/CdSe/CdS, and (*3*) cotton/CdTe/CdS NW fibers. Corresponding Raman barcodes obtained from each material are also shown. Reprinted with permission from [3]. Copyright 2014 American Chemical Society

under dark conditions, little current was observed. However, upon exposure to visible light the device current increased by more than two orders of magnitude. Figure 4.20a, shows typical current-voltage characteristics of these cotton/NW photodetectors in the dark and under illumination. Corresponding photocurrent action spectra of these cotton/CdSe and cotton/CdTe NW devices correlate with their linear absorption spectra. This indicates that the NWs are responsible for observed photocurrents in the devices (Fig. 4.20b). Similar results were observed for analogous NW (or NW yarn) based photodetectors [2, 4].

It was found that device responsivity could be improved by post-synthesis treatment of the NWs or by creating heterostructured NW networks (Fig. 4.20a, c). In the former case, NWs treated with pyridine to remove insulating species on the NW surface exhibited improved transport behavior across wires. In the latter case, NW mixtures composed of wires with Type II band offsets relative to each other yielded improved device charge separation efficiencies [50, 72]. Both approaches, in turn, resulted in corresponding enhancements of device responsivities.

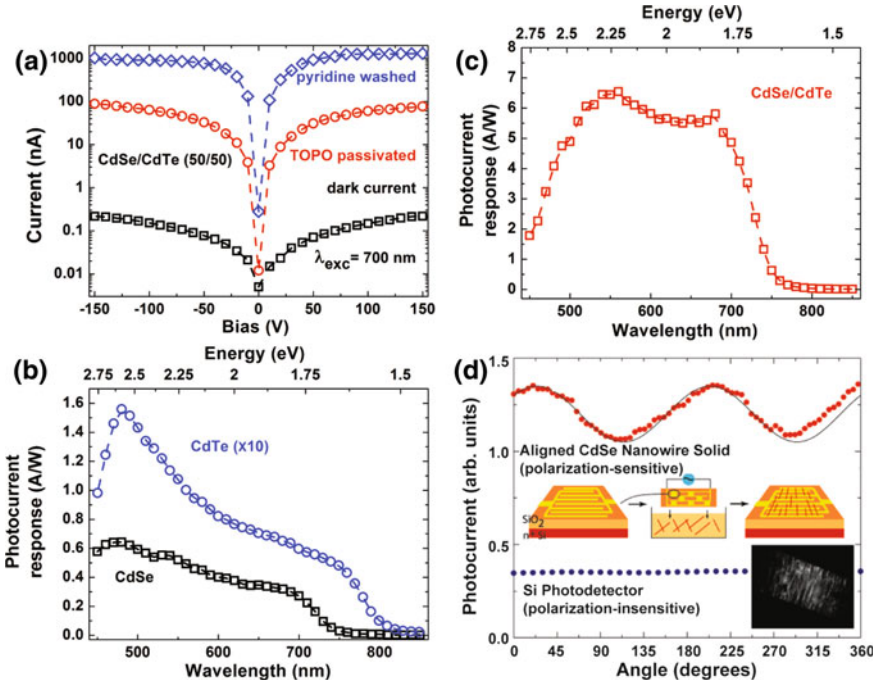

Fig. 4.20 **a** I–V characteristics and **b**, **c** photocurrent action spectra of CdSe, CdTe, and homogeneously mixed (50/50) CdSe/CdTe NWs deposited onto cotton fabrics. **d** Plot of the photocurrent polarization anisotropy from an aligned CdSe NW ensemble and comparison to the response of a commercial Si photodetector. **a**–**c** adapted with permission from [3]. Copyright 2014 American Chemical Society. **d** Adapted with permission from Singh [4]. Copyright 2007 American Chemical Society

Because NWs can be aligned using various techniques, resulting photodetectors are also polarization sensitive (Fig. 4.20d). In the case where AC DEP-aligned NWs have been used to make devices, corresponding photocurrent polarization anisotropies take values on the order of 0.13. This is similar to previously seen absorption (emission) anisotropy measurements of AC DEP-aligned NW ensembles ρ_{abs} = 0.24 (ρ_{em} = 0.27). They are also consistent with photocurrent polarization anisotropy measurements carried out on NW yarn photodetectors (ρ = 0.13–0.24) [1, 2]. The polarization sensitivity of NW photodetectors should be contrasted to the case of commercial Si photodetectors, which are not polarization sensitive.

4.3.4 NW Solar Cells

II–VI NWs are also potentially useful materials for creating nanostructured solar cells. Their anisotropic shape, favorable band gaps and large absorption cross sections make them useful active elements in solar cells. In this regard, there have been several recent demonstrations of solar cells built using SLS-produced NWs. A few examples are described below.

In a first study, Yu et al. demonstrated the use of CdSe NWs in a photoelectrochemical solar cell [8]. The device architecture consisted of indium tin oxide coated glass (ITO) as a transparent conductive substrate, a close packed NW absorber layer, sodium sulfide as an electrolyte and Pt as the counter electrode. The device also included colloidal CdSe quantum dots to fill in voids between NWs within the close packed NW absorber layer. The use of quantum dots made of the same material and possessing similar conduction and valence band levels was intended to improve the overall charge connectivity of the nanowire network. The energy level diagram illustrating the relative photoelectrochemical energies of different materials in the system is shown in Fig. 4.21a.

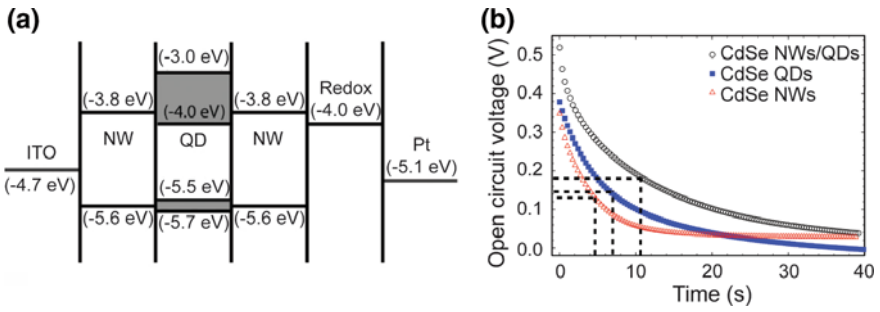

Fig. 4.21 **a** Energy level diagram and **b** open circuit voltage decays for photoelectrochemical solar cells system based on CdSe NWs and QDs. (A CdSe nanowire/quantum dot hybrid architecture for improving solar cell performance [8]. Copyright 2010 WILEY-VCH Verlag GmbH & Co. KGaA, Weinheim)

Experimentally, QD-modified NW solar cells show significant improvements in incident-photon-to-carrier conversion-efficiencies (IPCE) over comparable NW only cells. Values were seen to rise from 13 to 25 %. Furthermore, complementary open circuit voltage decay (OCVD) lifetimes increased from $t_{1/2}$ = 4.5 to 10.6 s (Fig. 4.21b). This demonstrated that QDs within the NW layer prevented back electron transfer to the electrolyte, enhancing overall charge separation efficiencies of the system. Consequently, device power conversion efficiencies were observed to rise from $\eta \sim 0.007$ to $\eta \sim 0.012$ % under simulated 1 sun conditions.

In a later example, CdSe NW solar cells were made using carbazole as a hole mediator [5]. Cells were built using fluorine doped tin oxide (FTO) coated glass as a conductive transparent substrate, ZnO as a compact (hole blocking) layer, a NW absorber layer, carbazole intercalated into the NW layer, sodium sulfide and sulfur as electrolytes and Cu_2S with reduced graphene oxide deposited on FTO as the counter electrode.

The purpose of the carbazole molecules was to achieve rapid hole extraction from the NWs, given their favorable HOMO level compared to the bulk CdSe valence band. Consequently, this would act to suppress unwanted charge recombination in the NWs following photoexcitation and would, in turn, improve device performance.

Figure 4.22a shows IPCE values recorded at different incident light wavelengths for CdSe NW devices with and without carbazole treatment. In the visible region of the spectrum, the maximum solar cell IPCE for untreated CdSe NWs was ~10 %. In the case of carbazole treated CdSe NWs, however, IPCE values were seen to rise up to ~45 %. Corresponding power conversion efficiencies also showed dramatic improvements from η = 0.01 % without carbazole to η = 0.46 % with carbazole. Complementary OCVD measurements confirm the effectiveness of charge separation in carbazole treated devices. Specifically, the apparent half-life of electrons in these solar cells increased from $t_{1/2}$ = 1.3 s without carbazole to 3.3 s with carbazole. This is illustrated in Fig. 4.22b.

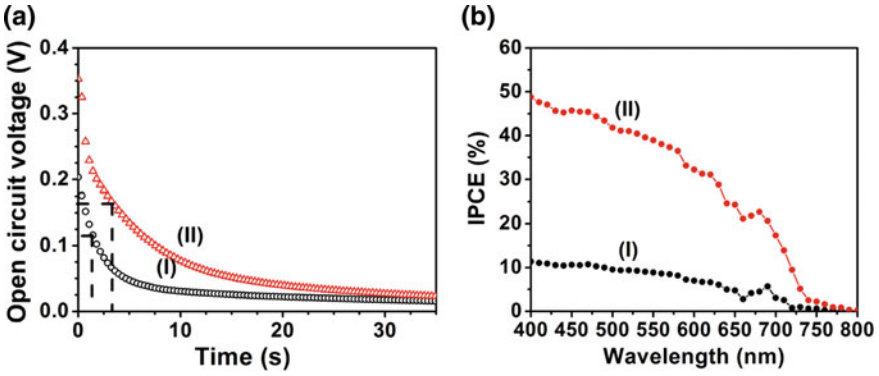

Fig. 4.22 **a** IPCE spectra and **b** open circuit voltage decays of solar cells based on CdSe NWs before (*I*) and after (*II*) carbazole treatment [5]. Reproduced by permission of The Royal Society of Chemistry

Along the same lines, Choi et al. used CdS NWs co-sensitized with squaraine dye to improve solar cell photoconversion efficiencies by extending their spectral response into the red and near infrared [7]. In this case, the organic dye was intended to act as an additional photosensitizer, adding to the absorption of NWs in the device. Choi's work subsequently showed that ~20 fold improvements in solar cell power conversion efficiencies were possible, from $\eta \sim 0.02$ to $\eta \sim 0.45$ %, using NW/squaraine composites.

Finally, Choi et al. explored using CdSe and CdS NW multilayers to improve solar cell performance [9]. The device consisted of FTO as an optically transparent substrate, ZnO as a blocking layer, stacked CdSe and CdS NW absorber layers, sodium sulfide and sulfur as electrolytes and reduced graphene oxide mixed with Cu_2S on FTO as the counter electrode. The underlying concept behind this solar cell was to exploit Type-II band offsets between CdSe and CdS NWs to achieve efficient charge separation following photoexcitation. Experimentally, multilayer CdSe and CdS cells were found to exhibit an order of magnitude improvement in power conversion efficiencies over comparable CdSe or CdS NW solar cells. Resulting power conversion efficiencies were $\eta \sim 1$ %.

4.3.5 NW-Based Photocatalysts for Hydrogen Generation

Semiconductor nanostructures with suitable band gaps ($E_g \sim 1.7$–3.1 eV) and electrochemical potentials ($E_{CB} \leq -0.41$ V and $E_{VB} \geq +0.82$ V vs. NHE at pH = 7) represent promising materials for use in photocatalytic hydrogen generation. This is because they absorb a good fraction of the incident solar radiation while their energetics enable charge transfer events that can carry out relevant chemistries. Furthermore, semiconductor nanostructures possess many advantages over their bulk counterparts due to their large surface-to-volume ratios, size-dependent optical properties, large absorption cross sections and ease of heterojunction fabrication.

On this last point, semiconductor nanostructures are interesting systems because of the relative ease of making heterojunctions with them. Implementing semiconductor/semiconductor heterointerfaces can dramatically improve not only the lifetime but also the spatial separation of photogenerated charges. Furthermore, nanostructures which feature metal/semiconductor heterojunctions should posses enhanced photocatalytic hydrogen generation activities since, in many cases, metal NPs possess suitable proton binding energies and simultaneously act as acceptors for photogenerated electrons.

We have previously illustrated in Sects. 4.2.2 and 4.2.3 how NW heterostructures can be made through the creation of core/shell morphologies as well as through the decoration of NWs with metal nanoparticles. Such NW-based heterostructures can, in turn, be used for photocatalytic hydrogen generation studies. Specific systems that have been investigated therefore include CdSe, CdSe/CdS core/shell, CdSe/Au NP, CdSe/Pt NP, CdSe/CdS/Au NP and CdSe/CdS/Pt NP NW photocatalysts. In all cases, UV-visible illumination of these photocatalysts in

aqueous solution and in the presence of sulfite/sulfide leads to hydrogen generation. Corresponding H_2 generation efficiencies have been quantified to better rationalize the role these semiconductor/semiconductor and metal/semiconductor heterojunctions play in dictating NW photocatalyst efficiencies.

Gas phase chromatography sampling of H_2 generation measurements generally reveal that CdSe NWs alone exhibit low H_2 generation efficiencies. Creating core/shell structures or decorating these NWs with metal nanoparticles, however, dramatically improves their H_2 generation efficiencies. Figure 4.23 shows specific results obtained from Pt NP decorated CdSe NW photocatalysts. Table 4.1 provides a fuller summary of observed hydrogen generation efficiencies across different CdSe NW systems.

Qualitatively, CdSe NWs show low H_2 generation efficiencies because of unwanted charge recombination processes in these wires. Table 4.1 shows that all other systems with semiconductor/semiconductor and metal/semiconductor junctions exhibit improved efficiencies. This indicates the importance of suppressing fast non-radiative processes in CdSe NWs or finding way to extract charges on timescales competitive with these events. Consequently, CdSe/CdS core/shell systems likely show enhancements due to improved carrier lifetimes stemming from the passivation of CdSe NW surface defects while metal NP decorated counterparts exhibit enhancements because of improved charge separation efficiencies.

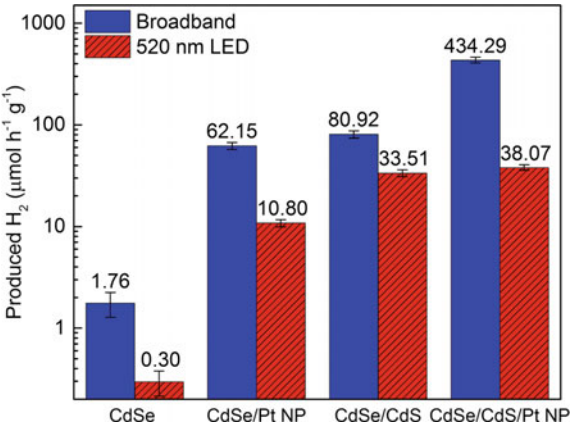

Fig. 4.23 Hydrogen generation efficiencies of CdSe NW-based photocatalysts [11]. Reproduced by permission of The Royal Society of Chemistry

Table 4.1 Summary of hydrogen generation efficiencies of CdSe NW-based photocatalysts under broadband and 520 nm illumination

NW system	Broadband illumination (μmol/h/g)	520 nm illumination (μmol/h/g)
CdSe	1.76, 1.98	0.30
CdSe/AuNP	2.61	
CdSe/CdS/Au NP	38.05	
CdSe/Pt NP	62.15	10.80
CdSe/CdS	58.06, 80.92	33.51
CdSe/CdS/Pt NP	434.29	38.07

To develop a more quantitative understanding of the results in Table 4.1 and why double heterojunction CdSe/CdS/Pt NP NWs show the largest H_2 generation efficiencies, transient differential absorption (TDA) experiments were conducted on each system. The technique enables one to follow the fate of photoexcited carriers in NWs following photoexcitation. In this regard, TDA spectroscopy is an important tool for probing the photophysics of semiconductor nanostructures because it allows one to spectroscopically follow the kinetics of excited carriers. For II–VI materials such as CdS and CdSe, observed TDA bleaches reflect the population of excited conduction band electrons given their relatively small effective mass [73]. Thus, by monitoring the temporal evolution of TDA bleaches, electron transfer reactions in II–VI nanostructures as well as their kinetics can be studied.

In what follows, only CdSe, CdSe/CdS and their Pt NP decorated counterparts are discussed. This is because the relatively poor performance of Au NP decorated systems ultimately stems from the slow electron discharge kinetics of Au, which inhibits reduction processes [74, 75]. Figure 4.24a first shows linear absorption spectra of CdSe, CdSe/CdS and CdSe/CdS/Pt NP NWs. Next the bottom of Fig. 4.24a shows experimental transient absorption bleaches observed after

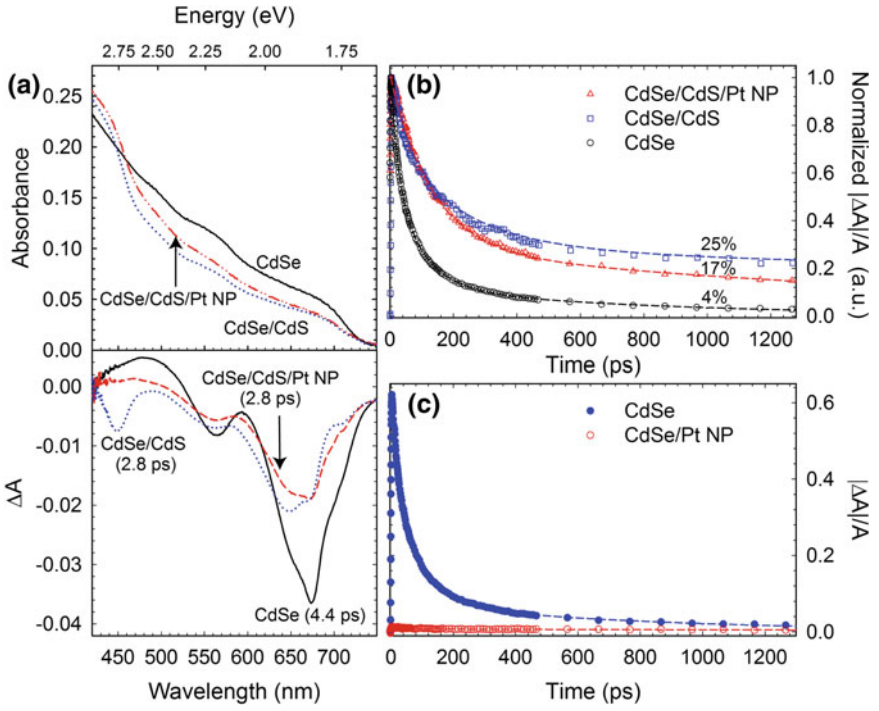

Fig. 4.24 **a** Linear absorption (*top panel*) and TDA (*bottom panel*) spectra of CdSe, CdSe/CdS and CdSe/CdS/Pt NP NWs. **b** Band edge bleach kinetics of CdSe, CdSe/CdS and CdSe/CdS/Pt NP NWs when excited at 387 nm. **c** Band edge bleach kinetics of CdSe and CdSe/Pt NP NWs when excited at 387 nm [11]. Reproduced by permission of The Royal Society of Chemistry

photoexciting each system. Negative going bleaches are seen at energies corresponding to features in the linear absorption and reflect the carrier population of different bands in the system. From the growth and decay kinetics of these bleaches, especially CdSe's band edge bleach at ~683 nm the kinetics of various electron transfer processes can subsequently be extracted.

In the case of CdSe NWs, Fig. 4.24b shows that their band edge bleach recovery occurs quickly within ~200 ps. This indicates that most of the photogenerated electrons in CdSe NWs recombine quickly in a non-radiative fashion due to the presence of defects on or within the wires. At 1 ns, only 4–8 % of the initially generated electrons remain wherein these long-lived species are most likely responsible for H_2 generation.

In the case of CdSe/CdS core/shell NWs, electron lifetimes noticeably increase due to the passivation of surface defects by the CdS shell. This has been observed directly in TDA measurements through increases in the remaining charge fraction at 1 ns when only the core of core/shell NWs has been excited [10, 11]. At 1 ns, between 25 and 33 % of the initially generated electrons remain available for chemical reduction, rationalizing why core/shell wires possess better H_2 generation efficiencies than their core only counterparts (Table 4.1).

In tandem, the Type-I heterojunction between the CdSe core and the CdS shell means that photogenerated electrons created in the shell also add to those in the core [10]. In the TDA measurement, this has been directly observed as a decrease of the CdS bleach at 450 nm accompanied by a growth of the CdSe bleach at 683 nm.

An interesting conclusion from these TDA measurements is that H_2 generation in CdSe/CdS core/shell NWs occurs not on the CdS shell but rather predominantly on the CdSe core [10]. This is because long-lived photogenerated electrons, responsible for the reduction, are seen to accumulate in the CdSe core. These H_2 generation results thus highlight the porosity of the CdS shell in CdSe/CdS NWs [10].

Next, in the case of Pt NP decorated systems, TDA measurements show ultrafast electron transfer into Pt. This can be seen in Fig. 4.24c where TDA kinetics of the CdSe band edge bleach show that the addition of Pt NPs causes an immediate (<1 ps) recovery of the band edge bleach. This ultrafast charge transfer, in turn, improves CdSe/Pt NP NW H_2 generation efficiencies since a larger fraction of CdSe's photogenerated electrons are transferred to Pt which possesses favorable proton binding affinities and electron discharge kinetics [74, 75], ultimately resulting in efficient H_2 generation.

Finally, in the case of Pt NP decorated CdSe/CdS NWs, the CdS shell passivates surface defects of the core. The CdS shell also contributes electrons to CdSe when excited. At the same time, the CdS shell contributes electrons to its surface adsorbed Pt NPs. Consequently, TDA measurements suggest a buildup of electrons in the CdSe core as well as in surface adsorbed Pt NPs when CdSe/CdS/Pt NP NWs are excited. This suggests that H_2 generation occurs in two places within this double heterojunction system—at the surface of the CdSe core and at the surface of the Pt NPs. The large H_2 generation efficiencies of this system (Table 4.1) can thus be rationalized as stemming from the combined effects of (i) the efficient surface passivation of CdSe NWs, which increases carrier lifetimes, (ii) the contribution of

additional electrons to the CdSe core from the CdS shell, which increases overall carrier densities, (iii) the efficient transfer of electrons from the CdS shell to surface adsorbed Pt NPs and (iv) the optimal proton binding affinities and electron discharge kinetics of Pt, which enable efficient proton reduction.

4.4 Conclusions and Outlook

In this chapter, we have discussed the synthesis of high quality semiconductor NWs using SLS growth. The method allows highly crystalline NWs to be grown at low temperatures. It also enables the growth of wires with tunable compositions, straight and branched morphologies and, more interestingly, the growth of wires within the confinement regime of a number of important systems. Various NW heterostructures can subsequently be fabricated using SLS-derived wires. This includes heterostructures exhibiting semiconductor/semiconductor and semiconductor/metal heterojunctions. Resulting NW architectures exhibit enhanced properties such as extended carrier lifetimes, improved emission quantum yields and enhanced charge separation efficiencies. The extent to which SLS NWs can be tuned, engineered, and assembled thus demonstrates their potential use within a broad range of applications. As illustrations, several examples, within the context of NW solar cells and photocatalysts, have been described.

Despite this great promise, however, challenges remain towards eventually implementing SLS-derived wires into commercial devices. This includes: (i) demonstrating scalable syntheses, (ii) developing a better understanding of NW surface defects so that their impact can be controlled and/or mitigated, (iii) developing high emission quantum yield NWs, (iv) improving the control of interfaces in heterostructured NWs, and (v) realizing the scalable, macroscopic assembly of these wires. Consequently, continued research and development on various fronts is needed, which portends exciting future developments for SLS NWs yet to come.

Acknowledgments PT thanks the Royal Thai Government Scholarship for financial support. MZ thanks the Notre Dame Innovation Postdoc Fund and ND Energy for financial support. MK thanks the NSF (CHE1208091) for financial support. We thank Rusha Chatterjee for assistance in editing this chapter.

References

1. R. Zhou, H.-C. Chang, V. Protasenko, M. Kuno, A.K. Singh, D. Jena, H.G. Xing, CdSe nanowires with illumination-enhanced conductivity: induced dipoles, dielectrophoretic assembly, and field-sensitive emission. J. Appl. Phys. **101**, 073704 (2007)
2. N. Petchsang, M.P. McDonald, L.E. Sinks, M. Kuno, Light induced nanowire assembly: the electrostatic alignment of semiconductor nanowires into functional macroscopic yarns. Adv. Mater. **25**, 601–605 (2013)

3. M. Zhukovskyi, L. Sanchez-Botero, M.P. McDonald, J. Hinestroza, M. Kuno, Nanowire-functionalized cotton textiles. ACS Appl. Mater. Interfaces **6**, 2262–2269 (2014)
4. A. Singh, X. Li, V. Protasenko, G. Galantai, M. Kuno, H.G. Xing, D. Jena, Polarization-sensitive nanowire photodetectors based on solution-synthesized CdSe quantum-wire solids. Nano Lett. **7**, 2999–3006 (2007)
5. H. Choi, M. Kuno, G.V. Hartland, P.V. Kamat, CdSe nanowire solar cells using carbazole as a surface modifier. J. Mater. Chem. A **1**, 5487–5491 (2013)
6. Z. Feng, Q. Zhang, L. Lin, H. Guo, J. Zhou, Z. Lin, ⟨0001⟩-Preferential growth of CdSe nanowires on conducting glass: template-free electrodeposition and application in photovoltaics. Chem. Mater. **22**, 2705–2710 (2010)
7. H. Choi, P.V. Kamat, CdS nanowire solar cells: dual role of squaraine dye as a sensitizer and a hole transporter. J. Phys. Chem. Lett. **4**, 3983–3991 (2013)
8. Y. Yu, P.V. Kamat, M. Kuno, A CdSe nanowire/quantum dot hybrid architecture for improving solar cell performance. Adv. Funct. Mater. **20**, 1464–1472 (2010)
9. H. Choi, J.G. Radich, P.V. Kamat, Sequentially layered CdSe/CdS nanowire architecture for improved nanowire solar cell performance. J. Phys. Chem. C **118**, 206–213 (2014)
10. P. Tongying, V.V. Plashnitsa, N. Petchsang, F. Vietmeyer, G.J. Ferraudi, G. Krylova, M. Kuno, Photocatalytic hydrogen generation efficiencies in one-dimensional CdSe heterostructures. J. Phys. Chem. Lett. **3**, 3234–3240 (2012)
11. P. Tongying, F. Vietmeyer, D. Aleksiuk, G.J. Ferraudi, G. Krylova, M. Kuno, Double heterojunction nanowire photocatalysts for hydrogen generation. Nanoscale **6**, 4117–4124 (2014)
12. Y. Yang, J. Li, H. Wu, E. Oh, D. Yu, Controlled ambipolar doping and gate voltage dependent carrier diffusion length in lead sulfide nanowires. Nano Lett. **12**, 5890–5896 (2012)
13. W. Liang, O. Rabin, A.I. Hochbaum, M. Fardy, M. Zhang, P. Yang, Thermoelectric properties of p-type PbSe nanowires. Nano Res. **2**, 394–399 (2009)
14. M. Fardy, A.I. Hochbaum, J. Goldberger, M.M. Zhang, P. Yang, Synthesis and thermoelectrical characterization of lead chalcogenide nanowires. Adv. Mater. **19**, 3047–3051 (2007)
15. R. Graham, C. Miller, E. Oh, D. Yu, Electric field dependent photocurrent decay length in single lead sulfide nanowire field effect transistors. Nano Lett. **11**, 717–722 (2011)
16. S.Y. Jang, Y.M. Song, H.S. Kim, Y.J. Cho, Y.S. Seo, G.B. Jung, C.-W. Lee, J. Park, M. Jung, J. Kim, B. Kim, J.-G. Kim, Y.-J. Kim, Three synthetic routes to single-crystalline PbS nanowires with controlled growth direction and their electrical transport properties. ACS Nano **4**, 2391–2401 (2010)
17. Y. Yang, X. Peng, D. Yu, High intensity induced photocurrent polarity switching in lead sulfide nanowire field effect transistors. Nanotechnology **25**, 195202 (2014)
18. R.S. Wagner, W.C. Ellis, Vapor-liquid-solid mechanism of single crystal growth. Appl. Phys. Lett. **4**, 89–90 (1964)
19. R.L. Penn, J.F. Banfield, Imperfect oriented attachment: dislocation generation in defect-free nanocrystals. Science **281**, 969–971 (1998)
20. J.D. Holmes, K.P. Johnston, R.C. Doty, B.A. Kogel, Control of thickness and orientation of solution-grown silicon nanowires. Science **287**, 1471–1473 (2000)
21. T.J. Trentler, K.M. Hickman, S.C. Goel, A.M. Viano, P.C. Gibbons, W.E. Buhro, Solution-liquid-solid growth of crystalline III-V semiconductors: an analogy to vapor-liquid-solid growth. Science **270**, 1791–1794 (1995)
22. H. Yu, P.C. Gibbons, K.F. Kelton, W.E. Buhro, Heterogeneous seeded growth: a potentially general synthesis of monodisperse metallic nanoparticles. J. Am. Chem. Soc. **123**, 9198–9199 (2001)
23. F. Wang, R. Tang, H. Yu, P.C. Gibbons, W.E. Buhro, Size- and shape-controlled synthesis of bismuth nanoparticles. Chem. Mater. **20**, 3656–3662 (2008)
24. H. Yu, J. Li, R.A. Loomis, L.-W. Wang, W.E. Buhro, Two- versus three-dimensional quantum confinement in indium phosphide wires and dots. Nat. Mater. **2**, 517–520 (2003)

25. H. Yu, W.E. Buhro, Solution–liquid–solid growth of soluble GaAs nanowires. Adv. Mater. **15**, 416–419 (2003)
26. H. Yu, J. Li, R.A. Loomis, P.C. Gibbons, L.-W. Wang, W.E. Buhro, Cadmium selenide quantum wires and the transition from 3D to 2D confinement. J. Am. Chem. Soc. **125**, 16168–16169 (2003)
27. J.W. Grebinski, K.L. Richter, J. Zhang, T.H. Kosel, M. Kuno, Synthesis and characterization of Au/Bi core/shell nanocrystals: a precursor toward II–VI nanowires. J. Phys. Chem. B **108**, 9745–9751 (2004)
28. D.D. Fanfair, B.A. Korgel, Bismuth nanocrystal-seeded III-V semiconductor nanowire synthesis. Cryst. Growth Des. **5**, 1971–1976 (2005)
29. Z. Li, A. Kornowski, A. Myalitsin, A. Mews, Formation and function of bismuth nanocatalysts for the solution–liquid–solid synthesis of CdSe nanowires. Small **4**, 1698–1702 (2008)
30. J. Puthussery, T.H. Kosel, M. Kuno, Facile synthesis and size control of II-VI nanowires using bismuth salts. Small **5**, 1112–1116 (2009)
31. J.W. Grebinski, K.L. Hull, J. Zhang, T.H. Kosel, M. Kuno, Solution-based straight and branched CdSe nanowires. Chem. Mater. **16**, 5260–5272 (2004)
32. M. Kuno, O. Ahmad, V. Protasenko, D. Bacinello, T.H. Kosel, Solution-based straight and branched CdTe nanowires. Chem. Mater. **18**, 5722–5732 (2006)
33. Z. Li, Ö. Kurtulus, N. Fu, Z. Wang, A. Kornowski, U. Pietsch, A. Mews, Controlled synthesis of CdSe nanowires by solution–liquid–solid method. Adv. Funct. Mater. **19**, 3650–3661 (2009)
34. F. Wang, A. Dong, J. Sun, R. Tang, H. Yu, W.E. Buhro, Solution–liquid–solid growth of semiconductor nanowires. Inorg. Chem. **45**, 7511–7521 (2006)
35. A. Dong, F. Wang, T.L. Daulton, W.E. Buhro, Solution–liquid–solid (SLS) growth of ZnSe–ZnTe quantum wires having axial heterojunctions. Nano Lett. **7**, 1308–1313 (2007)
36. D.D. Fanfair, B.A. Korgel, Twin-related branching of solution-grown ZnSe nanowires. Chem. Mater. **19**, 4943–4948 (2007)
37. N. Petchsang, L. Shapoval, F. Vietmeyer, Y. Yu, J.H. Hodak, I.M. Tang, T.H. Kosel, M. Kuno, Low temperature solution-phase growth of ZnSe and ZnSe/CdSe core/shell nanowires. Nanoscale **3**, 3145–3151 (2011)
38. M.L. Steigerwald, C.R. Sprinkle, Application of phosphine tellurides to the preparation of Group II-VI (2–16) semiconductor materials. Organometallics **7**, 245–246 (1988)
39. C.B. Murray, D.J. Norris, M.G. Bawendi, Synthesis and characterization of nearly monodisperse CdE (E = S, Se, Te) semiconductor nanocrystallites. J. Am. Chem. Soc. **115**, 8706–8715 (1993)
40. M. Kuno, An overview of solution-based semiconductor nanowires: synthesis and optical studies. Phys. Chem. Chem. Phys. **10**, 620–639 (2008)
41. M. Koguchi, H. Kakibayashi, M. Yazawa, K. Hiruma, T. Katsuyama, Crystal structure change of GaAs and InAs whiskers from zinc-blende to wurtzite type. Jpn. J. Appl. Phys. **31**, 2061–2065 (1992)
42. Q. Li, X. Gong, C. Wang, J. Wang, K. Ip, S. Hark, Size-dependent periodically twinned ZnSe nanowires. Adv. Mater. **16**, 1436–1440 (2004)
43. K.L. Hull, J.W. Grebinski, T.H. Kosel, M. Kuno, Induced branching in confined PbSe nanowires. Chem. Mater. **17**, 4416–4425 (2005)
44. K.-T. Yong, Y. Sahoo, K.R. Choudhury, M.T. Swihart, J.R. Minter, P.N. Prasad, Control of the morphology and size of PbS nanowires using gold nanoparticles. Chem. Mater. **18**, 5965–5972 (2006)
45. J. Sun, W.E. Buhro, The use of single-source precursors for the solution–liquid–solid growth of metal sulfide semiconductor nanowires. Angew. Chem. Int. Ed. **47**, 3215–3218 (2008)
46. A.C. Onicha, N. Petchsang, T.H. Kosel, M. Kuno, Controlled synthesis of compositionally tunable ternary $PbSe_xS_{1-x}$ as well as binary PbSe and PbS nanowires. ACS Nano **6**, 2833–2843 (2012)

47. J.K. Hyun, S. Zhang, L.J. Lauhon, Nanowire heterostructures. Annu. Rev. Mater. Res. **43**, 451–479 (2013)
48. Z. Li, X. Ma, Q. Sun, Z. Wang, J. Liu, Z. Zhu, S.Z. Qiao, S.C. Smith, G.M. Lu, A. Mews, Synthesis and characterization of colloidal core–shell semiconductor nanowires. Eur. J. Inorg. Chem. **27**, 4325–4331 (2010)
49. J.A. Goebl, R.W. Black, J. Puthussery, J. Giblin, T.H. Kosel, M. Kuno, Solution-based II–VI core/shell nanowire heterostructures. J. Am. Chem. Soc. **130**, 14822–14833 (2008)
50. S. Schäfer, A. Reich, Z. Wang, T. Kipp, A. Mews, Charge separation in CdSe/CdTe hetero-nanowires measured by electrostatic force microscopy. Appl. Phys. Lett. **100**, 022110 (2012)
51. S. Kim, B. Fisher, H.-J. Eisler, M. Bawendi, Type-II quantum dots: CdTe/CdSe(core/shell) and CdSe/ZnTe(core/shell) heterostructures. J. Am. Chem. Soc. **125**, 11466–11467 (2003)
52. X. Peng, M.C. Schlamp, A.V. Kadavanich, A.P. Alivisatos, Epitaxial growth of highly luminescent CdSe/CdS core/shell nanocrystals with photostability and electronic accessibility. J. Am. Chem. Soc. **119**, 7019–7029 (1997)
53. M.A. Hines, P. Guyot-Sionnest, Synthesis and characterization of strongly luminescing ZnS-capped CdSe nanocrystals. J. Phys. Chem. **100**, 468–471 (1996)
54. B.O. Dabbousi, J. Rodriguez-Viejo, F.V. Mikulec, J.R. Heine, H. Mattoussi, R. Ober, K.F. Jensen, M.G. Bawendi, (CdSe)ZnS core–shell quantum dots: synthesis and characterization of a size series of highly luminescent nanocrystallites. J. Phys. Chem. B **101**, 9463–9475 (1997)
55. R. Costi, A.E. Saunders, U. Banin, Colloidal hybrid nanostructures: a new type of functional materials. Angew. Chem. Int. Ed. **49**, 4878–4897 (2010)
56. A. Vaneski, A.S. Susha, J. Rodríguez-Fernández, M. Berr, F. Jäckel, J. Feldmann, A.L. Rogach, Hybrid colloidal heterostructures of anisotropic semiconductor nanocrystals decorated with noble metals: synthesis and function. Adv. Funct. Mater. **21**, 1547–1556 (2011)
57. U. Banin, Y. Ben-Shahar, K. Vinokurov, Hybrid semiconductor–metal nanoparticles: from architecture to function. Chem. Mater. **26**, 97–110 (2014)
58. P. Guo, J. Xu, X. Zhuang, W. Hu, X. Zhu, H. Zhou, L. Tang, A. Pan, Surface plasmon resonance enhanced band-edge emission of CdS–SiO_2 core–shell nanowires with gold nanoparticles attached. J. Mater. Chem. C **1**, 566–571 (2013)
59. X. Peng, J. Wickham, A.P. Alivisatos, Kinetics of II–VI and III–V colloidal semiconductor nanocrystal growth: "focusing" of size distributions. J. Am. Chem. Soc. **120**, 5343–5344 (1998)
60. D.V. Talapin, A.L. Rogach, M. Haase, H. Weller, Evolution of an ensemble of nanoparticles in a colloidal solution: theoretical study. J. Phys. Chem. B **105**, 12278–12285 (2001)
61. D.V. Talapin, H. Yu, E.V. Shevchenko, A. Lobo, C.B. Murray, Synthesis of colloidal PbSe/PbS core–shell nanowires and PbS/Au nanowire–nanocrystal heterostructures. J. Phys. Chem. C **111**, 14049–14054 (2007)
62. I. Jen-La Plante, S.E. Habas, B.D. Yuhas, D.J. Gargas, T. Mokari, Interfacing metal nanoparticles with semiconductor nanowires. Chem. Mater. **21**, 3662–3667 (2009)
63. G. Menagen, J.E. Macdonald, Y. Shemesh, I. Popov, U. Banin, Au growth on semiconductor nanorods: photoinduced versus thermal growth mechanisms. J. Am. Chem. Soc. **131**, 17406–17411 (2009)
64. S.E. Habas, P. Yang, T. Mokari, Selective growth of metal and binary metal tips on CdS nanorods. J. Am. Chem. Soc. **130**, 3294–3295 (2008)
65. Y. Huang, X. Duan, Q. Wei, C.M. Lieber, Directed assembly of one-dimensional nanostructures into functional networks. Science **291**, 630–633 (2001)
66. A. Theron, E. Zussman, A.L. Yarin, Electrostatic field-assisted alignment of electrospun nanofibres. Nanotechnology **12**, 384–390 (2001)
67. A. Tao, F. Kim, C. Hess, J. Goldberger, R. He, Y. Sun, Y. Xia, P. Yang, Langmuir–Blodgett silver nanowire monolayers for molecular sensing using surface-enhanced Raman spectroscopy. Nano Lett. **3**, 1229–1233 (2003)
68. S. Schäfer, Z. Wang, R. Zierold, T. Kipp, A. Mews, Laser-induced charge separation in CdSe nanowires. Nano Lett. **11**, 2672–2677 (2011)

69. J. Giblin, M. Syed, M.T. Banning, M. Kuno, G. Hartland, Experimental determination of single CdSe nanowire absorption cross sections through photothermal imaging. ACS Nano **4**, 358–364 (2010)
70. V. Protasenko, D. Bacinello, M. Kuno, Experimental determination of the absorption cross-section and molar extinction coefficient of CdSe and CdTe nanowires. J. Phys. Chem. B **110**, 25322–25331 (2006)
71. J. Giblin, M. Kuno, Nanostructure absorption: a comparative study of nanowire and colloidal quantum dot absorption cross sections. J. Phys. Chem. Lett. **1**, 3340–3348 (2010)
72. I. Gur, N.A. Fromer, M.L. Geier, A.P. Alivisatos, Air-stable all-inorganic nanocrystal solar cells processed from solution. Science **310**, 462–465 (2005)
73. V.I. Klimov, Optical nonlinearities and ultrafast carrier dynamics in semiconductor nanocrystals. J. Phys. Chem. B **104**, 6112–6123 (2000)
74. A. Wood, M. Giersig, P. Mulvaney, Fermi level equilibration in quantum dot–metal nanojunctions. J. Phys. Chem. B **105**, 8810–8815 (2001)
75. J.U. Bang, S.J. Lee, J.S. Jang, W. Choi, H. Song, Geometric effect of single or double metal-tipped CdSe nanorods on photocatalytic H_2 generation. J. Phys. Chem. Lett. **3**, 3781–3785 (2012)

Chapter 5
Rare Earth Based Anisotropic Nanomaterials: Synthesis, Assembly, and Applications

Chun-Hua Yan, Ling-Dong Sun, Chao Zhang, Chun-Jiang Jia, Guang-Ming Lyu, Hao Dong, Xiao-Yu Zheng, Yan-Jie Wang, Shuo Shi, Pei-Zhi Zhang and Lin-Dong Li

Abstract Rare earths (RE) refer to the lanthanide elements La–Lu together with Sc and Y. Conventionally, they have found applications in phosphors, magnets, catalysts, fuel cell electrodes/electrolyte. Here in this chapter, we discuss the synthesis, assembly and applications of rare earth based anisotropic nanomaterials. Regarding synthesis, the anisotropic growth behaviors of these nanocrystals are predominantly governed by their own unique crystal structures. Yet for wet-chemistry synthetic methods where a number of parameters could be finely tuned, the addition of particular coordination agents, templating agents or mineralizers has proven to be an effective way to direct the growth of nanocrystals into some anisotropic structures. Regarding applications, anisotropic nanomaterials, compared to their isotropic counterparts, often exhibit distinct properties. For example, the luminescence of anisotropic nanomaterials can display polarization and site-specific features. As for rare earth nanomaterials as magnetic resonance imaging (MRI) contrast agents, the high surface area of anisotropic nanostructures can give rise to superior performances. And for catalysis applications, anisotropic nanomaterials expose rich, highly active facets, which is of great importance for facet-selective catalytic reactions. In the chapter, we will start with introduction of the crystal structures of rare earth compounds, then briefly summarize the synthesis and assembly of rare earth anisotropic nanomaterials, and discuss their properties and applications in three realms, namely, luminescence, magnetism and catalysis.

C.-H. Yan (✉) · L.-D. Sun · C. Zhang · G.-M. Lyu · H. Dong · X.-Y. Zheng · Y.-J. Wang
S. Shi · P.-Z. Zhang · L.-D. Li
Beijing National Laboratory for Molecular Sciences, State Key Laboratory of Rare Earth Materials Chemistry and Applications, PKU-HKU Joint Laboratory in Rare Earth Materials and Bioinorganic Chemistry, College of Chemistry of Molecular Engineering, Peking University, Beijing, China
e-mail: yan@pku.edu.cn

C.-J. Jia
School of Chemistry and Chemical Engineering, Shandong University, Jinan, China

Q. Li (ed.), *Anisotropic Nanomaterials*, NanoScience and Technology,
DOI 10.1007/978-3-319-18293-3_5

5.1 Crystal Structures of Rare Earth Compounds

5.1.1 Rare Earth Oxides

As rare earth elements show strong affinity to oxygen, they can be easily synthesized in the air, and rare earth oxides enjoy the most investigation among its solid compounds. Rare earth oxides mostly take the form of sesquioxides (RE_2O_3) due to their trivalency, while some elements can also exist as divalent or tetravalent ions in their oxides, thus forming monoxides, dioxides or mixed valence oxides with a complex crystal structure [1]. Europium and ytterbium monoxides are the only two rare earth monoxides that are stable in solid form, and they are readily oxidized in the air. Praseodymium and terbium usually exist as both trivalent and tetravalent ions in their oxides, thus forming mixed valence oxides with non-stoichiometric formulas of Pr_6O_{11} and Tb_4O_7, respectively. Cerium exists exclusively as tetravalent ions in its most stable oxide, CeO_2 [2].

Rare earth sesquioxides are the most common category of rare earth oxides. Depending on their cationic radii, rare earth sesquioxides can be most stable in hexagonal phase (A phase), monoclinic phase (B phase) or body-centered cubic phase (C phase) under ambient conditions (as shown in Fig. 5.1). In both hexagonal (A phase) and monoclinic (B phase) sesquioxides, a rare earth cation is coordinated by seven oxygen ions, with six oxygen ions forming an octahedron around the cation. In hexagonal sesquioxides, the last oxygen ion rests on one of the octahedron's faces, while in monoclinic sesquioxides, the last oxygen ion locates exceptionally far from the cation. Light rare earth sesquioxides such as La_2O_3, Ce_2O_3, Pr_2O_3 and Nd_2O_3 usually exist in hexagonal phase due their large cationic radii, while Sm_2O_3 usually takes monoclinic phase due to its smaller cationic radius. In body-centered cubic (C phase) sesquioxides, a rare earth cation is coordinated by six oxygen ions, resembling a cubic fluoride structure with two anions removed. The cation occupies two different kinds of vacancies formed by differently removed surrounding anions. Y_2O_3 and all lanthanide oxides heavier than Sm_2O_3 (Eu_2O_3 to Lu_2O_3) exist in C phase.

EuO and YbO have a cubic halite structure and the space group *Fm3m* with the cation coordinated by six oxygen ions. The monoxides can also be mixed with the corresponding sesquioxides in 1:1 ratio to form the mixed valence oxides of Eu_3O_4 and Yb_3O_4, respectively.

As one of the most studied rare earth compound, CeO_2 is a notable exception to the sesquioxide norm. CeO_2 has a cubic fluorite structure and the space group *Fm3m*, with the cation coordinated by eight oxygen atoms. As the valence of cerium can alternate between Ce(III) and Ce(IV), Ce^{4+} in the lattice can be reduced to Ce^{3+} under reductive conditions, accompanied by the generation of oxygen vacancies that serve as highly active catalytic sites and oxygen storage centers. Despite the formation of Ce^{3+}, CeO_2 can maintain its cubic fluorite structure under intense reduction. This excellent chemical stability combined with its thermal stability makes it a versatile catalyst and oxygen sensor under rigorous conditions [3].

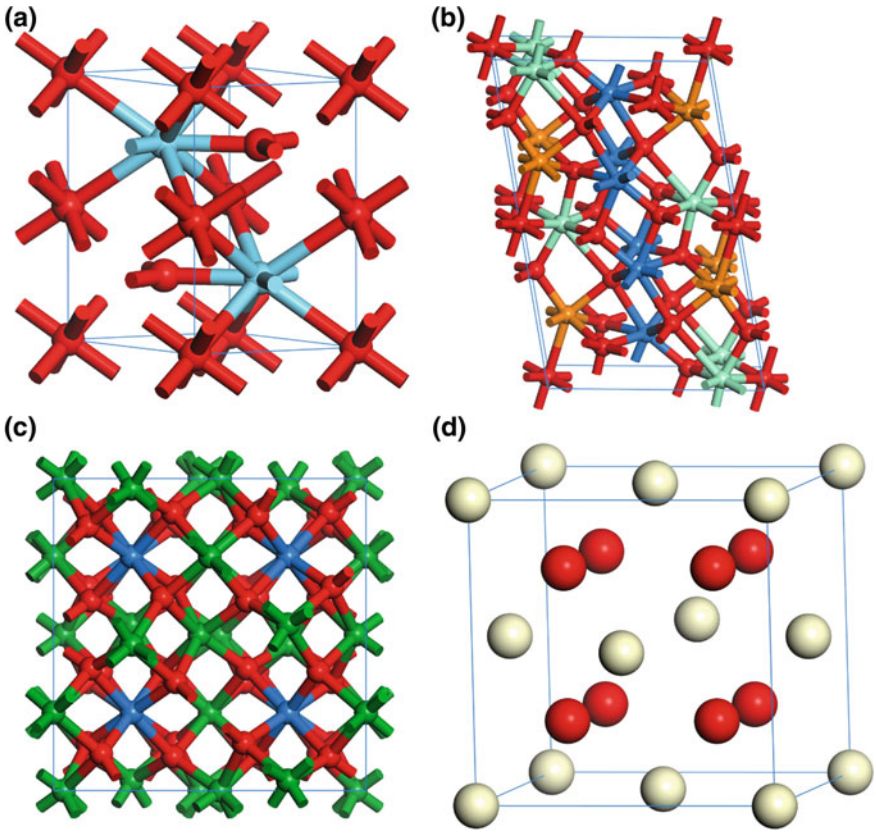

Fig. 5.1 Crystal structures of rare earth oxides. **a** Hexagonal sesquioxide. *Blue spheres* denote RE^{3+}; *red sphere* O^{2-}. **b** Monoclinic sesquioxide. *Blue*, *green* and *orange spheres* denote RE^{3+} in three different coordination environments; *red spheres* O^{2-}. **c** Cubic sesquioxide unit cell projected along the *c* axis. *Blue* and *red spheres* denote RE^{3+} in two different coordination environments; *red spheres* O^{2-}. **d** Cubic fluorite CeO_2. *White spheres* denote Ce^{4+}; *red spheres* O^{2-}

PrO_2 and TbO_2 also possess a cubic fluorite structure similar to CeO_2. The sesquioxides of praseodymium and terbium adopt a body-centered cubic structure as described above, enabling them to mix with their cubic fluorite dioxides to form mixed valence oxides.

5.1.2 Rare Earth Fluorides

Binary rare earth fluoride REF_3 has two kinds of crystal structures: trigonal fluocerite structure and orthorhombic β-YF_3 structure. Trigonal REF_3 has a

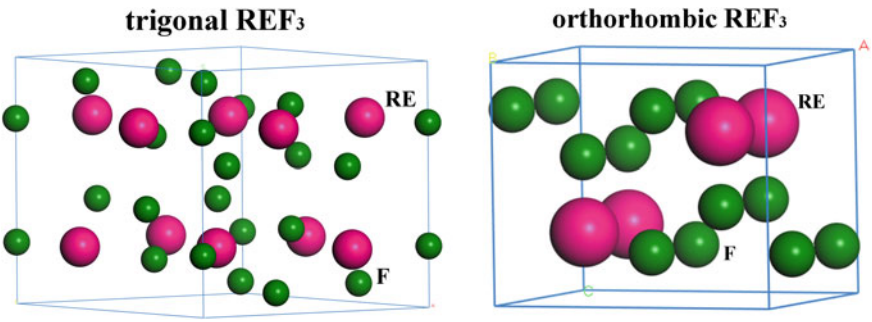

Fig. 5.2 Crystal structures of trigonal REF_3 and orthorhombic REF_3 (built by CERIUS2 software (http://www.accelrys.com/cerius2)

hexagonal phase with the space group of *P*-3*c1*. The rare earth cations lie on a twofold rotation axis. There are nine fluorine atoms near each rare earth atom. The distance of RE^{3+} and F^- ions is between 0.242 and 0.264 nm. There are two F^- ions far from the RE^{3+} ions with a distance of 0.301 nm. Rare earth atom is nine-coordinated via 9 fluorine atoms. Each F^- anion bonds with three RE^{3+} cations in a three-bridged configuration. β-YF_3 belongs to orthorhombic structure, *Pnma* space group. In this system, it is a three-dimensional (3D) network molecule with a F^- anion as a bridged atom. Each F^- anion bonds with three Y^{3+} as three bridges. There are nine F^- anions coordinated with Y^{3+}, eight of them close to the Y, while the other one is a little far. The nine F^- anions form a triangular prism coordination polyhedron (shown in Fig. 5.2).

REF_2 has a cubic fluorite structure, *Fm3m* space group. REF_2 can produce some complex fluorides. EuF_2 and CsF can form perovskite $CsEuF_3$. EuF_2 and MgF_2 can form orthogonal $SmMgF_4$ and $EuMgF_4$. EuF_2 and AlF_2 can form cubic solid solution (Eu, Al) $F_{2.00\text{-}2.44}$ and tetragonal system $EuAlF_5$. EuF_2 can form $EuZrF_6$, $EuSiF_6$, $EuThF_6$ with ZrF_4, SiF_4 and ThF_4 respectively.

5.1.3 Rare Earth Complex Fluorides

According to the coordination states of rare earths, the rare earth complex halide A_mREX_n (A = alkali and/or alkaline earth metal; RE = rare earth; X = halide) compounds can take the following forms: (1) $AREX_4$, a fourfold coordination of rare earth cations is accompanied by twofold or threefold coordination of the alkali and/or alkaline earth atom. (2) A_2REX_5, rare earth cations are in a fivefold coordination configuration, energetically more stable than a fourfold one. (3) A_3REX_6, the fivefold and sixfold coordination of rare earth cations are energetically competitive. For both A_2REX_5 and A_3REX_6, each coordination state can be realized in various forms that differ in detail but are close in energy.

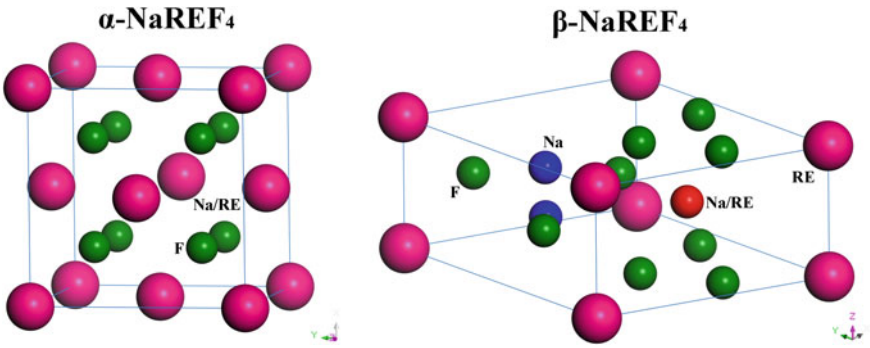

Fig. 5.3 Crystal structures of α-$NaREF_4$ and *β*-$NaREF_4$ built by CERIUS2 software (http://www.accelrys.com/cerius2)

Common structure types of the $AREF_4$ include tetragonal anti-scheelite ($LiYF_4$), hexagonal ($NaNdF_4$), trigonal ($KErF_4$), and orthorhombic ($KCeF_4$) type [4–6]. In addition, a high-temperature modality exists which has A^+ and RE^{3+} cations at the Ca^{2+} sites of cubic CaF_2 structure with statistical distribution.

As shown in Fig. 5.3, α-$NaREF_4$ has a cubic phase with the space group of *Fm3m*. *β*-$NaREF_4$ has a hexagonal phase (space group: *P*-6 *or* $P6_3/m$). In the cubic-phase α-$NaRF_4$, Na^+ and RE^{3+} cations are randomly distributed in the cationic sublattice. In the hexagonal-phase β-$NaREF_4$, the cation sites contain three types: a onefold site occupied by RE^{3+}, a onefold site occupied randomly by 1/2 Na^+ and 1/2 RE^{3+}, and a twofold site occupied randomly by Na^+ and vacancies [7].

5.1.4 Rare Earth Oxyhalides

Rare earth oxyhalides have two structures: tetragonal phase (*P4/nmm* space group) and trigonal phase (*R3m* space group), as shown in Fig. 5.4 [8, 9]. In the tetragonal phase, RE^{3+} cations occupy the position with C_{4v} symmetry. The tetragonal phase is thermodynamically less stable, and tends to form nonstoichiometric compounds with more complex structures. In the hexagonal phase, RE^{3+} cations occupy the position with C_{3v} symmetry. At high temperature, the hexagonal phase can transform into cubic structure.

5.1.5 Rare Earth Phosphates and Vanadates

For rare earth orthophosphates ($REVO_4$), there exist four different phases, mostly depending on the cationic radius of rare earth element: monazite, xenotime, rhabdophane, and churchite [10]. Rare earth orthovanadates ($REVO_4$) have two

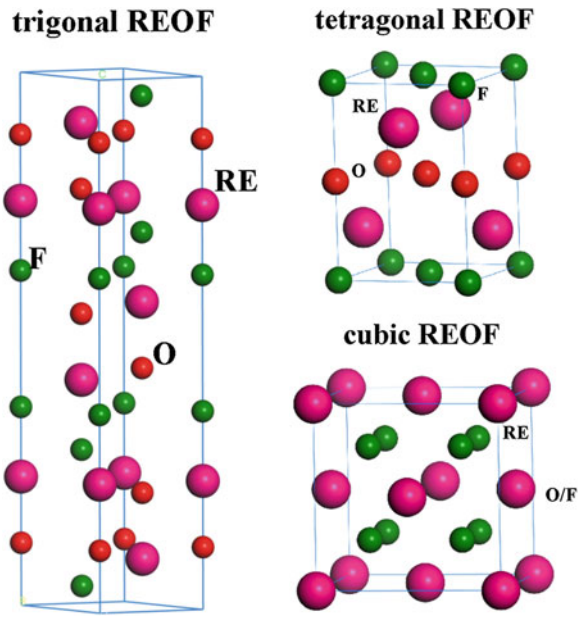

Fig. 5.4 Crystal structures of trigonal REOF, tetragonal REOF and cubic REOF built by CERIUS2 software (http://www.accelrys.com/cerius2)

isomorphic phase structures, namely, monoclinic (*m*-) monazite type, and tetragonal (*t*-) zircon type. The phase selectivity for $REVO_4$ relies on the radius of RE^{3+}, only zircon type is observed for all rare earth orthovanadates excluding $LaVO_4$ and $CeVO_4$ that can crystallize in both monoclinic and tetragonal phased structure [11, 12].

5.2 Synthesis, Assembly of Rare Earth Based Anisotropic Nanomaterials

5.2.1 One-Dimensional (1D) Nanostructures

One-dimensional (1D) nanostructures include nanorods, nanowires, and nanotubes. Many solid materials naturally grow into 1D nanostructures, the growth direction of which is usually dominated by the crystallographic symmetry [13–17]. However, rare earth oxides often have isotropic structures; for example, CeO_2 crystals has a face-centered cubic (fcc) structure (space group: *Fm3m*). Therefore, CeO_2 nanocrystals tend to present high-symmetry morphologies, such as cubes and octahedra. To obtain low-symmetry morphologies, templating or capping agents are generally needed to differentiate the surface energy of each facet and to direct anisotropic growth and the formation of 1D structures. Therefore, various templating methods have been established for preparing CeO_2 nanorods and nanowires. Porous anodic

alumina membranes (AAM) are commonly used in such synthesis as hard templates by virtue of their modulated pore diameters, ideally rod-shaped pores and exceptionally narrow size distribution [18–20]. CeO_2 nanowires were successfully synthesized with an improved sol–gel method within the hexagonally ordered nanochannels of the AAM. Ce^{3+} cations and corresponding anions reacted directly inside the nanochannels to form intermediates with 1D nanostructures. After post-treatment, the intermediates were transformed into the arrays of CeO_2 nanowires within the pores of AAM template [20].

CeO_2 nanorods can also be synthesized with solvothermal/hydrothermal methods [21–23], which generally feature controlled composition and morphology, low aggregation and high crystallinity, because of the diffusion-controlled growth in solvent media in a closed system. Yan's group prepared high-aspect-ratio ceria nanorods through a facile hydrothermal treatment without addition of any templates [24]. Using $Ce(NO_3)_3$ as the precursor, hexagonal $Ce(OH)_3$ intermediate was formed in the presence of OH^- anions (6 mol L^{-1}). After drying, white $Ce(OH)_3$ nanocrystals were converted into yellow $CeO_2 \cdot nH_2O$ in ambient atmosphere, without any change in their shape. Very recently, Yan's group have obtained lanthanide-doped CeO_2 nanowires through a modified hydrothermal route in the presence of NaOH and NaCl without any additional capping agents (as shown in Fig. 5.5) [25]. Such preparation process can be described with the following equations:

$$Ce^{3+}_{(aq)} + xLn^{3+}_{(aq)} + yOH^-_{(aq)} \rightarrow Ce(OH)_3{:}x\%Ln_{(s)} \tag{5.1}$$

$$Ce(OH)_3{:}x\%Ln_{(s)} + yO_{2(g)} \rightarrow CeO_2{:}x\%Ln_{(s)} + zH_2O \tag{5.2}$$

In this approach, Ce^{3+} precursor was dissolved in a high-concentration alkaline solution, forming one-dimensional $Ce(OH)_3$ intermediates with hexagonal structure. Upon calcination at 300 °C for 1 h, the nanowires transformed into CeO_2:Ln nanowires without prominent change in shape.

Zink's group reported a facile template-free hydrothermal method to obtain hierarchical architectures of CeO_2 nanorods in an acidic medium (as shown in Fig. 5.6) [26]. Na_3PO_4, as a mineralizer, plays a key role in controlling the morphology of CeO_2 nanostructures by adjusting the electrostatic potential and surface energy of CeO_2 nanorods. They investigated the mechanisms of nucleation and crystal growth process by varying the cerium precursors and concentration, concentration of phosphate, reaction temperature, pH of the reaction mixture, seeding and secondary treatment. Aspect ratios of these CeO_2 nanorods and nanowires can be precisely controlled and finely tuned from 4.1 to more than 100. The single-crystalline CeO_2 nanorods/nanowires grew along the [211] direction by an "oriented attachment" mechanism, followed by Ostwald ripening. Both phosphate and chloride ions were critical to the synthesis of one-dimensional CeO_2 nanorods and nanowires in both primary and secondary hydrothermal process. The strong coordination effect of phosphate with cerium ions was the driving force for the

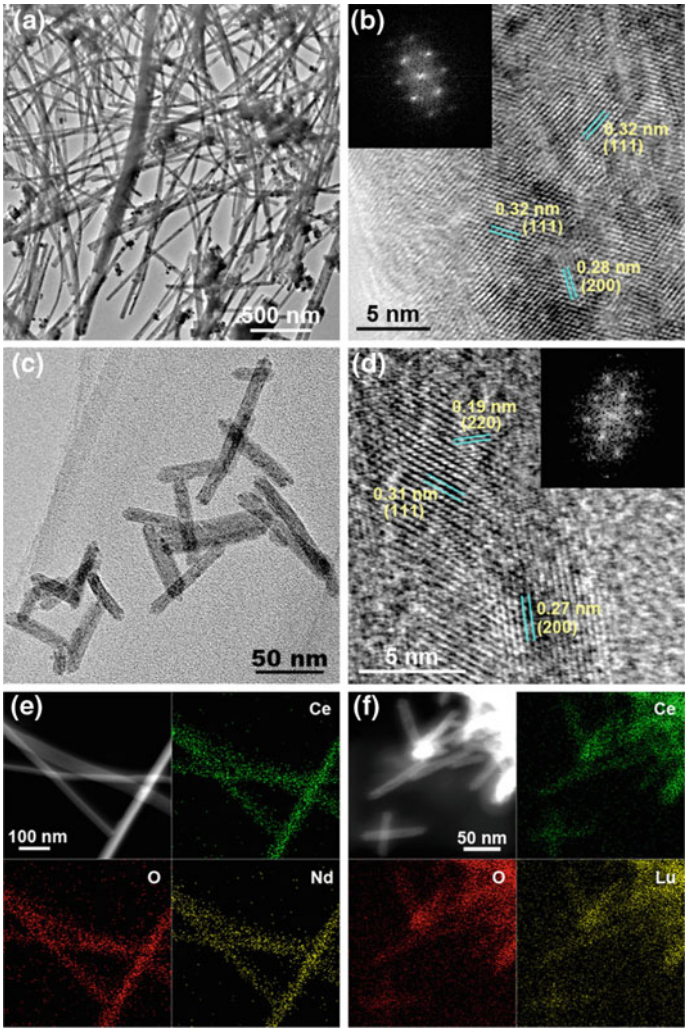

Fig. 5.5 TEM (**a**, **c**), HRTEM (**b**, **d**), and HAADF-STEM EDS elemental mapping (**e**, **f**) images of CeO_2:Nd (**a**, **b**, **e**) and CeO_2:Lu nanocrystals (**c**, **d**, **f**). (Reprinted with permission from [25]. Copyright 2013 American Chemical Society)

"dissolution" of nanorods under highly acidic condition. Chloride ions acted as a stabilizing agent in maintaining the rod/wire structure.

Rare earth oxide nanotubes have received extensive interests since the synthesis of carbon nanotubes in 1991 because they might offer unique properties and lead directly to original technological applications [27]. Han et al. first reported a facile method to synthesize CeO_{2-x} nanotubes by a hydrothermal route with mild reaction conditions [28]. By elevating the precipitation temperature and prolonging the

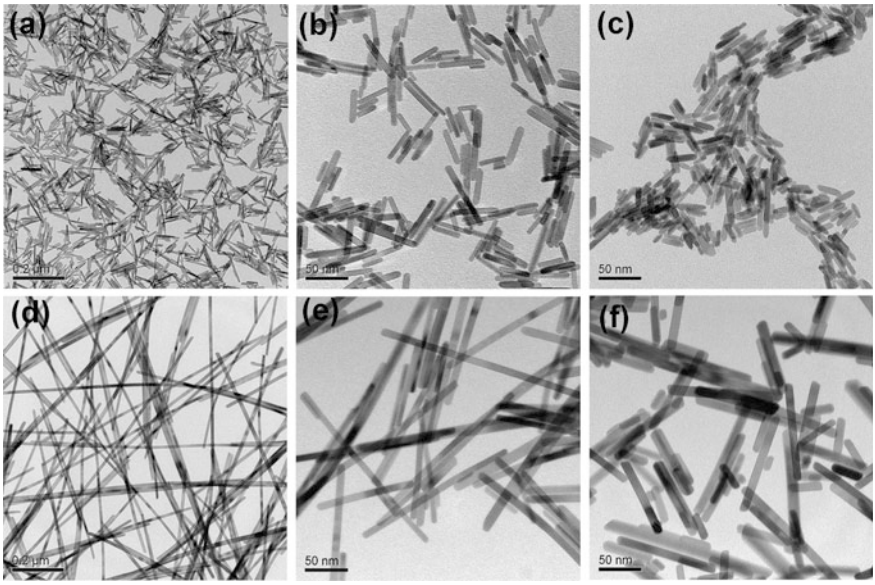

Fig. 5.6 TEM analyses of CeO_2 nanorods obtained from (**a**–**c**) primary and (**d**–**f**) secondary synthesis. (Reprinted with permission from [26]. Copyright 2012 American Chemical Society)

aging time, a large amount of nanotubes were formed. Nevertheless, this method had a few disadvantages, such as the time-consuming procedures, excessive by-products and difficulties for purification.

Yang's group developed an effective hydrothermal method to synthesize CeO_2 nanotubes with large cavities, thin walls and high quality [29]. A facile oxidation-coordination-assisted dissolution process of the hydroxide precursors was involved. First, $Ce(OH)_3$ nanowires were used as the starting materials; then the outer wall of $Ce(OH)_3$ nanostructures was partially oxidized by air. The oxidation-coordination-assisted dissolution process was limited inside the 1D nanomaterials. Finally, the ceria nanotubes with large cavities and thin walls were formed.

Chane-Ching et al. reported a general method for the synthesis of nanostructured materials with large surface area through the self-assembly of functionalized nanoparticles in a liquid-crystal phase [30]. Surface-functionalized ceria nanoparticles with the protonated amino acid interact directly with the ethylene oxide (CH_2CH_2O) groups of the copolymer. Based upon the weak interactions between the surfaces of the nanoparticles and the template, organized hexagonal arrays of CeO_2 nanoparticles are obtained and the symmetry of the arrays was preserved after calcination at 500 °C.

Seal et al. developed a very simple, green chemical route to guide self-assembly and time-dependent evolution of ceria nanoparticles into ultralong polycrystalline ceria nanorods [31]. By freezing and subsequent aging of an aqueous solution, CeO_2 nanoparticles trapped in voids (which form in ice) gradually evolve into

polycrystalline nanorods by localized oriented attachment process. MD simulations also predicted that the type of morphology evolution observed for the ceria nanostructures can be driven by the dimensional constraints.

Yan's group obtained four types of self-organized monolayer patterns (i.e., isolated particles, short chainlike (pseudo-1D aggregated), pearl necklace-like (1D aggregated), and dendritic (pseudo-2D aggregated) alignments during a PVP-assisted alcohothermal synthesis of ceria nanocrystals [32]. Possible self-organization mechanism of the nanosized CeO_2 colloids from isolated particle to 1D and 2D aggregated alignments were associated with the delicate balance of the attractive and repulsive forces caused by the adsorbed hydroxyls, PVP, and alkylammonium cations on the surfaces of CeO_2 nanocrystals during the irreversible evaporation of the solvent.

Using block copolymer Pluronic P123 as the template and ceric nitrate and zirconium oxide chloride as the precursors, highly ordered 2D hexagonal mesoporous $Ce_{1-x}Zr_xO_2$ solid solutions with a 2D hexagonal (p6mm) structure were synthesized via a novel direct and reproducible method as shown in Fig. 5.7 [33]. The overall synthesis strategy is based on a sol-gel process combined with evaporation-induced self-assembly in ethanol, without any extra reagents to adjust the pH of the sol-gel reaction. A series of mesoporous $Ce_{1-x}Zr_xO_2$ with different Ce/Zr ratios can be obtained under the optimized conditions, such as appropriate precursors, surfactants, and reaction temperature.

Nanosized rare earth fluorides and complex fluorides usually adopt plate-like morphologies due to their crystal structures, yet under certain conditions (for example, in the presence of shape-directing surfactants), 1D nanostructures can also be obtained. Chen et al. employed a precipitation method and prepared orthorhombic and hexagonal phase EuF_3 nanocrystals with various shapes, including nanospheres, nanobundles, nanorods, nanowires and nanoplates [34, 35]. Through a hydrothermal route, Li et al. obtained monodisperse LaF_3 and $NaLaF_4$ nanorods

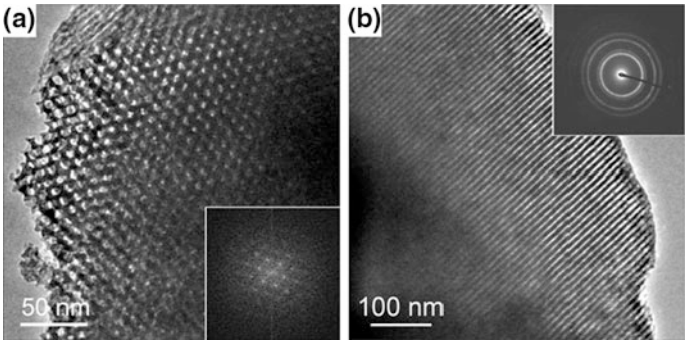

Fig. 5.7 TEM images of the mesoporous $Ce_{1-x}Zr_xO_2$ ($x > 0.5$) recorded along the **a** [001] and **b** [110] orientations. The *inset* in (**a**) is the corresponding FFT (fast Fourier transform) diffraction image, and the one in **b** is the corresponding SAED pattern. (Reprinted with permission from [33]. Copyright 2007 American Chemical Society)

with different aspect ratios [36]. They also developed a solvothermal method to prepare $NaYF_4$ nanocrystals by controlling the reactant concentration, temperature and duration, rod-like nanocrystals with good crystallinity and different sizes and aspect ratios were obtained [37–40]. Using YCl_3, NaF and EDTA as the starting materials, Qian et al. obtained spindle-like YF_3 with a hydrothermal method [41]. Interestingly, Zhao et al. discovered hexagonally ordered arrays of $NaYF_4$ nanotubes in a solvothermal reaction [42]. Yan's group developed a general thermolysis method to prepare rare earth fluorides and complex fluorides in high-boiling solvents (such as octadecene, oleic acid and oleylamine) using trifluoroacetate salts of rare earths and alkali metal; with proper ratio of Na to rare earth, hexagonal-phase $NaYF_4$ nanorods were obtained [43]. Using a similar approach, they obtained ultrathin EuOF nanowires with diameter below 2 nm [44]. The nanowires are highly flexible and can form ordered superstructures in a parallel configuration on substrates. A proper ratio of Eu precursor and surfactant oleic acid was found to be crucial for obtaining such wire-like structures.

For orthophosphates of light lanthanides (La–Gd), hexagonal rhabdophane and monazite phase rod-like or wire-like products could be obtained (as shown in Fig. 5.8) [45, 46]. With a temperature of l80–240 ºC, the products become the monazite phase with the morphology strongly affected by the acidity [47]. $LaPO_4$:Ln^{3+}(Ln^{3+} = Ce^{3+}, Tb^{3+}) and $LaPO_4$:Ce^{3+},Tb^{3+}/$LaPO_4$ core/shell nanowires have been synthesized on a large scale through a direct precipitation in a water-based system under moderate conditions without the assistance of any surfactant, catalyst, or template [48]. The diameters of the obtained nanowires are about 15 nm, and the lengths range from hundreds of nanometers to several micrometers. For heavy lanthanides (Ho–Lu) and Y, a synthesis temperature as low as 70 ºC is required to obtain hydrated monoclinic churchite phase, for example, YPO_4 nanowires [49]. Higher temperature leads to tetragonal zircon phase. Usually, a particle-like morphology is obtained with acidic conditions. When a chelating agent like EDTA is introduced, the hydrated hexagonal nanorods of YPO_4 could be obtained [50]. For intermediate lanthanides (Gd, Tb, Dy), hexagonal, tetragonal, and monoclinic phases may coexist. Therefore, results are more complex. Typically, rhabdophane type $TbPO_4$ nanorods form at low temperature and zircon type $TbPO_4$ nanocubes form at high temperature, both with acidic mother liquors [46]. Hexagonal $DyPO_4$ nanorod bundles form at low temperature [51]. Usually, the rhabdophane products of light rare earths convert to monazite products, while the churchite phase converts to zircon products with heat treatment [52].

Surfactants, chelating agents, as well as block copolymers are used to control the size and shape of rare earth phosphate nanocrystals. Bu et al. reported a P123-assisted hydrothermal synthesis of $CePO_4$:Tb single-crystalline thin nanorods of 10–12 nm in width. The surfactant Pluronic P123 was found to play a crucial role both to improve luminescence properties and nanorod homogeneity [53]. When the pH value of reaction system is adjusted to below 1.0, uniform spindle like nanowire bundles of $LaPO_4$ could be obtained [54]. Xing et al. reported the synthesis of uniform $CePO_4$ nanorods by reaction of aqueous [$(CTA)_3PO_4$] micelles with [Ce$(AOT)_3$] reverse micelles prepared in isooctane [55]. Ghosh et al. reported the

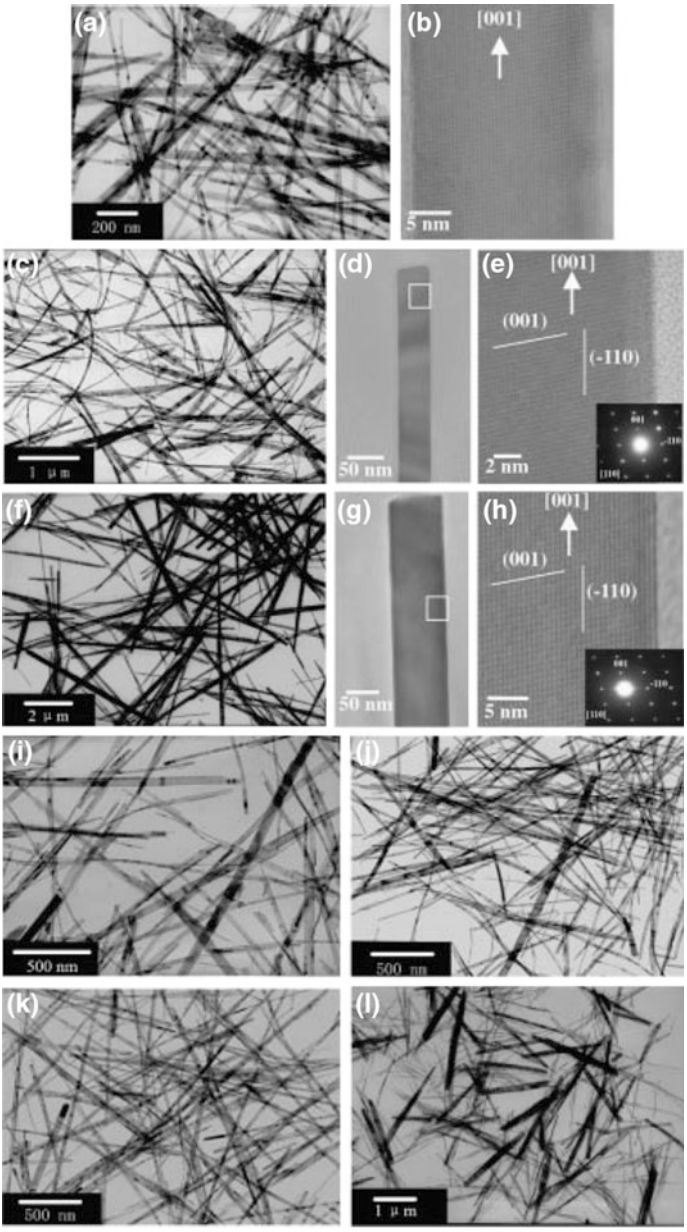
(a)
200 nm
(b)
[001]
5 nm
(c)
1 μm
(d)
50 nm
(e)
[001]
(001)
(-110)
2 nm
(f)
2 μm
(g)
50 nm
(h)
[001]
(001)
(-110)
5 nm
(i)
500 nm
(j)
500 nm
(k)
500 nm
(l)
1 μm

◀ **Fig. 5.8** **a** TEM image of $LaPO_4$ nanowires; **b** HRTEM image of a single 23 nm $LaPO_4$ nanowire; **c** TEM image of $SmPO_4$ nanowires; **d** TEM image of a uniform 50 nm $SmPO_4$ nanowire; **e** HRTEM image of a single $SmPO_4$ nanowire taken from the highlighted section with inset showing the electron diffraction pattern; **f** TEM image of $EuPO_4$ nanowires; **g** TEM image of a uniform 80 nm $EuPO_4$ nanowire; **h** HRTEM image of a single $EuPO_4$ nanowire taken from the highlighted section with inset showing the electron diffraction pattern; **i** TEM image of $CePO_4$ nanowires; **j** TEM image of $PrPO_4$ nanowires; **k** TEM image of $NdPO_4$ nanowires; and **l** TEM image of $GdPO_4$ nanowires/nanorods. (Reprinted with permission from [46]. Copyright 2003 Wiley-VCH.)

synthesis of $LaPO_4$:Er,Yb and $LaPO_4$:Er@$YbPO_4$ nanorods using a reverse micelles system [56]. Li et al. reported an OA-assisted solvothermal routes in mixed solution of water and ethanol for the synthesis of uniform hexagonal $REPO_4 \cdot nH_2O$ nanocrystals at 140 ºC (as shown in Fig. 5.9) [57]. The synthesis in high-boiling solvents gives out a number of advantageous features for the synthesis of doped $REPO_4$ nanocrytals. Yan et al. reported a series of high-quality dispersible $REPO_4$ nanocrytals with shapes of nanopolyhedra, quasinanorods, nanorods, and nanowires which are synthesized at 180–260 ºC in oleic acid and oleylamine solvents via a limited anion-exchange mechanism [58]. The assembly behavior during the synthesis of rare earth orthophosphates has been observed. Li et al. reported a one-pot synthesis of $CePO_4$ nanowires attached to CeO_2 octahedral micrometer crystals [59]. $Ce(NO_3)_3 \cdot 6H_2O$ and $(NH_4)_2HPO_4$ are used in a molar ratio of 2:1, pH value is tuned to be about 1, and the treatment temperature is 180 ºC. The photoluminescence properties of $CePO_4$ nanowires attached to CeO_2 octahedral micrometer crystals are enhanced strongly in comparison with pure $CePO_4$ nanowires.

For anisotropic orthovanadates, the first example reported is $LaVO_4$. Different from YVO_4 that only crystallizes in tetragonal phased structure, $LaVO_4$ exhibits both monoclinic and tetragonal phased structure. Therefore, phase modulation is the first task for the synthesis of $LaVO_4$-based materials. Wet chemistry routes always show superiority on the selective synthesis of nanomaterials with desired phase structure and morphology [60]. Sun et al. contributed several reports on this subject. In their synthesis, they used $NaVO_3$ and $La(NO_3)_3$ as the starting agents. The phase structure and morphology of $LaVO_4$ are dominated by aqueous pH value. Below pH 3.5, $LaVO_4$ crystallizes into irregular shaped *m*-phase nanoparticles. The *t*-phase nanorods only form in the pH range of 4.5–6.0. It is noticed that at early stage, $NaVO_3$ and $La(NO_3)_3$ solution were mixed to form a yellow suspension of *m*-$LaVO_4$. Then, the crude precipitates were transformed into *t*-$LaVO_4$ nanorods during a 48 h hydrothermal treatment at 180 °C with pH value of 4.5–6.0. The obtained nanorods had average diameters of 20 nm and lengths close to 100 nm along [001] direction. Besides the direct precipitation combining hydrothermal treatment, introducing chelating agent is also a powerful tool to restrict crystal growth, regulate the crystallization and get anisotropic materials. Yan et al. firstly used EDTA-assisted hydrothermal method to prepare *t*-$LaVO_4$ nanorods. The transformation from monoclinic phase to the metastable tetragonal structure dramatically enhanced the luminescence intensity of $LaVO_4$:Eu, validating the

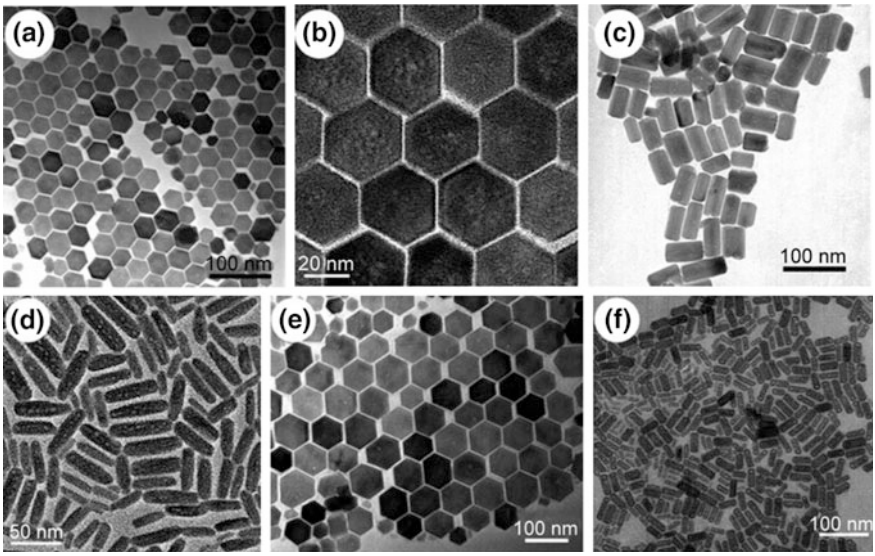

Fig. 5.9 TEM image of $REPO_4 \cdot nH_2O$ nanocrystals: **a** Dy, **b** Er, **c** Ho, **d** Tm, **e** Yb, and **f** Lu. (Reprinted with permission from [57]. Copyright 2007 Wiley-VCH)

correlation between structure and properties of materials [61]. They subsequently found that weak coordinating ligands, like sodium acetate or sodium citrate, only promote the crystallization of *m*-$LaVO_4$, also benefits the homogeneous doping of other rare earth ions in $LaVO_4$ lattice [61], but have no effect on the polymorph selection for the tetragonal phase. Also, by varying the ratio of [EDTA]/[La^{3+}], the aspect ratio of the $LaVO_4$ nanorods/nanowires also could be tuned (as shown in Fig. 5.10) [62, 63]. Employing a reverse microemulsion system with SDS (sodium dodecylsulfate) as the surfactant, Fan et al. obtained *t*-$LaVO_4$ nanowires and nanotubes after 170 °C treatment [64]. By altering the SDS concentration, the morphology of $LaVO_4$ was variable between nanowires and nanorods, and the aspect ratio along the [001] direction could reach 100.

5.2.2 Two-Dimensional (2D) Nanostructures

Recently, 2D nanomaterials, such as nanoplates and nanosheets have attracted broad attention because of their special structures and properties coming from the quantum confinement of electrons [65–68]. However, the facile synthesis of 2D rare earth oxide nanomaterials remains a challenge [69, 70]. Yan's group synthesized a series of dispersible rare earth oxide nanocrystals using rare earth benzoylacetonates [71], acetylacetonates, or acetates [72] as precursors by thermal deposition method

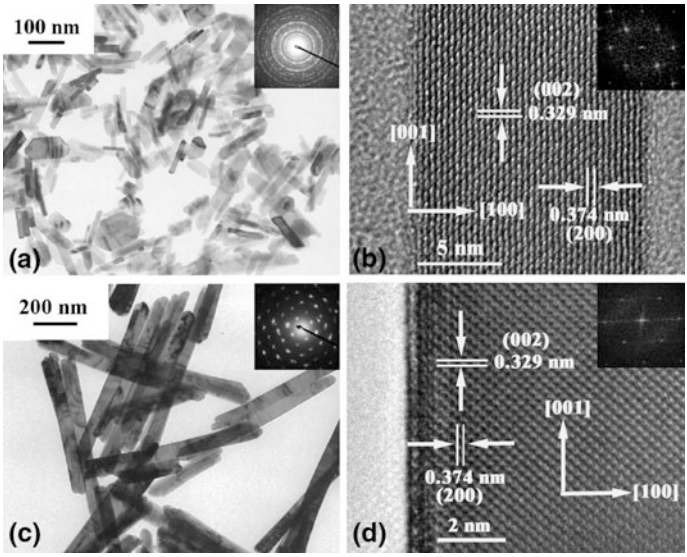

Fig. 5.10 TEM and HRTEM images of as-obtained *t*-$LaVO_4$ nanocrystals (**a** and **b**) and *t*-$LaVO_4$ nanorods (**c** and **d**). (Reprinted with permission from [63]. Copyright 2005 American Association)

(as shown in Fig. 5.11). Interesting, these nanocrystals exhibit a striking ability to self-assemble into large-area nanoarrays. By tuning the polarity of the dispersant, the RE_2O_3 nanocrystals could be aligned to form "side-to-side" or "face-to-face" self-assembly nanoarrays on carbon-coated copper grids [71, 72]. Rare earth oxides with different morphologies, including nanopolyhedra, nanoplates, and nanodisks, were synthesized in oleic acid/oleylamine mixed solvents. The nature of metal cations as well as the selective adsorption of the capping ligands plays a critical role in the shape-controlled growth process.

Murray et al. synthesized ultrathin 2D ceria nanoplates via a thermal decomposition method in the presence of mineralizers (sodium diphosphate) [73]. Many reaction parameters, such as precursor ratio, concentration, and reaction time, were varied to tune the morphology of nanoplates. Sodium diphosphate proved to be critical for accelerating the crystallization process and controlling the morphology of ceria nanocrystals. The obtained CeO_2 nanoplates exhibit much higher oxygen storage capacity than that of 3D CeO_2 nanomaterials prepared with other methods due to their higher theoretical surface-area-to-volume ratio and desirable (100) surfaces.

Generally, metal oxides with a cubic crystal structure, including ceria, inherently do not show any preference for 2D anisotropic growth behaviors. However, Xia et al. prepared ultrathin, single-crystalline ceria nanosheets with a thickness of approximately 2.2 nm and lateral dimension up to 4 μm by a simple aqueous route (as shown in Fig. 5.12) [74]. A balance of the anisotropic hydrophobic attraction and the electrostatic interactions may govern the spontaneous 2D self-organization

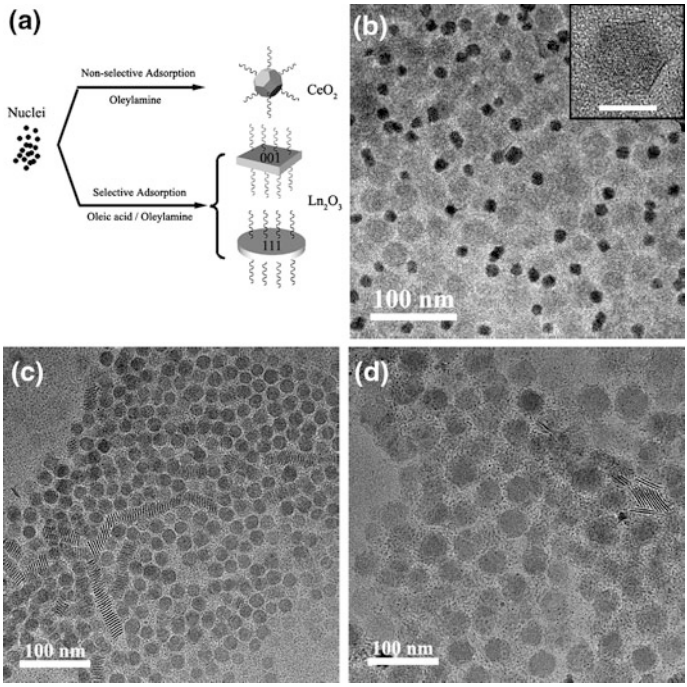

Fig. 5.11 **a** Formation of rare earth oxide nanopolyhedra, nanoplates, and nanodisks. **b–d** TEM images of the as-obtained Eu_2O_3: **b** OA/OM = 1:7, 310 °C, 1 h (*inset* HRTEM image of an Eu_2O_3 nanoparticle; *scale bar* 10 nm); **c** OA/OM = 3:5, 310 °C, 20 min; **d** OA/OM = 3:5, 330 °C, 1 h. (Reprinted with permission from [71]. Copyright 2005 John Wiley and Sons)

of initially formed small ceria nanocrystals. Subsequently, the nanosheets were formed through a recrystallization process. Due to the quantum size effect associated with the extremely small thickness, these ceria nanosheets hold great potentials for fundamental studies.

In order to study the role of active sites in catalysis, Xie's group successfully synthesized three-atom-layer thin CeO_2 sheets with about 20 % pits occupancy using an "ultrafast open space transformation" strategy [75]. An intermediate of ultrathin $CeCO_3OH$ sheets with thin 2D structures were obtained using sodium oleate, $CeCl_3$ and $NH_3 \cdot H_2O$ as the starting materials. Subsequently, freestanding ultrathin CeO_2 sheets with numerous surface pits were synthesized after direct heating of the $CeCO_3OH$ intermediate at 400 °C for 2 min in air. By contrast, they prepared clean three-atom-thick CeO_2 sheets without surface pits by elevating the heating temperature to 550 °C and shortening the duration to 10 s.

Rare earth fluorides and complex fluorides often take 2D shapes. Li et al. synthesized uniform LaF_3 nanoplates with Yb^{3+}/Er^{3+} and Yb^{3+}/Ho^{3+} dopants in a hydrothermal autoclave [76]. Yan's group employed the thermolysis approach with the single precursor $La(CFCOO)_3$ and obtained highly monodisperse LaF_3

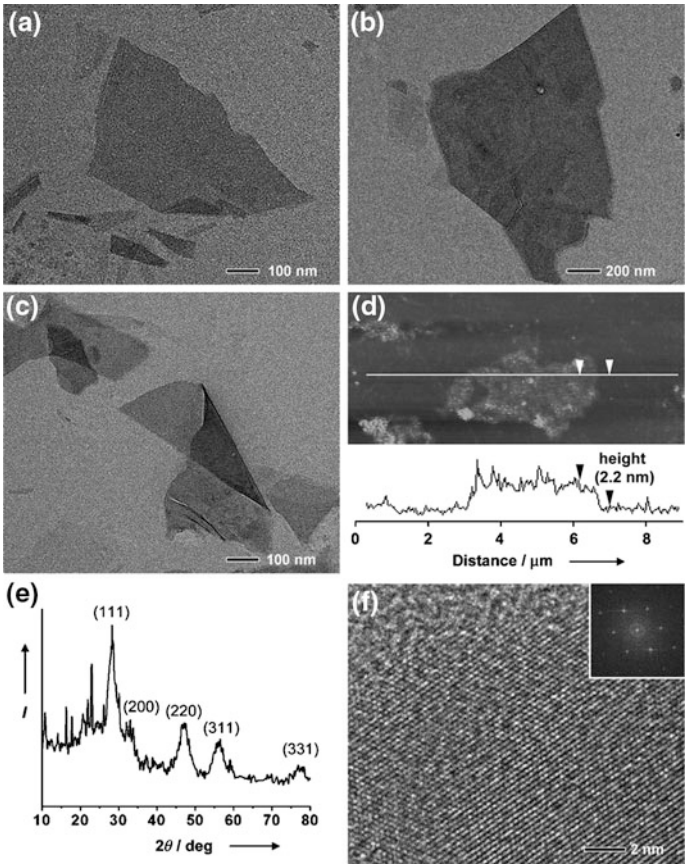

Fig. 5.12 Characterization of ceria nanosheets. **a**, **b** TEM images of nanosheets with different sizes. **c** TEM image of a self-folded nanosheet. **d** Tapping-mode AFM image and the height along the *line* shown in the AFM image. **e** Powder XRD pattern. **f** HRTEM image and the corresponding FT pattern (*inset*). (Reprinted with permission from [74]. Copyright 2010 John Wiley and Sons)

triangular nanoplates [77]. By altering the solvent, the nanoplates can self-assemble into highly ordered superlattices on substrates in a side-by-side or face-to-face manner (as shown in Fig. 5.13). They subsequently obtained monodisperse ultrathin LaOCl nanoplates (*ca.* 4.0 nm in thickness) using a similar method [78], and found that when different long chain amines (oleylamine, hexadecylamine and octadecylamine) were used as the surfactant, the LaOCl nanoplates could self-organize into face-to face and side-by-side superstructures, nanowire-like and nanorod-like superstructures. The different interaction strengths of amine capping ligands were presumed to be responsible for the different behaviors in self-assembly configurations. Apart from self-assembly, the same group also employed Langmuir-Blodgett technique to fabricate dense monolayers of a variety of differently shaped hydrophobic nanostructures [79], including sphere-like $NaYF_4$ and $LiYF_4$ polyhedra, 1D

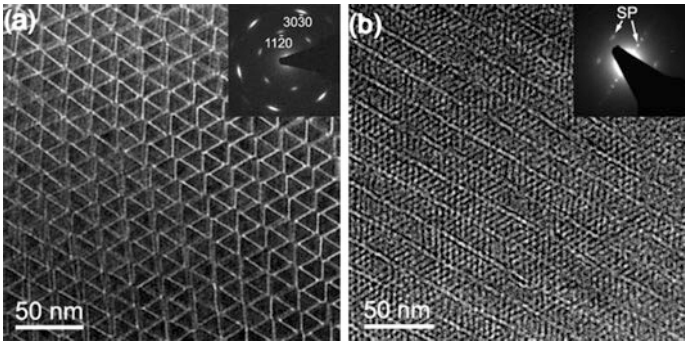

Fig. 5.13 TEM images of the **a** side-by-side and **b** face-to-face superlattices of LaF_3 nanoplates. Insets are the SAED patterns. (Reprinted with permission from [77]. Copyright 2005 American Chemical Society)

$NaYF_4$ nanorods, 2D LaF_3 triangular nanoplates, CaF_2 square nanoplates and EuF_3 hexagonal nanoplates. The effects of size, shape symmetry on the assembly kinetics were discussed.

Examples of 2D rare earth phosphates and vanadates are relatively rare, since they usually take rod-like or spindle-like shapes due to their crystal structures. Li et al. reported an oleic-acid-assisted solvothermal routes in mixed solution of water and ethanol for the synthesis of uniform $REPO_4 \cdot nH_2O$ nanocrystals at 140 ºC [57]. Hexagonal nanoplates with sub-100 nm diagonal diameter could be obtained, which self-assembled on substrate into ordered hexagonal monolayers. Qian et al. synthesized a series of rare earth vanadates and compared the effect of different chelating ligands including trisodium citrate, sodium tartrate and sodium malate [80]. They found when the amount of citrate or tartrate was higher than twofold molar ratio of Y^{3+}, a preferential growth would arise, yielding YVO_4 nanoplates with a donut-like morphology (as shown in Fig. 5.14). This method can be extended to vanadates of heavy lanthanide elements, such as $DyVO_4$ and $ErVO_4$. Li et al. prepared $LaVO_4$:Eu square nanoplates using a hydrothermal method with the assistance of oleic acid as surfactant [81]. The monodisperse 40 nm × 40 nm × 10 nm nanoplates tend to self-organize into ordered 2D arrays. They also synthesized a series of *t*-$REVO_4$ colloidal nanocrystals by using the same method [82]. They found the preferential growth direction of nanocrystals was decided by the steric repulsions of active points on crystal facets. $LaVO_4$, $CeVO_4$, and $PrVO_4$ nanocrystals revealed a square sheet-like morphology since their [100] and [010] directions had smaller rejection. With reducing ionic radius, YVO_4, $NdVO_4$, $SmVO_4$, and $EuVO_4$ showed similar square morphology, but the corners and edges of the nanoplates were broken or damaged. From $EuVO_4$ to $LuVO_4$, the breakage on nanocrystals edges became more pronounced and the proportion of irregular nanocrystals gradually increased. For $TmVO_4$ and $LuVO_4$, the selectivity of crystalline growth direction almost disappeared.

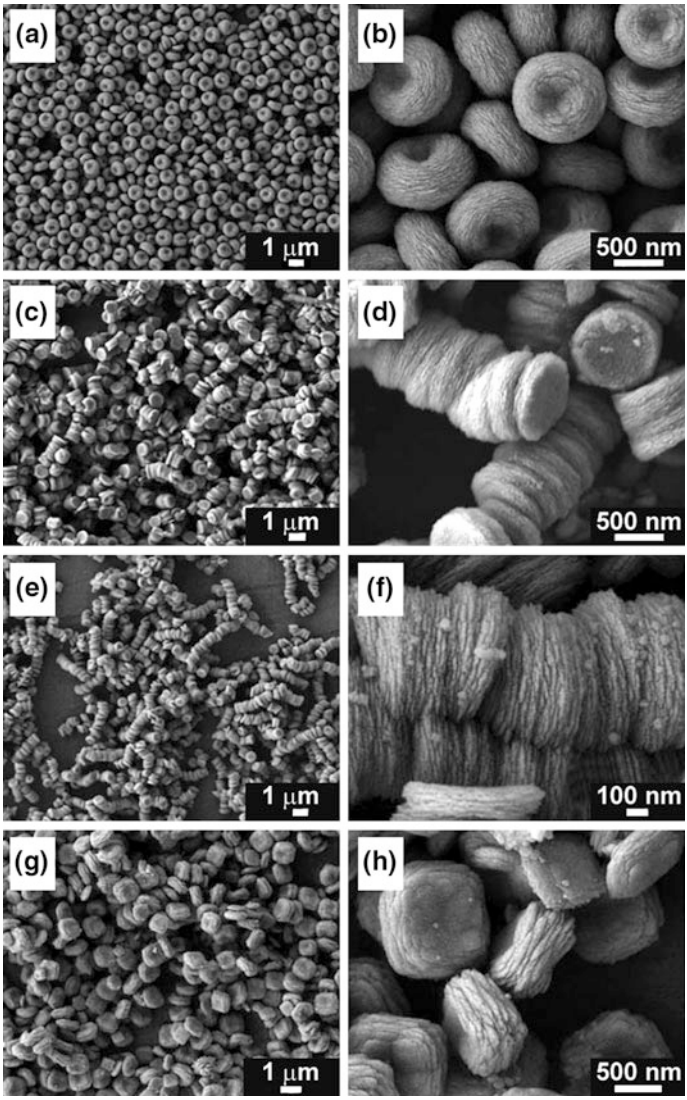

Fig. 5.14 SEM images of monodisperse YVO_4 assemblies obtained from 24 h hydrothermal reaction at 140 °C. Different chelating agents were used. **a**, **b** 2:1 molar ratio of citrate/Y^{3+}; **c**, **d**, 3:1 molar ratio of citrate/Y^{3+}; **e**, **f**, 4:1 molar ratio of citrate/Y^{3+}; **g**, **h**, 2:1 molar ratio of tarate/Y^{3+}. (Reprinted with permission from [80]. Copyright 2009 Wiley-VCH)

5.3 Applications of Rare Earth Based Anisotropic Nanomaterials

5.3.1 Luminescence Properties and Optical Applications

5.3.1.1 General Introduction of the Luminescence Properties of Rare Earths

Featuring abundant energy levels of 4f electron configurations, trivalent rare earth ions activated nanocrystals exhibit unique and fascinating luminescence properties [83]. Compared with semiconductor quantum dots and organic dyes, rare earth activated nanocrystals possess excellent photostability, large Stokes/anti-Stokes shifts, sharp-band emissions, and long luminescence lifetimes [84]. Benefiting from these advantages, RE-activated nanocrystals are promising candidates for applications in lighting and displays [85], optical fibers and amplifiers [86], bioimaging [87], photoactivation reactions [88], and photovoltaic devices [89].

With differently arranged energy levels, various rare earth activators are endowed with distinctive transition pathways. Ce^{3+}, widely studied and used for phosphor activators, is featured by its broadband 4f → 5d transition [90]. For other RE^{3+} activators, intra-configurational 4f → 4f transitions are the main intrinsic mechanism for their luminescence processes. Three different pathways for intra-configurational transition may occur in rare earth ions, namely, down-shifting, quantum-cutting (also known as downconversion), and upconversion (as shown in Fig. 5.15). In a down-shifting process, a high-energy excitation photon results in a low-energy one emitted, with the quantum efficiency below 100 %. Tb^{3+}, Eu^{3+}, Sm^{3+} and Dy^{3+} are typical activators for the down-shifting studies [91]. Due to their sufficiently high efficiencies and long luminescence lifetimes, down-shifting-based nanocrystals have been employed as candidates for lighting and displays and

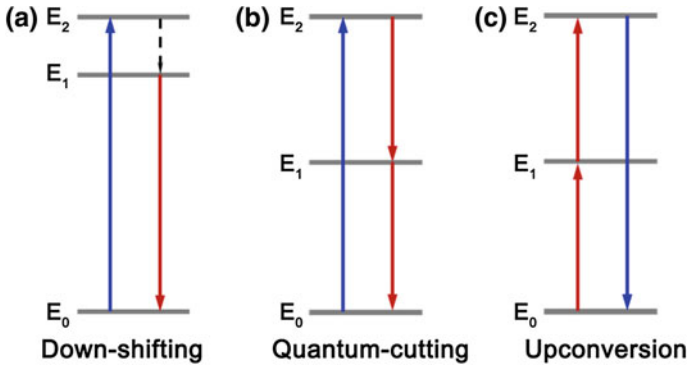

Fig. 5.15 Simplified illustration of intra-configurational transition pathways for rare earth ions. **a** Down-shifting. **b** Quantum-cutting (or downconversion). **c** Upconversion. The *upward*, *downward* and *dashed arrows* represent excitation, emission and relaxation processes, respectively

time-resolved biodetection applications [92, 93]. In a quantum-cutting process, one high-energy excitation photon splits into two (or more) low-energy ones by cascading down the ladder-like energy levels, with the quantum efficiency above 100 %. Nanocrystals with Pr^{3+}/Gd^{3+}–RE^{3+} (RE = Eu, Tb, Er) pairs and Yb^{3+}–RE^{3+} (RE = Tb, Tm, Pr) pairs dominate the quantum-cutting studies [94]. Considering the high quantum efficiency and specific visible or near-infrared (NIR) emissions, quantum-cutting-based nanocrystals are promising in lighting, displays, and particularly, improvement for solar cells [95, 96]. The photon upconversion process refers to a non-linear optical process where two (or more) low-energy excitation photons generate a high-energy one assisted by real intermediate excited states, with the quantum efficiency below 100 % [97]. In this section, we will mainly discuss the photon upconversion processes and extended optical applications of rare earth activated anisotropic nanocrystals.

5.3.1.2 Photon Upconversion in Rare Earth Anisotropic Nanostructures

Due to the high conversion efficiency, energy transfer upconversion (ETU) emissions have been widely studied. Two different types of luminescent centers, namely, a sensitizer and an activator, are involved in the ETU process [98–100]. Yb^{3+}, with only one excited state ($^2F_{5/2}$) and a large absorption cross-section at 980 nm, is an outstanding sensitizer for the ETU process. Moreover, the energy of $^2F_{5/2}$ state matches well with that of most rare earth ions, which also facilitates Yb^{3+} as a commendable sensitizer. With ladder-like arranged energy levels, long-lived intermediate excited states and excellent resonance with the energy gap from $^2F_{7/2}$ to $^2F_{5/2}$ of Yb^{3+}, Er^{3+}, Tm^{3+}, and Ho^{3+} (especially Er^{3+} and Tm^{3+}) ions are ideal pairing activators for the ETU process. In addition, the host matrices also have significant influences on the upconversion behaviors of doped luminescent centers. Generally, rare earth based fluorides and complex fluoride salts are considered as optimal host matrices due to their low phonon energy and high transparency for NIR photons [101–103].

In Yb^{3+}–Er^{3+} activated nanocrystals, three-photon 415 nm emission ($^2H_{9/2} \rightarrow {}^4I_{15/2}$), two-photon 525, 545 and 655 nm emissions ($^2H_{11/2} \rightarrow {}^4I_{15/2}$, $^4S_{3/2} \rightarrow {}^4I_{15/2}$, $^4F_{9/2} \rightarrow {}^4I_{15/2}$) can be observed after the successive energy transfer from Yb^{3+} to Er^{3+} (Fig. 5.16a) [104]. In Yb^{3+}–Ho^{3+} activated nanocrystals, three-photon 485 nm emission ($^5F_3 \rightarrow {}^5I_8$), two-photon 545 nm emission ($^5F_4$, $^5S_2 \rightarrow {}^5I_8$) and 650 nm emission ($^5F_5 \rightarrow {}^5I_8$) are the typical upconversion spectral fingerprints (Fig. 5.16b) [105]. The densely arranged energy levels of Er^{3+} and Ho^{3+} determine that multiple photon upconversion processes are scarcely observed in Yb^{3+}–Er^{3+} and Yb^{3+}–Ho^{3+} activated nanocrystals. However, multiple photon upconversion emissions, coming from three-, four-, and five-photon transitions, can be frequently detected in Yb^{3+}–Tm^{3+} activated nanocrystals. This should be attributed to the discretely arranged energy levels of Tm^{3+}, which, to a large extent, reduce the non-radiative relaxation processes. Therefore, two-photon 800 and 695 nm emissions

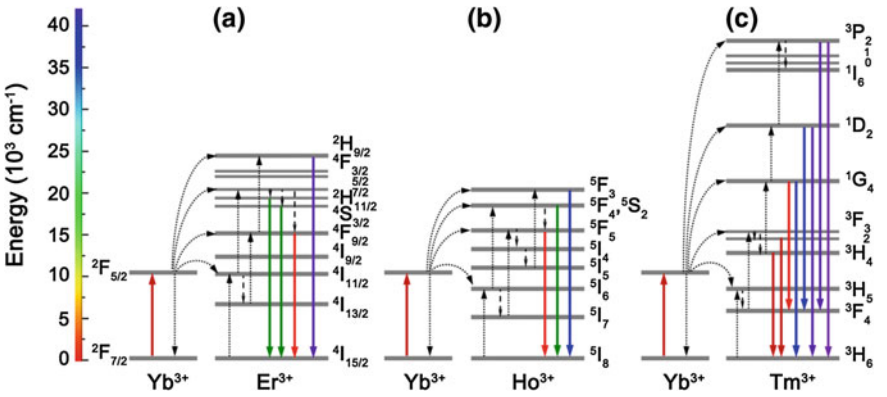

Fig. 5.16 Proposed upconversion energy transfer pathways in **a** Yb^{3+}–Er^{3+}, **b** Yb^{3+}–Ho^{3+} and **c** Yb^{3+}–Tm^{3+} pairs. Excitation and emission processes are represented by *upward* and *downward solid arrows*, respectively. The *dotted* and *dashed arrows* denote energy transfer and non-radiative relaxation processes, respectively

($^3H_4 \rightarrow {}^3H_6$, $^3F_3 \rightarrow {}^3H_6$), three-photon 645 and 475 nm emissions ($^1G_4 \rightarrow {}^3F_4$, $^1G_4 \rightarrow {}^3H_6$), four-photon 450 and 365 nm emissions ($^1D_2 \rightarrow {}^3F_4$, $^1D_2 \rightarrow {}^3H_6$), and even five-photon 345 and 290 nm emissions ($^1I_6 \rightarrow {}^3F_4$, $^1I_6 \rightarrow {}^3H_6$) can be simultaneously released from Yb^{3+}–Tm^{3+} pairs (Fig. 5.16c) [106].

When rare earth activated nanocrystals adopt anisotropic morphologies, their upconversion properties differ greatly from those with isotropic ones, especially the polarized upconversion emissions. Qiu et al. for the first time investigated the polarized upconversion emissions from Yb^{3+}–Tm^{3+} activated hexagonal phased $NaYF_4$ single nanorod [107]. Upon excitation with a 980 nm linearly polarized laser, sharp energy level splitting of the $^1D_2$ and $^1G_4$ states of Tm^{3+} was observed at room temperature, generating singlet-to-triplet emissions at 735 nm ($^1D_2 \rightarrow {}^3F_3$) and 768 nm ($^1G_4 \rightarrow {}^3H_5$), which previously were assumed to be partially forbidden (Fig. 5.17a). In the meanwhile, the multiple discrete emission intensity periodic variation with polarized direction was also observed (Fig. 5.17b). Moreover, the aspect ratio of nanorod was studied for the effect on the polarization property (Fig. 5.17c). Hexagonal-phased $NaYF_4$:Yb,Tm single nanorod and single nanodisk were found to possess quite similar fitting contours in each transition of Tm^{3+}, suggesting a negligible effect of aspect ratio on the polarization anisotropy. However, when Gd^{3+} ions were doped into the nanorods, the polarization anisotropy became distinctly different. Two different kinds of intensity variation states were observed for each transition. The authors reasoned that the different local symmetry of Tm^{3+} in $NaYF_4$:Gd,Yb,Tm nanorods should be responsible. Based on the comprehensive studies, the intrinsic transition properties and crystal local symmetry should dominate the polarization anisotropy.

Apart from the polarization anisotropy, the pleochroism of upconversion emissions is also embodied in anisotropic nanocrystals. Yan et al. prepared a series of hexagonal phased $NaYF_4$:Yb,Er nanocrystals with different sizes ranging from

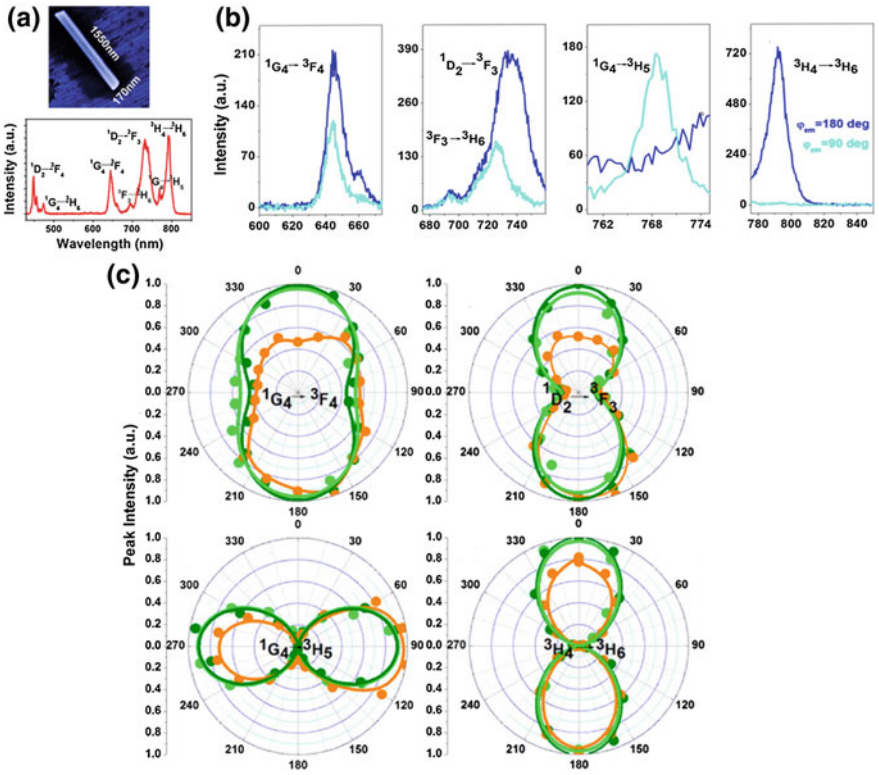

Fig. 5.17 **a** Scanning electron microscopy image of $NaYF_4$:Yb,Er nanorod and its upconversion emission spectrum upon excitation with a 980 nm linearly polarized laser. **b** Polarization angle (φ_{em}) dependent upconversion emission spectra. **c** Polar plots of the upconversion peak intensity as a function of the emission polarization angle, which is corresponding to the transitions of Tm^{3+} in $NaYF_4$:Yb,Er nanorod, nanodisk, and $NaYF_4$:Gd,Yb,Er nanorod. (Reprinted with permission from [107]. Copyright 2013 American Chemical Society)

$\sim$20 to $\sim$300 nm. As the size increased, the morphology of the nanocrystals changed from spherical to disk-like. And the green-to-red emission ratio of Er^{3+} was found to increase with the nanocrystals from isotropic to anisotropic (Fig. 5.18) [104, 108]. Furthermore, the authors investigated the upconversion behavior of one-dimensional $NaMgF_3$:Yb,Er nanorods. Different from the upconversion profile of hexagonal-phased $NaYF_4$:Yb,Er nanodisks, for which the green emission dominated the visible regime, the green emission from $NaMgF_3$:Yb,Er nanorods was significantly weaker than the red emission [109]. Recently, they developed a novel structure of $NaYF_4$:Yb,Er nanocages, deriving from the removal of NaCl in NaCl/$NaYF_4$:Yb,Er core/cage nanocomposites. The upconversion behavior of $NaYF_4$:Yb,Er nanocages and nanospheres were examined. It was found that the red-to-green emission ratio of Er^{3+} decreased to 0.44 in nanocages from 1.89 in nanospheres [110]. Zhu et al. compared the upconversion profiles of orthorhombic

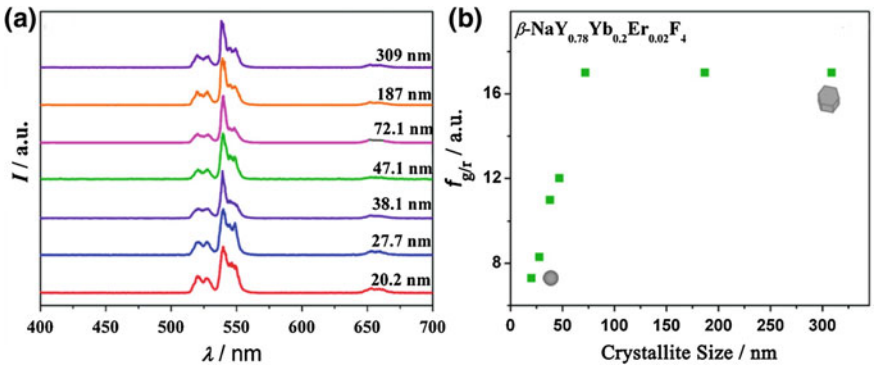

Fig. 5.18 **a** Upconversion emission spectra of different sized hexagonal $NaYF_4$:Yb,Er nanocrystals in cyclohexane. **b** Diagram of *green* to *red* emission ratio versus the size of $NaYF_4$:Yb,Er nanocrystals, with *insets* representing the morphology transition from isotropic to anisotropic. (Reprinted with permission from [104]. Copyright 2007 American Chemical Society)

KSc_2F_7:Yb,Er nanorods with hexagonal $NaYF_4$:Yb,Er nanorods [111]. They observed greatly enhanced red and violet emissions of Er^{3+} in KSc_2F_7:Yb,Er nanorods. Liu et al. prepared 1D orthorhombic KYb_2F_7:Yb,Er nanorods, where Yb^{3+} ions were localized as tetrad clusters. The spectral results exhibited that multiphoton violet emission of Er^{3+} was significantly enhanced compared with that in hexagonal $NaYF_4$ nanodisks [112]. Moreover, the violet emission of Er^{3+} was assigned as a four-photon emission.

When multiple activators are embedded in anisotropic nanocrystals, the upconversion emissions become more intriguing. Li et al. studied the upconversion behavior of hexagonal phased $NaYF_4$:Yb,Ho nanorods after Ce^{3+} doping [113]. They observed that the red-to-green emission ratio of Ho^{3+} increased after the introduction of Ce^{3+}, with the emission output from pure green to greenish-yellow. Moreover, unusual $^5G_5 \rightarrow {}^5I_7$ and $^5F_2$, $^3K_8 \rightarrow {}^5I_7$ transitions of Ho^{3+} and 5d → 4f transitions of Ce^{3+} can be simultaneously observed. Qin et al. modulated the red-to-green emission ratio of Er^{3+} in hexagonal-phased $NaYF_4$ one-dimensional microtubes by precisely defining the doping ratio of Tm^{3+} dopant [114]. An increased red-to-green emission ratio of Er^{3+} was detected with elevated content of Tm^{3+} from 0 to 2 mol%, with the emission output altering from green to red. Multiphoton cross-relaxations within Tm^{3+}–Er^{3+} pairs were proposed to account for the spectral variation. Lee et al. fabricated a series of quasi-two-dimensional anisotropic core/shell nanostructures, where the shell layers preferentially grew on the side faces (100) of the hexagonal phased $NaYF_4$ nanocrystals. Er^{3+} and Tm^{3+} ions were separately embedded in the core and shell regions, respectively, giving out multicolor upconversion emissions upon NIR excitation [115]. Recently, Liu et al. employed an end-on growth of upconversion nanocrystals compromising Tm^{3+} and Er^{3+} ions onto the hexagonal one-dimensional $NaYF_4$ nanorods. The emission output was further modulated by tuning the molar ratio of sensitizer and activator.

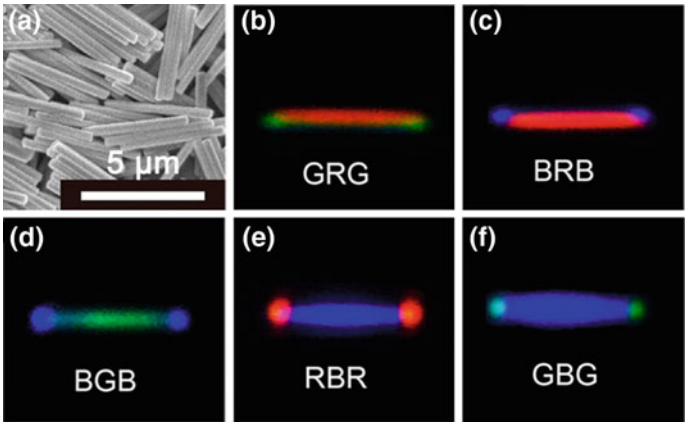

Fig. 5.19 **a** Scanning electron microscopy image of $NaYF_4$ based nanorod. **b–f** Optical micrographs showing five sets of dual-color-banded upconversion nanorods. Note that the appearance of a tinge color at the tip junction is due to the chromatic aberration and limited resolution of the microscope. (Reprinted with permission from [116]. Copyright 2014 American Chemical Society)

A series of dual-color upconversion nanorods displaying different combinations of the three primary colors were obtained (Fig. 5.19). With the dual-color emitting nanorods, they achieved some prototype models for barcoding for anti-counterfeiting application [116].

Recent progresses show that upconversion emissions from anisotropic nanocrystals can be tailored by the other co-assembled nanomaterials. Yan et al. investigated the upconversion emissions from a two-dimensional dense film of $NaYF_4$:Yb,Er nanocrystals by co-assembling with Ag nanowires [117]. They noticed 2.3 fold and 3.7 fold enhancement for the green and red emissions, respectively. And the large scattering efficiency of Ag nanowires was proposed to account for the enhancement. Kagan et al. studied the upconversion emission in an assembly comprising single $NaYF_4$:Yb,Er nanodisk and single Au nanorod (as shown in Fig. 5.20) [118]. The longitudinal surface plasmon resonance of the Au rod was tuned to match the 977 nm excitation wavelength of the $NaYF_4$:Yb,Er nanodisk by tailoring the dimension of the rod. And the spatial distance between the two composites was within the range of the intense near-fields surrounding the Au rod tips. As a result, two and threefold enhancements were achieved for the green and red emissions of Er^{3+}, respectively. Moreover, the enhancements exhibited a strong dependence on the polarization of the excitation light relative to the Au rod axis. The longitudinal polarization exhibited more spectral changes than the transverse one. Zink et al. encapsulated single $NaYF_4$:Yb,Er nanorod and single smaller superparamagnetic Fe_3O_4 nanocrystal into one mesoporous silica nanoparticle, and further exposed the nanocomposites to oscillating magnetic field [119]. The upconversion behavior of $NaYF_4$:Yb,Er nanorod was modulated by heat magnetically induced by Fe_3O_4 inside the nanocomposites. Spectral results showed

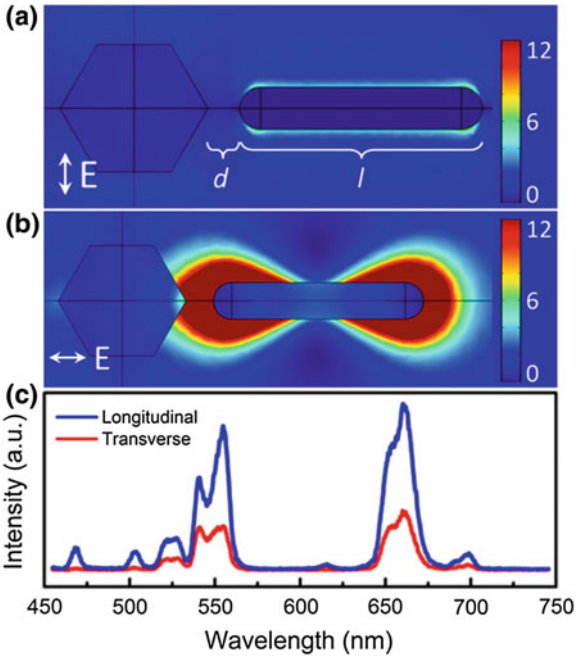

Fig. 5.20 Simulated field intensity enhancement maps for **a** transverse and **b** longitudinal excitation polarization. **c** Representative upconversion emission spectra from the center of the $NaYF_4$:Yb,Er nanodisk under longitudinal (*blue*) and transverse (*red*) incident polarization for the Au–$NaYF_4$:Yb,Er assembly. (Reprinted with permission from [118]. Copyright 2014 American Chemical Society)

that the emission ratio of 525 to 545 nm of Er^{3+} enhanced with elevated temperature, which resulted from prolonged exposure time to the magnetic field.

The excitation pathways can be modulated in anisotropic nanocrystals as well. Yan et al. extended the NIR excitation band of Yb^{3+}–RE^{3+} (RE = Er, Tm) pairs by introducing Nd^{3+} into a separated layer with an array of Yb^{3+} ions as the energy bridgers (Fig. 5.21) [120]. As a result, almost similarly efficient upconversion emissions can be obtained upon 980 nm (for Yb^{3+}) and 808 nm (for Nd^{3+}) excitations. Moreover, the potential overheating issue induced by longtime 980 nm irradiation was largely minimized by shifting the excitation wavelength to 808 nm. Similarly, Wang et al. also realized energy transfer management in multishell structured anisotropic nanorods upon 808 nm excitation [121]. Besides spatial separation of Nd^{3+} and activators, Han [122] and Liu [123] also achieved cascade sensitization of upconversion emissions by co-doping Nd^{3+} and Er^{3+}/Tm^{3+} in the same layer.

5.3.1.3 Optical Applications

The past few years witnessed the rapid development of rare earth upconversion nanocrystals in various aspects, including bioimaging studies [124], theranostics [125], sensing and detection [126], photovoltaic devices [127], and photoactivation

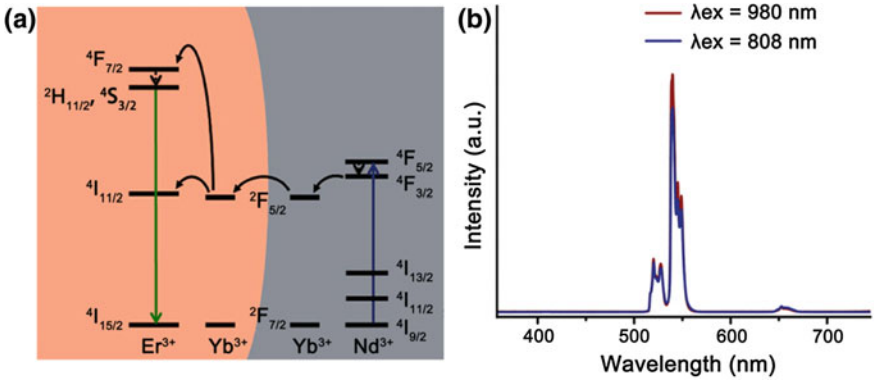

Fig. 5.21 **a** Proposed energy transfer pathways for Nd^{3+} activated upconversion emissions. **b** Typical upconversion emission spectra of Yb^{3+}–Er^{3+} activated nanocrystals upon 980 and 808 nm excitations. (Reprinted with permission from [120]. Copyright 2013 American Chemical Society)

reactions [128]. In this part, we will present a brief summary of rare earth upconversion nanocrystals for applications in biology and photoresponsive materials.

Due to the specific NIR excitation, resolvable UV to NIR emission and deep tissue penetration, rare earth upconversion nanocrystals have been widely used as biomarkers for biological studies. Various models, such as cells [129], *C. elegans* [130], rats [131] and rabbits [132], have been employed to assess the bioimaging performance of rare earth upconversion nanocrystals. Yan et al. examined the bioimaging capability and assessed the toxicity of $NaYF_4$:Yb,Tm nanocrystals in vitro and in vivo [133]. After incubation with the upconversion nanocrystals, bright upconversion emission signals can be collected from HeLa cells and *C. elegans* (Fig. 5.22). Moreover, no obvious toxicity effect was found for both cells and *C. elegans*. Li et al. synthesized sub-10 nm hexagonal $NaLuF_4$:Gd,Yb,Er nanocrystals and applied them for sensitive in vivo imaging. Subcutaneous imaging of 50 KB cells and intramouse imaging of 1000 KB cells after intravenous injection were obtained [134].

Besides single-modal optical imaging, rare earth upconversion nanocrystals have also been assembled with magnetic nanocrystals, noble metal nanocrystals and photosensitive molecules to support multi-modal imaging, theranostic and biodetection applications. Liu et al. deposited Au and Fe_3O_4 nanocrystals onto hexagonal $NaYF_4$:Yb,Er nanodisks to conduct photothermal therapy, magnetic resonance imaging and upconversion imaging studies [135]. Yan et al. fabricated multifunctional $NaGdF_4$:Yb,Er@CaF_2@SiO_2 nanocomposites, which were further grafted with photosensitizers to generate singlet oxygen, for upconversion imaging, magnetic resonance imaging and photodynamic therapy [136]. Li et al. decorated NIR cyanine dye hCy7 molecules on hexagonal $NaYF_4$:Yb,Er,Tm nanocrystals. When $MeHg^+$ ions were added to the nanocomposites, the red emission of Er^{3+} became significantly enhanced while the NIR emission of Tm^{3+} sharply decreased.

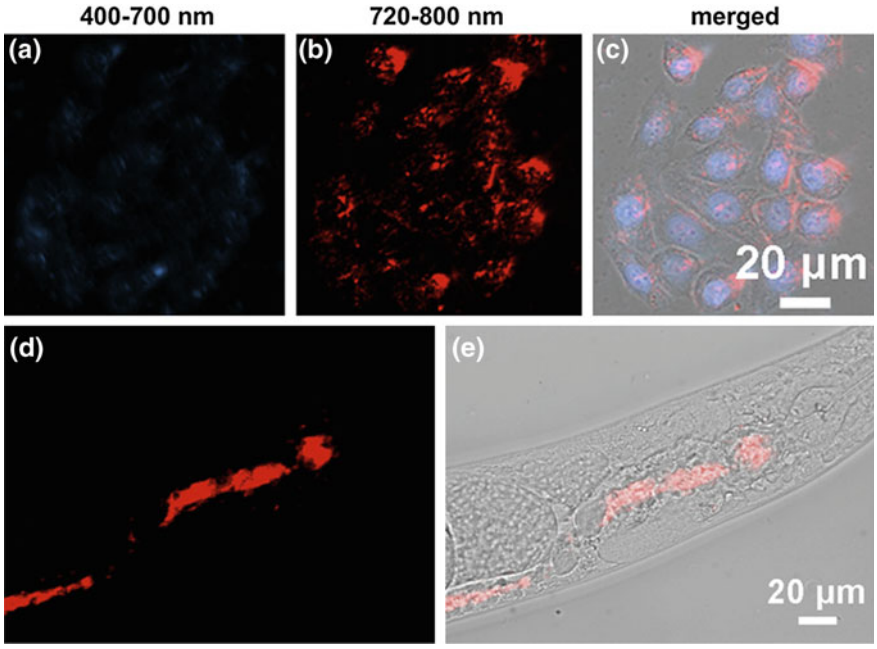

Fig. 5.22 In vitro and in vivo bioimaging of $NaYF_4$:Yb,Tm nanocrystals. **a**, **b** False-colored upconversion emission signals in visible (400–700 nm) and NIR (720–800 nm). **c** Merged images of HeLa cells and upconversion emissions. **d**, **e** False-colored NIR upconversion emission signal and the merged image of *C. elegans*. (Reprinted with permission from [133]. Copyright 2011 Elsevier B.V.)

They realized both in vitro and in vivo detection of $MeHg^+$ ions with the detection limit of 0.18 ppb [137].

Upconversion emissions from rare earth activated nanocrystals are also demonstrated to trigger photoactivation reactions. Diarylethene derivatives, *o*-nitrobenzyl containing molecules, and azobenzenes are typical photoresponsive molecules. Branda et al. used alternative irradiation of upconversion emissions from $NaYF_4$:Yb, Tm and $NaYF_4$:Yb,Er nanocrystals to remotely control the photoswitching process of diarylethene derivatives [138]. By precisely defining the composition of upconversion nanocrystals and tuning the NIR excitation power, reversible photoswitching process of diarylethene derivatives was achieved [139]. Xing et al. reported a novel type of nanocomposites for controllable release of D-luciferin molecules, which were decorated on the surface of $NaYF_4$:Yb,Tm nanocrystals via the *o*-nitrobenzyl group. Upon NIR excitation, UV emissions from Tm^{3+} can trigger the disassociation of D-luciferin molecules [140]. Recently, Yan and Li et al. fabricated a NIR-light-responsive self-organized helical superstructure by doping chiral azobenzenes and two-dimensional (2D) Yb^{3+}–Tm^{3+} activated nanodisks into a liquid crystal host. Upon high power excitation, UV emissions (Fig. 5.23a) from Tm^{3+} can direct the

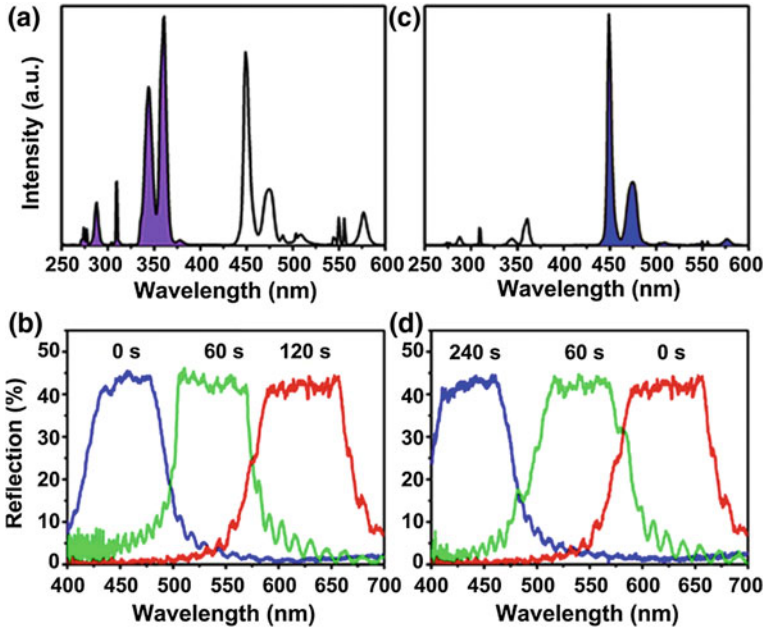

Fig. 5.23 Upconversion emission spectra from Yb^{3+}–Tm^{3+} activated nanodisks and reflection spectra of liquid crystal upon high power excitation (**a**, **b**) and low power excitation (**c**, **d**). (Reprinted with permission from [141]. Copyright 2014 American Chemical Society)

trans to *cis* isomerization of azobenzenes, resulting a red-shifted reflection wavelength of the liquid crystal (Fig. 5.23b). At low power excitation, the blue emissions (Fig. 5.23c) from Tm^{3+} are observed to trigger the reversible process of the blue-shifted absorption of liquid crystal (Fig. 5.23d) [141].

5.3.2 Magnetic Properties and MRI Applications of Anisotropic Rare Earth Nanostructures

The rare earth elements are well known for their superior magnetic properties. Their trivalent ions are characterized by f^n configurations, which renders them large paramagnetic susceptibility (expect Sc^{3+}, Y^{3+}, La^{3+} and Lu^{3+}, due to their lack of 4f unpaired electrons) [142]. Different from the 3d electrons of some transition metal ions (Fe^{3+}, Mn^{2+} and Co^{2+}, etc.), the 4f electrons of rare earth ions are less influenced by the microenvironment, as they are shielded by outer-shell ($5s^25p^6$) electrons. Besides, some of their compounds possess distinctive magnetic properties, such as large saturation magnetization, large magnetocrystalline anisotropy constant, large magnetostriction constant and remarkable magneto-optic effect [143]. As a result, rare earth materials have been widely used in traditional magnet

Table 5.1 Ground state, g values, calculated and experimental room temperature χT value for Ln (III) ions

Ln (III)	Configuration	Ground state	g_J	χT^{a}_{cal} (emu mol^{-1} K)	χT_{exp} (emu mol^{-1} K)
Ce	f^1	$^2F_{5/2}$	6/7	0.8	0.66–0.78
Pr	f^2	$^3H_4$	4/5	1.6	1.45–1.62
Nd	f^3	$^4I_{9/2}$	8/11	1.64	1.45–1.53
Pm	f^4	$^5I_4$	3/5	0.9	1.05
Sm	f^5	$^6H_{5/2}$	2/7	0.09	0.32
Eu	f^6	$^7F_0$	0	0	1.53
Gd	f^7	$^8S_{7/2}$	2	7.88	7.61–7.8
Tb	f^8	$^7F_6$	3/2	11.82	11.76–12.01
Dy	f^9	$^6H_{15/2}$	4/3	14.17	13.01–14.05
Ho	f^{10}	$^5I_8$	5/4	14.07	13.26–13.78
Er	f^{11}	$^4I_{15/2}$	6/5	11.48	11.05–11.28
Tm	f^{12}	$^3H_6$	7/6	7.15	7.03
Yb	f^{13}	$^2F_{7/2}$	8/7	2.57	2.53

Reprinted with permission from [142]. Copyright 2009 Springer Science and Business Media
[a] $\chi T_{cal} = (1/8)\ g_J^2[J(J+1)]$

technology over the past decades, for example, $SmCo_5$ and $Nd_2Fe_{14}B$ are well-known permanent magnets for their large static magnetic field; yttrium barium copper oxide are famous for displaying high-temperature superconductivity. With the development of nanotechnology, rare earth magnetic materials also have proved their great potential for applications in nanoscale, particularly in the field of magnetic resonance imaging (MRI) (Table 5.1).

As a very powerful noninvasive detection protocol, MRI has superb advantages, such as fast scan time, deep penetration, high spatial resolution, and no radiochemical damage [144, 145]. Nevertheless, the low imaging sensitivity hampered its further application. MRI contrast agents (CAs), which are able to alter the relaxation time of surrounding protons, have been utilized to improve the sensitivity both in clinical diagnosis and biological research [146]. Longitudinal relaxation enhancement is mainly related to the inner-sphere regime that chemically exchanges directly with the paramagnetic centers, while transverse relaxation enhancement is mainly related to proton's effective diffusion and interaction with magnetic dipolar moment in outer-sphere regime (Fig. 5.24) [147]. The ability of CAs to shorten longitudinal relaxation time (T_1) and transverse relaxation time (T_2) is evaluated by longitudinal relaxivity (r_1) and transverse relaxivity (r_2), respectively. Generally, CAs with low r_2 to r_1 ratio (r_2/r_1) are used for T_1-weighted images, while CAs with high r_2/r_1 are used for T_2-weighted images. For clinic, Gd-based chelates (especially Gd-DTPA) and superparamagnetic iron oxide nanoparticles (SPIO) are most widely used T_1 and T_2 CAs, respectively. To lower the risks of free Gd^{3+}, [148] most clinical lanthanide CAs are used in form of chelates, so as to stabilize Gd^{3+} by coordination [149, 150]. However, the leakage of Gd^{3+} is

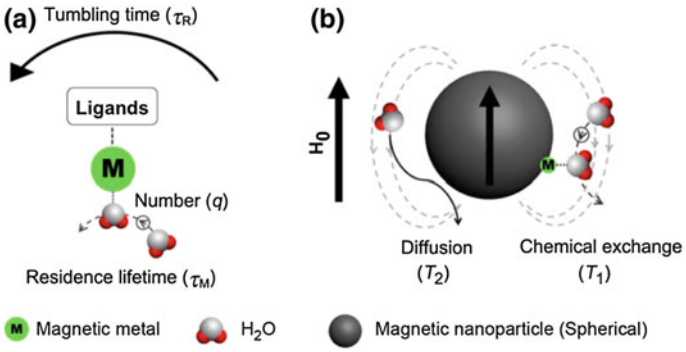

Fig. 5.24 Schematic illustrations of proton phenomena in magnetic systems relating to T_1 and T_2 relaxations. **a** Paramagnetic metal complex system and the selected key parameters to T_1 relaxation of protons: molecular tumbling time (τ_R), proton residence lifetime (τ_M), and the coordinating water molecular number (q), while the magnetic gradient field around paramagnetic center is neglected. **b** Phenomena of proton interaction with a spherical magnetic nanoparticle system: water molecular diffusion and chemical exchange with surface magnetic metals, related to their T_2 and T_1 contrast enhancements, respectively. (Reprinted with permission from [147]. Copyright 2014 American Chemical Society)

inevitable due to coordination equilibrium. Moreover, the Gd^{3+}-based chelates usually have small molecular weight, resulting in rapid clearance from human body. Aiming to solve the present problems of chelate CAs, the concept of nanoparticulate CAs has been raised [151]. The advantages of nanoparticle-based CAs include: (1) rigid inorganic structure could minimize the leakage of Gd^{3+}; (2) high payload of Gd^{3+} per nanoparticle could ensure large local contrast enhancement; (3) larger size than chelates could prolong not only the circulation time in vivo, but also the rotational correlation time (τ_R); (4) multi-functional bio-applications can be realized through doping and further surface engineering.

5.3.2.1 Gd-Based Anisotropic Nanostructures as MRI CAs

With seven unpaired electrons and isotropic orbitals, Gd^{3+} has both large magnetic moment and long electric relaxation time (due to the negligible spin–orbit interaction), and is widely accepted as the best choice for longitudinal proton relaxation enhancement [150]. Nano-sized gadolinium oxide nanoparticles were first evaluated for their physicochemical and NMR properties by McDonald et al. in 2003 [152], which opened the research field of rare earth-based nanoparticulate MRI CAs. Up to now, the studies of Gd-based T_1 CAs have been extended from gadolinium oxides (Gd_2O_3) to gadolinium hydroxide ($Gd(OH)_3$), gadolinium fluoride (GdF_3), sodium gadolinium fluoride ($NaGdF_4$) and gadolinium oxysalts (such as

$GdPO_4$), etc. Besides, doping Gd^{3+} into other inorganic matrices has become an effective strategy to combine MRI with other imaging modalities [153].

Relaxivity is one of the most important indexes for CAs, which could reflect the contrast enhancement efficacy. High relaxivity is always pursued, since it will bring benefits including improved image quality, reduced injection dose and lower risks. However, the r_1 value of Gd-DTPA is quite low (about 4 s^{-1} mM^{-1} at 1.5 T) [154]. Although Gd-based nanoparticles were supposed to have higher relaxivities than Gd-DTPA in the beginning, the r_1 values of those nanoparticles in early stage were still not sufficiently high. This probably could be explained by the immaturity of synthetic methods, since those nanoparticles usually had irregular shapes and wide size distribution. In recent years, with the development of synthetic method, uniform and monodispersed nanoparticles could be readily obtained, and size has been found to significantly affect the relaxivity. Lee et al. synthesized ultrasmall paramagnetic Gd_2O_3 nanoparticles with the size around 1 nm and a large r_1 was estimated (9.9 s^{-1} mM^{-1}) [155]. They discussed the size dependence of r_1 in two terms, surface to volume ratio (*S/V*) and cooperative induction effect. On one hand, it is indicated that only surface Gd^{3+} significantly contribute to the longitudinal relaxation. Therefore, decreasing the size will lead to larger *S/V* and more surface Gd^{3+}, and positively influence the r_1. On the other hand, several surface Gd^{3+} could possibly accelerate the longitudinal relaxation of water protons by cooperative induction. When the size is too small to produce this effect, the r_1 value would decrease. The optimal range of particle size that they suggested is 1–2.5 nm (Fig. 5.25). van Veggel et al. reported on the size-tunable synthesis of $NaGdF_4$ nanoparticles below 10 nm [156]. Through the analysis of the relationship between

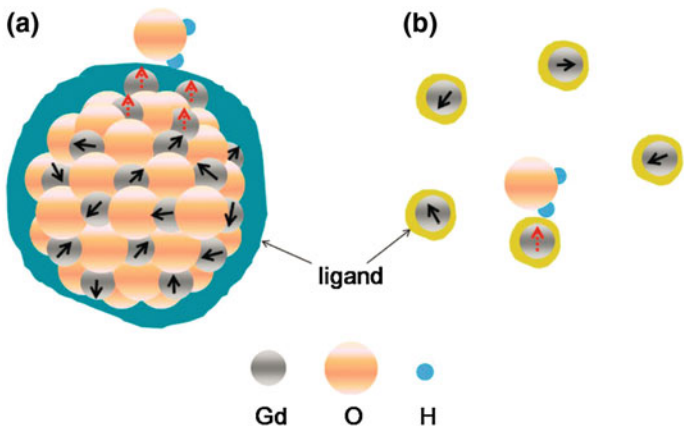

Fig. 5.25 Schematic diagram showing that **a** four surface Gd(III) ions as an example cooperatively induce the longitudinal relaxation of the water proton, whereas **b** such an effect does not exist in individual Gd(III)−chelates. The interacting and non-interacting Gd(III) ions with a water proton are denoted as *dotted* and *solid arrows* for their spins, respectively. The ligands are drawn arbitrarily. (Reprinted with permission from [155]. Copyright 2009 American Chemical Society)

particle size and r_1, they revealed that surface Gd^{3+} are the major contributors to the relaxivity enhancement, and surface Gd^{3+} on a larger nanoparticle affect the relaxivity more strongly than those on a smaller nanoparticle.

Besides *S/V*, τ_R is another important parameter affecting relaxivity, which is mainly determined by hydrated radii of nanoparticles [157]. For 0D nanomaterials, the τ_R value shortens with decreasing size, counteracting the effect of *S/V* towards relaxivity. Whereas for rare earth based nanomaterials with anisotropic morphology, the effect of *S/V* and τ_R could be consistent, as a result, high relaxivity could be realized through rational design of anisotropic nanoparticles.

For 1D nanostructures, most of the Gd-based nanomaterials have rod-like morphology. Suzuki et al. synthesized dextran coated rod-like $GdPO_4$ nanoparticles, with 20–30 nm in the major axis and 6–15 nm in the minor axis [157]. The nanoparticles showed high r_1 and r_2 values of 13.9 and 15.0 s^{-1} mM^{-1}, respectively, and 1.1 as the r_2/r_1 value at 0.47 T. The tumors in rabbit could be effectively visualized with only 1/10 of the applied dose compared to the clinically used Gd-DTPA [158].

Rod-like $Gd(OH)_3$ nanoparticles with the length of 150 nm were synthesized by Gillis et al., showing r_1 and r_2 of 4.03 and 8.0 s^{-1} mM^{-1}, respectively, at 1.5 T [159]. As the magnetic field increased to 7 T, the r_1 slightly decreased and r_2 increased linearly with the field. Zhao et al. synthesized $GdPO_4$ nanorods (up to $\sim$100 nm in length and $\sim$10 nm in diameter) in the presence of PVP molecules [160]. The r_1 of $GdPO_4$ was 2.08 s^{-1} mM^{-1} at 4.7 T. Size-dependent MRI relaxivity of Eu-doped $GdPO_4$ rod-like nanoparticles was investigated by Talham et al. [161]. They found although ionic molar relaxivity decreases for larger particles, the relaxivity per nanoparticle can be significantly greater. By doping light-emitting lanthanide ions into $GdPO_4$ host matrix, bimodal nanoprobe (luminescent and magnetic) could be obtained.

Tan et al. demonstrated a simple synthetic strategy for the fabrication of Tb and Yb/Er doped Gd_2O_3 nanorods [162]. As refluxing progressed, monodispersed quasi-spherical Gd_2O_3 nanocrystals were produced at first, and then fused into nanorods (18.8 ± 5.7 nm in length). The Yb/Er co-doped Gd_2O_3 nanorods exhibit good T_1-weighted MRI contrast enhancing and upconversion fluorescence properties. They also prepared $NaDyF_4$:Yb^{3+}/$NaGdF_4$:Yb^{3+},Er^{3+} nanorods, with the average diameter and length of 21 and 45 nm, respectively [163]. The r_1 (0.321 s^{-1} mM^{-1}) is quite small, and the presence of Dy^{3+} is inferred to affect the T_1 induced by Gd^{3+}. However the r_2 (437.97 s^{-1} mM^{-1}) is much higher than other reported Dy-based materials, probably due to the additional synergistic contribution of T_2 shortening by the Gd^{3+} sitting adjacent to Dy^{3+} in the nanorods.

Jin et al. reported a facile solvothermal approach to synthesize monodispersed ultrathin GdF_3 nanowires (lengths of 20–40 nm and diameters of *ca.* 2 nm) [164]. The nanowires were formed through assembly of GdF_3 nanocrystals. The surface capping ligands anchored to some specific GdF_3 surfaces selectively, and thus facilitated the oriented attachment along the no (or less) capped crystal planes. After modificated with the surfactant Pluronic F127, the GdF_3 nanowires showed high r_1

of 15.0 s^{-1} mM^{-1} at 7 T. The large length in 1D direction and low symmetry of nonspherical structure prolonged their τ_R compared to 0D nanoparticles, which was believed to be responsible for the high r_1.

2D nanostructures have also been well studied. Murray et al. reported shape-controlled synthesis of Gd_2O_3 tripodal and triangular nanoplates [165]. With an increase of magnetic field strength from 9.4 to 14.1 T, the r_1 of PEI-capped Gd_2O_3 tripodal nanoplates decreased from 1.41 to 0.89 s^{-1} mM^{-1}, and r_2 increased from 140 to 193 s^{-1} mM^{-1}. Reduced spectral density at higher magnetic field strengths results in less efficient dipole-dipole relaxation and a corresponding decrease in r_1. The magnetic moment of paramagnetic nanoparticles is proportional to local magnetic field strength, resulting in more effective dephasing of proton and thus increased r_2 at higher fields.

Colvin et al. synthesized Gd_2O_3 nanoplates via a thermal decomposition method [166]. The nanoplates have a core diameter varying from 2 to 22 nm and a thickness of 1–2 nm. When coated with an octylamine modified poly(acrylic acid) polymer layer, the r_1 of 2 nm Gd_2O_3 nanoplates reached 47.2 s^{-1} mM^{-1} at 1.41 T, about 10 times higher than that of Gd-DTPA.

Li et al. reported the synthesis of lanthanide ion doped $GdVO_4$ tetragonal nanosheets (with a thickness of $\sim$5 nm and a width of $\sim$150 nm) using a facile solvothermal reaction [167, 168]. After the ligand exchange reaction with poly (acrylic acid), the hydrophilic nanosheets showed excellent paramagnetic properties (r_1 reached 37.8 s^{-1} mM^{-1} at 0.5 T). This high r_1 was attributed to the special 2D nanostructure, since most of the Gd^{3+} were exposed on the surface of nanosheets and water-soluble polymer coating may offer a hydrophilic interface between the surface of the nanosheets and water molecules.

Alexandrou et al. synthesized Eu-doped $GdVO_4$ nanoparticles which combine magnetic resonance contrast enhancing properties with luminescence properties and hydrogen peroxide sensing features [169]. The 2D projection of the nanoparticles is an ellipse with the two major axes having lengths of 13.1 ± 1.1 and 26.6 ± 4.8 nm, respectively. The paramagnetic nanoparticles showed high r_1 (8.18 s^{-1} mM^{-1}) and r_2 (9.38 s^{-1} mM^{-1}).

5.3.2.2 Ln^{3+}(Other Than Gd^{3+})-Based Anisotropic Nanostructures as MRI CAs

Currently, the development of MRI is towards high field to further increase the signal-to-noise ratio, and to further improve the temporal and spatial resolution [170]. Unfortunately, the efficiencies of current clinically used CAs are reduced when field strength increased to higher than 3 T [145, 171, 172]. Therefore, CAs with high performance under high magnetic field are in urgent need. Paramagnetic trivalent RE^{3+} ions other than Gd^{3+} are less efficient T_1 relaxation agents, mainly

due to their short electronic relaxation time. However, those paramagnetic RE^{3+} with large magnetic moments (such as Tb^{3+}, Dy^{3+}, Ho^{3+} and Er^{3+}) can induce field inhomogeneities, resulting in transverse relaxation enhancement of protons [173]. The r_2 of lanthanide nanoparticles appeared to be proportional to the magnetic field strength and to the square of the effective moment of the lanthanide [174]. Thus, lanthanide-based nanomaterials hold great potential as T_2 CAs for high field MRI [171, 175].

Same with T_1 CAs, relaxivity properties of T_2 CAs are also believed to be influenced significantly by size and shape. van Veggel et al. synthesized $NaDyF_4$ nanoparticles with different sizes, and studied size dependence of r_2 [176]. They found larger nanoparticles show higher r_2 than smaller ones, and attributed this to spin-canting effects. With the decrease in the nanoparticle size, the *S/V* ratio increases and curvature of nanoparticles becomes more pronounced. Spins located near the surface tend to be slightly tilted, resulting in low magnetization value for small nanoparticles. Zeng et al. reported the synthesis of $NaErF_4$ with different shapes and discussed the shape induced magnetic properties [177]. They speculated that the different shape anisotropy leads to the difference of magnetization, and consequently the rod-like morphology had highest magnetization. After doping with Yb^{3+}, multi-functional $NaErF_4$ nanorods were obtained, combining upconversion emission, X-ray attenuation and negative relaxation enhancement properties [178].

Shen et al. reported Co^{2+}-doped $NaYF_4$:Yb^{3+},Tm^{3+} nanorods (mean width of 19.8 nm and mean length of 33.2 nm) as dual-modality imaging nanoprobes [179]. The r_2 of nanorods was up to 1544 s^{-1} mM^{-1}, due to the doping of Co^{2+}. Except the aforementioned sodium lanthanide fluoride, hydroxides with rod-like morphology have also been reported. Lee et al. reported water-soluble and biocompatible D-glucuronic acid coated $Dy(OH)_3$ nanorods (20 × 300 nm) and $Eu(OH)_3$ nanorods (9.0 × 118.3 nm) [180, 181]. The r_1 and r_2 of $Dy(OH)_3$ was 0.97 and 181.57 s^{-1} mM^{-1} at 1.5 T, respectively, while both of r_1 and r_2 were very small for $Eu(OH)_3$, probably due to the insufficient surface coating. To compensate for the deficiencies of individual imaging modalities, $NaDyF_4$ nanorods coated with α-cyclodextrin and modified with Gd-DTPA were prepared by Liao et al. [182] Dy^{3+} in the host matrix induces a high X-ray attenuation ability for CT and negative enhancement for T_2-weighted MRI (r_2 = 7.68 s^{-1} mM^{-1}), while Gd-DTPA induces positive enhancement for T_1-weighted MRI (r_1 = 4.65 s^{-1} mM^{-1}).

Reports of 2D lanthanide-based nanomaterials as MRI CAs are quite rare, probably due to the relatively large *S/V* ratio, which is unfavorable for T_2 CAs as we discussed above. Lanthanide (Gd, Dy and Yb) oxides nanodisks were produced with high-temperature colloidal syntheses by Helms et al. [183]. These nanodisks were 10–14 nm in diameter with a thickness of a single unit cell. For Dy_2O_3 nanodisks, their r_2 values showed *ca.* 1.7-fold enhancement over Gd-DTPA when passivated with poly(acrylic acid)-methoxy-terminated polyethylene oxides alongside Gd-DTPA at 1.41 T.

5.3.3 Catalytic Application of Rare Earth Anisotropic Nanostructures

The catalytic applications of rare earth nanomaterials draw large attention due to the unique electronic structures as rare earth elements possess 4f orbitals without full electron occupancy and lanthanide contraction. In particular, La and Ce are extensively used as catalyst or catalytic components. Among the compounds of La and Ce, ceria is the most representative catalyst and has been widely used in a number of catalytic reactions. Ceria can uptake and release oxygen owing to the transformation between Ce^{3+} and Ce^{4+} [184]. When the size decreases to nanometer scale, ceria exhibits more excellent performances due to high ratio of atoms exposed and thus high specific area. A large number of researches related to the controllable synthesis and applications of ceria nanomaterials have been conducted in the past decade. Therefore, here in this section, we will mainly focus on nanoceria to demonstrate the properties and applications of rare earth nanomaterials.

5.3.3.1 Basic Properties of Ceria Nanocrystals

As mentioned before, CeO_2 crystals are in fluorite structure, consisting of a face-centered cubic (fcc) unit cell of cations with anions occupying the octahedral interstitial sites [185]. In this structure, each cerium cation is coordinated by eight nearest-neighboring oxygen anions, and each oxygen anion is coordinated by four nearest-neighboring cerium cations. Of note, there exist both +3 and +4 oxidation states for cerium, and the transformation between Ce^{3+} and Ce^{4+} is reversible. Ceria can form a non-stoichiometric oxide (CeO_{2-x}) through releasing or uptaking oxygen at the ambient partial pressure of oxygen, while maintaining the crystal structure [186]. However, owing to the transformation between Ce^{3+} and Ce^{4+}, the discrepancy in the number of atomic neighbors and interatomic distances can cause surface defects in ceria, which is often responsible for the catalytic activity of ceria [17]. The main defect in CeO_2 is the formation of oxygen vacancies. The fluorite structure allows oxygen atoms for rapid diffusion as a function of the number of oxygen vacancies. This character endows ceria nanomaterials the capacity to store and release oxygen. In order to maintain the charge balance, the oxygen vacancies form and disappear during the transformation between Ce^{3+} and Ce^{4+} [187]. Oxygen vacancies can be produced via the following defect reaction:

$$\mathrm{Oo} + 2\mathrm{Ce_{Ce}} = 1/2\mathrm{O_2} + \mathrm{V\ddot{o}} + 2\mathrm{Ce'_{Ce}} \quad (1)$$

in which Ce_{Ce}, Oo, Vö and Ce'_{Ce} represent Ce^{4+}, O^{2-}, oxygen vacancies and Ce^{3+}, respectively. Oxygen vacancies play an important role in the activity of ceria nanomaterials for the various catalytic reactions like CO oxidation [188]. Besides the defect properties, ceria also possesses versatile acid–base properties [189].

The defect and acid–base properties are the bases of catalytic applications of ceria nanomaterials.

There are three low-index lattice planes on the surface of CeO_2 nanocrystals: (100), (110) and (111) [185]. According to density functional theory calculations, their stability follows this sequence: (111) > (110) > (100), while their activity follows the opposite order [190, 191]. And the oxygen vacancies are different on three planes. The energy required to generate oxygen vacancies on (111) plane surface is greater than those on (110) and (100) plane surfaces. Therefore, (110) and (100) planes in ceria are favorable in catalytic reactions owing to more vacancies. Generally, the shape of CeO_2 will determine the exposed lattice planes. For example, ceria nanoparticles consisting of octahedra or truncated octahedral shapes mainly expose the most stable (111) facets, while nanorods can be enclosed by (110) and (100) planes, and nanocubes can expose (100) planes. So there are more oxygen vacancies on the surface of nanorods and nanocubes. In view of the intrinsic activity of different planes, the catalytic performance and applications are considered to be closely linked to morphologies of ceria nanomaterials. Recently, ceria nanomaterials have been applied in a number of catalytic reactions, such as carbon monoxide (CO) oxidation, photocatalysis, organic chemistry and bio-anti-oxidation.

5.3.3.2 Catalysis for CO Oxidation

Ceria nanomaterials have been extensively applied in heterogeneous catalysis based on its ability to release and uptake oxygen [192]. CO oxidation is a simple but most extensively studied reaction in heterogeneous catalytic reaction. The reports on catalytic application of ceria nanomaterials for CO oxidation are abundant. Recently, the morphology-dependent catalytic properties of ceria nanomaterials have been investigated including 0D nanostructures (nanocube [193, 194], nanopolyhedron [194]), 1D nanostructures (nanowire [193, 195], nanorod [193, 196], nanotube [193, 196]) and 2D nanostructures (nanoplate [196]).

The morphology-dependent activities toward CO oxidation of ceria nanomaterials are essential for developing advanced catalysts. The activities of ceria toward CO oxidation are regulated through controlling morphologies by the modulation of specific area, exposed facets and oxygen vacancies. Ceria nanomaterials with high specific area which have more active sites show superior catalytic performance [197]. For example, Li et al. [197] prepared CeO_2 hollow spheres via a layer-by-layer method and observed the activity of the CeO_2 hollow spheres was higher than that of the non-hollow counterpart. Furthermore, CeO_2 nanotube also exhibited better catalytic performance in CO oxidation due to the exposed inner and outer surface [198]. Therefore, multifold ceria nanomaterials with high specific area were investigated so as to design favorable catalyst, such as spindle-like CeO_2 [198], platelet-like CeO_2 [199] and mesoporous CeO_2 [200].

However, specific area is not the sole factor influencing the catalytic activity toward CO oxidation. For example, Zhou et al. [22] reported that single CeO_2

nanorods are more active for CO oxidation than irregular nanoparticles. The higher activity was attributed to more exposed reactive crystal planes (100) and (110). Recently, morphology-controlled synthesis of ceria nanomaterials, such as nanocubes, 1D nanomaterials (wire, rods and tubes) and 2D nanomaterials (plates), provide an opportunity for designing excellent catalytic materials with desirable exposed planes. For example, Yan et al. [24] focused on the shape-dependent oxygen storage capacity of ceria nanocrystals with various shapes (nanopolyhedra, exposing (111) and (100); nanorods, (110) and (100), and nanocubes, (100)). The results showed that nanorods and nanocubes were more active than nanopolyhedra. Therefore, the design of highly active catalyst with well-defined crystal planes has been attractive and challenging in CO oxidation. Wu et al. [201, 202] investigated CO oxidation over ceria nanocrystals with defined surface planes including rods, cubes, and octahedra. They revealed that the reducibility of these ceria nanoparticles is in accordance with their CO oxidation activity, following the sequence: rods > cubes > octahedral. In addition, the intrinsic factor for this order was surface oxygen vacancies on different planes. The redox activity of ceria is proposed to be controlled by the nature of the oxygen vacancies which is critical for ceria catalysis. Wu et al. [201] probed defect sites on CeO_2 nanocrystals with well-defined surface planes by Raman spectroscopy and O_2 adsorption. They observed nanorods have the most abundant intrinsic defect sites, followed by nanocubes and nanooctahedra when ceria was oxidized. In addition, when ceria was reduced, more defect sites induced are clustered on nanorods than on nanocubes. However, very few defect sites can be generated on the nanooctahedra due to its lowest reducibility. Moreover, increasing the proportion of active planes is an efficient approach for enhancing the catalytic activity. Both CeO_2 nanorods and CeO_2 nanowires prepared by Tana et al. [203] predominantly exposed the reactive {110} and {100} planes. However, the CeO_2 nanowires exhibited higher activity for CO oxidation than nanorods because CeO_2 nanowires expose a larger proportion of active planes on the surface. Other 1D and 2D ceria nanomaterials were also assessed in CO oxidation, such as CeO_2 nanotubes, spindle-like CeO_2, platelet-like CeO_2, CeO_2 nanoplates. The CO oxidation properties of nanorods, nanoplates, and nanotubes were investigated by Pan et al. [14]. They observed an enhanced catalytic activity for CeO_2 nanoplates compared with CeO_2 nanotubes and nanorods, and the crystal surfaces (100) of CeO_2 nanoplates were considered to play an important role in determining their catalytic oxidation properties.

In addition, even if the morphology of ceria is the same, the activity can be modulated by synthetic conditions. For example, Liu et al. [188] prepared two nanorod samples by changing the precursor. Sample A with exposed (100) and (111) facets showed lower activity than Sample B with exposed (100) and (110) facets. The difference could be attributed to the difference of oxygen defects. Therefore, in summary, the activity of nanoceria for CO oxidation is dependent on the morphology, due to the differences in specific area, exposed planes and oxygen vacancies.

5.3.3.3 Photocatalysis

The researches regarding to photocatalytic applications of ceria nanomaterials are mainly focused on the degradation of organic pollutants, including methylene blue, methyl orange, Congo red and so on [204–207]. For example, Lu et al. [206] reported the application of ceria nanowire in removing the Congo red. In addition, ceria nanomaterials also exhibit activity in photolysis of water [208]. Lu et al. [208] observed that CeO_2 nanorods with (110) planes showed considerable photocatalytic activity for hydrogen evolution due to their redox capacity.

5.3.3.4 Catalysis of Organic Chemistry Reactions

The redox and acid–base properties of ceria are important factors that allow for activating complex organic molecules and selectively orienting their transformation [189]. Sato's group conducted significant research on catalytic application of ceria nanomaterials in organic synthesis, including alcohol dehydration reaction, alkylation reaction, condensation reaction and so on. For example, they reported CeO_2 (111) facets have active sites for the reactions of butanediols and of propanoic acid [209]. In addition, ceria nanomaterials also exhibit excellent catalytic properties in redox organic reaction. Lv et al. [210] reported that CeO_2 nanocube with exposed (100) facets showed exclusive selectivity for the oxidation of toluene to benzaldehydes in liquid phase by O_2. CeO_2 nanoplates prepared by Zhang et al. can selectively catalyze the reduction of nitro-aromatic compounds [211, 212].

5.3.3.5 Catalysis for Anti-oxidation

Recently, ceria nanomaterials attract large attention as an excellent anti-oxidant due to the reversible conversion between Ce^{3+} and Ce^{4+} [213]. It was reported that ceria nanomaterials can promote the decomposition of superoxide anion ($O_2^{\bullet -}$), hydrogen peroxide (H_2O_2) and hydroxyl radical [213–215]. Biologically, owing to the oxygen defects on the surface acting as sites for free radical scavenging, ceria nanoparticles exhibit excellent anti-oxidation performance in protecting cells from radiation, inflammation, ischemic strokes and so on [26, 216–218]. Kim et al. reported that ceria nanoparticles can protect against ischemic stroke [216]. Chen et al. showed that nanoceria particles can prevent increases in the intracellular concentrations of ROIs in primary cell cultures of rat retina and, in vivo, prevent loss of vision due to light-induced degeneration of photoreceptor cells [217]. The results reported by Nel et al. showed that CeO_2 nanoparticles can suppress the generation of reactive oxygen species (ROS) production, induce cellular resistance to an exogenous source of oxidative stress and protect cells from oxidant injury [218].

Most published studies show that nanoceria is well tolerated in living organisms. However, the bio-response was closely linked to the morphology of ceria.

Therefore, the bio-safety of ceria nanomaterials with particular morphology should be concerned, such as nanorods. Nel group conducted the systematic study about the effect of aspect ratio (R) of ceria nanorods on lysosomal damage, cytotoxicity, and 1L-1β production by the human myeloid cell line (THP-1) [26]. Their results showed that short CeO_2 nanorods with R = 1–16 were nontoxic. The nanorods with intermediary aspect ratios (R = 22, 31) did not cause any obvious cell death but did induce IL-1β production. The two nanowire samples with the highest aspect ratio led to significant IL-1β release as well as cell death. They also performed comparative studies in mouse and gastrointestinal tract (GIT) of zebrafish larvae in order to verify this toxicological paradigm for large-aspect-ratio CeO_2 nanoparticles [219].

5.3.3.6 Other Applications

Ceria as catalyst is also applied in other catalytic reactions, such as steam reforming [220], reduction of nitrogen oxide [221], gas sensitivity [222] and so on. Han et al. studied the application of CeO_2 nanotubes in steam reforming reaction [220], and observed that CeO_2 nanotubes showed higher activity than bulk CeO_2. In addition, rare earth composite nanomaterials are also widely used in industrial catalysis acting as catalyst. Besides acting as the active component in catalytic field, CeO_2 possess extensive applications acting as support. For example, the composite catalyst, consisting of CeO_2 and noble metal, was applied in three way catalyst, CO oxidation, reforming reaction, water–gas shift reaction, NO reduction and so on [223–227].

5.4 Perspective

The research field of rare earth based anisotropic nanomaterials has witnessed a rapid development during the past few decades, due to their rich interests in numerous applications. Though tremendous success has been achieved, a few scientific challenges are yet to be addressed:

(1) Synthesis mechanism. The synthesis mechanism for plenty of systems remain unclear or ambiguous, or simply still in the phase of presumption. This issue is largely owing to the lack of powerful, in situ and real-time characterization tools to monitor and document the reaction process. Therefore, developing some general and highly sensitive on-line monitoring methodologies is urgently necessary for investigating the synthesis mechanism. And undoubtedly, a more in-depth understanding of the synthesis mechanism would help scientists to design synthetic routes for nanostructures with desired morphologies, even those thermodynamically unfavorable ones.

(2) Synthetic methods. The synthetic methods developed so far generally require stringent conditions, such as high temperature, high pressure and inert gas atmosphere. In addition, quite a few methods have to be conducted in non-aqueous solutions, affording nanoparticles with strong hydrophobicity and poor biocompatibility. And up to date, most synthetic procedures are performed only in the lab in small batches, and can hardly be scaled up to an industrially relevant level. Therefore, the research field still calls for advanced synthetic methods that are green, facile, high-throughput, and readily scalable.
(3) Defect management. Defects in/on nanocrystals are inevitable, and can have both positive and negative effects. For optical applications, it is generally expected that the phosphors should possess good crystallinity and minimal defects, and display high luminescence efficiency; whereas for catalysis applications, defects in/on nanocrystals can usually serve as active catalytic sites owing to their inherent high-energy states. Therefore, it is still desired to develop novel methods for effectively annihilating or generating defects in/on nanocrystals, whether during or after the synthesis.

References

1. Q. Su, *Rare Earth Chemistry* (Henan Science and Technology Press, Zhengzhou, 1993)
2. G.X. Xu (ed.), *Rare Earth*, vol. 1. (Metallurgical Industry Press, Beijing, 1995)
3. G.H. Liu (ed.), *Rare Earth Materials Science* (Chemical Industry Press, Beijing, 2007)
4. G. Brunton, The crystal structure of KBF_4. J. Am. Chem. Soc. **25**, 2161–2162 (1969)
5. J.H. Burns, Crystal structure of hexagonal sodium neodymium fluoride and related compounds. Inorg. Chem. **6**, 881–886 (1965)
6. R.E. Thoma, C.F. Weaver, H.A. Friedman, Phase equilibria in the system LiF-YF3. J. Phys. Chem. **65**, 1096–1099 (1961)
7. R.E. Thoma, H. Insley, G.M. Hebert, The sodium fluoride-lanthanide trifluride systems. Inorg. Chem. **7**, 1222–1229 (1966)
8. Q. Su (ed.), *Rare Earth Chemistry* (Henan Science and Technology Press, Zhengzhou, 1993)
9. K.A. Gschneidner (ed.), *Handbook on the Physics and Chemistry of Rare Earths* (Elsevier, Amsterdam, 2011)
10. M.S. Wickleder, Inorganic lanthanide compounds with complex anions. Chem. Rev. **102**, 2011–2087 (2002)
11. C.H. Yan, Z.G. Yan, Y.P. Du, J. Shen, C. Zhang, W. Feng, L.D. Sun, Y.W. Zhang, *Handbook on the Physics and Chemistry of Rare Earths*, vol. 999. Controlled Synthesis and Properties of Rare Earth Based Nanomaterials (Elsevier, 2009)
12. C.H. Yan, C. Zhang, L.D. Sun, *Rare Earth Nanotechnology*. Synthesis of Rare Earth Nanomaterials (Pan Stanford Publishing Pte. Ltd., 2012)
13. Y. Xia, P. Yang, Y. Sun, Y. Wu, B. Mayers, B. Gates, Y. Yin, F. Kim, H. Yan, One-dimensional nanostructures: synthesis, characterization, and applications. Adv. Mater. **15**, 353–389 (2003)
14. Y.W. Jun, J.S. Choi, J. Cheon, Shape control of semiconductor and metal oxide nanocrystals through nonhydrolytic colloidal routes. Angew. Chem. Int. Ed. **45**, 3414–3439 (2006)
15. Z.G. Yan, C.H. Yan, Controlled synthesis of rare earth nanostructures. J. Mater. Chem. **18**, 5046–5059 (2008)

16. Q. Yuan, H.H. Duan, L.L. Li, L.D. Sun, Y.W. Zhang, C.H. Yan, Controlled synthesis and assembly of ceria-based nanomaterials. J. Colloid Interface Sci. **335**, 151–167 (2009)
17. C.W. Sun, H. Li, L.Q. Chen, Nanostructured ceria-based materials: synthesis, properties, and applications. Energy Environ. Sci. **5**, 8475–8505 (2012)
18. R.J. La, Z.A. Hu, H.L. Li, X.L. Shang, Y.Y. Yang, Template synthesis of CeO_2 ordered nanowire arrays. Mater. Sci. Eng. A **368**, 145–148 (2004)
19. G.S. Wu, T. Xie, X.Y. Yuan, B.C. Cheng, L.D. Zhang, An improved sol–gel template synthetic route to large-scale CeO_2 nanowires. Mater. Res. Bull. **39**, 1023–1028 (2004)
20. L. González-Rovira, J.M. Sánchez-Amaya, M. López-Haro, E. del Rio, A.B. Hungría, P. Midgley, J.J. Calvino, S. Bernal, F.J. Botana, Single-step process to prepare CeO_2 nanotubes with improved catalytic activity. Nano Lett. **9**, 1395–1400 (2009)
21. C.W. Sun, H. Li, H.R. Zhang, Z.X. Wang, L.Q. Chen, Controlled synthesis of CeO_2 nanorods by a solvothermal method. Nanotechnology **16**, 1454–1463 (2005)
22. K. Zhou, X. Wang, X. Sun, Q. Peng, Y. Li, Enhanced catalytic activity of ceria nanorods from well-defined reactive crystal planes. J. Catal. **229**, 206–212 (2005)
23. A. Vantomme, Z.Y. Yuan, G.H. Du, B.L. Su, Surfactant-assisted large-scale preparation of crystalline CeO_2 nanorods. Langmuir **21**, 1132–1135 (2005)
24. H.X. Mai, L.D. Sun, Y.W. Zhang, R. Si, W. Feng, H.P. Zhang, H.C. Liu, C.H. Yan, Shape-selective synthesis and oxygen storage behavior of ceria nanopolyhedra, nanorods, and nanocubes. J. Phys. Chem. B **109**, 24380–24385 (2005)
25. J. Ke, J.W. Xiao, W. Zhu, H. Liu, R. Si, Y.W. Zhang, C.H. Yan, Dopant-induced modification of active site structure and surface bonding mode for high-performance nanocatalysts: CO oxidation on capping-free (110)-oriented CeO_2: Ln (Ln = La-Lu) nanowires. J. Am. Chem. Soc. **135**, 15191–15200 (2013)
26. Z. Ji, X. Wang, H. Zhang, S. Lin, H. Meng, B. Sun, S. George, T. Xia, A.E. Nel, J.I. Zink, Designed synthesis of CeO_2 nanorods and nanowires for studying toxicological effects of high aspect ratio nanomaterials. ACS Nano **6**, 5366–5380 (2012)
27. S. Iijima, Helical microtubules of graphitic carbon. Nature **354**, 56–58 (1991)
28. W.Q. Han, L. Wu, Y. Zhu, Formation and oxidation state of CeO_{2-x} nanotubes. J. Am. Chem. Soc. **127**, 12814–12815 (2005)
29. K. Zhou, Z. Yang, S. Yang, Highly reducible CeO_2 nanotubes. Chem. Mater. **19**, 1215–1217 (2007)
30. J.Y. Chane-Ching, F. Cobo, D. Aubert, H.G. Harvey, M. Airiau, A. Corma, A general method for the synthesis of nanostructured large-surface-area materials through the self-assembly of functionalized nanoparticles. Chem. Eur. J. **11**, 979–987 (2005)
31. A.S. Karakoti, S.V.N.T. Kuchibhatla, D.R. Baer, S. Thevuthasan, D.C. Sayle, S. Seal, Self-assembly of cerium oxide nanostructures in ice molds. Small **4**, 1210–1216 (2008)
32. R. Si, Y.W. Zhang, L.P. You, C.H. Yan, Self-organized monolayer of nanosized ceria colloids stabilized by poly(vinylpyrrolidone). J. Phys. Chem. B **110**, 5994–6000 (2006)
33. Q. Yuan, Q. Liu, W.G. Song, W. Feng, W.L. Pu, L.D. Sun, Y.W. Zhang, C.H. Yan, Ordered mesoporous $Ce_{1-x}Zr_xO_2$ solid solutions with crystalline walls. J. Am. Chem. Soc. **129**, 6698–6699 (2007)
34. H. Wang, Q.L. Huang, J.M. Hong, X.T. Chen, Z.L. Xue, Selective synthesis and characterization of nanocrystalline EuF_3 with orthorhombic and hexagonal structures. Cryst. Growth Des. **6**, 1972–1974 (2006)
35. H. Wang, Q.L. Huang, J.M. Hong, X.T. Chen, Z.L. Xue, Controlled synthesis and characterization of nanostructured EuF_3 with different crystalline phases and morphologies. Cryst. Growth Des. **6**, 2169–2173 (2006)
36. X. Wang, J. Zhuang, Q. Peng, Y.D. Li, Hydrothermal synthesis of rare-earth fluoride nanocrystals. Inorg. Chem. **45**, 6661–6665 (2006)
37. X. Liang, X. Wang, J. Zhuang, Q. Peng, Y.D. Li, Synthesis of $NaYF_4$ nanocrystals with predictable phase and shape. Adv. Funct. Mater. **17**, 2757–2765 (2007)
38. X. Liang, X. Wang, J. Zhuang, Q. Peng, Y.D. Li, Branched $NaYF_4$ nanocrystals with luminescent properties. Inorg. Chem. **46**, 6050–6055 (2007)

39. L.Y. Wang, P. Li, Y.D. Li, Down- and up-conversion luminescent nanorods. Adv. Mater. **19**, 3304–3307 (2007)
40. J.H. Zeng, J. Su, Z.H. Li, R.X. Yan, Y.D. Li, Synthesis and upconversion luminescence of hexagonal-phase $NaYF_4$:Yb, Er^{3+} phosphors of controlled size and morphology. Adv. Mater. **17**, 2119–2123 (2005)
41. M.F. Zhang, H. Fan, B.J. Xi, X.Y. Wang, C. Dong, Y.T. Qian, Synthesis, characterization, and luminescence properties of uniform Ln^{3+}-doped YF_3 nanospindles. J. Phys. Chem. C **111**, 6652–6657 (2007)
42. F. Zhang, Y. Wan, T. Yu, F.Q. Zhang, Y.F. Shi, S.H. Xie, Y.G. Li, L. Xu, B. Tu, D.Y. Zhao, Uniform nanostructured arrays of sodium rare-earth fluorides for highly efficient multicolor upconversion luminescence. Angew. Chem. Int. Ed. **46**, 7976–7979 (2007)
43. H.X. Mai, Y.W. Zhang, R. Si, Z.G. Yan, L.D. Sun, L.P. You, C.H. Yan, High-quality sodium rare-earth fluoride nanocrystals: controlled synthesis and optical properties. J. Am. Chem. Soc. **128**, 6426–6436 (2006)
44. Y.P. Du, Y.W. Zhang, Z.G. Yan, L.D. Sun, C.H. Yan, Highly luminescent self-organized sub-2-nm EuOF nanowires. J. Am. Chem. Soc. **131**, 16364–16365 (2009)
45. Z.G. Yan, Y.W. Zhang, L.P. You, R. Si, C.H. Yan, General synthesis and characterization of monocrystalline 1D-nanomaterials of hexagonal and orthorhombic lanthanide orthophosphate hydrate. J. Cryst. Growth **262**, 408–414 (2004)
46. Y.W. Zhang, Z.G. Yan, L.P. You, R. Si, C.H. Yan, General synthesis and characterization of monocrystalline lanthanide orthophosphate nanowires. Eur. J. Inorg. Chem. **2003**, 4099–4104 (2003)
47. H. Meyssamy, K. Riwotzki, A. Kornowski, S. Naused, M. Haase, Wet-chemical synthesis of doped colloidal nanomaterials: particles and fibers of $LaPO_4$:Eu, $LaPO_4$:Ce, and $LaPO_4$:Ce, Tb. Adv. Mater. **11**, 840–844 (1999)
48. M. Yang, H. You, K. Liu, Y. Zheng, N. Guo, H. Zhang, Low-temperature coprecipitation synthesis and luminescent properties of $LaPO_4$:Ln^{3+}(Ln^{3+}=Ce^{3+}, Tb^{3+}) nanowires and $LaPO_4$:Ce^{3+}, Tb^{3+}/$LaPO_4$ core/shell nanowires. Inorg. Chem. **49**, 4996–5002 (2010)
49. W.H. Di, X.X. Zhao, S.Z. Lu, X.J. Wang, H.F. Zhao, Thermal and photoluminescence properties of hydrated YPO_4:Eu^{3+} nanowires. J. Solid State Chem. **180**, 2478–2484 (2007)
50. R.X. Yan, Y.D. Li, Down/up conversion in Ln^{3+}-Doped YF_3 nanocrystals. Adv. Funct. Mater. **15**, 763–770 (2005)
51. Y.P. Fang, A.W. Xu, R.Q. Song, H.X. Zhang, L.P. You, J.C. Yu, H.Q. Liu, Systematic synthesis and characterization of single-crystal lanthanide orthophosphate nanowires. J. Am. Chem. Soc. **125**, 16025–16034 (2003)
52. Y.P. Fang, A.W. Xu, A.M. Qin, R.J. Yu, Selective synthesis of hexagonal and tetragonal dysprosium orthophosphate nanorods by a hydrothermal method. Cryst. Growth Des. **5**, 1221–1225 (2005)
53. W.B. Bu, H.R. Chen, Z.L. Hua, Z.C. Liu, W.M. Huang, L.X. Zhang, J.L. Shi, Surfactant-assisted synthesis of Tb(III)-doped cerium phosphate single-crystalline nanorods with enhanced green emission. Appl. Phys. Lett. **85**, 4307–4309 (2004)
54. W.B. Bu, L.X. Zhang, Z.L. Hua, H.R. Chen, J.L. Shi, Synthesis and characterization of uniform spindle-shaped microarchitectures self-assembled from aligned single-crystalline nanowires of lanthanum phosphates. Cryst. Growth Des. **7**, 2305–2309 (2007)
55. Y. Xing, M. Li, S.A. Davis, S. Mann, Synthesis and characterization of cerium phosphate nanowires in microemulsion reaction media. J. Phys. Chem. B **110**, 1111–1113 (2006)
56. P. Ghosh, J. Oliva, E. De la Rosa, K.K. Haldar, D. Solis, A. Patra, Enhancement of upconversion emission of $LaPO_4$:Er@Yb core−shell nanoparticles/nanorods. J. Phys. Chem. C **112**, 9650–9658 (2008)
57. Z.Y. Huo, C. Chen, D. Chu, H.H. Li, Y.D. Li, Systematic synthesis of lanthanide phosphate nanocrystals. Chem. Eur. J. **13**, 7708–7714 (2007)
58. H.X. Mai, Y.W. Zhang, L.D. Sun, C.H. Yan, Orderly aligned and highly luminescent monodisperse rare-earth orthophosphate nanocrystals synthesized by a limited anion-exchange reaction. Chem. Mater. **19**, 4514–4522 (2007)

59. G.C. Li, K. Chao, H.R. Peng, K.Z. Chen, Z.K. Zhang, Facile synthesis of $CePO_4$ nanowires attached to CeO_2 octahedral micrometer crystals and their enhanced photoluminescence properties. J. Phys. Chem. C **112**, 16452–16456 (2008)
60. W.L. Fan, W. Zhao, L.P. You, X.Y. Song, W.M. Zhang, H.Y. Yu, S.X. Sun, A simple method to synthesize single-crystalline lanthanide orthovanadate nanorods. J. Solid State Chem. **177**, 4399–4403 (2004)
61. C.J. Jia, L.D. Sun, Z.G. Yan, Y.C. Pang, S.Z. Lü, C.H. Yan, Monazite and zircon type $LaVO_4$:Eu nanocrystals-synthesis, luminescent properties, and spectroscopic identification of the Eu^{3+} sites. Eur. J. Inorg. Chem. **18**, 2626–2635 (2010)
62. C.J. Jia, L.D. Sun, F. Luo, X.C. Jiang, L.H. Wei, C.H. Yan, Structural transformation induced improved luminescent properties for $LaVO_4$: Eu Nanocrystals. Appl. Phys. Lett. **84**, 5305–5307 (2004)
63. C.J. Jia, L.D. Sun, L.P. You, X.C. Jiang, F. Luo, Y.C. Pang, C.H. Yan, Selective synthesis of monazite- and zircon-type $LaVO_4$ nanocrystals. J. Phys. Chem. B **109**, 3284–3290 (2005)
64. W.L. Fan, X.Y. Song, S.X. Sun, X. Zhao, Microemulsion-mediated hydrothermal synthesis and characterization of zircon-type $LaVO_4$ nanowires. J. Solid State Chem. **180**, 284–290 (2007)
65. K.S. Novoselov, A.K. Geim, S.V. Morozov, D. Jiang, Y. Zhang, S.V. Dubonos, I.V. Grigorieva, A.A. Firsov, Electric field effect in atomically thin carbon films. Science **306**, 666–669 (2004)
66. H. Li, J. Wu, Z. Yin, H. Zhang, Preparation and applications of mechanically exfoliated single-layer and multilayer MoS_2 and WSe_2 nanosheets. Acc. Chem. Res. **47**, 1067–1075 (2014)
67. M. Chhowalla, H.S. Shin, G. Eda, L.-J. Li, K.P. Loh, H. Zhang, The chemistry of two-dimensional layered transition metal dichalcogenide nanosheets. Nat. Chem. **5**, 263–275 (2013)
68. Q.H. Wang, K. Kalantar-Zadeh, A. Kis, J.N. Coleman, M.S. Strano, Electronics and optoelectronics of two-dimensional transition metal dichalcogenides. Nat. Nano. **7**, 699–712 (2012)
69. H. Imagawa, S.H. Sun, Controlled synthesis of monodisperse CeO_2 nanoplates developed from assembled nanoparticles. J. Phys. Chem. C **116**, 2761–2765 (2012)
70. X.H. Guo, C.C. Mao, J. Zhang, J. Huang, W.N. Wang, Y.H. Deng, Y.Y. Wang, Y. Cao, W. X. Huang, S.H. Yu, Cobalt-doping-induced synthesis of ceria nanodisks and their significantly enhanced catalytic activity. Small **8**, 1515–1520 (2012)
71. R. Si, Y.W. Zhang, L.P. You, C.H. Yan, Rare-earth oxide nanopolyhedra, nanoplates, and nanodisks. Angew. Chem. Int. Ed. **44**, 3256–3260 (2005)
72. R. Si, Y.W. Zhang, H.P. Zhou, L.D. Sun, C.H. Yan, Controlled-synthesis, self-assembly behavior, and surface-dependent optical properties of high-quality rare-earth oxide nanocrystals. Chem. Mater. **19**, 18–27 (2006)
73. D. Wang, Y. Kang, V. Doan-Nguyen, J. Chen, R. Küngas, N.L. Wieder, K. Bakhmutsky, R.J. Gorte, C.B. Murray, Synthesis and oxygen storage capacity of two-dimensional ceria nanocrystals. Angew. Chem. Int. Ed. **50**, 4378–4381 (2011)
74. T. Yu, B. Lim, Y. Xia, Aqueous-phase synthesis of single-crystal ceria nanosheets. Angew. Chem. Int. Ed. **49**, 4484–4487 (2010)
75. Y. Sun, Q. Liu, S. Gao, H. Cheng, F. Lei, Z. Sun, Y. Jiang, H. Su, S. Wei, Y. Xie, Pits confined in ultrathin cerium(IV) oxide for studying catalytic centers in carbon monoxide oxidation. Nat. Commun. **4**, 2899–2907 (2013)
76. H. Hu, Z.G. Chen, T.Y. Cao, Q. Zhang, M.G. Yu, F.Y. Li, T. Yi, C.H. Huang, Hydrothermal synthesis of hexagonal lanthanide-doped LaF_3 nanoplates with bright upconversion luminescence. Nanotechnology **19**, 375702 (2008)
77. Y.W. Zhang, X. Sun, R. Si, L.P. You, C.H. Yan, Single-crystalline and monodisperse LaF_3 triangular nanoplates from a single-source precursor. J. Am. Chem. Soc. **127**, 3260–3261 (2005)

78. Y.P. Du, Y.W. Zhang, L.D. Sun, C.H. Yan, Atomically efficient synthesis of self-assembled monodisperse and ultrathin lanthanide oxychloride nanoplates. J. Am. Chem. Soc. **131**, 3162–3163 (2009)
79. H.P. Zhou, C. Zhang, C.H. Yan, Controllable assembly of diverse rare-earth nanocrystals via the Langmuir-Blodgett technique and the underlying size- and symmetry-dependent assembly kinetics. Langmuir **25**, 12914–12925 (2009)
80. L.W. Qian, J. Zhu, Z. Chen, Y.C. Gui, Q. Gong, Y.P. Yuan, J.T. Zai, X.F. Qian, Self-assembled heavy lanthanide orthovanadate architecture with controlled dimensionality and morphology. Chem. Eur. J. **15**, 1233–1240 (2009)
81. J.F. Liu, Y.D. Li, Synthesis and self-assembly of luminescent Ln^{3+}-doped $LaVO_4$ uniform nanocrystals. Adv. Mater. **19**, 1118–1122 (2007)
82. J.F. Liu, Y.D. Li, General synthesis of colloidal rare earth orthovanadate nanocrystals. J. Mater. Chem. **17**, 1797–1803 (2007)
83. J.-C.G. Bünzli, C. Piguet, Taking advantage of luminescent lanthanide ions. Chem. Soc. Rev. **34**, 1048–1077 (2009)
84. J. Shen, L.D. Sun, C.H. Yan, Luminescent rare earth nanomaterials for bioprobe applications. Dolton Trans. **42**, 5687–5697 (2008)
85. S. Ye, F. Xiao, Y.X. Pan, Y.Y. Ma, Q.Y. Zhang, Phosphors in phosphor-converted white light-emitting diodes: recent advances in materials, techniques and properties. Mater. Sci. Eng. A **71**, 1–34 (2010)
86. J.W. Stouwdam, F.C.J.M. van Veggel, Near-infrared emission of redispersible Er^{3+}, Nd^{3+}, and Ho^{3+} doped LaF_3 nanoparticles. Nano Lett. **7**, 733–737 (2002)
87. J. Shen, L.D. Sun, J.D. Zhu, L.H. Wei, H.F. Sun, C.H. Yan, Biocompatible bright YVO_4: Eu nanoparticles as versatile optical bioprobes. Adv. Funct. Mater. **20**, 3708–3714 (2010)
88. C.-J. Carling, F. Nourmohammadian, J.-C. Boyer, N.R. Branda, Remote-control photorelease of caged compounds using near-infrared light and upconverting nanoparticles. Angew. Chem. Int. Ed. **49**, 3782–3785 (2010)
89. L.T. Su, S.K. Karuturi, J.S. Luo, L.J. Liu, X.F. Liu, J. Guo, T.C. Sum, R.R. Deng, H.J. Fan, X.G. Liu, A.L.Y. Tok, Photon upconversion in hetero-nanostructured photoanodes for enhanced near-Infrared light harvesting. Adv. Mater. **25**, 1603–1607 (2013)
90. W.-Y. Huang, F. Yoshimura, K. Ueda, Y. Shimomura, H.-S. Sheu, T.-S. Chan, H.F. Greer, W.Z. Zhou, S.-F. Hu, R.-S. Liu, J.P. Attfield, Nanosegregation and neighbor-cation control of photoluminescence in carbidonitridosilicate phosphors. Angew. Chem. Int. Ed. **52**, 8012–8016 (2013)
91. Z.H. Xu, X.J. Kang, C.X. Li, Z.Y. Hou, C.M. Zhang, D.M. Yang, G.G. Li, J. Lin, Ln^{3+} (Ln = Eu, Dy, Sm, and Er) ion-doped YVO4 nano/microcrystals with multiform morphologies: hydrothermal synthesis, growing mechanism, and luminescent properties. Inorg. Chem. **49**, 6706–6715 (2010)
92. X.G. Zhang, L.Y. Zhou, Q. Pang, J.X. Shi, M.L. Gong, Tunable luminescence and $Ce^{3+} \rightarrow Tb^{3+} \rightarrow Eu^{3+}$ energy transfer of broadband-excited and narrow line red emitting Y_2SiO_5:Ce^{3+}, Tb^{3+}, Eu^{3+} Phosphor. J. Phys. Chem. C **118**, 7591–7598 (2014)
93. Y.S. Liu, S.Y. Zhou, D.T. Tu, Z. Chen, M.D. Huang, H.M. Zhu, E. Ma, X.Y. Chen, Amine-functionalized lanthanide-doped zirconia nanoparticles: optical spectroscopy, time-resolved fluorescence resonance energy transfer biodetection, and targeted imaging. J. Am. Chem. Soc. **134**, 15083–15090 (2012)
94. Q.Y. Zhang, X.Y. Huang, Recent progress in quantum cutting phosphors. Prog. Mater Sci. **55**, 353–427 (2010)
95. R.T. Wegh, H. Donker, K.D. Oskam, A. Meijerink, Visible quantum cutting in $LiGdF_4$:Eu^{3+} through downconversion. Science **283**, 663–666 (1999)
96. B.M. van der Ende, L. Aarts, A. Meijerink, Lanthanide ions as spectral converters for solar cells. Phys. Chem. Chem. Phys. **11**, 11081–11095 (2009)
97. F. Auzel, Upconversion and anti-stokes processes with f and d ions in solids. Chem. Rev. **104**, 139–173 (2004)

98. F. Wang, X.G. Liu, Recent advances in the chemistry of lanthanide-doped upconversion nanocrystals. Chem. Soc. Rev. **38**, 976–989 (2009)
99. M. Haase, H. Schäfer, Upconverting nanoparticles. Angew. Chem. Int. Ed. **50**, 5808–5829 (2011)
100. H. Dong, L.D. Sun, C.H. Yan, Basic understanding of the lanthanide related upconversion emissions. Nanoscale **5**, 5703–5714 (2013)
101. N. Menyuk, K. Dwight, J.W. Pierce, NaYF4:Yb, Er-an efficient upconversion phosphor. Appl. Phys. Lett. **21**, 159–161 (1972)
102. S. Heer, K. Krömpe, H.-U. Güdel, M. Haase, Highly efficient multicolor upconversion emission in transparent colloids of lanthanide-doped $NaYF_4$ nanocrystals. Adv. Mater. **16**, 2102–2105 (2004)
103. G.F. Wang, Q. Peng, Y.D. Li, Upconversion luminescence of monodisperse CaF_2:Yb^{3+}/Er^{3+} nanocrystals. J. Am. Chem. Soc. **131**, 14200–14201 (2010)
104. H.X. Mai, Y.W. Zhang, L.D. Sun, C.H. Yan, Highly efficient multicolor up-conversion emissions and their mechanisms of monodisperse NaYF4:Yb, Er core and core/shell-structured nanocrystals. J. Phys. Chem. C **111**, 13721–13729 (2007)
105. J.C. Boyer, F. Vetrone, J.A. Capobianco, A. Speghini, M. Bettinelli, Yb^{3+} ion as a sensitizer for the upconversion luminescence in nanocrystalline $Gd_3Ga_5O_{12}$:Ho^{3+}. Chem. Phys. Lett. **390**, 403–407 (2004)
106. A.X. Yin, Y.W. Zhang, L.D. Sun, C.H. Yan, Colloidal synthesis and blue based multicolor upconversion emissions of size and composition controlled monodisperse hexagonal $NaYF_4$: Yb, Tm nanocrystals. Nanoscale **2**, 953–959 (2010)
107. J.J. Zhou, G.X. Chen, E. Wu, G. Bi, B.T. Wu, Y. Teng, S.F. Zhou, J.R. Qiu, Ultrasensitive polarized up-conversion of Tm_{3+}−Yb_{3+} doped β-$NaYF_4$ single nanorod. Nano Lett. **13**, 2241–2246 (2013)
108. H.X. Mai, Y.W. Zhang, L.D. Sun, C.H. Yan, Size- and phase-controlled synthesis of monodisperse $NaYF_4$:Yb, Er nanocrystals from a unique delayed nucleation pathway monitored with upconversion spectroscopy. J. Phys. Chem. C **111**, 13730–13739 (2007)
109. Y.P. Du, Y.W. Zhang, Z.G. Yan, L.D. Sun, S. Gao, C.H. Yan, Single-crystalline and near-monodispersed $NaMF_3$ (M = Mn Co, Ni, Mg) and $LiMAlF_6$ (M = Ca, Sr) nanocrystals from cothermolysis of multiple trifluoroacetates in solution. Chem. Asian J. **2**, 965–974 (2007)
110. F. Wang, L.D. Sun, J. Gu, Y.F. Wang, W. Feng, Y. Yang, J.F. Wang, C.H. Yan, Selective heteroepitaxial nanocrystal growth of rare earth fluorides on sodium chloride: synthesis and density functional calculations. Angew. Chem. Int. Ed. **51**, 8796–8799 (2012)
111. Y.J. Ding, X. Teng, H. Zhu, L.L. Wang, W.B. Pei, J.J. Zhu, L. Huang, W. Huang, Orthorhombic KSc_2F_7:Yb/Er nanorods: controlled synthesis and strong red upconversion emission. Nanoscale **5**, 11928–11932 (2013)
112. J. Wang, R.R. Deng, M.A. MacDonald, B. Chen, J.K. Yuan, F. Wang, D.Z. Chi, T.S.A. Hor, P. Zhang, G.K. Liu, Y. Han, X.G. Liu, Enhancing multiphoton upconversion through energy clustering at sublattice level. Nat. Mater. **13**, 157–162 (2014)
113. G.F. Wang, Q. Peng, Y.D. Li, Luminescence tuning of upconversion nanocrystals. Chem. Eur. J. **16**, 4923–4931 (2010)
114. L.J. Huang, L.L. Wang, X.J. Xue, D. Zhao, G.S. Qin, W.P. Qin, Enhanced red upconversion luminescence in Er–Tm codoped $NaYF_4$ phosphor. J. Nanosci. Nanotechnol. **11**, 9498–9501 (2011)
115. C. Zhang, J.Y. Lee, Prevalence of anisotropic shell growth in rare earth core-shell upconversion nanocrystals. ACS Nano **7**, 4393–4402 (2013)
116. Y.H. Zhang, L.X. Zhang, R.R. Deng, J. Tian, Y. Zong, D.Y. Jin, X.G. Liu, Multicolor barcoding in a single upconversion crystal. J. Am. Chem. Soc. **136**, 4893–4896 (2014)
117. W. Feng, L.D. Sun, C.H. Yan, Ag nanowires enhanced upconversion emission of $NaYF_4$:Yb, Er nanocrystals via a direct assembly method. Chem. Commun. **29**, 4393–4395 (2009)
118. N.J. Greybush, M. Saboktakin, X.C. Ye, C.D. Giovampaola, S.J. Oh, N.E. Berry, N. Engheta, C.B. Murray, C.R. Kagan, Luminescence in single nanophosphornanorod

heterodimers formed through template-assisted self-assembly. ACS Nano **8**, 9482–9491 (2014)
119. J.Y. Dong, J.I. Zink, Taking the temperature of the interiors of magnetically heated nanoparticles. ACS Nano **8**, 5199–5207 (2014)
120. Y.F. Wang, G.Y. Liu, L.D. Sun, J.W. Xiao, J.C. Zhou, C.H. Yan, Nd^{3+}-sensitized upconversion nanophosphors: efficient *in vivo* bioimaging probes with minimized heating effect. ACS Nano **7**, 7200–7206 (2013)
121. H.L. Wen, H. Zhu, X. Chen, T.F. Hung, B.L. Wag, G.Y. Zhu, S.F. Yu, F. Wang, Upconverting near-infrared light through energy management in core–shell–shell nanoparticles. Angew. Chem. Int. Ed. **52**, 13419–13423 (2013)
122. J. Shen, G.Y. Chen, A.-M. Vu, W. Fan, O.S. Bilsel, C.-C. Chang, G. Han, Engineering the upconversion nanoparticle excitation wavelength: cascade sensitization of tri-doped upconversion colloidal nanoparticles at 800 nm. Adv. Opt. Mater. **1**, 644–650 (2013)
123. X.J. Xie, N.Y. Gao, R.R. Deng, Q. Sun, Q.H. Xu, X.G. Liu, Mechanistic investigation of photon upconversion in Nd^{3+}-sensitized core−shell nanoparticles. J. Am. Chem. Soc. **135**, 12608–12611 (2013)
124. J. Zhou, Z. Liu, F.Y. Li, Upconversion nanophosphors for small-animal imaging. Chem. Soc. Rev. **41**, 1323–1349 (2012)
125. Z.J. Gu, L. Yan, G. Tian, S.J. Li, Z.F. Chai, Y.L. Zhao, Recent advances in design and fabrication of upconversion nanoparticles and their safe theranostic applications. Adv. Mater. **25**, 3758–3779 (2013)
126. H.C. Guo, S.Q. Sun, Lanthanide-doped upconverting phosphors for bioassay and therapy. Nanoscale **4**, 6692–6706 (2012)
127. X.Y. Huang, S.Y. Han, W. Huang, X.G. Liu, Enhancing solar cell efficiency: the search for luminescent materials as spectral converters. Chem. Soc. Rev. **42**, 173–201 (2013)
128. B. Yan, J.-C. Boyer, N.R. Branda, Y. Zhao, Near-infrared light-triggered dissociation of block copolymer micelles using upconverting nanoparticles. J. Am. Chem. Soc. **133**, 19714–19717 (2011)
129. Y.F. Wang, L.D. Sun, J.W. Xiao, W. Feng, J.C. Zhou, J. Shen, C.H. Yan, Rare-earth nanoparticles with enhanced upconversion emission and suppressed rare-earth-ion leakage. Chem. Eur. J. **18**, 5558–5564 (2012)
130. S.F. Lim, R. Riehn, W.S. Ryu, N. Khanarian, C.-K. Tung, D. Tank, R.H. Austin, In vivo and scanning electron microscopy imaging of upconverting nanophosphors in *Caenorhabditis elegans*. Nano Lett. **6**, 169–174 (2006)
131. D.K. Chatterjee, A.J. Rufihah, Y. Zhang, Upconversion fluorescence imaging of cells and small animals using lanthanide doped nanocrystals. Biomaterials **29**, 937–943 (2009)
132. T.S. Yang, Y. Sun, Q. Liu, W. Feng, P.Y. Yang, F.Y. Li, Cubic sub-20 nm $NaLuF_4$-based upconversion nanophosphors for high-contrast bioimaging in different animal species. Biomaterials **33**, 3733–3742 (2012)
133. J.C. Zhou, Z.L. Yang, W. Dong, R.J. Tang, L.D. Sun, C.H. Yan, Bioimaging and toxicity assessments of near-infrared upconversion luminescent $NaYF_4$:Yb, Tm nanocrystals. Biomaterials **32**, 9059–9067 (2011)
134. Q. Liu, Y. Sun, T.S. Yang, W. Feng, C.G. Li, F.Y. Li, Sub-10 nm hexagonal lanthanide-doped $NaLuF_4$ upconversion nanocrystals for sensitive bioimaging in vivo. J. Am. Chem. Soc. **133**, 17122–17125 (2011)
135. L. Cheng, K. Yang, Y.G. Li, J.H. Chen, C. Wang, M.W. Shao, S.-T. Lee, Z. Liu, Facile preparation of multifunctional upconversion nanoprobes for multimodal imaging and dual-targeted photothermal therapy. Angew. Chem. **123**, 7523–7528 (2011)
136. X.F. Qiao, J.C. Zhou, J.W. Xiao, Y.F. Wang, L.D. Sun, C.H. Yan, Triple-functional core–shell structured upconversion luminescent nanoparticles covalently grafted with photosensitizer for luminescent, magnetic resonance imaging and photodynamic therapy *in vitro*. Nanoscale **4**, 4611–4623 (2012)

137. Y. Liu, M. Chen, T.Y. Cao, Y. Sun, C.Y. Li, Q. Liu, T.S. Yang, L.M. Yao, W. Feng, F.Y. Li, A cyanine-modified nanosystem for in vivo upconversion luminescence bioimaging of methylmercury. J. Am. Chem. Soc. **135**, 9869–9876 (2013)
138. C.-J. Cailing, J.-C. Boyer, N.R. Branda, Remote-control photoswitching using NIR light. J. Am. Chem. Soc. **131**, 10838–10839 (2009)
139. J.-C. Boyer, C.-J. Carling, B.D. Gates, N.R. Branda, Two-way photoswitching using one type of near-infrared light, upconverting nanoparticles, and changing only the light intensity. J. Am. Chem. Soc. **132**, 15766–15772 (2010)
140. Y.M. Yang, Q. Shao, R.R. Deng, C. Wang, X. Teng, K. Cheng, Z. Cheng, L. Huang, Z. Liu, X.G. Liu, B.G. Xing, In vitro and in vivo uncaging and bioluminescence imaging by using photocaged upconversion nanoparticles. Angew. Chem. Int. Ed. **51**, 3125–3129 (2012)
141. L. Wang, H. Dong, Y.N. Li, C.M. Xue, L.D. Sun, C.H. Yan, Q. Li, Reversible near-infrared light directed reflection in a self-organized helical superstructure loaded with upconversion nanoparticles. J. Am. Chem. Soc. **136**, 4480–4483 (2014)
142. B.W. Wang, S.D. Jiang, X.T. Wang, Magnetic molecular materials with paramagnetic lanthanide ions. Sci. China Ser. B **52**, 1739–1758 (2009)
143. Q. Su (ed.), *Chemistry of Rare Earths* (Henan Science and Technology Press, Zhengzhou, 1993)
144. M. Bottrill, L.K. Nicholas, N.J. Long, Lanthanides in magnetic resonance imaging. Chem. Soc. Rev. **35**, 557–571 (2006)
145. P. Caravan, Strategies for increasing the sensitivity of gadolinium based MRI contrast agents. Chem. Soc. Rev. **35**, 512–523 (2006)
146. C. Geraldes, S. Laurent, Classification and basic properties of contrast agents for magnetic resonance imaging. Contrast Media Mol. Imaging **4**, 1–23 (2009)
147. Z.J. Zhou, Z.H. Zhao, H. Zhang, Z.Y. Wang, X.Y. Chen, R.F. Wang, Z. Chen, J.H. Gao, Interplay between longitudinal and transverse contrasts in Fe_3O_4 nanoplates with (111) exposed surfaces. ACS Nano **8**, 7976–7985 (2014)
148. P.J. Klemm, W.C. Floyd, D.E. Smiles, J.M.J. Frechet, K.N. Raymond, Improving T_1 and T_2 magnetic resonance imaging contrast agents through the conjugation of an esteramide dendrimer to high-water-coordination Gd(III) hydroxypyridinone complexes. Contrast Media Mol. Imaging **7**, 95–99 (2012)
149. S. Aime, M. Fasano, E. Terreno, Lanthanide(III) chelates for NMR biomedical applications. Chem. Soc. Rev. **27**, 19–29 (1998)
150. P. Caravan, J.J. Ellison, T.J. McMurry, R.B. Lauffer, Gadolinium(III) chelates as MRI contrast agents: Structure, dynamics, and applications. Chem. Rev. **99**, 2293–2352 (1999)
151. H.B. Na, I.C. Song, T. Hyeon, Inorganic nanoparticles for MRI contrast agents. Adv. Mater. **21**, 2133–2148 (2009)
152. M.A. McDonald, K.L. Watkin, Small particulate gadolinium oxide and gadolinium oxide albumin microspheres as multimodal contrast and therapeutic agents. Invest. Radiol. **38**, 305–310 (2003)
153. F. Chen, W. Bu, S. Zhang, J. Liu, W. Fan, L. Zhou, W. Peng, J. Shi, Gd^{3+}-ion-doped upconversion nanoprobes: relaxivity mechanism probing and sensitivity optimization. Adv. Funct. Mater. **23**, 298–307 (2013)
154. M. Rohrer, H. Bauer, J. Mintorovitch, M. Requardt, H.J. Weinmann, Comparison of magnetic properties of MRI contrast media solutions at different magnetic field strengths. Invest. Radiol. **40**, 715–724 (2005)
155. J.Y. Park, M.J. Baek, E.S. Choi, S. Woo, J.H. Kim, T.J. Kim, J.C. Jung, K.S. Chae, Y. Chang, G.H. Lee, Paramagnetic ultrasmall gadolinium oxide nanoparticles as advanced T_1 MR1 contrast agent: account for large longitudinal relaxivity, optimal particle diameter, and in vivo T_1 MR images. ACS Nano **3**, 3663–3669 (2009)
156. N.J.J. Johnson, W. Oakden, G.J. Stanisz, R.S. Prosser, F.C.J.M. van Veggel, Size-tunable, ultrasmall $NaGdF_4$ nanoparticles: insights into their T_1 MRI contrast enhancement. Chem. Mater. **23**, 3714–3722 (2011)

157. H. Hifumi, S. Yamaoka, A. Tanimoto, D. Citterio, K. Suzuki, Gadolinium-based hybrid nanoparticles as a positive MR contrast agent. J. Am. Chem. Soc. **128**, 15090–15091 (2006)
158. H. Hifumi, S. Yamaoka, A. Tanimoto, T. Akatsu, Y. Shindo, A. Honda, D. Citterio, K. Oka, S. Kuribayashi, Dextran coated gadolinium phosphate nanoparticles for magnetic resonance tumor imaging. J. Mater. Chem. **19**, 6393–6399 (2009)
159. Y. Gossuin, A. Hocq, Q.L. Vuong, S. Disch, R.P. Hermann, P. Gillis, Physico-chemical and NMR relaxometric characterization of gadolinium hydroxide and dysprosium oxide nanoparticles. Nanotechnology **19**, 475102 (2008)
160. W. Ren, G. Tian, L. Zhou, W.Y. Yin, L. Yan, S. Jin, Y. Zu, S.J. Li, Z.J. Gu, Y.L. Zhao, Lanthanide ion-doped $GdPO_4$ nanorods with dual-modal bio-optical and magnetic resonance imaging properties. Nanoscale **4**, 3754–3760 (2012)
161. Y.C. Li, T. Chen, W.H. Tan, D.R. Talham, Size-dependent MRI relaxivity and dual imaging with $Eu_{0.2}Gd_{0.8}PO_4$ center dot H_2O nanoparticles. Langmuir **30**, 5873–5879 (2014)
162. G.K. Das, B.C. Heng, S.C. Ng, T. White, J.S.C. Loo, L. D'Silva, P. Padmanabhan, K.K. Bhokoo, S.T. Selvan, T.T.Y. Tan, Gadolinium oxide ultranarrow nanorods as multimodal contrast agents for optical and magnetic resonance imaging. Langmuir **26**, 8959–8965 (2010)
163. Y. Zhang, G.K. Das, V. Vijayaragavan, Q.C. Xu, P. Padmanabhan, K.K. Bhakoo, S.T. Selvan, T.T.Y. Tan, "Smart" theranostic lanthanide nanoprobes with simultaneous up-conversion fluorescence and tunable T_1-T_2 magnetic resonance imaging contrast and near-infrared activated photodynamic therapy. Nanoscale **6**, 12609–12617 (2014)
164. Y. Tian, H.Y. Yang, K. Li, X. Jin, Monodispersed ultrathin GdF_3 nanowires: Oriented attachment, luminescence, and relaxivity for MRI contrast agents. J. Mater. Chem. **22**, 22510–22516 (2012)
165. T. Paik, T.R. Gordon, A.M. Prantner, H. Yun, C.B. Murray, Designing tripodal and triangular gadolinium oxide nanoplates and self-assembled nanofibrils as potential multimodal bioimaging probes. ACS Nano **7**, 2850–2859 (2013)
166. M. Cho, R. Sethi, J.S.A. Narayanan, S.S. Lee, D.N. Benoit, N. Taheri, P. Decuzzi, V.L. Colvin, Gadolinium oxide nanoplates with high longitudinal relaxivity for magnetic resonance imaging. Nanoscale **6**, 13637–13645 (2014)
167. H. Hu, D. Li, S. Liu, M.Z. Wang, R. Moats, P.S. Conti, Z.B. Li, Integrin α2β1 targeted GdVO4: Eu ultrathin nanosheet for multimodal PET/MR imaging. Biomaterials **35**, 8649–8658 (2014)
168. H. Hu, S. Liu, D. Li, M.Z. Wang, R. Moats, H. Shan, P.S. Conti, Z.B. Li, The synthesis of lanthanide-doped $GdVO_4$ ultrathin nanosheets with great optical and paramagnetic properties for FRET biodetection and in vivo MR imaging. J. Mater. Chem. B **2**, 3998–4007 (2014)
169. M. Abdesselem, M. Schoeffel, I. Maurin, R. Ramodiharilafy, G. Autret, O. Clement, P.L. Tharaux, J.P. Boilot, T. Gacoin, C. Bouzigues, Multifunctional rare-earth vanadate nanoparticles: luminescent labels, oxidant sensors, and MRI contrast agents. ACS Nano **8**, 11126–11137 (2014)
170. D.H. Geschwind, G. Konopka, Neuroscience in the era of functional genomics and systems biology. Nature **461**, 908–915 (2009)
171. E. Terreno, D.D. Castelli, A. Viale, S. Aime, Challenges for molecular magnetic resonance imaging. Chem. Rev. **110**, 3019–3042 (2010)
172. L. Helm, Optimization of gadolinium-based MRI contrast agents for high magnetic-field applications. Future Med. Chem. **2**, 385–396 (2010)
173. M. Norek, J.A. Peters, MRI contrast agents based on dysprosium or holmium. Prog. Nucl. Magn. Reson. Spectrosc. **59**, 64–82 (2011)
174. M. Norek, E. Kampert, U. Zeitler, J.A. Peters, Tuning of the size of Dy_2O_3 nanoparticles for optimal performance as an MRI contrast agent. J. Am. Chem. Soc. **130**, 5335–5340 (2008)
175. S. Viswanathan, Z. Kovacs, K.N. Green, S.J. Ratnakar, A.D. Sherry, Alternatives to gadolinium-based metal chelates for magnetic resonance imaging. Chem. Rev. **110**, 2960–3018 (2010)

176. G.K. Das, N.J.J.Johnson, J. Cramen, B. Blasiak, P. Latta, B.Tomanek, C.J.M. van Veggel, $NaDyF_4$ nanoparticles as T_2 contrast agents for ultrahigh field magnetic resonance imaging. J. Phys. Chem. Lett. **3**, 524–529 (2012)
177. H. Wang, Z. Yi, L. Rao, H.R. Liu, S.J. Zeng, High quality multi-functional $NaErF_4$ nanocrystals: structure-controlled synthesis, phase-induced multi-color emissions and tunable magnetic properties. J. Mater. Chem. C **1**, 5520–5526 (2013)
178. H. Wang, W. Lu, T. Zeng, Z. Yi, L. Rao, H. Liu, S. Zeng, Multi-functional NaErF4: Yb nanorods: enhanced red upconversion emission, in vitro vell, in vivo X-ray, and T2-weighted magnetic resonance imaging. Nanoscale **6**, 2855–2860 (2014)
179. A. Xia, X. Zhang, J. Zhang, Y.Y. Deng, Q. Chem, S. S. Wu, X. H. Huang, J. Shen. Enhanced dual contrast agent, Co^{2+}-doped $NaYF_4$:Yb^{3+}, Tm^{3+} nanorods, for near infrared-to-near infrared upconversion luminescence and magnetic resonance imaging. Biomaterials **35**, 9167–9176 (2014)
180. K. Kattel, J.Y. Park, W. Xu, H.G. Kim, E.J. Lee, B.A. Bony, W.C. Heo, S. Jin, J.S. Baeck, Y. Chang, Paramagnetic dysprosium oxide nanoparticles and dysprosium hydroxide nanorods as T_2 MRI contrast agents. Biomaterials **33**, 3254–3261 (2012)
181. K. Kattel, J.Y. Park, W. Xu, B.A. Bony, W.C. Heo, T. Tegafaw, C.R. Kim, M.W. Ahmad, S. Jin, J.S. Baeck, Surface coated $Eu(OH)_3$ nanorods: a facile synthesis, characterization, MR relaxivities and in vitro cytotoxicity. J. Nanosci. Nanotechnol. **13**, 7214–7219 (2013)
182. J. Zhou, Z.G. Lu, G.G. Shan, S.H. Wang, Y. Liao, Gadolinium complex and phosphorescent probe-modified $NaDyF_4$ nanorods for T_1- and T_2-weighted MRI/CT/phosphorescence multimodality imaging. Biomaterials **35**, 368–377 (2014)
183. M.J. Bailey, R. van der Weegen, P.J. Klemm, S.L. Baker, B.A. Helms, Stealth rare earth oxide nanodiscs for magnetic resonance imaging. Adv. Healthc. Mater. **1**, 437–442 (2012)
184. A. Trovarelli, A.C.D. Leitenburg, M. Boaro, G. Dolcetti, The utilization of ceria in industrial catalysis. Catal. Today. **50**, 353–367 (1999)
185. Z.L. Wang, X.D. Feng, Polyhedral shapes of CeO_2 nanoparticles. J. Phys. Chem. B **107**, 13563–13566 (2003)
186. D.S. Zhang, X.J. Du, L.Y. Shi, R.H. Gao, Shape-controlled synthesis and catalytic application of Ceria nanomaterials. Dalton Trans. **41**, 14455–14475 (2012)
187. E. Shoko, M.F. Smith, R.H. McKenzie, Charge distribution near bulk oxygen vacancies in cerium oxides. J. Phys.: Condens. Matter **22**, 223201–223218 (2010)
188. X.W. Liu, K.B. Zhou, L. Wang, B.Y. Wang, Y.D. Li, Oxygen vacancy clusters promoting reducibility and activity of ceria nanorods. J. Am. Chem. Soc. **131**, 3140–3141 (2009)
189. L. Vivier, D. Duprez, Ceria-based solid catalysts for organic chemistry. ChemSusChem. **3**, 654–678 (2010)
190. J.C. Conesa, Computer modeling of surfaces and defects on cerium dioxide. Surf. Sci. **339**, 337–352 (1995)
191. D.C. Sayle, S.A. Maicaneanu, G.W. Watson, Atomistic models for CeO_2 (111), (110), and (100) nanoparticles, supported on yttrium-stabilized zirconia. J. Am. Chem. Soc. **124**, 11429–11439 (2002)
192. E. Aneggi, C.D. Leitenburg, J. Llorca, A. Trovarelli, Higher activity of diesel soot oxidation over polycrystalline ceria and ceria–zirconia solid solutions from more reactive surface planes. Catal. Today **197**, 119–126 (2012)
193. C.S. Pan, D.S. Zhang, L.Y. Shi, J.H. Fang, Template-free synthesis, controlled conversion, and CO oxidation properties of CeO_2 nanorods, nanotubes, nanowires, and nanocubes. Eur. J. Inorg. Chem. **2008**, 2429–2436 (2008)
194. X. Wang, Z.Y. Jiang, B.J. Zheng, Z.X. Xie, L.S. Zheng, Synthesis and shape-dependent catalytic properties of CeO_2 nanocubes and truncated octahedral. CrystEngComm **14**, 7579–7582 (2012)
195. X. W. Lu, X.Z. Li, J.C. Qian, Z.G. Chen, The surfactant-assisted synthesis of CeO_2 nanowires and their catalytic performance for CO oxidation. Powder Technol. **239**, 415–421 (2013)

196. C.S. Pan, D.S. Zhang, L.Y. Shi, CTAB assisted hydrothermal synthesis, controlled conversion and CO oxidation properties of CeO_2 nanoplates, nanotubes, and nanorods. J. Solid State Chem. **181**, 1298–1306 (2008)
197. X.Z. Li, F. Chen, X.W. Lu, C.Y. Ni, X.B. Zhao, Z.G. Chen, Layer-by-layer synthesis of hollow spherical CeO_2 templated by carbon spheres. J. Porous Mater. **17**, 297–303 (2010)
198. C. Ho, J.C. Yu, T. Kwong, A.C. Mak, S.Y. Lai, Morphology-controllable synthesis of mesoporous CeO_2 nano- and microstructures. Chem. Mater. **17**, 4514–4522 (2005)
199. C.W. Sun, L.Q. Chen, Controllable synthesis of shuttle-shaped ceria and its catalytic properties for CO oxidation. Eur. J. Inorg. Chem. **2009**, 3883–3887 (2009)
200. X. Liang, J.J. Xiao, B.H. Chen, Y.D. Li, Catalytically stable and active CeO_2 mesoporous spheres. Inorg. Chem. **49**, 8188–8190 (2010)
201. Z.L. Wu, M.J. Li, J. Howe, H.M. Meyer, S.H. Overbury, Probing defect sites on CeO_2 nanocrystals with well-defined surface planes by Raman spectroscopy and O_2 adsorption. Langmuir **26**, 16595–16606 (2010)
202. Z.L. Wu, M.J. Li, S.H. Overbury, On the structure dependence of CO oxidation over CeO_2 nanocrystals with well-defined surface planes. J. Catal. **285**, 61–73 (2012)
203. Z.M. Tana, J. Li, H. Li, Y. Li, W. Shen, Morphology-dependent redox and catalytic properties of CeO_2 nanostructures: nanowires, nanorods and nanoparticles. Catal. Today **148**, 179–183 (2009)
204. B. Choudhury, P. Chetri, A. Choudhury, Oxygen defects and formation of Ce^{3+} affecting the photocatalytic performance of CeO_2 nanoparticles. RSC Adv. **4**, 4663–4671 (2014)
205. P.F. Ji, J.L. Zhang, F. Chen, M. Anpo, Ordered mesoporous CeO_2 synthesized by nanocasting from cubic *Ia3d* mesoporous MCM-48 silica: formation, characterization and photocatalytic activity. J. Phys. Chem. C **112**, 17809–17813 (2008)
206. X.H. Lu, D.Z. Zheng, J.Y. Gan, Z.Q. Liu, C.L. Liang, P. Liu, Y.X. Tong, Porous CeO_2 nanowires/nanowire arrays: electrochemical synthesis and application in water treatment. J. Mater. Chem. **20**, 7118–7122 (2010)
207. Z.J. Yan, J.J. Wei, H.X. Yang, L. Liu, H. Liang, Y.Z. Yang, Mesoporous CeO_2 hollowspheres prepared by Ostwald ripening and their environmental applications. Eur. Inorg. Chem. **2010**, 3354–3359 (2010)
208. X.H. Lu, T. Zhai, H.N. Cui, J.Y. Shi, S.L. Xie, Y.Y. Huang, C.L. Liang, Y.X. Tong, Redox cycles promoting photocatalytic hydrogen evolution of CeO_2 nanorods. J. Mater. Chem. **21**, 5569–5572 (2011)
209. M. Kobune, S. Sato, R. Takahashi, Surface-structure sensitivity of CeO_2 for several catalytic reactions. J. Mol. Catal. A: Chem. **279**, 10–19 (2008)
210. J.G. Lv, Y. Shen, L.M. Peng, X.F. Guo, W.P. Ding, Exclusively selective oxidation of toluene to benzaldehyde on ceria nanocubes by molecular oxygen. Chem. Commun. **46**, 5909–5911 (2010)
211. Y. Zhang, F. Hou, Y.W. Tan, CeO_2 nanoplates with a hexagonal structure and their catalytic applications in highly selective hydrogenation of substituted nitroaromatics. Chem. Commun. **48**, 2391–2393 (2012)
212. I. Celardo, J.Z. Pedersen, E. Traversa, Pharmacological potential of cerium oxide nanoparticles. Nanoscale **3**, 1411–1420 (2011)
213. C. Korsvik, S. Patil, S. Seal, W.T. Self, Superoxide dismutase mimetic properties exhibited by vacancy engineered ceria nanoparticles. Chem. Commun. **10**, 1056–1058 (2007)
214. T. Pirmohamed, J.M. Dowding, S. Singh, B. Wasserman, E. Heckert, A.S. Karakoti, J.E.S. King, S. Seal, W.T. Self, Nanoceria exhibit redox state-dependent catalase mimetic activity. Chem. Commun. **46**, 2736–2738 (2010)
215. Y. Xue, Q.F. Luan, D. Yang, X. Yao, K.B. Zhou, Direct evidence for hydroxyl radical scavenging activity of cerium oxide nanoparticles. J. Phys. Chem. C **115**, 4433–4438 (2011)
216. C.K. Kim, T. Kim, I.Y. Choi, M. Soh, D. Kim, Y.-J. Kim, H. Jang, H.-S. Yang, J.Y. Kim, H.-K. Park, Ceria nanoparticles that can protect against ischemic stroke. Angew. Chem. Int. Ed. **51**, 1–6 (2012)

217. J. Chen, S. Patil, S. Seal, J.F. Mcginnis, Rare earth nanoparticles prevent retinal degeneration induced by intracellular peroxides. Nat. Nanotechnol. **1**, 142–150 (2006)
218. A. Nel, T. Xia, L. Madler, N. Li, Toxic potential of materials at the nanolevel. Science **311**, 622–627 (2006)
219. S.J. Lin, X. Wang, Z.X. Ji, C.H. Chang, Y. Dong, H. Meng, Y.P. Liao, M.Y. Wang, T.B. Song, S. Kohan, Aspect ratio plays a role in the hazard potential of CeO_2 nanoparticles in mouse lung and zebrafish gastrointestinal tract. ACS Nano **8**, 4450–4464 (2014)
220. W.Q. Han, W. Wen, J.C. Hanson, X. Teng, N. Marinkovic, J.A. Rodriguez, One-dimensional ceria as catalyst for the low-temperature water-gas shift reaction. J. Phys. Chem. C **113**, 21949–21955 (2009)
221. C. Fang, D.S. Zhang, L.Y. Shi, R.H. Gao, H.R. Li, L.P. Ye, J.P. Zhang, Highly dispersed CeO_2 on carbon nanotubes for selective catalytic reduction of NO with NH_3. Catal. Sci. Technol. **3**, 803–811 (2013)
222. D. Barreca, A. Gasparotto, C. Maccato, C. Maragno, E. Tondello, E. Comini, G. Sberveglieri, Columnar CeO_2 nanostructures for sensor application. Nanotechnology **18**, 125502 (2007)
223. H. He, H.X. Dai, L.H. Ng, K.W. Wong, C.T. Au, Pd-, Pt-, and Rh-loaded $Ce_{0.6}Zr_{0.35}Y_{0.05}O_2$ three-way catalysts: an investigation on performance and redox properties. J. Catal. **206**, 1–13 (2002)
224. X. Yu, L. Kuai, B.Y. Geng, CeO_2/rGO/Pt sandwich nanostructure: rGO-Enhanced electron transmission between metal oxide and metal nanoparticles for anodic methanol oxidation of direct methanol fuel cells. Nanoscale **4**, 5738–5743 (2012)
225. H.P. Zhou, H.S. Wu, J. Shen, A.X. Yin, L.D. Sun, C.H. Yan, Thermally stable Pt/CeO_2 hetero-nanocomposites with high catalytic activity. J. Am. Chem. Soc. **132**, 4998–5011 (2010)
226. X.N. Lu, C.Y. Song, S.H. Jia, Z.S. Tong, X.L. Tang, Y.X. Teng, Low temperature selective catalytic reduction of NO_x with NH_3 over amorphous MnO_x catalysts prepared by three methods. Catal. Commun. **8**, 329–334 (2007)
227. R. Si, M. Flytzani-Stephanopoulos, Shape and crystal plane effects of nanoscale ceria on the activity of Au-CeO_2 catalysts for the water-gas shift reaction. Angew. Chem. Int. Ed. **47**, 2884–2887 (2008)

Chapter 6
Liquid Crystalline Anisotropic Nanoparticles: From Metallic and Semiconducting Nanoparticles to Carbon Nanomaterials

Hari Krishna Bisoyi and Quan Li

Abstract Anisotropic nanomaterials made of metals, semiconductors, or carbon are of special interest for their mechanical, electrical, magnetic, optical, chemical and other spectacular properties in the bottom-up fabrication of advanced functional materials and devices in the field of nanoscience and nanotechnology. To widen their applicability, it is necessary to process these anisotropic building blocks into different well-defined assembly structures with preferred orientations. This chapter deals with the liquid crystalline properties of one- and two-dimensional (1D and 2D) anisotropic nanoparticles such as nanorods, nanotubes, nanodiscs and graphene derivatives. The different strategies developed for the realization of liquid crystal phases from metallic, semiconducting and carbon based anisotropic nanoparticles have been discussed. High performance materials and devices fabricated by processing via liquid crystalline route of these materials have also been highlighted.

6.1 Introduction

Liquid crystals (LCs) represent a state of matter which is characterized by a unique combination of order and mobility of the building blocks. The building blocks of the LC phase can be organic, inorganic or organometallic in nature. LC phase is a true thermodynamic stable state of matter and has been accepted as the fourth state of matter after solid, liquid and gas. Because of its occurrence between the crystalline solid and isotropic liquid, this phase of matter is often referred to as

H.K. Bisoyi · Q. Li (✉)
Liquid Crystal Institute and Chemical Physics Interdisciplinary Program, Kent State University, Kent, OH 44242, USA
e-mail: qli1@kent.edu

Q. Li (ed.), *Anisotropic Nanomaterials*, NanoScience and Technology,
DOI 10.1007/978-3-319-18293-3_6

mesophase (intermediate phase). The constituents of the mesophases are known as mesogens. LCs have been regarded as unique functional soft materials from both scientific and technological point of view [1–7]. The counterintuitive combination of order and dynamics (fluidity) of the building blocks in this fascinating state of matter yields soft materials with anisotropic (direction dependent) properties that are extremely responsive under the influence of small external stimuli [8]. Owing to their dynamic nature, thermally, photochemically or mechanically induced structure changes of LCs have been used for the construction of multifunctional stimuli-responsive materials. The domains of LCs span multiple discipline of pure and applied science including materials science and bioscience [9, 10]. Moreover, LCs can be considered as prototype supramolecular systems which furnish well-defined self-assembled architectures via different non-covalent secondary interactions. Furthermore, LCs persuasively demonstrate the powerful organization principle of matter by maximizing the interaction energy and minimizing the excluded volume. The most common and commercial application of LCs is in flat panel information display devices popularly recognized as LC displays (LCD). Some of the LCD devices which enrich the comfort of our everyday modern life are computer-, laptop- and television-monitors, mobile phone and camera screens, projectors etc. In addition to their display applications, recently numerous beyond display applications of LCs are emerging [1].

LCs are commonly classified into two broad classes: thermotropic and lyotropic. Thermotropic LCs can be obtained either by heating (thermal effect) crystalline solids or by cooling isotropic liquids. Thermotropic LCs are widely used in flat panel LCD devices. On the other hand, lyotropic LCs can be realized by dissolving amphiphilic molecules with sufficient concentrations in suitable solvents. Often water is used as the solvent and such anisotropic aqueous solutions find their applications in food and cosmetic industry, soap and detergent industry including drug delivery, gene therapy etc. [11]. In addition to flexible surfactant molecules, it has been observed that tobacco mosaic virus (TMV), *fd* virus, deoxyribo nucleic acid (DNA) and other biomacromolecules exhibit lyotropic liquid crystalline phases in water [12–17]. LC nanoscience is currently emerging as an interesting field which deals with the application of nanoscience and nanotechnology to LC science [18, 19]. In this context, the design and synthesis of LC anisotropic nanoparticles are very appealing. Since anisotropic nanoparticles exhibit many fascinating characteristics, it has been shown that through LC phase processing functional materials and devices with well aligned nanoparticles can be fabricated in a bottom-up approach [20–33]. Moreover, lyotropic LC phases can be realized and stabilized by dispersing anisometric nanoparticles such as rods and discs in appropriate concentrations under suitable conditions. The theoretical aspects of the LC phases of the colloids of anisotropic particles (rods and plates) were investigated by Onsager in 1949 [34]. He rationalized the formation of the nematic phase by excluded volume effects working among the particles. As the concentration increases, the colloid transits from the isotropic phase to the isotropic/nematic biphase, and eventually to the nematic phase. At a larger aspect ratio and high particle concentration, the loss in orientational entropy is compensated and

outweighed by the gain in translational entropy. Thus an anisotropic colloid transits from isotropic to LC state.

In this chapter, LC phase behaviors of anisotropic metallic, semiconducting as well as carbon based one-dimensional (1D) and two-dimensional (2D) nanoparticles are covered. Different physical and chemical methods used for dispersion and LC phase formation of nanoparticles under appropriate conditions are discussed. By tuning the size and shape of the particles and their mutual interactions, novel and interesting phase behavior has been observed. Exploitation of functional materials fabricated through LC phase processing of the anisotropic nanoparticles has also been highlighted.

6.2 Liquid Crystals of One Dimensional (1D) Nanoparticles

6.2.1 Liquid Crystalline Nanorods

Nanorods are a fascinating class of 1D nanomaterials with promising applicable properties. The physical properties of nanorods can be modulated by varying their length, diameter and aspect ratios (the ratio between length and diameter). Compared to their spherical counterparts, nanorods exhibit unique properties. Both metallic and semiconducting nanorods have been extensively synthesized by top-down and bottom-up approaches and are studied as enabling building blocks in nanoscience and nanotechnology. Tremendous attention is devoted to the exploration of novel electric and optical properties of 1D nanoscale materials such as nanowires, nanotubes and nanorods. Buining et al. reported in 1993 that dispersions of sterically stabilized rodlike boehmite particles undergo an isotropic-nematic phase separation [35]. The phase separation process was studied with polarizing optical microscopy (POM). The boehmite core particles were sterically stabilized by grafting a layer of poly(isobutene) on their surface. The boehmite particles were 200 nm long and 10 nm wide. Gold nanorods (GNRs) are a promising class of metallic anisotropic nanoparticles which have been investigated widely in different areas of nanoscience and nanotechnology as well as in biological sciences and sensing. The anisotropic nanoparticles are known to self-assemble in different structures. Interestingly, these ensembles exhibit unique properties that are different from those of the individual GNRs and bulk materials. GNRs exhibit two kinds of localized surface plasmon resonance because of coherent oscillations of the conduction band electrons in parallel and perpendicular directions to the GNR long axis, these are known as longitudinal and transverse plasmon resonance respectively. These plasmonic nanoparticles can form LC phases under suitable conditions. Jana et al. synthesized GNRs in aqueous surfactant solution using a seed mediated growth approach [36]. High aspect ratio GNRs were found to form LC phases in concentrated solutions. The LC phases were characterized by POM,

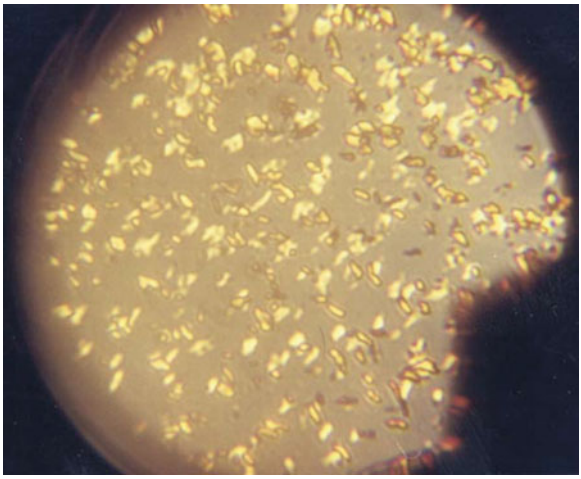

Fig. 6.1 Polarizing optical microscopy texture of LC GNRs. Reproduced with permission from [36]. Copyright The Royal Society of Chemistry 2002

transmission electron microscopy (TEM) and X-ray scattering techniques (Fig. 6.1). These phases possess concentration dependent orientational order.

LC phase formation has also been observed in low aspect ratio (4) GNRs during drop drying on glass substrates. These drops exhibit characteristic birefringence under POM with crossed polarizers and sparkling due to fluctuations in the director field [37]. Characterizing the self-assembly of GNRs on TEM grids shows the formation of nematic phase. Namatic and smectic-like arrays of mesogen functionalized GNRs have been observed upon slow evaporation of solution in an organic solvent on TEM grids (Fig. 6.2). Interestingly, these arrays can be reoriented by applying external magnetic field from planar to vertical orientation [38].

Lyotropic nematic LC phase formation in dispersions of silver nanowires and nanoparticles in ethylene glycol and water has been reported [39]. The silver nanowires and nanoparticles are coated with polyvinylpyrrolidone and their mixtures are dispersed in ethylene glycol and water. In the mixtures, the nanoparticles partition to a separate phase and enable the nanowires LC phase formation at lower than expected concentrations. Nanowire-rich LC phase exhibits a strand like morphology and upon shearing, the LC phase results in significant nanowire alignment. Because of silver's excellent electrical, optical, thermal and antimicrobial properties, the silver coatings obtained from the dispersions are promising materials for a range of applications.

Lanthanum phosphate ($LaPO_4$) mineral LC suspensions with outstanding stability for electro-optical applications have been fabricated [40]. The colloidal stability of $LaPO_4$ nanorod LCs was improved by transfer of particles from water toward ethylene glycol. These nanorods were devoid of chemical functionalization on their surface. POM and X-ray scattering studies revealed nematic and columnar mesophases of the nanorods (Fig. 6.3). When an external alternative electric field is applied, a very efficient orientation of the nanorods was obtained in the LC phase. Such switchable nanorods can potentially be used in electro-optical devices.

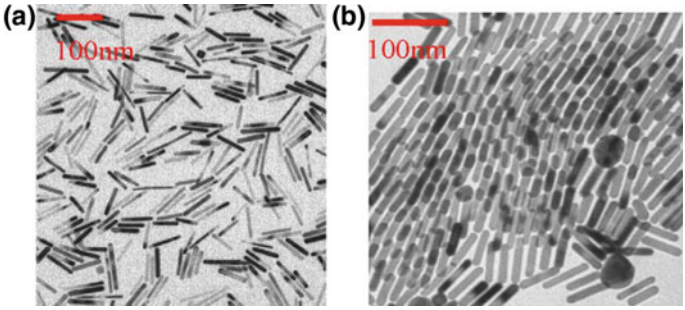

Fig. 6.2 TEM images of GNRs assembly. **a** Isotropic phase, **b** nematic-like assembly. Reproduced with permission from [37]. Copyright 2009 Elsevier

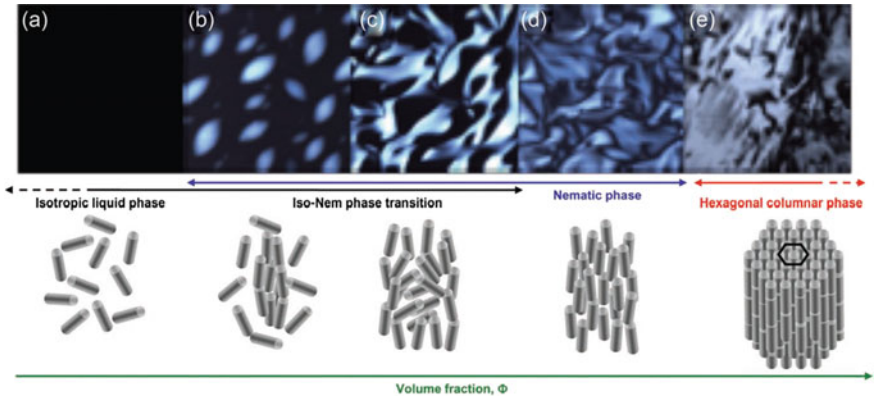

Fig. 6.3 LC phases of lanthanum phosphate. Reproduced with permission from [40]. Copyright 2012 Wiley-VCH Verlag GmbH & Co. KGaA, Weinheim

Monodisperse silica nanorods with micrometer lengths were found to self-assemble into LC phases in concentrated dispersions [41]. These nanorod LCs were studied quantitatively on the single particle level in three-dimensional real-space using confocal microscopy. The isotropic phase of silica rods in dimethyl sulfoxide (DMSO) can be turned into a paranematic phase when an AC electric field was applied as studied by confocal microscopy. In dispersions of higher aspect ratio rods, a smectic phase was observed (Fig. 6.4). The ability of the system to form smectic phases as well as isotropic and nematic phases makes it unique and very suitable as a model system for the real-space study of colloidal LCs. Lyotropic smectic LC phase behavior of silica nanorods in binary mixtures of DMSO and water has also been reported [42]. It was observed that the phase behavior of the system is affected by nanorod size polydispersity and DMSO concentration in the binary solvent.

Kanie et al. reported thermotropic mesophases formed by hybridization of LC phosphates and monodisperse spindle-shaped α-Fe_2O_3 particles [43]. Due to the

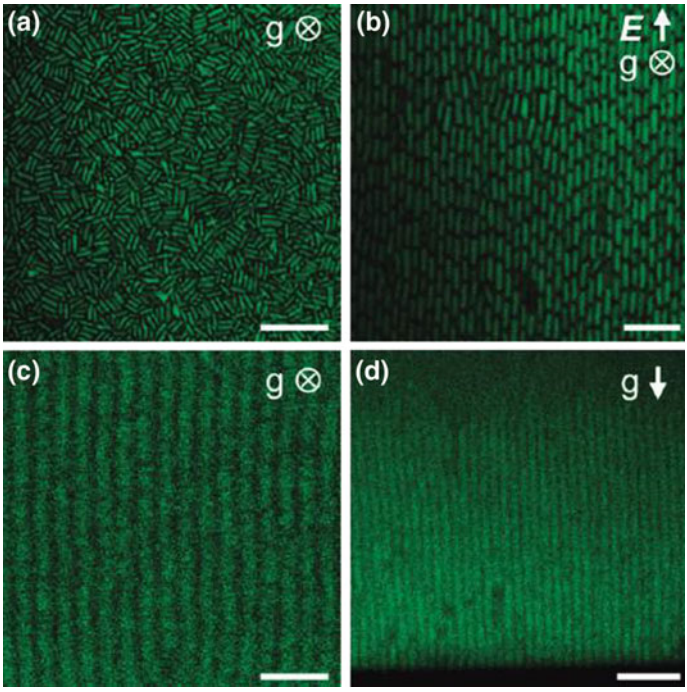

Fig. 6.4 Confocal microscopy images of silica nanorods in isotropic **a** and paranematic phase **b** induced by electric field. For larger aspect rods a smectic phase is observed without application of electric field. The smectic planes are visible in **c** and **d**. Reproduced with permission from [41]. Copyright 2011 American Chemical Society

strong adsorption of phosphate ions on the particles, phosphate terminated mesogens were designed to functionalize the particle surfaces. Upon mesogen functionalization, the organic-inorganic hybrids exhibited thermotropic phase behavior and nematic phase was identified. Recently, polymer coated iron oxide nanoparticles forming lyotropic LC phases were reported [44]. The nanoparticles were functionalized with brush-like layers of polystyrene or polyisoprene having different molecular weights. The lyotropic phases in toluene can be shear aligned to obtain macroscopic highly ordered single crystalline nanoparticle superlattices. Moreover, within the ordered phases, the distance between adjacent nanoparticles can be varied systematically via concentration and attached polymer molecular weight.

Goethite (α-FeOOH) is mostly used as pigment in industry. Interestingly, goethite particles have a permanent magnetic moment along their long axis, presumably due to uncompensated spins within their antiferromagnetic crystal structure. In contrast, their magnetic easy axis is along the shortest particle dimension. Therefore, the particles have the opposing tendencies to align with their long axis parallel to the field at a low magnetic field strength and to orient perpendicular to a higher magnetic field. This magnetic property of goethite nanorods has been

exploited to align them in their LC suspensions [45–52]. Goethite nanorods form nematic phases in their aqueous suspensions. The nematic phase aligns in a very low magnetic field. Interestingly, both parallel and perpendicular alignments to the field have been observed depending on the field strength. Lemaire et al. further showed that aqueous suspensions of goethite nanorods can display a rectangular columnar phase at higher volume fractions. Interestingly, the nematic phase can transition to columnar phase under a magnetic field and this magnetic-field-induced transition is fully reversible and reproducible. Subsequently Vroege et al. found smectic liquid crystalline order in suspensions of highly polydisperse goethite nanorods in addition to nematic and columnar phases [47]. It seems very likely that the fractionation and sedimentation-induced macroscopic separation associated with the isotropic-nematic phase transition help to create the circumstances to form a smectic phase upon storage for a prolonged time. The effect of fractionation on the LC phase behavior of colloidal goethite dispersions with different polydispersity has been studied in detail by the combination of X-ray scattering and TEM. The occurrence of strong fractionation in highly polydisperse systems was found. Nematic and smectic phases were observed in all the investigated systems, however the occurrence of columnar phase was found only in systems with high polydispersity above some critical value [48]. Biaxial nematic and biaxial smectic phases were found in the suspensions of goethite particles with a board like shape [51]. In these systems, macroscopic domains were oriented by a magnetic field and the phase structures were revealed by small angle X-ray scattering (Fig. 6.5). This study showed that biaxial phases can be readily obtained by a proper choice of the particle shape. It should be mentioned that in the uniaxial nematic phase the particles have orientational ordering along one direction, i.e. the principal axis, in the biaxial nematic phase the particles exhibit orientational ordering along two orthogonal directions. Magnetic field induced nematic-nematic phase separation in goethite nanorods has been demonstrated recently. Small angle X-ray scattering measurements proved that the two resulting nematic phases have orthogonal orientations, a uniaxial nematic phase with particles parallel to the field and a biaxial nematic phase with particles perpendicular to the field [52]. Maeda et al. prepared

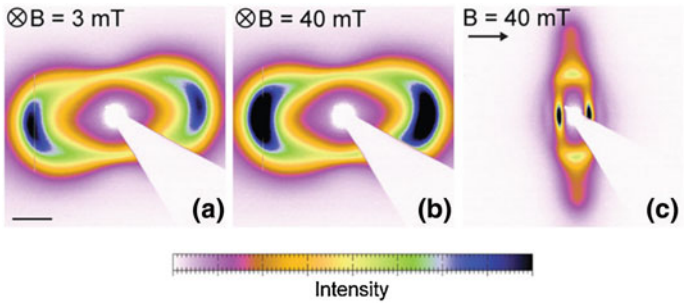

Fig. 6.5 X-ray scattering patterns of biaxial nematic phase in goethite suspensions. Reproduced with permission from [51]. Copyright 2009 The American Physical Society

monodisperse colloidal β-FeOOH particles and found that smectic ordering occurs over a wide region from evaporating suspensions of the particle on substrates. Subsequently they prepared monodisperse rodlike colloidal particles with a wide range of aspect ratios. In their suspensions, nematic and smectic phases spontaneously appeared [53, 54]. The low aspect ratio particles exhibit isotropic-smectic phase transition while the particles with high aspect ratio undergo isotropic-nematic-smectic phase transitions. The larger size of the particles enabled the observation of their arrangement and dynamics with an optical microscope.

Semiconductor nanorods of CdSe form LC phases [55–57]. This has been achieved by the recent advances in the control of the size and shapes of inorganic nanocrystals during their synthesis. Li et al. made CdSe nanorods by pyrolysis of organometallic precursors of Cd and Se in a surfactant mixture. The CdSe nanorods are functionalized with amphiphilic molecules, such that a polar functional group is bound to the nanocrystal surface and long alkyl chains are projecting outward. The alkyl chains provide high solubility of the nanorods in organic solvents. A solution of CdSe nanorods in cyclohexane forms LC phase as the concentration is increased (Fig. 6.6). Since CdSe nanorods have tunable and linearly polarized photoluminescence and anisotropic nonlinear optical properties, LCs of CdSe nanorods can potentially be used as functional components in electro-optical devices. Subsequently their assembly on a substrate as well as isotropic-LC phase diagram has been studied in detail.

TiO_2 is a versatile material that has widespread industrial use as pigment, in solar cells, as catalyst support, as photo catalyst etc. Achieving good colloidal stability of

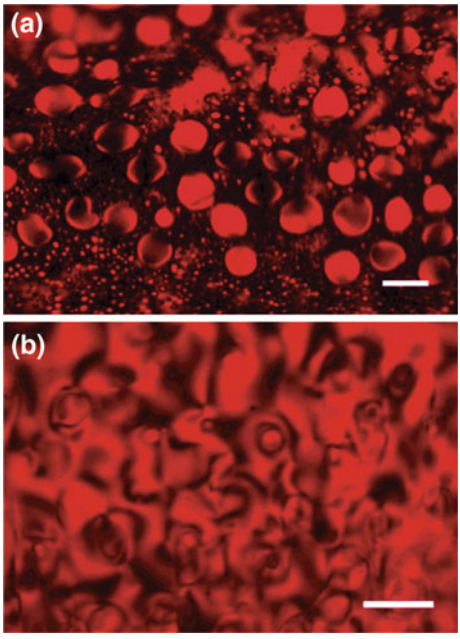

Fig. 6.6 POM textures of the LC phase of semiconductor CdSe nanorods. Reproduced with permission from [55]. Copyright 2002 American Chemical Society

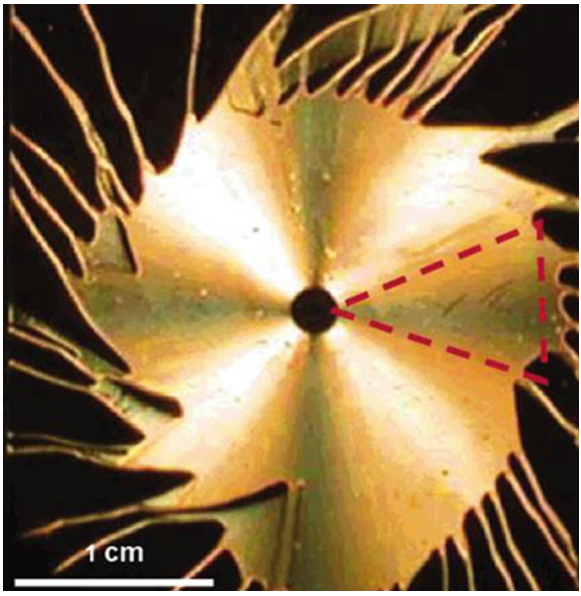

Fig. 6.7 Dried film of rutile nanorods fabricated from their LC phase. Reproduced with permission from [58]. Copyright 2007 American Chemical Society

aqueous suspensions of rutile nanorods is quite challenging. The van der Waals attractions between particles are strong. However, suitable methods have been developed to prepare stable rutile nanorod suspensions in water. Because of their anisotropic shape, TiO_2 nanorods at sufficiently high concentrations yield nematic LC phase [58]. The LC phase has been characterized by POM and X-ray diffraction (XRD) techniques. Very well aligned rutile films on glass substrates were produced by spin-coating (Fig. 6.7), and the potential application of these rutile films in photocatalysis was demonstrated. The photocatalytic properties were investigated by monitoring the decomposition of methylene blue under polarized UV light which showed that the rutile films exhibit anisotropic photocatalytic properties.

Organic-inorganic hybrid LCs have been obtained by mesogen functionalization of spindle shaped anisotropic nanoparticles of anatase TiO_2 [59]. The strong adsorption of amines onto the surface of TiO_2 has inspired their functionalization with amine terminated rodlike mesogens. This yields stable thermotropic LC phase. The nematic phase behavior of this hybrid was investigated by POM and XRD studies. Meuer et al. adopted a different approach to obtain LCs from TiO_2 nanorod mesogens in organic solvents [60]. They designed and synthesized dopamine-functionalized diblock copolymers which were subsequently linked to TiO_2 nanorods. These polymer coated nanorods were well dispersible in organic solvents. Encouraged by these results, they prepared polymethyl-methacrylate (PMMA) functionalized nanorods and found that these nanorods form LC phases in polyethylene glycol (PEG) oligomers. Interestingly, the clearing points of the LC phases were found to depend on the concentration of the nanorods. With increasing volume fraction of the nanorods, the clearing temperature was observed to rise.

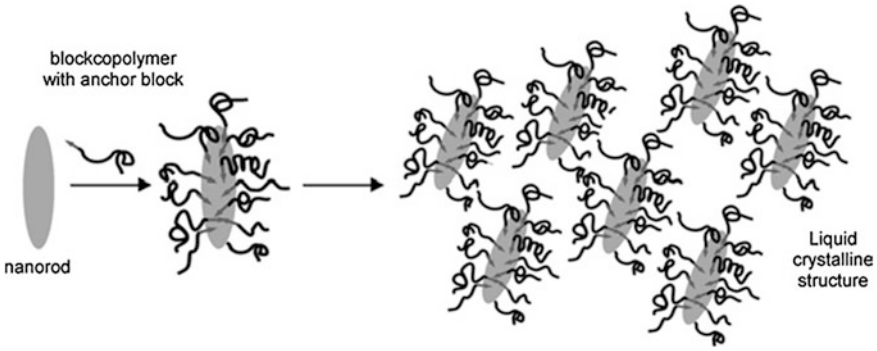

Fig. 6.8 LC phase formation in polymer functionalized semiconducting nanorods. Reproduced with permission from [61]. Copyright The Royal Society of Chemistry 2008

In attempts to combine the properties of inorganic nanorods and organic polymers, Zentel and co-workers have designed and synthesized a range of hybrid materials [61–63]. Various nanorods were functionalized with diblock copolymers containing anchor groups via grafting-to method. Stable dispersions of these hairy rod hybrids form lyotropic LC phases (Fig. 6.8) at suitable concentrations in organic solvents and thermotropic LC phases in oligomeric and polymeric matrices. The transition temperatures of the LC phases were found to depend on the length of the nanorods and the organic matrix.

ZnO semiconducting nanorods were grafted with hole conducting block copolymers to enhance their solubility in organic solvents and compatibility in oligomer matrices. These organic-inorganic hybrid nanorods furnish stable dispersions in solvents such as tetrahydrofuran, dioxane, toluene and xylene. At higher concentration, the nanorods form LC phases in various solvents and in low T_g oligomers [62]. While the nanorods exhibit lyotropic phase behavior in the organic solvents, they display temperature-dependent phase behavior in oligomer matrices. Highly oriented nanorod assemblies can be fabricated by processing from the LC phase. It should be noted that the same strategy has been employed to obtain LC phases from other semiconducting nanorods like SnO_2 and CdTe. Block copolymer grafted ZnO nanorods forming LC phase in a polystyrene oligomer matrix show a switching behavior under an applied AC electric field. The alignment of the nanorod mesogens can be switched from planar to homeotropic under the electric field (Fig. 6.9) [63]. Dielectric measurements show that the switching behavior arises due to the cooperative LC behavior since the ZnO nanorods themselves exhibit a very small effective dipole moment. The orientation switching has been visualized by scanning electron microscopy (SEM) owing to the large size of the mesogen nanorods. These observations can potentially lead to new optoelectronic devices based on reorientation of ZnO nanorods.

Zhang et al. prepared single-crystal ZnO nanowires with high aspect ratio which upon appropriate functionalization formed nematic phases in organic and aqueous media [64]. The LCs were readily processed to produce films with large-area

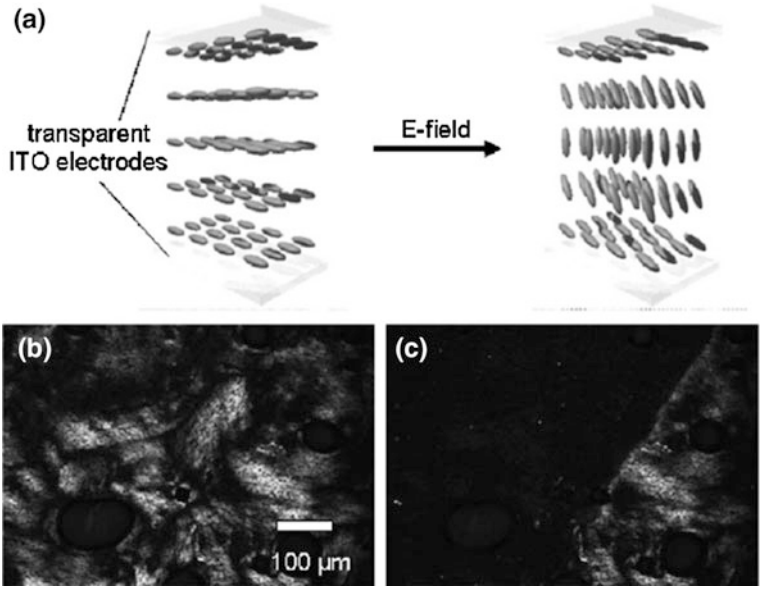

Fig. 6.9 Electric field induced reorientation of ZnO nanorods and the corresponding POM textures. Reproduced with permission from [63]. Copyright 2010 Wiley-VCH Verlag GmbH & Co. KGaA, Weinheim

monodomains of aligned nanowires. Interestingly, the director field displays bend deformation in organic mesophase dried films whereas the splay deformation is observed in the aqueous case. The nanowires functionalized with an *n*-alkyl chain display a propensity for bend distortion of the nematic director field in dry films whereas carboxylic-acid-functionalized films were dominated by splay distortion (Fig. 6.10). This suggests that the elasticity of the system can be tuned via appropriate surface functionalization. The LC phase also provides a solution based route for the fabrication of optoelectronic devices based on semiconductor nanowires. They further synthesized transition-metal Co and Mn-doped ZnO nanowires which exhibited characteristic paramagnetic behavior. The suspensions of these surface-functionalized magnetic nanowires spontaneously form stable homogeneous nematic LC phases in organic solvent above a critical concentration. Large-area uniaxially aligned thin films of doped nanowires were obtained from the lyotropic phase by applying either mechanical shear or magnetic field [65].

6.2.2 Liquid Crystalline Carbon Nanotubes

Carbon nanotubes (CNTs) are 1D hollow cylinders of graphite with high aspect ratio. Generally, CNTs are classified into two categories based on their structure and

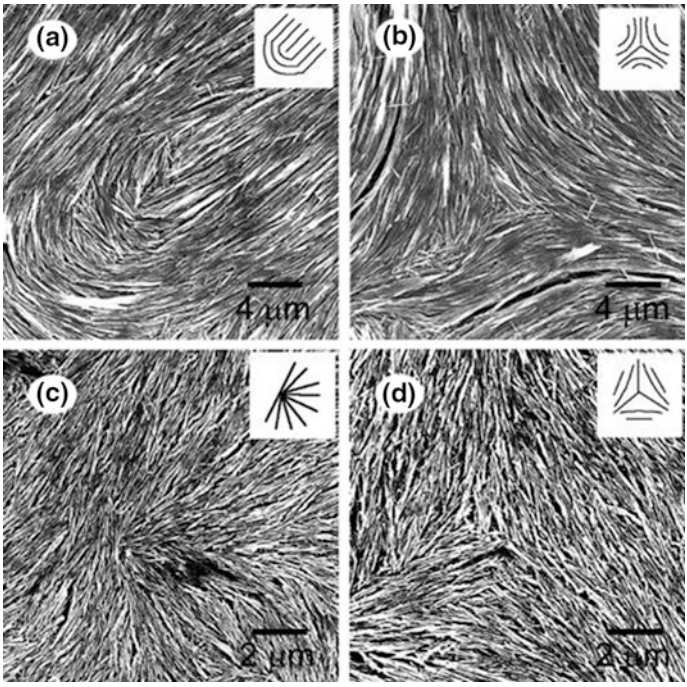

Fig. 6.10 Defect structures of the dried films of LC ZnO nanowire suspensions. Reproduced with permission from [64]. Copyright 2011 American Chemical Society

dimensions: single walled CNTs (SWNTs), which consist of one layer of cylindrical graphene; and multi-walled CNTs (MWNTs), which contain several concentric graphene sheets. Both SWNTs and MWNTs display unprecedented physical and chemical properties. The combination of superlative mechanical, thermal and electronic properties displayed by CNTs makes them ideal for a wide range of applications such as conductive and high strength composites, catalyst supports in heterogeneous catalysis, energy-storage and energy-conversion devices, field emitters, transistors, sensors, gas storage media, and molecular wires. Depending on their geometry, nanotubes can be metallic or semiconducting, with a strong anisotropy of conductivity being observed; they are primarily conductive along the tubes and hardly conductive across them. Despite the extraordinary promise of CNTs their realistic application as 1D conductors or semiconductors has been restricted because of difficulties in dispersing and aligning them in the desired direction. Well aligned CNTs are highly desirable for the preparation of variety of nanodevices particularly where 1D charge migration is important.

CNTs can be viewed as highly anisometric rigid rod-like particles. Like other anisotropic and one dimensional molecule, CNTs can form lyotropic LC phase under suitable conditions [66, 67]. Windle group first reported the LC phase behavior of carboxylic acid functionalized water soluble MWNTs [68]. They found

that when the concentration of the CNTs aqueous dispersions reached 4.3 % by volume there was the phase transition from the isotropic to nematic phase characterized by Schlieren texture typical of lyotropic nematic phase. The evaporation of the solvent from the dispersions gave solid samples with very similar microstructure to the original dispersion which has been characterized by scanning electron microscope (SEM) at a resolution sufficient to view the organization of individual nanotubes. Song et al. studied in detail the isotropic-nematic phase transition in dispersions of MWNTs [69–72]. They observed the coexistence of the two phases over a significantly wide range of concentration which was attributed to the polydispersity of nanotubes dimensions and their straightness. It was found that longer and thicker nanotubes preferentially separate into the anisotropic nematic phase. Subsequently they have investigated size-dependence and elasticity of LC CNTs. Recently, they reported the fabrication of macroscopic fibers of well-aligned MWNTs by wet spinning from the LC using ethylene glycol as the solvent. The electrical conductivity of these CNT fibers has been found to be highly anisotropic. Nanotubes were found to be highly aligned within these fibers due to the combination of shear forces and the LC phase.

Smalley et al. reported the exfoliation of CNT bundles with the help of a superacid [73–77]. SWNTs can be dispersed at high concentration in superacid, the protonation of CNTs sidewalls eliminates wall-wall van der Waals interactions and promotes the dispersion process. The tubes are stabilized against aggregation by the formation of an electrostatic double layer of protons and negative counter-ions. At very low concentration, CNTs in superacids dissolve as individual tubes. At higher concentration, solvated CNTs form nematic phase with polydomains (Fig. 6.11). Under anhydrous condition, the LC phase can be processed into highly aligned fibers with controlled morphology of pure CNTs without the aid of any surfactants or polymers.

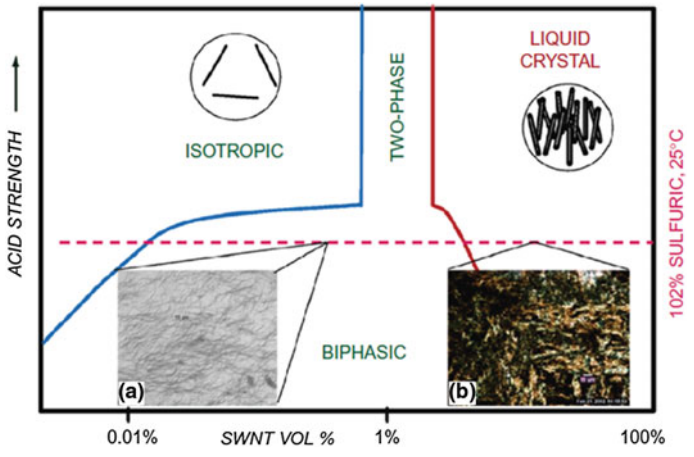

Fig. 6.11 Isotropic to nematic phase transition in CNTs. Reproduced with permission from [74]. Copyright 2006 American Chemical Society

Badaire et al. reported the formation of LC phase of CNTs by non-covalent functionalization with single strand DNA in water [78–80]. They observed that a nematic-isotropic coexistence is formed for nanotubes concentrations between 2 and 4 weight%. Above 4 weight%, the system forms a single nematic phase of unmodified and freely dispersed nanotubes. Poulin et al. uniformly aligned the nematic aqueous suspensions of nanotubes in thin cells by mechanical shearing. Homogeneous anisotropic thin films were obtained by drying the nematic phase. The order parameter is measured by polarized Raman spectroscopy and found to be quite weak due to entanglement of the nanotubes. Recently, Puech et al. showed that bile-salt stabilized SWNTs exhibit a first order transition to a nematic LC phase. The nematic phase expresses itself in the form of micron-sized spindle shaped nematic droplet freely floating in the isotropic host dispersion confirmed by polarization microscopy. Furthermore, the director field was found to be uniform in these nematic droplets. They later reported that shortening the bile salt stabilized nanotubes by high power ultrasonication and centrifugation allows the formation of LCs that can easily be oriented under the form of large macroscopic monodomains. The orientational order parameter of the LC was measured by polarized Raman spectroscopy which was found to approach the value theoretically expected for LCs made of rigid rods in solution. LC phase behavior of CNTs dispersed in biological hyaluronic acid solutions has been stabilized and studied [82]. Another biopolymer dispersant gellan gum is used to achieve aqueous dispersions of highly concentrated SWNTs which exhibit LC phase [83]. Large-scale aligned-nanotube composites membranes have been successfully prepared from such highly concentrated CNT suspensions. Such membranes with improved alignment of CNTs may find potential application in high-performance biocomposite functional materials such as sensors and actuators. Recently, the first lyotropic cholesteric LC phase has been realized by dispersing SWNTs in aqueous solutions of double-stranded DNA (dsDNA) [84]. Interestingly, depending on the dispersion methodology the polydomain nematic phase could also be obtained in these systems. The typical finger print texture of CNT cholesteric LC phase is shown in Fig. 6.12. This controlled phase behavior could open new routes for producing SWNT films with controlled morphology and optical properties of cholesteric films.

Noncovalent functionalization of SWNTs is particularly attractive avenue for dispersion because it enables modification of material properties without altering the chemical structure of the nanotubes. Dispersion of SWNTs at high concentrations in organic solvents, as alternative to water, provides increased flexibility for incorporating various chemical functionalities, tuning morphologies, and as a result controlling the properties of the resulting composite material. Among suitable dispersants, conjugated polymers are promising candidates owing to their ability to undergo pi-pi stacking with SWNTs. Organic solvent based nematic lyotropic LC phase of noncovalently functionalized CNTs has been reported by Bao et al. [85]. They reported a high-concentration dispersion of SWNTs in organic solvents by conjugated polymers and for the first time its transition into the nematic LC phase. The polymer-SWNT LC composites can be easily aligned through simple shearing

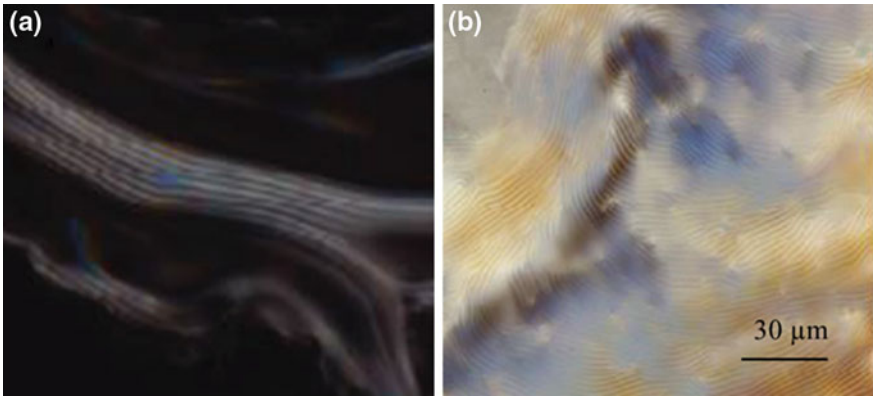

Fig. 6.12 Finger print texture in CNT LC. Reproduced with permission from [84]. Copyright 2011 American Chemical Society

by pushing a drop of the polymer/SWNT dispersion with the edge of a glass pipette tip on a glass substrate, resulting in large monodomains of uniform brightness. Anisotropy in electrical conductance was observed in those shear-aligned SWNT films. The conductance of a given film along the shearing direction is always at least twice its conductance perpendicular to the shearing direction. The aligned SWNT films fabricated from the nematic phase are potentially useful as electrodes and are capable of alignment of LC materials and other molecular materials deposited on them. Pyrene functionalized poly(methyl methacrylate) (PMMA) was found to be highly efficient to solubilize and disentangle MWNTs in solutions that self-organize as LC phases in PMMA and polyethylene glycol (PEG) 400 matrices (these oligomeric matrices that are still mobile but do not evaporate like a solvent) [86]. High concentration of oriented domains offers the potential to align CNTs at high volume fractions.

Stable dispersions of CNTs have been achieved by dissolving purified CNTs in aqueous sodium dodecyl sulphate solution by sonication and centrifugation [87]. LC processing of highly oriented CNT arrays for thin-film transistors from the above dispersions has been demonstrated by Tsukruk et al. It is further demonstrated that the performance of thin-film transistors based on densely packed and uniformly oriented CNT arrays is largely improved compared to random CNTs as shown in Fig. 6.13. This approach has great potential in processing of high-performance electronic devices based on high density oriented CNT films with good device characteristics.

Recently Jiang et al. reported the formation of LC phase by SWNT polyelectrolytes in DMSO [88]. It was found that small-diameter nanotubes were preferentially functionalized when the polyelectrolytes are dispersed in DMSO. While both nematic and chiral nematic phases of pure and functionalized CNTs have been observed both in aqueous and organic mediums, however, smectic mesophase has not been observed yet. The polydispersity of CNTs seems to be the preventing factor to smectic phase formation. Moreover, thermotropic phase behavior of CNTs remains elusive [89] and is still a challenging task.

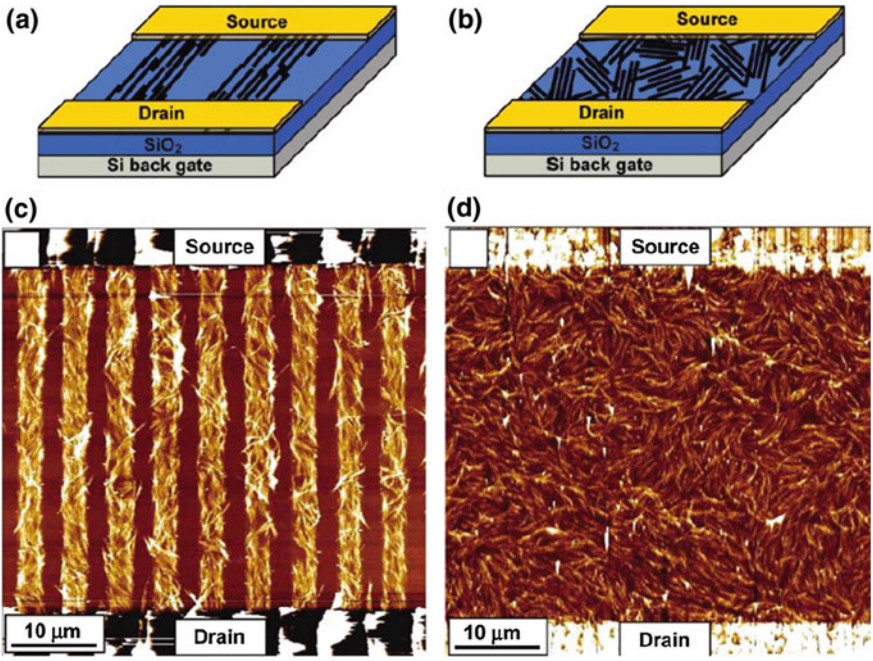

Fig. 6.13 Thin film transistors fabricated from CNT LC. Reproduced with permission from [87]. Copyright 2006 American Chemical Society

6.3 Liquid Crystals of Two-Dimensional (2D) Nanoparticles

6.3.1 Liquid Crystalline Nanodiscs

Like the LC ordering of collection of 1D rod-shaped nanoparticles and nanotubes in concentrated dispersions, collections of disc-shaped 2D nanoparticles should also exhibit orientational order with sufficient concentration and narrow size and shape distributions. Disc-like colloidal objects are experimentally observed to exhibit nematic, smectic and columnar type mesophases in consistent with theoretical predictions [90–92]. It should be noted that Langmuir had discovered in 1938 that bentonite clay particles exhibit a discotic nematic phase [22], much before the discovery of discotic LCs themselves.

Gabriel et al. described a lyotropic LC lamellar phase comprising an aqueous suspension of planar sheets of phosphatoantimonate $H_3Sb_3P_2O_{14}$ (Fig. 6.14) [93]. These highly organized materials can be mechanically or magnetically aligned over large temperature ranges. The structure of the LC phase has been investigated by small angle X-ray scattering studies. Aligned single domains of aqueous

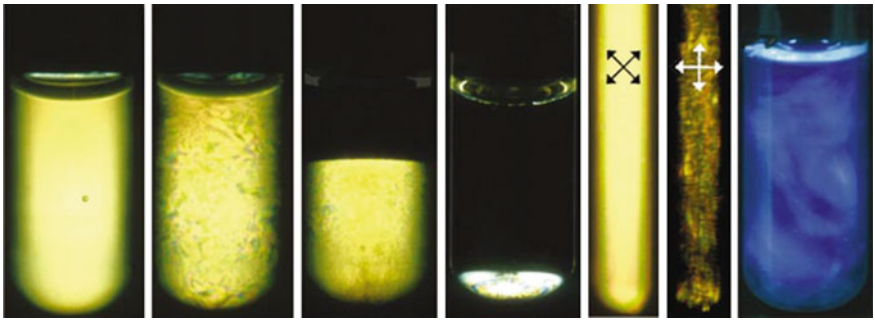

Fig. 6.14 LC phases of phosphatoantimonate in water. Reproduced with permission from [93]. Copyright 2001 Macmillan Magazines Ltd

suspensions of $H_3Sb_3P_2O_{14}$ have been used to measure residual dipolar couplings for the structure determination of biomolecules by liquid-state nuclear magnetic resonance (NMR).

Monodisperse $Ni(OH)_2$ platelets were found to form LC phase in their concentrated dispersions [94]. In the LC phase, interparticle interactions were varied by changing salt concentration and were found to influence the phase behavior. Columnar or layer structures were identified in this system by neutron diffraction studies. Layered double hydroxides (LDHs) are an interesting class of plate-like inorganic compounds which have received extensive attention as materials for catalysts, catalyst supports, adsorbents, anion exchangers, and promising materials for nanocomposites. Liu et al. reported the LC phase formation of colloidal Mg/Al LDH [95]. At larger concentrations, the aqueous dispersions formed nematic phases as confirmed by *Schlieren* textures under POM (Fig. 6.15). Later, they reported the observation of lamellar phase in the colloidal dispersions of positively charged LDH platelets [96]. The lamellar phase was characterized by XRD studies.

Lekkerkerker and coworkers reported the LC phase behavior of gibbsite ($Al(OH)_3$) platelets in a series of systematic studies [97–100]. Nematic, lamellar and columnar phase formations have been observed and characterized in gibbsite suspensions. The first system consists of sterically stabilized gibbsite platelets dispersed in toluene. Polyisobutene was employed as a steric stabilizer. Polarising optical microscopy (POM) revealed that the LC phase of these colloidal platelets was nematic. Subsequently, they described the observation of isotropic, nematic and columnar phases in the suspension of polydisperse plate like particles upon increasing the concentration of particles (Fig. 6.16).

By varying the ionic strength of the suspension of charged gibbsite platelets, they find isotropic-nematic and isotropic-columnar phase transitions. Through the variation of ionic strength, they were able to tune the effective aspect ratio of the platelets which enabled multiple phase transitions in one colloidal suspension. In this system the formation of triphasic suspension was noticed on prolonged standing a biphasic suspension indicating the effect of gravity on phase separation. Recently, the formation of unexpected smectic B phase has been reported in a

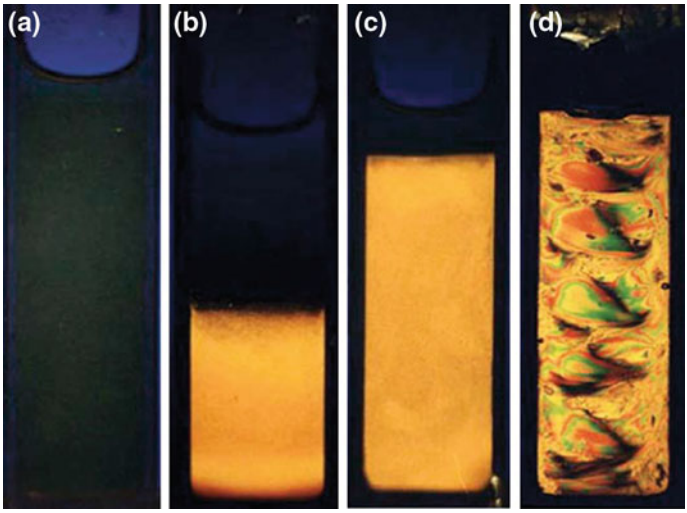

Fig. 6.15 LC phases of layered double hydroxide. Reproduced with permission from [95]. Copyright The Royal Society of Chemistry 2005

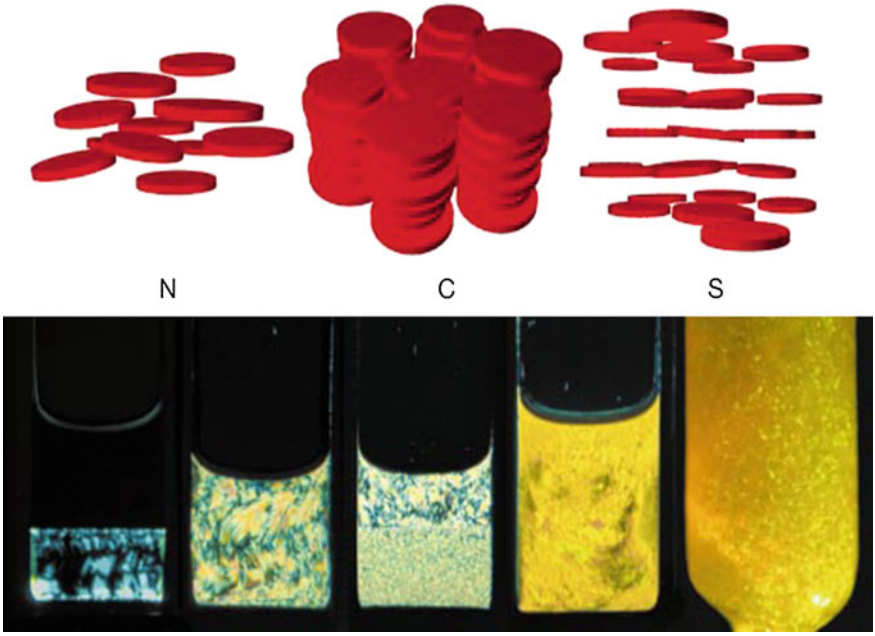

Fig. 6.16 LC phases of gibbsite nanodiscs. Reproduced with permission from [98]. Copyright 2000 Macmillan Magazines Ltd

system of charged colloidal gibbsite platelets suspended in DMSO. It is believed that the use of this polar aprotic solvent leads to a long range electrostatic Coulomb repulsion between platelets which drives the formation of smectic B phase consisting of hexagonally ordered particles. The phase structure has been identified by high-resolution X-ray scattering experiments (Fig. 6.17). This study shows that manipulating interactions leads to a new richness in the phase behavior of colloids.

Copper sulfide nanomaterials are *p*-type semiconductors that are being explored for application in photovoltaics, electrochemical sensors, and battery electrodes. Copper sulfide nanodiscs were observed to spontaneously self-assemble with face-to-face close packing when the solvent is evaporated from their concentrated dispersions. Isotropic to hexagonal columnar phase transition was observed during solvent evaporation and in the columnar phase the discs were not periodically ordered within the columns [101]. Bryks et al. demonstrated that self-assembly of copper alkanethiolates results liquid crystalline mesophase [102]. Well-ordered copper sulfide nanodiscs have been prepared by processing the copper alkanethiolates from their LC phase.

Gadolinium trifluoride (GdF_3) nanoplates have been observed to self-assemble into LC phases displaying long-range orientational and positional order [103]. LC

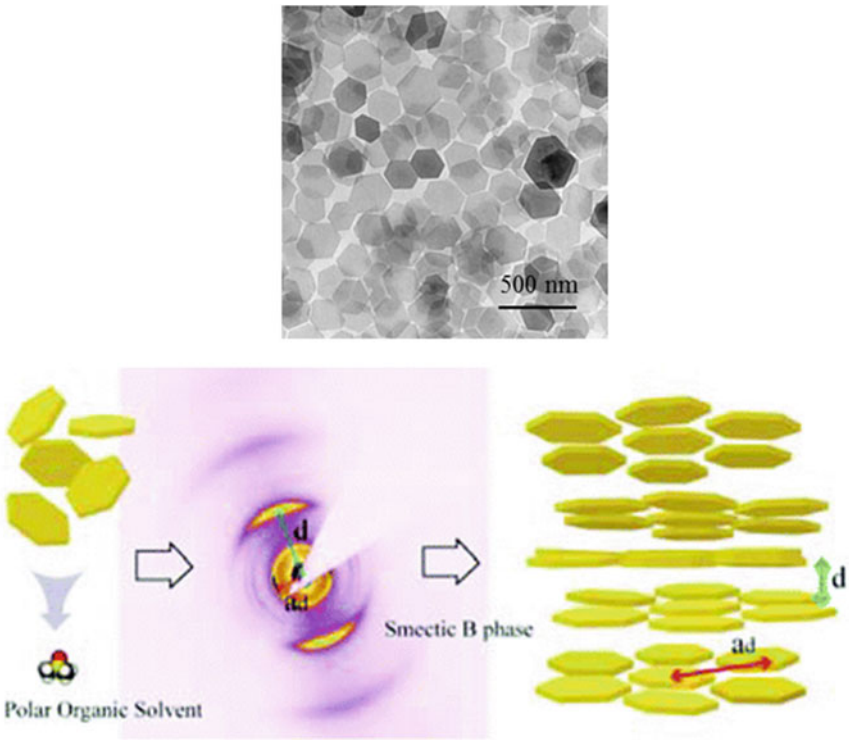

Fig. 6.17 Smectic B LC phase of gibbsite nanodiscs. Reproduced with permission from [100]. Copyright 2012 American Chemical Society

phases are formed using a liquid interfacial assembly, in which a drop of a nanocrystal suspension in a volatile solvent is slowly dried on glycol-type polar subphases. The assembled structures are characterized by a combination of TEM and XRD studies. The choice of subphase is found to be an important factor, a more polar subphase favors lamellar LC structure and a less polar subphase favors columnar assembly. Thermo-sensitive discotic LCs have been obtained by grafting poly(*N*-isopropylacrylamide) onto zirconium phosphate platelets [104]. The aspect ratio dependence of these soft discs on I-N transitions has been investigated and it was found that the nematic phase is stable for wide aspect ratio of the discs. By adjusting temperature, the aspect ratio of the disc can be varied since the grafted polymers change their conformation from extended to coiled with temperature.

6.3.2 Liquid Crystalline Graphene Derivatives

Graphene, the 2D nanoform of carbon, is a single layer of carbon atoms arranged in a honeycomb lattice. Graphite, made up of stacked graphene layers, exists in nature; however graphene is not known to exist naturally. This 2D allotrope of carbon is recently found to display outstanding optical, electrical, thermal and mechanical properties. Consequently, it has been demonstrated in various materials and device applications to modify physico-chemical properties including gas and energy storage, optoelectronics, energy conversion, catalysis and biological labeling. Liquid phase exfoliation can be employed to produce graphene based composites or films, which are key components for many applications such as thin-film transistors, and conductive transparent electrodes in light-emitting diodes and photovoltaics. Surfactant-assisted and surfactant-free methods of liquid phase exfoliation of graphene in aqueous and organic solutions have been developed. Since graphene can be considered as disc-like nano-object with very large aspect ratio, it has been shown that upon dispersion in sufficiently high concentrations it exhibits lyotropic LC phase behavior. In the following, we discuss the different methods used to obtain LC phases of graphene and its derivatives.

Pasquali et al. observed that graphite spontaneously exfoliates into single-layer graphene in chlorosulphonic acid and dissolves at isotropic concentrations as high as 2 mg/ml [105]. Under such conditions, graphite exfoliates into the solution owing to the protonation of their surface planes and remains dispersed because of the repulsive interaction among the graphene sheets. However, when the precipitated soluble graphene powder was redispersed in about 20 mg/ml concentration and centrifuged, spontaneous formation of LC phase was observed. The observed LC *Schlieren* texture is very similar to typical discotic nematic samples. Many potential applications of graphene including electronics and nanocomposites require that graphene-based materials be dispersed and processed in a fluid phase. In this context, such high concentration LC solutions could be particularly useful for making flexible electronic devices and multifunctional fibers since this route does

not compromise with the intrinsic properties of graphene. However, the processing of such a LC phase in the superacid requires very harsh conditions.

Graphene oxide (GO) is the oxygenated form of a graphene monolayer platelet with chemical functionalization capability, and extremely large surface area. GO is mass-producible from natural graphite by chemical oxidation and subsequent exfoliation. The hydrophilic surface functional groups, such as epoxide, hydroxyl and carboxyl groups that decorate the basal plane and the edge of GO, enable monolayer exfoliation in common polar solvents including water. Similar to graphene layers, GO layers also exhibit nematic LC phase behavior upon dispersion in high concentrations in suitable solvent medium. Kim et al. first introduced GO LCs as a versatile new class of carbon-based LCs [106]. They characterized the nematic phase of aqueous GOs by POM and freeze-fracture SEM (FF-SEM) (Fig. 6.18). Interestingly, the liquid crystallinity could be maintained upon the decoration of the GO platelets with nanoparticles or by including an additional polymer component in the solvent medium. Moreover, the orientation of GO LCs could be manipulated by a magnetic field or mechanical deformation. The liquid crystallinity of GO offers a versatile route to control the molecular organization and the corresponding properties of the carbon-based materials.

Xu et al. reported the formation and salt-dependent phase behavior of GO LCs [107–110]. Rheological measurements showed that GO aqueous dispersions

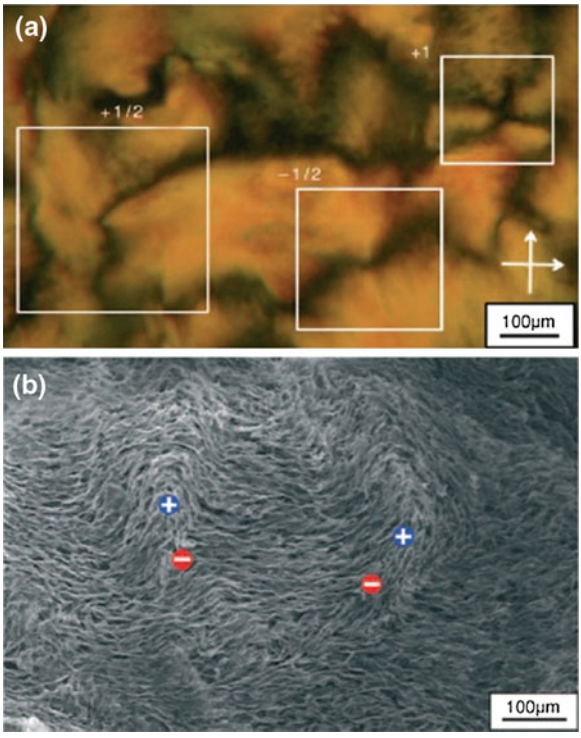

Fig. 6.18 POM and SEM images of GO LC. Reproduced with permission from [106]. Copyright 2011 Wiley-VCH Verlag GmbH & KGaA, Weinheim

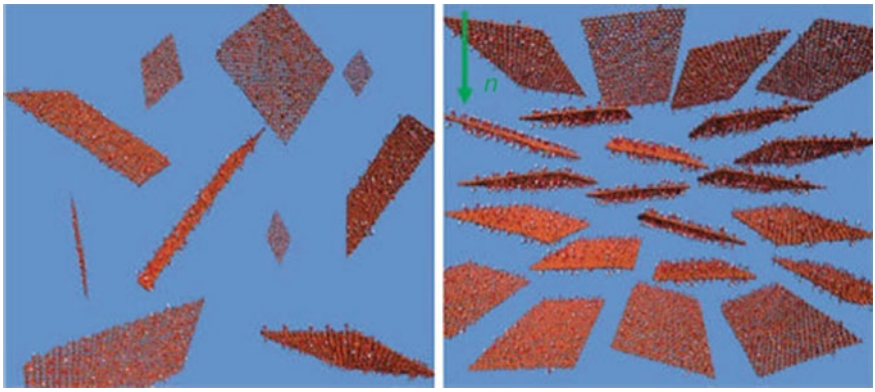

Fig. 6.19 Orientation of GO flakes in nematic and isotropic phases. Reproduced with permission from [107]. Copyright 2011 American Chemical Society

display typical shear flow and confirm the isotropic-nematic transition. The ordering of GO sheets in aqueous dispersions and in the solid state has been demonstrated by the characterization techniques of POM, small angle X-ray scattering, SEM and TEM. The direct, real-time fluorescent inspections by confocal laser microscopy further reveal that the individually dispersed fluorescent GO sheets align with orientational directions along their long axes (Fig. 6.19).

Subsequently Gao et al. disclosed that GO sheets at very high concentrations above the nematic phase can exhibit chiral LCs in a twist-grain-bondary phase-like model with simultaneous lamellar ordering and long-range helical frustrations. Such GO LCs were continuously spun into metres of macroscopic GO fibers which upon subsequent chemical reduction furnished neat graphene fibers with high conductivity and good mechanical performance. The flexible, strong graphene fibers were knitted into designed patterns and into directionally conductive textiles. Such multifunctional graphene fibers have promise in versatile applications such as next-generation functional textiles, flexible and wearable sensors, and supercapacitor devices. Very recently, the same group has reported lyotropic LC of polyacrylonitrile-grafted GOs in polar organic solvents such as dimethylformamide (DMF) and DMSO forming nematic and lamellar LCs upon increasing concentrations. Polyacrylonitrile chains were covalently and uniformly grafted onto GO surfaces via a simple free radical polymerization process.

Dan et al. reported the fabrication of discotic nematic LC phase by giant GO flakes with very high aspect ratio (10^4) in water [111, 112]. It was observed that higher aspect ratio leads to a dramatic change in mesomorphic behavior and the phase transition takes place at concentrations one order of magnitude lower than usually observed. The gel-like LC exhibits an unusual defect-free uniform director alignment over hundreds of nanometers which enabled them to characterize the nematic order parameter, optical birefringence and elastic properties of the mesophase. In order to directly visualize the orientation of GO flakes in the nematic phase, they used two different types of anisotropic colloidal inclusions such as gold

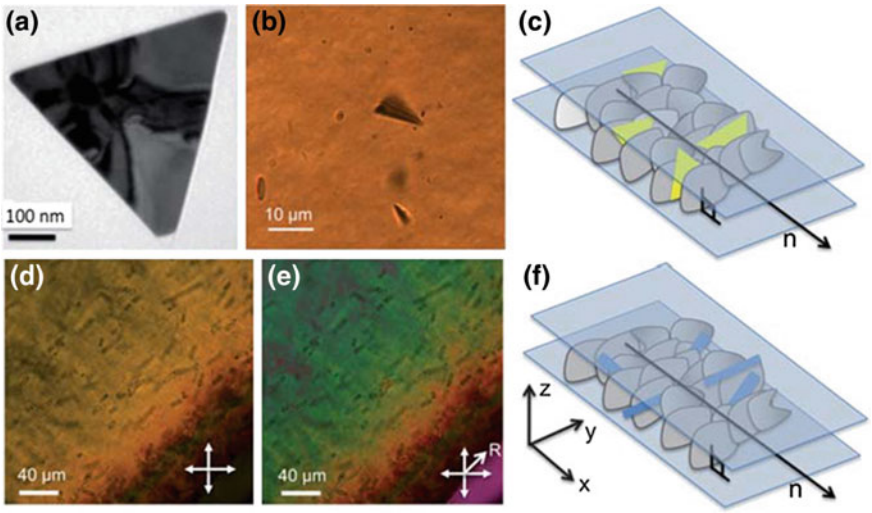

Fig. 6.20 GO LC and dispersion of nanodiscs and nanorods into it. Reproduced with permission from [111]. Copyright The Royal Society of Chemistry 2011

triangles and glass microrods. Gold triangular platelets spontaneously oriented with their large-area faces parallel to GO flakes whereas glass microrods spontaneously aligned with their long axes parallel to GO flakes as observed by POM (Fig. 6.20). They have further studied the dipolar and quadrupolar distortions of the director field by suspending colloidal microspheres in the nematic phase. Recently, Senyuk et al. have used nonlinear photoluminescence for fully 3D label-free imaging of structures of isotropic and orientational order of LC phases formed by aqueous GO flakes [112].

Kim et al. have developed a solution-phase synthesis method of ultralarge GO sheets involving pre-exfoliation of graphite flakes. Such large GO sheets spontaneously form lyotropic nematic phase at a very low concentration in water [113]. They produced self-assembled brick-like GO nanostructures by simple casting of GO dispersions and drying in ambient conditions. These free-standing GO papers can be potentially applied in many areas such as electrodes in energy-storage devices and nanocomposites with high degree of orientation. Hydration-responsive folding and unfolding in GO LC phases have been observed and studied by Guo et al. [114]. They investigated surface anchoring, complex fluid flow and microconfinement of GO LCs. It was observed that ordered GO phases undergo drying and rehydration cycles in which the GO layers fold and unfold to give unique anisotropic swelling behavior. The detailed investigations of hydration-responsive folding and unfolding open the potential for LC derived GO phases as smart stimuli-responsive materials. Zhu et al. reported the formation and transformation of GO LC structures in the synthesis and deformation of tough GO nanocomposite hydrogels [115]. Addition of poly(*N*-vinylpyrrolidone) and acrylamide, which are capable of forming hydrogen bonding with GO nanosheets, shifts the isotropic-

nematic transition to a lower volume fraction and enhances the formation of nemaic droplets. The LC domains have been found to be highly oriented under a high tensile strain. The LC nanocomposite hydrogels synthesized in this work have excellent mechanical properties. Recently, Tour group fabricated LC phases of GO nanoribbons and chemically reduced graphene nanoribbons in chlorosulphonic acid [116]. The starting material GO nanoribbons were obtained from the oxidative unzipping of MWNTs. The LC solutions were spun directly into hundreds of meters of continuous macroscopic fibers with high performances. GO LCs with controllable alignments can make use of the advantageous properties of graphene based materials especially in electro-optic devices. Shen et al. showed that GO LCs with weak interflake interactions can be macroscopically aligned by applying low electric fields [117]. It was observed that the GO LCs possess large Kerr coefficients which facilitated the fabrication of electro-optic devices with well-aligned defect-free GO over wide areas.

Organic solvent-based GO LCs have been reported by Jalili et al. which overcomes the practical limitations imposed on processing in water [118–121]. A wide range of common organic solvents including ethanol, acetone, tetrahydrofuran, DMF, etc. have been found to enable the fabrication of GO LC phase. This study contributes to the fundamental understanding of the solvophobic effect and the parameters affecting the self-assembly process and could provide practical solutions to the processibility of a wide range of GO based materials that require organic solvents because of solubility issues, water sensitivity etc. The research group has successfully demonstrated wet-spinning of graphene fibers and yarns from LC dispersions of aqueous GO. Based on rheological and POM investigations, they have been able to propose the relation between sheet size and polydispersity, concentration, liquid crystallinity and spinnability. The thermal conductivity of continuous spun, fully oriented and robust graphene fibers is found to be much higher than polycrystalline graphite. Outstanding mechanical performance has been obtained in large GO sheets reinforced elastomeric composite fibers. In this report, the insights into how both the GO sheet size dimension and dispersion parameters influence the mechanical behavior at various applied strains are discussed. A large-scale flexible fabrication of highly porous high-performance multifunctional GO and reduced GO fibers and yarns was demonstrated (Fig. 6.21). This fabrication method takes advantage of the intrinsic soft self-assembly behavior of ultralarge GO LC dispersions. The yarns were found to be mechanically robust, and exhibit high electric conductivity and high specific surface area.

Colloidal self-assembly is an efficient and inexpensive approach for the fabrication of photonic crystal structures. Li et al. reported photonic structures based on GO LCs exhibiting tunable structural color over the entire visible light spectrum [122]. The light reflected from the GO photonic dispersion can be tuned to cover the entire visible spectrum simply by varying the GO concentration. This finding show feasibility of development of novel graphene based materials for potential applications in sensors, tunable reflective filters, and many other optoelectronic devices. Residual dipolar couplings have proven to be an invaluable anisotropic (NMR) parameter for the structural elucidation of complex biopolymers and organic

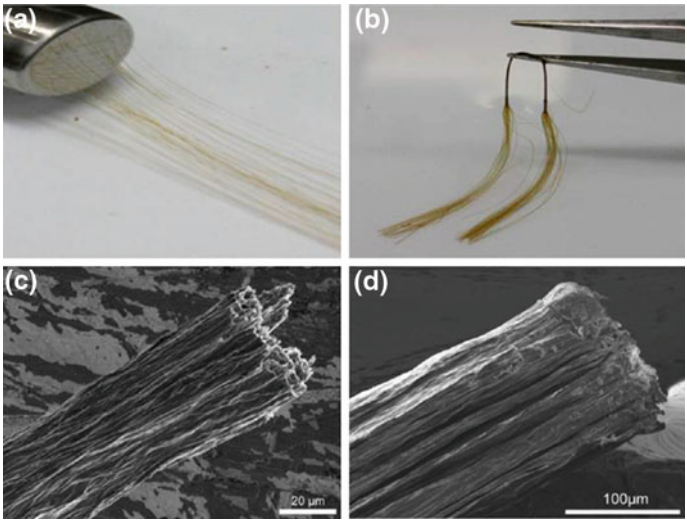

Fig. 6.21 GO fibers and yarns produced through LC phase processing. Reproduced with permission from [120]. Copyright 2014 American Chemical Society

molecules. Lei et al. demonstrated that GO LCs can act as versatile and tunable alignment medium for the measurement of residual dipolar couplings in organic solvents [123]. The LCs were found to be maintainable at very low concentrations and to be remarkably stable and broadly compatible with both aqueous and organic solvents. Compared with other alignment media, very clean and high-quality NMR spectra were acquired with the GO molecules in solution because of their rigidity and high molecular weight. Lee et al. used the liquid crystallinity of GO for size selection of large size GO and subsequently demonstrated size-dependent N-doping and oxygen reduction catalysis [124]. This work demonstrated that large GO may provide a better catalytic activity with controlled dopant structures.

Reduced GO (rGO) can be obtained by chemical reduction of GO. Chemical reduction of GO to produce rGO allows partial restoration of its electronic conjugation and graphene properties, but this recovery is also associated with a gain in hydrophobicity with a loss of water solubility, which hinders the formation of LC phase. Poulin et al. reported an approach that allows the formation of aqueous lyotropic LCs using rGO despite their lack of water solubility [125]. The objective was to combine the advantages of rGO materials and the easy processing of GO flakes in the LC phase. In this approach, the rGO particles are stabilized by bile salts (BSs), which act as surfactants. Surfactant-stabilized rGO flakes are shown to form LCs in water. The LC structures are characterized by small-angle X-ray scattering experiments that confirm the exfoliation of single-layer graphene flakes. The LCs formed with rGO offer opportunities to develop new materials that combine the advantages of liquid crystallinity for processing and ordering with the richer transport properties of rGO compared with GO. Graphite oxide (GtO) containing dozens of oxidized graphene

sheets have been reported to exhibit LC phase behavior [126]. Alignment of GtO LC under electric field has been demonstrated. It may be possible to fabricate functional materials by processing the GtO from its LC phase.

6.4 Conclusions and Outlook

LC phase formation by anisotropic nanoparticles is currently a vibrant field of research with an exciting future. Metallic, semiconducting and carbon based 1D and 2D anisotropic nanoparticles have been appropriately functionalized by either physical or chemical methods to exhibit LC phase behavior under suitable conditions. Thus, lyotropic LC phase behaviors of anisotropic nanoparticles have been realized both in aqueous and organic solutions. Nematic, biaxial nematic, lamellar and columnar phases have been observed. Interesting mechanical, optical, electrical and magnetic properties of the anisotropic building blocks have been exploited to fabricate functional materials and devices. Owing to their preferred orientation and ordering, anisotropic nanoparticles have been organized into a diverse array of well-defined higher-order architectures via processing through their LC phases. The research and development presented in this chapter undoubtedly contributes toward our fundamental understanding of phase behavior of anisotropic particles and provides economic routes for the facile processing of these intriguing materials. However, commercial exploitation of these materials is still in its infancy. The number of anisotropic building blocks exhibiting lyotropic LC phases has steadily increased. A critical parameter is the dispersity in the size of the particles. Indeed, polydispersity usually prevents long range positional ordering. Therefore, it is of paramount importance to fabricate LC phases from monodisperse anisotropic nanoparticles. Given the contemporary significance of 1D and 2D nanobuilding blocks, it is anticipated that the combination of outstanding and unprecedented properties of tailored anisotropic nanoparticles with processibility and alignment properties of LCs can lead to useful materials and devices with promising properties and performances.

Acknowledgments The preparation of this chapter benefited from the support to Quan Li by US Air Force Office of Scientific Research (AFOSR), US Department of Energy (DOE), US Army Research Office (ARO), US Department of Defense Multidisciplinary University Research Initiative (DoD MURI), US National Aeronautics and Space Administration (NASA), and US National Science Foundation (NSF), and Ohio Third Frontier.

References

1. Q. Li (ed.), *Liquid Crystals Beyond Displays: Physics, Chemistry, and Applications* (Wiley, Hoboken, 2012)
2. Q. Li (ed.), *Self-organized Organic Semiconductors: From Materials to Device Applications* (Wiley, Hoboken, 2011)

3. H.K. Bisoyi, Q. Li, *Liquid Crystals Kirk-Othmer Encyclopedia of Chemical Technology* (Wiley-VCH, New York, 2014), pp. 1–52
4. P.G. de Gennes, J. Prost, *The Physics of Liquid Crystals* (Oxford University Press, Oxford, 1993)
5. P.J. Collings, M. Hird, *Introduction to Liquid Crystals: Chemistry and Physics* (Taylor & Francis, London, 1997)
6. S. Kumar, *Chemistry of Discotic Liquid Crystals: From Monomers to Polymers* (CRC Press, Boca Raton, 2011)
7. J.W. Goodby, P.J. Collings, T. Kato, C. Tschierske, H. Glesson, P. Raynes (eds.), *Handbook of Liquid Crystals*, 2nd edn. (Wiley-VCH, Weinheim, 2014)
8. Q. Li (ed.), *Intelligent Stimuli Responsive Materials: From Well-Defined Nanostructures to Applications* (Wiley, Hoboken, 2013)
9. G.H. Brown, J.J. Wolken, *Liquid Crystals and Biological Structures* (Academic Press, New York, 1979)
10. S.J. Woltman, G.D. Jay, G.P. Crawford (eds.), *Liquid Crystals: Frontiers in Biomedical Applications* (World Scientific, New Jersey, 2007)
11. A.G. Petrov, *The Lyotropic state of Matter: Molecular Physics and Living Matter Physics* (Gordon & Breach Science Publishers, Amsterdam, 1999)
12. F.C. Bawden, N.W. Pirie, J.D. Bernal, I. Fankuchen, Liquid crystalline substances from virus infected plants. Nature **138**, 1051 (1936)
13. Z. Dogic, S. Fraden, Ordered phases of filamentous viruses. Curr. Opin. Colloid. Inter. Sci. **11**, 47–55 (2006)
14. Z. Dogic, S. Fraden, Cholesteric phase in virus suspensions. Langmuir **16**, 7820–7824 (2000)
15. Z. Dogic, S. Fraden, Smectic phase in a colloidal suspension of semiflexible virus particles. Phys. Rev. Lett. **78**, 2417–2420 (1997)
16. M. Nakata, G. Zanchetta, B.D. Chapman, C.D. Jones, J.O. Cross, R. Pindak, T. Bellini, N.A. Clark, Science **318**, 1276–1279 (2007)
17. G. Zanchetta, M. Nakata, M. Buscaglia, T. Bellin, N.A. Clark, Proc. Natl. Acad. Sci. U.S.A. **105**, 1111–1117 (2008)
18. Q. Li (ed.), *Nanoscience with Liquid Crystals: From Self-Organized Nanostructures to Applications* (Springer, Heidelberg, 2014)
19. H.K. Bisoyi, S. Kumar, Liquid crystal nanoscience: an emerging avenue of soft self-assembly. Chem. Soc. Rev. **40**, 306–319 (2011)
20. G.J. Vroege, H.N.W. Lekkerkerker, Phase transitions in lyotropic colloidal and polymer liquid crystals. Rep. Prog. Phys. **55**, 1241 (1992)
21. H.N.W. Lekkerkerker, G.J. Vroege, Liquid crystal phase transitions in suspensions of mineral colloids: new life from old roots. Phil. Trans. R. Soc. A **371**, 20120263 (2013)
22. S.C. Glotzer, M.J. Solomon, Anisotropy of building blocks and their assembly into complex structures. Nat. Mater. **6**, 557–562 (2007)
23. P. Davidson, J.-C.P. Gabriel, Mineral liquid crystals. Curr. Opin. Collod. Inter. Sci. **9**, 377–383 (2005)
24. N. Miyamoto, T. Nakato, Liquid crystalline inorganic nanosheet colloids derived from layered materials. Isr. J. Chem. **52**, 881–894 (2012)
25. H.K. Bisoyi, S. Kumar, Carbon based liquid crystals: art and science. Liq. Cryst. **38**, 1427–1449 (2011)
26. T. Hegmann, H. Qi, V.M. Marx, Nanoparticles in liquid crystals: synthesis, self-assembly, defect formation and potential applications. J. Inorg. Organomet. Polym Mater. **17**, 483–508 (2007)
27. J.P.F. Lagerwall, G. Scalia, A new era for liquid crystal research: applications of liquid crystals in soft matter nano-, bio- and microtechnology. Curr. Appl. Phys. **12**, 1387–1412 (2012)
28. G.L. Nealon, R. Greget, C. Dominguez, Z.T. Nagy, D. Guillon, J.-L. Gallani, B. Donnio, Liquid-crystalline nanoparticles: hybrid design and mesophase structures. Beilstein J. Org. Chem. **8**, 349–370 (2012)

29. J.-C.P. Gabriel, P. Davidson, New trends in colloidal liquid crystals based on mineral moieties. Adv. Mater. **12**, 9–20 (2000)
30. J.P. Gabriel, P. Davidson, Mineral liquid crystals from self-assembly of anisotropic nanosystems. Top. Curr. Chem. **226**, 119–172 (2003)
31. A.S. Sonin, Inorganic lyotropic liquid crystals. J. Mater. Chem. **8**, 2557–2574 (1998)
32. F. Guo, R. Hurt, Supramolecular synthesis of graphenic mesogenic materials. Macromol. Chem. Phys. **213**, 1164–1174 (2012)
33. Z. Xu, C. Gao, Graphene in macroscopic order: liquid crystals and wet-spun fibers. Acc. Chem. Res. **47**, 1267–1276 (2014)
34. L. Onsager, The effect of shape on the interaction of colloidal particles. Ann. N. Y. Acad. Sci. **51**, 627–659 (1949)
35. P.A. Buining, H.N.W. Lekkerkerker, Isotropic-nematic separation of a dispersion of organophilic boehmite rods. J. Phys. Chem. **97**, 11510–11516 (1993)
36. N.R. Jana, L.A. Gearheart, S.O. Obare, C.J. Johnson, K.J. Edler, S. Mann, C.J. Murphy, Liquid crystalline assemblies of ordered gold nanorods. J. Mater. Chem. **12**, 2909–2912 (2002)
37. V. Sharma, K. Park, M. Srinivasarao, Colloidal dispersion of gold nanorods: historical background, optical properties, seed-mediated synthesis, shape separation and self-assembly. Mater. Sci. Eng., R **65**, 1–38 (2009)
38. S. Umadevi, X. Feng, T. Hegmann, Large area self-assembly of nematic liquid-crystal-functionalized gold nanorods. Adv. Funct. Mater. **23**, 1393–1403 (2012)
39. S. Murali, T. Xu, B.D. Marshall, M.J. Kayatin, K. Pizarro, V.K. Radhakrishnan, D. Nepal, V. A. Davis, Lyotropic liquid crystalline self-assembly in dispersions of silver nanowires and nanoparticles. Langmuir **26**, 11176–11183 (2010)
40. J. Kim, A. de la Cotte, R. Deloncle, S. Archambeau, C. Biver, J.-P. Cano, K. Lahlil, J.-P. Boilot, E. Grelet, T. Gacoin, $LaPO_4$ Mineral liquid crystalline suspensions with outstanding colloidal stability for electro-optical applications. Adv. Funct. Mater. **22**, 4949–4956 (2012)
41. A. Kuijk, A. van Blaaderen, A. Imhof, Synthesis of monodisperse, rodlike silica colloids with tunable aspect ratio. J. Am. Chem. Soc. **133**, 2346–2349 (2011)
42. T. Xu, V.A. Davis, Liquid crystalline phase behavior of silica nanorods in dimethyl sulfoxide and water. Langmuir **30**, 4806–4813 (2014)
43. K. Kanie, A. Maramatsu, Organic-inorganic hybrid liquid crystals: thermotropic mesophases formed by hybridization of liquid crystalline phosphates and monodispersed alpha-Fe_2O_3 particles. J. Am. Chem. Soc. **127**, 11578–11579 (2005)
44. S.M. Taheri, S. Fischer, M. Trebbin, S. With, J.H. Schroder, J. Perlich, S.V. Roth, S. Forster, Lyotropic phase behavior of polymer-coated iron oxide nanoparticles. Soft Matter **8**, 12124–12131 (2012)
45. J. Tang, S. Fraden, Magnetic-field-induced isotropic-nematic phase transition in a colloidal suspension. Phys. Rev. Lett. **71**, 3509–3512 (1993)
46. B.J. Lemaire, P. Davidson, J. Ferre, J.P. Jamet, P. Panine, I. Dzov, J.P. Jolivet, Outstanding magnetic properties of nematic suspensions of goethite (α-FeOOH) nanorods. Phys. Rev. Lett. **88**(125507), 1–4 (2002)
47. S. Belli, A. Patti, M. Dijkstra, R. van Roij, Polydispersity stabilizes biaxial nematic liquid crystals. Phys. Rev. Lett. **107**(148303), 1–4 (2011)
48. G.J. Vroege, D.M.E. Thies-Weesie, A.V. Petukhov, B.J. Lemaire, P. Davidson, Smectic liquid-crystalline order in suspensions of highly polydisperse goethite nanorods. Adv. Mater. **18**, 2565–2568 (2006)
49. E. van den Pol, D.M.E. Thies-Weesie, A.V. Petukhov, G.J. Vroege, K. Kvashnina, Influence of polydispersity on the phase behavior of colloidal goethite. J. Chem. Phys. **129**(164715), 1–8 (2008)
50. B.J. Lemaire, P. Davidson, P. Panine, J.P. Jolivet, Magnetic-field-induced nematic-columnar phase transition in aqueous suspensions of goethite (α-FeOOH) nanorods. Phys. Rev. Lett. **93**(267801), 1–4 (2004)

51. E. van den Pol, A.V. Petukhov, D.M.E. Thies-Weesie, D.V. Byelov, G.J. Vroege, Experimental realization of biaxial liquid crystal phases in colloidal dispersions of boardlike particles. Phys. Rev. Lett. **103**(258301), 1–4 (2009)
52. E. Van den Pol, A. Lupascu, M.A. Diaconeasa, A.V. Petukhov, D.V. Byelov, G.J. Vroege, Onsager revisited: magnetic field induced nematic-nematic phase separation in dispersions of goethite nanorods. J. Phys. Chem. Lett. **1**, 2174–2178 (2010)
53. H. Maeda, Y. Maeda, Liquid crystal formation in suspensions of hard rodlike colloidal particles: direct observation of particle arrangement and self-ordering behavior. Phys. Rev. Lett. **90**(018303), 1–4 (2003)
54. H. Maeda, Y. Maeda, An atomic force microscopy study of surface structures of colloidal β-FeOOH particles forming smectic layers. Nano Lett. **2**, 1073–1077 (2002)
55. L. Li, J. Walda, L. Manna, A.P. Alivisatos, Semiconductor nanorod liquid crystals. Nano Lett. **2**, 557–560 (2002)
56. L.-S. Li, A.P. Alivisatos, Semiconductor nanorod liquid crystals and their assembly on substrate. Adv. Mater. **15**, 408–411 (2003)
57. L. Li, M. Marjanska, G.H.J. Park, A. Pines, A.P. Alivisatos, Isotropic-liquid crystalline phase diagram of a CdSe nanorods solution. J. Chem. Phys. **120**, 1149–1152 (2004)
58. A. Dessombz, D. Chiche, P. Davidson, P. Panine, C. Chaneac, J.-P. Jolivet, Design of liquid-crystalline aqueous suspensions of rutile nanorods: evidence of anisotropic photocatalytic properties. J. Am. Chem. Soc. **129**, 5904–5909 (2007)
59. K. Kanie, T. Sugimoto, Organic-inorganic hybrid liquid crystals: hybridization of calamitic liquid crystalline amines with monodispersed anisotropic TiO_2 nanoparticles. J. Am. Chem. Soc. **125**, 10518–10519 (2003)
60. S. Meuer, K. Fischer, I. Mey, A. Janshoff, M. Schmidt, R. Zentel, Liquid crystals from polymer-functionalized TiO_2 nanorod mesogens. Macromolecules **41**, 7946–7952 (2008)
61. M. Zorn, S. Meure, M.N. Tahir, Y. Khalavka, C. Sonnichsen, W. Tremel, R. Zentel, Liquid crystalline phases from polymer functionalized semiconducting nanorods. J. Mater. Chem. **18**, 3050–3058 (2008)
62. M. Zorn, R. Zentel, Liquid crystalline orientation of semiconducting nanorods in a semiconducting matrix. Macromol. Rapid Commun. **29**, 922–927 (2008)
63. M. Zorn, M.N. Tahir, B. Bergmann, W. Tremel, C. Grigoriadis, G. Floudas, R. Zentel, Orientation and dynamics of ZnO nanorods liquid crystals in electric fields. Macromol. Rapid Commun. **31**, 1101–1107 (2010)
64. S. Zhang, P.W. Majewski, G. Keskar, L.D. Pfefferle, C.O. Osuji, Lyotropic self-assembly of high-aspect-ratio semiconductor nanowires of single-crystal ZnO. Langmuir **27**, 11616–11621 (2011)
65. S. Zhang, C.I. Pelligra, G. Keskar, P.W. Majewski, F. Ren, L.D. Pfefferle, C.O. Osuji, Liquid crystalline order and magnetocrystalline anisotropy in magnetically doped semiconducting ZnO nanowires. ACS Nano **5**, 8357–8364 (2011)
66. S. Zhang, S. Kumar, Carbon nanotubes as liquid crystals. Small **4**, 1270–1283 (2008)
67. C. Zakri, C. Blanc, E. Grelet, C. Zamora-Ledezma, N. Puech, E. Anglaret, P. Poulin, Liquid crystals of carbon nanotubes and graphene. Phil. Trans. R. Soc. A **371**(20120499), 1–15 (2013)
68. W. Song, I.A. Kinloch, A.H. Windle, Nematic liquid crystallinity of multiwall carbon nanotubes. Science **302**, 1363–1363 (2003)
69. S. Zhang, I.A. Kinloch, A.H. Windle, Mesogenicity drives fractionation in lyotropic aqueous suspensions of multiwall carbon nanotubes. Nano Lett. **6**, 568–572 (2006)
70. S. Zhang, K.K.K. Koziol, I.A. Kinloch, A.H. Windle, Macroscopic fibers of well-aligned carbon nanotubes by wet spinning. Small **4**, 1217–1222 (2008)
71. W. Song, A.H. Windle, Isotropic-nematic phase transition of dispersions of multiwall carbon nanotubes. Macromolecules **38**, 6181–6188 (2005)
72. W. Song, A.H. Windle, Size-dependence and elasticity of liquid-crystalline multiwalled carbon nanotubes. Adv. Mater. **20**, 3149–3154 (2008)

73. V.A. Davis, L.M. Ericson, A.N.G. Parre-Vasquez, H. Fan, Y. Wang, V. Prieto, J.A. Longoria, S. Ramesh, R.K. Saini, C. Kittrell, W.E. Billups, W.W. Adams, R.H. Hauge, R.E. Smalley, M. Pasquali, Phase behavior and rheology of SWNTs in superacids. Macromolecules **37**, 154–160 (2004)
74. P.K. Rai, R.A. Pinnick, A.N.G. Parra-Vasquez, V.A. Davis, H.K. Schmidt, R.H. Hauge, R.E. Smalley, M. Pasquali, J. Am. Chem. Soc. **128**, 591–595 (2006)
75. S. Ramesh, L.M. Ericson, V.A. Davis, R.K. Saini, C. Kittrell, M. Pasquali, W.E. Billups, W. W. Adams, R.H. Hauge, R.E. Smalley, Dissolution of pristine single walled carbon nanotubes in superacids by direct protonation. J. Phys. Chem. B **108**, 8794–8798 (2004)
76. V.A. Davis, A.N.G. Parra-Vasquez, M.J. Green, P.K. Rai, N. Behabtu, V. Prieto, R.D. Booker, J. Schmidt, E. Kesselman, W. Zhou, H. Fan, W.W. Adams, R.H. Hauge, J.E. Fischer, Y. Cohen, Y. Talmon, R.E. Smalley, M. Pasquali, True solutions of single-walled carbon nanotubes for assembly into macroscopic materials. Nature Nanotech. **4**, 830–834 (2009)
77. L.M. Ericson, H. Fan, H. Peng, H. Peng, V.A. Davis, W. Zhou, J. Sulpizio, Y. Wang, R. Booker, J. Vavro, C. Guthy, A.N.G. Parra-Vasquez, M.J. Kim, S. Ramesh, R.K. Saini, C. Kittrell, G. Lavin, H. Schmidt, W.W. Adams, W.E. Billups, M. Pasquali, W.-F. Hwang, R.H. Hauge, J.E. Fischer, R.E. Smalley, Macroscopic, neat, single-walled carbon nanotubes fiers. Science **305**, 1447–1450 (2004)
78. S. Badaire, C. Zakri, M. Maugey, A. Derre, J.N. Barisci, G. Wallace, P. Poulin, Liquid crystals of DNA-stabilized carbon nanotubes. Adv. Mater. **17**, 1673–1676 (2005)
79. C. Zamora-Ledezma, C. Blanc, M. Maugey, C. Zakri, P. Poulin, E. Anglaret, Anisotropic thin films of single wall carbon nanotubes from aligned lyotropic nematic suspensions. Nano Lett. **8**, 4103–4107 (2008)
80. N. Puech, C. Blanc, E. Grelet, C. Zamora-ledezma, M. Maugey, C. Zakri, E. Anglaret, P. Poulin, Highly ordered carbon nanotubes nematic liquid crystals. J. Phys. Chem. C **115**, 3272–3278 (2011)
81. N. Puech, E. Grelet, P. Poulin, C. Blanc, P. van der Schoot, Nematic droples in aqueous dispersions of carbon nanotubes. Phys. Rev. E **82**(020702), 1–4 (2010)
82. S.E. Moulton, M. Maugey, P. Poulin, G.G. Wallace, Liquid crystal behavior of single-walled carbon nanotubes dispersed in biological hyaluronic acid solutions. J. Am. Chem. Soc. **129**, 9452–9457 (2007)
83. L. Lu, W. Chen, Large-scale aligned carbon nanotubes from their purified, highly concentrated suspension. ACS Nano **4**, 1042–1048 (2010)
84. G. Ao, D. Nepal, M. Aono, V.A. Davis, Cholesteric and nematic liquid crystalline phase behavior of double-stranded DNA stabilized single-walled carbon nanotubes dispersions. ACS Nano **5**, 1450–1458 (2011)
85. H.W. Lee, W. You, S. Barman, S. Hellstrom, M.C. Leieux, J.H. Oh, S. Liu, T. Fujiwara, W. M. Wang, B. Chen, Y.W. Jin, J.M. Kim, Z. Bao, Lyotropic liquid-crystalline solutions of high-concentration dispersions of single-walled carbon nanotubes with conjugated polymers. Small **5**, 1019–1024 (2009)
86. S. Meuer, L. Braun, R. Zentel, Solubilization of multi-walled carbon nanotubes by alpha-purene functionalized PMMA and their liquid crystalline self-organization. Chem. Commun. 3166–3168 (2008)
87. H. Ko, V.V. Tsukruk, Liquid-crystalline processing of highly oriented carbon nanotubes arrays for thin film transistors. Nano Lett. **6**, 1443–1445 (2006)
88. C. Jiang, A. Saha, C. Xiang, C.C. Young, J.M. Tour, M. Pasquali, A.A. Marti, Increased solubility, liquid-crystalline phase, and selective functionalization of single-walled carbon nanotubes polyelectrolyte dispersions. ACS Nano **7**, 4503–4510 (2013)
89. S. Kumar, H.K. Bisoyi, Aligned carbon nanotubes in the supramolecular order of discotic liquid crystals. Angew. Chem. Int. Ed. **46**, 1501–1503 (2007)
90. J.A.C. Veerman, D. Frenkel, Phase behavior of disklike hard-core mesogens. Phys. Rev. A **45**, 5632–5648 (1992)

91. A. Patti, S. Belli, R. van Roij, M. Dijkstra, Relaxation dynamics in the columnar liquid crystal phase of hard platelets. Soft Matter **7**, 3533–3545 (2011)
92. M.A. Bates, D. Frenkel, Nematic-isotropic transition in polydisperse systems of infinitely thin hard platelets. J. Chem. Phys. **110**, 6553–6559 (1999)
93. J.-C.P. Gabriel, F. Camerel, B.J. Lemaire, H. Desvaux, P. Davidson, P. Betail, Swollen liquid-crystalline lamellar phase based on extended solid-like sheets. Nature **413**, 504–508 (2001)
94. A.B.D. Brown, S.M. Clarke, A.R. Rennie, Ordered phase of platelike particles in concentrated dispersions. Langmuir **14**, 3129–3132 (1998)
95. S. Liu, J. Zhang, N. Wang, W. Liu, C. Zhang, D. Sun, Liquid-crystalline phases of colloidal dispersions of layered double hydroxide. Chem. Mater. **15**, 3240–3241 (2003)
96. N. Wang, S. Liu, J. Zhang, Z. Wu, J. Chen, D. Sun, Lamellar phase in colloidal suspensions of positively charged LDHs platelets. Soft Matter **1**, 428–430 (2005)
97. F.M. van der Kooij, H.N.W. Lekkerkerker, Formation of nematic liquid crystals in suspensions of hard colloidal platelets. J. Phys. Chem. B **102**, 7829–7832 (1998)
98. F.M. van der Kooij, K. Kassapidou, H.N.W. Lekkerkerker, Liquid crystal phase transitions in suspensions of polydisperse plate-like particles. Nature **406**, 868–871 (2000)
99. D. van der Beek, H.N.W. Lekkerkerker, Liquid crystal phases of charged colloidal platelets. Langmuir **20**, 8582–8586 (2004)
100. D. Kleshchanok, P. Holmqvist, J.-K. Meijer, H.N.W. Lekkerkerker, Lyotropic smectic B phase formed in suspensions of charged colloidal platelets. J. Am. Chem. Soc. **134**, 5985–5990 (2012)
101. A.E. Saunders, A. Ghezelbash, D. Smilgies, M.B. Sigman, B.A. Korgel, Columnar self-assembly of colloidal nanodisks. Nano Lett. **6**, 2959–2963 (2006)
102. W. Bryks, M. Wette, N. Velez, S.-W. Hsu, A.R. Tao, Supramolecular precursors for the synthesis of anisotropic Cu_2S nanocrystals. J. Am. Chem. Soc. **136**, 6175–6178 (2014)
103. T. Paik, D.-K. Ko, T.R. Gordon, V. Doan-Nguyen, C.B. Murray, Studies of liquid crystalline self-assembly of GdF_3 nanoplates by in-plane, out-of-plane SAXS. ACS Nano **5**, 8322–8330 (2011)
104. X. Wang, D. Zhao, A. Diaz, I.B.N. Medina, H. Wang, Z. Cheng, Thermo-sensitive discotic colloid liquid crystals. Soft Matter **10**, 7692–7695 (2014)
105. N. Behabtu, J.R. Lomeda, M.J. Green, A.L. Higginbotham, A. Sinitskii, D.V. Kosynkin, D. Tsentalovich, A.N.G. Parra-vasquez, J. Schmidt, E. Kesselman, Y. Cohen, Y. Talmon, J.M. Tour, M. Pasquali, Spontaneous high-concentration dispersions and liquid crystals of graphene. Nature Nanotech. **5**, 406–411 (2010)
106. J.E. Kim, T.H. Han, S.H. Lee, J.Y. Kim, C.W. Ahn, J.M. Yun, S.O. Kim, Graphene oxide liquid crystals. Angew. Chem. Int. Ed. **50**, 3043–3047 (2011)
107. Z. Xu, C. Gao, Aqueous liquid crystals of graphene oxide. ACS Nano **5**, 2908–2915 (2011)
108. Z. Xu, C. Gao, Graphene chiral liquid crystals and macroscopic assembled fibers. Nature Commun. **2**(571), 1–9 (2011)
109. Z. Xu, H. Sun, X. Zhao, C. Gao, Ultastrong fibers assembled from giant graphene oxide sheets. Adv. Mater. **25**, 188–193 (2013)
110. Z. Liu, Z. Xu, X. Hu, C. Gao, Lyotropic liquid crystal of polyacrylonitrile-grafted graphene oxide and its assembled continuous nacre-mimetic fibers. Macromolecules **46**, 6931–6941 (2013)
111. B. Dan, N. Behabtu, A. Martinez, J.S. Evans, D.V. Kosynkin, J.M. Tour, M. Pasquali, I.I. Smalyukh, Liquid crystals of aqueous, giant grapheme oxide flakes. Soft Matter **7**, 11154–11159 (2011)
112. B. Senyuk, N. Behabtu, B.G. Pacheco, T. Lee, G. Ceriotti, J.M. Tour, M. Pasquali, I.I. Smalyukh, Nonlinear photoluminescence imaging of isotropic and liquid crystalline dispersions of graphene oxide. ACS Nano **6**, 8060–8066 (2012)
113. S.H. Aboutalebi, M.M. Gudarzi, Q.B. Zheng, J.-K. Kim, Spontaneous formation of liquid crystals in ultalarge graphene oxide dispersions. Adv. Funct. Mater. **21**, 2978–2988 (2011)

114. F. Guo, F. Kim, T.H. Han, V.B. Shenoy, J. Huang, R.H. Hurt, Hydration-Responsive Folding and unfolding in graphene oxide liquid crystal phases. ACS Nano **5**, 8019–8025 (2011)
115. Z. Zhu, G. Song, J. Liu, P.G. Whitten, L. Liu, H. Wang, Liquid crystalline behavior of graphene oxide in the formation and deformation of tough nanocomposite hydrogels. Langmuir **30**, 14648–14657 (2014)
116. C. Xiang, N. Behabtu, Y. Liu, H.G. Chae, C.C. Young, B. Genorio, D.E. Tsentalovich, C. Zhang, D.V. Kosynkin, J.R. Lomeda, C.-C. Hwang, S. Kumar, M. Pasquali, J.M. Tour, Graphene nanoribbons as an advanced precursor for making carbon fiber. ACS Nano **7**, 1628–1637 (2013)
117. T.-Z. Shen, S.-H. Hong, J.-K. Song, Electro-optical switching of graphene oxide liquid crystals with an extremely large Kerr coefficient. Nat. Mater. **13**, 394–399 (2014)
118. R. Jalili, S.H. Aboutalebi, D. Esrafilzadeh, K. Konstantinov, S.E. Moulton, J.M. Razal, G.G. Wallace, Organic solvent-based graphene oxide liquid crystals: a facile route toward the next generation of self-assembled layer-by-layer multifunctional 3D architectures. ACS Nano **7**, 3981–3990 (2013)
119. R. Jalili, S.H. Aboutalebi, D. Esrafilzadeh, R.L. Shepherd, J. Chen, S. Aminorroaya-Yamini, K. Konstantinov, A.I. Minett, J.M. Razal, G.G. Wallace, Scalable, one-step wet-spinning of graphene fibers and yarns from liquid crystalline dispersions of graphene oxide: Towards multifunctional textiles. Adv. Funct. Mater. **23**, 5345–5354 (2013)
120. S.H. Aboutalebi, R. Jalili, D. Esrafilzadeh, M. Salari, Z. Gholamvand, S.A. Yamini, K. Konstantinov, R.L. Shepherd, J. Chen, S.E. Moulton, P.C. Innis, A.I. Minett, J.M. Razal, G. G. Wallace, High-Performance multifunctional graphene yarns: towards wearable all-carbon energy storage textiles. ACS Nano **8**, 2456–2466 (2014)
121. M.Z. Seyedin, J.M. Razal, P.C. Innis, R. Jalili, G.G. Wallace, Achieving outstanding mechanical performance in reinforced elastomeric composite fibers using large sheets of graphene oxide. Adv. Funct. Mater. **25**, 94–104 (2014)
122. P. Li, M. Wong, X. Zhang, H. Yao, R. Ishige, A. Takahara, M. Miyamoto, R. Nishimura, H.-J. Sue, Tunable lyotropic photonic liquid crystal based on graphene oxide. ACS Photonics **1**, 79–86 (2014)
123. X. Lei, Z. Xu, H. Sun, S. Wang, C. Griesinger, L. Peng, C. Gao, R.X. Tan, Graphene oxide liquid crystals as a versatile and tunable alignment medium for the measurement of residual dipolar couplings in organic solvents. J. Am. Chem. Soc. **136**, 11280–11283 (2014)
124. K.E. Lee, J.E. Kim, U.N. Maiti, J. Lim, J.O. Hwang, J. Shim, J.J. Oh, T. Yun, S.O. Kim, Liquid crystal size selection of large-size graphene oxide for size-dependent N-doped and oxygen reduction catalysis. ACS Nano **8**, 9073–9080 (2014)
125. C. Zamora-Ledezma, N. Puech, C. Zakri, E. Grelet, S.E. Moulton, G.G. Wallace, S. Gambhir, C. Blanc, E. Anglaret, P. Poulin, Liquid crystallinity and dimensions of surfactant-stabilized sheets of reduced graphene oxide. J. Phys. Chem. Lett. **3**, 2425–2430 (2012)
126. L. Tong, W. Qi, M. Wang, R. Huang, R. Su, Z. He, Long-range ordered graphite oxide liquid crystals. Chem. Commun. **50**, 7776–7779 (2014)

Chapter 7
Self-assembled 1D Semiconductors: Liquid Crystalline Columnar Phase

Manoj Mathews, Ammathnadu S. Achalkumar and Quan Li

Abstract Organic semiconducting materials have emerged as potential alternative to inorganic silicon based semiconductors for the production of low-cost, flexible and light weight plastic electronic devices. When compared with crystalline and polymeric structures, liquid crystalline (LC) ordering in organic semiconductors favors their self-assembly into large area monodomain thin-film structures with carrier mobilities in the range from 10^{-3} cm^2 V^{-1} s^{-1} to 10^{-1} cm^2 V^{-1} s^{-1}. The LC nature enables a self-healing process of structural defects such as grain boundaries within the material which is especially exploited during post production thermal treatment for device improvement. The main objective of this chapter is to review the research progress in the field of columnar LC semiconductors with the emphasis on molecular structure—charge transport property relationship, control of alignment, and their prospective applications in molecular electronics.

7.1 Introduction

Intense multidisciplinary research efforts of the past two decades have generated considerable progress in the field of organic semiconductors. When compared with inorganic semiconducting materials, organic molecules offer the advantage of low-cost synthesis and easy manufacture of large-area films by solution processing for

M. Mathews (✉)
Post Graduate & Research Department of Chemistry, St. Joseph's College, Devagiri, Calicut 673008, India
e-mail: mathewsmanoj@gmail.com

A.S. Achalkumar
Department of Chemistry, Indian Institute of Technology, Guwahati 781039, India

Q. Li (✉)
Liquid Crystal Institute and Chemical Physics Interdisciplinary Program, Kent State University, Kent, OH 44242, USA
e-mail: qli1@kent.edu

Q. Li (ed.), *Anisotropic Nanomaterials*, NanoScience and Technology,
DOI 10.1007/978-3-319-18293-3_7

the fabrication of cost-effective, lightweight plastic electronic products in the form of thin-film transistors, light-emitting diodes, solar cells, and sensors [1–4]. All organic semiconductors share in common a π-conjugated electron system, that is, alternating single and double bonds throughout the molecule. In a conjugated system, π-orbitals of adjacent carbon atoms overlap and the electrons occupying such orbitals become relatively delocalized to form energy band gaps (1.5–3 eV) in the semiconducting range. Organic semiconductors can be categorized into crystalline, amorphous, and liquid crystalline (LC) based on the morphology of the materials. The efficiency of these materials is directly related to the mobility of the charges achievable in their semiconducting thin-films. Crystalline organic semiconductors usually exhibit charge carrier mobilities over 10^{-1} cm^2 V^{-1} s^{-1}. The highest charge-carrier mobilities (>2 cm^2 V^{-1} s^{-1}) have been measured in organic single crystals of pentacene and rubrene [5, 6]. Polycrystalline films of polymeric semiconducting materials such as oligothiophenes have mobilities exceeding that of amorphous silicon (>1.0 cm^2 V^{-1} s^{-1}) [7–9]. Charge mobilities for amorphous solids are generally found to be below 10^{-3} cm^2 V^{-1} s^{-1}. Liquid crystalline semiconductors exhibit carrier mobilities in the range from 10^{-3} cm^2 V^{-1} s^{-1} to 10^{-1} cm^2 V^{-1} s^{-1}, i.e. between those of organic amorphous and crystalline materials [10]. Although very high carrier mobilities are observed for single crystalline materials, their slow growth and lack of processability prevent them from being integrated in low-cost, large-area devices on flexible substrates. For industrial applications, cost-effective approaches are sought after, particularly on solution processing techniques such as spin-coating, casting, or printing at ambient conditions. Moreover, device fabrication requires a precise control of material organization in the semiconducting layer. Although amorphous organic semiconductors based on π-conjugated polymers can be conveniently processed from solution, because of high structural disorder they show poor mobilities on the order of 10^{-3} cm^2 V^{-1} s^{-1} or less. On the other hand, when compared with amorphous solids or polycrystalline materials, LC semiconductors exhibit relatively high charge-carrier mobility and allow melt/solution processing. Higher carrier mobility is attributed to self-healing of defects as well as self-organizing nature of the LC phase. The emergence of LC phases associated with electronic charge carrier transport has triggered a rapid intensification of fundamental and technological research on this class of organic semiconductors.

7.2 Liquid Crystalline (LC) Semiconductors

Chemical structures of LC semiconductors have a similarity in terms of the aromatic π-conjugated system called a core and hydrocarbon chains. LC phases or mesophases are thermodynamically stable states of matter with an intermediate degree of order between crystals and liquids. LC phases can be induced in some shape-anisotropic (e.g. rod or disc shaped) molecules by alkyl chain substitutions. Liquid crystals or mesogens (LC phase forming materials) can be broadly classified

into thermotropic or lyotropic depending on whether the phase transitions are induced by change in temperature alone (thermotropic) or by the influence of both temperature and solvent (lyotropic) [11, 12]. Conventionally, rod-like and disc-shaped mesogens; they are popularly known as calamitics and discotics respectively exhibit thermotropic mesomorphism. Phase segregation arising from chemically and conformationally different molecular parts drives the self-organization of these molecules into hierarchically ordered mesophases such as nematic, smectic and columnar phases. Nematic and smectic phases of calamitic molecules have found commercial applications in liquid crystal displays (LCDs) and continue to attract research in view of other technological and biomedical applications [13, 14]. Discotic molecules exhibit two types of mesophases namely, nematic (N) phase and columnar (Col) phase. The discovery of columnar phase in discotic liquid crystals (DLCs) dates back to the report of Chandrasekhar et al. in 1977 in hexa-substituted esters of benzene **1** [15]. Subsequently, numerous disc-shaped molecules with different central aromatic cores and peripheral substitutions showing various mesophases have been reported. Figure 7.1 shows a general structural template for disk-shaped mesogens and the molecular structures of the most prominent DLC cores. With the natural tendency of π-orbitals of adjacent discotic molecules to maximally overlap, they self-assemble into columnar phases where molecules stack one on top of the other like pile of coins. Columnar phases exhibit rich polymesomorphism and are identified experimentally by the combined use of polarizing optical microscopy (for textural observation), differential scanning calorimetry (DSC, for phase transition temperatures), and X-ray diffraction studies (for molecular ordering in the phase). Columnar phases are further classified depending upon their phase symmetry and varying degrees of molecular order within the columns [16]. For example, upright columns forming a hexagonal columnar phase (Col_h) and tilted columns resulting in a rectangular columnar phase (Col_r) are the two most common types of columnar phases. In some cases, the columns are liquid-like, that is, there is no ordering of discs within or between the columns (disordered hexagonal columnar phase, Col_{hd}), while in others they are arranged in an ordered fashion (ordered hexagonal columnar phase, Col_{ho}). More ordered phases such as columnar oblique (Col_{ob}), columnar plastic (Col_p), and columnar helical (H) mesophases are not as common. Figure 7.2 shows the most common phase structures of the discotic molecules. Depending upon the molecular structure, the disk-like mesogens exhibit nematic (N), nematic columnar (N_{Col}) and chiral nematic (N*) phases. The nematic phase, like its calamitic analogue, is the least ordered mesophase and the least viscous. It possesses orientational order, while long-range positional order is absent, as illustrated in Fig. 7.3. In contrast to their calamitic counterparts, the short axis of the disc-shaped mesogens orient along the director (n) of the nematic phase. Hence, the discs align perpendicular to the director. Consequently, they show negative birefringence. Nematic DLCs are commercially useful as an optical compensator film for improving the viewing angle of LCDs [17]. It is noteworthy that not only the DLC compounds but also molecules with unconventional shapes such as linear

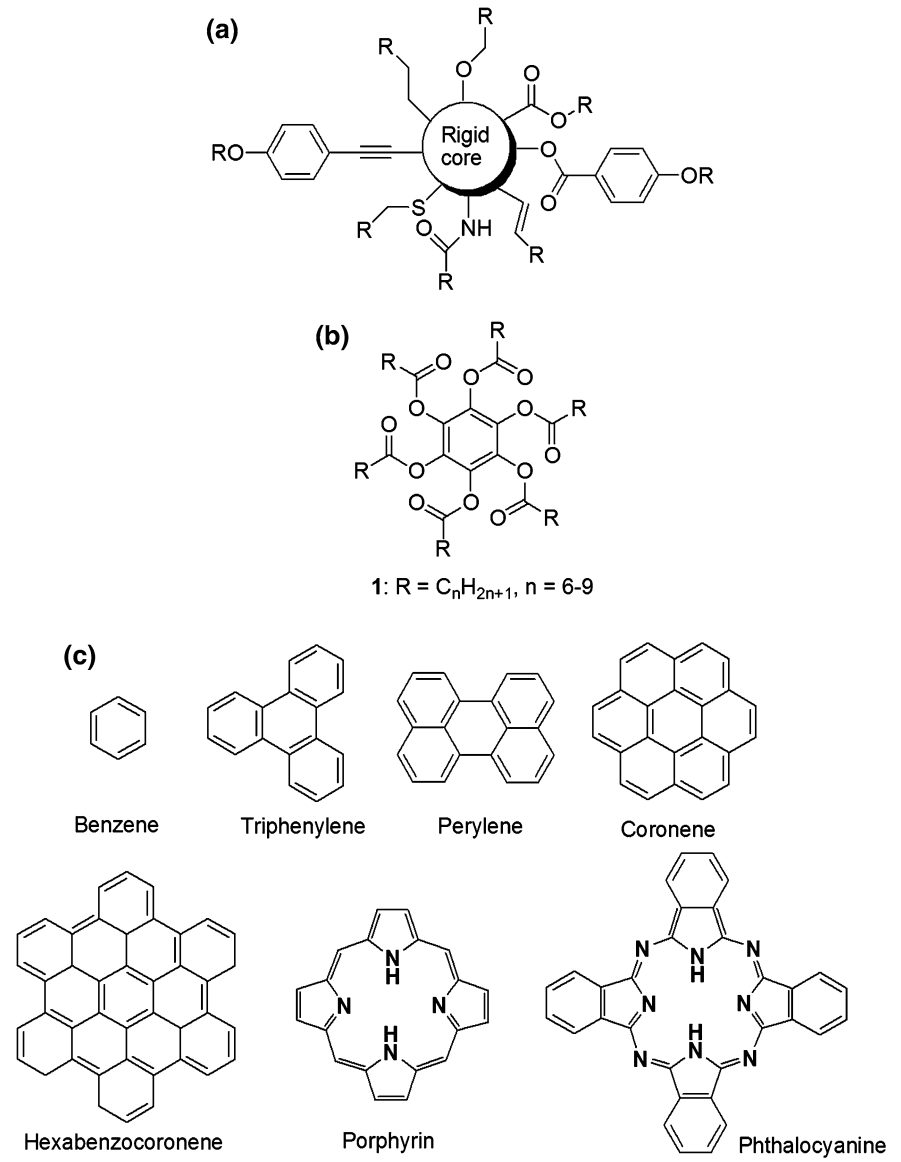

Fig. 7.1 **a** A general structural template for disk-shaped mesogens. **b** Molecular structure of hexa-ester benzene **1**. **c** Most studied aromatic cores as discotic mesogens

π-conjugated oligomers, rings, cones, and bowls have been shown to self-assemble into columnar phases [18]. Some of bent-core molecules, amphiphiles and dendrimers also exhibit uncommon columnar mesophase.

DLC molecules with a delocalized π-electron system can self-organize spontaneously into highly ordered columnar mesophase structures that are capable of

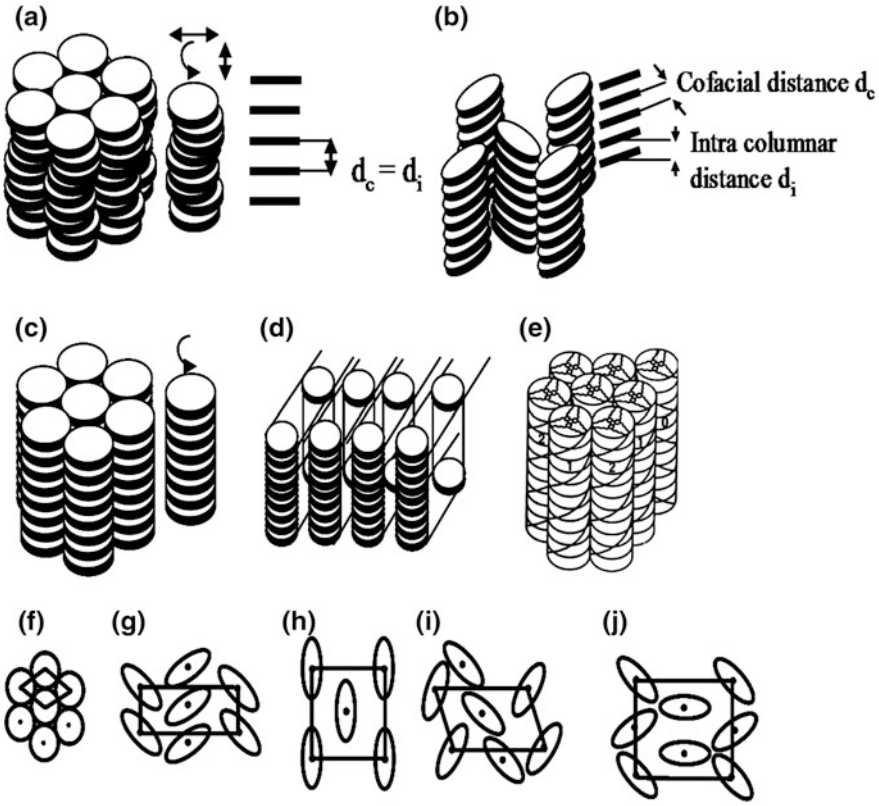

Fig. 7.2 Schematic illustration of the columnar phases of discotic liquid crystals. **a** Columnar hexagonal (Col_h) phase; **b** columnar rectangular (Col_r) phase; **c** columnar plastic (Col_p) phase; **d** columnar lamellar (Col_L) phase and **e** helical (H) phase. Also shown are top views of the two-dimensional lattices (ellipses denote disks that are tilted with respect to Col axis): **f** hexagonal; **g** and **j** rectangular; **h** rectangular face-centred and **i** oblique

electronic conduction in one dimension. Electronic charge carrier transport in the columnar mesophases of DLCs was confirmed in early 1990s [19]. Parallel to discotic columnar phases, charge carrier transport was also confirmed in the smectic phases of π-conjugated calamitic liquid crystals [20]. While the carrier transport is limited within a column in discotic LCs, it is within a layer in the semiconducting smectic liquid crystals. Therefore, conduction in columnar and smectic liquid crystals is said to be one-dimensional (1D) and two-dimensional (2D), respectively. Charge carrier mobility values as high as 0.5 $cm^2\ V^{-1}\ s^{-1}$ had been reported in the highly ordered smectic phases [10]. In contrast to the smectic and columnar phases in which efficient electronic transport is possible due to large intermolecular π-orbital overlap, only ionic conduction had been observed for a long time in the nematic and cholesteric phases. However, hole transport was recently confirmed in

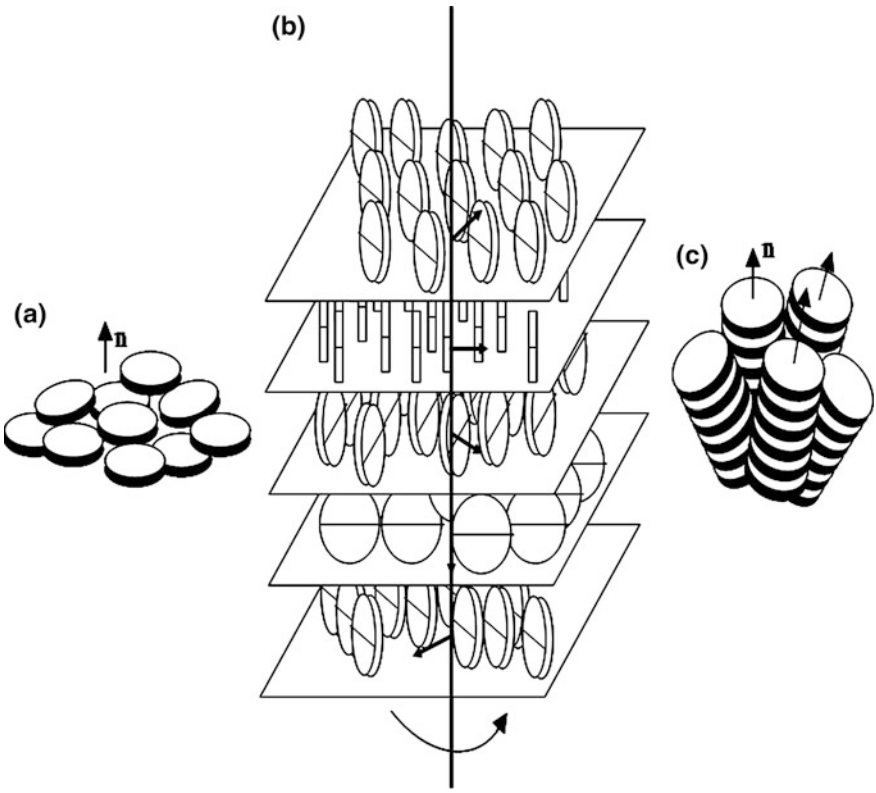

Fig. 7.3 Schematic representation of the molecular organization in the nematic (**a**), chiral nematic (**b**) and nematic columnar (**c**) phases of discotic mesogens

the nematic and cholesteric phases of calamitic liquid crystals bearing large π-conjugated cores [21, 22]. Sustained efforts led to the development of LC semiconductors that combine high charge-carrier mobility with several other advantages including long-range self-assembling, self-healing, ease of processing and solubility in organic solvents all of which are highly desirable for device applications. During the last decade, serious efforts have been made to exploit LC semiconductors in various organic electronic devices such as organic field-effect transistors (OFET), organic light-emitting diodes (OLED), and photovoltaic cells. Electroluminescence devices emitting polarized light were produced using uniaxially aligned photopolymerizable nematic and smectic LC semiconductors [23]. A large number of columnar and smectic liquid crystals had been prepared to study their charge transport and semiconducting applications. This chapter primarily focuses on semiconducting columnar phases of DLCs and we refer readers to some recent articles for information on advances in the field of calamitic and polymeric LC semiconductors [10, 20–23].

7.3 Discotic Columnar Liquid Crystalline Semiconductors

Formation of columnar structures (with typical inter core distances of about 3.5 Å) facilitates long-range π-orbital overlap between the adjacent molecules ensuring 1D intracolumnar charge-transport, that is, the charges move preferentially along the conducting aromatic cores of the columns (Fig. 7.4). The formation of 1D functional macrodomains that induces enhanced anisotropic functions is more easily achieved in columnar liquid crystals than in single crystals and crystalline polymers. Most discotic molecules have a very low intrinsic carrier concentration because of the fairly large energy band gap (2–4 eV) and behave as insulators in the pure state. Charge carriers must be injected into the molecules by chemical doping, pulse radiolysis, photoirradiation or from an electrode surface. Efficient charge transport requires that the charges be able to move from molecule to molecule and not be trapped or scattered. Therefore, charge carrier mobilities are influenced by many factors including molecular structure, mesophase order and alignment, presence of impurities, charge-carrier density etc. Depending on the extent of aromatic core conjugation and the degree of order in the columnar stacking, charge-carrier mobility in discotic columns can vary from 10^{-3} to 1.0 $cm^2\ V^{-1}\ s^{-1}$. The charge transport in LC semiconductors with low mobility values (<0.1 $cm^2\ V^{-1}\ s^{-1}$) is described via a one-dimensional hopping process while a banded conduction that involves the formation of conduction bands across several molecules is proposed to explain the high carrier mobilities (>0.1 $cm^2\ V^{-1}\ s^{-1}$) [10, 24, 25].

The charge carrier mobility in DLCs are generally determined by pulse radiolysis-time-resolved microwave conductivity (PR-TRMC), time of flight (TOF), steady-state space charge-limited current (SCLC), and field-effect transistor (FET) configuration techniques. By TOF method, both the hole and electron mobilities can be obtained independently. Although TOF mobilities up to 0.2 $cm^2\ V^{-1}\ s^{-1}$

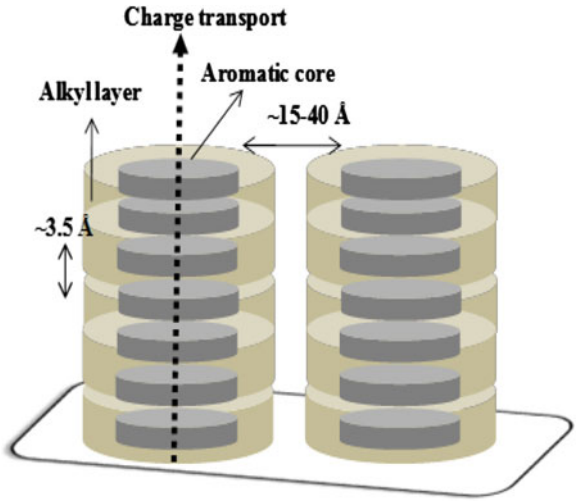

Fig. 7.4 Schematic representation of the self-assembly of discotic mesogens into one-dimensionally conducting 'wires'

have been reported for some cases, most DLCs exhibit values on the order of 10^{-3} cm^2 V^{-1} s^{-1} [26]. The charge mobilities determined by the TOF method are often found to be lower than the corresponding PR-TRMC values obtained for a sample. This is because PR-TRMC method yields charge mobility at local level which is relatively insensitive to defects and therefore relatively higher values. By PR-TRMC method, the mobility of intrinsic charge carriers can be determined even for nonaligned multidomain samples. With this technique, mobility values as high as 1.1 cm^2 V^{-1} s^{-1} have been measured in a discotic hexabenzocoronene derivative [27]. A variation on this method has been introduced in which a laser pulse is used to produce the electron-hole pair, which is a technique known as flash photolysis, time resolved, microwave conductivity or FP-TRMC [28]. The mobilities can also be obtained from the current-voltage (*I*/*V*) characteristics measured in a field-effect transistor (FET) configuration [29]. An organic FET is constituted by three electrodes, the gate, the source and the drain), an insulating (or dielectric) layer, and the organic semiconductor layer. In FETs, the charges migrate at the interface between the organic semiconductor and the dielectric. Charge transport is affected by trap states created by the presence of impurities or structural defects within the organic layer or at the interface and polarity of the dielectric. Therefore both TOF and FET methods measure mobility at macroscopic scale. Unlike the TOF experiment, which requires a homeotropic alignment of the DLC, FET experiments require a planar alignment (columns running parallel to the surface) with control of the azimuthal angle of the director, so that the preferred conduction pathway is from source to drain electrode. SCLC mobility is calculated from the current-voltage characteristics of thin organic films sandwiched between injecting electrodes [30]. The SCLC technique is sensitive to the structural defects of the macroscopic alignment and to the charge injection effectiveness at the electrodes. There are several studies comparing the charge carrier mobilities of discotic mesogens by different measurement techniques [30, 31]. Though there are some differences in the reported mobility values depending on the measurement technique used, in general it is observed that the mobility is discontinuous at crystalline, LC, and isotropic boundaries and tends to decrease at each phase transition because of the decreasing molecular order. Furthermore, studies had also revealed that different discotic systems have a strong correlation between the core size and the charge mobility, i.e. the mobility values increase with the size of the aromatic core [32].

7.4 Discotic Liquid Crystals with High Charge-Carrier Mobility

DLCs are synthesized following a general design template with a central disc connected to flexible peripheral tails through various types of linking groups (Fig. 7.1). Apart from tuning the LC properties, one can also tailor the semiconducting properties of DLCs by varying the nature of the central core and the peripheral alkyl chains. To ensure high charge-carrier mobility in DLCs, it is

essential to have a high degree of molecular order within the columnar mesophase. This can be achieved either by structural design or by physical processing. One of the successful design strategies to obtain high charge-carrier mobility has been to increase the size of the central rigid core, which in turn enhances the π-orbital overlap within the columnar structure. Various noncovalent interactions like charge transfer complexes, metal coordination, and hydrogen bonding have been used to decrease the inter-disc distance within the columnar phase and enhance the π-π stacking of the molecules.

Presence of peripheral alkyl chains on the discotic cores helps in inducing liquid crystallinity and solubility. Additionally, by varying the chain length and its chemical nature, a certain degree of control over LC order and alignment can be accomplished. It is necessary to obtain DLCs that have good thermal and oxidation stability. In addition, electronic properties such as HOMO and LUMO energy levels must be tunable for the practical device applications. This is because HOMO and LUMO energy levels of a molecule not only determine its semiconducting properties (*p*-type or *n*-type) but also affect the hole or electron injection barrier at the metal-semiconductor interface in devices. These intrinsic electronic properties can often be tailored by introducing electron-donating or electron-withdrawing substitutions on the discotic core.

Pure DLCs are intrinsically insulating and hence charge carriers (electrons or holes) must be introduced into the system to make it semiconducting. Optimization of charge-carrier mobility of DLCs is decisive for their potential device application. Simon and co-workers first discussed the concept of using DLCs as quasi-one-dimensional conductors in 1982 [33]. Early studies on the charge transport behavior of columnar discotics involved chemical doping of charge carriers using strong oxidants. For example, when 1 mol% of electron acceptor $AlCl_3$ was doped to electron-rich hexahexyloxytriphenylene derivative **2c** (Fig. 7.5), the conductivity σ increased from an undoped value of less than 10^{-9} S m^{-1} to about 10^{-3} S m^{-1}. The conductivity along the columns (σ∥) was found to be three orders of magnitude greater than that in the perpendicular direction (σ⊥) [34, 35]. However, liquid crystallinity is highly reliant on the purity of the materials, and doping often alters these properties. In early 1990s, as an alternate method to generate charge carriers, researchers employed ionizing radiation/photoirradiation in chemically pure (non-doped) DLC molecules and measured the charge carrier mobility by PR-TRMC or TOF technique. Porphyrin and phthalocyanine derivatives were the first examples of DLCs studied for the conductivity by a PR-TRMC method [36, 37]. In the year 1993, Adam et al. measured photoinduced charge-carrier mobility of 1×10^{-3} cm^2 V^{-1} s^{-1} in the columnar phase of hexapentyloxytriphenylene (**2b**) by the TOF technique [19]. This study provided valuable insights into the charge transport in DLCs, because for the first time this enabled the identification of the nature of charge carriers (whether holes or electrons). It was shown that nondispersive transport of charge carriers along the column axis is independent of temperature and field. From then onwards, the major research focus on DLCs has shifted from simple structure-mesophase property relationship studies to

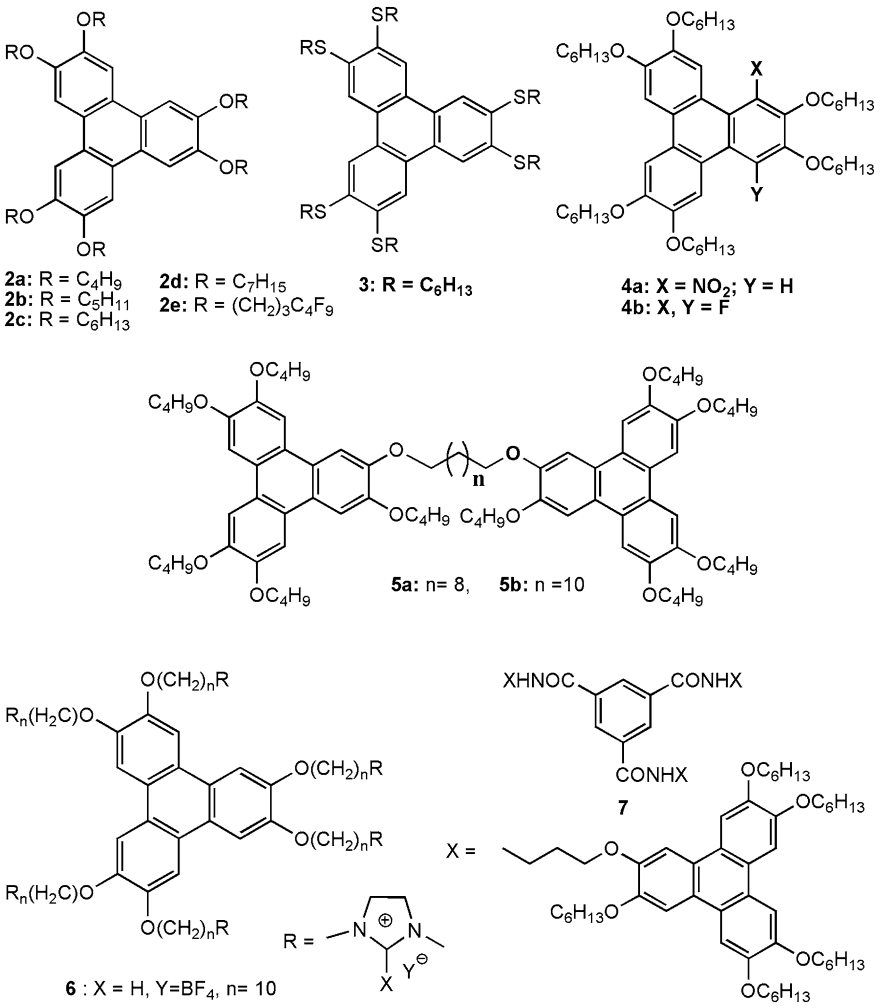

Fig. 7.5 Molecular structures of DLCs **2–7**

understanding of charge transport and to develop new high-mobility systems for various practical applications.

7.4.1 **p-*Type Discotic Molecules***

The majority of DLCs known today are derived from electron-rich aromatic cores like triphenylenes, hexa-*peri*-benzocoronenes, porphyrins, phthalocyanines etc. and are known as hole carriers. It is well known that the extent of π-overlap between the

core units of DLCs is the most important factor for the charge transport process in DLCs. Hence, a molecule with a larger π-conjugated core is expected to show higher charge-carrier mobility. Furthermore, there is a strong correlation between the charge carrier mobility with the order present in the mesophases. Systematic charge mobility studies carried out on triphenylene-based DLCs (**2–3**) reaffirmed this phenomenon. For example, carrier mobilities of the order of 10^{-3} cm^2 V^{-1} s^{-1} for holes were measured in the Col_h phase of triphenylene DLC **2b** [19]. More ordered plastic columnar phase of a lower homologue **2a** exhibited approximately an order of magnitude increase in the hole transport [38]. Even higher hole mobility value (1×10^{-1} cm^2 V^{-1} s^{-1}) was found in the three-dimensionally ordered helical columnar phase of triphenylene DLC **3** [39]. Short-side chain derivatives of triphenylenes, **2a–b**, permit better interaction of the cores, resulting in higher mobilities in comparison with the long-side chain analogs **2c–d** [40]. DLC compounds in which the alkyl chains are coupled to the core via sulfur (compound **3**) show, in general, considerably higher charge mobility values than those in which the chains are coupled either directly or via oxygen. This increase in charge-carrier mobility is attributed to the higher mesophase order induced by the sulfur atoms. Compound **3** on cooling from isotropic state undergoes phase transitions to Col_h phase, from Col_h to the more ordered columnar helical (H) phase, and from H phase to the crystal phase below 40 °C. A very low mobility of 1×10^{-4} cm^2 V^{-1} s^{-1} is observed in the isotropic liquid phase due to the absence of any columnar order. There is an increase in charge-carrier mobility from 5×10^{-3} cm^2 V^{-1} s^{-1} in the Col_h to 0.1 cm^2 V^{-1} s^{-1} in the helical columnar phase (Fig. 7.6). The sum of the one-dimensional charge-carrier mobilities, μ_{1D}, of about 0.4 cm^2 V^{-1} s^{-1} has been obtained from the PR-TRMC technique for **3** in its crystalline phase [31]. This increase in short-range carrier

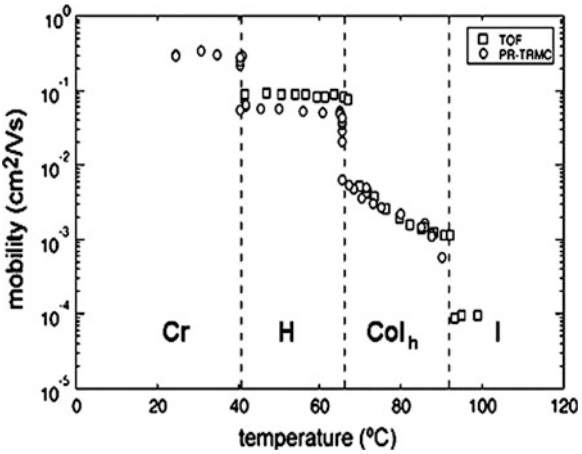

Fig. 7.6 The charge-carrier mobility in different phases of **3** measured by TOF (μ_h; *squares*) and sum of one-dimensional intracolumnar mobility $\sum\mu_{1D}$ (*open circles*) estimated by PR-TRMC experiments while cooling the sample from its isotropic phase. Reproduced with permission from [31]

mobility on transition from mesophase to crystal phase is a common feature of a number of discotics and is ascribed to the greater short-range structural order within the crystal packing of the molecules. It is found that molecular order within the columnar phase of discotic triphenylenes can also be changed by the variation of the lateral chain or by direct polar substitutions (compound **4**) on the aromatic core [41, 42]. van de Crats et al. reported TOF and PR-TRMC hole mobilities of about 0.01 $cm^2\ V^{-1}\ s^{-1}$ in the columnar phase of triphenylene dimer **5** [43]. Aida and co-workers reported ionic DLCs (iDLCs) **6** consisting of triphenylene core and charged hexaimidazolium side chains [44]. Compounds stabilized Col_h and bicontinuous cubic (Cub_{bi}) mesophases. Charge carrier mobility of about $3 \times 10^{-4}\ cm^2\ V^{-1}\ s^{-1}$ was measured in columnar phase by PR-TRMC method. Although these values are low when compared with mobility values of $>10^{-2}\ cm^2\ V^{-1}\ s^{-1}$ found in the Col_h phase of neutral DLCs, it revealed for the first time that iDLCs can function as organic semiconductors. Recently, ambipolar charge transport (electron as well as hole charge transport) in the columnar phases of **2a** and **3** was observed by improving the sample purity [45, 46]. For both compounds, the carrier mobility for electrons was found to be as fast as the hole mobility. There are several strategies developed for improved charge transport in triphenylene based columnar phases. An order of magnitude higher hole mobilities in the columnar phase is reported for binary mixtures formed by addition of a large core discogen to the triphenylene molecules [47]. This is attributed to the more stable columnar structure in the mixtures. Hydrogen bonding interactions are known to enhance mesophase order and hence the charge transport in columnar phases. Paraschiv et al. reported high charge mobility of 0.2 $cm^2\ V^{-1}\ s^{-1}$ in a highly ordered columnar hexagonal plastic phase of an intermolecularly hydrogen-bonded 1,3,5-benzenetrisamide derivative **7** with three pendant hexaalkoxytriphenylene groups [48]. Kato and co-workers succeeded in showing that physical gelation of molecules **2b–d** with hydrogen-bonded fibers to enhance the hole carrier mobility by suppression of molecular fluctuations in the columnar phase [49]. Several studies revealed that DLCs could well disperse nanoparticles (NPs) in their columnar phases. Six orders of magnitude increase in electrical conductivity in the Col_h phase of a triphenylene DLC was achieved upon doping it with discotic covered gold NPs or methylbenzene thiol-covered gold NPs [50, 51]. Not only gold NPs but doping of quantum dots (QDs) is also reported to enhance conductivity in DLCs [52].

Müllen and co-workers developed DLCs based on polycyclic aromatic hydrocarbon (PAH) cores such as hexa-*peri*-benzocoronenes (HBCs) (Fig. 7.7) having large mesophase range and high charge-carrier mobility [53]. In the columnar mesophases, charge-carrier mobility was in the range of 0.2–0.4 $cm^2\ V^{-1}\ s^{-1}$ and in the crystal phase these values were exceeding 1.1 $cm^2\ V^{-1}\ s^{-1}$ for HBC derivative (**8a**) as found by the PR-TRMC method [27]. By the TOF technique, long-range hole mobilities in the order of $10^{-3}\ cm^2\ V^{-1}\ s^{-1}$ have been recorded at room temperature for compound **8c** [53]. The high charge-carrier mobility found in discotic HBCs can be attributed to their unique, highly ordered columnar phase structures with large intermolecular π-orbital overlap between the aromatic cores. Several HBC derivatives have so far been successfully utilized as active conducting

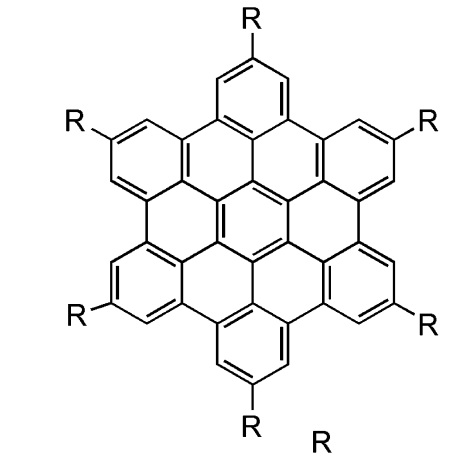

8a: R = C_nH_{2n+1}, n = 10, 12, 14
8b: R = Ph-$C_{12}H_{25}$
8c: R = $CH(C_9H_{19})_2$
8d: R =

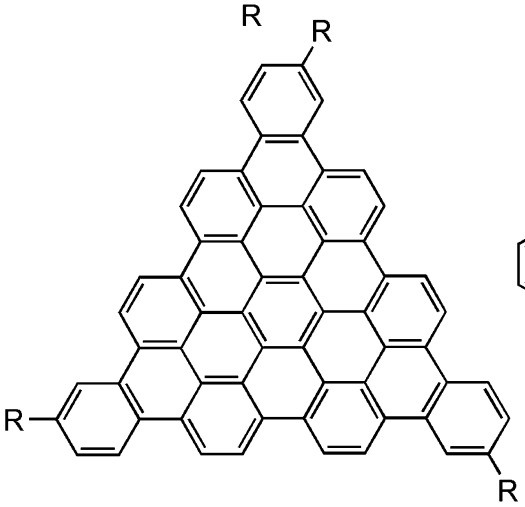

9a: R = C_{10} or $_6$; **9b:** R = C_{14} or$_{10}$

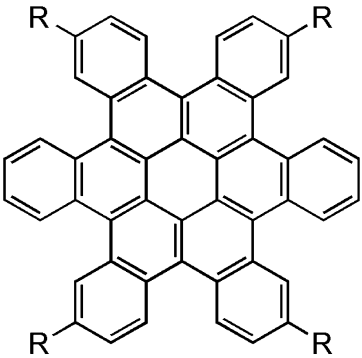

10: R = $OC_{12}H_{25}$

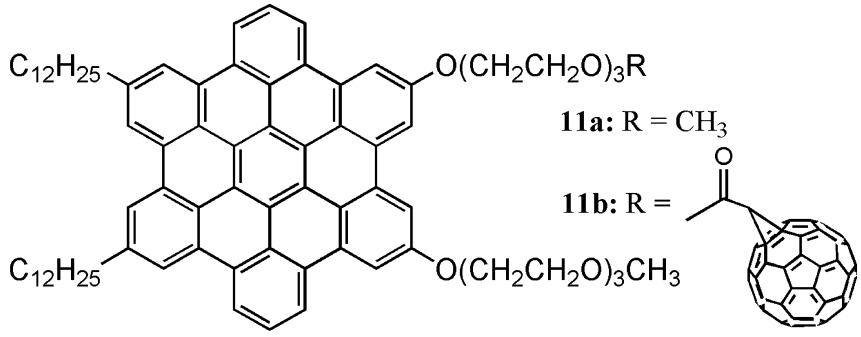

11a: R = CH_3

11b: R =

Fig. 7.7 Molecular structures of DLCs **8–11**

layers in molecular devices such as organic FETs and solar cells [54]. HBC is a planar aromatic molecule consisting of 13 fused six-membered rings. Studies on larger discotic molecules derived from peripherally alkyl-substituted PAH cores consisting of 42, 60, 78, 96, and 132 carbon atoms revealed that there is no substantial increase in charge-carrier mobility with increasing core size. This observation was in contrast to the expectation that increasing core size increases the charge mobility. HBCs and their larger derivatives mentioned above possess sixfold (D_{6h}) symmetry. Müllen's research group theoretically predicted higher charge transport in triangle-shaped molecules with threefold symmetry and went onto synthesize PAHs (**9a–b**) having the same number of carbons as fullerene and achieved improved photovoltaic performance [55]. Nuckolls and co-workers reported the stabilization of columnar mesophase in a contorted HBC derivative **10** [56]. Relatively high carrier mobilities and current modulation ($\mu = 0.02$ cm^2 V^{-1} s^{-1}; on-off current ratio of 106:1) were observed in FETs made with the LC films of **10**. Aida and co-workers designed gemini-shaped HBC derivatives **11a–b** with two hydrophobic dodecyl chains on one side of the core and two hydrophilic triethylene glycol chains on the other [57]. Solution cast films of **11a** exhibited hole mobility of about 1.0×10^{-4} cm^2 V^{-1} s^{-1}. On the other hand, C_{60}-appended HBC **11b** self-assembled into a coaxial nano-tube with an ambipolar field effect mobility ($\mu_e = 1.1 \times 10^{-5}$ cm^2 V^{-1} s^{-1} and $\mu_h = 9.7 \times 10^{-7}$ cm^2 V^{-1} s^{-1}). More interestingly, mixing 10 mol% of **11b** in **11a** resulted in co-assembled nanotube structures with intratubular hole mobility of 2.0 cm^2 V^{-1} s^{-1}, as determined by the flash-photolysis time-resolved conductivity (FP-TRMC) technique.

Phthalocyanine and porphyrin aromatic cores substituted with alkyl chains at the periphery were known to self-assemble into columnar mesophases from the early research on DLCs [33, 58]. Systematic studies revealed the role of chain length and metal ion on phase transition temperatures, mesophase range, and carrier mobilities. Charge-carrier mobility measurements on porphyrin **12a–b** and phthalocyanine **13a** (Fig. 7.8) by PR-TRMC revealed $\sum\mu_{1D}$ values in excess of 0.1 cm^2 V^{-1} s^{-1} [36, 37]. It was believed that electron-rich organic semiconductors like porphyrins and phthalocyanines are hole carriers. In contrary to this, Ohta and coworkers found ambipolar charge transport (negative charge mobility of 2.4×10^{-3} cm^2 V^{-1} s^{-1} and a positive mobility of 2.2×10^{-3} cm^2 V^{-1} s^{-1}) in the Col_h of a phthalocyanine metallomesogen compound **14** [59]. Bushby and colleagues achieved high hole mobility (~0.2 cm^2 V^{-1} s^{-1}) in the Col_r phase of an octaalkyl-phthalocyanine **15** [60]. Mobility values up to 0.7 cm^2 V^{-1} s^{-1} were reported for alkylthio-substituted phthalocyanine rare-earth metal sandwich complexes [61].

Porphyrin cores are good candidates for photovoltaic applications because porphrin is the basic structure of the best photoreceptor in nature, i.e. chlorophyll and the energy levels are matched well with the electron acceptors and anode materials to facilitate charge separation and transfer. The challenge is to obtain highly ordered columnar phase with high charge carrier mobility. Li and co-workers synthesized porphyrin based DLCs (**16a–d**) (Fig. 7.9) in high chemical purity. In addition to the ease of synthesis and wide temperature range stabilization of

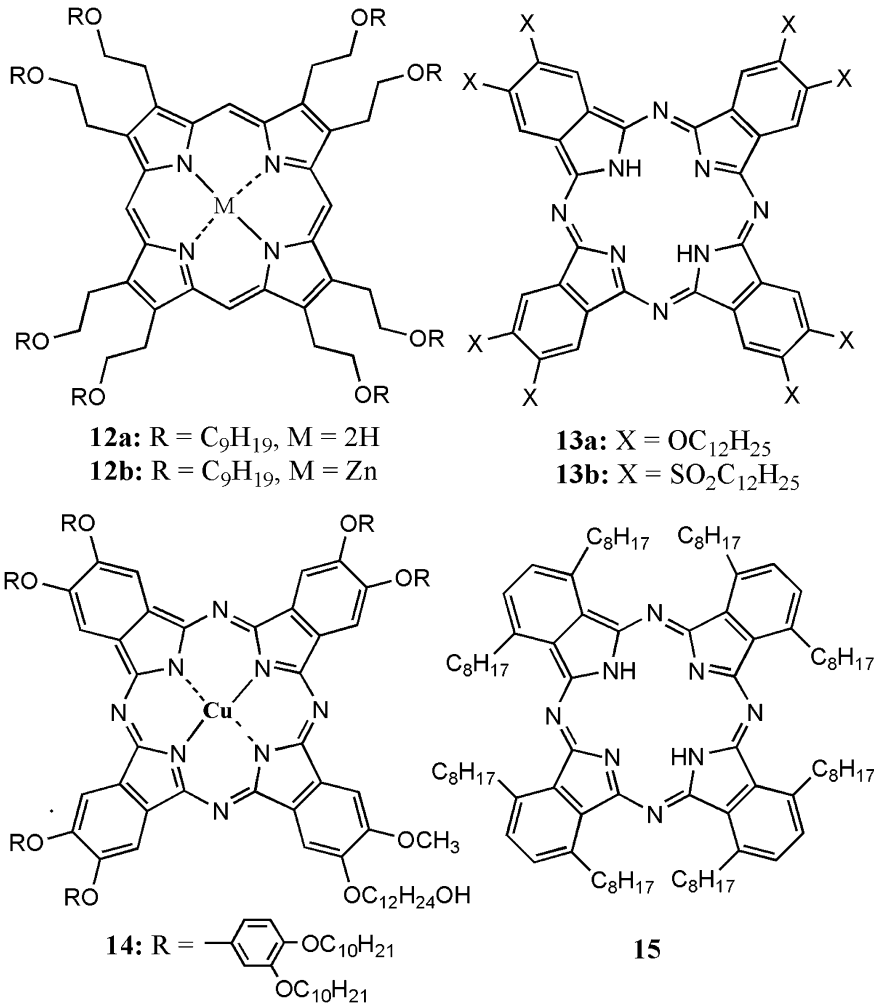

Fig. 7.8 Molecular structures of DLCs **12–15**

columnar phase, these DLCs spontaneously aligned into homeotropic orientation [62, 63]. Formation of defect-free large-area monodomain films is critical for photovoltaic applications. The power conversion efficiency achieved under ambient conditions for solution processed bilayer- and bulk-heterojunction photovoltaic cells based on **16a–b** appears to be one of the best values achieved for solar cells using columnar DLC materials [64]. Aida and co-workers induced liquid crystallinity in a fused Cu porphyrin dimer core by attaching dodecyl and semifluoroalkyl side chains to its periphery [65]. Interestingly, compound **17a** with dodecyl and semifluoroalkyl side chains exhibited a rectangular columnar phase with electron

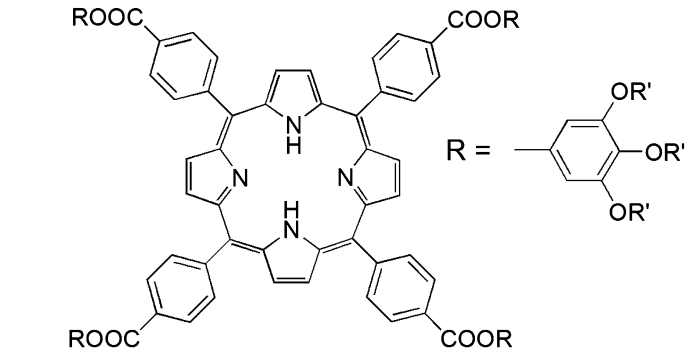

16a R' = $C_{12}H_{25}$;**16b** R' = $C_{14}H_{29}$

16c R' = $C_{16}H_{33}$;**16d** R' = $(CH_2)_{10}C_4F_9$

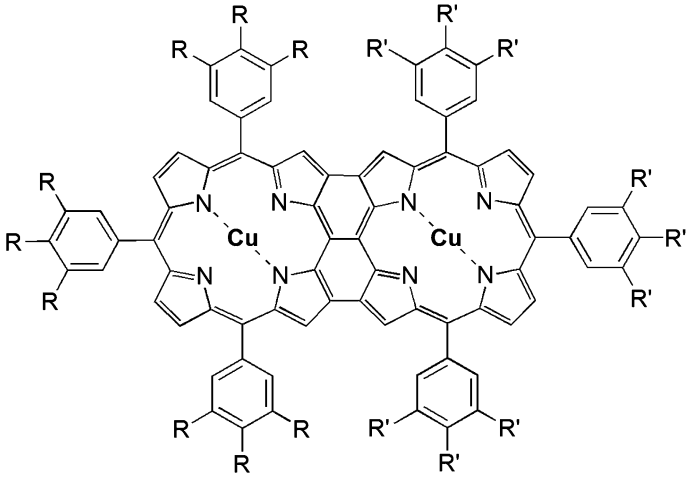

17a R = -$O(CH_2)_{11}CH_3$, R' = -$O(CH_2)_6(CF_2)_3CF_3$

17b R = R' = -$O(CH_2)_6(CF_2)_3CF_3$

Fig. 7.9 Molecular structures of DLCs **16** and **17**

transport (μ_{TOF} 1.3×10^{-3} cm^2 V^{-1} s^{-1}) while **17b** with semifluoroalkyl side chains alone exhibited a hole (μ_{TOF} 4.3×10^{-3} cm^2 V^{-1} s^{-1}) transporting orthorhombic columnar phase. Although the influence of chemical nature of side chains on the structural order of columnar phases is well known, electron or hole transport in the columnar phase determined by its side chains appears to be quite encouraging for diversification of organic semiconductors from limited available structural motifs.

7.4.2 n-*Type Discotic Molecules*

Vast majority of the known DLCs are relatively rich in electrons and are better hole transporters (donor materials) than electrons. Electron-transporting materials (acceptor materials) with high mobility are essential for applications in solar cells, bipolar transistors and OLEDs. Therefore several electron-deficient DLCs were synthesized and characterized as *n*-type materials. Electron-deficient DLCs were obtained either by substitution of electron-withdrawing peripheral groups onto a *p*-type discotic core or by designing new electron-deficient heterocyclic aromatic cores. Substitution of electron-withdrawing groups lowers both the LUMO and HOMO levels in π-conjugated systems and enhances the electron transport. The electron transport in the columnar mesophase was first evidenced in an electron-deficient thioether-substituted tricycloquinoxaline derivative **18a** (Fig. 7.10) [66]. Doping of compound **18a** with 6 mol% of potassium metal, an electron donor, resulted in conductivity (σ‖) of about 2.9×10^{-5} S m^{-1} in the columnar phase. It was found that replacing the hexylthio side chains in **18a** with ethyleneoxy chains (**18b**) to enhance the K^+ solubility, leading to higher doping levels and higher conductivities (σ‖ = 1.1×10^{-3} S m^{-1}). Photoconductivity studies on **18b** revealed transient photocurrents for both electrons ($\sim 10^{-4}$ cm^2 V^{-1} s^{-1}) and holes [67]. Hexaazatriphenylene (**19** and **20**) is another example of an electron-deficient aromatic heterocyclic core exhibiting a columnar mesophase. Meijer and co-workers utilized DLC **19** as an electron-acceptor material in blend films with a well-known donor material poly(3-hexylthiophene) [68].

In another study, Gearba et al. reported ∑μ1D mobilities up to 2.0×10^{-2} cm^2 V^{-1} s^{-1} in the columnar mesophase of hydrogen-bonded hexaazatriphenylene **20** [69]. The interdisc distance of 3.18 Å achieved in **20** is attributed to the presence of intermolecular hydrogen bonding. Demenev et al. reported electron mobility of 2.0×10^{-3} cm^2 V^{-1} s^{-1} in the hexagonal columnar mesophases of a benzotristhiophene derivative **21** [70]. Interestingly, the charge carrier mobility was found to be temperature independent even across the phase transitions between the two mesophases of **21** because of the presence of an intracolumnar hydrogen bonding. Lehmann et al. reported DLCs based on electron-deficient hexaazatrinaphthylene core (for example, **22**) [71]. The electron-deficient character of **22** was demonstrated by cyclic voltammetry. By PR-TRMC measurements, charge carrier mobilities of 0.9 and 0.3 cm^2 V^{-1} s^{-1}, respectively, for crystalline and columnar LC phases of **22** were found. Zang et al., designed DLC **23** with benzene core and three (trialkoxyaryl)oxadiazole arms and reported TOF electron mobility of 1.0×10^{-3} cm^2 V^{-1} s^{-1} in the columnar phase [72]. Geert's group reported metal free phthalocyanine based DLCs bearing peripheral alkylsulfonyl substituents (for example, **13b**) as potential air-stable *n*-type semiconductors [73].

Among the high-performance, *n*-type DLC materials are the perylene derivatives functionalized with electron-withdrawing imide substituents **24–28** (Fig. 7.11). Photoconductivity and *n*-type semiconducting properties of these materials have found applications in prototype devices such as solar cells, OFETs, and OLEDs.

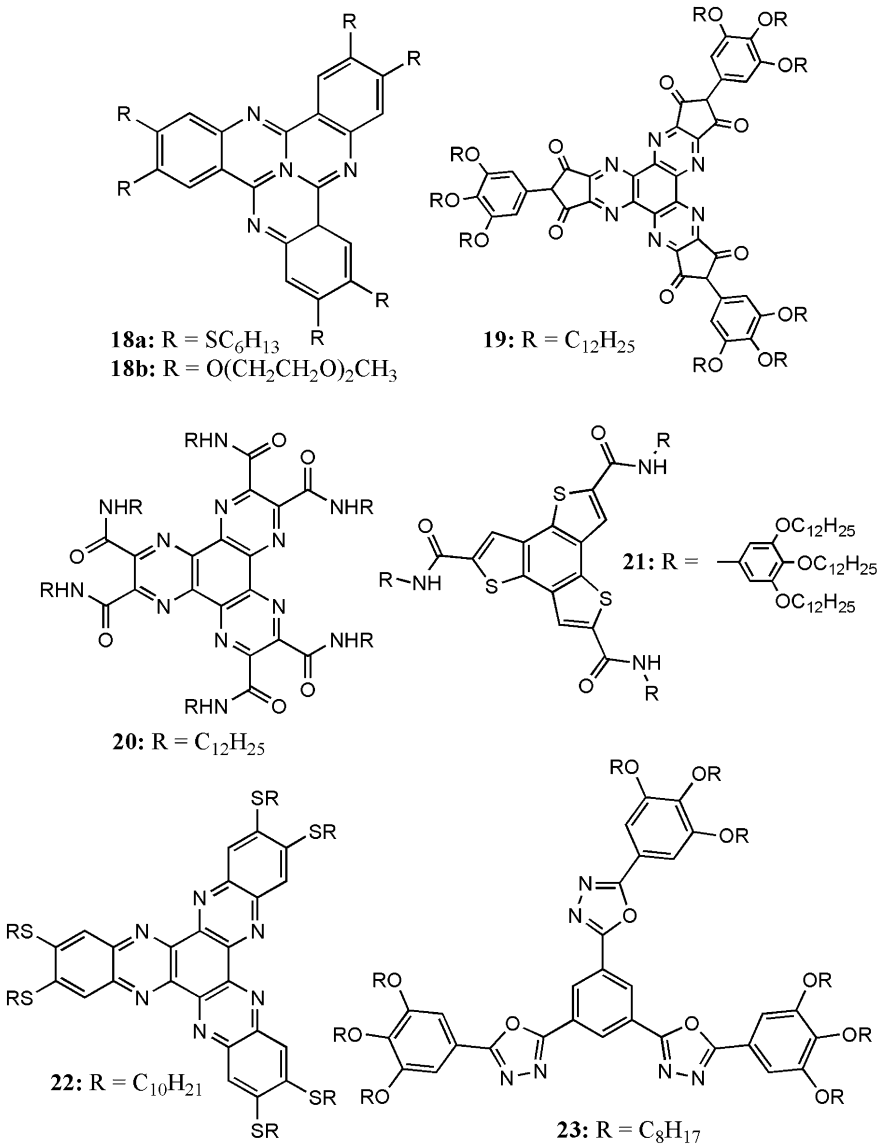

Fig. 7.10 Molecular structures of DLCs **18–23**

First report on the charge transport properties in perylene-based DLCs came from Struijk et al. [74]. They measured mobilities of 0.1 $cm^2\ V^{-1}\ s^{-1}$ and 0.2 $cm^2\ V^{-1}\ s^{-1}$ in the LC and crystalline phases, respectively, for *N,N′*-alkylperylenetetracarboxylicdiimide (PTCBI) **24d** by the PR-TRMC method. TOF measurements of mobility on a similar compound **24a** yielded similar mobility values

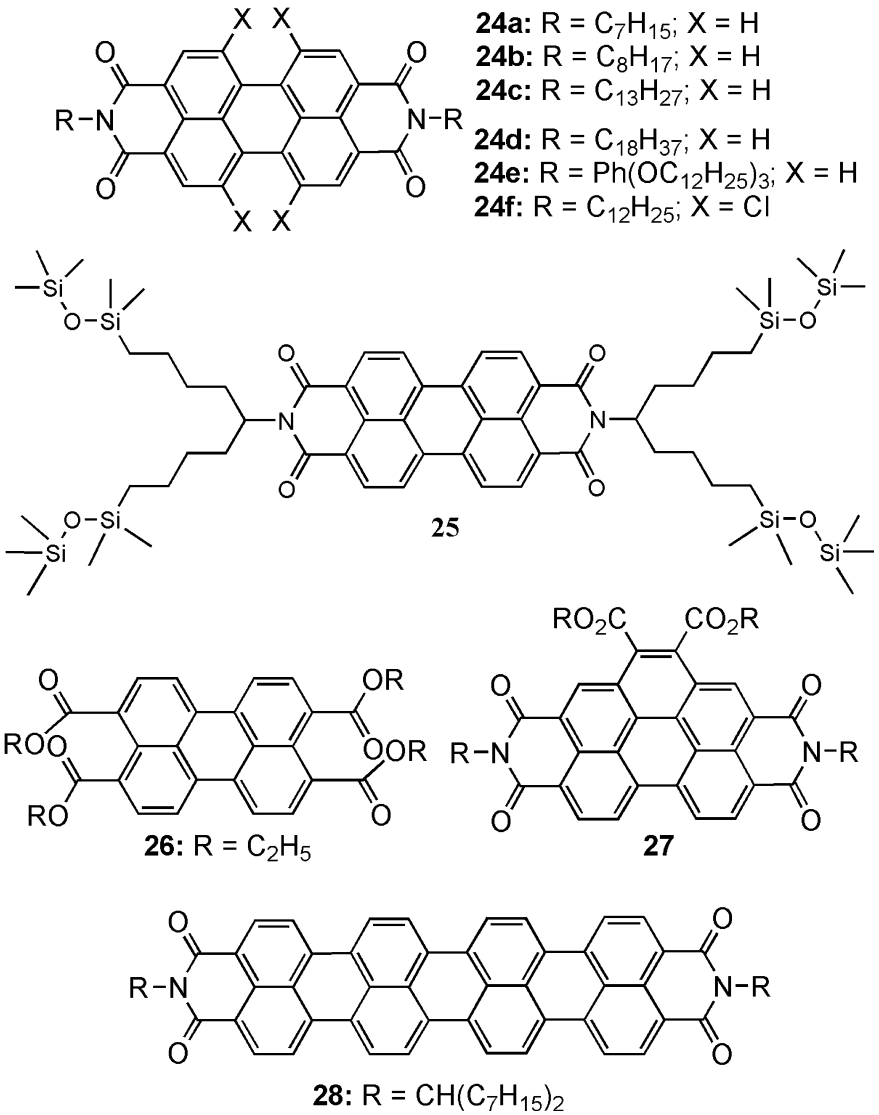

Fig. 7.11 Molecular structures of DLCs **24–28**

with evidence for ambipolar charge transport [75]. Field-effect mobility up to 0.6 $cm^2\ V^{-1}\ s^{-1}$ and current on/off ratios $>10^5$ were obtained for thin-film transistors based on perylenebisimide **24b**, when operated under nitrogen atmosphere [76]. Charge-carrier mobility values as high as $1.1 \times 10^{-2}\ cm^2\ V^{-1}\ s^{-1}$ have been found in the room-temperature Col_h phase of perylenebisimide **24e** [77]. Functionalization of perylenebisimide cores at bay positions proved to be a good

strategy to enhance charge carrier mobility as reported for tetrachloro-substituted perylenebisimide **24f** in comparison to a nonchlorinated analog compound [78]. Funahashi et al. synthesized PTCBI derivatives **25** bearing oligosiloxane chains. Compound **25** exhibited columnar phases at room temperature with TOF electron mobility exceeding 0.1 $cm^2\ V^{-1}\ s^{-1}$ [79].

Destruel and co-workers achieved red light emission in a bilayer OLED device by combining electron-deficient perylenetetraester compound **26** with electron-rich triphenylene **2a** (as a hole transport material) [80]. Columnar LC diimide-diester compounds (**27**) are known to support electron transport in their mesophases because of the presence of strong electron-withdrawing substituents. By combining **27** with LC benzoperylenetriester compounds in bilayer, OLED device yielded red color emission [81]. Higher perylenediimides like terrylene and quaterrylenetetracarboxyldiimides exhibit columnar mesophases with attractive semiconducting properties [82]. For example, a "swallow-tailed" quaterrylenetetra carboxyldiimide **28** was utilized as an active semiconducting layer in an ambipolar thin-film transistor [83]. Postproduction thermal annealing of the device resulted solely in an electron transport. Other DLC cores like coronene, decacyclene, and rufigallol are known to exhibit electron transport in their columnar mesophases when appropriately substituted with electron-withdrawing substituents. A coronene derivative **29** (Fig. 7.12) is reported to show a room-temperature columnar phase with charge carrier mobility of $\sim 0.2\ cm^2\ V^{-1}\ s^{-1}$ [84]. Hashimoto and co-workers found photoinduced electron transfer in discotic 1,7,13-heptanoyldecacyclene **30** by combing it with a *p*-type semiconducting polymer [85]. Kumar and Bisoyi reported room-temperature Col_h phase in a series of electron-deficient rufigallol derivatives **31** [86]. More recently, Kumar and coworkers reported wide range stabilization of the Col_h phase in DLC oligomers **32**, wherein an electron-rich triphenylene moiety was combined with an electron-deficient anthraquinone moiety to obtain donor-acceptor-donor triads [87]. Although charge transport behavior of these compounds has not yet been reported, such study can be highly useful for potential application in devices like solar cells where a pure single compound with the capability to form separate charge conduction pathways for electrons and holes is highly desirable. In another interesting study, Bunning et al. reported electrons as majority carriers in a triblock copolymer with a main chain polymeric triphenylene liquid crystal capped at either end with poly(ethylene oxide) chains [88].

Highly fluorescent discotic columnar phases are beneficial for OLED applications. However, majority of the DLCs discussed so far (except for some perylene derivatives) are only weakly fluorescent in their mesophases. Recently, pyrene-based DLCs have been synthesized in order to induce strong fluorescence in the columnar mesophase [89, 90]. Shimizu and co-workers reported ambipolar charge transport in the Col_h phase of a pyrene derivative **33** (Fig. 7.12) with charge mobilities on the order of $10^{-3}\ cm^2\ V^{-1}\ s^{-1}$ [90]. Interestingly, when the Col_h phase of **33** was super cooled to room temperature, a rigid glassy state was formed (with structural features of the preceding Col_h phase) without disrupting the charge transport.

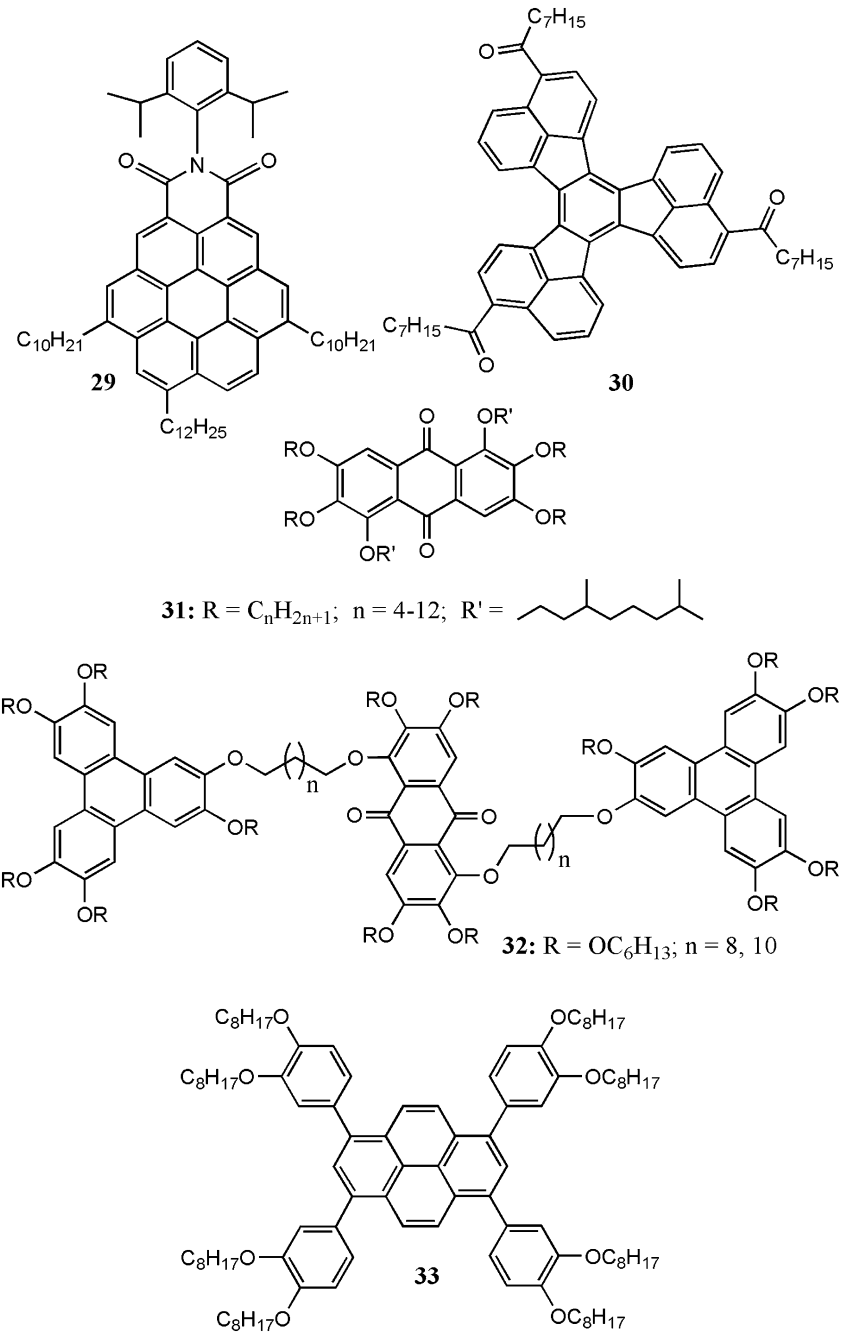

Fig. 7.12 Molecular structures of DLCs **29–33**

7.4.3 p-n *Type Dyad Discotic Molecules*

Only a few examples of DLC semiconductors such as triphenylenes and phthalocyanines exhibiting ambipolar characteristics have been reported. Yasuda and coworkers reported ambipolar charge transport in triazine-based columnar liquid crystals **34** (Fig. 7.13). The molecular design was such that central 1,3,5-triazine core possesses an electron affinity served as an electron-accepting unit, whereas the thiophene-based peripheral substituents provide electron-donating properties. TOF experiments had revealed that the compounds exhibit hole and electron mobilities on the order of 10^{-5} and 10^{-3} cm^2 V^{-1} S^{-1}, respectively, in the Col_h phase [91]. In another interesting molecular design, ambipolar charge transport in DLCs was obtained by covalently linking donor-acceptor (D-A) DLC dyads. Imahori et al.

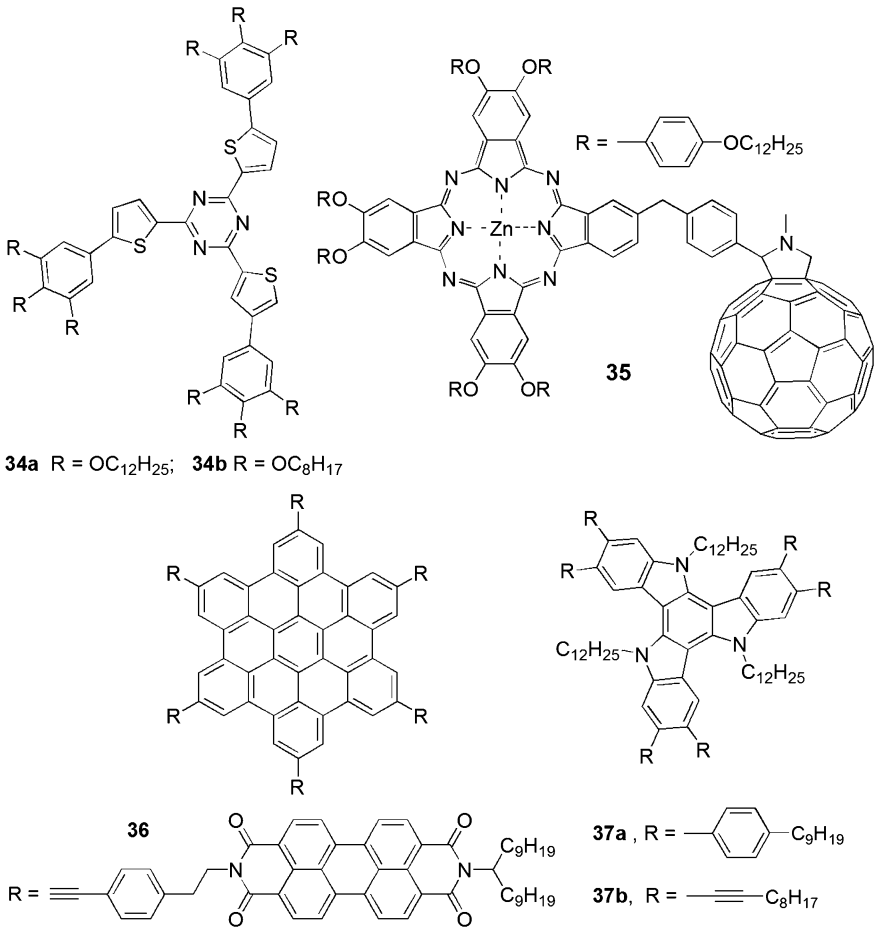

Fig. 7.13 Molecular structures of DLCs **34–37**

reported ambipolar charge transport in a molecular dyad **35** consisting of covalently linked discotic phthalocyanine (donor) and fullerene (acceptor) [92]. The dyad molecule self-assembled to form segregated D-A columns in the mesomorphic state. In the TOF measurements, DLC **35** exhibited high hole (0.26 $cm^2\ V^{-1}\ s^{-1}$) and electron (0.11 $cm^2\ V^{-1}\ s^{-1}$) mobilities. Recently, Mullen and co-workers reported dyad DLC **36** with *n*-type PTCBI moieties covalently linked around *p*-type hexabenzocoronene core. Dyad **36** assembled into columnar structures with nanosegregated stacks of HBC and PDI such that an electron-donating 1D core is surrounded by an electron accepting shell mantle [93]. In contrary to the expectations, photoinduced electron transfer between HBC and PDI did not occur within these molecular dyad because of the limited D-A orbital overlap in the plane of the molecule which in turn is attributed to the distance of more than 1 nm between donor and acceptor. However, nanosegregated stacks formed of *p*-type and *n*-type moieties are expected to provide ambipolar charge transport channels in bulk state.

In recent years, several other π-conjugated systems based on triindole [94, 95], corannulenes [96], ovalenes [97], tris(*N*-salicylideneanilines) [98], and dibenzophenazine [99] have been identified as promising DLC cores. Golemme and co-workers found charge carrier mobilities of 0.03 $cm^2\ V^{-1}\ s^{-1}$ and 0.09 $cm^2\ V^{-1}\ s^{-1}$ in the Col_h and crystal phase respectively in a triindole DLC derivative [94]. More recently, they synthesized DLCs **37a** and **37b** with difference only in nature of the side chain. On replacing the nonylphenyl with the octylethynyl side chain the intermolecular distance in π-stacking of columnar phase decreased from 4.4 in **37a** to 3.9 Å in **37b** and achieved four orders of magnitude increase in charge mobility [100].

7.5 Alignment of Discotic Columnar Phase

All the proposed commercial applications of DLCs rely on our ability to control the surface alignment of the columnar phase. This is because charge transport in columnar phase is quasi-one-dimensional, i.e., charge-carrier conduction is much faster along the columnar stacks than between columns. Flexible alkyl chains linked to the rigid core act as an insulating hydrocarbon matrix and decrease intercolumnar tunneling of the charge carriers. This anisotropy of charge transport implies that columns must be appropriately aligned in a direction that the current is desired to flow. DLCs can align either perpendicular to the substrate surface, referred to as homeotropic alignment, or parallel to the substrate surface, referred to as planar alignment (Fig. 7.14). While a planar alignment (also referred as homogeneous or "face-on" orientation) of the columnar mesophase is required for devices such as OFETs, a homeotropic alignment (where columns normal to the surface) of columns is essential for OLEDs and photovoltaic cells. The problems encountered when attempting to orient discotic LCs are related to the strong intermolecular interactions in these materials, which translate into a comparatively high viscosity and high mesophase temperatures. Apart from alignment requirements, obtaining a

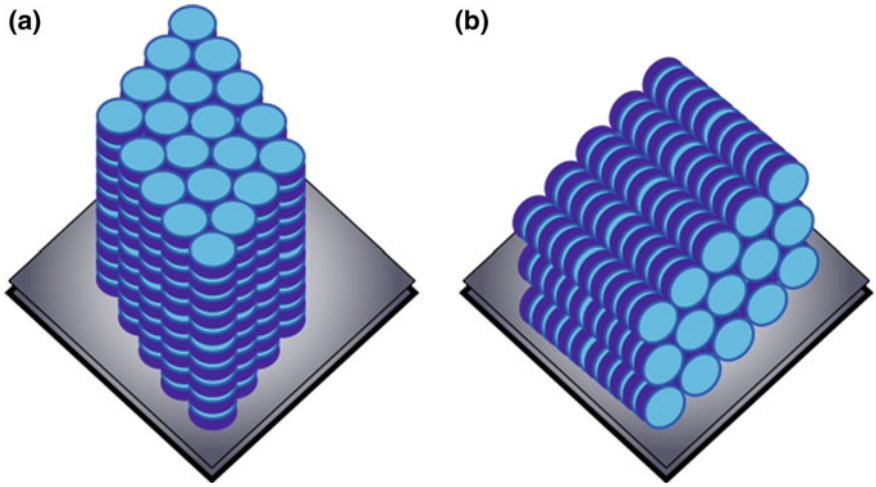

Fig. 7.14 Schematic representations of **a** "Face-on" or homeotropic alignment of columnar DLC and **b** "Edge-on", homogeneous, or planar alignment of columnar DLC

highly ordered monodomain thin-film structures free of local defects significantly influence the device performance. Local defects at domain boundaries in unoriented layers can trap charge carriers and significantly decrease device performance. Although, alignment of calamitic liquid crystals on surfaces is an advanced technology, it is seldom applicable to columnar mesophases [101]. Different parameters like molecular structure, film thickness, surface interactions and processing techniques are known to control the alignment and monodomain formation in discotic columnar mesophases. A brief discussion on different alignment methods is described below. The first part will deal with molecular design strategies while the second part focuses on different processing techniques.

7.5.1 Alignment Control of Columnar Phase Through Molecular Design

Although DLCs self-organize readily into columnar phases, the alignment of columns is neither uniform nor monodomain in nature. Several attempts have been made to align DLC molecules onto a substrate by tailoring molecular core or the functional groups in the side chains. Triphenylene, phthalocyanine, porphyrin, and hexabenzocoronene (HBC) derivatives are the most commonly used DLCs for mesophase evaluation and alignment control. They can be aligned on a single substrate, in between two substrates, or in microscopic and nanoscopic pores by processing either from solution or from isotropic liquid. In general, homeotropic anchoring is the most common at the substrate–liquid crystal interfaces, whereas

planar anchoring is preferred at the liquid crystal–air interface (single substrate). DLCs have been shown to adapt a homeotropic alignment in their columnar mesophases in relatively thick films (a few micrometers) when the material is confined between two substrates and slowly cooled from their isotropic state. In most cases, the uniform alignment requires a slow cooling rate. However, high viscosity of the columnar mesophase often promotes multidomains and prevents the perfect homeotropic alignment over a large area. As a molecular design strategy, attempts have been made to decrease the isotropic melt viscosity of mesogens either by incorporating hetero atoms in the flexible side chains or by introducing sterically hindering groups on to the mesogenic core. Incorporating heteroatoms near the rigid core of triphenylene and phthalocyanine discotic molecules is known to enhance the ease of homeotropic alignment [102]. A systematic study of triphenylene DLCs on various substrates revealed that the homeotropic alignment is thermodynamically favored in the columnar phases, while the alignment changes to planar when kept in the glassy or crystalline state [103]. Some other studies focused on modifying the surface affinity of molecules by changing the chemical nature of the side chains. It was shown that the introduction of a fluoroalkyl group into the peripheral chains of triphenylene mesogens could provide a strong tendency towards homeotropic alignment of the hexagonal columnar (Col_h) mesophase on a variety of substrates, indicating a new concept of molecular design for the alignment control of a columnar mesophase [104]. Pisula et al. have made extensive structural studies with modifications of HBC derivatives, having different core sizes, side chain lengths and substituents. Bulky branched side chains facilitated face-on alignment from melts by drastically decreasing the isotropization temperature, however, such side chains tended to introduce intracolumnar disorder in higher coverage films because of steric crowding [105]. Introduction of ether linkages within the side chains of HBC derivatives was found to enhance the affinity of the discotic molecules towards polar surfaces, resulting in homeotropic self-assembly when the compounds are processed from the isotropic state between two surfaces and as a thin film on a single surface [105]. Li and coworkers achieved spontaneous homeotropic alignment in porphyrin-based DLCs (**16a–d**) by varying the film thickness, thermal annealing process, and mechanical shearing [106]. Samples deposited on a single substrate displayed multiple homeotropic and randomly oriented planar domains. The preferential orientation of these materials between two substrates was found to be homeotropic. Slow cooling at a rate of $\sim$2 °C/min from the isotropic phase of **16a–c** promotes selective nucleation and slow growth of homeotropic domains, while abrupt cooling results in multidomain structures. However, shearing and annealing the sample film resulted in highly ordered planar alignment along the shear direction. It was much easier to obtain a large-area defect-free homeotropically aligned thin film of perfluoroalkylated discotic porphyrins (**16d**). Another interesting aspect of these porphyrin DLCs is their capability to retain stable homeotropic alignment through room temperature.

Hydrogen bonding groups incorporated into the cores of the DLC molecules are known to aid in “templating” the deposition of ordered columnar phases on various substrates [107]. Following this molecular design strategy, attempts were also made

to achieve alignment control by incorporation of hydrogen bonding groups in the side chains of the DLC molecules. Phenomenologically, an edge-on arrangement results from the minimization of the surface contact of molecules with a substrate of different polarity. Although there is some success, a more general molecular design principle that chemical modifications of a mesogen provided a certain controllability of the molecular alignment for a columnar mesophase without changing the mesomorphism is yet to achieve.

7.5.2 Alignment Control of Columnar Phase Through Physical Methods

For technological applications, it is important to align semiconducting columnar phase of DLCs in thin films and sandwiched devices. In general, it is observed that a homeotropically aligned columnar mesophase can be obtained by slow cooling from the isotropic phase. Alignment of DLCs by thermal annealing is achieved when the material is stable above its clearing temperatures and it wets the substrate in both its isotropic and LC phases. Representative examples of triphenylene, phthalocyanine, porphyrin, and hexabenzocoronene DLCs have been shown to adapt homeotropic alignment in their columnar mesophases spontaneously in relatively thick films (a few micrometers) when the material is confined between two substrates. Planar alignment of columnar LC films is favoured in relatively thin films (≤100 nm) and on a single substrate. In spite of spontaneous self-assembly of discotic molecules into Col phases, obtaining large area mono domain LC films in a desired alignment is often very challenging. It can be achieved by combining molecular design strategies with various film processing techniques. These techniques include surface treatment, Langmuir–Blodgett (LB) deposition, self-assembled monolayers, zone casting and zone melting, application of magnetic and electric fields, use of infrared radiation and confinement in nanoscopic and microscopic porous templates.

7.5.2.1 Surface Treatment

Calamitic liquid crystals for LCD display applications are predominantly aligned by interactions with specially treated surfaces. Polyimide is widely used as a coating reagent to obtain a homogeneous alignment for rod-like liquid crystals. For DLCs, it is reported that the discotic nematic (N_D) phase of 2,3,6,7,10,11-hexakis(4-*n*-octyloxybenzoyloxy) triphenylene exhibits a spontaneous homeotropic alignment on the polyimide-coated substrate. Alignment layers made for calamitic liquid crystals do not provide specific orientations for the columnar phase of most DLCs. On the other hand, oriented polytetrafluoroethylene (PTFE) coated surfaces was successfully used for aligning DLCs. Zimmermann et al. first reported the planar

orientation of a triphenylene DLC in its hexagonal plastic columnar phase by spin coating the material onto a PTFE alignment layer [108]. Uniaxial "in-plane" orientation of columnar phase was also achieved in HBC, phthalocyanine, pyrene, and benzoperylene derivatives by spin-casting the LC material onto a PTFE orientation layer [109–111]. Homeotropic alignement on the substrate can also be obtained by deposition of dilute solution of discotic molecules onto MoS_2 or highly oriented pyrolytic graphite, as reported for discotic triphenylenes, hexaazatriphenylene and HBCs [112–114]. In these cases, the main driving force for the face-on organization is the interaction between the disc and the surface. Friend and co-workers reported planar alignment of HBC on rubbed-PTFE layer and obtained field-effect mobility as high as 0.5×10^{-3} cm^2 V^{-1} s^{-1} even without the need for an annealing step in the mesophase [115]. Homeotropic alignment of discotic Col phase can conveniently be achieved in submicron thick open films by controlling the growth kinetics of the columnar domains by thermal annealing. When the film thickness is reduced to the typical value required in organic solar cells, i.e. 50–100 nm the homeotropic alignment is disfavored over the planar orientation, and dewetting occur during annealing leading to strongly inhomogeneous films. Moreover, PTFE layers can be insulating and are not ideal for photovoltaic devices where good charge transport throughout the device is essential. Addressing this issue, ultrathin films of a columnar mesophase of a benzoperylene DLC was stabilized in homeotropic alignment by thermal annealing on an ITO electrode that was subjected to either UV-ozone or nitrogen plasma surface treatment [116]. Geerts and co-workers reported alignment switching in a phthalocyanine compound bearing eight oligo (ethyleneoxy) peripheral substituents by varying the nature of the solid substrate from a hydrophilic to hydrophobic one. Homeotropically aligned films were obtained on a hydrophilic surface, whereas planar alignment with a random distribution of the column directors occurred on the hydrophobic surface [117].

In another interesting method, homeotropic alignment of discotic columns in open films (50–300 nm) for a phthalocyanine mesogen was achieved by the use of a polymer sacrificial layer [118]. Here "face-on" alignment is imposed by thermal annealing of the confined LC film with a top sacrificial polymer layer that is later removed by washing with a selective solvent. But annealing of these structures, after the sacrificial layer was removed, suggested reintroduction of disorder into these films. Planar alignment of triphenylene and phthalocyanine columnar DLCs with control of the azimuthal angle was achieved by isotropic phase dewetting on chemically patterned surfaces [119]. Spin-coating of triphenylamine-based DLCs on the SWNT-coated substrate is reported to exhibit homeotropic alignment in thin films in its hexagonal columnar phase [120].

7.5.2.2 Langmuir–Blodgett (LB) Deposition

The Langmuir–Blodgett technique is a simple way to control molecular organization at the air–water interface (see Fig. 7.15) [121]. This technique had been successfully employed to homogeneously align amphiphilic derivatives of

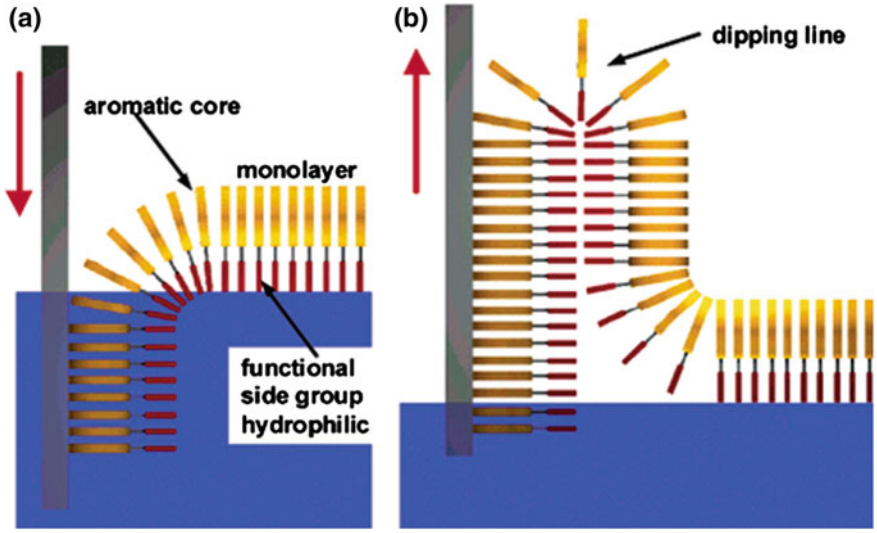

Fig. 7.15 Schematic illustration of the deposition of discotic molecules onto a substrate with the edge-on arrangement using the Langmuir-Blodgett technique. Reproduced with permission from [121]

triphenylenes, phthalocyanines, and HBC DLCs [122, 123]. The molecules form well-defined monolayer when spread from a solution at the air–water interface (the Langmuir film). Efficient transfer of the monolayer to substrate by vertical dipping gives well defined multilayer films. DLCs pack with uniformity in orientation, parallel to the vertical dipping direction used for Langmuir-Blodgett thin film fabrication. Armstrong and co-workers fabricated thin-film transistors based on a discotic phthalocyanine molecule on silicon substrates by the LB technique [124].

7.5.2.3 Templating from Self-assembled Monolayers

Alignment of DLCs on self-assembled monolayers (SAMs) has been the subject of many studies [125–128]. The application of SAMs opens new opportunities because of the ease with which they can be patterned, with nanometer resolution and over macroscopic areas. It is well known that thiols, disulfides, and thioethers interact strongly with gold covered substrates to form highly ordered SAMs by spontaneous adsorption from solution. Therefore SAMs of DLCs on gold surfaces was anticipated from different discoid molecules containing thioether, thiol, or disulfide substituents. Accordingly, discotic liquid crystalline hexaalkylthio-substituted triphenylenes and tricycloquinazolines, and derivatized triphenylenes with a single long ω-thioalkyl or ω-dithioalkyl substituent, were shown to self-assemble from dilute solution onto gold surfaces [125]. The discotic hexaalkyl thioethers assembled homeotropically onto the gold substrate. The alkyl chains

were found to lie flat on the gold but cover the aromatic cores. In contrast, aromatic cores of the molecules of the monosubstituted triphenylene discoids with a single thiol or disulfide substituent in the monolayers were aligned in a planar orientation [126]. Monobe et al. reported planar alignment behavior in the columnar mesophase of a triphenylene derivative on SAMs consisting of an asymmetrical disulfide, i.e. butyl hexadecyl disulfide. But such an alignment was not observed on SAMs consisting of a hexadecanethiol highlighting the fact that alignment of discotic liquid crystal molecules is affected by the morphological state of monolayer [127]. High mechanical stability and electrical "conductivity" across thin films of a thiol derivative of HBC had been reported in a metal–SAM–metal junction. Electrical measurements across SAMs indicated that electron transport through the HBC core is extremely efficient, when compared to the aliphatic part of the monolayer [128].

7.5.2.4 Zone Casting and Zone Crystallization

The zone-cast films offer high macroscopic uniaxial orientation of the columns with a molecular edge-on arrangement on the substrate. In zone-casting, a solution of the material is continuously deposited through a nozzle onto a moving substrate which is being withdrawn at a controlled rate, so that a meniscus is formed between a flat nozzle and the substrate [129]. The concentration gradient within the meniscus guides the molecules to uniaxially aligned columns parallel to the moving substrate (Fig. 7.16). The film morphology depends on processing conditions such as evaporation temperature, polarity of the solvent, concentration, solvent flow, substrate velocity, as well as the distance between the nozzle and the substrate. Various materials including low-molecular-weight semiconductors, discotic molecules, and block copolymers were successfully processed using this technique. Some of these materials were already shown to have good properties as active layers in field-effect transistors. For example, Mullen and co-workers achieved an order of magnitude higher field effect mobility (1×10^{-2} cm^2 V^{-1} s^{-1}) in zone-cast films of discotic HBC derivative when compared to a PTFE aligned FET device of the same material [130]. Recently, Tracz et al. reported on a room temperature LC phthalocyanine

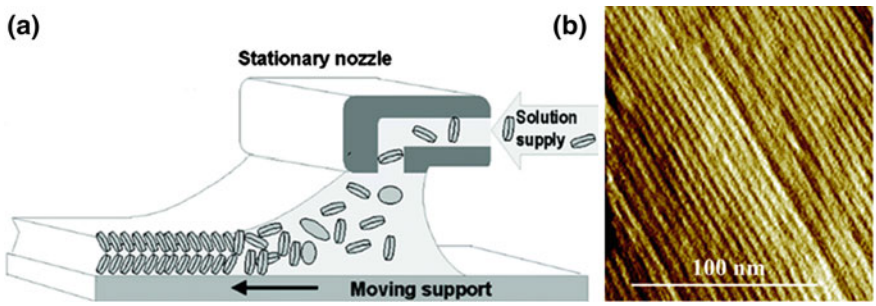

Fig. 7.16 **a** Zone-casting alignment rechnique; and, **b** zone-cast thin film of hexadodecyl HBC Reprinted with permission from [129]. Copyright 2003, American Chemical Society

processed by zone casting method. Highly oriented films that are uniform over several square centimeters were obtained on glass support from a mixed solvent (1:1 mixture of toluene and ethylene chloride) solution [131].

Zone casting and zone crystallization techniques are very similar in principle and differ only in processing conditions. While the former method involves solution processing, the latter depends on melt processing of the sample. Amorphous or polycrystalline films of DLCs have been recrystallized into single-crystal-like thin films of micrometer thickness by a zone-melting technique. In the zone crystallization method, the sample in its isotropic phase is moved in a defined velocity from a hot substrate to a cold substrate, allowing the material to crystallize along the temperature gradient as an aligned film [132]. Discotic HBC derivatives with branched long alkyl substituents were successfully processed into macroscopically ordered domains with "edge-on" orientation by using this technique [133].

7.5.2.5 Application of Electric Field and Magnetic Field

It is well known for rod-like LC molecules to align unidirectionally under the influence of an electric field. However, most DLCs do not respond to an applied electric field. Many recent studies focused on designing DLC molecules that are responsive to an applied electric field. Thus, alignment by electric field was achieved in the columnar phases of corannulene, triphenylene, hexaphenylbenzene, hexabenzocoronene and phthalocyanine based DLCs. In one of the first demonstrations, a solution of hexa(para-*n*-dodecylphenyl)hexabenzocoronene (**8b**) was applied to a glass surface by drop-casting and the molecules were oriented into highly ordered planar aligned columnar structures by an electric field during solvent evaporation [134]. An amide-substituted corannulene derivative with branched paraffinic side chains was shown to self-assemble into a columnar phase that responds to an applied electric field and align homeotropically to the electrode surface [135]. As a molecular design strategy, Miyajima et al. introduced aromatic amides with branched paraffinic tails onto mesogenic discotic cores such as corannulene, triphenylene and hexaphenylbenzene to serve as an electric-field-responsive handle that enables large-area unidirectional orientation of columnarly assembled LC molecules [136]. Very recently, a novel hexa-peri-hexabenzocoronene/oligothiophene hybrid DLC was shown to self-assemble into a hexagonal columnar LC phase, and respond to applied electric fields resulting in uniform homeotropic or planar alignment depending upon the electrode structure [137]. Furthermore, the columnar orientation was maintained even after removal of the electric field until the material was heated above the clearing temperature.

A magnetic field has been utilized for producing highly oriented films of DLCs. On the basis of this method, a substituted hexabenzocoronene DLC was solution-processed into planar orientation and field-effect transistors (FET) were constructed

with charge carrier mobilities up to 10^{-3} cm^2 $V^{-1}s^{-1}$ [138]. Choi and co-workers designed discotic metallomesogens, i.e. cobalt octa(*n*-alkylthio) porphyrazine derivatives that can interact with an external magnetic field to uniaxially align columnar phase [139, 140]. Planar alignment was achieved, by simultaneously utilizing an applied magnetic field (1.0 T) and the interaction of the discotic metallomesogen with an octadecyltrichlorosilane (OTS) functionalized substrate.

7.5.2.6 Application of IR Irradiation

In this technique, the vibrational mode of a selected chemical bond in a mesogen is excited by application of IR irradiation to induce alignment control. Shimizu and co-workers reported selective switching between planar and homeotropic alignments in the Col_h phase of the triphenylene mesogen by the excitation of C–C stretching vibration of the molecule using a combination of linearly and circularly polarized infrared irradiation [141]. Recently, this technique was extended to achieve alignment control of plastic columnar and helical columnar mesophases of other triphenylene derivatives [142].

7.5.2.7 Alignment in Pores and Channels

In recent years, several researchers looked upon molecular confinement within pores and channels as a tool to align DLC molecules. Wendorff and co-workers obtained aligned LC triphenylene nanowires within porous alumina templates [143]. Nanowire formation was found to depend on various factors like thermal history of the sample, pore geometry and the interfacial phenomena. In another study, polymer/liquid-crystal tubes consisting of an approximately 30 nm thick poly (methyl methacrylate) (PMMA) layer on the outside and a 5–10 nm thick discotic LC layer on the inside of the porous alumina template tubes had been prepared [144]. An HBC DLC derivative has been melt processed into nano-and macroscopic inorganic membrane pore templates to obtain supramolecular organization in the form of bundles and nanorods [145]. Uniform carbon nanotubes with ordered graphene orientations were obtained by carbonization of preorganized discotic hexabenzocoronene in porous alumina template [146]. Mouthuy et al. reported alignment of the columnar phases of a phthalocyanine-based DLC in SiO_2 channels [147]. These nano scale channels were fabricated using E-beam lithography and the samples were filled by spin-coating. Recently, Bushby and coworkers achieved planar alignment of triphenylene and phthalocyanine DLCs using microchannels made of SU8 polymer [148]. The advantage of this method lies in the easiness of fabrication of the SU8 channels in micrometer length scales and filling up of samples by capillary action.

7.6 Applications of Discotic Columnar Semiconductors

The semiconducting and self-assembling properties of columnar DLCs have stimulated intense research toward their application in organic electronic devices such as solar cells, OLEDs and OFETs. In OLEDs, charge carriers (holes and electrons) are injected from the electrodes into the organic semiconductor and emit light when they meet. Solar cells have an opposite working principle compared to OLEDs: light is absorbed and dissociated into charge carriers that migrate to the electrodes to give rise to an electric current. OFET plays the role of current modulator in electronic circuits by tuning the current flowing in its channel. A comparison of their device performance with those comprising analogous organic systems provides clear evidence that the DLC compounds are an important class of material in organic electronics and are extremely attractive alternatives to traditionally used inorganic semiconductors.

OLEDs generate light by electroluminescence. The basic structure of an OLED is shown in Fig. 7.17. It consists of a thin film of an organic semiconducting layer sandwiched in-between two electrodes, one with a high work function, the anode (generally transparent Indium Tin Oxide) able to inject positive charge carriers (holes) and one with a low work function, the cathode (calcium, aluminium, magnesium etc.) that injects negative charge carriers (electrons). Organic layer is composed of a hole transport layer, an emission layer, and an electron transport layer. With application of a voltage across the OLED, electrons and holes drift through their respective transporting layers and recombine near the interface (emission layer) to emit light with an energy hν. The external quantum efficiency η characterizes the efficiency of the OLEDs and is given by the ratio of the number of photons produced and the number of charges injected. In many cases, an electron-transporting layer and the light-emitting layer are combined into a single layer. Progress achieved on the performance of OLEDs regarding brightness, efficiency, and stability had resulted in their commercial applications in various portable display devices [149].

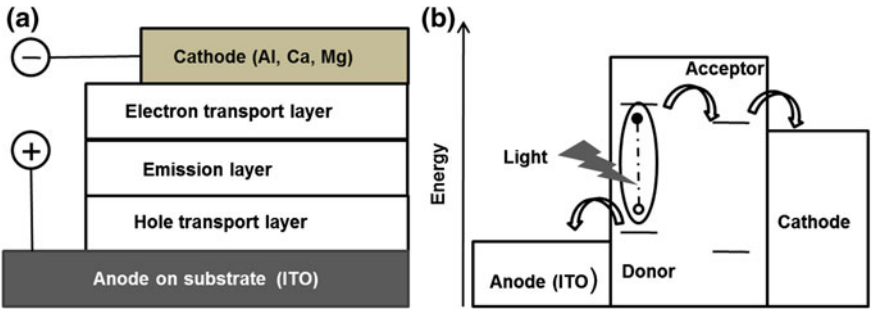

Fig. 7.17 Schematic representation of **a** an organic light-emitting diode architecture, **b** the charge recombination process in OLEDs

It is possible to combine the efficient charge transport properties of the columnar mesophase with luminescence properties through molecular design both of which are important material properties required for OLED applications. Wendorff and coworkers were the first to demonstrate the use of columnar discotics for applications in single layer OLEDs. Bacher et al. fabricated bilayer OLEDs by combining discotic triphenylene compounds as hole transporting material and the tris(8-quinolinolato) aluminum(III) complex (Alq3) as electron transport and emitting material [150–152]. Destruel and coworkers were the first to fabricate an all columnar bilayer organic red light-emitting diode with both an electron-rich columnar liquid crystal as hole transport material and an electron-deficient tetraethyl perylenetetracarboxylate fluorescent columnar liquid crystal as electron transport material [80]. They later achieved red, green, and blue color emissions by combining electron-deficient triphenylene and perylene discotic derivatives (as an electron transport layer) with a non-LC hole-transporting layer in multilayer OLED devices [153]. Saturated red light emission was observed in diodes made of an electron rich triphenylene derivative as hole transport material and an electron deficient fluorescent perylene derivative as electron transport material with both materials exhibiting a columnar LC phase. Figure 7.18 shows the current-voltage characteristics of the all columnar OLED made of ITO-coated glass/triphenylene hexaether/perylene tetraester/aluminum configuration. The current density was reported to reach as high as 28 mA cm^{-1} at 26 V. The light turn on occurred at 16 V and brightness up to 45 cd m^{-1} at 28 V was reported [154]. Performances of DLC based OLEDs are expected to improve significantly in the coming years with design of highly fluorescent DLCs and additional improvements on orientational order of the semiconducting molecules which can lead to high charge carrier mobility.

Photovoltaic or solar cells absorb solar light to convert it into an electrical current. OPV devices are constituted by an organic layer sandwiched between two

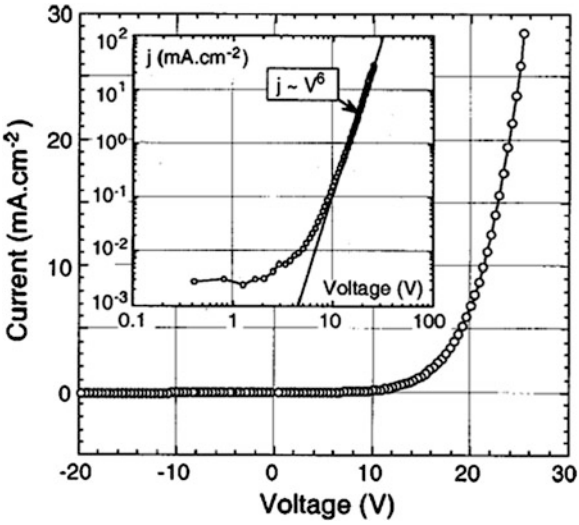

Fig. 7.18 Current density-voltage characteristics of the EL device. Reprinted with permission from [154]. Copyright 2001, American Institute of Physics

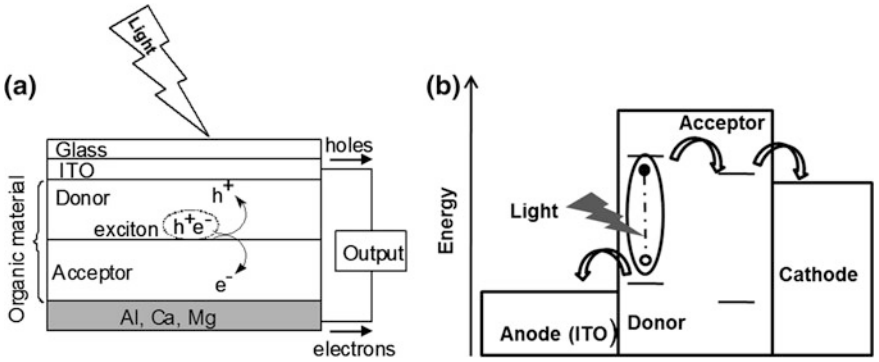

Fig. 7.19 Schematic representation of **a** a bilayer solar cell and **b** the photo-induced charge generation process responsible of the creation of an electric current

electrodes. The highest workfunction electrode (often ITO, a transparent material that allows light to enter the devices) collects holes whereas the lowest work-function collects electrons, resulting from the dissociation of the excitons (tightly bound holes and electrons) created by the absorption of photons (see Fig. 7.19). The photovoltaic efficiency η is defined as the ratio of the number of charge collected at the electrodes and the number of photons absorbed in the device. In solar cells, the UV-VIS absorption profile of the materials is very important, as it directly relates to the quantity of photons that the device can potentially capture. Equally important are the relative energy levels of the donor and acceptor materials. The energy gap between HOMO of the donor and LUMO of the acceptor determine the potential output (open-circuit voltage) of the device. Therefore, the performance of a solar cell device critically depends on several factors such as optical absorption and exciton formation, exciton migration to the donor-acceptor interface, exciton dissociation into charge carriers, charge-carrier mobility, and charge collection at the electrodes [155]. Discotic columns as an active semiconducting layer in OPV cells have a number of advantages over other organic materials. Apart from the ease of solution processibility into large-area thin films on flexible substrates, the highly ordered columnar mesophase of DLCs offers large exciton diffusion length and high charge-carrier mobilities both of which are key parameters for the device efficiency.

Several DLC derivatives of porphyrin, phthalocyanine, HBC, triphenylene, and perylene cores have been employed for solar cell applications. Some representative examples are discussed below. Gregg et al. first reported photovoltaic effect in a discotic porphyrin LC film sandwiched between ITO-coated glass electrodes [156]. Several years later, Petritsch et al. demonstrated photovoltaic performance in a bilayer heterojunction (BHJ) cell comprising a discotic phthalocyanine derivative as an electron donor and a perylene derivative as an electron-acceptor material, albeit with poor external quantum efficiencies (EQE $\sim$ 0.5 %) [157]. Schmidt-Mende et al. reported a significant improvement in photovoltaic performance by combining discotic HBC **8b** (electron donor) with an *n*-type perylene tetracarboxdiimide

molecule in a BHJ device [158]. They achieved power conversion efficiency around 2 % under monochromatic illumination (490 nm). Authors attribute this result to the nanophase segregation of perylene and HBC systems in the blend films to form separate percolation pathways for electron and hole transport. Further improvement in performance, i.e. an external quantum efficiency of 29.5 % at 460 nm and an open-circuit voltage of 0.70 V was achieved by controlling the film morphology by annealing of the HBC-perylene tetracarboxdiimide blend deposited on an elastomeric stamp of low-surface roughness [159]. Destruel's group reported preparation of an OPV device with ITO/triphenylene derivative/perylene derivative/Al cell structure and reported an external quantum efficiency of around 3 % [160].

Li et al. fabricated both bilayer- and bulk-heterojunction solar cells by spin-coating discotic porphyrin as a donor and C_{60} and its derivative PCBM as electron acceptor [64]. Bilayer and bulk-heterojunction devices were fabricated on ITO anode coated with a conducting polymeric mixture, i.e. poly(3,4-ethylenedioxythiophene) (PEDO)/poly(styrenesulfonate) (TPSS). In the bilayer solar cell, an active layer composed of a porphyrin DLC was spin coated from its chlorobenzene solution followed by thermal deposition of a C_{60} layer (deposited under vacuum). A blend thin film of the porphyrin DLC **16a** or **16b** and PCBM (1:1 *w*/*w* and 230–250 nm thick spin coated from a chlorobenzene solution) was used as the active layer in the bulk heterojunction device. On top of the active layer, Ca/Al cathode was deposited. Compared to the bilayer PV cells, BHJ devices showed better performance. After thermal annealing, BHJ cells exhibited a short-circuit current density (J_{SC}) of 3.990 mA/cm^2 and a power conversion efficiency (PCE) of 0.712 % (Fig. 7.20).

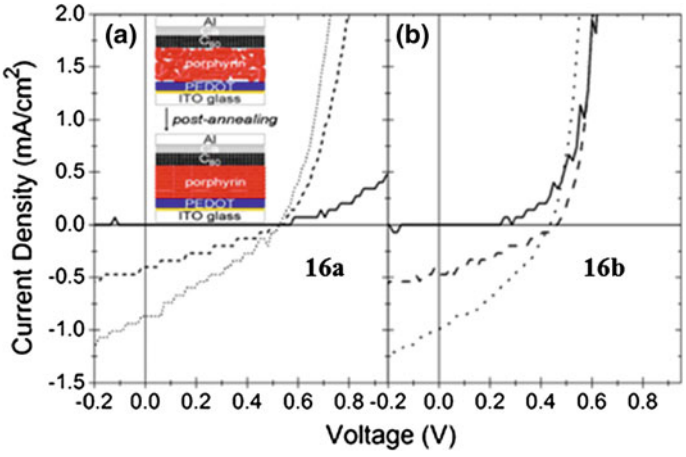

Fig. 7.20 *J-V* characteristics of the bilayer solar cells based on (**a**) **16a** and (**b**) **16b** under dark (*solid line*), and before (*dash line*) and after (*dot line*) annealing under the illumination of AM 1.5 G and 100 mW/cm^2. The *inset* of (**a**) schematically shows possible ordering of active porphyrin layer before and after annealing. Reproduced with permission from [64]

High external quantum efficiency of more than 70 % and an energy conversion efficiency of 3.1 % were achieved recently in a solution processable discotic phthalocyanine based bulk heterojunction solar cell [161]. For improvement in the performance of bulk heterojunction organic solar cells, the incorporation of *p*-type and *n*-type segments in a single molecule was sought. Accordingly, molecular DLC dyads such as HBC-pyrene [162], HBC-anthraquinone [163] and HBC-perylene-tetracarboxy diimide [93] were reported. Although OPV cells employing discotic molecules are yet to match the performance of polymer based devices, the progress that we are making with respect to the synthesis of new molecules and design of novel molecular architectures has been very encouraging.

Another important application of organic semiconductors is in the field of transistors. Transistors play the role of logical gates in an electrical circuit. The current in the circuit is modulated by varying the voltage between the electrodes. Basically, an organic field-effect transistor (OFET) is constituted by three electrodes (the gate, the source and the drain), an insulating (or dielectric) layer, and the organic semiconductor layer. An OFET can be fabricated in either top- or bottom contact geometry (Fig. 7.21). In "top-contact" geometry, the drain and source electrodes are deposited on top of the semiconducting layer, while the electrodes are positioned under the active layer in "bottom-contact" geometry. The geometries have their own advantages but the bottom contact devices are more often used since it is easier to integrate them in low-cost manufacturing processes. Commercial applications of OFETs are envisioned in active matrix displays, sensors, smart cards, and radiofrequency identification tags (RFIDs) [164].

Notable among high-performance DLCs for OFET applications are the derivatives of HBCs, phthalocyanines, and perylenes [29]. Van de Crats et al. constructed an OFET device by spin coating discotic HBC **8d** on to an aligned PTFE layer and reported field-effect mobilities of 0.5–1.0 × 10^{-3} cm^2 V^{-1} s^{-1} with a turn-on voltage of −5 to −10 V and on/off ratios of more than 10^4 [106]. Mullen and co-workers achieved an order of magnitude higher field effect mobility (1 × 10^{-2} cm^2 V^{-1} s^{-1}) in zone-cast films of discotic HBC derivative when compared with a PTFE aligned FET device of the HBC **8a** (n = 12), see Fig. 7.22 [130]. With magnetic field aligned HBC **8a**, FET charge carrier mobility of 10^{-3} cm^2 V^{-1} s^{-1} was achieved

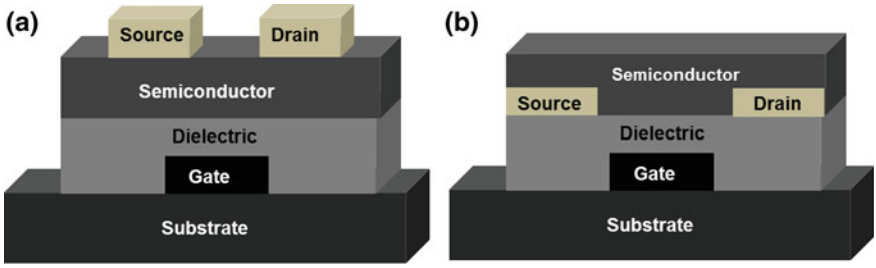

Fig. 7.21 Schematic representation of field-effect transistors in **a** *top* contact and **b** *bottom* contact geometries

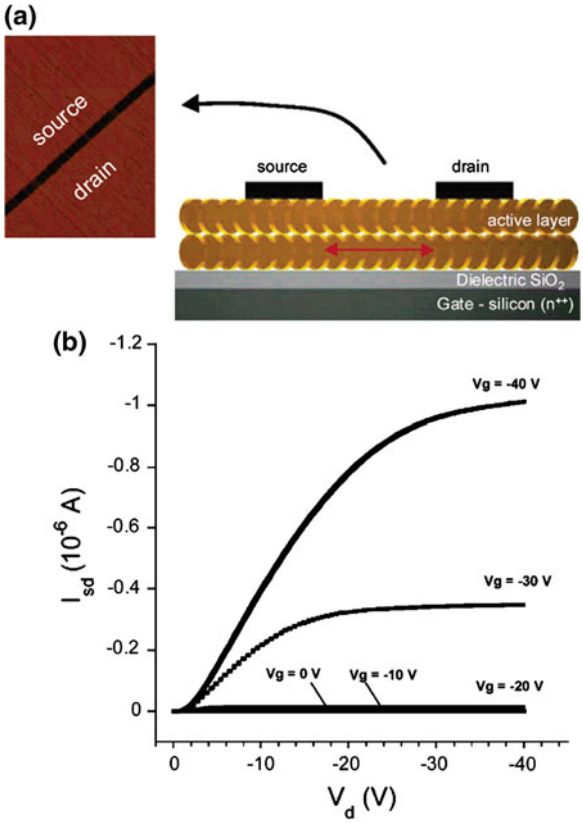

Fig. 7.22 **a** Schematic side-view representation of the top contact device configuration with contacts evaporated onto the 20 nm thick zone-cast HBC **4a** (n = 12) aligned film. The discs represent the tilted molecules in edge-on arrangement. The red arrow indicates the charge transport direction. The optical image shows the aligned layer in a 25 μm long channel of a FET. **b** I-V output characteristics of the zone-cast HBC **4a** (n = 12) as an active layer. (Reprinted with permission from [130]. Copyright 2005 John Wiley & Sons, Inc.)

with on-off ratio of 10^4 and turn-on voltage of ~5 V [165]. Nuckolls and coworkers reported OFETs (top contact with Au as source and drain electrode) based on nonplanar HBC **10** with high charge-carrier mobilities (0.02 $cm^2\ V^{-1}\ s^{-1}$), high on/off ratios (10^6), and low turn-on voltages (−3 V) [56]. Recently they reported the fabrication of stable high performance photosensitive OFETs, by integrating HBC **10** with single-walled carbon nanotubes (SWNT) as point contacts, with resistance up to 8.99×10^9 Ω [166]. Armstrong and coworkers fabricated bottom-contact transistors based on a discotic Cu-phthalocyanine derivative on silicon substrates with the LB alignment technique, and their devices showed field mobility of 10^{-2} $cm^2\ V^{-1}\ s^{-1}$ [124].

Perylene diimide derivatives are one of the most important *n*-type semiconducting mesogenic materials with high charge-carrier mobility. High field effect mobilities have been demonstrated in *n*-channel thin-film transistors using vapor-deposited perylene diimide derivatives. In 2002, Malenfant et al. reported *n*-channel OFETs based on **19b** with saturation electron mobilities ranging from 0.3 to 0.6 $cm^2\ V^{-1}\ s^{-1}$ and on-off ratios greater than 10^5 in a bottom-contact configuration [73]. Chesterfield et al. reported electron mobility up to 1.7 $cm^2\ V^{-1}\ s^{-1}$ with an on-

off current ratio of 10^7 in an OFET device based on **19b**. Higher performance of the device is attributed to the formation of well-organized thin films formed under controlled growth conditions [142].

Single-channel OFETs with simultaneous or selective transport of electrons and/or holes (ambipolar charge transport) are highly desirable owing to their application in complementary-like circuits. Using discotic quaterrylene tetracarboxdiimide **28**, bottom-gate ambipolar OFETs were fabricated on hexamethyldisilazane (HDMS) treated SiO_2 substrates [83]. Saturated electron and hole mobilities were found to be 1.5×10^{-3} cm^2 V^{-1} s^{-1} and 1.0×10^{-3} cm^2 V^{-1} s^{-1}, respectively. However, postproduction thermal annealing of these devices resulted solely in electron transport. To realize the advantages of LC organic semiconductors in practical applications, the FETs (both *n*-channel and *p*-channel) should at least provide field-effect mobilities above 1 cm^2 and on-off ratios in the range of 10^6 and operate under ambient conditions, preferably in a bottom-contact configuration.

7.7 Conclusions and Outlook

During the last two decades, significant progress has been made to develop organic semiconducting materials for electronic devices. In this chapter, we have described recent advances in the field of discotic columnar liquid crystals as semiconductors. An overview of structural and mesomorphic properties of molecules with emphasis on charge transport in terms of novel DLC cores, control of alignment and applications is provided through selected examples. DLCs exhibit carrier mobilities in between those of organic amorphous and crystalline materials. Molecular structure-charge mobility studies reveal ways to systematically improve charge carrier mobility by proper variation of the electronic and steric structure of the constituting molecules and to reach charge carrier mobilities that are comparable to amorphous silicon. DLCs as semiconductors combine quasi-one-dimensional charge transport with several other advantages including long-range self-assembling, self-healing of defects, solubility in organic solvents etc., all of which are highly desirable for low-cost lightweight plastic electronic products such as thin-film transistors, light-emitting diodes, solar cells, and sensors. For all of these proposed applications, it is necessary to have discotic columns to be macroscopically and uniformly aligned with planar or homeotropic orientation. Although several alignment techniques have been developed for DLCs it is yet to match the control that we had achieved in the calamitic liquid crystals. Despite achieving some good performance in OFETs and OPVs, research on applications of semiconducting DLCs is still in its infancy when stability and efficiency have to be compared with the performances of silicon based cells. Therefore, the development of new mesomorphic compounds is very important. Performances of these devices are expected to improve significantly in the coming years with design of robust DLCs and additional improvements on alignment of columnar phase on surfaces. Furthermore, dynamically functional anisotropic properties of columnar liquid crystals can be tuned or enhanced by the

formation of heterogeneous structures by the development of new composite materials based on liquid crystals with nanofibers, nanoparticles and carbon materials.

References

1. Q. Li (ed.), *Self-Organized Organic Semiconductors: From Materials to Device Applications* (Wiely, Hoboken, 2011)
2. S.R. Forrest, The path to ubiquitous and low-cost organic electronic appliances on plastic. Nature **428**, 911–918 (2004)
3. H. Klauk, (ed.), *Organic Electronics: Materials, Manufacturing and Applications* (Wiley-VCH, Weinheim, 2006)
4. J. Roncali, P. Leriche, A. Cravino, From one-to three-dimensional organic semiconductors: In search of the organic silicon. Adv. Mater. **19**, 2045–2060 (2007)
5. O.D. Jurchescu, J. Baas, T.T.M. Palstra, Effect of impurities on the mobility of single crystal pentacene. Appl. Phys. Lett. **84**, 3061–3063 (2004)
6. V. Podzorov, S.E. Sysoev, E. Loginova, V.M. Pudalov, M.E. Gershenson, Single-crystal organic field effect transistors with the hole mobility ~ 8 cm^2/Vs. Appl. Phys. Lett. **83**, 3 504–3506 (2003)
7. G. Hadziioannou, G. G. Malliavas (eds.), *Semiconducting Polymers: Chemistry, Physics and Engineering* (Wiley-VCH, Weinheim, 2007)
8. H. Pan, Y. Li, Y. Wu, P. Li, B.S. Ong, S. Zhu, G. Xu, Low-temperature, solution-processed, high-mobility polymer semiconductors for thin-film transistors. J. Am. Chem. Soc. **129**, 4112–4113 (2007)
9. H. Yan, Z. Chen, Y. Zheng, C. Newman, J.R. Quinn, F. Dotz, M. Kastler, A. Facchetti, A high-mobility electron-transporting polymer for printed transistors. Nature **457**, 679–686 (2009)
10. J. Hanna, A. Ohno, H. Iino, Charge carrier transport in liquid crystals. Thin Solid Films **554**, 58–63 (2014)
11. D. Demus, J. Goodby, G.W. Gray, H.-W. Spiess, V. Vill, (eds.), *Handbook of Liquid Crystals*, vol. 2A (Wiley-VCH, Weinheim, 1998)
12. P.J. Collings, M. Hird (eds.), *Introduction to Liquid Crystals: Chemistry and Physics*, (Taylor & Francis Ltd, London, 1997)
13. Q. Li (ed.), *Nanoscience with Liquid Crystals: From Self-Organized Nanostructures to Applications* (Springer, Heidelberg, 2014)
14. Q. Li (ed.), *Liquid Crystals Beyond Displays: Chemistry, Physics, and Applications* (Wiley, Hoboken, 2012)
15. S. Chandrasekhar, B.K. Sadashiva, K.A. Suresh, Liquid crystals of disc-like molecules. Pramana **9**, 471–480 (1977)
16. S. Kumar, Self-organization of disc-like molecules: chemical aspects. Chem. Soc. Rev. **35**, 83–109 (2006)
17. K. Kawata, Orientation control and fixation of discotic liquid crystal. Chem. Record. **2**, 59–80 (2002)
18. T. Kato, T. Yasuda, Y. Kamikawa, M. Yoshio, Self-assembly of functional columnar liquid crystals. Chem. Commun. **2009**, 729–739 (2009)
19. D. Adam, F. Closs, T. Frey, D. Funhoff, D. Haarer, H. Ringsdorf, P. Schuhmacher, K. Siemensmeyer, Transient photoconductivity in a discotic liquid crystal. Phys. Rev. Lett. **70**, 457–460 (1993)
20. M. Funahashi, J. Hana, Fast hole transport in a new calamitic liquid crystal of 2-(4-heptyloxyphenyl)-6-dodecylthiobenzothiazole. Phys. Rev. Lett. **78**, 2184–2187 (1997)

21. K.L. Woon, M.P. Aldred, P. Vlachos, G.H. Mehl, T. Stirner, S.M. Kelly, M. O'Neill, Electronic charge transport in extended nematic liquid crystals. Chem. Mater. **18**, 2311–2317 (2006)
22. M. Funahashi, N. Tamaoki, Electronic conduction in the chiral nematic phase of an oligothiophene derivative. ChemPhysChem **7**, 1193–1197 (2006)
23. M.P. Aldred, A.E.A. Contoret, S.R. Farrar, S.M. Kelly, D. Mathieson, M. O'Neill, W.C. Tsoi, P. Vlachos, A full-color electroluminescent device and patterned photoalignment using light-emitting liquid crystals. Adv. Mater. **17**, 1368–1372 (2005)
24. V. Lemaur, D.A. da Silva, V. Coropceanu, M. Lehmann, Y. Geerts, J. Piris, M.G. Debije, A. M. van de Craats, K. Senthilkumar, L.D.A. Siebbles, J.M. Warman, J.L. Bredas, J. Cornil, Charge transport properties in discotic liquid crystals: a quantum-chemical insight into structure–property relationships. J. Amer. Chem. Soc. **126**, 3271–3279 (2004)
25. L.J. Lever, R.W. Kelsall, R.J. Bushby, Band transport for discotic liquid crystals. Phys. Rev. B. **72**, 035130 (2005)
26. W. Pisula, M. Zorn, J.Y. Chang, K. Mullen, R. Zental, Liquid crystalline ordering and charge transport in semiconducting materials. Macromol. Rapid Commun. **30**, 1179–1202 (2009)
27. A.M. Van de Craats, J.M. Warman, A. Fechtenkötter, J.D. Brand, M.A. Harbison, K. Müllen, Record charge carrier mobility in a room-temperature discotic liquid crystalline derivative of hexabenzocoronene. Adv. Mater. **11**, 1469–1472 (1999)
28. J. Piris, W. Pisula, J.M. Warman, Anisotropy of the optical absorption and photoconductivity of a zone-cast film of a discotic hexabenzocoronene. Synth. Met. **147**, 85–89 (2004)
29. Y. Shimizu, K. Oikawa, K. Nakayama, D. Guillon, Mesophase semiconductors in field effect transistors. J. Mater. Chem. **17**, 4223–4229 (2007)
30. B. Domercq, J. Yu, B.R. Kaafarani, T. Kondo, S. Yoo, J.N. Haddock, S. Barlow, S.R. Marder, B. Kippelen, A comparative study of charge mobility measurements in a diamine and in a hexaazatrinaphthylene using different techniques. Mol. Cryst. Liq. Cryst. **481**, 80–93 (2008)
31. A.M. Van de Craats, J.M. Warman, M.P. De Haas, D. Adam, J. Simmerer, D. Haarer, P. Schuhmacher, The mobility of charge carriers in all four phases of the columnar discotic material hexakis (hexylthio) triphenylene: Combined TOF and PR-TRMC results. Adv. Mater. **8**, 823–826 (1996)
32. A.M. Van de Craats, J.M. Warman, The core-size effect on the mobility of charge in discotic liquid crystalline materials. Adv. Mater. **13**, 130–133 (2001)
33. C. Piechocki, J. Simon, A. Skoulios, D. Guillon, P. Weber, Discotic mesophases obtained from substituted metallophthalocyanines. Toward liquid crystalline onedimensional conductors. J. Am. Chem. Soc. **104**, 5245–5247 (1982)
34. N. Boden, R.J. Bushby, J. Clements, M.V. Jesudason, P.F. Knowles, G. Williams, One-dimensional electronic conductivity in discotic liquid crystals. Chem. Phys. Lett. **152**, 94–99 (1988)
35. N. Boden, R. Borner, D.R. Brown, R.J. Bushby, J. Clements, ESR studies of radical cations produced on doping discotic liquid crystals with lewis acids. Liq. Cryst. **11**, 325–334 (1992)
36. P.G. Schoten, J.M. Gorman, M.P. deHaas, M.A. Fox, H.L. Pan, Charge migration in supramolecular stacks of peripherally substituted porphyrins. Nature **353**, 736–737 (1991)
37. P.G. Schoten, J.M. Gorman, M.P. deHaas, J.F. van der Pol, J.W. Zwikker, Radiation-induced conductivity in polymerized and nonpolymerized columnar aggregates of phthalocyanine. J. Am. Chem. Soc. **114**, 9028–9034 (1992)
38. J. Simmerer, B. Glusen, W. Paulus, A. Kettner, P. Schuhmacher, D. Adam, K.-H. Etzbach, K. Siemensmeyer, J.H. Wendorff, H. Ringsdorf, D. Haarer, Transientphotoconductivity in a discotic hexagonal plastic crystal. Adv. Mater. **8**, 815–819 (1996)
39. D. Adam, P. Schumacher, J. Simmerer, L. Haussling, K. Siemensmeyer, K.H. Etzbachi, H. Ringsdorf, D. Haarer, Fast photoconduction in the highly ordered columnar phase of a discotic liquid crystal. Nature **371**, 141–143 (1994)

40. H. Bengs, F. Closs, T. Frey, D. Funhoff, H. Ringsdorf, K. Siemensmeyer, Highly photoconductive discotic liquid crystals: Structure–property relations in the homologous series of hexa-alkoxytriphenylenes. Liq. Cryst. **15**, 565–574 (1993)
41. J.A. Rego, S. Kumar, H. Ringsdorf, Synthesis and characterization of fluorescent, low-symmetry triphenylene discotic liquid crystals: Tailoring of mesomorphic and optical properties. Chem. Mater. **8**, 1402–1409 (1996)
42. A. Kettner, J.H. Wendorff, Modifications of the mesophase formation of discotic triphenylene compounds by substituents. Liq. Cryst. **26**, 483–487 (1999)
43. J.M. Warman, A.M. van De Craats, Charge mobility in discotic materials studied by PR-TRMC. Mol. Cryst. Liq. Cryst. **396**, 41–72 (2003)
44. M.A. Alam, J. Motoyanagi, Y. Yamamoto, T. Fukushima, J. Kim, K. Kato, M. Takata, A. Saeki, S. Seki, S. Tagawa, T. Aida, "Bicontinuous cubic" liquid crystalline materials from discotic molecules: A special effect of paraffinic side chains with ionic liquid pendants. J. Am. Chem. Soc. **131**, 17722–17723 (2009)
45. H. Iino, J. Hanna, C. Jager, D. Haarer, Fast electron transport in discotic columnar phase of triphenylene derivative, hexabutyloxytriphenylene. Mol. Cryst. Liq. Cryst. **436**, 217–224 (2005)
46. H. Iino, Y. Takayashiki, J. Hanna, R.J. Bushby, D. Haarer, High electronmobility of 0.1 cm^{-1} V^{-1} s^{-1} in the highly ordered columnar phase of exahexylthiotriphenylene. Appl. Phys. Lett. **87**, 192105 (2005)
47. B.R. Wegewijs, L.D.A. Siebbeles, N. Boden, R.J. Bushby, B. Movaghar, O.R. Lozman, Q. Liu, A. Pecchia, L.A. Mason, Charge-carrier mobilities in binary mixtures of discotic triphenylene derivatives as a function of temperature. Phys. Rev. B Condens. Matter Mater. Phys. **65**, 245112/1–245112/8 (2002)
48. I. Paraschiv, K. de Lange, M. Giesbers, B. van Lagen, F.C. Grozema, R.D. Abellon, L.D.A. Siebbeles, E.J.R. Sudholter, H. Zuilhof, A.T.M. Marcelis, Hydrogen-bond stabilized columnar discotic benzenetrisamides with pendant triphenylene groups. J. Mater. Chem. **18**, 5475–5481 (2008)
49. N. Mizoshita, H. Monobe, M. Inoue, M. Ukon, T. Watanabe, Y. Shimizu, K. Hanabusa, T. Kato, The positive effect on hole transport behaviour in anisotropic gels consisting of discotic liquid crystals and hydrogen-bonded fibres. Chem. Commun. 2002, 428–429 (2002)
50. S. Kumar, S.K. Pal, P.S. Kumar, V. Lakshminarayanan, Novel conducting nanocomposites: synthesis of triphenylene-covered gold nanoparticles and their insertion into a columnar matrix. Soft Matter **3**, 896–900 (2007)
51. L.A. Holt, R.J. Bushby, S.D. Evans, A. Burgess, G. Seeley, A 106-fold enhancement in the conductivity of a discotic liquid crystal doped with only 1 % (w/w) gold nanoparticles. J. Appl. Phys. **103**, 063712 (2008)
52. S. Kumar, L.K. Sagar, CdSe quantum dots in a columnar matrix. Chem. Commun. **47**, 12182–12184 (2011)
53. J. Wu, W. Pisula, K. Mullen, Graphenes as potential material for electronics. Chem. Rev. **107**, 718–747 (2007)
54. M.G. Debije, J. Piris, M.P. de Haas, J.M. Warman, Z. Tomovic, C.D. Simpson, M.D. Watson, K. Mullen, The optical and charge transport properties of discotic materials with large aromatic hydrocarbon cores. J. Am. Chem. Soc. **126**, 4641–4645 (2004)
55. X. Feng, M. Liu, W. Pisula, M. Takase, J. Li, K. Mullen, Supramolecular organization and photovoltaics of triangle-shaped discotic graphenes with swallowtailed alkyl substituents. Adv. Mater. **20**, 2684–2689 (2008)
56. S. Xiao, M. Myers, Q. Miao, S. Sanaur, K. Pang, M.L. Steigerwald, C. Nuckolls, Molecular wires from contorted aromatic compounds. Angew. Chem. Int. Ed. **44**, 7390–7394 (2005)
57. Y. Yamamoto, G. Zhang, W. Jin, T. Fukushima, N. Ishii, A. Saeki, S. Seki, S. Tagawa, T. Minari, K. Tsukagoshi, T. Aida, Ambipolar-transporting coaxial nanotubes with a tailored molecular graphene–fullerene heterojunction. PNAS **106**, 21051–21056 (2009)
58. J.W. Goodby, P.S. Robinson, B.-K. Teo, P.E. Cladi, The discotic phase of uroporphyrin octa-*N*-dodecyl ester. Mol. Cryst. Liq. Cryst. **56**, 303–309 (1980)

59. H. Fujikake, T. Murashige, M. Sugibayashi, K. Ohta, Time-of-flight analysis of charge mobility in a Cu-phthalocyanine-based discotic liquid crystal semiconductor. Appl. Phys. Lett. **85**, 3474 (2004)
60. H. Iino, J. Hanna, R.J. Bushby, B. Movaghar, B.J. Whitaker, M.J. Cook, Very high time-of-flight mobility in the columnar phases of a discotic liquid crystal. Appl. Phys. Lett. **87**, 132102 (2005)
61. K. Ban, K. Nishizawa, K. Ohta, A.M. Craats, J.M. Warman, I. Yamamoto, H. Shirai, Discotic liquid crystals of transition metal complexes 29: mesomorphism and charge transport properties of alkylthio-substituted phthalocyanine rare-earth metal sandwich complexes. J. Mater. Chem. **11**, 321–331 (2001)
62. S.W. Kang, Q. Li, B.D. Chapman, R. Pindak, J.O. Cross, L. Li, M. Nakata, S. Kumar, Microfocus x-ray diffraction study of the columnar phase of porphyrinbased mesogens. Chem. Mater. **19**, 5657–5663 (2007)
63. L. Li, S.W. Kang, J. Harden, Q. Sun, X. Zhou, L. Dai, A. Jakli, S. Kumar, Q. Li, Nature-inspired light-harvesting liquid crystalline porphyrins for organic photovoltaics. Liq. Cryst. **35**, 233–239 (2008)
64. Q. Sun, L. Dai, X. Zhou, L. Li, Q. Li, Bilayer-and bulk-heterojunction solar cells using liquid crystalline porphyrins as donors by solution processing. Appl. Phys. Lett. **91**, 253505 (2007)
65. T. Sakurai, K. Tashiro, Y. Honsho, A. Saeki, S. Seki, A. Osuka, A. Muranaka, M. Uchiyama, J. Kim, S. Ha, K. Kato, M. Takata, T. Aida, Electron- or hole-transporting nature selected by side-chain-directed π-stacking geometry: Liquid crystalline fused metalloporphyrin dimers. J. Am. Chem. Soc. **133**, 6537–6540 (2011)
66. N. Boden, R.C. Borner, R.J. Bushby, J. Clements, First observation of an *n*-doped quasi-one-dimensional electronically-conducting discotic liquid crystal. J. Am. Chem. Soc. **116**, 10807–10808 (1994)
67. N. Boden, R.J. Bushby, K. Donovan, Q. Liu, Z. Lu, T. Kreouzis, A. Wood, 2,3,7,8,12,13-Hexakis [2-(2-methoxyethoxy) ethoxy] tricycloquinazoline: a discogen which allows enhanced levels of *n*-doping. Liq. Cryst. **28**, 1739–1748 (2001)
68. K. Pieterse, P.A. van Hal, R. Kleppinger, J.A.J.M. Vekemans, R.A.J. Janssen, E.W. Meijer, An electron-deficient discotic liquid-crystalline material. Chem. Mater. **13**, 2675–2679 (2001)
69. R.I. Gearba, M. Lahmann, J. Levin, D.A. Ivanov, M.H.J. Koch, J. Barbera, M.G. Debije, J. Piris, Y.H. Geerts, Tailoring discotic mesophases: Columnar order enforced with hydrogen bonds. Adv. Mater. **15**, 1614–1618 (2003)
70. A. Demenev, S.H. Eichhorn, T. Taerum, D.F. Perepichka, S. Patwardhan, F.C. Grozeme, L. D.A. Siebbeles, R. Klenkler, Quasi temperature independent electron mobility in hexagonal columnar mesophases of an H-bonded benzotristhiophene derivative. Chem. Mater. **22**, 1420–1428 (2010)
71. M. Lehmann, G. Kestemont, R. Gomez Aspe, C. Buess-Herman, M.H.J. Koch, M.G. Debije, J. Piris, M.P. de Haas, J.M. Warman, M.D. Watson, High chargecarrier mobility in p-deficient discotic mesogens: Design and structure-property relationship. Chem. Eur. J. **11**, 3349–3362 (2005)
72. Y.-D. Zhang, K.G. Jespersen, M. Kempe, J.A. Kornfield, S. Barlow, B. Kippelen, S.R. Marder, Columnar discotic liquid-crystalline oxadiazoles as electron-transport materials. Langmuir **19**, 6534–6536 (2003)
73. B. Tylleman, G. Gbabode, C. Amato, C. Buess-Herman, V. Lemaur, J. Cornil, R. Go'mez Aspe, Y.H. Geerts, S. Sergeyev, Metal-free phthalocyanines bearing eight alkylsulfonyl substituents: Design, synthesis, electronic structure, and mesomorphism of new electron-deficient mesogens. Chem. Mater. **21**, 2789–2797 (2009)
74. C.W. Struijk, A.B. Sieval, J.E.J. Dakhorst, M. van Dijk, P. Kimkes, R.B.M. Koehorst, H. Donker, T.J. Schaafsma, S.J. Picken, A.M. van de Craats, Liquid crystalline perylene diimides: Architecture and charge carrier mobilities. J. Am. Chem. Soc. **122**, 11057–11066 (2000)

75. J.Y. Kim, I.J. Chung, Y.C. Kim, J.W. Yu, Mobility of electrons and holes in a liquid crystalline perylene diimide thin film with time of flight technique. Chem. Phys. Lett. **398**, 367–371 (2004)
76. P.R.L. Malenfant, C.D. Dimitrakopoulos, J.D. Gelorme, L.L. Kosbar, T.O. Graham, A. Curioni, W. Andreoni, N-type organic thin-film transistor with high field-effect mobility based on a N, N -dialkyl-3,4,9,10-perylene tetracarboxylic diimide derivative. Appl. Phys. Lett. **80**, 2517 (2002)
77. Z. An, J. Yu, S.C. Jones, S. Barlow, S. Yoo, B. Domercq, P. Prins, L.D.A. Siebbeles, B. Kippelen, S.R. Marder, High electron mobility in room-temperature discotic liquid-crystalline perylene diimides. Adv. Mater. **17**, 2580–2583 (2005)
78. Z. Chen, M.G. Debije, T. Debaerdemaeker, P. Osswald, F. Wuerthner, Tetrachloro-substituted perylene bisimide dyes as promising *n*-type organic semiconductors: studies on structural, electrochemical and charge transport properties. Chem. Phys. Chem. **5**, 137–139 (2004)
79. M. Funahashi, A. Sonoda, High electron mobility in a columnar phase of liquid-crystalline perylenetetracarboxylic bisimide bearing oligosiloxane chains. J. Mater. Chem. **22**, 25190–25197 (2012)
80. I. Seguy, P. Destruel, H. Bock, An all-columnar bilayer light-emitting diode. Synth. Met. **111**, 15–18 (2000)
81. S. Alibert-Fouet, S. Dardel, H. Bock, M. Oukachmih, S. Archambeau, I. Seguy, P. Jolinat, P. Destruel, Electroluminescent diodes from complementary discotic benzoperylenes. Chem. Phys. Chem. **4**, 983–985 (2003)
82. F. Nolde, W. Pisula, S. Muller, C. Kohl, K. Mullen, Synthesis and selforganization of core-extended perylene tetracarboxdiimides with branched alkyl substituents. Chem. Mater. **18**, 3715–3725 (2006)
83. H.N. Tsao, W. Pisula, Z. Liu, W. Osikowicz, W.R. Salaneck, K. Müllen, From ambi-to unipolar behavior in discotic dye field-effect transistors. Adv. Mater. **20**, 2715–2719 (2008)
84. U. Rohr, C. Kohl, K. Müllen, A. Craats, J. Warman, Liquid crystalline coronene derivatives. J. Mater. Chem. **11**, 1789–1799 (2001)
85. K. Hirota, K. Tajima, K. Hashimoto, Physicochemical study of discotic liquid crystal decacyclene derivative and utilization in polymer photovoltaic devices. Synth. Met. **157**, 290–296 (2007)
86. H.K. Bisoyi, S. Kumar, Room-temperature electron-deficient discotic liquid crystals: facile synthesis and mesophase characterization. New J. Chem. **32**, 1974–1980 (2008)
87. S.K. Gupta, V.A. Raghunathan, S. Kumar, Microwave-assisted facile synthesis of discotic liquid crystalline symmetrical donor–acceptor–donor triads. New J. Chem. **33**, 112–118 (2009)
88. J.C. Bunning, K.J. Donovan, R.J. Bushby, O.R. Lozman, Z. Lu, Electron photogeneration in a triblock co-polymer discotic liquid crystal. Chem. Phys. **312**, 145–150 (2005)
89. A. Hayer, V. de Halleux, A. Kohler, A. El-Garoughy, E.W. Meijer, J. Barbera, J. Tant, J. Levin, M. Lehmann, J. Gierschner, J. Cornil, Y.H. Geerts, Highly fluorescent crystalline and liquid crystalline columnar phases of pyrene-based structures. J. Phys. Chem. B **110**, 7653–7659 (2006)
90. M.J. Sienkowska, H. Monobe, P. Kaszynski, Y. Shimizu, Photoconductivity of liquid crystalline derivatives of pyrene and carbazole. J. Mater. Chem. **17**, 1392–1398 (2007)
91. T. Yasuda, T. Shimizu, F. Liu, G. Ungar, T. Kato, Electro-functional octupolar π-conjugated columnar liquid crystals. J. Am. Chem. Soc. **133**, 13437–13444 (2011)
92. H. Hayashi, W. Nihashi, T. Umeyama, Y. Matano, S. Seki, Y. Shimizu, H. Imahori, Segregated donor–acceptor columns in liquid crystals that exhibit highly efficient ambipolar charge transport. J. Am. Chem. Soc. **133**, 10736–10739 (2011)
93. L.F. Dössel, V. Kamm, I.A. Howard, F. Laquai, W. Pisula, X. Feng, C. Li, M. Takase, T. Kudernac, S. De Feyter, K. Müllen, Synthesis and controlled self-assembly of covalently linked hexaperi-hexabenzocoronene/perylene diimide dyads as models to study fundamental energy and electron transfer processes. J. Am. Chem. Soc. **134**, 5876–5886 (2012)

94. M. Talarico, R. Termine, E.M. Garcia-Frutos, A. Omenat, J.L. Serrano, B. Gomez-Lor, A. Golemme, New electrode-friendly triindole columnar phases with high hole mobility. Chem. Mater. **20**, 6589–6591 (2008)
95. B. Zhao, B. Liu, R.Q. Png, K. Zhang, K.A. Lim, J. Luo, J. Shao, P.K.H. Ho, C. Chi, J. Wu, New discotic mesogens based on triphenyl-fused triazatruxenes: Synthesis, physical properties, and self-assembly. Chem. Mater. **22**, 435–449 (2010)
96. D. Miyajima, K. Tashiro, F. Araoka, H. Takezoe, J. Kim, K. Kato, M. Takata, T. Aida, Liquid crystalline corannulene responsive to electric field. J. Am. Chem. Soc. **131**, 44–45 (2009)
97. S.S. Besbes, E. Grelet, H. Bock, Soluble and liquid-crystalline ovalenes. Angew. Chem. Int. Ed. **45**, 1783–1786 (2006)
98. C.V. Yelamaggad, A.S. Achalkumar, D.S. Shankar Rao, S.K. Prasad. Self-assembly of C_{3h} and C_s symmetric keto-enamine forms of tris(*N*salicylideneanilines) into columnar phases: A new family of discotic liquid crystals. J. Am. Chem. Soc. **126**, 6506–6507 (2004)
99. C. Lavigueur, E.J. Foster, V.E. Williams, Self-assembly of discotic mesogens in solution and in liquid crystalline phases: effects of substituent position and hydrogen bonding. J. Am. Chem. Soc. **130**, 11791–11800 (2008)
100. E.M. García-Frutos, U.K. Pandey, R. Termine, A. Omenat, J. Barberá, J.L. Serrano, A. Golemme, B. Gómez-Lor, High charge mobility in discotic liquid-crystalline triindoles: just a core business? Angew. Chem. **50**, 7399–7402 (2011)
101. S.H. Eichhorn, A. Adavelli, H.S. Li, N. Fox, Alignment of discotic liquid crystals. Mol. Cryst. Liq. Cryst. **397**, 47–58 (2003)
102. S. Sergeyev, W. Pisula, Y.H. Geerts, Discotic liquid crystals: A new generation of organic semiconductors. Chem. Soc. Rev. **36**, 1902–1929 (2007)
103. J.K. Vij, A. Kocot, T.S. Perova, Order parameter, alignment and anchoring transition in discotic liquid crystals. Mol. Cryst. Liq. Cryst. **397**, 231–244 (2003)
104. N. Terasawa, H. Monobe, K. Kiyohara, Y. Shimizu, Strong tendency towards homeotropic alignment in a hexagonal columnar mesophase of fluoroalkylated triphenylenes. Chem. Commun. 2003, 1678–1679 (2003)
105. W. Pisula, Z. Tomovic, B. El Hamaoui, M.D. Watson, T. Pakula, K. Mullen, Control of the homeotropic order of discotic hexa-*peri* -hexabezocoronenes. Adv. Funct. Mater. **15**, 893–904 (2005)
106. X. Zhou, S.W. Kang, S. Kumar, Q. Li, Self-assembly of discotic liquid crystal porphyrin into more controllable ordered nanostructure mediated by fluorophobic effect. Liq. Cryst. **36**, 269–274 (2009)
107. N. Kumaran, P.A. Veneman, B.A. Minch, A. Mudalige, J.E. Pemberton, D.F. O'Brien, N.R. Armstrong, Self-organized thin films of hydrogen-bonded phthalocyanines: characterization of structure and electrical properties on nanometer length scales. Chem. Mater. **22**, 2491–2501 (2010)
108. S. Zimmermann, J.H. Wendorff, C. Weder, Uniaxial orientation of columnar discotic liquid crystals. Chem. Mater. **14**, 2218–2223 (2002)
109. O. Bunk, M.M. Nielsen, T.I. Solling, A.M. van de Craats, N. Stutzmann, Induced alignment of a solution-cast discotic hexabenzocoronene derivative for electronic devices investigated by surface X-ray diffraction. J. Am. Chem. Soc. **125**, 2252–2258 (2003)
110. R.I. Gearba, D.V. Anokhin, A.I. Bondar, W. Bras, M. Jahr, M. Lehmann, D.A. Ivanov, Homeotropic alignment of columnar liquid crystals in open films by means of surface nanopatterning. Adv. Mater. **19**, 815–820 (2007)
111. E. Charlet, E. Grelet, Anisotropic light absorption, refractive indices, and orientational order parameter of unidirectionally aligned columnar liquid crystal films. Phys. Rev. E: Stat. Nonlinear, Soft Matter Phys. **78**, 041707/1–041707/8 (2008)
112. S.D. Xu, Q.D. Zeng, J. Lu, C. Wang, L.J. Wan, C.L. Bai, The two-dimensional self-assembled n-alkoxy-substituted stilbenoid compounds and triphenylenes studied by scanning tunneling microscopy. Surf. Sci. **538**, L451–L459 (2003)

113. M. Palma, J. Levin, V. Lemaur, A. Liscio, V. Palermo, J. Cornil, Y. Geerts, M. Lehmann, P. Samori, Self-organization and nanoscale electronic properties of azatriphenylene-based architectures: a scanning probe microscopy study. Adv. Mater. **18**, 3313–3317 (2006)
114. R. Friedlein, X. Crispin, C.D. Simpson, M.D. Watson, F. Jackel, W. Osikowicz, S. Marciniak, M.P. de Jong, P. Samori, S.K.M. Jonsson, M. Fahlman, K. Mullen, J.P. Rabe, W. R. alaneck, Electronic structure of highly ordered films of self-assembled graphitic nanocolumns. Phys. Rev. B **68**, 195414 (2003)
115. A.M. van de Craats, N. Stutzmann, O. Bunk, M.M. Nielsen, M. Watson, K. Mullen, H.D. Chanzy, H. Sirringhaus, R.H. Friend, Meso-epitaxial solution-growth of self-organizing discotic liquid-crystalline semiconductors. Adv. Mater. **15**, 495–499 (2003)
116. E. Charlet, E. Grelet, P. Brettes, H. Bock, H. Saadaoui, L. Cisse, P. Destruel, N. Gherardi, I. Seguy, Ultrathin films of homeotropically aligned columnar liquid crystals on indium tin oxide electrodes. Appl. Phys. Lett. **92**, 024107 (2008)
117. S. Sergeyev, J. Levin, J.-Y. Balandier, E. Pouzet, Y.H. Geerts, Homeotropic alignment in films of a mesogenic phthalocyanine depends on the nature of interactions with the surface. Mendeleev Commun. **19**, 185–186 (2009)
118. E. Pouzet, V.D. Cupere, C. Heintz, J.W. Andreasen, D.W. Breiby, M.M. Nielsen, P. Viville, R. Lazzaroni, G. Gbabode, Y.H. Geerts, Homeotropic alignment of a discotic liquid crystal induced by a sacrificial layer. J. Phys. Chem. C **113**, 14398–14406 (2009)
119. J.P. Bramble, D.J. Tate, D.J. Revill, K.H. Sheikh, J.R. Henderson, F. Liu, X. Zeng, G. Ungar, R.J. Bushby, S.D. Evans, Planar alignment of columnar discotic liquid crystals by isotropic phase dewetting on chemically patterned surfaces. Adv. Funct. Mater. **20**, 914–920 (2010)
120. T.D. Choudhury, N.V.S. Rao, R. Tenent, J. Blackburn, B. Gregg, I.I. Smalyukh, Homeotropic alignment and director structures in thin films of triphenylamine-based discotic liquid crystals controlled by supporting nanostructured substrates and surface confinement. J. Phys. Chem. B **115**, 609–617 (2011)
121. T. Bjornholm, T. Hassenkam, N. Reitzel, Supramolecular organization of highly conducting organic thin films by the Langmuir-Blodgett technique. J. Mater. Chem. **9**, 1975–1990 (1999)
122. B.W. Laursen, K. Norgaard, N. Reitzel, J.B. Simonsen, C.B. Nielsen, J. Als-Nielsen, T. Bjornholm, T.I. Solling, M.M. Nielsen, O. Bunk, K. Kjaer, N. Tchebotareva, M.D. Watson, K. Mullen, J. Piris, Macroscopic alignment of graphene stacks by Langmuir–blodgett deposition of amphiphilic hexabenzocoronenes. Langmuir **20**, 4139–4146 (2004)
123. N. Reitzel, T. Hassenkam, K. Balashev, T.R. Jensen, P.B. Howes, K. Kjaer, A. Fechtenkotter, N. Tchebotareva, S. Ito, K. Mullen, T. Bjornholm, Langmuir and Langmuir-Blodgett films of amphiphilic hexa-peri-hexabenzocoronene: New phase transitions and electronic properties controlled by pressure. Chem. Eur. J. **7**, 4894–4901 (2001)
124. S. Cherian, C. Donley, D. Mathine, L. LaRussa, W. Xia, N. Armstrong, Effects of field dependent mobility and contact barriers on liquid crystalline phthalocyanine organic transistors. J. Appl. Phys. **96**, 5638–5643 (2004)
125. N. Boden, R.J. Bushby, P.S. Martin, Triphenylene-based liquid crystals as self-assembled monolayers. Langmuir **15**, 3790–3797 (1999)
126. H. Schönherr, F.J.B. Kremer, S. Kumar, J.A. Rego, H. Wolf, H. Ringsdorf, M. Jaschke, H.-J. Butt, E. Bamberg, Self-assembled monolayers of discotic liquid crystalline thioethers, discoid disulfides, and thiols on gold: molecular engineering of ordered surfaces. J. Am. Chem. Soc. **118**, 13051–13057 (1996)
127. H. Monobe, H. Azehara, Y. Shimizu, M. Fujihira, Alignment of discotic nematic and columnar phases on self-assembled monolayers of alkanethiol and asymmetrical disulfide. Chem. Lett. **30**, 1268–1269 (2001)
128. M. Duati, C. Grave, N. Tebeborateva, J. Wu, K. Mullen, A. Shaporenko, M. Zharnikov, J.K. Kriebel, G.M. Whitesides, M.A. Rampi, Electron transport across Hexa-peri-hexabenzocoronene units in a metal-self-assembled monolayer-metal junction. Adv. Mater. **18**, 329–333 (2006)

129. A. Tracz, J.K. Jeszka, M. Watson, W. Pisula, K. Müllen, T. Pakula, Uniaxial alignment of the columnar super-structure of a hexa(alkyl) hexa-*peri*-hexabenzocoronene on untreated glass by simple solution processing. J. Am. Chem. Soc. **125**, 1682–1683 (2003)
130. W. Pisula, A. Menon, M. Stepputat, I. Lieberwirth, U. Kolb, A. Tracz, H. Sirringhaus, T. Pakula, K. Mullen, A zone-casting technique for device fabrication of field effect transistors based on discotic hexa-peri-hexabenzocoronene. Adv. Mater. **17**, 684–689 (2005)
131. A. Tracz, T. Makowski, S. Masirek, W. Pisula, Y.H. Geerts, Macroscopically aligned films of discotic phthalocyanine by zone casting. Nanotechnology **18**, 485303 (2007)
132. C.Y. Liu, A.J. Bard, In-situ regrowth and purification by zone melting of organic single-crystal thin films yielding significantly enhanced optoelectronic properties. Chem. Mater. **12**, 2353–2362 (2000)
133. W. Pisula, M. Kastler, D. Wasserfallen, T. Pakula, K. Müllen, Exceptionally long-range self-assembly of hexa-peri-hexabenzocoronene with dove-tailed alkyl substituents. J. Am. Chem. Soc. **126**, 8074–8075 (2004)
134. A. Cristadoro, G. Lieser, H.J. Rader, K. Mullen, Field-force alignment of disc-type π systems. ChemPhysChem **8**, 586–591 (2007)
135. D. Miyajima, K. Tashiro, F. Araoka, H. Takezoe, J. Kim, K. Kato, M. Takata, T. Aida, Liquid crystalline corannulene responsive to electric field. J. Am. Chem. Soc. **131**, 44–45 (2009)
136. D. Miyajima, F. Araoka, H. Takezoe, J. Kim, K. Kato, M. Takata, T. Aida, Electric-field-responsive handle for large-area orientation of discotic liquid-crystalline molecules in millimeter-thick films. Angew. Chem. Int. Ed. **50**, 7865–7869 (2011)
137. N. Hu, R. Shao, Y. Shen, D. Chen, N.A. Clark, D.M. Walba, An electric-field-responsive discotic liquid-crystalline hexa-peri-hexabenzocoronene/ oligothiophene hybrid. Adv. Mater. **26**, 2066–2071 (2014)
138. I.O. Shklyarevskiy, P. Jonkheijm, N. Stutzmann, D. Wasserberg, H.J. Wondergem, P.C.M. Christianen, A.P.H.J. Schenning, D.M. de Leeuw, Z. Tomovic, J. Wu, K. Mullen, J.C. Maan, High anisotropy of the field-effect transistor mobility in magnetically aligned discotic liquid-crystalline semiconductors. J. Am. Chem. Soc. **127**, 16233–16237 (2005)
139. J.-H. Lee, S.-M. Choi, B.D. Pate, M.H. Chisholm, Y.-S. Han, Magnetic uniaxial alignment of the columnar superstructure of discotic metallomesogens over the centimetre length scale. J. Mater. Chem. **16**, 2785–2791 (2006)
140. H.-S. Kim, S.-M. Choi, J.-H. Lee, P. Busc, S.J. Koza, E.A. Verploegen, B.D. Pate, Uniaxially oriented, highly ordered, large area columnar superstructures of discotic supramolecules using magnetic field and surface interactions. Adv. Mater. **20**, 1105–1109 (2008)
141. H. Monobe, K. Awazu, Y. Shimizu, Alignment control of a columnar liquid crystal for a uniformly homeotropic domain using circularly polarized infrared irradiation. Adv. Mater. **18**, 607–610 (2006)
142. H. Monobe, K. Awazu, Y. Shimizu, Alignment change of hexahexylthiotriphenylene in the helical columnar phase by infrared laser irradiation. Thin Solid Films **518**, 762–766 (2009)
143. M. Steinhart, S. Zimmermann, P. Goring, A.K. Schaper, U. Gosele, C. Weder, J.H. Wendorff, Liquid crystalline nanowires in porous alumina: geometric confinement versus influence of pore walls. Nano Lett. **5**, 429–434 (2005)
144. M. Steinhart, S. Murano, A.K. Schaper, T. Ogawa, M. Tsuji, U. Gosele, C. Weder, J.H. Wendorff, Morphology of polymer/liquid-crystal nanotubes: influence of confinement. Adv. Funct. Mater. **15**, 1656–1664 (2005)
145. W. Pisula, M. Kastler, D. Wasserfallen, R.J. Davies, M.C.G. Gutierrez, K. Mullen, From macro- to nanoscopic templating with nanographenes. J. Am. Chem. Soc. **128**, 14424–14425 (2006)
146. L. Zhi, J. Wu, J. Li, U. Kolb, K. Mullen, Carbonization of disclike molecules in porous alumina membranes: toward carbon nanotubes with controlled graphene-layer orientation. Angew. Chem. Int. Ed. **44**, 2120–2123 (2005)

147. P.O. Mouthuy, S. Melinte, Y.H. Geerts, A.M. Jonas, Uniaxial alignment of nanoconfined columnar mesophases. Nano Lett. **7**, 2627–2632 (2007)
148. J. Cattle, P. Bao, J.P. Bramble, R.J. Bushby, S.D. Evans, J.E. Lydon, D.J. Tate, Controlled planar alignment of discotic liquid crystals in microchannels made using SU8 photoresist. Adv. Funct. Mater. **23**, 5997–6006 (2013)
149. C.R. McNeill, N.C. Greenham, Conjugated-polymer blends for optoelectronics. Adv. Mater. **21**, 1–11 (2009)
150. T. Christ, B. Glusen, A. Greiner, A. Kellner, R. Sander, V. Stumpflen, V. Tsukruk, J.H. Wendorff, Columnar discotics for light emitting diodes. Adv. Mater. **9**, 48–51 (1997)
151. I.H. Stapff, V. Stümpflen, J.H. Wendorff, D.B. Spohn, D. M¨obius, Multi-layer light emitting diodes based on columnar discotics. Liq. Cryst. **23**, 613–617 (1997)
152. A. Bacher, I. Bleyl, C.H. Erdelen, D. Haarer, W. Paulus, H.W. Schmidt, Low molecular weight and polymeric triphenylenes as hole transport materials in organic two-layer LEDs. Adv. Mater. **9**, 1031–1035 (1997)
153. T. Hassheider, S.A. Benning, H.S. Kitzerow, M.F. Achard, H. Bock, Colortuned electroluminescence from columnar liquid crystalline alkyl arenecarboxylates. Angew. Chem. Int. Ed. **40**, 2060–2063 (2001)
154. I. Seguy, P. Jolinat, P. Destruel, J. Farenc, R. Mamy, H. Bock, J. Ip, T.P. Nguyen, Red organic light emitting device made from triphenylene hexaester and perylene tetraester. J. Appl. Phys. **89**, 5442–5448 (2001)
155. B.P. Rand, J. Genoe, P. Heremans, J. Poortmans, Solar cells utilizing small molecularweight organic semiconductors. Prog. Photovolt: Res. Appl. **15**, 659–676 (2007)
156. B.A. Gregg, M.A. Fox, A.J. Bard, Photovoltaic effect in symmetrical cells of a liquid crystal porphyrin. J. Phys. Chem. **94**, 1586–1598 (1990)
157. K. Petritsch, R.H. Friend, A. Lux, G. Rozenberg, S.C. Moratti, A.B. Holmes, Liquid crystalline phthalocyanines in organic solar cells. Synth. Met. **102**, 1776–1777 (1999)
158. L. Schmidt-Mende, A. Fechtenkotter, K. Mullen, E. Moons, R.H. Friend, J.D. MacKenzie, Self-organized discotic liquid crystals for high-efficiency organic photovoltaics. Science **293**, 1119–1122 (2001)
159. J.P. Schmidtke, R.H. Friend, M. Kastler, K. Müllen, Control of morphology in efficient photovoltaic diodes from discotic liquid crystals. J. Chem. Phys. **124**, 174704 (2006)
160. M. Oukachmih, P. Destruel, I. Seguy, G. Ablart, P. Jolinat, S. Archambeau, M. Mabiala, S. Fouet, H. Bock, New organic discotic materials for photovoltaic conversion. Sol. Energy Mater. Sol. Cells **85**, 535–543 (2005)
161. T. Hori, N. Fukuoka, T. Masuda, Y. Miyake, H. Yoshida, A. Fujii, Y. Shimizu, M. Ozaki, Bulk heterojunction organic solar cells utilizing 1,4,8,11,15,18,22,25-octahexylphthalocyanine. Sol. Energy Mater. Sol. Cells **95**, 3087–3092 (2011)
162. N. Tchebotareva, X. Yin, M.D. Watson, P. Samori, J.P. Rabe, K. Müllen, Ordered architectures of a soluble hexa-peri-hexabenzocoronene-pyrene dyad: Thermotropic bulk properties and nanoscale phase segregation at surfaces. J. Am. Chem. Soc. **125**, 9734–9739 (2003)
163. P. Samori, X. Yin, N. Tchebotareva, Z. Wang, T. Pakula, F. Jackel, M.D. Watson, A. Venturini, K. Müllen, J.P. Rabe, Self-assembly of electron donor-acceptor dyads into ordered architectures in two and three dimensions: Surface patterning and columnar double cables. J. Am. Chem. Soc. **126**, 3567–3575 (2004)
164. H. Sirringhaus, Device physics of solution-processed organic field-effect transistors. Adv. Mater. **17**, 2411–2425 (2005)
165. I.O. Shklyarevskiy, P. Jonkheijm, N. Stutzmann, D. Wasserberg, H.J. Wondergem, P.C.M. Christianen, A.P.H.J. Schenning, D.M. De Leeuw, Z. Tomovic, J. Wu, K. Mullen, J.C. Maan, High anisotropy of the field-effect transistor mobility in magnetically aligned discotic liquid-crystalline semiconductors. J. Am. Chem. Soc. **127**, 16233–16237 (2005)
166. X. Guo, S. Xiao, M. Myers, Q. Miao, M.L. Steigerwald, C. Nuckolls, Photoresponsive nanoscale columnar transistors. PNAS **106**, 691–696 (2009)

Chapter 8
Directed Assembly and Self-organization of Metal Nanoparticles in Two and Three Dimensions

S. Holger Eichhorn and Jonathan K. Yu

Abstract Properties of metals and other compounds change in comparison to their bulk materials when they are prepared as sufficiently small particles, usually in the 1–50 nm range. A myriad of applications for these nanoparticles have been conceived and tested and their presence in consumer products is already ubiquitous. It was established right from the beginning that the properties of materials containing nanoparticles not only depend on their size, shape, and composition but also their spatial arrangement. Most prominent are predictable changes to their optical properties when nanoparticles are positioned in ordered arrays and sufficiently close to permit electronic interactions. This chapter describes the recent advancements in the arrangement of metal nanoparticles into defined structures of two- and three-dimensional order by the Langmuir-Blodgett technique, layer-by-layer deposition, and the self-organization of liquid crystalline and amphiphilic metal nanoparticles. The large volume of work on the (directed) self-assembly of nanoparticles is just briefly presented in the introduction as it has been extensively and comprehensively reviewed by others. While the Langmuir-Blodgett technique can generate monolayer and multilayer materials, the other two techniques (layer-by-layer deposition and the self-organization) are predominantly applied to the preparation of three-dimensionally ordered materials. Discussed in great detail is how the purity and size-distribution of employed metal nanoparticles and the structure of their protective layer(s) affect their ability to generate two- and three-dimensionally ordered arrangements of high quality and persistence length by any of the three techniques. Processing conditions are described in less detail because they do not differ from those used for molecular materials, although they are equally important to the preparation of structures of long-range order. Finally, possible applications and properties of materials prepared by the Langmuir-Blodgett technique, Layer-by-layer deposition, and self-organization are described if deemed important.

S. Holger Eichhorn (✉) · J.K. Yu
Department of Chemistry and Biochemistry, University of Windsor,
401 Sunset Avenue, Windsor, ON N9B 3P4, Canada
e-mail: eichhorn@uwindsor.ca

Q. Li (ed.), *Anisotropic Nanomaterials*, NanoScience and Technology,
DOI 10.1007/978-3-319-18293-3_8

8.1 Introduction

Both, molecular and supramolecular structures affect the properties of molecular materials and must be optimized for every desired application. Similarly, properties of materials comprised of metal nanoparticles (MNPs) are controlled not only by the structure and composition of MNPs but also their arrangement in space. In fact, an increasing proportion of the recent research on MNPs has focused on their controlled processing into specific one-, two-, and three-dimensional structures. Self-assembly and self-assembly directed or assisted by directional chemical interactions, external fields, and template surfaces, are the most prominent methodologies applied to control the spatial arrangement of nanoparticles (NPs) but structures of two- and three-dimensional order have also been obtained with other techniques, such as the formation of Langmuir-Blodgett (LB) films, Layer-by-Layer (LbL) deposition, and the self-organization of liquid crystalline or amphiphilic MNPs (Fig. 8.1). It is the application of the latter three techniques this chapter is concerned with, in addition to being focused on MNPs, since the application of self-assembly and related processes has been recently and extensively reviewed by others [1–5]. Brief summaries of selected review articles on the controlled assembly

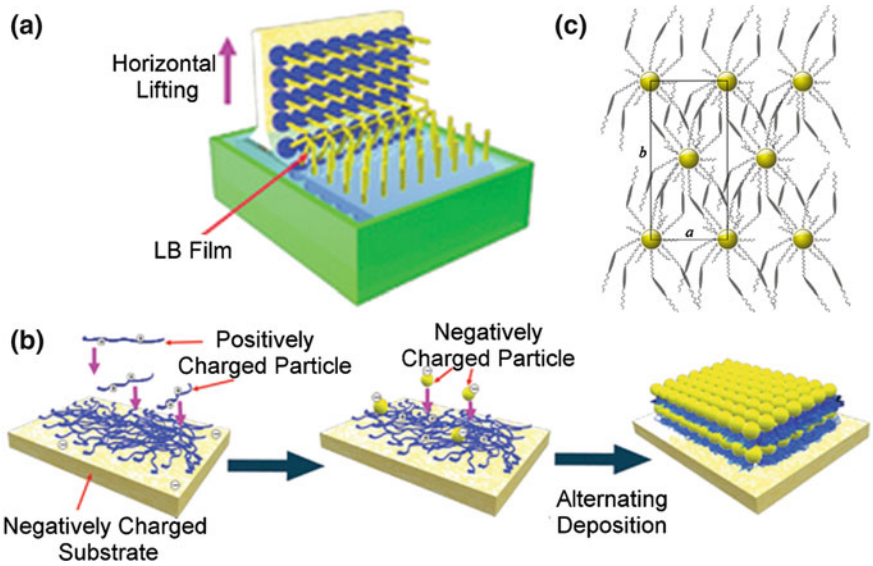

Fig. 8.1 Cartoons of ordered structures generated by **a** LB films, **b** LbL deposition [6], and **c** the self-organization of liquid crystalline or amphiphilic MNPs [7]. Adapted by permission from Macmillan Publishers Ltd.: NPG Asia Materials [6], copyright 2012. Reprinted (adapted) with permission from [7]. Copyright 2013 American Chemical Society

of nanoparticles by techniques not covered here are provided below as guidance for the interested reader.

Grzelczak et al. review mainly the directed self-assembly of spherical gold NPs and, in more general terms, to what extent self-assembly can be controlled by either changing the energy or entropy landscapes via the use of templates or applied external fields [1]. The first part is concerned with the interactions between chemically modified gold NPs and templates and the template free self-assembly of chemically modified gold NPs due to directional interactions. Provided examples include DNA mediated assembly of gold NPs and investigations of anisotropic and Janus-type MNPs. The second part briefly describes the influence of various external fields on the self-assembly process, which inevitably includes examples of metal oxide, modified polymer, silica, and other NPs. Besides the common application of a single field (electric, magnetic, and flow), the authors also highlight the high potential for simultaneous application of several directing fields. This second part also includes a short overview of self-assembly of NPs at liquid-liquid interfaces but the interested reader may rather be directed to a comprehensive review on self-assembly at liquid-liquid interfaces by Böker et al. [2].

Although already 7 years old, the review on self-assembly of NPs by Kinge et al. is still one of the most comprehensive description of different self-assembly processes and their principles [3]. At the centre of this review is the description of different self-assembly methods and their underlying principles, such as drying mediated assembly, self-assembled monolayers, self-assembly via H-bonding, electrostatic assembly including LbL deposition, directed assembly aided by electrical, magnetic, and optical fields, and assembly at interfaces that includes a short section on LB films. Also described is the use of inorganic and biological templates, microcontact and other printing methods, as well as shape-selective assembly of non-spherical NPs. Following the part on general concepts and methodology is an extensive list of examples that is structured based on the dimensionality (one, two, and three) of the self-assembly and the review concludes with a brief description of specific properties of self-assembled NPs. A more concise and recent account on techniques for self-assembly of NPs is provided by Nie et al., which also gives a more comprehensive description of the properties of derived materials and their potential applications [4]. The authors in particular emphasize properties that derive from plasmonic interactions and the same research group has recently devoted an entire review to the subject of self-assembled plasmonic nanostructures [5]. This review, in contrast to all other reviews mentioned here, also contains a part on the computational modelling of self-organization of NPs and discusses the dynamic and static nature of NP assemblies. A quotation from this review will serve us as a final remark: “We note that although a particular force may dominate the self-assembly process, in reality, the formation of a particular structure originates from the interplay of several forces.”

8.2 Langmuir-Blodgett Films of Metal Nanoparticles (MNPs)

8.2.1 Introduction

The Langmuir-Blodgett (LB) technique is probably the oldest methodology for the generation of defined monomolecular layers and their layer-by-layer transfer onto substrates. So, it is not surprising that NPs were processed into monolayers by the LB technique as soon as they became available as soluble, discrete, and well characterized entities. In the early 1990s Peng and co-workers already described the formation of LB films of Fe_2O_3 NPs with stearate layers in between the NP layers [8]. Since then, the LB technique has been applied to many other types of NPs, such as NPs made of metal [9] and metal oxides [10], NPs with core-shell structures [11], and NPs that are semiconductors [12] or magnetic [13]. This review is mainly concerned with metal NPs (MNPs) but NPs generated from metal oxides and inorganic semiconductors may be mentioned where appropriate. Not covered is the synthesis of MNPs used for LB deposition although specific purity or shape requirements may be indicated.

When compared to other assembling methods, such as self-assembled monolayer templates and lithographic patterning, the LB method has several important advantages: (a) relatively large areas can be uniformly coated (square centimeters) for comparatively low cost, (b) the spacing between MNPs can be relatively easily varied by adjusting the surface pressure, (c) basically all soluble MNPs can be processed by this method, (d) monolayers of two-dimensional order and multilayers of three-dimensional order can be generated [14]. Important deficiencies of the LB method are limited scalability and the incompatibility with continuous coating processes.

In general, the formation of LB films of MNPs involves the following four steps: (1) The MNPs must be dissolved in a sufficiently volatile solvent that is immiscible with the mostly aqueous subphase of the trough. (2) This solution is spread onto the water surface to generate a Langmuir film after the evaporation of the solvent. (3) The physical state of the Langmuir film is controlled and changed with moveable barriers that adjust the available surface area and, consequently, surface pressure. (4) The Langmuir film is transferred, usually by vertical dipping (Langmuir-Blodgett technique) or horizontal lifting (Langmuir-Schäfer technique), onto a substrate at a surface pressure below the collapse pressure of the film to generate a LB film [15, 16].

All MNPs used for depositions by the LB method are coated with a monolayer or bilayer layer of organic protecting ligands or with a polymer layer to prevent particle growth by coalescence [17] and to impart sufficiently high solubility in the spreading solvent and perhaps an amphiphilic character. A stable and adequate spacing between metal cores of MNPs is particularly important when the film is compressed to avoid coalescence, which usually results in a loss of the assembled structure due to precipitation [18, 19]. Compression to surface pressures of 10 mN/m and larger is essential for the generation of uniform films of close-packed

MNPs. L-films with collapse pressures much larger than 15 mN/m usually require sufficiently amphiphilic MNPs, which is not easily achieved [20]. Two common approaches to amphiphilic MNPs is the preparation of Janus MNPs, nanoparticles that possess two different chemical functionalities at each hemisphere, such as one hydrophobic and one hydrophilic side [21], or the coating with amphiphilic polymers [22]. Alternatively, less amphiphilic MNPs have been co-deposited with an amphiphilic reagent (surfactant), which certainly is the most straightforward approach and avoids complex synthetic pathways [23]. Clearly, many properties of the MNPs important to the formation of L- and LB-films are controlled by their protective coating, which is why we structured the following part of individual contributions based on the types of coatings, with the exception of the part on magnetic MNPs.

Before we begin with the discussion of individual papers we should provide some general information on the processing of MNPs by the LB method and guidance on how to interpret published results. We start with typical conditions for the processing of L-films and LB-films. Most common spreading solvents are chloroform and toluene but limited solubility especially of charged MNPs required the use of solvent mixtures such as dimethyl sulfoxide (DMSO) and chloroform. Concentrations of the MNPs in the spreading solvent are rarely provided because their low solubility usually requires 1–5 mL of saturated solution. These large volumes must be carefully and dropwise added at different locations of the liquid subphase to avoid early formation of three-dimensional aggregates. MNPs much larger than 20 nm in diameter are usually not sufficiently soluble and are spread as dispersions after extensive sonication. The most common subphase still is ultrapure water but especially hydrophobic MNPs have been reported to spread better on ethylene glycol and diethylene glycol [24].

A common problem with MNPs is their strong propensity for self-aggregation into islands of solid domains or even three-dimensional aggregates. This may be circumvented by a careful spreading procedure and fast enough compression of the L-film. Typical reported compression rates are between 5 and 15 cm^2/min and maximum surface pressures before buckling of the L-film occurs are 10–15 mN/m. However, much higher collapse pressures of 30 mN/m and larger have also been reported. Defects in the rigid monolayers may be improved by compression-expansion cycles if the compression is at least partially reversible [25]. Both, the collapse pressure and the packing order of MNPs in the L-film critically depend on the purity of the MNPs and their size distribution, which complicates the comparison of results obtained by different groups. Especially the presence of excess protective ligand or polymer is often not carefully evaluated and may be the main reason for a less ordered packing. We also note that the evaluation of the phase behaviour in L-films solely based on pressure-area isotherms can be rather misleading. Studies of the phase behaviour must be accompanied at least by Brewster angle microscopy while the analysis of transferred LB films may not provide reliable information on the structure of the preceding L-film, especially if transferred at low surface pressures.

Transfer of L-films onto hydrophilic and hydrophobic substrates is usually achieved by vertical up-stroke (LB-technique) or horizontal lift-up (Langmuir-Schäfer technique) at speeds of 0.1–1.0 mm/min. In some studies the up-stroke angle was altered to values of around 105° to minimize film ruptures or the L-film was lowered onto a submerged substrate by removing a part of the liquid subphase [19]. Transferred (LB) films are typically studied by tunneling and scanning electron microscopy (TEM) (SEM), atomic force microscopy (AFM), and grazing-incidence small angle X-ray scattering (GIXD). We note that only the latter technique provides reliable information on the long-range order of close-packed arrangements of MNPs.

Most common applications of LB-films of MNPs are photonic devices [26, 27] and substrates for surface enhanced resonance measurements [28–31]. One advantage of the LB method is that the electronic and magnetic interactions between MNPs can be altered by varying the average interparticle distances through variation of the surface pressure. Also tested has been the incorporation into bulk-heterojunction polymer solar cells [32], sensors for mercury detection [33] and organic acids and phenols [34], and catalysts for CO oxidation [35, 36].

8.2.2 LB-Films of MNPs Protected by Alkylamine and Alkylthiolate Ligands

MNPs, especially gold NPs, protected by a self-assembled monolayer of alkylthiolates or alkylamines have been most widely studied because of their relatively straightforward synthesis. With increasing length of the ligand's alkyl chains, these MNPs become increasingly hydrophobic since the partially charged surface of the metal core is better shielded from the outer surface of the MNP by longer alkyl groups. Still, even the most hydrophobic MNPs may form reasonably stable L- and LB-films if their size distribution is sufficiently narrow and their protective layer is adequately stable. However, the collapse pressures of their L-films were often small with values between 5 mN/m for weakly attached laurylamine ligands [23] and 15 mN/m for dodecanethiolate [37] on gold NPs. A change from dodecanethiolate to pentanethiolate protective ligands resulted in the expected decrease in surface area per NP from 11 to 6 nm^2 and a shorter distance between gold cores as confirmed by GIXD studies. Unexpected was the twice as high collapse pressure (30 mN/m) of the pentanethiolate protected gold NPs when compared to the dodecanethiolate protected NPs because ligands with longer alkyl chains generally provide a higher stability to the NPs. However, compressed monolayers of both gold NPs displayed the expected hexagonally close-packed arrangement at the air-water interface.

Similar values were reported by Medina-Plaza et al., Chen et al., and James et al. Medina-Plaza et al. generated LB monolayers of dodecanethiolate protected gold NPs on ITO electrodes for applications in electrochemical sensing [34]. They reported the formation and successful transfer of L-films of mostly hexagonally

close-packed gold NPs at a surface pressure of 10 mN/m and a surface area per MNP of 30 nm^2 for NPs with a diameter of 4.9 ± 0.5 nm. However, the L- and LB-films consist of small domain structures with no long-range order and frequent defect sites. Chen et al. deposited LB monolayers of dodecanethiolate protected gold NPs on ITO electrodes to enhance the efficiency of photovoltaic devices [32]. They reported similar optimum surface pressures of about 10 mN/m for the transfer of close-packed L-films of gold NPs of core diameters 3, 6, 10, and 16 nm. However, TEM images revealed many more defects, especially empty areas, for the LB films of the larger gold NPs (10 and 16 nm) than for the smaller MNPs. The authors also observed the often reported self-aggregation and island formation at low surface pressures.

James et al. utilized commercially available 4-*tert*-butylthiophenol protected gold NPs of 4.3 nm diameter with a standard deviation of 2.5 nm for the preparation of L- and LB-monolayers on quartz [33]. Close-packed films were obtained at a surface pressure of 15 mN/m while films with larger interparticle spacing were generated at a lower surface pressure of 8 mN/m. The less densely packed films were less sensitive for mercury vapour measurements by about 50 % but provided a faster mass flux of mercury. The authors also tested the heat stability of the films for thermal recovery and observed coalescence of gold NPs at 513 K to MNPs of about 8 nm diameter.

Changes in collapse pressure as observed for dodecanethiolate and pentanethiolate protected gold NPs may be caused by differences in size distributions but different degrees of crystallinity of the alkyl chains will also contribute to the observed differences. Thiolate ligands with alkyl chains of 12 or more carbon atoms usually generate crystalline domains of alkyl groups while shorter alkyl chains do not. So, alkylthiolate protected MNPs with shorter alkyl chains may be "softer" than those with longer alkyl chains, which is counterintuitive at first glance. In fact, a recent study on the chain length dependence of collapse pressures of alkylthiolate protected gold NPs confirmed increases in collapse pressure of more than 30 mN/m for the NPs with longer alkyl chains (Fig. 8.2) [38]. The authors could show that this is mainly an effect of the order-to-disorder (melting) transition of the alkyl chains. Alkyl chains with even numbered carbons of 14 or more are crystalline and generate L-films of much higher collapse pressure if the L-film studies are conducted at 22 °C.

Matsumoto et al. performed LB studies on almost monodisperse Au_{147} and Au_{55} NPs with hexylthiolate (NP diameter = 3 nm and core diameter = 1.8 nm) and octadecylthiolate ligands (NP diameter = 5 nm and core diameter = 1.3 nm), respectively [39]. Both gold NPs formed L-films that could be transferred onto TiO_2 (110) surfaces at surface pressures of 10 and 3 mN/m. TEM analysis of the films obtained at 10 mN/m revealed an ordered hexagonal packing over distances larger than 1 µm and interparticle distances in agreement with the sizes of the MNPs (Fig. 8.3a). However, investigations by scanning transmission microscopy (STM) clearly demonstrated the labile character of these films as NPs were moved and removed by the STM tip (Fig. 8.3b, c). The low density films transferred at 3 mN/m

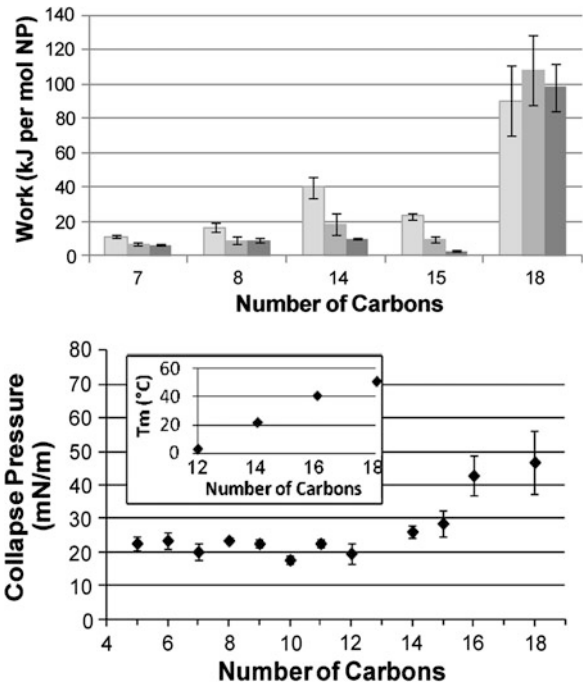

Fig. 8.2 *Top graph* Work required to collapse a monolayer of gold NPs protected by alkanethiols of different length at 13 °C (*left bar*), 22 °C (*centre bar*), and 40 °C (*right bar*). *Bottom graph* Collapse pressures of monolayers of gold NPs protected by alkanethiols of different length. Reprinted (adapted) with permission from [38]. Copyright 2012 American Chemical Society

were even more loosely packed and could not be studied by TEM and STM because of the high mobility of gold NPs on the surface.

In an early LB study, Heath et al. reported the formation of long-range hexagonally close-packed two-dimensional layers for alkylthiolate protected gold and silver NPs that have the right combination of core size and alkyl chain length if the size distribution is sufficiently small [40]. They proposed that the assembly of MNPs strongly depends on the amount of excess (conical) volume (V_e) available to the passivating ligands. For $V_e > 0.35$ nm^3, large interpenetration of the alkyl chains of adjacent particles generates extended one-dimensional structures at low surface pressures and two-dimensional foam-like phases at high pressures. Attractive dispersion forces between metal cores dominate for $V_e < 0.35$ nm^3 but are sufficiently reversible to generate long-range hexagonally close-packed two-dimensional layers of MNPs for V_e values larger than 0.15 nm^3. V_e values below 0.15 nm^3 result in the often observed irreversible self-aggregation of MNPs.

Clearly, the behavior of MNPs protected with alkylamines and—thiolates in L- and LB-films is complex because it depends on many different parameters such as size, size distribution, linking group, length of alkyl chain, spreading solvent, pH and temperature of subphase, and the ligand to gold ratio. An exact comparison of results reported by different groups may be possible if only one parameter changes but the preparation of two identical batches of monolayer protected MNPs is already a challenge due to synthetic limitations. However, the reliable and

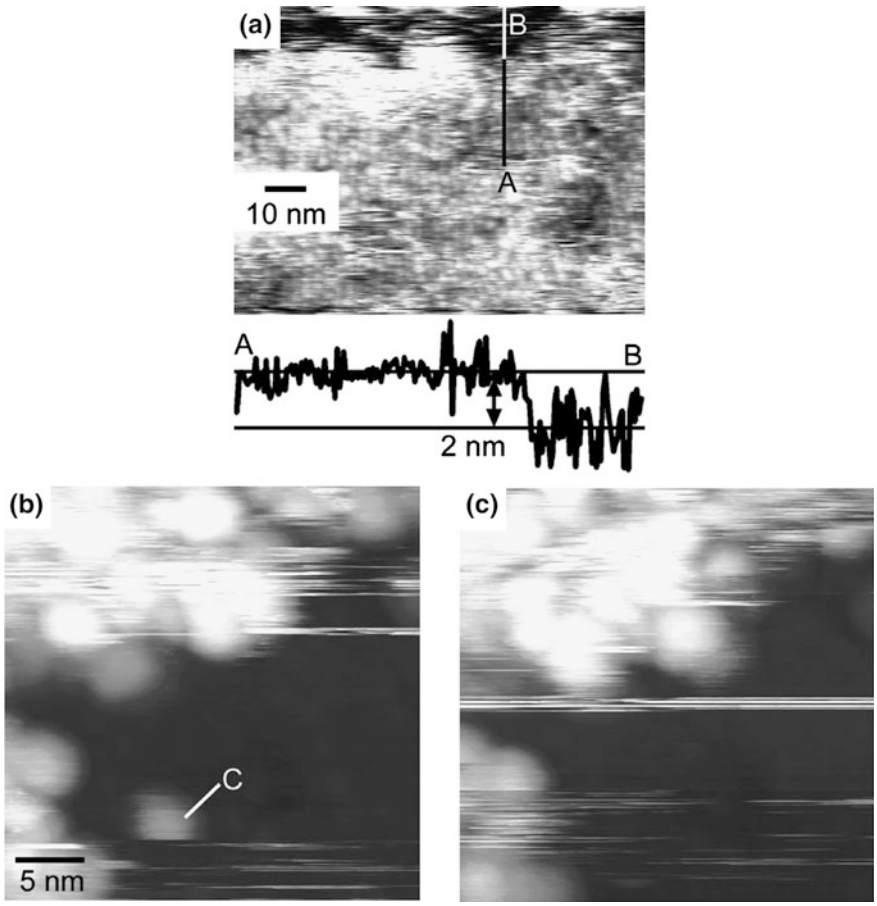

Fig. 8.3 **a** SEM image of hexagonal pattern of hexaylthiolate protected gold NPs on a TiO_2 (110) substrate. STM images of the same gold NPs on TiO_2 that reveal the removal of NP C in image (**b**) by the STM tip to give image (**c**) [39]. Reprinted from [39], Copyright 2007, with permission from Elsevier

reproducible preparation of layers consisting of hexagonally close-packed MNPs of long-range order, as required for many applications, does not seem to be feasible. A central problem is the self-aggregation of hydrophobic and most other MNPs at the air-water interface that generates floating islands of irreversibly associated MNPs. The glass-like rigid structure of these island phases prevent rearrangements of MNPs that are required for the formation of defect free films with long range packing order upon compression at the air-water interface. Many research groups chose the addition of a second spreading component, such as excess ligand, a surfactant, or just alkanes, as a versatile option to improve the interfacial properties of monolayer protected MNPs.

In a recent study, Gagnon et al. demonstrated that a simple addition of alkanes to gold NPs protected by tetradecylthiolate generates a liquid expanded phase of improved fluidity and reversibility as confirmed by compression–expansion hysteresis measurements [41]. The added alkane is assumed to be incorporated into the alkyl layer of the gold NPs to minimize the conical free volume of the ligand shell. This incorporation is reversible as the alkanes are assumed to be partially squeezed out upon compression. Particularly interesting is the reported dependence on temperature and length of the added alkane. In this study good mixing between the tetradecylthiolate protected gold NPs and an alkane only occurs at temperatures below the melting point of the alkyl chains attached to the MNP (order-to-disorder transition) and if the added alkane has at least the same number of carbon atoms as the alkyl group of the ligand. However, defect free films with long-range hexagonally close-packed order were not obtained and the addition of alkanes either lowered the collapse pressure or generated featureless pressure-area isotherms for all fluid liquid expanded films.

A unique approach to more stable L-films of alkylthiolate protected gold NPs was reported by Sanders et al. [42]. They added a solution of 1,12-dithioldodecane to L-films of alkylthiolate protected gold NPs with alkyl chains ranging from 6 to 18 carbon atoms at a low surface pressure of 0.2 mN/m. Expectedly, the L-films of MNPs with alkyl chain lengths of 6–14 carbon atoms had collapse pressures of below 15 mN/m, were rather disordered, and difficult to transfer as intact films. Addition of 1,12-dithioldodecane increased collapse pressures to values above 20 mN/m (Fig. 8.4), generated larger areas of close-packed order, and allowed a transfer by the LB and Langmuir-Schäfer techniques. This change in properties was reasoned with an apparent cross-linking of the MNPs at the air-water interface. Other evidence of cross-linking was provided by TEM images that revealed membrane like properties of the L-films (Fig. 8.5). In contrast, collapse pressures of gold NPs protected by hexa- and octadecylthiolates were larger than 30 mN/m and decreased upon addition 1,12-dithioldodecane and so did the degree of order of their assembly. This is not surprising as the dithiolate is much shorter than the interparticle distance between these MNPs and probably also does not easily insert into the more crystalline ligand layer of hexa- and octadecylthiolates.

8.2.3 LB-Films of MNPs Containing Polar Ligands

Another and more widely approach to L- and LB-films with larger collapse pressures is the addition of surfactant molecules or ligands with polar terminal groups to hydrophobic alkylthiolate and alkylamine protected MNPs. Experimentally most straightforward is the co-deposition of hydrophobic MNPs protected by outer alkyl groups with an amphiphilic compound. Swami et al. showed that laurylamine protected gold NPs do not form stable L-films and are not amenable to transfer onto substrates [23]. Addition of water insoluble octadecanol to the spreading solution of laurylamine protected gold NPs significantly improved the amphiphilicity and

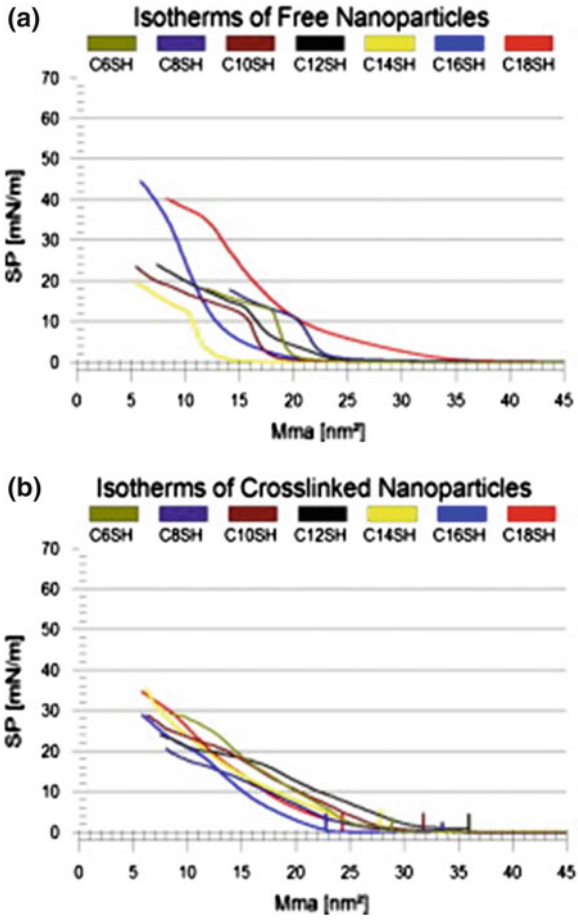

Fig. 8.4 Pressure-area isotherms of **a** free and **b** crosslinked gold NPs protected by alkylthiols of different length [42]. Reprinted from [42], Copyright 2014, with permission from Elsevier

stability of the L-film that could now be transferred onto substrates to form mono- and multi-layer LB-films. Unfortunately, large increases in surface pressure over time after spreading and surface areas per cluster that were four times the maximum estimated area indicated structural rearrangements of the MNPs. This assumption was corroborated by a comparison of TEM images of as prepared laurylamine protected gold NPs and after their deposition as LB monolayer that revealed an overall increase in size and in size distribution of the gold cores from initially 5 (±0.5) nm to 8–28 nm. Clearly, the weakly attached laurylamine ligands do not provide sufficient stability for LB studies and probably rearrange and exchange in the presence of octadecanol. The increased area per cluster are likely generated by areas just covered with octadecanol as the amount of octadecanol that inserts into the alkyl layer of the gold NPs is limited and will likely change with surface pressure.

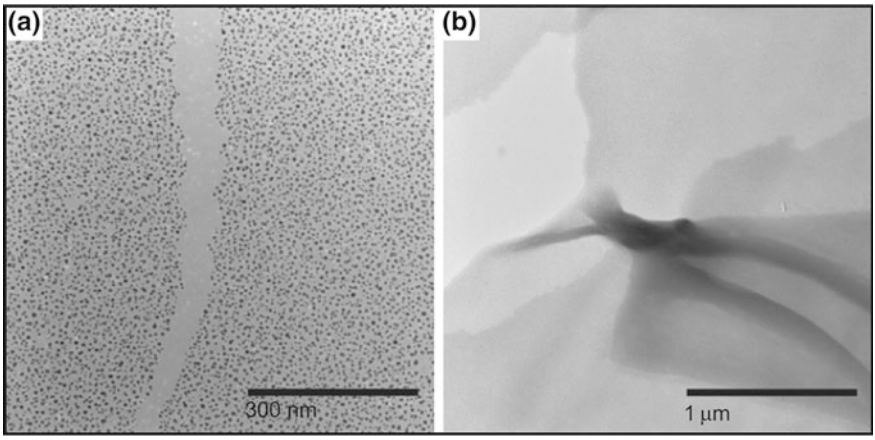

Fig. 8.5 High (**a**) and low (**b**) resolution TEM images of crosslinked hexanethiol protected gold NP that reveal uniform particle distribution, symmetric tears, and possible folding of the flexible film. Reprinted from [42], Copyright 2014, with permission from Elsevier

Bjørnholm and co-workers conducted a comparable study with more stable alkylthiolate protected gold NPs and, perhaps more importantly, they added the amphiphilic compound as a functionalized alkylthiolate to generate gold NPs with two different types of ligands (e.g. dodecanethiolate and 11-hydroxyundecanethiolate) [37]. The most important outcome of these studies is that the randomly attached thiolate ligands are sufficiently mobile to rearrange at the air-water interface. Amphiphilic Janus type gold NPs are generated since most of the ligands bearing terminal hydroxyl groups migrated so that they face the aqueous phase (Fig. 8.6). Expectedly, the collapse pressures of their L-films increased from 15 mN/m for just dodecanethiolate ligands to over 30 mN/m for a 5:1 mixture of dodecanethiolate and 11-hydroxyundecanethiolate. The authors also could show by GIXD studies that entirely hydrophobic gold NPs protected by a mixture of dodecanethiolate and pentanethiolate also respond to the interfacial conditions by generating more elongated NPs when compressed as L-film. The observed packing distances agree with an expulsion of the long-chain ligands from the plane of the monolayer as a response to the increased surface pressure. Similar rearrangements of ligands have also been observed in self-organizing MNPs discussed later.

Most widely applied has been the addition of amphiphilic molecules that likely add a second layer of ligands by interdigitation of the aliphatic chains. In the simplest case, it is the addition of excess ligand as recently reported by Lau et al. [43]. They prepared nearly monodisperse gold NPs of 8.0 nm core diameter that were protected by a monolayer of oleylamine. These NPs do not form defect free monolayers at the air-water interface because of their strong tendency to aggregate. Addition of an extra amount of oleylamine diminished self-aggregation so that L- and LB-films of long-range hexagonally close-packed order were obtained

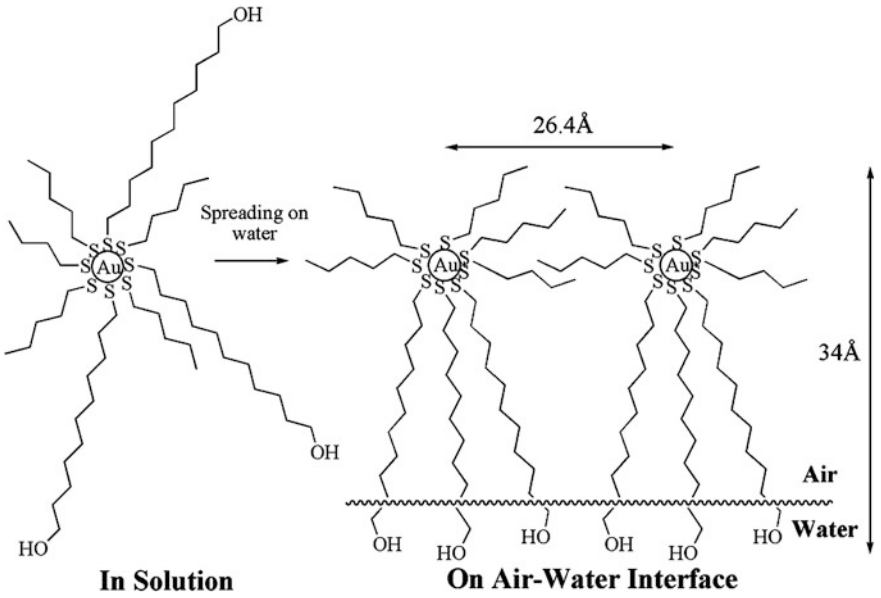

Fig. 8.6 Randomly attached alkylthiolate and 11-hydroxyundecanethiolate ligands rearrange on a gold NP surface to generate amphiphilic Janus-type NPs at the air-water interface. Reproduced from [37] with permission of The Royal Society of Chemistry

(Fig. 8.7). It is assumed that the extra amount of oleylamine attaches to the NPs so that their aliphatic chains mix (interdigitate), which generates amine and ammonium groups at the outer surface of the gold NPs. Amine groups provide a better interaction with the aqueous phase while ammonium groups prevent strong self-aggregation due to charge repulsion. Notably, the excess oleylamine may also be added to compressed L-films of oleylamine protected gold NPs that already contain multilayers and other defects to generate L-films of similar long-range hexagonally close-packed order described above (Fig. 8.8).

An elegant approach to the synthesis of surfactant protected silver NPs was presented by Lee et al. [44]. They reported the formation of stearate protected silver NPs by thermal decomposition of a multilayer film of silver stearate at 550 K. The obtained MNPs of 4 nm diameter readily form monolayer assemblies at the air-water interface with an astonishing collapse pressure of 59 mN/m, which is higher than for a monolayer of just stearate molecules. The high stability of the NP monolayer is reasoned with significant interdigitation between the alkyl chains of stearate ligands on adjacent silver NPs. Interdigitation between ligands was supported by interparticle distances of 3–3.5 nm measured by TEM, which was 0.5–1.0 nm smaller than the predicted diameter based on the length of stearate ligands (Fig. 8.9). Also successful was the transfer of these stearate protected silver NPs onto substrates by the LB technique.

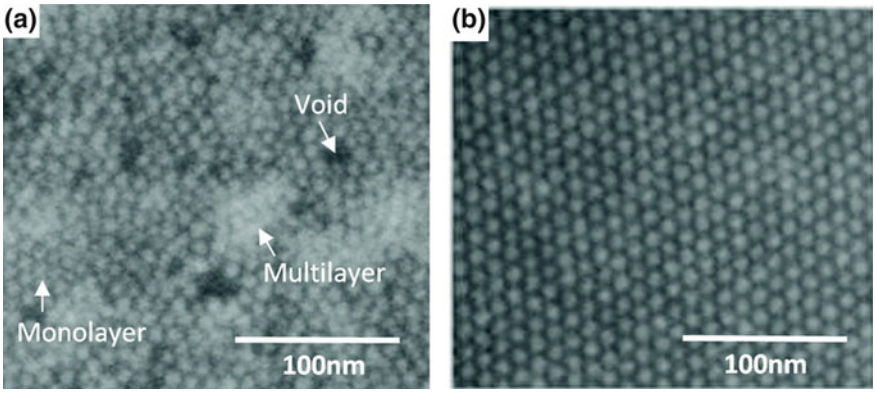

Fig. 8.7 SEM images of LB films of oleylamine protected gold NPs transferred onto silicon substrates without (**a**) and with excess oleylamine (**b**). Reprinted (adapted) with permission from [43]. Copyright 2012 American Chemical Society

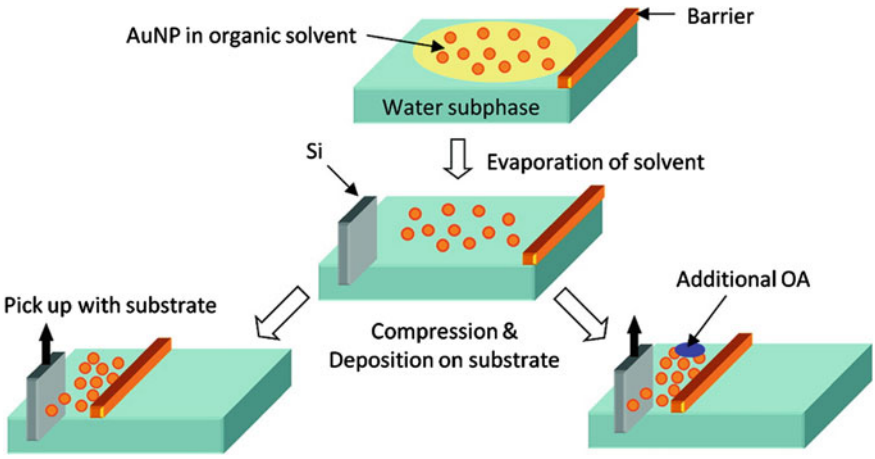

Fig. 8.8 LB assembly process of oleylamine protected gold NPs with and without addition of excess oleylamine (OA) [43]. Reprinted (adapted) with permission from [43]. Copyright 2012 American Chemical Society

Similarly, the addition of fatty acid ω-tricosenoic acid to mercaptoaniline protected palladium NPs significantly improved their interfacial properties [45]. L-films of the pure mercaptoaniline protected palladium NPs with a core diameter of 1.5–2.0 nm collapsed at surface pressures larger than 6 nm/m but assembled into a monolayer at very low pressure of 2 mN/m. Addition of ω-tricosenoic acid to the spreading solution increased the film's robustness to a surface pressure of 30 mN/m and these mixed L-films could be readily transferred by vertical dipping while the pure monolayer could only be transferred horizontally by trough draining.

Fig. 8.9 TEM image of stearate protected silver NPs obtained by thermal decomposition of a multilayer film of silver stearate at 550 K [44]. Springer and the original publisher/The European Physical Journal D-Atomic, Molecular, Optical and Plasma Physics, 16, 2001, 293–296, Phase Behavior of organic-inorganic crystal, S.J. Lee, S.W. Han, H.J. Choi, and K. Kim, Fig. 8.3, original copyright notice) with kind permission from Springer Science and Business Media

A comparison of the surface areas per entity of the pure components and the mixture as well as IR studies agree with a side-by-side arrangement of palladium NPs and ω-tricosenoic acid in the L- and LB-films and no significant H-bonding between the aniline and carboxylic acid groups.

8.2.4 LB-Films of MNPs Protected by Ionic Surfactants

Ionic surfactants have also been used as additives, which allows for a combined application of electrostatic assembly with the LB technique. In addition, these MNPs are more biocompatible especially if fatty acids and amines or other chargeable biomolecules are incorporated. Sastry et al. generated MNPs with an outer layer of carboxylic acid or amine groups by adding neutral fatty acid or amine molecules to alkylthiolate protected silver and gold NPs [9, 46]. At carefully controlled conditions interdigitation between aliphatic chains of the fatty acid or amine and the alkyl groups of the ligands results in the formation of a bilayer. This phenomenon appears to be unique to NPs as a similar bilayer formation is not observed for self-assembled monolayers of alkylthiolates on flat silver and gold surfaces, probably because of insufficient free volume. At pH = 9 a carboxylic acid terminated bilayer MNP is charged and dissolves in the aqueous subphase but

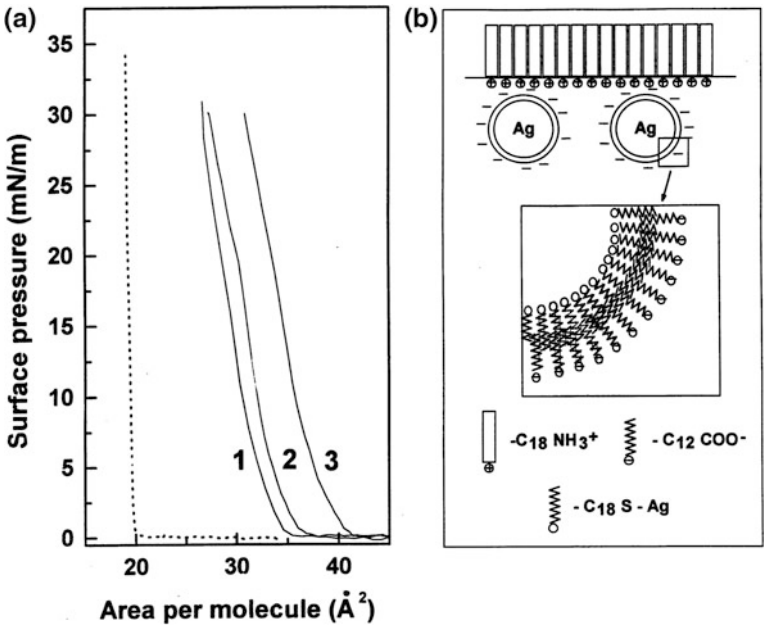

Fig. 8.10 **a** Pressure-area isotherms of octadecylamine before and after the exposure to lauric acid protected silver NPs dissolved in the aqueous subphase for 15 min (*Line 1*), 60 min (*Line 2*), and 120 min (*Line 3*). **b** Cartoons of the octadecylamine L-film after exposure to lauric acid protected silver NPs and the proposed interdigitated bilayer of lauric acid on the surface of the silver NPs [9]. Copyright 1998 American Chemical Society

attaches electrostatically to an oppositely charged L-film of fatty amines that are also charged at this pH (Fig. 8.10). Obviously, amine and acid groups may also be exchanged and oppositely charged MNPs may also be used for electrostatic assembly. Complex multilayers were generated at the air-water interface by alternating addition of oppositely charged species, including single-stranded DNA and other charged biomolecules, to the aqueous subphase. Transfer of these electrostatically assembled multilayer L-films onto substrates is possible but the authors also highlight other processing options based on thermally evaporated fatty lipid films. We note that these charged MNPs may also be processed by electrostatic layer-by-layer deposition without the help of the LB technique as described later.

Cationic monomeric and gemini imidazolium surfactants were studied as protective ligands for silver NPs by Datta et al. [47]. Since the NPs were synthesized in aqueous solution it is assumed that polar imidazolium groups point towards the silver surface and towards the water phase to generate bilayers around the NPs. This structure probably remains unchanged upon transfer into chloroform as spreading solvent. The spacer length between imidazolium units in the gemini structures proved to be an important parameter as it affects the shape of the formed silver NPs and the order of the aggregates generated at the air water interface (Fig. 8.11). All

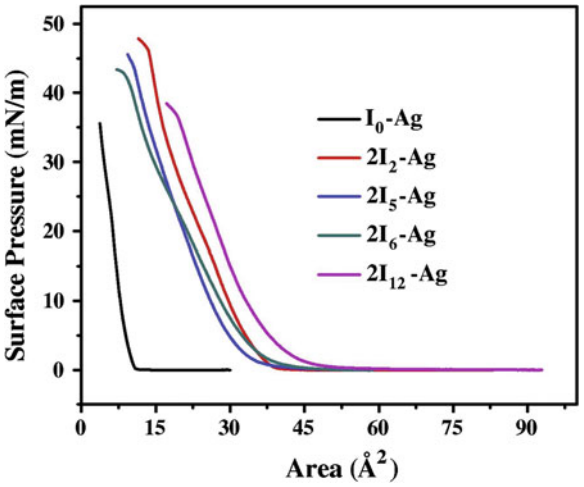

Fig. 8.11 Pressure-area isotherms for silver NPs protected with monomeric (I_0) and gemini imidazolium surfactants of varying spacer length (2–12 carbon atoms) at 28 °C. On average, an area of 40 ± 5 Å per silver NP protected by gemini surfactants is obtained for the extrapolated onset of surface pressure [47]. Reprinted from [47], Copyright 2014, with permission from Elsevier

silver NPs display the gas-analogous state at low pressures, the liquid-condensed phase at intermediate pressures, and a solid-analogous phase at high pressures, which is ideal for the formation of long-range ordered assemblies. However, especially silver NPs protected by gemini imidazolium surfactants with shorter spacers already self-aggregate at low surface pressures to generate islands of condensed phases of close-packed structures. AFM images of LB films confirmed the presence of islands and multilayer assemblies.

Charges may also be attached to MNPs via charged protective ligands. Sashuk et al. prepared gold and silver NPs that were protected by a mixture of two ligands [48]. One ligand was the hydrophobic 1-undecanethiol and the other ligand contained a charged or chargeable end group, such as 11-mercaptoundecyltrimethylammonium chloride and 11-mercaptoundecanoic acid. Attachment in solution should give a rather random distribution of the two ligands but the ligands are expected to rearrange at an air-water interface with the charged ligands facing the water surface. Similar rearrangements of polar and apolar thiolate ligands were reported by Bjørnholm and co-workers and described above [37]. To ensure insolubility in water not more than 15 % of the ligands per NP can be charged, which is sufficient to generate amphiphilic MNPs that form stable L- and LB-films (Fig. 8.12). Surprisingly, cationic MNPs with ammonium end groups gave higher ordered and more stable two-dimensional assemblies than anionic MNPs with carboxylic acid. For example, cationic MNPs withstood surface pressures of 40 mN/m whereas L-films of anionic MNPs already collapsed at 25 mN/m. This difference is explained with strong H-bonding between remaining carboxylic acid

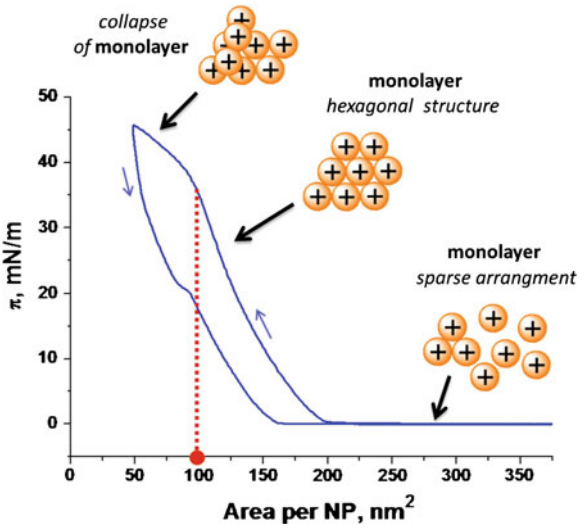

Fig. 8.12 Pressure-area isotherms on compression and expansion for positively charged MNPs with an onset of surface pressure at a surface area of about 200 nm^2/NP. The observed hysteresis is reasoned with a migration of MNPs into the aqueous phase [48]. Reprinted from [48], Copyright 2012, with permission from Elsevier

groups at the MNP's surface. However, long-range order of hexagonally close-packed NPs was neither achieved with cationic nor with anionic MNPs even though the former generated significantly larger defect-free domains.

8.2.5 L- and LB-Films of MNPs Protected by Polymers

Protection by MNPs by a polymer layer rather than ligand molecules usually increases the stability of the MNPs and their overall size because polymer layers tend to be thicker, denser, and less uniform than self-assembled monolayers of molecular ligands. A comparative study on gold NPs protected by a molecular surfactant oleylamine, which probably forms a partial bilayer, and poly(vinyl pyrrolidone) (PVP) was provided by Benkovičová et al. [49]. Unfortunately, the core sizes and size distributions of the two samples were significantly different with core diameters of 14.6 (±15) and 24.4 (±20) nm for oleylamine and PVP, respectively, although the thickness of the organic layer was almost identical with 0.7 and 0.8 nm, respectively. Nevertheless, both samples of gold NPs assembled into hexagonally close-packed arrays of relatively long-range order as LB-films on silica substrates and, more surprisingly, by drop casting onto silica substrates (Fig. 8.13). Clearly, the lower polydispersity of the oleylamine protected gold NPs is the main reason for the generation of more ordered self-assembled arrays. The authors do not mention any problems with self-aggregation of these comparatively large MNPs.

Polyvinylpyrrolidone was also used as protective layer for rhodium NPs (nanocrystals) by Zhang et al. [50]. L-films were deposited onto silicon wafers by the Langmuir-Schäffer method at different compression pressures. TEM analysis of

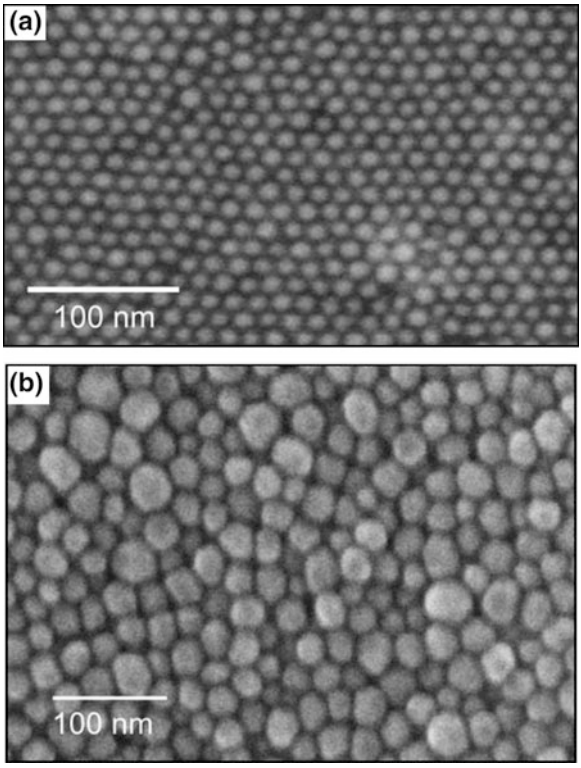

Fig. 8.13 SEM images of monolayers of gold NPs protected by oleylamine (**a**) and polyvinylpyrrolidone (**b**) obtained by drop casting onto silica substrates [49]. Springer and the original publisher, Chemical Papers, Preparation of sterically stabilized gold nanoparticles for plasmonic applications, 67, 2013, 1225–1230, Monika Benkovičová, Karol Végso, Peter Šiffalovič, Matej Jergel, Eva Majková, Štefan Luby, Alexander Šatka) with kind permission of Springer Science+Business Media

the monolayer LB-films revealed a constant increase in surface coverage with increasing surface pressure (11, 24, and 33 % at 4.4, 8.1, and 10.4 mN/m, respectively) in Fig. 8.14a. Buckling of the L-film to multilayers was observed at a surface pressure of 12.9 mN/m in Fig. 8.14b. However, smaller sized particles (6.5 and 8.3 nm in diameter) showed higher surface coverage than larger particles (13.5 nm) when compression pressures below 10 mN/m were applied, which was reasoned with a lower polydispersity of the smaller rhodium NPs. At surface pressures greater than 10 mN/m the samples showed large deviations in surface coverage (35–64 %) that are likely caused by the different geometric shapes of the formed rhodium nanocrystals. Interestingly, all tested LB-films showed catalytic activity for the hydrogenation of ethylene, which confirmed that active surface area was available on the rhodium NPs despite the polymer coating.

A rather unique approach was chosen by Genson et al. who attached an amphiphilic V-shaped polymer to gold NPs [51]. The structure of the attached ligand containing a hydrophobic polybutadiene chain and a hydrophilic poly(ethylene glycol) chain is given in Fig. 8.15a. These ligands were not attached by ligand

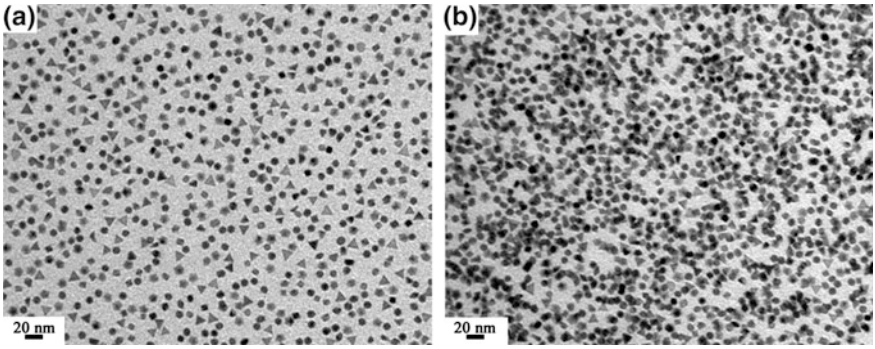

Fig. 8.14 TEM images of LB films of 8.3 nm Rh nanocrystals transferred at surface pressures of **a** 10.4 mN/m (monolayer) and **b** 12.9 mN/m (multilayer). Reprinted (adapted) with permission from [50]. Copyright 2007 American Chemical Society

exchange or during the formation of the MNPs but via an esterification of mercaptophenol protected gold NPs of 2 nm diameter to generate a dense organic layer. Due to their amphiphilic coating the MNPs spread well at the air-water interface with an onset of surface pressure at a surface area of 200–250 nm^2/MNP and a minimum area of 30 nm^2/MNP before collapse at a surface pressure of 18 mN/m. Compression was reversible and a condensed monolayer was obtained at a surface area per MNP of 140 nm^2. Comparison of the measured areas per MNP in the L-films and AFM studies on LB-films suggest a dissolution of most poly(ethylene glycol) chains in the aqueous subphase upon compression and a preferential arrangement of the polybutadiene chains at the air-water interface to generate MNPs of pancake-shape (Fig. 8.15b).

Tao et al. demonstrated that much larger MNPs can also be processed into LB-films of long-range order [52]. They prepared silver NPs (nanocrystals) of diameters of 100–250 nm and different polyhedral shapes that were protected by PVP. Transfer onto silicon wafers was accomplished at different surface pressures between 0 and 14 mN/m to change plasmonic properties by changing average interparticle distances from 40 nm to about 2 nm, respectively. Related work with PVP protected silver and gold NPs, nanocubes and nanocages, respectively, was reported by Mahmoud et al. [27]. Their MNPs were smaller in size with diameters of about 75 nm and surface pressure well above 30 mN/m could be reached before the L-films collapsed. However, LB-monolayers with uniform distribution of MNPs were obtained only at low particle density and with MNPs that contained only very small amounts of free PVP. Even smaller are the PVP protected platinum NPs reported by Song et al. with sizes of about 10 nm [26]. Samples with primary cubic, cuboctahedral, and octahedral shapes generated LB monolayers of similar order. However, surface pressures as low as 6 mN/m already generated LB-films with MNPs escaping into the third dimension.

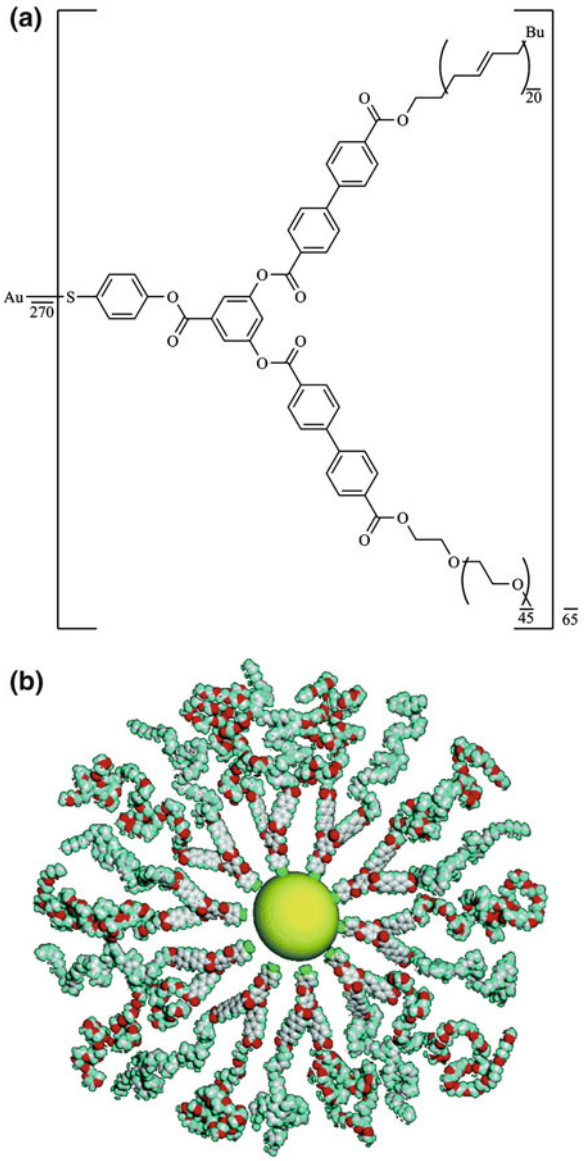

Fig. 8.15 **a** Chemical structure of a monomer unit of the V-shaped ligand $(PB\text{-}PEG)_n$ and **b** a simplistic molecular model of a gold NP coated with ten V-shaped ligands that have poly (ethylene glycol) chains in an amorphous state. Reprinted (adapted) with permission from [51]. Copyright 2006 American Chemical Society

8.2.6 L- and LB-Films of Magnetic MNPs

Many properties of magnetic MNPs also depend on their size, size distribution, and types of protective ligands as discussed above but we decided to grant them a separate part because of their unique magnetic interactions and properties. Magnetic dipole-dipole interactions may affect their assembly in L- and LB-films if the MNPs

have sufficiently large volumes and high magnetic moments. Magnetic dipolar interactions one order of magnitude stronger than the thermal energy of MNPs at room temperature have been reported as well as precipitation of 14 nm cobalt NPs due to too strong magnetic interactions. We refer to a recent review by Bellido et al. for more details on magnetic interactions and the processing of magnetic NPs in general [53]. Reviewed in the following are L- and LB-films of MNPs, not including metal oxide NPs, which reduces the number of examples to sufficiently air stable iron and cobalt containing NPs.

L- and LB-films of iron/platinum NPs have been reported by two groups. Wang et al. prepared iron/platinum NPs protected by oleic acid and oleylamine with a core diameter of 4 nm and a standard deviation of less than 10 % [54]. These mainly hydrophobic MNPs generated close-packed assemblies at the air-water interface and could be transferred onto substrates at surface pressures between 15 and 20 mN/m that equal a surface area per MNP of 60–70 nm^2. Unique of this study is the comparison of LB-film formation on substrates of different hydrophilicity according to surface contact angle measurements. Intact LB monolayers of close-packed MNPs were obtained only on substrates with contact angles of water larger than 65°, which is considered as the boundary between hydrophobic and hydrophilic behavior.

Less successful were Wen et al. with their attempt to generate LB films with 3–4 nm iron/platinum NPs protected by PVP [55]. Although pressure-area isotherms reveal high collapse pressures of larger than 50 mN/m for L-films of pure MNPs and their mixture with stearic acid, their transfer onto carbon-coated copper TEM grids generated discontinuous films with multilayer areas. We assume some of these feature are already present in the L-film and generated by the transfer process, which suggests the MNPs self-aggregate relatively strongly. This conclusion, however, is contrary to what the authors concluded.

Thorough LB studies with relatively air-stable cobalt NPs protected by tridodecylamine were presented by Johans et al. [19]. They illustrate the importance of Brewster Angle Microscopy measurements in conjunction with pressure-area isotherms to identify self-aggregation and island formation of the MNPs. Contrary to several reports on surfactant supported L-film formation discussed above, the authors concluded from careful comparative studies that the presence of excess tridodecylamine (cobalt NPs were not repeatedly washed to remove all excess tridodecylamine) does not aid the spreading of cobalt NPs but tridodecylamine competes for surface area and promotes self-aggregation that even led to the precipitation of aggregates of cobalt NPs from the interface. Most likely, the steric bulk of tridodecylamine makes it much less useful as amphiphilic additive when compared to conventional fatty acids and amines. Another interesting result is the observation that the MNPs spread much better and more reversibly on ethylene glycol than on water because of its lower polarity and surface tension. The authors also compared different spreading solvents (chloroform, toluene, and hexanes) that affected the types of self-aggregates that are formed (Fig. 8.16) but all these measures did not generate close-packed L-films that could be transferred onto substrates. The best quality L- and LB-films were obtained from mixtures of

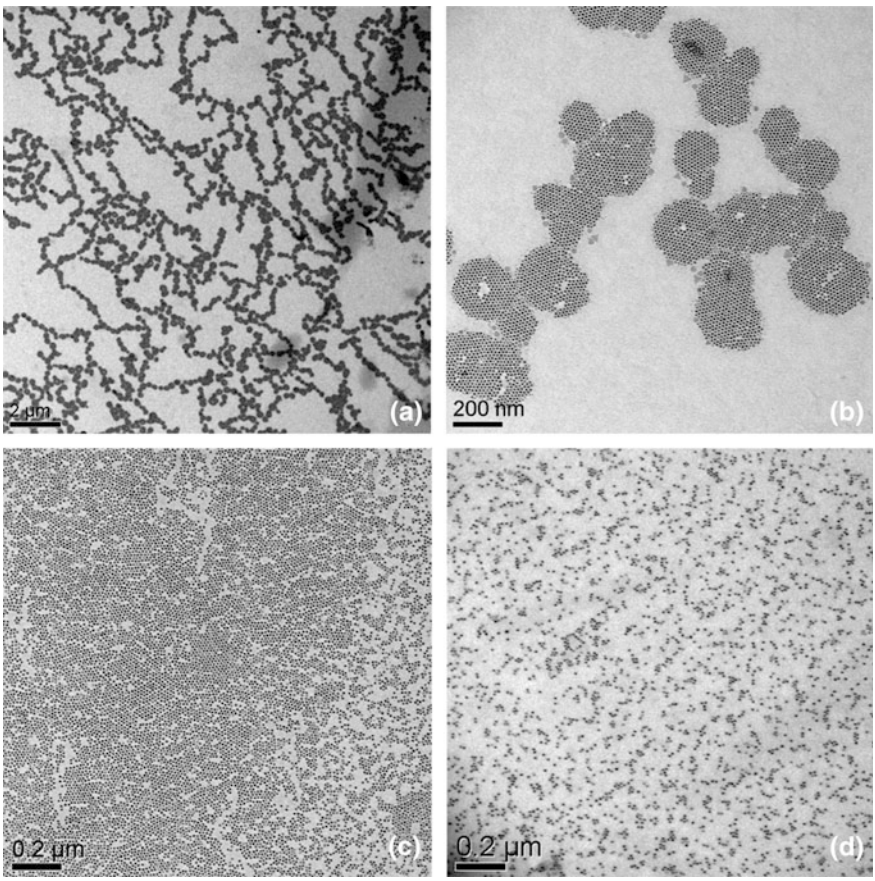

Fig. 8.16 TEM images of self-aggregated tridodecylamine protected cobalt NPs nanoparticles on ethylene glycol after evaporation of hexane (**a**, **b**) or toluene (**c**, **d**) solutions. Reprinted (adapted) with permission from [19]. Copyright 2010 American Chemical Society

tridodecylamine protected cobalt NPs with a block co-polymer PS-*b*-PEO on ethylene glycol as subphase. These films displayed superparamagnetic behavior at room temperature.

MNPs of cobalt alloys were studied in the groups of Singla [56] and Weller [24]. Singla and co-worker synthesized cobalt/nickel NPs of 8 nm diameter and reasonably small size distribution that were stabilized by PVP. Good quality L- and LB-films (up to six layers) were obtained when the spreading solution contained stearic acid and films were vertically transferred at a surface pressure of 30 mN/m and area per NP of 60–70 nm^2. AFM images of bilayers transferred onto glass slides are in agreement with a transfer of overall smooth, close-packed monolayers but some larger aggregates were also present. Weller and co-workers investigated 8 nm cobalt/platinum NPs of spherical and cubic shapes that were protected by

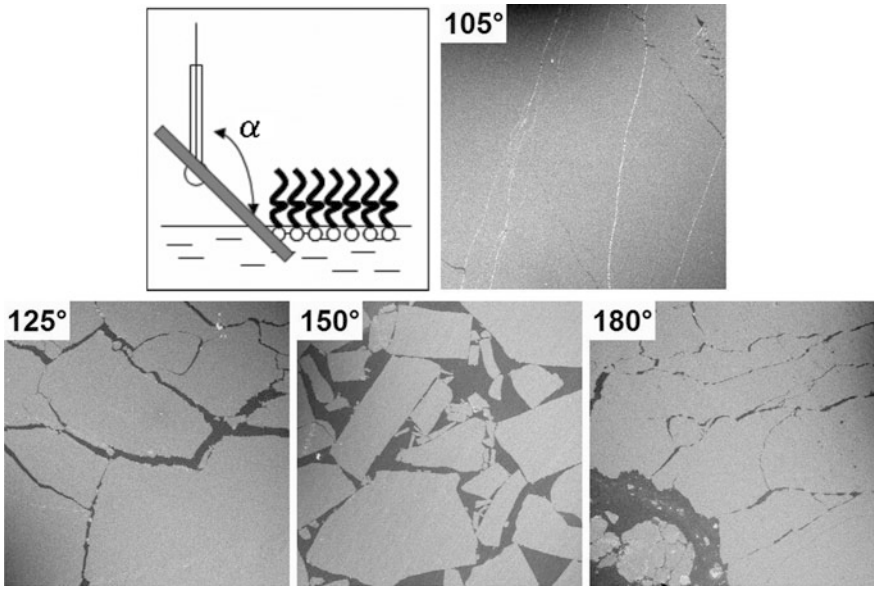

Fig. 8.17 SEM images of cobalt-platinum NPs monolayers transferred onto silicon wafers at various dipping angles. Light areas represent coverage by NPs while dark areas are uncovered by NPs. Reprinted (adapted) with permission from [24]. Copyright 2008 American Chemical Society

hexadecylamine. Essential for the formation of close-packed and relatively defect free L-films was a careful removal of excess hexadecylamine to avoid the formation of double layers of nanoparticles at domain boundaries and improve dispersion at the interface. The authors also demonstrated that good quality monolayers were formed on the less polar diethylene glycol but not on water as subphase, which seemed to be generally true for hydrophobic MNPs. The optimum surface pressure for transfer was determined to be 8 mN/m and a surface area per NP of 30 nm^2. Finally, they reduced the number of defects in transferred films by optimizing the dipping angle to 105°, in between vertical and horizontal transfer (Fig. 8.17).

8.2.7 LB Multilayers of MNPs

Most of the work presented above is focused on the preparation of monolayers whereas Kundu et al. presented some interesting results on the preparation of LB multilayers with dodecanethiol protected gold NPs of core diameters of 1.4 and 3.4 nm [57–59]. They succeeded in the formation of multilayers by sequential transfer of monolayer L-films onto H-terminated Si(001) substrates by vertical down-up cycles (LB method) at a surface pressure of 8 mN/m. To their surprise only odd numbered multilayers were generated, which they reasoned with a change

from Z-type to Y-type LB deposition after the first down-up cycle. In other words, no monolayer is deposited at the first down stroke but only at the first up-stroke. To reason this finding the authors hypothesized that the Si(001) substrate required some pre-wetting before deposition of gold NPs occurred.

Perhaps more surprising is that the authors apparently generated multilayer L-films by a simple increase in surface pressure beyond the collapse pressure of the monolayer. They reported the irreversible formation of bi-, tri-, and tetralayer films at surface pressures of 16, 21, and 25 mN/m, respectively. X-ray diffraction investigations of multilayer films transferred onto Si(001) substrates revealed some ordering of the MNPs and an unusually short interparticle distance between layers that suggested a strong interpenetration. However, the exact structures of the multilayer films remain unclear and, more importantly, are not stable over time. All multilayer films collapse over months into a monolayer of randomly assembled gold NPs of various but increased sizes [59]. Clearly, the close-packing of the gold NPs compromises their stability towards coalescence. The authors also show that the kinetic and mechanism of the collapse of the multilayer films depends on the chemical nature of the substrate surface by investigating the process not only on H-terminated Si(001) substrates but also Br- and HO-terminated Si(001) substrates [58].

8.3 Layer-by-Layer Deposition of Metal Nanoparticles

8.3.1 Introduction

Charged and uncharged MNPs may also be processed into thin films by a process called Layer-by-Layer (LbL) deposition that is somewhat related to the formation of LB-films but does not provide a direct control over the packing order and density within each layer. The method typically relies on electrostatic interactions between oppositely charged compounds, although examples that utilize H-bonding and other intermolecular forces have also been reported [60], and was initially developed for the LbL deposition of polyelectrolytes. However, many other molecular species have been incorporated into these multilayer films over the past two decades including charged MNPs and other colloidal particles [61–63]. In fact, the first reported electrostatic LbL deposition was actually utilizing colloidal particles and not polymers [64]. Charged MNPs are well suited for this technique because only a fraction of the attached charged groups can interact with the oppositely charged surface to leave a sufficient number of charges for the deposition of the next, oppositely charged layer. In other words, a non-stoichiometric excess of charged groups is deposited with each new layer relative to the preceding layer.

The generic process of LbL deposition is rather straightforward and illustrated in [65]: (a) A charged substrate is dipped into a solution containing oppositely charged material which will bind to the substrate. (b) The coated substrate is taken out of

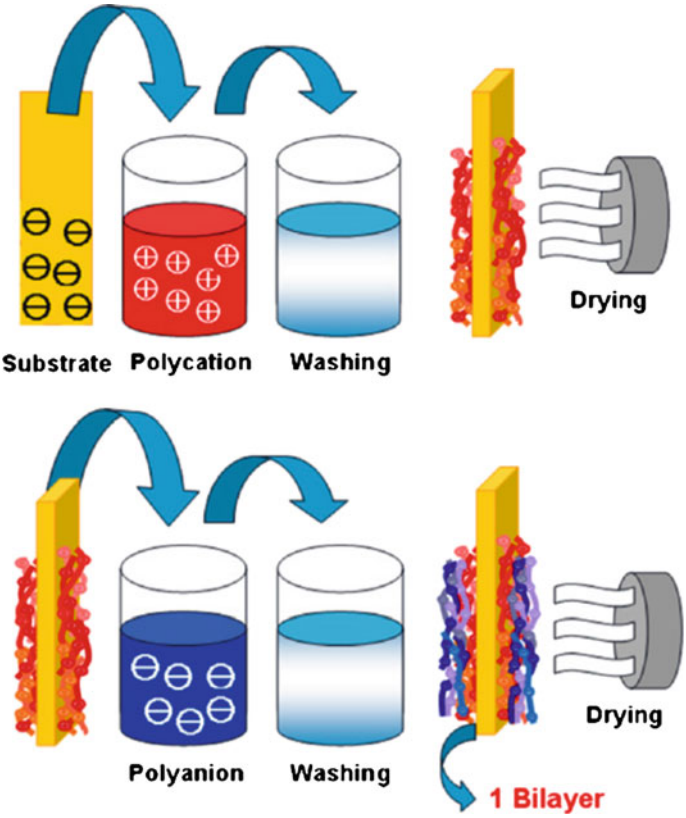

Scheme 8.1 Simplified cartoon of LbL assembly procedure driven by electrostatic attraction between adjacent films [65]. Reprinted from [65], Copyright 2010, with permission from Elsevier

solution and washed with solvent to remove excess material. (c) The substrate is then dried in air or a flow of inert gas to remove most solvent from the washing step. (d) The coated substrate is now immersed into a solution of an oppositely charged material to form the next layer on top. (e) The generated bilayer is again washed with solvent and dried before the process is repeated to build up multilayer films (Scheme 8.1).

One of the main attractions of the LbL method is its technical simplicity and applicability to many different types of surfaces but the apparent straightforward coating process may be deceptive since a range of different parameters must be taken into account to control the structural outcome. Important factors and properties that affect the structure of the formed LbL layer are the physical properties of the poly-charged species (e.g. elasticity and surface roughness), surface charge density, ionic strength and concentration of the solutions, the timeframe of adsorption, and the rinsing and drying process [66]. Each of these properties must

be optimized and accurately monitored to reproducibly generate the desired structure by LbL deposition.

Characterization of the generated LbL films depends on the same spectroscopic and diffraction methods as the characterization of LB-films. The lack of pressure-area isotherms and known exact amount of deposited compounds is often compensated for by quartz-crystal microbalance measurements.

8.3.2 LbL Deposition of Ionic MNPs

Ionic MNPs have been generated by the attachment of ionic ligand molecules, ionic dendrimers, and polyelectrolytes and have been deposited either as alternating layers of anionic and cationic MNPs or, more often, as alternating layers with oppositely charged polyelectrolytes. In all these cases electrostatic interactions dominate the LbL deposition and the structure of the resulting multilayer films depends on several processing parameters such as pH and ionic strength of the coating solutions and exposure time. However, highly ordered arrangements of MNPs, as achievable with the LB method, have rarely been generated by the LbL method. Also, in-plane packing distances between MNPs of the same charge remain low, surface coverage is often below 30 %, because of coulomb repulsion.

Most readily prepared charged gold NPs are citrate stabilized gold NPs in dilute aqueous solution but their application to the conventional LbL process is difficult because of their low stability. The electrostatic repulsion of citrate layers on the surface of gold NPs provides sufficient stability only at low concentration and ionic strength of the aqueous solution. However, Schmitt et al. successfully demonstrated their LbL deposition with the cationic polyelectrolyte poly(ally1 1-amine hydrochloride) to give surprisingly well ordered layers of MNPs [67]. The long term stability of these multilayer composite films remains questionable since citrate stabilized gold NPs likely coalesce over time in the given environment.

Abdelrahman et al. attempted to circumvent the problem of low stability by depositing layers of 1,4-benzenedimethanethiol in-between layers of citrate stabilized gold NPs [68, 69]. The thiols easily replace the citrate groups and generate a stable binding layer between each layer of gold NPs. Consequently, the process does not depend on electrostatic interactions but the formation of quasi covalent gold-sulfur bonds. However, the authors do observe growth of the gold NPs from 2.6 nm to 5–6 nm after the deposition despite the presence of dithiols. Clearly, the protection with citrate groups does not completely prevent coalescence of the gold NPs, which likely occurs before they are fully immobilized by the 1,4-benzenedimethanethiol linker molecules.

Bifunctional ligands with a thiol group at one end and a charged or chargeable group at the other end generate more stable charged MNPs. Hicks et al. reported the LbL deposition of hexanethiol/mercaptoundecanoic acid protected gold NPs with poly(allylamine hydrochloride) and hexanethiol/4-aminothiophenol protected gold NPs with poly(sodium 4-styrene sulfonate) [70]. They chose NPs with core

diameters of about 1.6 nm to match the thickness of each polymer layer but still observed multilayer deposition of gold NPs in one cycle, which they reasoned with entanglements between loose polymer chains and depositing gold NPs. Deposition kinetics were most drastically affected by changes in pH. This work was expanded by Song et al. who LbL deposited anionic gold NPs with a mixed monolayer of hexanethiol, ferrocenylhexanethiol, and mercaptoundecanoic acid alternating with poly(allyl 1-amine hydrochloride) [71]. Again, the adsorption density of the gold NPs in the multilayers greatly depended on pH and ionic strength of the polyelectrolyte solution. A pH of 5.8 was found to be optimal to ensure gold NPs and polyelectrolytes are sufficiently charged. Alternating LbL deposition of anionic hexanethiol/mercaptoundecanoic acid protected gold NPs with a cationic dendrimer instead of a polyelectrolyte also generated multilayers as demonstrated by Zhao et al. [72]. The methodology could be applied to gold NPs of smaller (3 nm) and larger (16 nm) core diameters and variations in ionic strength were used to alter interparticle distances.

Peter et al. attempted the LbL deposition of *N*,*N*,*N*-trimethyl-(11-mercaptoundecyl)ammonium chloride and mercaptoundecanoic acid protected gold NPs without the aid of polyelectrolytes or other mediating organic molecules [73]. Unfortunately, the oppositely charged gold NPs form clusters of sizes between 100 and 6000 MNPs instead of alternating monolayers. This result may not be particularly surprising considering the low density packing of the first layer of gold NPs on the substrate and the high affinity between oppositely charged MNPs. Cluster size distributions appeared to follow an exponentially decaying function, which may allow for a predictable nanostructuring of surfaces by this approach.

A more successful approach to the LbL deposition of oppositely charged MNPs was reported by Kawada et al. [74]. They coated silver NPs with polyethyleneimine and poly(sodium 4-styrenesulfonate) to give cationic and anionic MNPs of average diameters of 13.1 and 8.8 nm, respectively. Their alternating LbL deposition onto a supporting membrane of anodic aluminum oxide generated well-ordered layers of cationic and anionic MNPs that were tested as ultrafiltration membranes.

In general, protection of MNPs by polyelectrolytes generates more robust MNPs than a monolayer of protective organic ligands. For instance, gold NPs of a core diameter of 4.76 nm do not grow in size over a period of weeks if protected by poly (diallyldimethylammonium chloride) as confirmed by UV-vis spectroscopy [75]. LbL deposition of these gold NPs with an anionic polymer (s-119) produced stable multilayer films although the estimated layer thickness of 3.4 nm for each gold NP layer, determined by ellipsometry, is too small based on an overall NP diameter of >4.8 nm. This discrepancy may be reasoned with significant packing distances between gold NPs within each layer and interpenetrating layers.

Polymer coated MNPs may also be generated within a multilayer of cationic and anionic polyelectrolytes. A comparative study was provided by Rivero et al. who examined silver NPs capped with poly(acrylic acid, sodium salt) that were LbL deposited together with poly(allylamine hydrochloride) [76]. Alternating deposition of poly(acrylic acid) protected silver NPs with poly(allylamine hydrochloride) produced multilayers of distinct layer structure with progressive deposition of

MNPs, although the morphology of these multilayers may not be uniform. In contrast, silver NPs were formed only in the most outer layer when LbL deposited mulitlayers of poly(acrylic acid) and poly(allyl 1-amine hydrochloride) were first exposed to a solution of silver (I) ions and then to a solution of the reducing complex dimethylamine borane.

A major limitation of the use of charged MNPs for the formation of multilayer films by LbL deposition is the electrostatic repulsion between MNPs of the same charge because it causes a large spacing between MNPs and, consequently, a low surface coverage (<30 %). Cho and co-workers developed a methodology that incorporates initially hydrophobic MNPs into ionic or strongly polar multilayer films which they termed amphiphilic LbL assembly [77, 78]. They alternately deposit a poly(amidoamine) dendrimer or poly(ethylene imine) and silver or gold NPs protected by a hydrophobic, weakly binding ligand such as palmitic acid or tetraoctylammonium bromide. At the interface the hydrophobic ligands are partially replaced by the more strongly binding hydrophilic dendrimer or polymer and mostly replaced after the deposition of the next layer of hydrophilic dendrimer or polymer (Fig. 8.18). The group achieved in plane packing densities of MNPs up to 77 % and always above 50 %. If polyelectrolytes are used, such as poly(4-sodium, styrenesulfonic acid), the packing density of the initially hydrophobic MNPs could be increased by up to 20 % by an increase in ionic strength. For example, increase

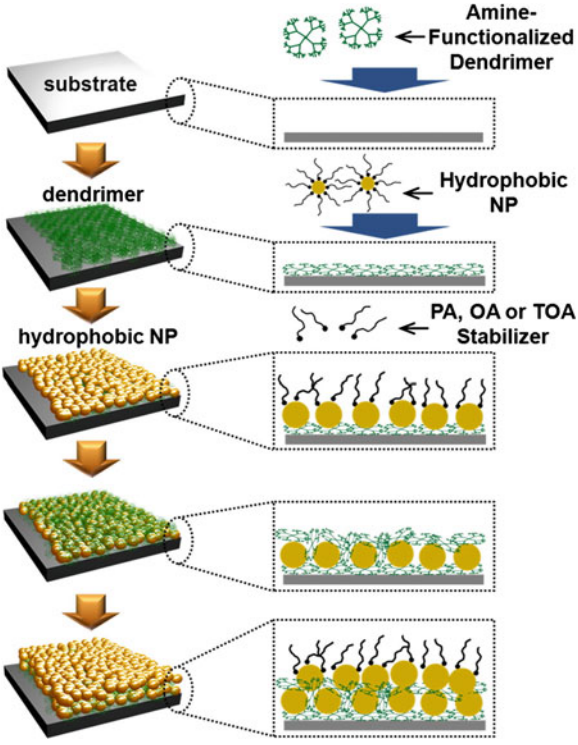

Fig. 8.18 Schematic diagram showing the preparation of $(dendrimer)_n$ multilayer films by LbL assembly of hydrophobic MNPs and hydrophilic dendrimer in organic media. Reprinted (adapted) with permission from [77]. Copyright 2013 American Chemical Society

of the concentration of NaCl in the coating solution increased the amount of deposited MNPs and poly(4-sodium, styrenesulfonic acid) until a concentration of 0.2 M was reached. The authors also demonstrated the general applicability of this procedure by processing other NPs such as metal oxides Fe_3O_4, TiO_2, and MnO.

8.3.3 LbL Deposition of Neutral MNPs Based on H- and Covalent Bonds as Well as Other Non-ionic Interactions

LbL deposition is also possible with non-ionic dendrimers based on poly(amido-amine) or poly(propylene imine) if functionalized with exo-amino groups for better attachment to gold NPs [79]. Dendrimers that attach to gold NPs with multiple amine groups were found to even replace alkanethiol ligands that individually bind stronger to the gold surface but the authors used dodecylamine protected gold NPs in this study. The conformational flexibility of these dendrimers also allows them to closer pack to the metal surface and more effectively fill spaces between MNPs. Binding between different layers is mainly facilitated by H-bonding between amine groups not involved in the binding to the gold surface and by van der Waals interactions. The overall morphology of these films is porous grainy due to deposition of spherical dendrimers with spherical MNPs.

Finally, LbL deposition may be achieved by covalently linking MNPs via bifunctional linker molecules or chemical reactions between two functional groups. Bifunctional linkers that have been applied to link NPs together contain thiol, amine, siloxane, alcohol, and isocyanide functional groups [80–82]. An early work by Brust et al. demonstrated the use of nonane-1,9-dithiol to LbL assemble gold NPs and CdSe particles [83]. Musick et al. used 2-mercaptoethanol as cross-linker between gold NPs to generate multilayer films but the morphology of the films is porous and no close-packing of gold NPs is observed [80].

However, 2-mercaptoethanol as spacer does not provide sufficient distance between gold NPs and coalescence of the gold cores is observed over time. A study by Supriya et al. demonstrates how the thermal stability of cross-linked gold NP films increases with increasing spacer length by comparing 2-mercaptoethanol, 1,6-hexanedithiol, and 1,10-decanedithiol [84]. In this study, coalescence of gold NPs was desired because conductive pathways are generated and was promoted by heat treatments at different temperatures and for different periods of time. The initial resistance of the films, for example, increased from 50 Ω to 1 MΩ and to >100 MΩ with increasing spacer length of the three different linker molecules.

Instead of using linker molecules with two terminal linking groups it is also possible to generate new chemical bonds between two protective ligands. An interesting example is the preparation of gold NPs that are coated with *O*-carboxymethyl chitosan and cross-linked in the multilayer by exposure to glutaraldehyde [85]. The chitosan polymer is assumed to coordinate to the gold NPs

predominantly through their carboxylic acid groups, which leaves the amine groups available for reactions with the dialdehyde cross-linker to generate diimines. Li et al. chose a different approach by LbL depositing polyphenylene dendrimer-stabilized gold nanoparticles with alkynes in their peripheries with a functional polymer that contains peripheral azide groups for "click" chemistry [86].

8.4 Self-organizing Metal Nanoparticles

Self-organization probably is the most powerful method at hands for the controlled three-dimensional nano-structuring of materials over macroscopic length scales, which is mainly aided by the cooperative behaviour between individual self-organizing units (usually molecules). Self-organization also is the central process underlying successful technologies such as liquid crystal displays. It is an intrinsically three-dimensional process, similar to crystallization, but can generate structures of various degrees of order and mobility. Equally important for its remarkable ability to nano-structure materials and to its technological success, however, its cooperative response to relatively weak external directional forces, such as electric and magnetic fields and surface alignment layers, that generate domains of uniform orientation and structure over centimeter length scales [87].

Phases formed by self-organizing compounds are named mesophases because their degree of order is in-between that of an isotropic liquid and a single crystal. Mesophases, by definition, are thermodynamically stable and mostly anisotropic phases, in contrast to kinetically trapped phases of similar structures. Bulk materials form mesophases by change of temperature (thermotropic mesophases) whereas the mesomorphism of solutions (lyotropic mesophases) depends on concentration and temperature. Thermotropic mesophases are subdivided based on their molecular (shape anisotropy) and supramolecular structures. Rod-shaped (calamitic) molecules form nematic phases, which display solely orientational order, and smectic phases that display orientational and one-dimensional positional order. However, smectic phases with higher positional order are also known. Disc-shaped (discotic) and wedge-shaped molecules preferentially self-organize into columnar mesophases of orientational and two-dimensional positional order but nematic phases with just orientational order have also been observed (discotic nematic), although they remain rare. Spherical and cone-shaped molecules usually arrange into cubic structures that are characterized by positional order and a lack of orientational order.

Early designs of compounds that self-organize into mesophases were mainly based on the shape anisotropy of rod-like molecules, which is sufficient for the introduction of anisotropy due to orientational order (nematic mesophases). Subsequently, microphase segregation and directed molecular interactions were added as design tools that gave access to layered (smectic) mesophases of rod-shaped molecules that may display positional order from one-dimension to quasi three-dimensions. After about 90 years of research on rod-shaped mesogens, disc-shaped structures were added to the tool kit in the 1970s as a new type of shape-

anisotropy. Concepts of self-organization and mesomorphism have seen a significant extension well beyond the classical structural motifs described above over the past 20 years. Judicious application of shape anisotropy, microphase segregation, directed molecular interactions, and self-assembly has converted molecules with low or unfavorable aspect ratios, including ionic molecules, into compounds that display mesophases over a wide range of temperatures. These new developments made it conceivable to convert quasi spherical nanoparticles into self-organizing structures, similar to what has been demonstrated for C_{60} [88, 89].

Most of the reported work on self-organizing MNPs has been concerned with gold NPs, although the first studies on self-organizing MNPs involved metal oxide NPs. A rather comprehensive review of all reported self-organizing MNPs was provided by Nealon et al. [90] while a more general overview of NPs in self-organizing materials was provided by Bisoyi and Kumar [91]. The following part will be mainly concerned with MNPs that self-organize into thermotropic mesophases but we note that micellar [92] and lyotropic [93] NPs have also been reported. Similarly, self-organizing materials that are generated by doping NPs into self-organizing compounds, usually liquid crystals, are not covered here [94, 95]. Finally, self-organizing rod-shaped and other metal nanoparticles of anisotropic shape are omitted because they have been discussed in the previous chapter.

The prominent role of gold NPs for the synthesis of self-organizing MNPs is easily explained by their well established and versatile coating with monolayers of organic molecules, mostly thiolates, and the relatively straightforward synthesis of gold NPs with small diameters between 1 and 5 nm [96]. They are either prepared directly in the presence of the final organic thiolate ligand (e.g. modified Brust–Schiffrin procedure [97, 98]) or by a two-step procedure in which the gold NPs are first synthesized in the presence of a weaker binding ligand (e.g. alkyl amine or thiolate with shorter alkyl chain) that is subsequently fully or partially exchanged by a stronger binding desired ligand via a solvent-mediated ligand exchange process [99]. Gold NPs prepared with weaker binding ligands usually display smaller size distributions but a complete removal of this ligand by exchange processes is often difficult. However, the presence of two different ligands appears to be advantages to the self-organization properties of MNPs because they can change the overall shape of MNPs and their interparticle interactions [100]. A similar response was observed for MNPs at interphases, e.g. when processed by the LB method, as described earlier in this chapter [37].

Regardless of the applied synthesis method, purification of the MNPs is a crucial and difficult step because of their high surface area and often overall amphiphilic character (charged metal surface partially covered with a monolayer of hydrophobic alkylthiolate ligands). Depending on the exact reaction conditions, excess of organic ligands, surfactant molecules, and side-products from the applied reducing agent must be removed, which is usually achieved by repetitive precipitation. However, particle sizes often increase with every precipitation step due to coalescence, which is an indication of the dynamic binding of thiolate ligands to gold NP surfaces and the incremental removal of soluble ligands with every precipitation step [17, 101]. Gold NPs with rather strongly bond thiolate ligands may also be

purified by gel-permeation chromatography [102]. Product purity and ligand ratios are usually determined by a combination of solution nuclear magnetic resonance (NMR) spectroscopy, thermal analysis (Differential scanning calorimetry (DSC) and thermogravimetric analysis (TGA)), elemental analysis, and TEM [103–105].

Mesomorphism of MNPs is investigated by three main methods, variable temperature polarized optical microscopy (POM), DSC, and variable temperature powder XRD. Most important for a structural analysis of mesophases of MNPs is powder XRD, ideally of aligned domains of the mesophases, although their interpretation may be complex because MNPs may adapt their shapes to the optimize packing within the geometrical restrictions of the displayed phase. The relatively small number of reflections makes an analytical solution of the XRD pattern impractical. Probably the most reliable approach to the analysis of these diffraction patterns is the comparison of simulated diffractions patterns based on calculated density distributions within simulated packing structures, which has been widely applied by Ungar and others.

Investigation of the mesomorphism of monolayer protected gold NPs is complicated mainly by the dynamic character of the organic layer, when compared to the self-organization of molecular structures. Thiolate ligands relatively easily move on the surface of gold NPs and also reversibly desorb and adsorb, especially at elevated temperatures [106, 107]. Consequently, the average diameter of the gold core may increase with time at temperatures above 100–150 °C due to coalescence of gold cores. Perhaps even more important is that the distribution of organic ligands on the surface of gold NPs changes depending on the environment. This can benefit the mesomorphism by rendering an isotorpic spherical structure to an anisotropic prolate spheroid (increase in shape anisotropy) [108] and similar structural changes of MNPs due to ligand mobility have been observed at interfaces as reported earlier in this chapter in the part on LB films [51].

The quasi spherical shape of MNPs with truncated octahedral or related metal structures would make them prime candidates for the formation of cubic mesophases but those are rarely observed in these materials. In fact, attachment of organic ligands that have no mesogenic structure, such as a simple alkylthiolates, has not generated self-organizing MNPs. A perhaps obvious remedy is the attachment of ligands that self-organize themselves (mesomorphic ligands) or have typical features of self-organizing compounds (mesogenic). This approach has broadly been applied not only to the conversion of MNPs into self-organizing compounds but also to generate MNPs that can be easily doped into liquid crystalline host materials [109]. Most of the attached mesomorphic and mesogenic ligands contain rod-shaped rigid structures and will be discussed first, while relatively few examples exist on ligands with disc-shaped rigid structures.

Although the number of self-organizing gold NPs is still limited, some general design criteria may be cautiously extracted from the studies that have been reported [90, 91]. All mesomorphic and mesogenic ligands that have been investigated have a flexible spacer between the rigid part and the linking group (usually thiolate) to the gold NP surface. Both length and structure of the spacer chain must ensure sufficient mobility for the rigid part to arrange (self-organize) into the most

favourable packing structure. A good source of guidance for the prediction of optimal spacer chains may be the large volume of work on liquid crystalline side-chain polymers. For most of the reported self-organizing MNPs the overall length of ligands is commensurate with the diameter of the MNP core, which limits the required size of the metal core to values well below 10 nm unless unusually large organic ligands are available. An increase in length (packing volume) of mesogenic ligands with regard to the metal core likely aids mesomorphism but may be synthetically challenging, while a significant decrease in length (packing volume) may not only compromise mesomorphism but also the stability of the MNPs. In addition to the average size of MNPs their size distribution also appears to be crucial. Experimental and theoretical studies suggest that an increase in size distribution diminishes the propensity for self-organization, similar to what has been observed for the self-assembly of MNPs.

8.4.1 LC MNPs with One Type of Ligand

Mesomorphic MNPs were first reported in 2001 by coating gold NPs with calamitic liquid crystals through thiolate linking groups. The rigid part of the ligands consisted of a (cyclohexyl)phenoxy group (Fig. 8.20) that provided sufficient shape anisotropy and microphase segregation for the formation of nematic and smectic mesophases. Attachment of these ligands to gold NPs of 3 nm core diameter generated mesomorphic MNPs that display mesophases at a wider temperature range than the free ligands but, unfortunately, the mesophase(s) were not investigated by XRD and their structure(s) remained unassigned [110] (Fig. 8.19).

Four years later a similar approach was reported that employed mesomorphic ligands with cyanobiphenyl as rigid parts (Fig. 8.20) [112]. Both, TEM and XRD data for the sample with dodecyl spacer chains and a gold core of 2.7 ± 0.5 nm diameter revealed a string-like arrangement of gold NPs in their mesophase with distances between strings of about 6 nm, an interparticle distance within each string of 2–3 nm, and an overall length of each string between 13 and 60 nm. These results provided the first evidence for an uneven distribution of mesomorphic ligands on the surface of gold NPs in an anisotropic mesophase. The observed distances agree with a packing model shown in Fig. 8.21 that proposes a preferential alignment of the ligands in-between strings to generate a likely partially interdigitated antiparallel double layer of cyanobiphenyl groups. However, the obtained data were still insufficient for an assignment of the type of mesophases but it likely is a nematic mesophases. The temperature range of 110–130 °C is significantly wider and higher in temperature than the free ligand, which forms a monotropic nematic mesophases between 75.9 and 71.7 °C. Corresponding gold NPs with shorter spacer chains given in Fig. 8.19 were studied much later and in more detail. The refined structural interpretation of the new data overall corroborated the initially proposed packing structures [108].

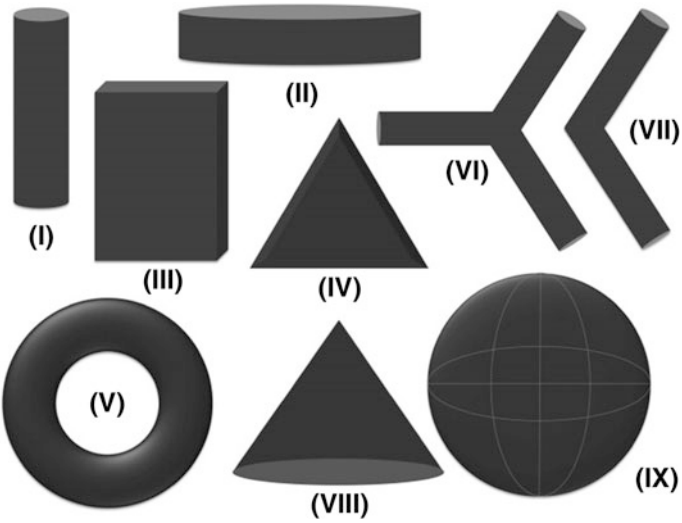

Fig. 8.19 Cartoons of shapes of molecular cores that have been successfully converted into liquid crystals: *I* calamitic; *II* discotic, *III* board-shaped, *IV* wedge-shaped, *V* ring-shaped, *VI* star-like, *VII* bent-rod, *VIII* conical, and *IX* spherical motifs. Reprinted from [111], with permission from Elsevier

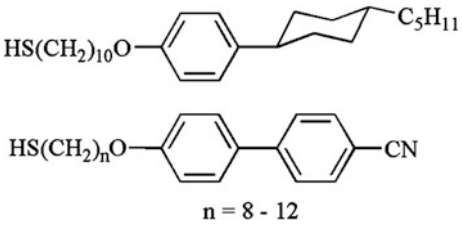

Fig. 8.20 Mesomorphic thiol ligands based on (cyclohexyl)phenoxy [110] and cyanobiphenyl rigid [112] parts that were used in early studies of mesomorphic gold NPs

However, the authors of the latter study presented a more sophisticated and general model that has been commonly accepted and applied in packing models for nematic, lamellar, and columnar mesophases (Fig. 8.22). They proposed the formation of hard pole areas with strong interactions between ligands and much less densely packed equator areas that results in a distortion from isotropic spheroidal to anisotropic prolate spheroidal structure. The described structural changes of the ligands are mainly based on conformational changes and require a relatively low density packing of ligands to provide sufficient space for these changes. Rearrangements of ligands, although possible, are likely not involved in this distortion of the ligand shell. MNPs that pack in local rectangular or hexagonal

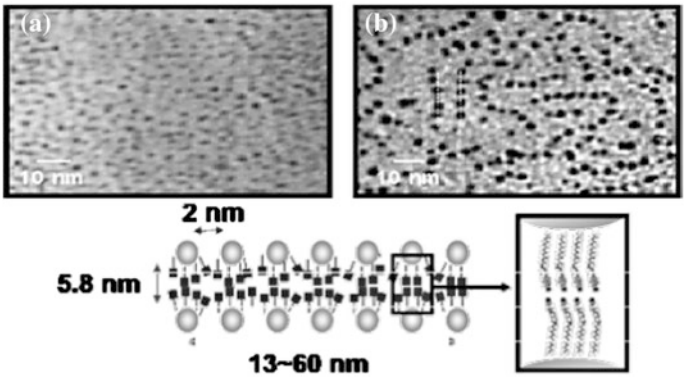

Fig. 8.21 TEM images of Au@6_{12} **a** before and **b** after thermal treatment. *Below* Proposed model of the nanoparticle arrangement within the strings. Reproduced by permission of The Royal Society of Chemistry. Shown to the right is a simplified illustration of a local rectangular arrangement of gold NPs in a mesophase. Reprinted with permission from [90]. Copyright 2012 Beilstein Institute

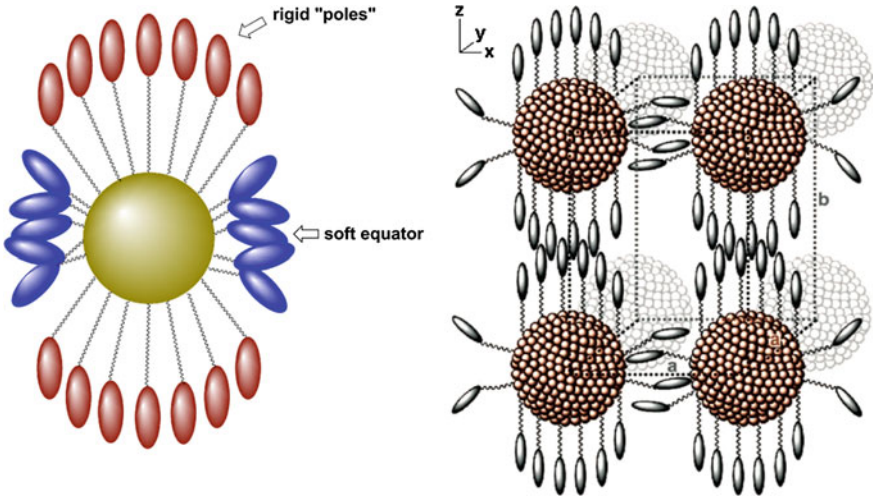

Fig. 8.22 Generation of rigid "poles" and soft equator areas by ligand deformation at the surface of gold NPs (*left*). Simplified illustration of a local rectangular arrangement of deformed gold NPs in a mesophase (*right*). Reprinted with permission from [90]. Copyright 2012 Beilstein Institute

structures display local A_2 order between the poles and local A_d order between the equators. These different environments may also explain why the observed XRD data suggest the coexistence of more than one packing structure.

8.4.2 LC MNPs with Two or More Types of Ligands

Overall, the attachment of just mesomorphic ligands appears to have serious limitations because attempts to generate mesomorphic gold NPs with more densely packing dendritic ligands and laterally attached rod-like ligands failed [113]. Much more versatile is the use of mixed ligands that is typically achieved by incomplete ligand exchange reactions of thiol ligands by other thiol ligands. Several comprehensive studies with alkylthiols as primary ligands that were partially exchanged by much larger mesomorphic ligands have been conducted by Mehl and Ungar and co-workers [114–116] and Gorecka and co-workers [117, 118]. It became apparent in all these studies that the ligands are not distributed evenly but the mesomorphic ligands form domains at the poles and the alkylthiols form domains at the equator to generate prolate spheroidal or even cylindrical shapes. In contrast to the previous examples of prolate spheroidal structures the mechanism is different here as it relies on the migration of ligands rather than conformational changes.

In addition to the application of mixed ligand layers both groups also employed more sophisticated mesomorphic ligands that display a range of nematic and smectic mesophases. Examples of ligands with terminal connections that were used by Gorecka and co-workers are given in Fig. 8.23. Typical ratios between primary alkylthiol ligands and mesomorphic ligands in molar ratios were 1:1–2:1 based on NMR studies but changes in ratios within this range had only minor effects on the mesomorphism. Variation of the chain lengths of the alkylthiols, on the other hand, had profound effects on the mesomorphism. For example, the increase from hexyl to octyl to dodecyl thiols changed the packing structures of the cylindrically shaped MNPs from smectic to modulated smectic to columnar as illustrated in Fig. 8.24. We note, however, that the organic domains in all of these materials appear to be in an amorphous state rather than any orientationally and/or positionally ordered state, which is consistent with the observed low birefringence.

The incorporation of ligands with two rigid parts (dimeric) was investigated in a recent publication by Gorecka and co-workers [119]. A comparison of the "dimeric ligands" with conventional "monomeric" ligands revealed distinct structural

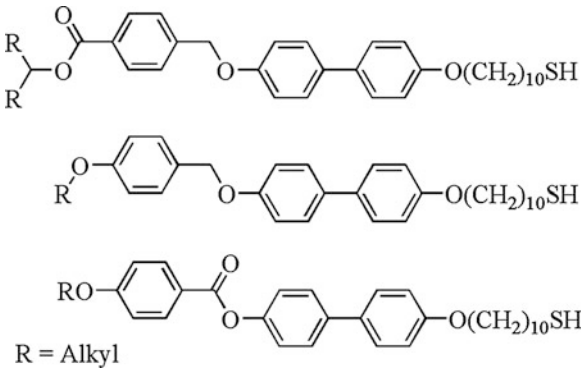

Fig. 8.23 Mesomorphic ligands for gold MNPs that display smectic and nematic polymorphism [117, 118]

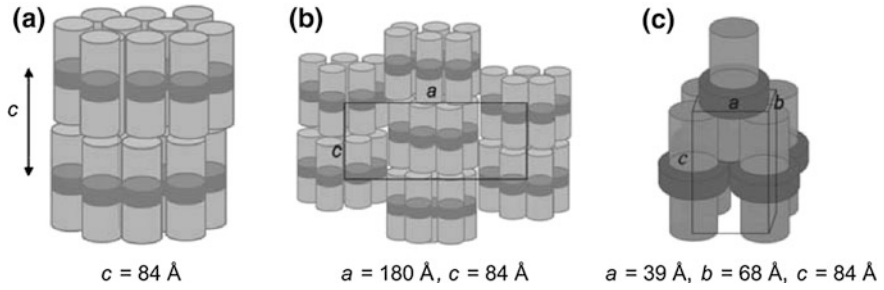

Fig. 8.24 Proposed structural models resulting from ligand migration at the NP surface: **a** smectic for hexyl thiol as primary ligand **b** modulated smectic for octyl thiol as primary ligand **c** columnar for dodecyl thiol as primary ligand, respectively. *Light grey* and *dark grey* indicate the disposition and form of the mesogenic groups and alkylthiols respectively. Reprinted with permission from [118]. Copyright 2010 Wiley-VCH Publishers

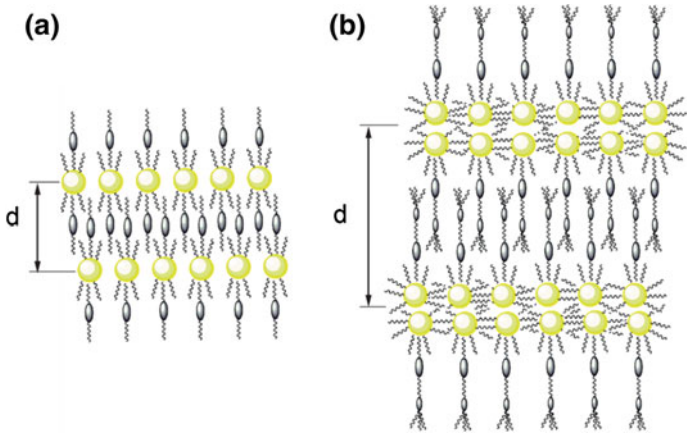

Fig. 8.25 Schematic drawing of the arrangement of the hybrid particles in a smectic phase for materials with **a** monomeric ligands (series AuL1) and **b** dimeric secondary ligands (series AuL2 and AuL3). For clarity of the picture only a limited number of molecules grafting the metallic clusters are shown. Reproduced from [119] with permission of The Royal Society of Chemistry

differences, most notably the formation of a bilayer of gold NPs in-between the organic layers of smectic mesophases (Fig. 8.25). Also important is the observation of orientational order in the organic layer that generates measurable birefringence. Another recent study clearly reveals the importance of the flexible spacer between the mesogenic unit and the MNP [7]. Longer spacers not only promote mesomorphism by lowering the melting temperatures of the MNPs but also affect what types of self-organized structures are formed. Observed here is the change from a 1D (lamellar) structure to 3D superlattices with base-centered

orthorhombic unit cells. Interestingly, the length of the alkylthiol has no effect on the formed structure.

Lateral attachment of mesomorphic ligands has been successfully demonstrated by Mehl and co-workers [114–116] and generates cylindrical MNP structures that preferentially arrange into columnar stacks. This seems to be a more general preference as it was also observed for related silsesquioxanes [120]. The rigid parts of the mesomorphic ligands are aligned parallel to the columnar stacks but the packing volume (length) of the alkylthiol ligands influences whether the columns are modulate or not. The former arrange into a rhombohedral phase whereas the latter arranges into a hexagonal phase (Fig. 8.26). Optical textures of these columnar mesophases are characteristic of a nematic phase, which implies the absence of longer range positional order.

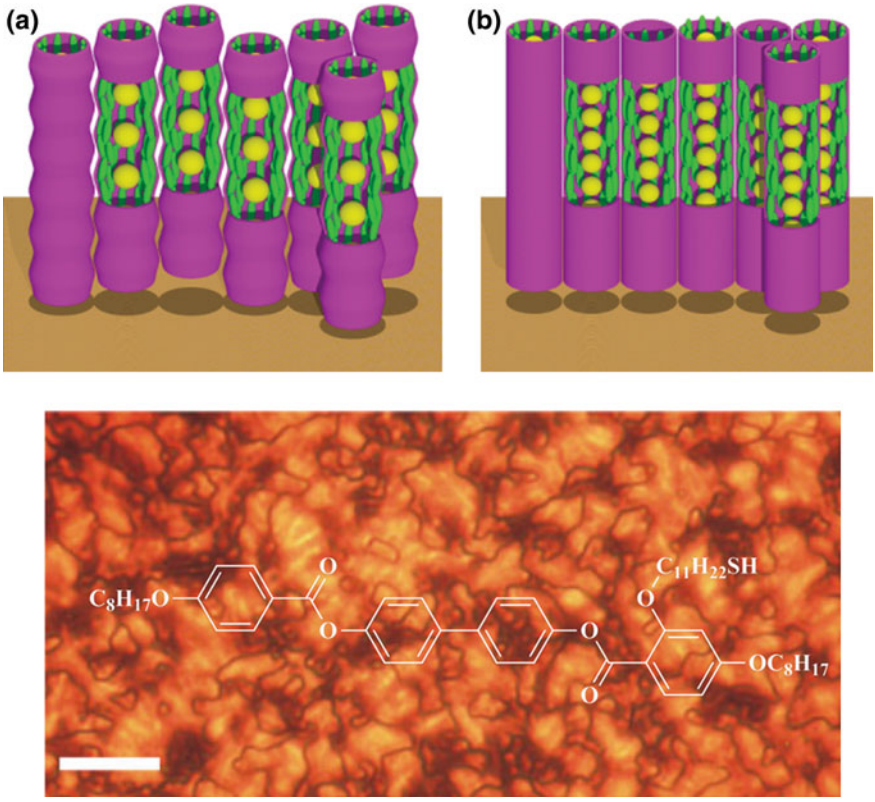

Fig. 8.26 Schematic models of the gold string structures (*top*). **a** Rhombohedral phase of gold NPs with dodecyl thiol as primary ligand and **b** hexagonal columnar phase of gold NPs with hexyl thiol as primary ligand; *yellow* gold nanoparticles, *green* mesogens. Threaded nematic texture of the MNP with dodecyl thiol as primary ligand and the shown mesogen as secondary ligand as observed by polarized optical microscopy at room temperature (*bottom*). Reprinted with permission from [114]. Copyright 2009 Wiley-VCH Publishers

Lateral attachment of bent-rod mesomorphic ligands has not generated any mesomorphic MNPs, which is often reasoned with the high melting temperatures of these ligands. Thiol desorption and subsequent growth of the MNPs occurs before the ligands actually melt into a more fluid phase [117, 121]. Dendritic and structural related ligands have been attached to gold NPs in an attempt to better fill the space around MNPs and to increase the volume fraction of the organic layer. Especially an increase of the volume fraction of the deformable and shape-directing organic layer should enhance the mesomorphic properties. This can be achieved by increasing the size of the ligands or decreasing the size of the gold cores. However, typical core diameters of the reported mesomorphic gold NPs are between 1 and 3 nm, which does not leave much room for a further decrease in core size.

Dendritic ligands have converted many different types of cores into mesomorphic compounds [122] but the first attempts of generating mesomorphic MNPs were unsuccessful [113], even though highly ordered arrangements of these MNPs on carbon-coated copper grids were observed. These findings were reasoned with the tight packing of the dendritic ligands that does not allow for distortions of the overall shape of the MNP by conformational changes and ligand migration. The first successful design employed dendrons that were attached to the MNP via a flexible spacer and, consequently, was conformationally more flexible [123]. These MNPs displayed cubic and 2-dimensional hexagonal mesophases. This report was followed by only one other successful attempt with MNPs [124] but several mesomorphic metal oxide NPs with dendritic ligands have been reported [125–127].

Finally, the attachment of discotic mesomorphic ligands to MNPs has not yet produced mesomorphic MNPs as neat material but drastically enhanced their ability to be doped into columnar mesophases of discotic liquid crystals of similar structures [128, 129]. However, only very few examples have yet been studied and it is likely that mesomorphic MNPs with discotic ligands will be successfully prepared in the near future.

Clearly, the development of self-organizing MNPs is still in its infant state and mainly concerned with structure property relations. Very few reports have been concerned with the properties of the obtained materials but, in principle, they should be similar to the interesting properties that have been reported for self-assembled MNPs. A recent publication, for example, reports the anisotropic plasmonic properties of silver and gold NPs in their lamellar mesophases [130].

8.5 Conclusions and Outlook

The ability to control packing structures and distances of metal nanoparticles (MNPs) in monolayers and multilayers is fundamental for many applications such as sensorics, catalysis, electronic devices, optical devices, spectroscopy, and membranes. Processing MNPs by the Langmuir-Blodgett technique has been particularly successful for the generation of two-dimensional hexagonal close-packed

monolayers of MNPs with tunable interparticle spacing. Although above examples exemplify the verge of fabricating highly-ordered, defect-free LB films, defects in the monolayers remain as an obstacle mainly due to polydisperse sizes and self-aggregation of nanoparticles. Enhanced LB properties are obtained with amphiphilic NPs such as Janus-type MNPs, which may produce highly-ordered LB films. The stability of these films may be improved by the use of multidentate ligands or by cross-linking deposited MNPs with ligands that contain two terminal linking groups.

Only few examples of LB multilayer films have been reported, which reflects the difficulty of controlling multiple depositions of ordered monolayers. Layer-by-Layer (LbL) deposition is more commonly applied to the fabrication of multilayer films that contain MNPs. Most of the early examples of LbL deposition relied on ionic MNPs but surface coverages of larger than 30 % are difficult to achieve because of coulomb repulsion between equally charged MNPs. Much higher packing densities of >75 % were achieved with neutral, hydrophobic MNPs and new processing techniques in non-polar solvents provide new options for the preparation of more ordered and stable LbL deposited monolayers.

Lastly, self-organizing MNPs give access to a range of different three-dimensionally ordered structures such as lamellar (smectic), columnar, and cubic arrangements of MNPs. The predominant design relies on the attachment of liquid crystalline ligand molecules via long flexible spacers. In fact, the length of the flexible spacer is critical as the formation of liquid crystal phases requires the conformational rearrangement of the ligands to generate overall more elongated NPs. Alternatively, the shape of MNPs containing a mixture of at least two ligands may change due to domain formation of specific ligands.

A major limitation is still the synthetic availability of monodisperse, compositionally defined, and stable MNPs. Especially LB-studies and self-organization of MNPs are strongly affected by impurities, such as excess of protective ligand, and polydispersity of their size, shape, and composition. Consequently, new synthetic strategies and designs that generate stable, monodisperse, and purer MNPs with the desired chemical functionality are at the heart of any advancement in this area of research.

References

1. M. Grzelczak, J. Vermant, E.M. Furst, L.M. Liz-Marzán, Directed self-assembly of nanoparticles. ACS Nano **4**, 3591–3605 (2010)
2. A. Boker, J. He, T. Emrick, T.P. Russell, Self-assembly of nanoparticles at interfaces. Soft Matter **3**, 1231–1248 (2007)
3. S. Kinge, M. Crego-Calama, D.N. Reinhoudt, Self-assembling nanoparticles at surfaces and interfaces. ChemPhysChem **9**, 20–42 (2008)
4. Z. Nie, A. Petukhova, E. Kumacheva, Properties and emerging applications of self-assembled structures made from inorganic nanoparticles. Nat. Nanotechnol. **5**, 15–25 (2010)

5. A. Klinkova, R.M. Choueiri, E. Kumacheva, Self-assembled plasmonic nanostructures. Chem. Soc. Rev. **43**, 3976–3991 (2014)
6. K. Ariga, Q. Ji, J.P. Hill, Y. Bando, M. Aono, Forming nanomaterials as layered functional structures toward materials nanoarchitectonics. NPG Asia Mater. **4**, 17 (2012)
7. W. Lewandowski, K. Jatczak, D. Pociecha, J. Mieczkowski, Control of gold nanoparticle superlattice properties via mesogenic ligand architecture. Langmuir **29**, 3404–3410 (2013)
8. X.G. Peng, Y. Zhang, J. Yang, B.S. Zou, L.Z. Xiao, T.J. Li, Formation of nanoparticulate Fe_2O_3-stearate multilayer through the Langmuir-Blodgett method. J. Phys. Chem. **96**, 3412–3415 (1992)
9. M. Sastry, K.S. Mayya, V. Patil, Facile surface modification of colloidal particles using bilayer surfactant assemblies: a new strategy for electrostatic complexation in Langmuir-Blodgett films. Langmuir **14**, 5921–5928 (1998)
10. K. Gmucova, M. Weis, V. Nadazdy, E. Majkova, Orientation ordering of nanoparticle Ag/Co cores controlled by electric and magnetic fields. ChemPhysChem **9**, 1036–1039 (2008)
11. H. Watanabe, M. Nishimura, Y. Fukui, K. Fujimoto, Development of a particle nanoimprinting technique by core-shell particles. Langmuir **30**, 1630–1635 (2014)
12. Y.C. Tian, J.H. Fendler, Langmuir-Blodgett film formation from fluorescence-activated, surfactant-capped, size-selected CdS nanoparticles spread on water surfaces. Chem. Mater. **8**, 969–974 (1996)
13. S.A. Iakovenko, A.S. Trifonov, M. Giersig, A. Mamedov, D.K. Nagesha, V.V. Hanin, E.C. Soldatov, N.A. Kotov, One- and two-dimensional arrays of magnetic nanoparticles by the Langmuir-Blodgett technique. Adv. Mater. **11**, 388–392 (1999)
14. A.R. Tao, J. Huang, P. Yang, Langmuir-Blodgettry of nanocrystals and nanowires. Acc. Chem. Res. **41**, 1662–1673 (2008)
15. K. Kolasinski, *Surface Science: Foundations of Catalysis and Nanoscience* (Wiley, 2002)
16. A.R. Tao, Nanocrystal assembly for bottom-up plasmonic materials and surface-enhanced Raman spectroscopy (SERS) sensing. Pure Appl. Chem. **81**, 61–71 (2009)
17. J.C. Love, L.A. Estroff, J.K. Kriebel, R.G. Nuzzo, G.M. Whitesides, Self-assembled monolayers of thiolates on metals as a form of nanotechnology. Chem. Rev. **105**, 1103–1169 (2005)
18. J.H. Fendler, Self-assembled nanostructured materials. Chem. Mater. **8**, 1616–1624 (1996)
19. E. Pohjalainen, M. Pohjakallio, C. Johans, K. Kontturi, J.V.I. Timonen, O. Ikkala, R.H.A. Ras, T. Viitala, M.T. Heino, E.T. Seppala, Cobalt nanoparticle Langmuir-Schaefer films on ethylene glycol subphase. Langmuir **26**, 13937–13943 (2010)
20. R.K. Gupta, K.A. Suresh, S. Kumar, Monolayer of amphiphilic functionalized gold nanoparticles at an air-water interface. Phys. Rev. E **78**, 032601 (2008)
21. A. Perro, S. Reculusa, S. Ravaine, E. Bourgeat-Lami, E. Duguet, Design and synthesis of Janus micro-and nanoparticles. J. Mater. Chem. **15**, 3745–3760 (2005)
22. H. Zhang, Y. Liu, D. Yao, B. Yang, Hybridization of inorganic nanoparticles and polymers to create regular and reversible self-assembly architectures. Chem. Soc. Rev. **41**, 6066–6088 (2012)
23. A. Swami, A. Kumar, P.R. Selvakannan, S. Mandal, M. Sastry, Langmuir-Blodgett films of laurylamine-modified hydrophobic gold nanoparticles organized at the air-water interface. J. Colloid Interface Sci. **260**, 367–373 (2003)
24. V. Aleksandrovic, D. Greshnykh, I. Randjelovic, A. Froemsdorf, A. Kornowski, S.V. Roth, C. Klinke, H. Weller, Preparation and electrical properties of cobalt-platinum nanoparticle monolayers deposited by the Langmuir-Blodgett technique. ACS Nano **2**, 1123–1130 (2008)
25. J.Y. Kim, S. Raja, F. Stellacci, Evolution of langmuir film of nanoparticles through successive compression cycles. small **7**(17), 2526–2532 (2011)
26. H. Song, F. Kim, S. Connor, G.A. Somorjai, P.D. Yang, Pt nanocrystals: shape control and Langmuir-Blodgett monolayer formation. J. Phys. Chem. B **109**, 188–193 (2005)
27. M.A. Mahmoud, M.A. El-Sayed, Comparative study of the assemblies and the resulting plasmon fields of Langmuir-Blodgett assembled monolayers of silver nanocubes and gold nanocages. J. Phys. Chem. C **112**, 14618–14625 (2008)

28. P.J.G. Goulet, D.S. dos Santos, R.A. Alvarez-Puebla, O.N. Oliveira, R.F. Aroca, Surface-enhanced Raman scattering on dendrimer/metallic nanoparticle layer-by-layer film substrates. Langmuir **21**, 5576–5581 (2005)
29. P.J.G. Goulet, N.P.W. Pieczonka, R.F. Aroca, Mapping single-molecule SERRS from Langmuir-Blodgett monolayers, on nanostructured silver island films. J. Raman Spectrosc. **36**, 574–580 (2005)
30. Y. Lu, G.L. Liu, L.P. Lee, High-density silver nanoparticle film with temperature-controllable interparticle spacing for a tunable surface enhanced Raman scattering substrate. Nano Lett. **5**, 5–9 (2005)
31. M.A. Mahmoud, C.E. Tabor, M.A. El-Sayed, Surface-enhanced Raman scattering enhancement by aggregated silver nanocube monolayers assembled by the Langmuir-Blodgett technique at different surface pressures. J. Phys. Chem. C **113**, 5493–5501 (2009)
32. X. Chen, X. Yang, W. Fu, M. Xu, H. Chen, Enhanced performance of polymer solar cells with a monolayer of assembled gold nanoparticle films fabricated by Langmuir-Blodgett technique. Mater. Sci. Eng., B **178**, 53–59 (2013)
33. J.Z. James, D. Lucas, C.P. Koshland, Gold nanoparticle films as sensitive and reusable elemental mercury sensors. Environ. Sci. Technol. Lett. **46**, 9557–9562 (2012)
34. C. Medina-Plaza, C. Garcia-Cabezon, C. Garcia-Hernandez, C. Bramorski, Y. Blanco-Val, F. Martin-Pedrosa, T. Kawai, J.A. de Saja, M.L. Rodriguez-Mendez, Analysis of organic acids and phenols of interest in the wine industry using Langmuir-Blodgett films based on functionalized nanoparticles. Anal. Chim. Acta **853**, 572–578 (2015)
35. J.Y. Park, Y. Zhang, M. Grass, T. Zhang, G.A. Somorjai, Tuning of catalytic CO oxidation by changing composition of Rh-Pt bimetallic nanoparticles. Nano Lett. **8**, 673–677 (2008)
36. Y.W. Zhang, M.E. Grass, W.Y. Huang, G.A. Somorjai, Seedless polyol synthesis and CO oxidation activity of monodisperse (111)- and (100)-oriented rhodium nanocrystals in sub-10 nm sizes. Langmuir **26**, 16463–16468 (2010)
37. K. Nørgaard, M.J. Weygand, K. Kjaer, M. Brust, T. Bjørnholm, Adaptive chemistry of bifunctional gold nanoparticles at the air/water interface. A synchrotron X-ray study of giant amphiphiles. Faraday Discuss. **125**, 221 (2004)
38. K.D. Comeau, M.V. Meli, Effect of alkanethiol chain length on gold nanoparticle monolayers at the air-water interface. Langmuir **28**, 377–381 (2012)
39. T. Matsumoto, P. Nickut, T. Sawada, H. Tsunoyama, K. Watanabe, T. Tsukuda, K. Al-Shamery, Y. Matsumoto, Deposition and fabrication of alkanethiolate gold nanocluster films on TiO_2(110) and the effects of plasma etching. Surf. Sci. **601**, 5121–5126 (2007)
40. J.R. Heath, C.M. Knobler, D.V. Leff, Pressure/temperature phase diagrams and superlattices of organically functionalized metal nanocrystal monolayers: the influence of particle size, size distribution, and surface passivant. J. Phys. Chem. B **101**, 189–197 (1997)
41. B.P. Gagnon, M.V. Meli, Effects on the self-assembly of n-alkane/gold nanoparticle mixtures spread at the air-water interface. Langmuir **30**, 179–185 (2014)
42. T.A. Sanders II, M.N. Sauced, J.A. Dahl, Langmuir isotherms of flexible, covalently crosslinked gold nanoparticle networks: increased collapse pressures of membrane-like structures. Mater. Lett. **120**, 159–162 (2014)
43. C.Y. Lau, H. Duan, F. Wang, C.B. He, H.Y. Low, J.K.W. Yang, Enhanced ordering in gold nanoparticles self-assembly through excess free ligands. Langmuir **27**, 3355–3360 (2011)
44. S.J. Lee, S.W. Han, H.J. Choi, K. Kim, Phase behavior of organic-inorganic crystal—temperature-dependent diffuse reflectance infrared spectroscopy of silver stearate. Eur. Phys. J. D **16**, 293–296 (2001)
45. H. Perez, R.M.L. de Sousa, J.P. Pradeau, P.A. Albouy, Elaboration and electrical characterization of Langmuir-Blodgett films of 4-mercaptoaniline functionalized platinum nanoparticles. Chem. Mater. **13**, 1512–1517 (2001)
46. M. Sastry, M. Rao, K.N. Ganesh, Electrostatic assembly of nanoparticles and biomacromolecules. Acc. Chem. Res. **35**, 847–855 (2002)

47. S. Datta, J. Biswas, S. Bhattacharya, How does spacer length of imidazolium gemini surfactants control the fabrication of 2D-Langmuir films of silver-nanoparticles at the air-water interface. J. Colloid Interface Sci. **430**, 85–92 (2014)
48. V. Sashuk, R. Holyst, T. Wojciechowski, M. Fialkowski, Close-packed monolayers of charged Janus-type nanoparticles at the air-water interface. J. Colloid Interface Sci. **375**, 180–186 (2012)
49. M. Benkovicova, K. Vegsoe, P. Siffalovic, M. Jergel, E. Majkova, S. Luby, A. Satka, Preparation of sterically stabilized gold nanoparticles for plasmonic applications. Chem. Pap. **67**, 1225–1230 (2013)
50. Y. Zhang, M.E. Grass, S.E. Habas, F. Tao, T. Zhang, P. Yang, G.A. Somorjai, One-step polyol synthesis and langmuir-blodgett monolayer formation of size-tunable monodisperse rhodium nanocrystals with catalytically active (111) surface structures. J. Phys. Chem. C **111**, 12243–12253 (2007)
51. K.L. Genson, J. Holzmueller, C. Jiang, J. Xu, J.D. Gibson, E.R. Zubarev, V.V. Tsukruk, Langmuir-Blodgett monolayers of gold nanoparticles with amphiphilic shells from V-shaped binary polymer arms. Langmuir **22**, 7011–7015 (2006)
52. A. Tao, P. Sinsermsuksakul, P. Yang, Tunable plasmonic lattices of silver nanocrystals. Nat. Nanotechnol. **2**, 435–440 (2007)
53. E. Bellido, N. Domingo, I. Ojea-Jimenez, D. Ruiz-Molina, Structuration and integration of magnetic nanoparticles on surfaces and devices. Small **8**, 1465–1491 (2012)
54. Y. Wang, M. Yang, B. Xu, Z. Yang, N. Hu, L. Wei, B. Cai, Y. Zhang, Controlled assembly of FePt nanoparticles monolayer on solid substrates. J. Colloid Interface Sci. **417**, 100–108 (2014)
55. M. Wen, E. Kejia, H. Qi, L. Li, J. Chen, Y. Chen, Q. Wu, T. Zhang, Langmuir-Blodgett self-assembly and electrochemical catalytic property of FePt magnetic nano-monolayer. J. Nanopart. Res. **9**, 909–917 (2007)
56. M. Kumar, A. Pathak, M. Singh, M.L. Singla, Fabrication of Langmuir-Blodgett film from polyvinylpyrrolidone stabilized NiCo alloy nanoparticles. Thin Solid Films **519**, 1445–1451 (2010)
57. S. Kundu, Layer-by-layer assembly of thiol-capped Au nanoparticles on a water surface and their deposition on H-terminated Si(001) by the Langmuir-Blodgett method. Langmuir **27**, 3930–3936 (2011)
58. S. Kundu, J.K. Bal, Reorganization of Au nanoparticle Langmuir-Blodgett films on wet chemically passivated Si(001) surfaces. J. Appl. Phys. **110** (2011)
59. S. Kundu, K. Das, O. Konovalov, Prolonged reorganization of thiol-capped Au nanoparticles layered structures. AIP Adv. **3** (2013)
60. M.M. de Villiers, D.P. Otto, S.J. Strydom, Y.M. Lvov, Introduction to nanocoatings produced by layer-by-layer (LbL) self-assembly. Adv. Drug Delivery Rev. **63**, 701–715 (2011)
61. G. Decher, J.B. Schlenoff (eds.), *Multilayer Thin Films: Sequential Assembly of Nanocomposite Materials* (Wiley-VCH Verlag GmbH & Co. KGaA, 2012)
62. A.N. Shipway, E. Katz, I. Willner, Nanoparticle arrays on surfaces for electronic, optical, and sensor applications. ChemPhysChem **1**, 18–52 (2000)
63. A.N. Shipway, I. Willner, Nanoparticles as structural and functional units in surface-confined architectures. Chem. Commun. **20**, 2035–2045 (2001)
64. R.K. Iler, Multilayers of colloidal particles. J. Colloid Interface Sci. **21**, 569–575 (1966)
65. J.R. Siqueira Jr, L. Caseli, F.N. Crespilho, V. Zucolotto, O.N. Oliveira Jr, Immobilization of biomolecules on nanostructured films for biosensing. Biosens. Bioelectron. **25**, 1254–1263 (2010)
66. K. Sato, J. Anzai, Dendrimers in layer-by-layer assemblies: synthesis and applications. Molecules **18**, 8440–8460 (2013)
67. J. Schmitt, G. Decher, W.J. Dressick, S.L. Brandow, R.E. Geer, R. Shashidhar, J.M. Calvert, Metal nanoparticle/polymer superlattice films: fabrication and control of layer structure. Adv. Mater. **9**, 61–65 (1997)

68. A.I. Abdelrahman, A.M. Mohammad, T. Okajima, T. Ohsaka, Fabrication and electrochemical application of three-dimensional gold nanoparticles: self-assembly. J. Phys. Chem. B **110**, 2798–2803 (2006)
69. A.I. Abdelrahman, A.M. Mohammad, M.S. El-Deab, T. Okajima, T. Ohsaka, Bisthiol-assisted multilayers' self-assembly of gold nanoparticles: synthesis, characterization, size control and electrocatalytic applications. Macromol. Symp. **270**, 74–81 (2008)
70. J.F. Hicks, Y. Seok-Shon, R.W. Murray, Layer-by-layer growth of polymer/nanoparticle films containing monolayer-protected gold clusters. Langmuir **18**, 2288–2294 (2002)
71. W. Song, M. Okamura, T. Kondo, K. Uosaki, Sequential layer-by-layer growth of Au nanoclusters protected by a mixed self-assembled monolayer with a polymer binding layer—effects of pH and ionic strength of the polymer solution. J. Electroanal. Chem. **612**, 105–111 (2008)
72. W.B. Zhao, J. Park, A.-M. Caminade, S.-J. Jeong, Y.H. Jang, S.O. Kim, J.-P. Majoral, J. Cho, D.H. Kim, Localized surface plasmon resonance coupling in Au nanoparticles/phosphorus dendrimer multilayer thin films fabricated by layer-by-layer self-assembly method. J. Mater. Chem. **19**, 2006–2012 (2009)
73. B. Peter, S. Kurunczi, D. Patko, I. Lagzi, B. Kowalczyk, Z. Rácz, B.A. Grzybowski, R. Horvath, Label-free in situ optical monitoring of the adsorption of oppositely charged metal nanoparticles. Langmuir **30**, 13478–13482 (2014)
74. S. Kawada, D. Saeki, H. Matsuyama, Development of ultrafiltration membrane by stacking of silver nanoparticles stabilized with oppositely charged polyelectrolytes. Colloids Surf. A **451**, 33–37 (2014)
75. Y. Liu, Y. Wang, R.O. Claus, Layer-by-layer ionic self-assembly of Au colloids into multilayer thin-films with bulk metal conductivity. Chem. Phys. Lett. **298**, 315–319 (1998)
76. P.J. Rivero, J. Goicoechea, I.R. Matias, F.J. Arregui, A comparative study of two different approaches for the incorporation of silver nanoparticles into layer-by-layer films. Nanoscale Res. Lett. **9**, 301–301 (2014)
77. Y. Ko, H. Baek, Y. Kim, M. Yoon, J. Cho, Hydrophobic nanoparticle-based nanocomposite films using in situ ligand exchange layer-by-layer assembly and their nonvolatile memory applications. ACS Nano **7**, 143–153 (2012)
78. M. Park, Y. Kim, Y. Ko, S. Cheong, S.W. Ryu, J. Cho, Amphiphilic layer-by-layer assembly overcoming solvent polarity between aqueous and nonpolar media. J. Am. Chem. Soc. **136**, 17213–17223 (2014)
79. N. Krasteva, I. Besnard, B. Guse, R.E. Bauer, K. Müllen, A. Yasuda, T. Vossmeyer, Self-assembled gold nanoparticle/dendrimer composite films for vapor sensing applications. Nano Lett. **2**, 551–555 (2002)
80. M.D. Musick, C.D. Keating, M.H. Keefe, M.J. Natan, Stepwise construction of conductive Au colloid multilayers from solution. Chem. Mater. **9**, 1499–1501 (1997)
81. M.D. Musick, C.D. Keating, L.A. Lyon, S.L. Botsko, D.J. Pena, W.D. Holliway, T.M. McEvoy, J.N. Richardson, M.J. Natan, Metal films prepared by stepwise assembly. 2. Construction and characterization of colloidal Au and Ag multilayers. Chem. Mater. **12**, 2869–2881 (2000)
82. T. Baum, D. Bethell, M. Brust, D.J. Schiffrin, Electrochemical charge injection into immobilized nanosized gold particle ensembles: potential modulated transmission and reflectance spectroscopy. Langmuir **15**, 866–871 (1999)
83. M. Brust, R. Etchenique, E.J. Calvo, G.J. Gordillo, The self-assembly of gold and SCd nanoparticle multilayer structures studied by quartz crystal microgravimetry. Chem. Commun. 1949–1950 (1996)
84. L. Supriya, R.O. Claus, Colloidal Au/linker molecule multilayer films: low-temperature thermal coalescence and resistance changes. Chem. Mater. **17**, 4325–4334 (2005)
85. J. Dhar, S. Patil, Self-assembly and catalytic activity of metal nanoparticles immobilized in polymer membrane prepared via layer-by-layer approach. ACS Appl. Mater. Interfaces **4**, 1803–1812 (2012)

86. H. Li, Z. Li, L. Wu, Y. Zhang, M. Yu, L. Wei, Constructing metal nanoparticle multilayers with polyphenylene dendrimer/gold nanoparticles via "click" chemistry. Langmuir **29**, 3943–3949 (2013)
87. J.W. Goodby, P.J. Collings, T. Kato, C. Tschierske, H. Gleeson, P. Raynes (eds.), *Handbook of Liquid Crystals* (Wiley-VCH Verlag & Co. KGaA, 2013)
88. M. Sawamura, K. Kawai, Y. Matsuo, K. Kanie, T. Kato, E. Nakamura, Stacking of conical molecules with a fullerene apex into polar columns in crystals and liquid crystals. Nature **419**, 702–705 (2002)
89. B. Donnio, S. Buathong, I. Bury, D. Guillon, Liquid crystalline dendrimers. Chem. Soc. Rev. **36**, 1495–1513 (2007)
90. G.L. Nealon, R. Greget, C. Dominguez, Z.T. Nagy, D. Guillon, J.-L. Gallani, B. Donnio, Liquid-crystalline nanoparticles: hybrid design and mesophase structures. Beilstein J. Org. Chem. **8**, 349–370 (2012)
91. H.K. Bisoyi, S. Kumar, Liquid-crystal nanoscience: an emerging avenue of soft self-assembly. Chem. Soc. Rev. **40**, 306–319 (2011)
92. J. van Herrikhuyzen, G. Portale, J.C. Gielen, P.C.M. Christianen, N.A.J.M. Sommerdijk, S. C.J. Meskers, A.P.H.J. Schenning, Disk micelles from amphiphilic Janus gold nanoparticles. Chem. Commun. 697–699 (2008)
93. P. Davidson, J.C.P. Gabriel, Mineral liquid crystals. Curr. Opin. Colloid Interface Sci. **9**, 377–383 (2005)
94. U. Shivakumar, J. Mirzaei, X. Feng, A. Sharma, P. Moreira, T. Hegmann, Nanoparticles: complex and multifaceted additives for liquid crystals. Liq. Cryst. **38**, 1495–1514 (2011)
95. T. Hegmann, Modulating the properties of liquid crystals using nanoparticles as dopants. Int. Innov. Rep. **9**, 53–55 (2013)
96. M.C. Daniel, D. Astruc, Gold nanoparticles: assembly, supramolecular chemistry, quantum-size-related properties, and applications toward biology, catalysis, and nanotechnology. Chem. Rev. **104**, 293–346 (2004)
97. M. Brust, M. Walker, D. Bethell, D.J. Schiffrin, R. Whyman, Synthesis of thiol-derivatised gold nanoparticles in a two-phase Liquid-Liquid system. J. Chem. Soc., Chem. Commun. 801–802 (1994)
98. P.J.G. Goulet, R.B. Lennox, New insights into Brust–Schiffrin metal nanoparticle synthesis. J. Am. Chem. Soc. **132**, 9582–9584 (2010)
99. N.R. Jana, X. Peng, Single-phase and gram-scale routes toward nearly monodisperse Au and other noble metal nanocrystals. J. Am. Chem. Soc. **125**, 14280–14281 (2003)
100. X. Mang, X. Zeng, B. Tang, F. Liu, G. Ungar, R. Zhang, L. Cseh, G.H. Mehl, Control of anisotropic self-assembly of gold nanoparticles coated with mesogens. J. Mater. Chem. **22**, 11101–11106 (2012)
101. X. Ji, D. Copenhaver, C. Sichmeller, X. Peng, Ligand bonding and dynamics on colloidal nanocrystals at room temperature: the case of alkylamines on CdSe nanocrystals. J. Am. Chem. Soc. **130**, 5726–5735 (2008)
102. R.C. Hedden, B.J. Bauer, A.P. Smith, F. Gröhn, E. Amis, Templating of inorganic nanoparticles by PAMAM/PEG dendrimer–star polymers. Polymer **43**, 5473–5481 (2002)
103. W. Jia, J. McLachlan, J. Xu, S.M. Tadayyon, P.R. Norton, S.H. Eichhorn, Characterization of Au and Pd nanoparticles by high-temperature TGA–MS. Can. J. Chem. **84**, 998–1005 (2006)
104. M. Iqbal, J. McLachlan, W. Jia, N. Braidy, G. Botton, S.H. Eichhorn, Ligand effects on the size and purity of Pd nanoparticles. J. Therm. Anal. Calorim. **96**, 15–20 (2009)
105. W. Jia, J. McLachlan, J. Xu, S.H. Eichhorn, Size and purity of gold nanoparticles changes with different types of thiolate ligands. J. Therm. Anal. Calorim. **100**, 839–845 (2010)
106. R. Ristau, R. Tiruvalam, P.L. Clasen, E.P. Gorskowski, M.P. Harmer, C.J. Kiely, I. Hussain, M. Brust, Electron microscopy studies of the thermal stability of gold nanoparticle arrays. Gold Bull. **42**, 133–143 (2009)

107. Y. Joseph, I. Besnard, M. Rosenberger, B. Guse, H.-G. Nothofer, J.M. Wessels, U. Wild, A. Knop-Gericke, D. Su, R. Schlögl, A. Yasuda, T. Vossmeyer, Self-assembled gold nanoparticle/alkanedithiol films: preparation, electron microscopy, XPS-analysis, charge transport, and vapor-sensing properties. J. Phys. Chem. B **107**, 7406–7413 (2003)
108. M. Draper, I.M. Saez, S.J. Cowling, P. Gai, B. Heinrich, B. Donnio, D. Guillon, J.W. Goodby, Self-assembly and shape morphology of liquid crystalline gold metamaterials. Adv. Funct. Mater. **21**, 1260–1278 (2011)
109. J. Mirzaei, M. Urbanski, H.-S. Kitzerow, T. Hegmann, Synthesis of liquid crystal silane-functionalized gold nanoparticles and their effects on the optical and electro-optic properties of a structurally related nematic liquid crystal. ChemPhysChem **15**, 1381–1394 (2014)
110. N. Kanayama, O. Tsutsumi, A. Kanazawa, T. Ikeda, Distinct thermodynamic behaviour of a mesomorphic gold nanoparticle covered with a liquid-crystalline compound. Chem. Commun. 2640–2641 (2001)
111. B. Donnio, Liquid-crystalline metallodendrimers. Inorg. Chim. Acta **409**, 53–67 (2014)
112. I. In, Y.-W. Jun, Y.J. Kim, S.Y. Kim, Spontaneous one dimensional arrangement of spherical Au nanoparticles with liquid crystal ligands. Chem. Commun. 800–801 (2005)
113. S. Frein, J. Boudon, M. Vonlanthen, T. Scharf, J. Barbera, G. Suess-Fink, T. Buergi, R. Deschenaux, Liquid-crystalline thiol- and disulfide-based dendrimers for the functionalization of gold nanoparticles. Helv. Chim. Acta **91**, 2321–2337 (2008)
114. X. Zeng, F. Liu, A.G. Fowler, G. Ungar, L. Cseh, G.H. Mehl, J.E. Macdonald, 3D ordered gold strings by coating nanoparticles with mesogens. Adv. Mater. **21**, 1746–1750 (2009)
115. L. Cseh, G.H. Mehl, The design and investigation of room temperature thermotropic nematic gold nanoparticles. J. Am. Chem. Soc. **128**, 13376–13377 (2006)
116. L. Cseh, G.H. Mehl, Structure-property relationships in nematic gold nanoparticles. J. Mater. Chem. **17**, 311–315 (2007)
117. M. Wojcik, W. Lewandowski, J. Matraszek, J. Mieczkowski, J. Borysiuk, D. Pociecha, E. Gorecka, Liquid-crystalline phases made of gold nanoparticles. Angew. Chem. Int. Ed. **48**, 5167–5169 (2009)
118. M. Wojcik, M. Kolpaczynska, D. Pociecha, J. Mieczkowski, E. Gorecka, Multidimensional structures made by gold nanoparticles with shape-adaptive grafting layers. Soft Matter **6**, 5397–5400 (2010)
119. J.M. Wolska, D. Pociecha, J. Mieczkowski, E. Gorecka, Gold nanoparticles with flexible mesogenic grafting layers. Soft Matter **9**, 3005–3008 (2013)
120. K. Kaneko, A. Mandai, B. Heinrich, B. Donnio, T. Hanasaki, Electric-field-induced reversible viscosity change in a columnar liquid crystal. ChemPhysChem **11**, 3596–3598 (2010)
121. V.M. Marx, H. Girgis, P.A. Heiney, T. Hegmann, Bent-core liquid crystal (LC) decorated gold nanoclusters: synthesis, self-assembly, and effects in mixtures with bent-core LC hosts. J. Mater. Chem. **18**, 2983–2994 (2008)
122. B.M. Rosen, C.J. Wilson, D.A. Wilson, M. Peterca, M.R. Imam, V. Percec, Dendron-mediated self-assembly, disassembly, and self-organization of complex systems. Chem. Rev. **109**, 6275–6540 (2009)
123. B. Donnio, P. García-Vázquez, J.L. Gallani, D. Guillon, E. Terazzi, Dendronized ferromagnetic gold nanoparticles self-organized in a termotropic cubic phase. Adv. Mater. **19**, 3534–3539 (2007)
124. K. Kanie, M. Matsubara, X. Zeng, F. Liu, G. Ungar, H. Nakamura, A. Muramatsu, Simple cubic packing of gold nanoparticles through rational design of their dendrimeric corona. J. Am. Chem. Soc. **134**, 808–811 (2012)
125. A. Demortiere, S. Buathong, B.P. Pichon, P. Panissod, D. Guillon, S. Begin-Colin, B. Donnio, Nematic-like organization of magnetic mesogen-hybridized nanoparticles. Small **6**, 1341–1346 (2010)
126. B. Donnio, A. Derory, E. Terazzi, M. Drillon, D. Guillon, J.-L. Gallani, Very slow high-temperature relaxation of the remnant magnetic moment in 2 nm mesomorphic gold nanoparticles. Soft Matter **6**, 965–970 (2010)

127. A. Demortiere, P. Panissod, B.P. Pichon, G. Pourroy, D. Guillon, B. Donnio, S. Begin-Colin, Size-dependent properties of magnetic iron oxide nanocrystals. Nanoscale **3**, 225–232 (2011)
128. S. Kumar, S.K. Pal, P.S. Kumar, V. Lakshminarayanan, Novel conducting nanocomposites: synthesis of triphenylene-covered gold nanoparticles and their insertion into a columnar matrix. Soft Matter **3**, 896–900 (2007)
129. Z. Shen, M. Yamada, M. Miyake, Control of stripelike and hexagonal self-assembly of gold nanoparticles by the tuning of interactions between triphenylene ligands. J. Am. Chem. Soc. **129**, 14271–14280 (2007)
130. W. Lewandowski, D. Constantin, K. Walicka, D. Pociecha, J. Mieczkowski, E. Gorecka, Smectic mesophases of functionalized silver and gold nanoparticles with anisotropic plasmonic properties. Chem. Commun. **49**, 7845–7847 (2013)

Chapter 9
Self-Organized 3D Photonic Superstructure: Blue Phase Liquid Crystal

Tsung-Hsien Lin, Chun-Wei Chen and Quan Li

Abstract Blue phase liquid crystals (BPLCs) have attracted considerable attention in recent years owing to their unique periodic structure and electro-optic properties. Besides the potential applications in the next generation display, BPLC with a cubic lattice structure can be regarded as a self-organized three-dimenstional (3D) photonic crystal that can be applied for photonic devices such as optical filter, optical attenuator, phase modulator, laser source and so on. This chapter will introduce the formation of BPLCs from both theoretical and experimental points of view. The stability and temperature range of BPLCs are also discussed followed by its photonic crystal structure, lattice orientation and phase identification. After a basic overview, this chapter will further introduce the applications of BPLCs, including controllability of photonic band gap with external fields, fast electro-optic Kerr effect, and optical nonlinear effect. This short summary shows that the century old intriguing BPLCs have diverse opportunities to offer in modern photonic materials and devices. Moreover, the current challenges in this area are expected to spark innovative ideas leading toward the design and engineering of new chiral materials that may furnish suitable BPLCs to produce advanced photonic materials that have desirable properties and functions.

9.1 Introduction

Blue phases (BPs) were observed the first time when the Austrian botanist Reinitzer discovered liquid crystals (LCs) in 1888 [1]. The name "blue phase" is due to the blue appearance of the phase when it was first observed in cholesteryl benzoate by

T.-H. Lin (✉) · C.-W. Chen
Department of Photonics, National Sun Yat-Sen University,
Lien-Hai Road, Kaohsiung, Taiwan
e-mail: jameslin@faculty.nsysu.edu.tw

Q. Li (✉)
Liquid Crystal Institute and Chemical Physics Interdisciplinary Program,
Kent State University, Kent, OH 44242, USA
e-mail: qli1@kent.edu

Q. Li (ed.), *Anisotropic Nanomaterials*, NanoScience and Technology,
DOI 10.1007/978-3-319-18293-3_9

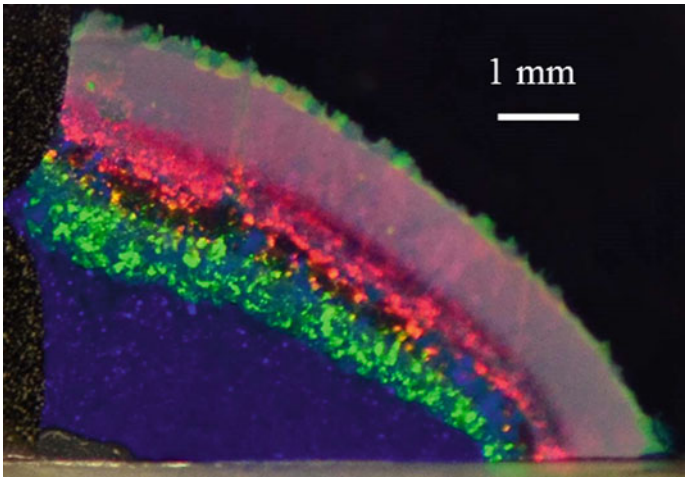

Fig. 9.1 Macroscopic view of liquid crystalline blue phases

Reinitzer. However blue phases can in fact have other colors [2]. Figure 9.1 reveals that BPLCs are, in fact, not all blue colored. The allure and beauty of such a class of mesophases originate mainly from their self-organized three-dimensional (3D) photonic crystal structure. With typical lattice spacing on the order of several hundred nanometers, selective Bragg reflection could be any color positioned in the visible region. They are thermodynamically stable between isotropic liquid state and cholesteric phase, which can be classified as BPIII, BPII and BPI in light of their emergence order. The high chirality in these materials forces the mesogenic molecules to twist with respect to each other (Fig. 9.2), resulting in the typical double twisted cylinder of BPs. This also explains why BPLCs ordinarily reflect visible [3] and ultraviolet light [4] while very few of them show reflection beyond the red end of the visible spectrum [5]. Usually, when chirality in LC system is high enough, double twist cylinder structure is more stable than a simple helical structure. However, DTC cannot be densely packed to fill the entire space and hence disclination lines appear at the interstices among the cylinders to form a stabilized 3D cubic structure.

9.2 Formation of Blue Phase (BP)

LC molecules, aligning with the lowest energy, form a specific stable phase. The formation of double-twist arrangement can be interpreted from the Oseen-Frank elastic model [6, 7]. In a chiral system, the elastic free energy density f_e can be expressed as [8]:

Fig. 9.2 Schematic depictions of director distribution in nematic phase (N), cholesteric phase (N*) and blue phase (BP)

$$f_e = \frac{1}{2}\Big\{k_{11}(\vec{\nabla}\cdot\vec{n})^2 + k_{22}(\vec{n}\cdot\vec{\nabla}\times\vec{n}+q_0)^2 + k_{33}\Big[\vec{n}\times(\vec{\nabla}\times\vec{n})\Big]^2 + (k_{22}+k_{24})\vec{\nabla}\cdot\Big[(\vec{n}\cdot\vec{\nabla})\vec{n} - (\vec{\nabla}\cdot\vec{n})\vec{n}\Big]\Big\},$$

where various k_{ij} is the anisotropic elastic coefficients, n represents the director, and q_0 is the wave vector of the chiral system which equals to $2\pi/P$, in which P denotes the pitch length. The first three terms are the well-known expression of splay, twist and bend distortions in the bulk. The last term, often called the saddle-splay deformation, is a surface-like contribution to the free energy. The surface part is frequently omitted for nematics and other non-frustrated mesophases, but of particular importance for those with topological defect structures such as BPs and twist grain boundary (TGB) phases. Simplified by taking all the elastic coefficients equal to k, the free energy is thus:

$$F_e = \frac{k}{2}\sum_{\alpha\beta}\left(\partial_\alpha n_\beta - q_0\varepsilon_{\alpha\beta\gamma}n_\gamma\right)^2 - q_0^2, \tag{9.2}$$

where α, β and γ index are the coordinates, ∂_α is the partial derivative with respect to α, and $\varepsilon_{\alpha\beta\gamma}$ is the antisymmetric dielectric tensor. The minimum free energy bottoms out when:

$$\partial_\alpha n_\beta = q_0\varepsilon_{\alpha\beta\gamma}n_\gamma, \tag{9.3}$$

That is, the director n twists along all directions perpendicular to the axis of a central director: this is called the "double-twist". The double-twist system is frustrated [9–11], which indicates a fairly finite expansion for the local orientational order on the plane parallel to the helical axes, compared to its non- and single-twist counterparts. Specifically, the double-twisted arrangement of the molecules near the centerline is more stable than those far from the centerline. This thereby leads to a cylindrical organization. DTC is the elementary building block of BPLCs, in which the director rotates 45° in total along the radius (Fig. 9.3a). The handedness of the

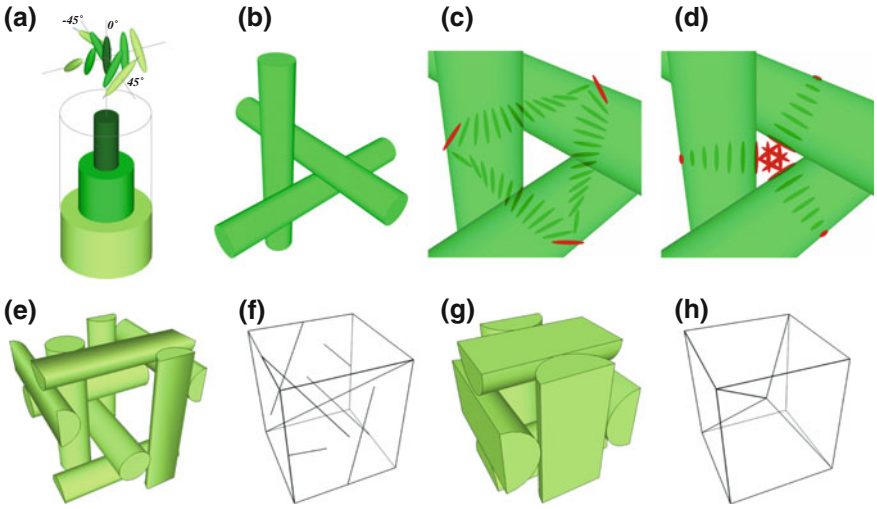

Fig. 9.3 Conceptual schemes: **a** director distribution in a DTC; **b** three-dimensional stacking of DTCs and the corresponding director distribution of the **c** continuous and **d** discontinuous portions; arrangements of DTCs and disclinations in **e**, **f** BPI and **g**, **h** BPII

twist is determined by the material. Curvature of cylinder implies that the double-twisted configuration cannot fill up the entire space; in other words, the system is unstable without the defects that fill up the vacancies, therefore DTCs must coexist with the defects. Based on the optical isotropy nature of BP, Saupe firstly conjectured that BP has the cubic symmetry [12]. Nowadays it is well known that, in BPI and BPII, cylinders stack orthogonally in three dimensions (Fig. 9.3b). While Fig. 9.3c depicts the continuous portions, in terms of the director field, at which every two DTCs touch; a defect is generated when conflicts arise at the triangular region, as interpreted in Fig. 9.3d. The manner of DTC packing varies as phase transition. On the aspect of lattice structure, BPI is body-centered cubic with $I4_132$ (O^8) symmetry, whereas BPII belongs to simple (primitive) cubic space group $P4_232$ (O^2) [6, 11, 13, 14]. The schematic depictions of the cylinder arrangement and disclination network in BPI as well as in BPII are presented respectively in Fig. 9.3e, f. On the contrary, the configuration of BPIII, the fog-like phase, has remained enigmatic. Numerous efforts were devoted to model BPIII but still inconclusive. An up-to-date series of simulation results [15] strongly suggested that BPIII is an amorphous network of disclinations. Inside the defects of all three phases, the local director alignment must be completely disordered (i.e. isotropic) so as to cancel the conflicting molecular interactions. On the other hand, the elastic continuum nature of LC gives rise to the destabilization of BPs. As a result, BPs are usually found to appear in a narrow temperature range (sub- to few Kelvin), hence hindering their applicability. Thermodynamic disruption of a cubic BP always leads to an increase in total free energy, and thereby decreases the stability of the system. It is noteworthy that there are two primary theories to describe the formation of

BPs: (i) Landau-de Gennes theory, in which the free energy is characterized by the order parameter, was developed by Brazovskii and Dmitriev [16], Hornreich and Shtrikman [17], Kleinert and Maki [18]. Though we will not give the introduction to the Landau-de Gennes theory in this review, more detailed accounts can be founded elsewhere [19–22]; (ii) Defect theory, developed by calculating the free energy of a disclination and its vicinity, was established by Meiboom et al. [23]. The total free energy of a disclination with unit length is given by:

$$F = F_{\mathrm{e}} + F_{\mathrm{disc}} + F_{\mathrm{intf}} = (F_{\mathrm{bulk}} + F_{\mathrm{surf}}) + F_{\mathrm{disc}} + F_{\mathrm{intf}}, \tag{9.4}$$

This expression comprehends the free energy of the disclination and the surrounding DTCs. As mentioned previously, the first term F_{e} includes deformations exerted in the bulk as well as at the interface. In this case, it is the integral taken over the surface of DTCs encircling an S = −1/2 disclination:

$$F_{\mathrm{surf}} = \frac{1}{2}(k_{22} + k_{24}) \int \left[\left(\vec{n} \cdot \vec{\nabla}\right)\vec{n} - \left(\vec{\nabla} \cdot \vec{n}\right)\vec{n} \right] \cdot d\vec{S} = -\frac{\pi}{2}(k_{22} + k_{24}), \tag{9.5}$$

The negative sign discloses that this is the segment which could lower the total free energy. The second term F_{disc} comes from the excess free energy of the disclination core. When the temperature T is close to the clearing point T_c, this term can be written as:

$$F_{\mathrm{disc}} = a(T_c - T)\pi R^2, \tag{9.6}$$

where the coefficient $a \sim 8$ kJ/m^{3}K can be estimated from the latent heat of the isotropic-cholesteric transition, and R is the core radius, generally estimated to be around 10 nm. It is apparent that a decrease in temperature would raise the free energy. The last term F_{intf} describes the contribution of the interfacial energy between the isotropic liquid (disclination) and the Chiral Liquid Crystal (CLC), given by:

$$F_{\mathrm{intf}} = 2\sigma\pi R, \tag{9.7}$$

where σ denotes the surface tension of the disclination. Further estimation through (i) approximating the S = –1/2 disclination of the BPs within a cut-off radius $R_{\max}$ to its nematic analogue; (ii) assuming $k_{11} = k_{22} = k_{33} = k$ and $k_{24} = 0$, the total free energy is thus:

$$F = \frac{\pi}{4} k \ln(R_{\max}/R) - \frac{\pi}{2} k + a(T_c - T)\pi R^2 + 2\sigma\pi R, \tag{9.8}$$

Herein, $R_{\max}$ is on the order of the distance between disclinations, approximately 100 nm. The disclination term F_{disc} is the only directly temperature related term, explaining why BPs are constrained in a very narrow temperature range.

9.3 Expansion of Temperature Range of BPs

Based on the defect theory, restraining the mesogenic interactions inside the disclinations is the key to preventing BP from structural breakdown. In a pristine BP, heat keeps the defects in the isotropic liquid state. However, the thermal energy would become insufficient as the ambient temperature moves out of the extremely narrow BP range. An effective measure would be to introduce solid nanostructures to separate the mesogenic molecules enclosing the defects. Luckily, since the defects can act as potential wells in the system, these impurities are trapped spontaneously in the defects. In the past few years, candidates including nanoparticles [24–26] and polymer network [27] were demonstrated to stabilize BPs either experimentally or theoretically [28–30]. Such stabilization raises not only the tolerance of thermal variation to a higher level but also the electro-optic threshold of lattice deformation [25] and phase transition to the cholesteric phase [31]. To date, the effect of nanoparticles on BP range broadening is still found to be finite. This might result from mobility of nanoparticles, thus the stabilization of the disclinations is not sufficient.

During the early 90s, Kitzerow et al. had stored the textures of three distinct BPs, respectively, in dense crosslinked networks, i.e. 100 % polymer [32]. Nonetheless, the electro-optic tunability is completely lost since they are no longer in the mesophases. Ten years later, the concept of polymer-stabilized blue phase (PSBP) was demonstrated by Kikuchi et al. [27], which has now become a widespread approach in this field. The first demonstration showed the presence of BPI over 60 K, paling the stabilization driven by nanoparticles. Unlike polymer-stabilized nematics and cholesterics which can be easily achieved by using only difunctional reactive mesogens, the reported prepolymer for PSBP consists of a mesogenic diacrylate RM257 and a non-mesogenic acrylate EHA, which are the key to the satisfied effect of stabilization. While the reactive mesogen could be dispersed homogeneously throughout the BPLC bulk, non-liquid crystalline monomer tends to diffuse to the isotropic liquid disclinations. Most of the polymer chains are thus formed in the defects. In subsequent development of PSBP, it was found that the acrylate EHA can be replaced by TMPTA, a non-mesogenic monomer having three functional groups, giving rise to a stronger polymer network [33, 34]. Some others argued that these successful recipes actually benefited from combining the difunctional crosslinker with a mono- or trifunctional one [35]. In contrast to nanoparticles, polymer network is firm and hardly mobile. This leads to a reproducible structure upon annealing from the isotropic phase. If the polymer is raised by up to 25 wt%, the PSBPLC could be peeled off resulting in a free-standing gel [36]. The gel is stretchable with reflection changing in color as a result of lattice distortion. Ojima et al. demonstrated that infiltrating a BPLC into a cast of randomly distributed polymer network could expand its temperature range [37]. This disclosed that

polymer stabilization can be done in both ways: either by generating crosslinked polymer chains in the disclinations or by having the disclinations match the network. Templating a BP is thus possible, and its pioneering case is accomplished by Castles et al. [38]. They washed out the nonreactive LCs and unpolymerized molecules from a PSBP, after which an achiral nematic was re-filled into the polymer template, yielding an extremely wide BP span from −125 to 125 °C.

Besides filling up the disclinations of BPs, according to Nakata et al. [39], doping a achiral bent-core mesogen P8PIMB in a chiral nematic gave rise to the existence of a BP, and the corresponding temperature range got widened as the concentration of bent-core mesogens was increased. Both Coles' and Takezoe's groups have reported on the observations of BPs ranging up to 40 K in bimesogens (mesogenic dimers) [40, 41]. Since the director field of the S = −1/2 disclination represents the splay-bend deformation, coincidentally matching the feature of flexoelectric mesogens in an electric field; and, both bent-core mesogens [42] and bimesogens [43] are highly flexoelectric. It was suggested that the observed high thermodynamic stability resulted from the introduction of localized flexoelectric polarization [44]. Others correlated the temperature range of BPs to the elastic coefficients via experiments [45]. By replacing a fraction of the calamitic nematic host of the BPLC with a bent-core mesogen, k_{11} (splay) was elevated while k_{33} (bend) declined. With a decrease in the proportion of k_{33} to k_{11}, the thermodynamic stability of BP was improved. An impressive progress was observed when k_{33} is smaller than k_{11}, which matched the theoretical predictions [46, 47]. This was also confirmed experimentally by Shibayama et al., adopting a dendron to modulate the elastic properties [48]. According to Fukuda et al. [47], the temperature range can be estimated by extending Meiboom's defect model with an additional term describing DTC's elastic energy, given by:

$$\Delta T = \frac{k}{8aR_{\max}^2} \exp\left(\frac{2k_{11} + 0.5k_{22} - 0.50k_{33}}{k} - 1\right), \tag{9.9}$$

where k, originating from the first term (F_{bulk}) of (9.8), has been reassumed as:

$$k = \frac{1}{2}(k_{11} + k_{33})\left[1 - \frac{25}{72}\left(\frac{k_{11} - k_{33}}{k_{11} + k_{33}}\right)^2\right], \tag{9.10}$$

A broadened BP range could arise from the enlarged k_{11} and k_{22} (twist) as well as shrunk k_{33}. This is in line with the numerical findings based on a modified Landau-de Gennes theory [49]. The stability of BP with reference to the bending angle of the bent-core molecule has been investigated by Zheng et al. [50]. It was found that the more the molecule bends, the wider the range extends. Also, we demonstrated the bent-core molecule induced BP stabilization by means of light-activated trans-cis isomerization. The photoresponsive BPLC employed consists of 5 wt% non-mesogenic azobenzene 4MAB. Without any external stimuli, the

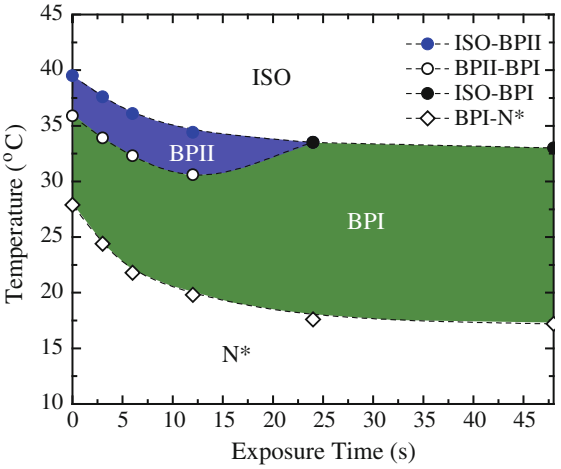

Fig. 9.4 Phase sequence of the 4MAB-dyed BPLC against the violet exposure time

azo-dye would exist at its trans form. Under 20 mW/cm^2 violet irradiation at λ_{pump} = 404 nm, the dye molecules began to undergo a conformation change from the linear trans form to the bent cis form. The medium eventually reach a cis-dominant equilibrium state at around 45 s. Figure 9.4 shows that the BP range had expanded by ~36 % from 11.6 to 15.8 K. The boomerang-like molecular structure of the cis isomer is believed to account for the observed widening of the temperature range. The prolonged relaxation time of the metastable cis-4MAB with the absence of the illumination enables the maintenance of the widened state for several hours. Additionally, the cis-to-trans back-isomerization can be accelerated by exposure to green light. Similar isomerization-induced range expansion had also been discovered [51].

Kishikawa et al. discussed that digging into the molecular design of the chiral additives is quite promising for BP range expansion [52]. Another measure that could be taken into account is to use hydrogen-bond based complexes, either by exploiting their flexible intramolecular bridging [53] or the generation of intermolecular twist [54]. The world record was set by a cyclosiloxane-based polymeric system which possesses a stable BP over 324.5 K ranging from 150 to −174.5 °C [55]. Nowadays, plenty of materials have been found to exhibit wide-ranged BPs, hence, offering ease of conducting fundamental study and creating possibility for use in applied optics. For example, large thermal hysteresis arises at the transition point between a BP and another mesophase in the materials having wide-ranged BPs [56]. This has found applications in bistable light shutter and reflective display [56, 57]. A detailed discussion on the molecular engineering of BPLC can be found in a recent review [58]. BPs have also been discovered in smectics [59], discotics [60] and metallomesogens [61].

9.4 Photonic Crystal Structure and Lattice Orientation

Abundance of valuable investigations on the photonic bandgaps in BPs was conducted in the 80s. As stated earlier, periodically intertwined DTCs and disclinations make BPLC form a cubic photonic crystal. While BPI is O^8 body-centered cubic (O^{8+} for the DTC packing and O^{8-} for the defect structure [13]), BPII has O^2 simple cubic. The photonic band structure of a BP can be calculated by solving Maxwell's equations for transverse waves in a director field structure constructed by the Landau-de Gennes theory [14, 62]. The simulation results indicate no full bandgap in BPs. Submicron-scaled lattice spacing (around 200–300 nm) gives rise to visible color reflection which satisfies the Bragg's law [13, 63–65], and the corresponding wavelength λ with respect to the lattice plane (hkl) can be estimated by the following equation [66]:

$$\lambda_{hkl} = 2nd_{hkl} \cdot \cos\theta = \frac{2na \cdot \cos\theta}{\sqrt{h^2 + k^2 + l^2}}, \tag{9.11}$$

where h, k and l are the Miller indices, n is the average refractive index, d_{hkl} denotes the interplanar spacing, a represents the lattice constant, and θ is the angle between the light incidence and the crystallographic direction [hkl]. By the cubic symmetry, all the directions in $\langle hkl \rangle$ are equivalent, and so are the planes in $\{hkl\}$. Figure 9.3 (cf. Sect. 9.2) implies that the size of a unit cell is different regarding the two BPs. The lattice constant corresponds to a cholesteric pitch in BPI (Fig. 9.3e) but half of a pitch in BPII (Fig. 9.3g).

Figure 9.5 presents the Bragg reflection of a BPLC examined under a polarizing optical microscope in the reflection mode (R-POM). Compared with a one-dimenstional (1D) cholesteric LC, the bandgaps of BPs are spiky and narrow with typical bandwidths ranging from 10 to 30 nm [5, 40, 67]. Consistent with the X-ray diffraction results from classic atom-based crystals, the Bragg's condition holds true for the selective reflection in primitive cubic crystals (BPII), while body-centered cubic crystals (BPI) must follow both the Bragg's and another selection rules resulting from the extra scattering centers, i.e. lattice points at unit-cell centers [64]. Forbidden reflection takes place at planes with the summation of the Miller indices, $h + k + l$, equal to an odd number, so the selective reflection occurs only at the summation with even number such as at {110}, {200}, and {112} [63]. Their cubic lattice nature can as well be revealed by measuring the Müller matrix [68] and Kössel diagram [69]. The Kössel diffraction technique is normally implemented by irradiating an electron- or proton-beam to excite X-rays from a single crystal. The resultant diffraction pattern provides clues to determine the crystal structure, such as the Miller indices and the crystallographic direction. However, for a photonic crystal like BPLC or colloidal crystal, visible monochromatic light can be used as the incident beam source. By applying the conventional R-POM setup [70], the back-scattered light would form a ring pattern on the focal plane, and each Kössel ring represents a lattice plane in the examined BP single crystal. Information including

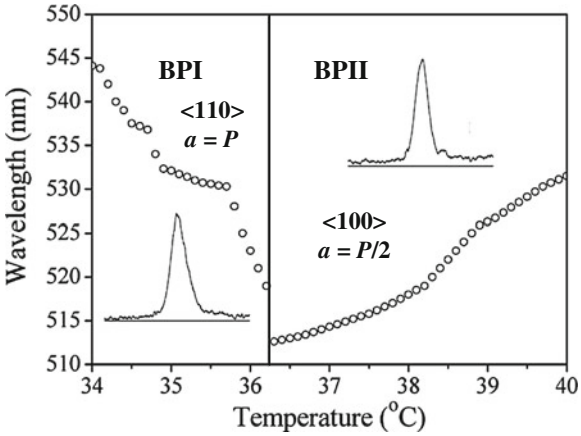

Fig. 9.5 Selective reflection wavelengths and sample spectra (*inset*) of cubic BPs against the temperature

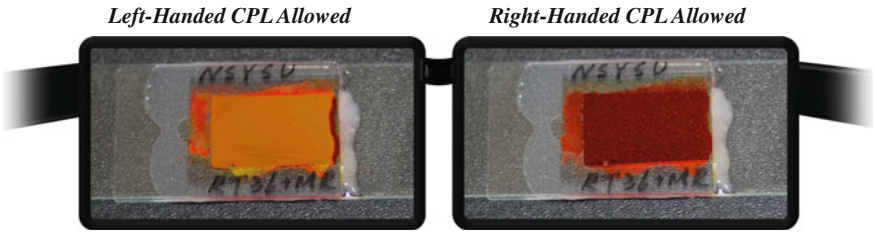

Fig. 9.6 Photographs of a S811-based BPLC sample seen through a pair of 3D glasses (circular polarizers with reverse handedness). **CPL* circularly polarized light; *the *red color* came from the addition of methyl red

crystal orientation and lattice spacing can be collected through in-depth Kössel analysis [60, 69–72]. Aside from those Bragg scattering detections, the periodic structures of BPs have been observed directly by means of transmission electron microscopy (TEM) [73], atomic force microscopy (AFM) [60] and confocal laser scanning microscopy (CLSM) [74]. Owing to the chiral nature, BPs interact directly with circularly polarized light having the same handedness with the helix [62, 65]. Putting on a pair of circularly polarized 3D glasses allows one to inspect the polarization dependency by closing one eye at a time, as demonstrated in Fig. 9.6.

As has been observed [67, 75, 76], a BP platelet usually grows with facets possessing sharp edges and corners at the very beginning. It then gets rounded and finally meets other domains. This behavior distinguishes BP from other mesomorphic phases, which normally form spherical droplets. Speaking of BP lattice orientation in a confined geometry, it depends strongly on where the nucleation occurs [77]. Upon cooling from the isotropic phase, homogeneous nucleation, i.e. BP nuclei sprout up in the bulk, would finally lead to randomly oriented platelets.

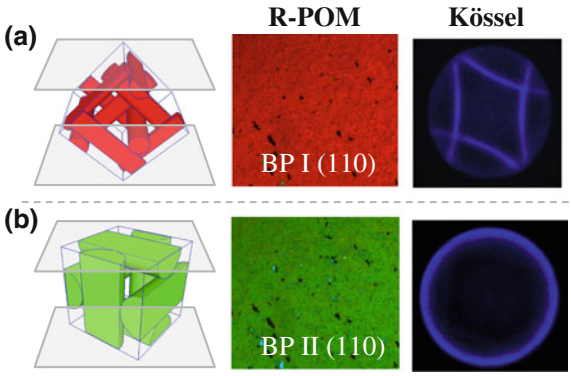

Fig. 9.7 Platelet textures and Kössel patterns of **a** BPI and **b** BPII observed in a surface-treated sample

By contrast, orientational constraints are imposed on those grown from the glass substrates—heterogeneous nucleation. BPI crystallites are likely to have their {110} and {112} facets parallel to the substrate [67, 75, 78]. To gain further control of the orientation, it would be well-advised to conduct surface treatment on the substrate [63, 79, 80]. Lowering the surface free energy, especially the polar component, could help cast a quasi-monocrystalline BP presenting {110} in BPI and {100} in BPII as displayed in Fig. 9.7 [81].

When it comes to bulk effects, inter-mesophase transitions play an important role in determining the lattice orientation since, in liquid crystal phases, elastic interactions between two adjacent molecules are strong. In this regard, ⟨110⟩-oriented BPI crystallites could be acquired by cooling from the ⟨100⟩-oriented BPII [82]. Heating from the planar-textured cholesteric phase to BPI leads to ⟨100⟩-oriented crystallites exhibiting direct reflection from {200} [83]. Using BPLCs with negative dielectric anisotropy, similar cholesteric-BPI transition had been performed isothermally by applying a vertical electric field [78]. Reorientation of grown crystals and crystal growth from a biased isotropic liquid are two commonly seen phenomena originating from the breaking of spatial isotropy by an electric field. According to Pierański et al. [77], exerting a field E on a cubic BP single crystal of a dipole moment p would produce a torque $\Gamma = p \times E$. Since only the third-order nonlinearity contributes to the torque, it is thus:

$$\begin{aligned}\vec{\Gamma} &= \Omega A \sum_{i=1}^{3} \left(\vec{n}_i \cdot \vec{E}\right)^3 \left(\vec{n}_i \times \vec{E}\right) \\ &= \Omega A \left[E_2 E_3 \left(E_2^2 - E_3^2\right)\vec{n}_1 + E_3 E_1 \left(E_3^2 - E_1^2\right)\vec{n}_2 + E_1 E_2 \left(E_1^2 - E_2^2\right)\vec{n}_3\right],\end{aligned} \tag{9.12}$$

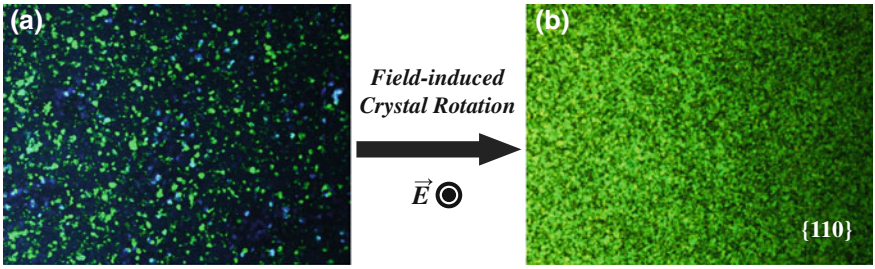

Fig. 9.8 Field-induced rotation of BPI crystallites from **a** random orientations to **b** ⟨110⟩//E. *Photographs taken at the field-off state

characterized by the crystal volume Ω, a material-related coefficient A [83] and unit vectors along the fourfold crystallographic axes n_m. Three possible conditions can be found in the equation to cancel the torque out: (i) $|E_1| = |E_2| = |E_3|$, i.e. ⟨111⟩//E; (ii) $|E_i| = |E_j|$ but $|E_m| = 0$, i.e. ⟨110⟩//E; (iii) $|E_i| = |E_j| = 0$ but $|E_m| \neq 0$, i.e. ⟨100⟩//E. They concluded that, in the case of $A > 0$ (attribute of general BPI and BPII), a BP crystal would be absolutely stable when orienting in ⟨100⟩ along the field, whereas the crystal aligns itself in ⟨111⟩//E if $A < 0$. ⟨110⟩//E is relatively unstable in both cases. This was in agreement with their close examination under R-POM. Similar conclusion was also drawn by Lubin and Hornreich [84] and by Dmitrienko [83] as they derived by minimizing the free energy under the influence of an electric field. Using a dielectrically negative BPLC, Heppke et al. had demonstrated an evolution of BPII-monocrystal rotation from ⟨112⟩ through ⟨110⟩ to ⟨100⟩ [71]. However, employing different materials, occurrence of ⟨110⟩//E in BPI has been observed [66, 85]. Figure 9.8 demonstrates the crystal rotation to ⟨110⟩//E in a BPLC having positive dielectric anisotropy. Moreover, biasing also helps shaping the polyhedral BP crystallites during the nucleation process [86]. This results from the competition between respective propagation of the lateral facets with reference to the field direction. The growth rate of a facet greatly depends on the phase (BPI or BPII), the type of the facet {hkl} and the strength of the field.

9.5 Phase Identification of BP

In most cases, cubic BPs can simply be recognized by the appearance of colored platelets under polarizing optical microscope (POM) [40], while BPIII, the fog-like phase, shows extremely weak reflection and scattering, which makes its identification relatively hard [51]. Precise phase identification of cubic BPs is often carried out in conjunction with certain supplementary approaches like Kössel diagram and reflection/transmission spectrum. Herein, a typical phase sequence of BPLC is demonstrated in Fig. 9.9 [87]. Cooling from the isotropic liquid, blue platelets and some invisibles nucleated and finally filled up the bulk. Using monochromatic light

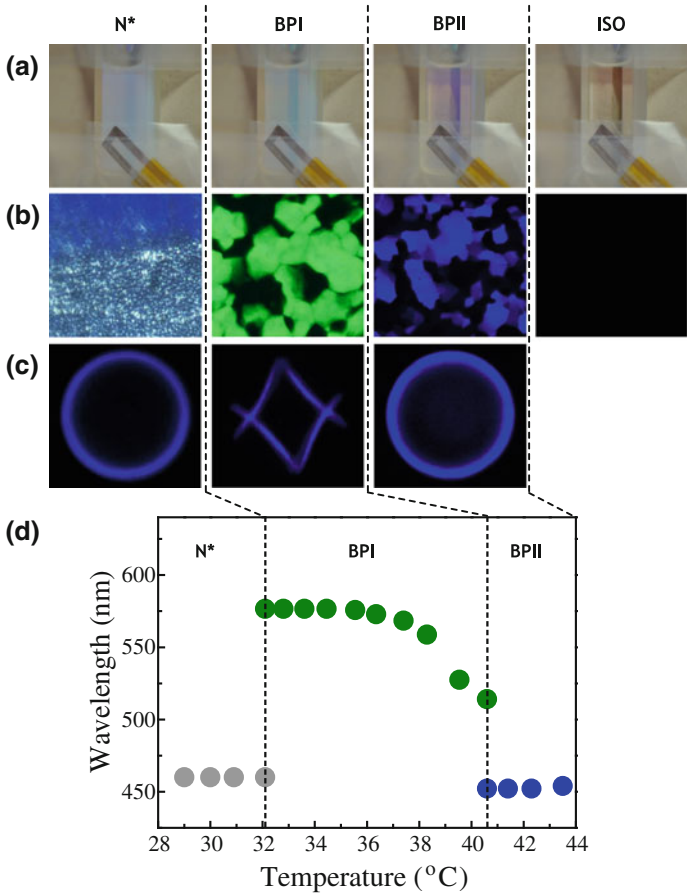

Fig. 9.9 Phase sequence of a BPLC—LK-40 [86] identified by means of **a** naked-eye macroscopic observation, **b** polarizing microscopic observation, **c** Kössel diagram and **d** selective reflection wavelength

at λ_{probe} = 440 nm to detect the Kössel diffraction pattern of a blue platelet, a circle was shown indicating an orientation of ⟨100⟩ in BPII [71]. This conjecture was confirmed by matching the examined reflection wavelength with the theoretical estimation from (9.11): $\lambda_{BPII\{100\}} = 2{\cdot}n{\cdot}a{\cdot}(h^2 + k^2 + l^2)^{-1/2} = n{\cdot}P{\cdot}(1^2 + 0^2 + 0^2)^{-1/2} = \lambda_N{}^*$, where $\lambda_N{}^*$ is the central reflection wavelength from the planar cholesteric. On further cooling to 40.7 °C, green platelets emerged and subsequently swallowed up the blue ones, leading to a jump of the reflection wavelength. The diffraction ring pattern disappeared to be replaced by four interwoven curves. These clues suggest a phase transition to BPI [5, 70]. The four Kössel lines represent four of the lattice planes in the {110} family viewed along the ⟨110⟩ axis. Finally, the cholesteric phase appeared on cooling, with the coexistence of planar and focal conic

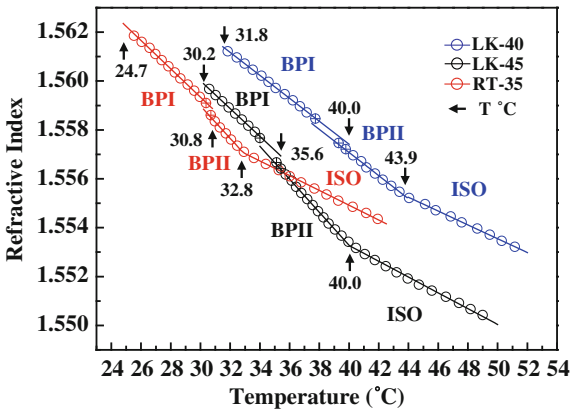

Fig. 9.10 Temperature-dependent refractive index in BPLCs—LK-40, LK-45 and RT-35. **ISO* denotes the isotropic phase

Table 9.1 Temperature dependence of the three BPLCs' refractive indices in BPI, BPII and ISO

BPLC	*dn/dT* of BPI ($°C^{-1}$)	*dn/dT* of BPII ($°C^{-1}$)	*dn/dT* of ISO ($°C^{-1}$)
LK-40	$-0.00049\ (\pm 2\times 10^{-5})$	$-0.00053\ (\pm 5\times 10^{-5})$	$-0.00029\ (\pm 7\times 10^{-5})$
LK-45	$-0.00044\ (\pm 3\times 10^{-5})$	$-0.00059\ (\pm 3\times 10^{-5})$	$-0.00032\ (\pm 2\times 10^{-5})$
RT-35	$-0.00057\ (\pm 1\times 10^{-5})$	$-0.00069\ (\pm 2\times 10^{-5})$	$-0.00034\ (\pm 4\times 10^{-5})$

textures. The characteristic Kössel pattern of a planar cholesteric, composed of superimposed spiral arcs, is also displayed.

Phase sequence of a BPLC could be identified by measuring its physical properties as a function of temperature including refractive index [87], density [88], elasticity [89], viscosity [89], heat capacity [89, 90], permittivity [91] and optical rotatory power (optical activity) [51, 92]. Quantitative characterization of these properties and their temperature dependency also help develop high-performance BP devices for advanced photonic applications. Figure 9.10 plots the temperature dependence of average refractive index in three BPLC sub-phases. As expected from its principal dependence on the density, the index change (*dn/dT*) in an identical phase is linear and negative. Just like other liquid crystalline phases, Table 9.1. reveals that the gradients in BPs are steeper than the isotropic phase. In the aspect of density-dependent index, this agrees with the Demus et al.'s investigation on the density of another BP system [88]. It is obvious as well that BPII shows a larger magnitude of the index slope than BPI, which might result from the lattice structure related thermal expansion coefficient. Speaking of phase transition, a smooth and continuous change of the index gradient suggests a second-order transition, from isotropic to BPII, whereas a jump in the refractive index within the region of coexistent BPII and BPI indicates a weakly first-order transition. These results are in line with the calorimetric study [89] and the dielectric behavior [91].

9.6 Control of BP Photonic Bandgap

As a soft photonic crystal, BPLC features remarkable bandgap tunability over wide range in response to different external stimuli. By varying the chiral fraction of a mixture, the lattice constant and the resultant spectral position of reflection can be predetermined [93]. Dynamic in situ bandgap tuning has been carried out effectively by exertion of heat [3], pressure [94], stress [36], bias [95], light [96], etc. According to (9.11), selective reflection is subject to both refractive index and lattice constant change (close relationship to the cholesteric pitch), factors which usually exhibit strong temperature dependency. In most of the cases, the bandgaps redshift with declining temperature within BPI, whereas the BPII bandgaps either stay constant or blueshift slightly (cf. Fig. 9.9). However, there are exceptions [40, 54, 92]. Also, while cooling a surface-treated sample, the reflected color normally suffers a sharp blue shift within BPII and gets pinned over the entire BPI range [3, 81]. According to Pollmann et al. [94], varying the pressure is equivalent to the control of density, so the resultant behavior resembles its thermal counterpart in phase sequence and bandgap shifting. All of their materials showed that pressurizing a BP would redshift the reflection or give rise to phase transition to a lower-chirality state, e.g. BPII to BPI. In terms of mechanically driven band gap tuning, Castles et al. recently demonstrated color change in selective reflection by stretching a free-standing BP gel [36]. As depicted in Fig. 9.11, under lateral stretching, the interplanar spacing along the surface normal would be condensed, thereby leading to blue shifted reflection.

Thus far, the most complex but functional way of controlling the selective reflection would be to apply an electric field. The field-induced effects include local director reorientation, lattice distortion, phase transition and crystal reorientation [95]. Local director reorientation is actually the fundamental of transmissive BP

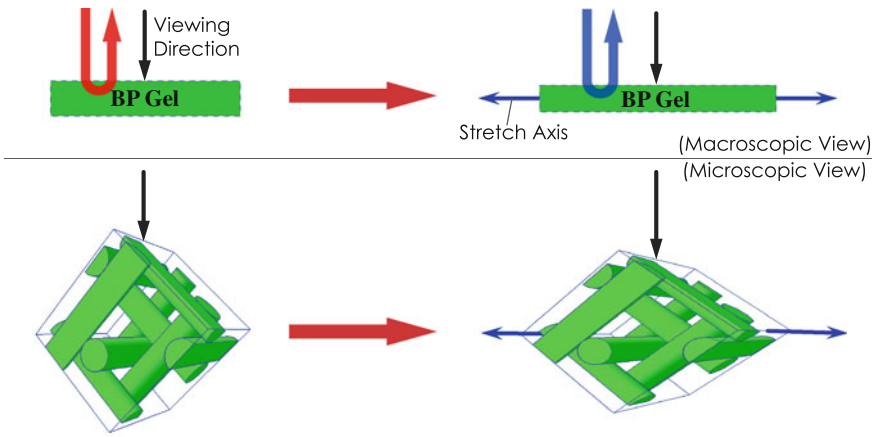

Fig. 9.11 Schematic depiction of stretch-induced bandgap shifting in a BP gel

displays (cf. Sect. 9.7). Biasing a BPLC makes mesogenic molecules tilt towards or away from the field axis depending on their intrinsic dielectric anisotropy. Since no structural change takes place, a reduction (rise) in effective refractive index along the field axis would cause a blue shift (red shift) of bandgaps in a dielectrically positive (negative) BPLC. However, lining the molecules up also indicates breaking of the DTCs and the corresponding periodicity of index distribution, bringing about a reduction in reflectivity. Because of the tightly wound director arrangement, such switching generally responds on the submillisecond scale, much faster than typical nematics (tens of milliseconds) [97]. Local reorientation is more likely to occur in a PSBP than a pristine BP in that polymer network could assist in preserving the cubic symmetry of the lattice from structural change like lattice distortion or phase transition [98].

The second possible response to the applied field is deformation of the lattice—the so-called electrostriction. This effect involves diffusion of molecules (flow reorientation), which in turn gives rise to noticeable and continuous change of crystal structure. Heppke et al. were the first to demonstrate electrostriction in cubic BPs [99]. Together with field-induced phase transition, they also presented the evolution of change in selective reflection from blue (BPII) through green (BPI) to red (BPI). Figure 9.12 summarizes the electrostriction behavior under various conditions concerning phase, crystal orientation and the sign of dielectric anisotropy [71, 72]. In BPII, the lattice would be stretched along the field axis if the intrinsic dielectric anisotropy is positive, while compression occurs in a negative one. As a result, the reflection shifts substantially towards the opposite end of the spectrum with respect to its local reorientation counterpart. Recently, the photonic band structure of the deformed BPII having $\langle 100 \rangle // E$ has been calculated [100]. The electrostriction in BPI seems anomalous in that the lattice distortion depends strongly on the crystal orientation with respect to the field axis. The $\langle 110 \rangle$-oriented

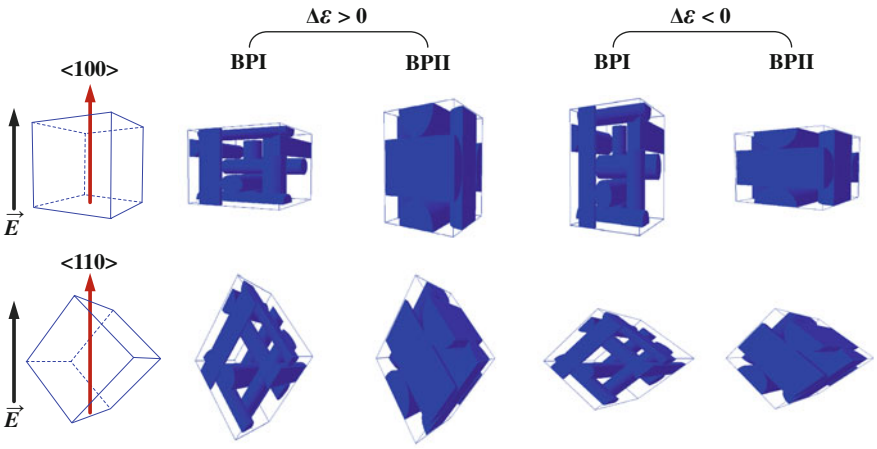

Fig. 9.12 Schematic depiction of electrostriction in cubic BPs

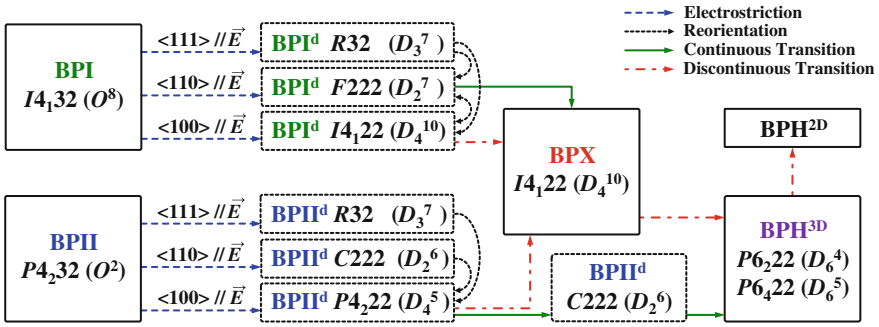

Fig. 9.13 Flow chart of possible crystal structures upon electrostriction or phase transition [95]

BPI lattice acts in the same manner as in BPII. However, in the case of ⟨100⟩ BPI// *E*, the interplanar spacing on the axis parallel to the field would shrink (extend) if the material is dielectrically positive (negative). Figure 9.13 outlines the structural change in terms of space group [95]. Under electrostriction, the crystal structure of BPII is distorted from cubic P4$_2$32 (O^2) to tetragonal P4$_2$22 (D_4^5) if ⟨100⟩//*E*, orthorhombic *C*222 (D_2^6) if ⟨110⟩//*E*, and trigonal *R*32 (D_3^7) if ⟨111⟩//*E*. In BPI, the crystal structure changes from cubic *I*4$_1$32 (O^8) to tetragonal *I*4$_1$22 (D_4^{10}) if ⟨100⟩// *E*, orthorhombic *F*222 (D_2^7) if ⟨110⟩//*E*, or trigonal *R*32 (D_3^7) if ⟨111⟩//*E*. To explain these experimental findings, Dmitrienko [84] and Trebin et al. [101] had modeled the lattice distortion of BPs from the theoretical aspects. Besides local reorientation, electrostriction often accompanies torque-induced irreversible crystal reorientation (cf. Sect. 9.4) as well [66]. Figure 9.14 gives a demonstration of two effects occurring simultaneously in BPI, namely distortion-induced redshift in reflection and crystal reorientation to ⟨110⟩//*E*. Field-driven dramatic change of reflectivity and subtle shift of color in BPIII has been frequently discussed in conjunction with the lattice distortion in cubic BPs. In general, strengthening the applied field would enhance (attenuate) the intensity and blue shift (red shift) the wavelength of BPIII reflection in a dielectrically negative (positive) BPLC [102]. Furthermore, such switching is thousand times faster than the electrostriction in BPI and BPII, tens of millisecond as opposed to tens of seconds [83].

Exerting an electric field stronger than that causing the aforementioned effects could possibly generate new BPs [69, 102, 103], namely: tetragonal BPX (BPE$_a$), three-dimensional hexagonal BPH^{3D}, two-dimensional hexagonal BPH^{2D} (BPE$_c$), and some undetermined BPE phases, where E stands for Electric field. Figure 9.13 depicts the possible BP-BPE transitions in response to the applied field [95]. In some of the transitions, the color (bandgaps) shifts continuously and so the corresponding Kössel diagram is essential for precise identification. The effects of molecular dielectric anisotropy have been summarized [95]. Decreasing the temperature toward the low end of the BP range can reduce the threshold for field-induced phase transitions to cholesteric and nematic [103]. Considering the molecular dielectric anisotropy, transition from the BP to a planar (focal conic)

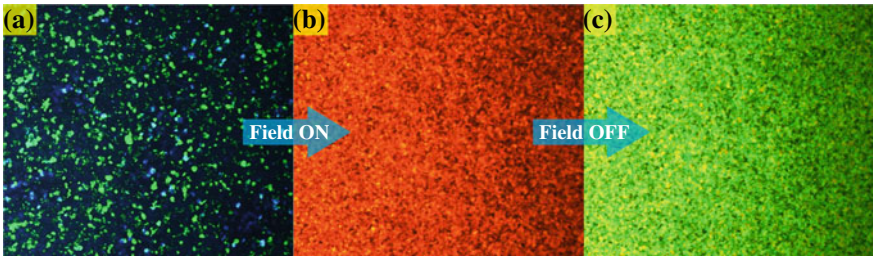

Fig. 9.14 Progression from **a** the initial state (randomly oriented platelets) through **b** the field-on state (simultaneous electrostriction/crystal reorientation) to **c** the relaxed state (uniformly oriented platelets)

cholesteric phase could be observed in dielectrically negative (positive) materials, and direct BP-nematic transition only took place in dielectrically positive PSBPs and a few pristine ones. With the aid of a field-induced metastable cholesteric phase, Wang et al. have achieved a reversible switching from ⟨110⟩ to ⟨200⟩ oriented BPI in a dielectrically negative system [78]. On cooling from the isotropic phase to BPI, the resulting polycrystal normally shows a majority of ⟨110⟩ and ⟨112⟩ oriented platelets. Applying a weak field makes BPI transit to a planar cholesteric state, while a strong field would cause electrohydrodynamic instability leading to a turbulent state (Fig. 9.15a). The intermediate field-induced state determines the orientation of the crystal upon removal of the field: the BPLC relaxes back to ⟨200⟩-oriented BPI from the planar state and ⟨110⟩-oriented BPI from the turbulent state (Fig. 9.15b). It is noteworthy that almost all the effects respond nonlinearly to the electric field, i.e. Kerr effect ($\propto E^2$) [71, 77]. This is because the cubic symmetry of BPs (the class 432 crystals—BPI: $I4_132$; BPII: $P4_232$) eliminates the second-order susceptibility. Comprehensive discussion on the electric field effects on BPs has been documented [95].

Due to the tremendous amount of scientific work on photoisomerizable functional dyes over the past few years, photoresponsive BPLCs were recently developed at a rapid pace. Light-activated reaction is often considered superior to those thermal, electrical, chemical and mechanical means as it features local addressability, remote control and self-modulation. It is known that an azobenzene has two isomers: trans and cis. The isomerization could take place under effective irradiation, which is related to the wavelength and intensity of the excitation. In a dye doped chiral LC, such a conformational change of the azobenzene may exert one of the following three possible effects: disarrangement, variation in chirality and photo-alignment. In general, the trans-isomer is linear and the cis-isomer is bent in shape. So calamitic molecules prefer to align with the trans form, but its cis counterpart may upset the order of the LC matrix. Disordering the orientational order usually leads to a drop in the clearing point as well as other transition temperatures [96]. Accordingly, the LC transits isothermally to a phase originally existing at higher temperatures, e.g. BPII to the isotropic phase at 37 °C in the case

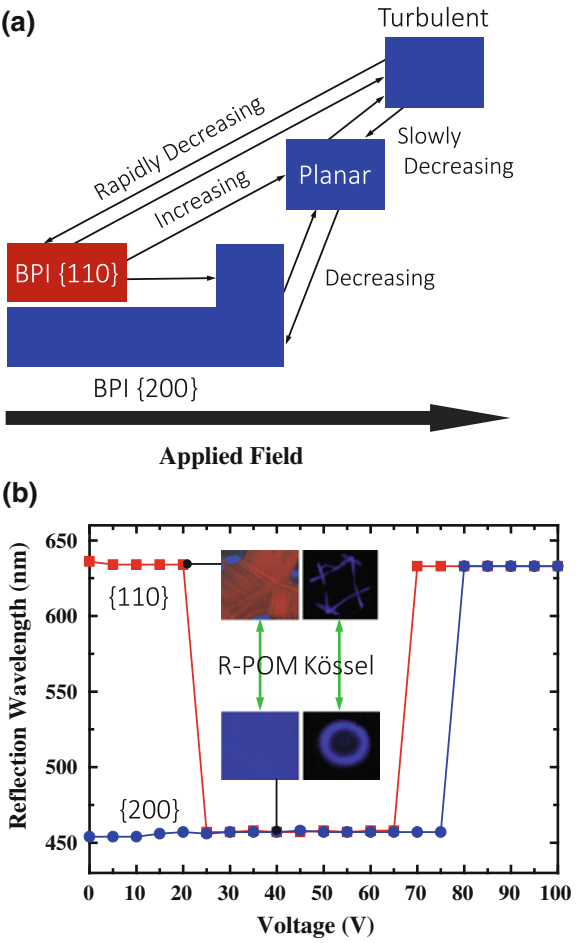

Fig. 9.15 Binary switching of crystal orientation in dielectrically negative BPI: **a** Driving scheme and **b** response to electrical pulses with different voltage

depicted in Fig. 9.4. Speaking of the photo-induced isotropic state, the findings from Lin et al.'s study on an azo-LC doped BP suggested that the isomerization might not utterly destroy the double-twist director arrangement [104]. The rapid laser-driven restoration to the colored platelet texture (within 120 ms) indicated that the photoisomerization just broke the cubic lattice structure into unorganized DTCs.

In contrast to electrostriction, photoisomerization-induced lattice expansion (or comprssion) is isotropic. Light-activated bandgap tuning over 100 nm was demonstrated in the supercooled BP (BPS) by Chanishvili et al. in their pioneering work on photoresponsive BPs [96]. Sharing the similarity of using achiral azobenzene, Liu et al. further confirmed the change of lattice spacing by Kössel diagrams [105]. So far, the largest tuning range in such systems, from red ($\sim$650 nm) to blue ($\sim$500 nm), was achieved by Chen et al. using azobenzene dimers [106]. A field-induced transition from BPI to the cholesteric phase was also observed. To

understand the underlying mechanism, Chanishvili et al. had investigated several BP mixtures regarding their optical tuning behavior and temperature dependence of the peak wavelength and bandwidth [96]. It was inferred that, in the achiral-azobenzene doped BPLCs, the photo-driven color shift of the stopband is a competition between the isomerization-induced variations in helical pitch and order parameter. Likewise, the pristine BPLC doped with a small amount of a chiral azobenzene gives rise to optically tunable bandgaps. The tuning range is governed by the difference between the helical twisting powers of the trans- and cis-isomers. Chiral bis(azobenzene) compounds, in particular, have frequently been employed to realize amazing phototunability in cholesteric LCs. In most cases, the twisting power at the cis state is weaker than that at the trans. Lin et al. were the first to perform bandgap tuning from ultraviolet through the entire visible spectrum to near infrared in a photoresponsive BPLC [81]. Figures 9.16 and 9.17 show that the selective reflection was invisible at the initial state. It was in fact a ⟨200⟩-oriented BPII crystal, confirmed by the Kössel diagram. Under violet irradiation at λ_{pump} = 408 nm, blue-colored platelets gradually came into view and subsequently turned aquamarine. Complementary Kössel and spectroscopic observations pointed to the occurrence of a continuous dilatation of the BPII lattice. More illumination would bring about a jump in reflection to green and a sudden change in Kössel pattern to interlaced curves from a ring, indicating a phase transition to {110}-oriented BPI. The tuning saturated at $\lambda_{BPI} \sim 720$ nm. On removal of the pump at any point in the phototuning process, the color ceased to change for several hours. Quick restoration could be carried out by green irradiation. Later, Jin et al. succeeded in demonstrating a continuous and reversible blue-to-red phototuning without any phase transition [107]. This was accomplished by doping a hydrogen-bonded chiral azobenzene into a BP mixture.

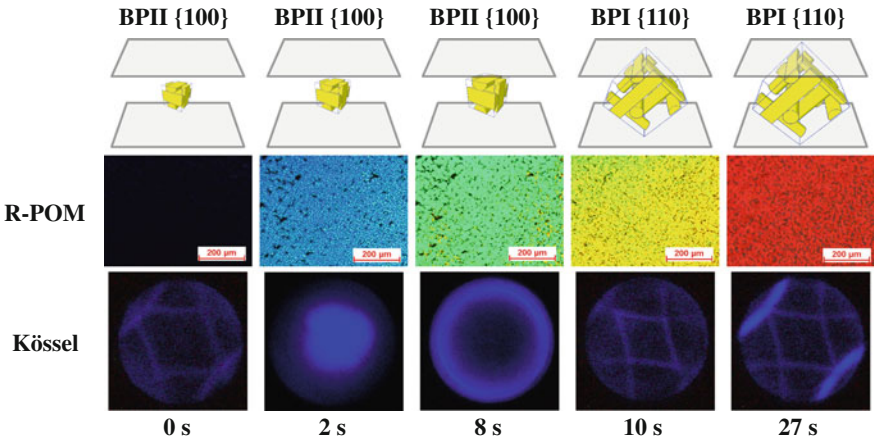

Fig. 9.16 Light-driven band gap tuning and phase transition: R-POM photographs and Kössel diagrams against the exposure time of violet laser (λpump = 408 nm)

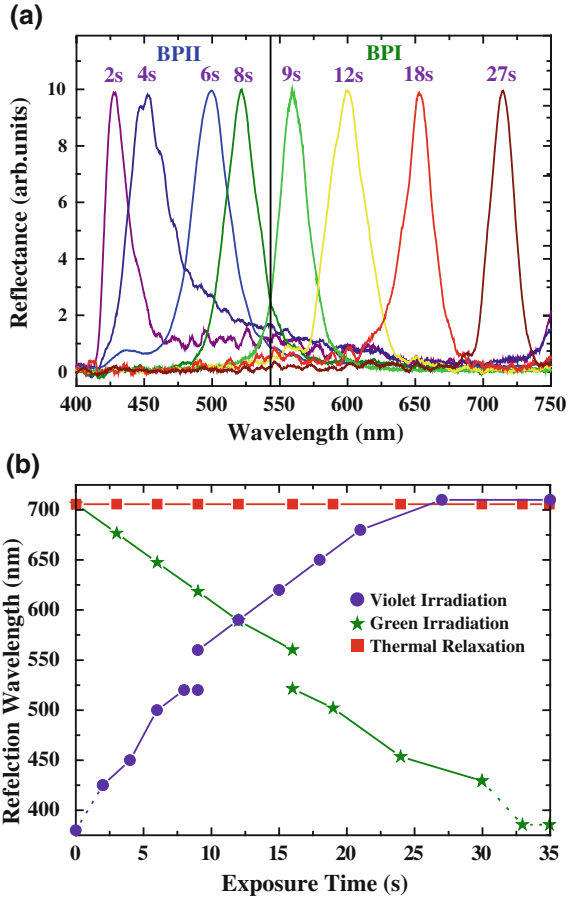

Fig. 9.17 Light-driven band gap tuning and phase transition: time dependence of reflection spectra and peak wavelength

As stated previously, surface anchoring could pin the lattice size to tolerate the variations in temperature. With the aid of methyl-red, Liu et al. photoaligned the dye doped BPLC to produce patterns of a thermal bandgaps (Fig. 9.18a) [3]. Figure 9.18 displays two different effects that both result in optically patterned BPI polycrystals: (a) bandgaps pinned by photoalignment and (b) band gaps shifted by variations of chirality and/or orientational order. It is noteworthy that, besides the bandgap tunability, some effort has gone into the development of phototropic BPLCs [96, 108].

In 2000, Etchegoin detected the presence of a stopband in BPI by measuring the emission spectrum of a dye doped sample [109]. A couple of years later, Cao et al. monitored the circularly polarized bandedge laser action in a single BPII crystal [110], emitting from the three orthogonal directions corresponding the ⟨100⟩-orientation of BPII crystal. This observation has encouraged the development of 3D

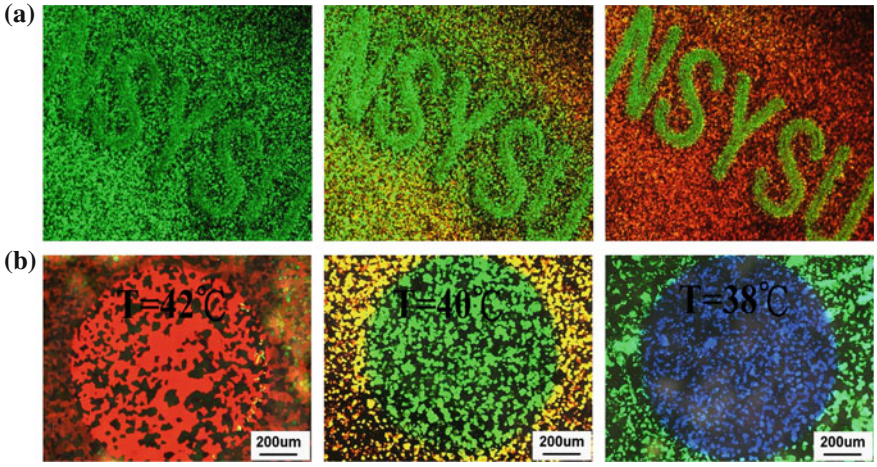

Fig. 9.18 Photo-patterned BP polycrystals: **a** optically pinned bandgaps (the word part) and **b** optically shifted bandgaps (the *circular* region)

tunable laser sources for integrated photonic circuit applications [104, 111]. Recently, Chen et al. observed the potential for dye doped cubic BPs to give off coherent random laser [112]. Much different from the bandedge lasing, interferences and recurrent multiple scattering arising from the grain boundaries in a BP polycrystal provides the optical feedbacks for such laser action. The platelet size, which can be easily controlled by the cooling rate, determines the mode stability of the random lasing (Fig. 9.19). Apart from lasers, sharp reflection peaks and fast director reorientation make BPLCs (especially PSBPs) promising for the use in full-color reflective displays [86, 95].

9.7 Optical Isotropy and Fast Electro-Optic Response

On the macro scale in BPs, the optical anisotropy of mesogen has been averaged in three dimensions by the tightly-wound director axis arrangement. This holds true for incident light satisfying at least one of the following conditions: (i) the handedness is opposite to the BP helices; (ii) the wavelength is not contained the stop band. In this regard, BP is optically isotropic. The bistable fiber-optic light valve proposed by Lee et al. [57] is an excellent example for the use of BP as an optically isotropic medium in the near infrared spectrum. As discussed earlier, birefringence could be induced under the influence of an electric field. BP is much different from the nematic LC in terms of electro-optic response. In nematic LC, the index changes as a result of bulk director reorientation, while the director axes in BP are orientated in a quasi-random manner inherently, indicating that no Fréedericksz transition exists. The field-induced index variation is thus the sum of local director

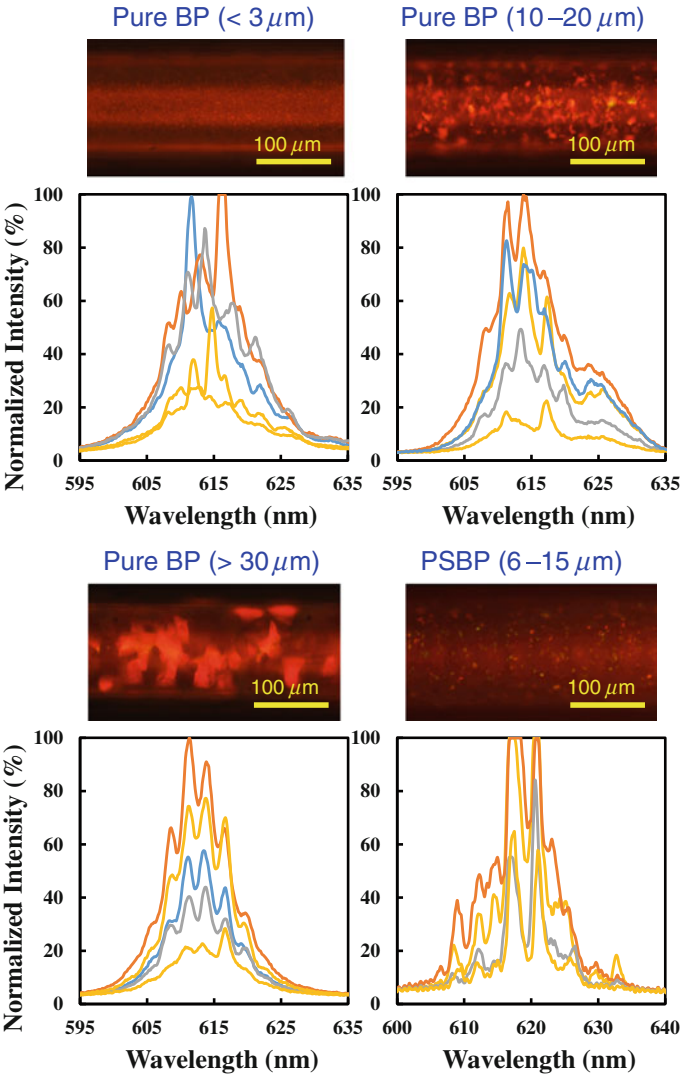

Fig. 9.19 Mode stability of random lasing in BPI under various conditions

reorientation. Such a change can be seen as the macroscopic deformation of an index ellipsoid from the isotropic sphere to anisotropic ellipsoid, where the optical axis is on the field axis. This offers considerable advantage for the design of polarization-independent optical elements. Moreover, in conventional PSBPs, prohibited molecular diffusion and associated disclination motion restrict the response to local director reorientation [98]. According to Gerber's model for the

relaxation time [97], the interaction length is on the order of the pitch P for the case of local reorientation. Therefore, the time constant τ can be estimated by the formula:

$$\tau = \frac{\gamma_1 P^2}{k(2\pi)^2}, \tag{9.13}$$

where γ_1 denotes the rotational viscosity, P is the pitch length and k is the effective elastic coefficient of the system (dominated by the twist deformation coefficient k_{22} from Kitzerow et al.'s derivation [83]). The response time, submilliseconds, is much faster than bulk reorientation of conventional nematics, i.e. tens of milliseconds. BPLCs are therefore considered as a promising alternative to nematics for electro-optic applications, including: gratings [113–115], lenses [113, 116], interferometric filters [117, 118], attenuator [119] and displays [86, 120, 121]. Most of these devices are made of PSBPs because the addition of polymer network could suppress the slow electrostriction effect (cf. Sect. 9.6) and enhance the thermal stability (cf. Sect. 9.3).

Figure 9.20 depicts the regular electro-optic response of BP [122]. The field-induced birefringence is defined as $\delta_n(E) = n_e(E) - n_o(E)$, where n_e and n_o are the induced extraordinary and ordinary indices respectively. Under a weak electric field, the index change is nearly in proportion to the square of the field strength, indicating a Kerr-like response. This is in accordance with the theoretical prediction that the second-order susceptibility vanishes in crystals of the class 432 and so the quadratic electro-gyration effect dominates the response. By continually increasing the field strength, the rising trend of induced birefringence gradually eases up and eventually leads to the saturation of induced birefringence. The deviation of δn from the Kerr fitting line may be caused by higher-order nonlinear effects. To fit well with the real response, Yan et al. modified the classical Kerr model:

$$\delta n = \lambda K E^2, \tag{9.14}$$

to a phenomenological one for BP [122]:

$$\delta n = \delta n_{\text{sat}} \left[1 - \exp\left(-\frac{E^2}{E_{sat}^2} \right) \right], \tag{9.15}$$

where K stands for the Kerr constant, δn_{sat} is the saturated index change and E is the saturation field. Gerber has generalized the relationship between the Kerr constant and the physical properties of the material [97]:

$$K \approx \frac{\Delta n \cdot \Delta \varepsilon \cdot \varepsilon_0}{k} \cdot \left(\frac{P}{2\pi} \right)^2, \tag{9.16}$$

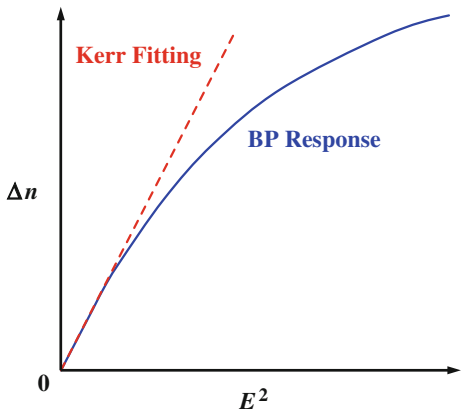

Fig. 9.20 Conceptual diagram: regular BP response and theoretical Kerr fitting of induced birefringence against the square of electric field strength

where Δn is the intrinsic birefringence, $\Delta\varepsilon$ is the dielectric anisotropy, while ε_0 is the vacuum permittivity, as aforementioned, k and P are the effective elastic coefficient and the cholesteric pitch, respectively. According to Choi et al. [123], the ratio of k_{33} (bend) to k_{11} (splay) is fairly influential to the coefficient k.

The Kerr constant directly affects the driving voltage of BP. Taking display as an example, the peak-transmittance voltage is inversely proportional to the square root of the Kerr constant. Besides the practicability, high driving voltage may bring about hysteresis, slow relaxation and residual birefringence. Herein, hysteresis is defined as the voltage difference at half-maximum transmittance in one cycle of increasing and decreasing field. These shortcomings primarily originate from electrostriction. Findings by Chen et al. [124] reveal that hysteresis and slow relaxation would emerge in pristine BPI as the voltage exceeds the threshold for lattice distortion, but not in BPII. When it comes to PSBP, though electrostriction is effectively restrained, the polymer network could still be deformed if the applied voltage is too high. It was reported that the electro-optic response of PSBP depends strongly on the polymerization and operating temperatures while almost independent on the phase on curing [125]. High curing temperature can reduce the driving voltage (Fig. 9.21a) as well as the critical field (Fig. 9.21b); meanwhile, the response time is prolonged. Figure 9.22a suggests that this is a consequence of weaker boundary anchoring caused by a looser polymer network. Taking the advantage of the curing temperature effect on the Kerr constant, Lin et al. designed a binary PSBP phase grating featuring polarization independency and fast response [114]. Similar relationship between network density and electro-optic response can be examined by varying the concentration of monomers [126]. While operating a PSBP close to its clearing point, the driving voltage rises significantly with increasing temperature (Fig. 9.22b). This is because both the dielectric and optical anisotropies are closely related to the order parameter. In addition, the hysteresis and residual birefringence are well suppressed in that the operating temperature is within the existing range of the pristine BP. Since the rising operating temperature diminishes the rotational viscosity, the relaxation process becomes faster (cf. 9.13)

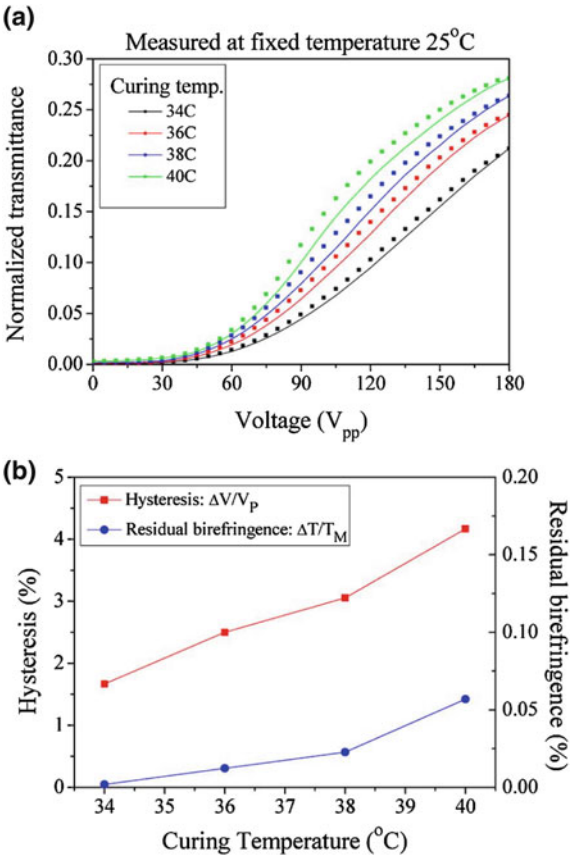

Fig. 9.21 **a** Voltage-dependent transmittance curves and **b** degrees of hysteresis and residual birefringence of PSBPs curing at 34 °C (BPI), 36 °C (BPI), 38 °C (BPII) and 40 °C (BPII)

[127]. The findings about the mode stability of BP random lasing indicate that the grain size and orientational uniformity are believed to play a crucial role in the stability of BP under the influence of external stimuli (cf. Fig. 9.19) [112]. Hysteresis can be seen as an outcome of an electrically disturbed BPs. Several reports have confirmed that both orientating and growing large platelets have positive impacts on the elimination of hysteresis [80, 128].

To reduce the driving voltage, researchers have been seeking for ways to enhance the Kerr constant over the past few years. One approach is to synthesize mesogens with large dielectric and/or optical anisotropies. However, achieving large dielectric anisotropy requires multiple polar groups, and high intrinsic birefringence indicates long molecular conjugation. BP compounds are hence bulky and viscous, which prolongs the response time and reduces the relaxation frequency [129]. Recently, a PSBP has been developed with $K \sim 33$ nm/V^2 and $\tau \sim 0.95$ ms, whose nematic host is JC-BP06 N, having $\Delta\varepsilon \sim 470$. Optimizing the recipe of the precursor, especially the mixing ratio of monomers, is also worth a shot [126, 130]. Since the Kerr constant is in quadratic proportion to the helical pitch P (cf. 9.16),

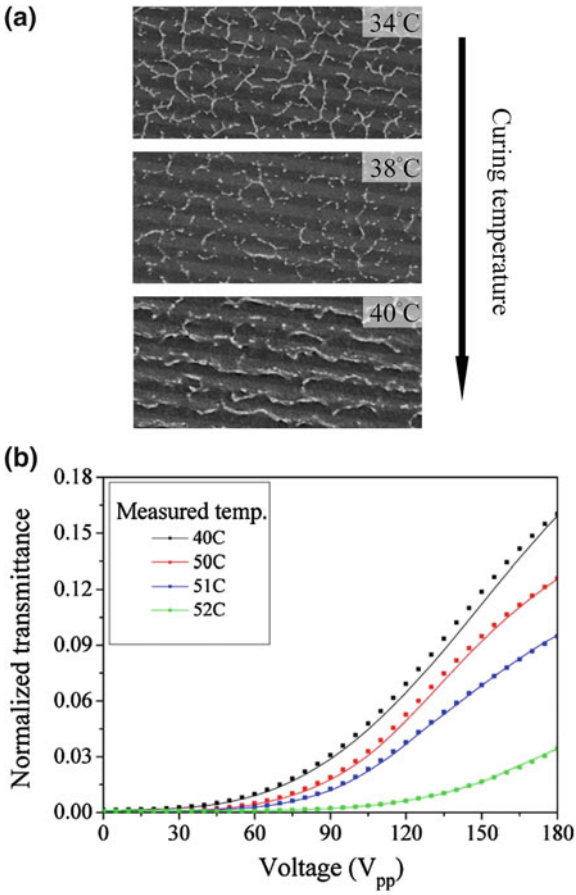

Fig. 9.22 **a** SEM images of the polymer networks formed at 34, 38 and 40 °C. **b** Voltage-dependent transmittance curves of the 38 °C-cured PSBP performed at 40, 50, 51 and 52 °C. *Tc = 53.2 °C

another strategy that could be taken is to shift the selective reflection from ultraviolet to visible [93]. By doing so, the optical rotatory power would be elevated [131], and the colored backscattering deteriorates the visual performance. To tackle the former problem, the included angle between the absorption axes of the crossed polarizers needs to be adjusted. But, replacing the linear polarizers by the circular ones could prove effective in avoiding both problems [132]. Aside from the Kerr constant, the design of electrode is as well essential to the resultant driving voltage. Considering normal incidence, an in-plane-switching (IPS) cell would generally be the first to pop up in mind because the induced birefringence would be parallel to the surface [133]. Due to its non-uniform field distribution and shallow interaction depth, the driving voltage is usually high and thus giving rise to hysteresis and residual birefringence. Several modified electrode structures [134–136] were proposed to improve the performance, while the difficulty of fabrication would be raised simultaneously. However, Jiao et al.'s design [135] implies the possibility of using a tilted vertical-field-switching (VFS) cell to modulate the polarization.

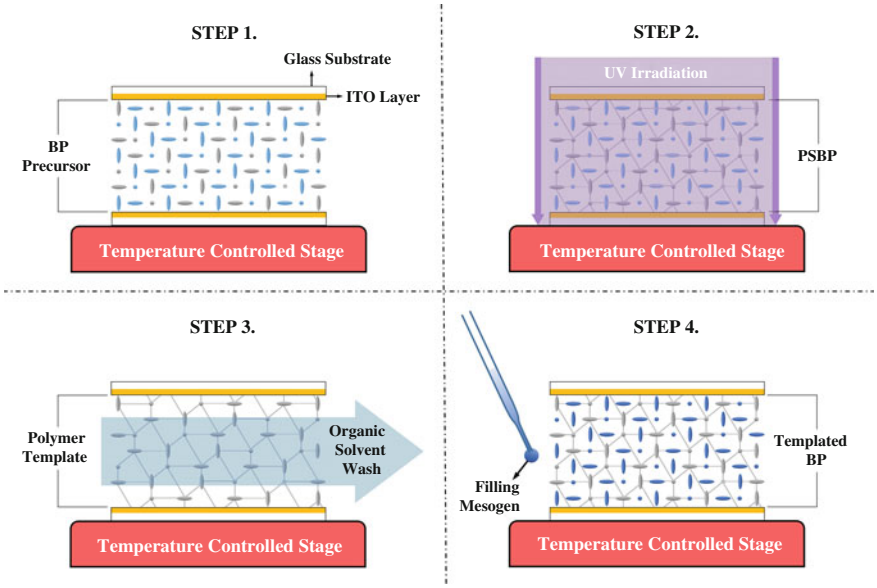

Fig. 9.23 Fabrication procedure of templated BP

In conjunction with a few external light-guiding layers, Cheng et al. demonstrated the first BP display driven by the VFS mode [120]. In VFS, the electric field could reach the entire bulk with a uniform field distribution. Their experimental data show high transmittance and low driving voltage in comparison with the IPS mode. The hysteresis and residual birefringence nearly vanished. Given the mature development of the operation modes for BP, many efforts were then shifted to embed BPLC in various display systems [86, 137]. The research and development on BP based LCDs have been documented in detailed discussions [34, 35, 138, 139].

Recently, the templating technique was applied to further improve the electro-optic performance of PSBP [140, 141]. Templated BP is usually fabricated by the following procedure (Fig. 9.23): (step 1) cooling or heating the precursor to a BP; (step 2) polymerizing the BP precursor; (step 3) removing the remaining chiral nematic, thereby obtaining a polymer film with the similar nanostructral with BP, that is so called BP polymer template; (step 4) infusing a mesogen into the polymer template. Using nematics as the filling material, both Lavrentovich's group [140] and Lin's group [141] discovered that the driving voltage dropped remarkably upon templating (Fig. 9.24a and 9.24b), but conflict arose from the response time (Fig. 9.24c). To find out the underlying mechanisms, Lin et al. correlated the electro-optic response to the chirality of the filling mesogen [141]. They concluded that the reduction of the driving voltage resulted not only from the enhanced optical and dielectric anisotropies, but also from the effect of elastic restoring force (ERF).

In a templated BP, the polymer cast compels the mesogenic molecules to orientate in the conformation of BP. An ERF is hence established owing to the

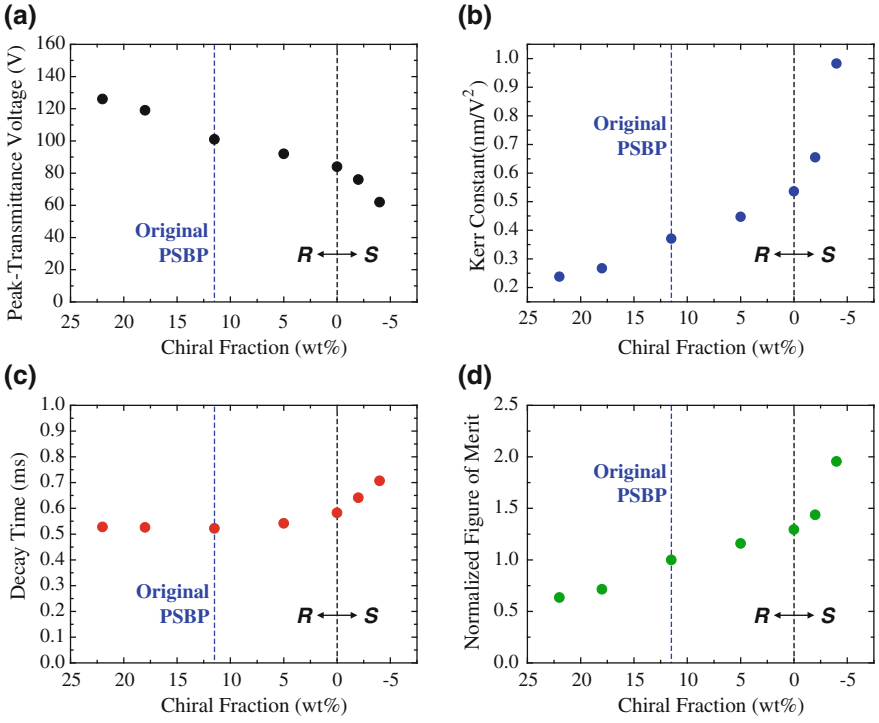

Fig. 9.24 **a** Peak-transmittance voltage, **b** Kerr constant, **c** decay time and **d** figure of merit (K/τ) against the chiral fraction of filling mesogen. **negative sign* of chiral fraction indicates that the filling mesogen has the opposite handedness to the original PSBP

chirality mismatch. The magnitude of the ERF is governed by both the twisting power and handedness of the filling mesogen relative to those of the original PSBP. When a voltage is applied, the ERF may help or hinder the electric field unwind the helical structure depending on the mesogen's chirality: (i) If the filling mesogen has the same handedness as that of the original PSBP but a shorter pitch, the ERF is exerted in the same direction as the polymer anchoring force. Thus, to acquire the same induced birefringence as the original PSBP, a stronger electric field is required to counteract the ERF; (ii) If the filling mesogen has the same handedness but a longer pitch, or even if it has no chirality (nematic), then the ERF acts synergistically with the electric field because the mesogen tends to be less twisted intrinsically; and (iii) If the filling mesogen exhibits reverse handedness, the ERF is even higher than that in the second situation due to the preferential twist in the opposite direction. If the ERF is exerted against the polymer anchoring force [situations (ii) and (iii)], they cancel each other out, leaving only the residual anchoring force to be resisted by the electric field. This phenomenon can cause a drop in the effective elastic coefficient k of the template BP system in comparison with the original PSBP (cf. 9.16). Similarly, k increases when both the ERF and the

polymer anchoring force are exerted in the same direction [situation (i)]. The exponential growth of the Kerr constant from filling achiral nematic to reverse handedness chiral nematic LCs implies that the ERF plays a key role in electro-optic response of templated BPs (Fig. 9.24b).

In general, the relaxation time is extended with the lowering of the driving voltage. However, such prolongation seemed not as obvious as expected empirically: the response time usually lies within the range from 0.5 to 0.7 ms. Although the ERF could reduce the magnitude of k, the decrease of the chiral fraction also made the filled mesogen less viscous (cf. 9.13). This might be the reason why the time constant increased sharply when the right-handed chiral additive was replaced by the left-handed one (Fig. 9.24c). Furthermore, the extent of the changes in k and γ_1 determine whether the relaxation time is extended or compressed [140, 141]. Figure of merit of a PSBP device is defined as the ratio of Kerr constant to response time [142]. Figure 9.24d reveals that reducing the chiral fraction can decrease the peak-transmittance voltage and slightly increase the time constant, therefore raise the figure of merit. If the filling material exhibits reverse handedness, the figure got improved further.

Speaking of phase manipulation, BPs feature ultrafast response and polarization independency in comparison with other mesophases. The PSBP can be integrated either inside or outside an optical cavity to realize an electrically tunable interferometric filter. By sandwiching a PSBP between two aluminium mirrors, a tunable Fabry–Pérot filter was thus fabricated [117]. Owing to the high reflectivity of the mirrors and optical transparency of the PSBP across an extremely broad spectrum, the etalon could be operated in both the visible and near infrared regions. Figure 9.25a shows that the tunability was $\sim$10 nm for the visible wavelengths and $\sim$15 nm for the near infrared. Because the light propagated along the field axis, the polarization direction had negligible effect on the filtering frequency or efficiency (Fig. 9.25b). Switching from 0 to 60 V took the etalon 0.66 ms to reach the stationary state, while the relaxation process took about 0.75 ms (Fig. 9.25c).

The ultrafast response and scattering-free nature make PSBP superior in design of tunable micro-ring resonators to nematic in practice [118]. Though the resonant wavelength only shifted $\sim$3 nm in total, the quality factor of the PSBP-clad resonator was retained above 20,000 during the tuning process (Fig. 9.26a), which pales that of those clothed in nematics [143]. With increasing field strength, the relaxation time was lengthened but kept within 1 ms, while the rise time was shortened (Fig. 9.26b). The remarkable extension of the relaxation time might result from the occurrence of electrostriction as the voltage exceeded 100 V.

9.8 Nonlinear Optical Response of BPs

Nonlinear optics is an emerging field of BP research. The first investigation of nonlinear optical response in BPs was carried out by Mayén-Mondragón and Yáñez-Limón in 2006 [144]. They monitored the dynamics of photothermal lens

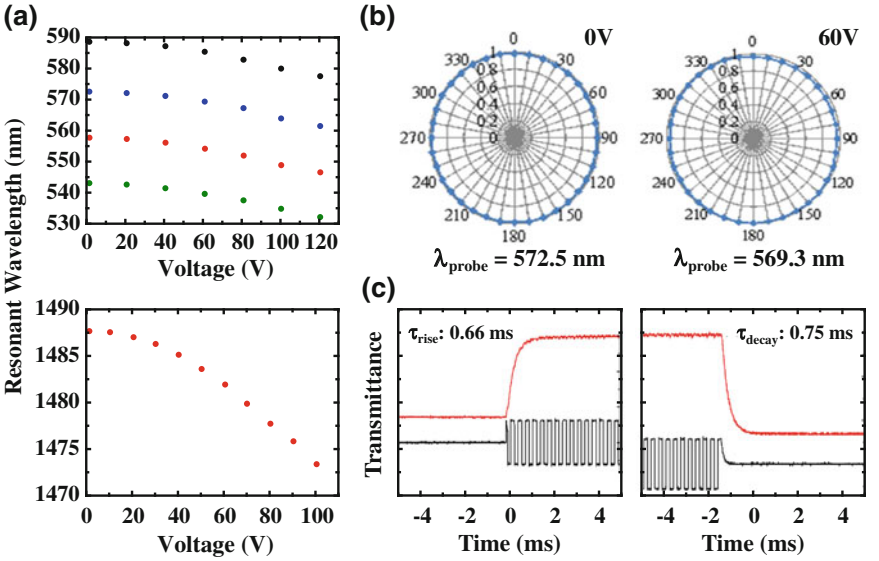

Fig. 9.25 Electro-optic response of a PSBP etalon: **a** voltage-dependent resonant wavelength, **b** transmittance against incident polarization (at the resonant wavelengths), **c** rise time and decay time

signals to study the kinetics of phase transitions in a dye doped BPLC (Carmín de Grana, 1 wt%) [144]. Recently, the nonlinear wave mixing experiments were carried out to examine the nonlinear index coefficient n_2 (Fig. 9.27a) [145]. By applying a green continuous-wave laser (λ = 532 nm), the pristine BPLC "RT-35" (cf. Fig. 9.10) did not show any self-diffraction effects. To enhance the nonlinear optical response, a small amount of azobenzene 'Methyl Red' (<0.1 wt%) were doped into the BPLC. Under weak irradiation (I $\sim$ 50 mW/cm^2), side diffractions became observable. The intensity of the diffraction signal took about few minutes to reach a steady state (Fig. 9.27b). It was also found that the steady-state signal did not vanish right after one of the pump beams was blocked. The nonlinear grating relaxed in several minutes or longer. Such nonlinear optical behavior implied the occurrence of lattice distortion, which might originate from photothermal indexing and isomerization-induced reorientation. By calculating the index change Δn from the expression of Raman-Nath diffraction efficiency: $\eta \sim (\pi \cdot d \cdot \Delta n/\lambda)^2$, the nonlinear index coefficient was thus obtained: $n_2 \sim \Delta n/\mathrm{I} \sim 10^{-3}$ cm^2/W. Herein, d is the film thickness and I is the pump intensity. It has to be noted that the magnitude of n_2 strongly depends on exposure time, wave-mixing angle and pump intensity. Besides the slow relaxation, the persistent grating would also disappear when the BPLC experiences a phase transition to the isotropic or cholesteric phase. To further magnify the response, a direct-current (DC) field can be applied to induce space charge. It has been suggested that the diffraction power could be improved by eight times larger, yielding a n_2 of $\sim$0.5 cm^2/W [146]. Ptasinski et al. recently designed an adiabatic racetrack resonator clad in the dye doped BP to achieve all-optical

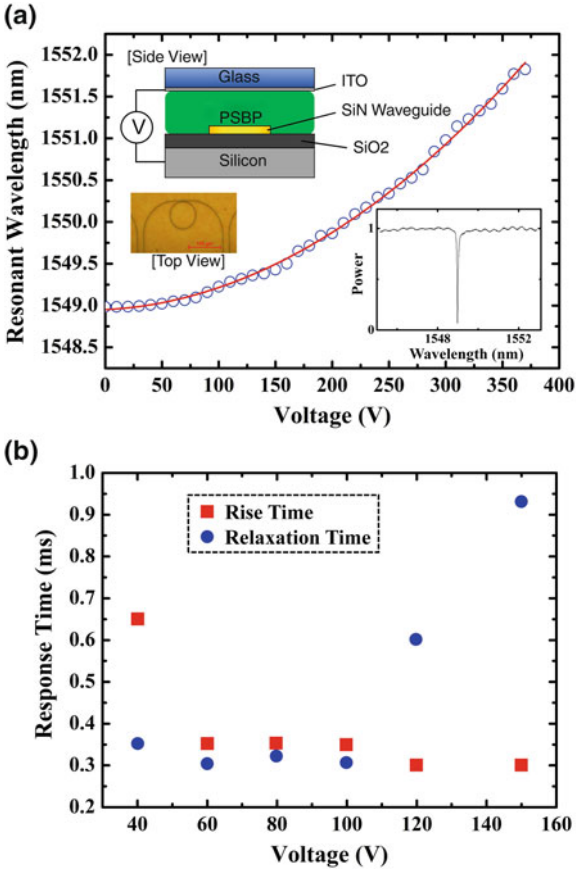

Fig. 9.26 Electro-optic response of a PSBP-clad micro-resonator: **a** voltage-dependent resonant wavelength and **b** voltage-dependent response time. **insets* are the conceptual drawing and microscopic image and transmission spectrum of the device

modulation [147]. Under the illumination of a broadband blue LED ($\lambda \sim 470$ nm), the resonant wavelengths shifted 1.23 nm at maximum.

Under prolonged irradiation by a succession of intense laser pulses ($\lambda = 532$ nm; $\tau_p = 10$ ns; repetition rate: 10 Hz), such nonvolatile grating diffraction was observed in a 1 mm-thick film of pristine RT-35. In this case, dye absorption-induced thermal and isomerization effects were absent in the sample. Instead, electrostriction-induced density effect and/or Maxwell stress-induced flow-reorientation and/or multiphoton absorption-induced thermal effect were responsible for the lattice distortion. Resulting from the accumulation of the effects upon multiple shots, the persistent nonlinear grating was slowly built up. In a separate experiment, momentary self-defocusing was perceptible under single-pulse pumping (Fig. 9.28a) [148]. As a nanosecond laser pulse shone on the BPII sample, the collinear He–Ne probe laser diverged as revealed in Fig. 9.28b. The transmitted light close to the propagation axis darkened abruptly and reached the minimum in $\sim$0.4 ms, while the out power detected outside the central (original) region underwent a sharp rise. They subsequently took $\sim$100 ms to return to the initial

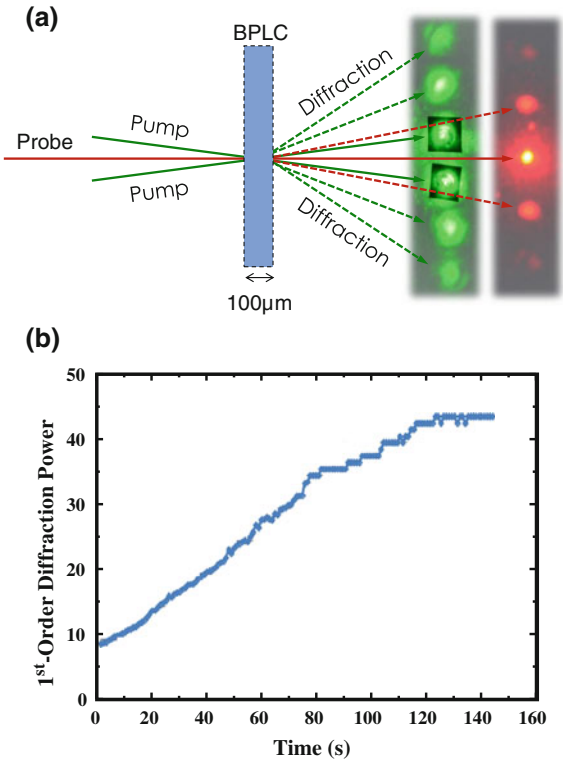

Fig. 9.27 **a** Schematic depiction of nonlinear wave mixing experiment and **b** dynamic evolution of the first-order diffraction signal

levels. These dynamical details are similar to those thermal and density effects observed in nematics. The defocusing effect was hence attributed to the negative index gradient (cf. Fig. 9.10) and possible density change. Detailed mechanisms of the pulsed laser-induced nonlinearities occurring in the pristine BP still await a thorough investigation and clarification.

On account of the low scattering loss, polarization independency and free surface alignment, BPLC is ideal for infiltrating long-propagation-length hollow fibers with respect to nematic LCs. Multiple nonlinear optical responses occurring in BPs give rise to light blocking in a period much shorter than the pulse duration. Taking these advantages, a BP-cored nonlinear optical fiber array was developed for eye/sensor protection from being damaged by unexpected intense agile lasers (Fig. 9.29) [149]. Such a device allows large-view and good-quality imaging for low-power input as well as optical limiting actions at high input intensity levels. To examine its feasibility a broadband (∼400–1200 nm) supercontinuum laser (τ_p = 100 ps; repetition rate: 80 MHz) was adopted. Beam profiles in Fig. 9.29 reveal a self-defocusing behavior: the negative index gradient led to self-defocusing and the subsequent core-to-cladding coupling of higher order guiding modes in BP-cores.

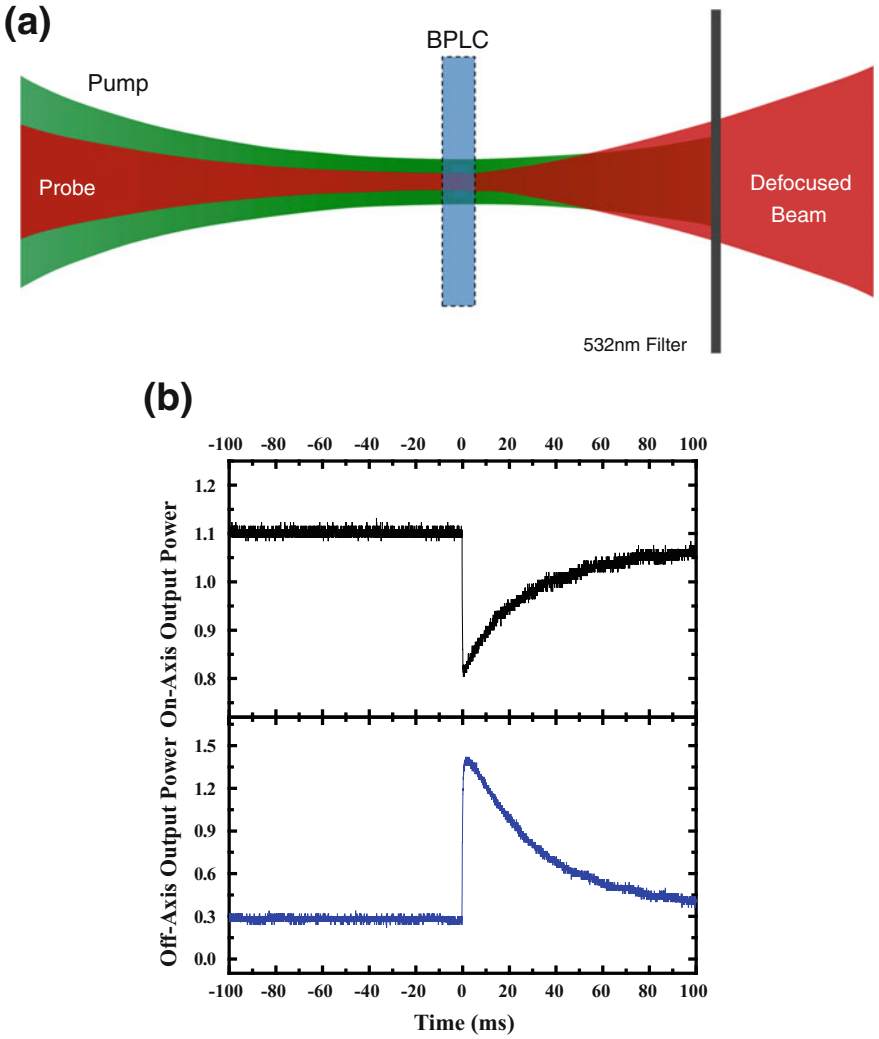

Fig. 9.28 **a** Schematic depiction of nonlinear self-defocusing experiment and **b** dynamic evolution of output power monitored *inside* (*top*) and *outside* (*bottom*) the central region

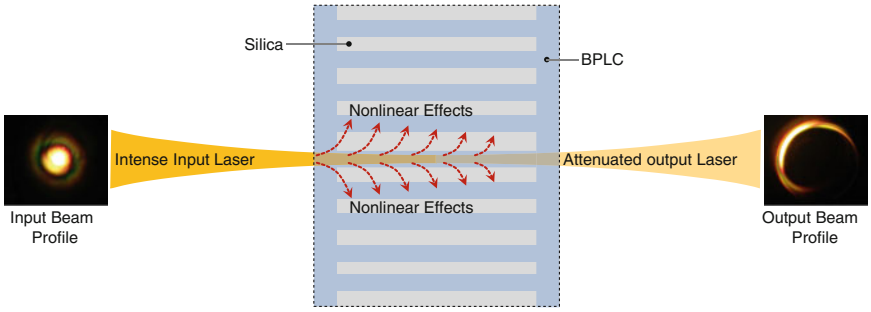

Fig. 9.29 Nonlinear transmission in BP-cored fiber array

9.9 Conclusions and Outlook

In this chapter, we have presented a brief overview about the BPLCs covering from their fundamentals to applications, mostly in the aspects of physics, optics and engineering. It is quite astonishing to think that such mesophases' fluid lattices can even form, since it is the delicate balance among many forces including elasticity, chirality and thermal energy. Yet, nature has found a narrow window between the isotropic phase and the positional order lacking cholesteric phase. In this highly chiral system, the director twists along all directions perpendicular to the axis of a central director forming the so called "double-twist cylinder" structure. Such structure can form three distinct sub-phases: BPI, BPII and BPIII. Both, BPI and BPII, are represented by the cylinder arrangement and disclination network forming, respectively a body-centered cubic lattice and simple cubic lattice. The morphology of the BPIII, however, is still debatable, although strong evidences suggest that it is an amorphous network of disclinations. Besides existing in a very narrow temperature interval for many materials, several works in the past two decades have greatly improved the usability of BPs by polymer stabilization, and with new, designed materials to increase the temperature interval to more than a hundred Kelvins. However, the BPs stabilized under ambient conditions are essential to unravel the detail structure-property relationships and to enhance the application potential of these intriguing materials. In this context, the recently developed chiral dopants with very high and widely tunable helical twisting powers as well as handedness inversion capability seem promising towards the fabrication of functional BPs [150, 151]. Moreover, the research involving addition of differently shaped anisotropic nanoparticles to widen the BP temperature range and to optimize their physical properties deserves systematic attention [152]. Due to their striking characteristics including 3D photonic crystal make-up, optical isotropy and ultrafast response, the future of BP seems bright. Indeed, this material presents incredible optical properties that can be controlled by several external stimuli, for example, color tuning by director reorientation or lattice deformation. There are abundant puzzling questions waiting to be resolved, for instance, the formation of BPIII. In comparison with their use as

optically isotropic and rapid responding materials, the photonic applications are still in the startup phase and many beyond-display applications may dominate the future BP research [153]. It is hoped that this introduction could help people to understand BPLCs and stimulate promising new ideas for further development.

References

1. F. Reinitzer, Beiträge zur Kenntniss des Cholesterins. Monatsh. Chem. **9**, 421–441 (1888)
2. H.K. Bisoyi, Q. Li, *Liquid Crystals*, *Kirk-Othmer Encyclopedia of Chemical Technology* (Wiley, Hoboken, 2014), pp. 1–52
3. H.-Y. Liu, C.-T. Wang, C.-Y. Hsu, T.-H. Lin, Pinning effect on the photonic bandgaps of blue-phase liquid crystal. Appl. Opt. **50**, 1606–1609 (2011)
4. H. Kikuchi, H. Higuchi, Y. Haseba, T. Iwata, Fast electro-optical switching in polymer-stabilized liquid crystalline blue phases for display application. SID Int. Symp. Dig. Tec. **38**, 1737–1740 (2007)
5. D.L. Johnson, J.H. Flack, P.P. Crooker, Structure and properties of the cholesteric blue phases. Phys. Rev. Lett. **45**, 641–644 (1980)
6. S. Meiboom, M. Sammon, W.F. Brinkman, Lattice of disclinations: the structure of the blue phases of cholesteric liquid crystals. Phys. Rev. A **27**, 438–454 (1983)
7. B. Pansu, Geometrical model of the tetragonal BPX blue phase. J. Phys. II France **5**, 573–585 (1995)
8. P.-G. De Gennes, J. Prost (ed.), *The Physics of Liquid Crystals* (Clarendon press, Oxford, 1993)
9. J.P. Sethna, D.C. Wright, N.D. Mermin, Relieving cholesteric frustration: the blue phase in a curved space. Phys. Rev. Lett. **51**, 467–470 (1983)
10. J.P. Sethna, Frustration, curvature, and defect lines in metallic glasses and the cholesteric blue phase. Phys. Rev. B **31**, 6278–6297 (1985)
11. E. Dubois-violette, B. Pansu, Frustration and related topology of blue phases. Mol. Cryst. Liq. Cryst. **165**, 151–182 (1988)
12. A. Saupe, On molecular structure and physical properties of thermotropic liquid crystals. Mol. Cryst. Liq. Cryst. **7**, 59–74 (1969)
13. S. Meiboom, M. Sammon, D.W. Berreman, Lattice symmetry of the cholesteric blue phases. Phys. Rev. A **28**, 3553–3560 (1983)
14. R.M. Hornreich, S. Shtrikman, C. Sommers, Photonic bands in simple and body-centered-cubic cholesteric blue phases. Phys. Rev. E **47**, 2067–2072 (1993)
15. O. Henrich, K. Stratford, M.E. Cates, D. Marenduzzo, Structure of blue phase III of cholesteric liquid crystals. Phys. Rev. Lett. **106**, 107801 (2011)
16. S. Brazovskii, S. Dmitriev, Phase transitions in cholesteric liquid crystals. Zh. Eksp. Teor. Fiz **69**, 979–989 (1975)
17. R.M. Hornreich, S. Shtrikman, A body-centered cubic structure for the cholesteric blue phase. J. Phys. France **41**, 335–340 (1980)
18. H. Kleinert, K. Maki, Lattice textures in cholesteric liquid crystals. Fortschr. Phys. **29**, 219–259 (1981)
19. R.M. Hornreich, S. Shtrikman, Landau theory of blue phases. Mol. Cryst. Liq. Cryst. **165**, 183–211 (1988)
20. D. Wright, N. Mermin, Crystalline liquids: the blue phases. Rev. Modern Phys. **61**, 385–432 (1989)
21. T. Seideman, The liquid-crystalline blue phases. Rep. Prog. Phys. **53**, 659 (1990)
22. P.P. Crooker, in *Chirality in Liquid Crystals*, eds. by H.-S. Kitzerow, C. Bahr. Blue Phases (Springer, New York, 2001), pp. 186–222

23. S. Meiboom, J.P. Sethna, P.W. Anderson, W.F. Brinkman, Theory of the blue phase of cholesteric liquid crystals. Phys. Rev. Lett. **46**, 1216–1219 (1981)
24. H. Yoshida, Y. Tanaka, K. Kawamoto, H. Kubo, T. Tsuda, A. Fujii, S. Kuwabata, H. Kikuchi, M. Ozaki, Nanoparticle-stabilized cholesteric blue phases. Appl. Phys. Express **2**, 121501 (2009)
25. L. Wang, W. He, X. Xiao, M. Wang, M. Wang, P. Yang, Z. Zhou, H. Yang, H. Yu, Y. Lu, Low voltage and hysteresis-free blue phase liquid crystal dispersed by ferroelectric nanoparticles. J. Mater. Chem. **22**, 19629–19633 (2012)
26. M. Lavri, G. Cordoyiannis, S. Kralj, V. Tzitzios, G. Nounesis, Z. Kutnjak, Effect of anisotropic MoS_2 nanoparticles on the blue phase range of a chiral liquid crystal. Appl. Opt. **52**, E47–E52 (2013)
27. H. Kikuchi, M. Yokota, Y. Hisakado, H. Yang, T. Kajiyama, Polymer-stabilized liquid crystal blue phases. Nature Mater. **1**, 64–68 (2002)
28. M. Ravnik, G.P. Alexander, J.M. Yeomans, S. Žumer, Three-dimensional colloidal crystals in liquid crystalline blue phases. Proc. Natl. Acad. Sci. U.S.A. **108**, 5188–5192 (2011)
29. B. Rožič, V. Tzitzios, E. Karatairi, U. Tkalec, G. Nounesis, Z. Kutnjak, G. Cordoyiannis, R. Rosso, E.G. Virga, I. Muševič, S. Kralj, Theoretical and experimental study of the nanoparticle-driven blue phase stabilisation. Eur. Phys. J. E Soft Matter **34**, 1–11 (2011)
30. J.-I. Fukuda, Stability of cholesteric blue phases in the presence of a guest component. Phys. Rev. E **86**, 041704 (2012)
31. S. Yabu, Y. Tanaka, K. Tagashira, H. Yoshida, A. Fujii, H. Kikuchi, M. Ozaki, Polarization-independent refractive index tuning using gold nanoparticle-stabilized blue phase liquid crystals. Opt. Lett. **36**, 3578–3580 (2011)
32. H.S. Kitzerow, H. Schmid, A. Ranft, G. Heppke, R.A.M. Hikmet, J. Lub, Observation of blue phases in chiral networks. Liq. Cryst. **14**, 911–916 (1993)
33. Y. Haseba, H. Kikuchi, T. Nagamura, T. Kajiyama, Large electro-optic Kerr effect in nanostructured chiral liquid-crystal composites over a wide temperature range. Adv. Mater. **17**, 2311–2315 (2005)
34. Y. Chen, S.-T. Wu, Recent advances on polymer-stabilized blue phase liquid crystal materials and devices. J. Appl. Polym. Sci. **131**, 40556 (2014)
35. J. Yan, S.-T. Wu, Polymer-stabilized blue phase liquid crystals: a tutorial. Opt. Mater. Express **1**, 1527–1535 (2011)
36. F. Castles, S.M. Morris, J.M.C. Hung, M.M. Qasim, A.D. Wright, S. Nosheen, S.S. Choi, B. I. Outram, S.J. Elston, C. Burgess, L. Hill, T.D. Wilkinson, H.J. Coles, Stretchable liquid-crystal blue-phase gels. Nature Mater. **13**, 817–821 (2014)
37. M. Ojima, T. Noma, H. Asagi, A. Fujii, M. Ozaki, H. Kikuchi, Pinning effect of mixed cellulose ester membrane on appearance of cholesteric blue phases. Appl. Phys. Express **2**, 021502 (2009)
38. F. Castles, F.V. Day, S.M. Morris, D.H. Ko, D.J. Gardiner, M.M. Qasim, S. Nosheen, P.J.W. Hands, S.S. Choi, R.H. Friend, H.J. Coles, Blue-phase templated fabrication of three-dimensional nanostructures for photonic applications. Nat. Mater. **11**, 599–603 (2012)
39. M. Nakata, Y. Takanishi, J. Watanabe, H. Takezoe, Blue phases induced by doping chiral nematic liquid crystals with nonchiral molecules. Phys. Rev. E **68**, 041710 (2003)
40. H.J. Coles, M.N. Pivnenko, Liquid crystal 'blue phases' with a wide temperature range. Nature **436**, 997–1000 (2005)
41. S. Aya, A. Zep, K. Aihara, K. Ema, D. Pociecha, E. Gorecka, F. Araoka, K. Ishikawa, H. Takezoe, Stable electro-optic response in wide-temperature blue phases realized in chiral asymmetric bent dimers. Opt. Mater. Express **4**, 662–671 (2014)
42. J. Harden, B. Mbanga, N. Éber, K. Fodor-Csorba, S. Sprunt, J.T. Gleeson, A. Jákli, Giant flexoelectricity of bent-core nematic liquid crystals. Phys. Rev. Lett. **97**, 157802 (2006)
43. H.J. Coles, M.J. Clarke, S.M. Morris, B.J. Broughton, A.E. Blatch, Strong flexoelectric behavior in bimesogenic liquid crystals. J. Appl. Phys. **99**, 034104 (2006)
44. F. Castles, S.M. Morris, E.M. Terentjev, H.J. Coles, Thermodynamically stable blue phases. Phys. Rev. Lett. **104**, 157801 (2010)

45. S.-T. Hur, M.-J. Gim, H.-J. Yoo, S.-W. Choi, H. Takezoe, Investigation for correlation between elastic constant and thermal stability of liquid crystalline blue phase I. Soft Matter **7**, 8800–8803 (2011)
46. M. Kléman, The coexistence of cholesteric and 2-dimensional orders. J. Phys. France **46**, 1193–1203 (1985)
47. J.-I. Fukuda, Stabilization of blue phases by the variation of elastic constants. Phys. Rev. E **85**, 020701 (2012)
48. S. Shibayama, H. Higuchi, Y. Okumura, H. Kikuchi, Dendron-stabilized liquid crystalline blue phases with an enlarged controllable range of the photonic band for tunable photonic devices. Adv. Funct. Mater. **23**, 2387–2396 (2013)
49. G.P. Alexander, J.M. Yeomans, Stabilizing the blue phases. Phys. Rev. E **74**, 061706 (2006)
50. Z. Zheng, D. Shen, P. Huang, Wide blue phase range of chiral nematic liquid crystal doped with bent-shaped molecules. New J. Phys. **12**, 113018 (2010)
51. H.-C. Jeong, K.V. Le, M.-J. Gim, S.-T. Hur, S.-W. Choi, F. Araoka, K. Ishikawa, H. Takezoe, Transition between widened BPs by light irradiation using photo-active bent-core liquid crystal with chiral dopant. J. Mater. Chem. **22**, 4627–4630 (2012)
52. K. Kishikawa, T. Sugiyama, T. Watanabe, S. Aoyagi, M. Kohri, T. Taniguchi, M. Takahashi, S. Kohmoto, Simple and efficient chiral dopants to induce blue phases and their optical purity effects on the physical properties of blue phases. J. Phys. Chem. B **118**, 10319–10332 (2014)
53. W. He, G. Pan, Z. Yang, D. Zhao, G. Niu, W. Huang, X. Yuan, J. Guo, H. Cao, H. Yang, Wide blue phase range in a hydrogen-bonded self-assembled complex of chiral fluoro-substituted benzoic acid and pyridine derivative. Adv. Mater. **21**, 2050–2053 (2009)
54. Y. Li, Y. Cong, H. Chu, B. Zhang, Blue phases induced by rod-shaped hydrogen-bonded supermolecules possessing no chirality or mesomorphic behaviour. J. Mater. Chem. C **2**, 1783–1790 (2014)
55. B.-Y. Zhang, F.-B. Meng, Y.-H. Cong, Optical characterization of polymer liquid crystal cell exhibiting polymer blue phases. Opt. Express **15**, 10175–10181 (2007)
56. C.-T. Wang, H.-C. Jau, T.-H. Lin, Bistable cholesteric-blue phase liquid crystal using thermal hysteresis. Opt. Mater. **34**, 248–250 (2011)
57. C.-H. Lee, C.-W. Wu, C.-W. Chen, H.-C. Jau, T.-H. Lin, Polarization-independent bistable light valve in blue phase liquid crystal filled photonic crystal fiber. Appl. Opt. **52**, 4849–4853 (2013)
58. A. Yoshizawa, Material design for blue phase liquid crystals and their electro-optical effects. RSC Adv. **3**, 25475–25497 (2013)
59. E. Grelet, Liquid crystals exhibiting a double geometrical frustration: the smectic blue phases. Mol. Cryst. Liq. Cryst. **412**, 37–47 (2004)
60. A. Hauser, M. Thieme, A. Saupe, G. Heppke, D. Kruerke, Surface-imaging of frozen blue phases in a discotic liquid crystal with atomic force microscopy. J. Mater. Chem. **7**, 2223–2229 (1997)
61. J. Buey, P. Espinet, H.-S. Kitzerow, J. Strauss, Metallomesogens presenting blue phases in a glassy state and in metallomesogen/nematic mixtures, Chem. Comm. **5**, 441–442 (1999)
62. Y. Ogawa, J.-I. Fukuda, H. Yoshida, M. Ozaki, Finite-difference time-domain analysis of cholesteric blue phase II using the Landau-de Gennes tensor order parameter model. Opt. Lett. **38**, 3380–3383 (2013)
63. S. Meiboom, M. Sammon, Structure of the blue phase of a cholesteric liquid crystal. Phys. Rev. Lett. **44**, 882–885 (1980)
64. R.M. Hornreich, S. Shtrikman, Optical selection rules and structures of cholesteric blue phases. Phys. Lett. A **82**, 345–349 (1981)
65. V.A. Kizel', V.V. Prokhorov, Structure of the blue phases of cholesteric liquid crystals. Zh. Eksp. Teor. Fiz **87**, 450–466 (1984)
66. F. Porsch, H. Stegemeyer, The effect of an electric field on the selective reflection bands of liquid crystalline blue phases. Chem. Phys. Lett. **125**, 319–323 (1986)
67. R. Barbet-Massin, P. Pierański, Blue phase one: first optical measurements of the order parameter. J. Phys. Lett. **45**, 799–806 (1984)

68. J.W. Gorman, P.P. Crooker, Mueller-matrix measurements in a two-component blue-phase mixture. Phys. Rev. A **31**, 910–913 (1985)
69. B. Jérôme, P. Pierański, Kossel diagrams of blue phases. Liq. Cryst. **5**, 799–812 (1989)
70. R.J. Miller, H.F. Gleeson, Lattice parameter measurements from the Kossel diagrams of the cubic liquid crystal blue phases. J. Phys. II France **6**, 909–922 (1996)
71. G. Heppke, B. Jérôme, H.-S. Kitzerow, P. Pieranski, Electrostriction of BPI and BPII for blue phase systems with negative dielectric anisotropy. J. Phys. France **50**, 549–562 (1989)
72. G. Heppke, B. Jérôme, H.-S. Kitzerow, P. Pieranski, Electrostriction of the cholesteric blue phases BPI and BPII in mixtures with positive dielectric anisotropy. J. Phys. France **50**, 2991–2998 (1989)
73. M.J. Costello, S. Meiboom, M. Sammon, Electron microscopy of a cholesteric liquid crystal and its blue phase. Phys. Rev. A **29**, 2957–2959 (1984)
74. K. Higashiguchi, K. Yasui, H. Kikuchi, Direct observation of polymer-stabilized blue Phase I structure with confocal laser scanning microscope. J. Am. Chem. Soc. **130**, 6326–6327 (2008)
75. R. Barbet-Massin, P.E. Cladis, P. Pieranski, Crystal habit of liquid-crystal blue phase I. Phys. Rev. A **30**, 1161–1164 (1984)
76. B. Pansu, E. Dubois-Violette, Blue phases: experimental survey and geometrical approach. J. Phys. Colloques **51**, C7-281-C287-296 (1990)
77. P. Pierański, P.E. Cladis, T. Garel, R. Barbet-Massin, Orientation of crystals of blue phases by electric fields. J. Phys. France **47**, 139–143 (1986)
78. C.-T. Wang, H.-Y. Liu, H.-H. Cheng, T.-H. Lin, Bistable effect in the liquid crystal blue phase. Appl. Phys. Lett. **96**, 041106 (2010)
79. P. Nayek, H. Jeong, H.R. Park, S.-W. Kang, S.H. Lee, H.S. Park, H.J. Lee, H.S. Kim, Tailoring monodomain in blue phase liquid crystal by surface pinning effect. Appl. Phys. Express **5**, 051701 (2012)
80. T.-H. Lin, Y. Li, C.-T. Wang, H.-C. Jau, C.-W. Chen, C.-C. Li, H.K. Bisoyi, T.J. Bunning, Q. Li, Red, green and blue reflections enabled in an optically tunable self-organized 3D cubic nanostructured thin film. Adv. Mater. **25**, 5050–5054 (2013)
81. S.-I. Yamamoto, Y. Haseba, H. Higuchi, Y. Okumura, H. Kikuchi, Lattice plane control of liquid crystal blue phase. Liq. Cryst. **40**, 639–645 (2013)
82. H.S. Kitzerow, P.P. Crooker, S.L. Kwok, J. Xu, G. Heppke, Dynamics of blue-phase selective reflections in an electric field. Phys. Rev. A **42**, 3442–3448 (1990)
83. V.E. Dmitrienko, Electro-optic effects in blue phases. Liq. Cryst. **5**, 847–851 (1989)
84. D. Lubin, R.M. Hornreich, Effect of a weak electric field on the cubic blue phases of cholesteric liquid crystals. Phys. Rev. A **36**, 849–857 (1987)
85. Y. Chen, S.-T. Wu, Electric field-induced monodomain blue phase liquid crystals. Appl. Phys. Lett. **102**, 171110 (2013)
86. P. Pierański, P.E. Cladis, R. Barbet-Massin, Shapes of blue phase crystals grown in electric fields. Liq. Cryst. **5**, 829–838 (1989)
87. C.-W. Chen, H.-C. Jau, C.-H. Lee, C.-C. Li, C.-T. Hou, C.-W. Wu, T.-H. Lin, I.C. Khoo, Temperature dependence of refractive index in blue phase liquid crystals. Opt. Mater. Express **3**, 527–532 (2013)
88. D. Demus, H.G. Hahn, F. Kuschel, Density measurements in cholesteryl myristate. Mol. Cryst. Liq. Cryst. **44**, 61–70 (1978)
89. R.N. Kleiman, D.J. Bishop, R. Pindak, P. Taborek, Shear modulus and specific heat of the liquid-crystal blue phases. Phys. Rev. Lett. **53**, 2137–2140 (1984)
90. D. Armitage, R.J. Cox, Liquid crystal blue phase to isotropic transition and electric field response. Mol. Cryst. Liq. Cryst. **64**, 41–50 (1980)
91. S.-C. Chen, P.-C. Wu, W. Lee, Dielectric and phase behaviors of blue-phase liquid crystals. Opt. Mater. Express **4**, 2392–2400 (2014)
92. V. Belyakov, E. Demikhov, V. Dmitrienko, V. Dolganov, Optical activity, transmission spectra, and structure of blue phases of liquid crystals. Zh. Eksp. Teor. Fiz **89**, 2035–2051 (1985)

93. H. Choi, H. Higuchi, H. Kikuchi, Electrooptic response of liquid crystalline blue phases with different chiral pitches. Soft Matter **7**, 4252–4256 (2011)
94. P. Pollmann, E. Voss, High pressure optical studies of the chirality and phase behaviour of liquid crystalline blue phases. Liq. Cryst. **23**, 299–307 (1997)
95. H.S. Kitzerow, The effect of electric fields on blue phases. Mol. Cryst. Liq. Cryst. **202**, 51–83 (1991)
96. A. Chanishvili, G. Chilaya, G. Petriashvili, P.J. Collings, Trans-cis isomerization and the blue phases. Phys. Rev. E **71**, 051705 (2005)
97. P.R. Gerber, Electro-optical effects of a small-pitch blue-phase system. Mol. Cryst. Liq. Cryst. **116**, 197–206 (1985)
98. H. Yoshida, S. Yabu, H. Tone, Y. Kawata, H. Kikuchi, M. Ozaki, Secondary electro-optic effect in liquid crystalline cholesteric blue phases. Opt. Mater. Express **4**, 960–968 (2014)
99. G. Heppke, M. Krumrey, F. Oestreicher, Observation of electro-optical effects in blue phase systems. Mol. Cryst. Liq. Cryst. **99**, 99–105 (1983)
100. Y. Ogawa, J.-I. Fukuda, H. Yoshida, M. Ozaki, Photonic band structure and transmission analysis of cholesteric blue phase II: electrostriction in the [100] direction. Opt. Express **22**, 3766–3772 (2014)
101. M. Żelazna, L. Longa, H.R. Trebin, H. Stark, Electrostriction tensor of the cubic blue phases: the role of amplitudes. Phys. Rev. E **57**, 6711–6716 (1998)
102. D.K. Yang, P.P. Crooker, Blue phase III of chiral liquid crystals in an electric field. Phys. Rev. A **37**, 4001–4005 (1988)
103. F. Porsch, H. Stegemeyer, The influence of chirality and dielectric anisotropy on the voltage-temperature phase diagram of blue-phase systems. Liq. Cryst. **5**, 791–798 (1989)
104. J.-D. Lin, Y.-M. Lin, T.-S. Mo, C.-R. Lee, Photosensitive and all-optically fast-controllable photonic bandgap device and laser in a dye-doped blue phase with a low-concentration azobenzene liquid crystal. Opt. Express **22**, 9171–9181 (2014)
105. H.-Y. Liu, C.-T. Wang, C.-Y. Hsu, T.-H. Lin, J.-H. Liu, Optically tuneable blue phase photonic band gaps. Appl. Phys. Lett. **96**, 121103 (2010)
106. X. Chen, L. Wang, C. Li, J. Xiao, H. Ding, X. Liu, X. Zhang, W. He, H. Yang, Light-controllable reflection wavelength of blue phase liquid crystals doped with azobenzene-dimers. Chem. Comm. **49**, 10097–10099 (2013)
107. O. Jin, D. Fu, J. Wei, H. Yang, J. Guo, Light-induced wide range color switching of liquid crystal blue phase doped with hydrogen-bonded chiral azobenzene switches. RSC Adv. **4**, 28597–28600 (2014)
108. R.K. Vijayaraghavan, S. Abraham, D.S.S. Rao, S.K. Prasad, S. Das, Light induced generation of stable blue phase in photoresponsive diphenylbutadiene based mesogen. Chem Comm. **46**, 2796–2798 (2010)
109. P. Etchegoin, Blue phases of cholesteric liquid crystals as thermotropic photonic crystals. Phys. Rev. E **62**, 1435–1437 (2000)
110. W. Cao, A. Munoz, P. Palffy-Muhoray, B. Taheri, Lasing in a three-dimensional photonic crystal of the liquid crystal blue phase II. Nat. Mater. **1**, 111–113 (2002)
111. A. Mazzulla, G. Petriashvili, M.A. Matranga, M.P. De Santo, R. Barberi, Thermal and electrical laser tuning in liquid crystal blue phase I. Soft Matter **8**, 4882–4885 (2012)
112. C.-W. Chen, H.-C. Jau, C.-T. Wang, C.-H. Lee, I.C. Khoo, T.-H. Lin, Random lasing in blue phase liquid crystals. Opt. Express **20**, 23978–23984 (2012)
113. C.-H. Lin, Y.-Y. Wang, C.-W. Hsieh, Polarization-independent and high-diffraction-efficiency Fresnel lenses based on blue phase liquid crystals. Opt. Lett. **36**, 502–504 (2011)
114. Y.-T. Lin, H.-C. Jau, T.-H. Lin, Polarization-independent rapidly responding phase grating based on hybrid blue phase liquid crystal. J. Appl. Phys. **113**, 063103 (2013)
115. S.-J. Ge, W. Ji, G.-X. Cui, B.-Y. Wei, W. Hu, Y.-Q. Lu, Fast switchable optical vortex generator based on blue phase liquid crystal fork grating. Opt. Mater. Express **4**, 2535–2541 (2014)
116. S.-H. Lin, L.-S. Huang, C.-H. Lin, C.-T. Kuo, Polarization-independent and fast tunable microlens array based on blue phase liquid crystals. Opt. Express **22**, 925–930 (2014)

117. Y.-H. Chen, C.-T. Wang, C.-P. Yu, T.-H. Lin, Polarization independent Fabry-Pérot filter based on polymer-stabilized blue phase liquid crystals with fast response time. Opt. Express **19**, 25441–25446 (2011)
118. C.-T. Wang, Y.-C. Li, J.-H. Yu, C.Y. Wang, C.-W. Tseng, H.-C. Jau, Y.-J. Chen, T.-H. Lin, Electrically tunable high Q-factor micro-ring resonator based on blue phase liquid crystal cladding. Opt. Express **22**, 17776–17781 (2014)
119. G. Zhu, B.-Y. Wei, L.-Y. Shi, X.-W. Lin, W. Hu, Z.-D. Huang, Y.-Q. Lu, A fast response variable optical attenuator based on blue phase liquid crystal. Opt. Express **21**, 5332–5337 (2013)
120. H.-C. Cheng, J. Yan, T. Ishinabe, N. Sugiura, C.-Y. Liu, T.-H. Huang, C.-Y. Tsai, C.-H. Lin, S.-T. Wu, Blue-phase liquid crystal displays with vertical field switching, display technology. J. Display Technol. **8**, 98–103 (2012)
121. H. Lee, H.-J. Park, O.-J. Kwon, S.J. Yun, J.H. Park, S. Hong, S.-T. Shin, The world's first blue phase liquid crystal display. SID Int. Symp. Dig. Tec. **42**, 121–124 (2011)
122. J. Yan, M. Jiao, L. Rao, S.-T. Wu, Direct measurement of electric-field-induced birefringence in a polymer-stabilized blue-phase liquid crystal composite. Opt. Express **18**, 11450–11455 (2010)
123. S.-W. Choi, S.-I. Yamamoto, Y. Haseba, H. Higuchi, H. Kikuchi, Optically isotropic-nanostructured liquid crystal composite with high Kerr constant. Appl. Phys. Lett. **92**, 043119 (2008)
124. K.-M. Chen, S. Gauza, H. Xianyu, S.-T. Wu, Hysteresis effects in blue-phase liquid crystals. J. Display Technol. **6**, 318–322 (2010)
125. C.-Y. Fan, H.-C. Jau, T.-H. Lin, F.C. Yu, T.-H. Huang, C. Liu, N. Sugiura, Influence of polymerization temperature on hysteresis and residual birefringence of polymer stabilized blue phase LCs. J. Display Technol. **7**, 615–618 (2011)
126. J. Yan, S.-T. Wu, Effect of polymer concentration and composition on blue phase liquid crystals. J. Display Technol. **7**, 490–493 (2011)
127. Y. Chen, J. Yan, J. Sun, S.-T. Wu, X. Liang, S.-H. Liu, P.-J. Hsieh, K.-L. Cheng, J.-W. Shiu, A microsecond-response polymer-stabilized blue phase liquid crystal. Appl. Phys. Lett. **99**, 201105 (2011)
128. P. Nayek, H. Jeong, S.-W. Kang, S.H. Lee, H.-S. Park, H.J. Lee, H.S. Kim, G.-D. Lee, Effect of the grain size on hysteresis of liquid-crystalline blue phase I. J. Soc. Inf. Display **20**, 318–325 (2012)
129. Y. Chen, D. Xu, S.-T. Wu, S.-I. Yamamoto, Y. Haseba, A low voltage and submillisecond-response polymer-stabilized blue phase liquid crystal. Appl. Phys. Lett. **102**, 141116 (2013)
130. Y. Chen, J. Yan, M. Schadt, S.-H. Liu, K.-L. Cheng, J.-W. Shiu, S.-T. Wu, Diluter effects on polymer-stabilized blue phase liquid crystals. J. Display Technol. **9**, 592–597 (2013)
131. Y. Liu, Y.-F. Lan, H. Zhang, R. Zhu, D. Xu, C.-Y. Tsai, J.-K. Lu, N. Sugiura, Y.-C. Lin, S.-T. Wu, Optical rotatory power of polymer-stabilized blue phase liquid crystals. Appl. Phys. Lett. **102**, 131102 (2013)
132. J. Yan, Z. Luo, S.-T. Wu, J.-W. Shiu, Y.-C. Lai, K.-L. Cheng, S.-H. Liu, P.-J. Hsieh, Y.-C. Tsai, Low voltage and high contrast blue phase liquid crystal with red-shifted Bragg reflection. Appl. Phys. Lett. **102**, 011113 (2013)
133. L. Rao, J. Yan, S.-T. Wu, Prospects of emerging polymer-stabilized blue-phase liquid-crystal displays. J. Soc. Inf. Display **18**, 954–959 (2010)
134. S. Yoon, M. Kim, M. Su Kim, B. Gyun Kang, M.-K. Kim, A. Kumar Srivastava, S. Hee Lee, Z. Ge, L. Rao, S. Gauza, S.-T. Wu, Optimisation of electrode structure to improve the electro-optic characteristics of liquid crystal display based on the Kerr effect. Liq. Cryst **37**, 201–208 (2010)
135. M. Jiao, Y. Li, S.-T. Wu, Low voltage and high transmittance blue-phase liquid crystal displays with corrugated electrodes. Appl. Phys. Lett. **96**, 011102 (2010)
136. H.-C. Jau, P.-H. Liao, H.-W. Li, H.-K. Hsu, C.-H. Chen, C.-C. Wang, T.-H. Lin, Improvement of electro-optical properties of PSBP LCD using a double-sided IPS electrode. J. Soc. Inf. Display **20**, 351–353 (2012)

137. S. He, J.-H. Lee, H.-C. Cheng, J. Yan, S.-T. Wu, Fast-response blue-phase liquid crystal for color-sequential projection displays. J. Display Technol. **8**, 352–356 (2012)
138. G. Nordendorf, A. Hoischen, J. Schmidtke, D. Wilkes, H.S. Kitzerow, Polymer-stabilized blue phases: promising mesophases for a new generation of liquid crystal displays. Polym. Adv. Technol. **25**, 1195–1207 (2014)
139. D.-K. Yang, S.-T. Wu, in *Fundamentals of Liquid Crystal Devices*. Polymer-Stabilized Blue Phase Liquid Crystals (Wiley, Hoboken, 2014) pp. 477–512
140. J. Xiang, O.D. Lavrentovich, Blue-phase-polymer-templated nematic with sub-millisecond broad-temperature range electro-optic switching. Appl. Phys. Lett. **103**, 051112 (2013)
141. H.-C. Jau, W.-M. Lai, C.-W. Chen, Y.-T. Lin, H.-K. Hsu, C.-H. Chen, C.-C. Wang, T.-H. Lin, Study of electro-optical properties of templated blue phase liquid crystals. Opt. Mater. Express **3**, 1516–1522 (2013)
142. Y. Jin, C. Yuan, W. Shin-Tson, S. Xiaolong, Figure of merit of polymer-stabilized blue phase liquid crystals. J. Display Technol. **9**, 24–29 (2013)
143. W. De Cort, J. Beeckman, T. Claes, K. Neyts, R. Baets, Wide tuning of silicon-on-insulator ring resonators with a liquid crystal cladding. Opt. Lett. **36**, 3876–3878 (2011)
144. R. Mayén-Mondragón, J.M. Yáñez-Limón, Study of blue phases transition kinetics by thermal lens spectroscopy in cholesteryl nonanoate. Rev. Sci. Instrum. **77**, 044903 (2006)
145. I.C. Khoo, T.-H. Lin, Nonlinear optical grating diffraction in dye-doped blue-phase liquid crystals. Opt. Lett. **37**, 3225–3227 (2012)
146. I.C. Khoo, DC-field-assisted grating formation and nonlinear diffractions in methyl-red dye-doped blue phase liquid crystals. Opt. Lett. **40**, 60–63 (2015)
147. J. Ptasinski, I.-C. Khoo, Y. Fainman, Enhanced optical tuning of modified-geometry resonators clad in blue phase liquid crystals. Opt. Lett. **39**, 5435–5438 (2014)
148. I.C. Khoo, C.-W. Chen, K.L. Hong, T.-H. Lin, S. Zhao, Nonlinear optics of nematic and blue phase liquid crystals. Mol. Cryst. Liq. Cryst. **594**, 31–41 (2014)
149. I.C. Khoo, K.L. Hong, S. Zhao, D. Ma, T.-H. Lin, Blue-phase liquid crystal cored optical fiber array with photonic bandgaps and nonlinear transmission properties. Opt. Express **21**, 4319–4327 (2013)
150. Y. Wang, Q. Li, Light-driven chiral molecular switches or motors in liquid crystals. Adv. Mater. **24**, 1926–1945 (2012)
151. H.K. Bisoyi, Q. Li, Light-directing chiral liquid crystal nanostructures: from 1D to 3D. Acc. Chem. Res. **47**, 3184–3195 (2014)
152. Q. Li (ed.), *Nanoscience with Liquid Crystals: From Self-organized Nanostructures to Applications* (Springer, Heidelberg, 2014)
153. Q. Li (ed.), *Liquid Crystals Beyond Displays: Physics, Chemistry, and Applications* (Wiley, Hoboken, 2012)

Chapter 10
Interfacial Interactions in 1D and 2D Nanostructure-Based Material Systems

Changhong Ke and Xiaoming Chen

Abstract One-dimensional (1D) and two-dimensional (2D) nanostructures possess many extraordinary structural and physical/chemical properties, and are pursued for a number of innovative devices and material systems in nano science and engineering, such as nano electronics, sensors and composites. Due to their large surface-to-volume ratios, the interface in these nanostructure-based material systems plays important roles in their functionalities and performance. In this chapter, we review the fundamental knowledge of interfacial interactions and their roles in the structural and physical properties, and applications of 1D and 2D nanostructures, and survey the recent advances on the characterization of interfacial interactions in 1D and 2D nanostructure-based material systems.

10.1 Introduction

One-dimensional (1D) and two-dimensional (2D) nanostructures are two types of fundamental low-dimensional nanomaterials. They are ideal building blocks for a large number of innovative nanoscale materials and systems, such as nano electronics, sensors and composites, which have led to substantial technology innovations cross many disciplines and industries. The exceptional functionality and performance of these innovative materials and systems mostly originate from the extraordinary structural, physical and chemical characteristics of the underlying 1D and 2D building blocks. The significance of low-dimensional nanostructure is partially recognized through a Nobel Prize bestowed in 2010 to the discovery of graphene, a single-atomic thick covalent carbon honeycomb network. For many of their applications, 1D and 2D nanostructures are either assembled into micro- or macro-scale structures (e.g. yarns, thin-films and porous sponges), or integrated

C. Ke (✉) · X. Chen
Department of Mechanical Engineering, State University of New York at Binghamton, Binghamton, NY, USA
e-mail: cke@binghamton.edu

Q. Li (ed.), *Anisotropic Nanomaterials*, NanoScience and Technology,
DOI 10.1007/978-3-319-18293-3_10

with other bulk materials to form heterogeneous material systems and devices (e.g. nanocomposites and solid-state electronics). Due to their exceptionally large surface-to-volume ratios, the interfaces formed between nanostructures themselves and between nanostructures and other material surfaces play important roles in the functionality and performance of nanostructure-based material systems. Characterization of the interfacial interactions in 1D and 2D nanostructure-based material systems is a critical step towards a complete understanding of the role of nanoscale interfaces and to the tuning of their design and manufacturing for optimal functionality and performance. For instance, for 1D nanostructure-based bistable nano switches [1–4], the adhesion strength between the nanostructure and the substrate material is of importance not only in defining the stable states of the device, but also in controlling the switching processes between the stable states. Another example is the interface in nanofiber-reinforced polymer nanocomposites. The interfacial strength between nanofibers and polymer matrices has a profound influence on the bulk mechanical properties (e.g. Young's modulus, yield strength, and toughness) of polymer nanocomposites. Interfacial failure, which is observed as the dominant failure mode for polymer nanocomposites, substantially compromises the reinforcing effect of the additive high-strength nanofibers. In this chapter, we present an overview of the nanoscale interfacial interactions in 1D and 2D nanostructure-based material systems and the recent theoretical and experimental advances in characterizing the nanoscale adhesion interactions in 1D and 2D nanostructures. This chapter is organized in three parts as follows: Part I, we review the structures, properties and applications of 1D and 2D nanostructures; Part II, we discuss the nanoscale adhesion interactions in 1D and 2D nanostructures; Part III, we survey the theoretical and experimental techniques and research advances of characterizing three major types of interfacial interactions, including binding interactions between nanostructures, adhesion interactions between nanostructures and flat surfaces, and interfacial bonding interactions between nanostructures and polymer matrices.

10.2 Overview of 1D and 2D Nanostructures

1D and 2D nanostructures are mostly in the forms of nanotubes (or nanowires) and nanosheets, respectively, which are macromolecules composed of single or multiple chemical elements and are of less than 100 nm in lateral or thickness dimension. Carbon nanotubes (CNTs) [5] have been the most studied tubular nanostructures due to their exceptional material properties and application prospects. Boron nitride nanotubes (BNNTs) are another type of promising 1D tubular nanostructure, and have garnered increasing attention from the research community [6, 7]. From a structural point of view, CNTs and BNNTs are of high similarity, and are formed through rolling a graphene sheet and a hexagonal boron nitride (h-BN) nanosheet, respectively. CNT is composed of seamless covalent C–C hexagonal bonding networks, while BNNT is composed of repeated and partially ionic B–N bonding

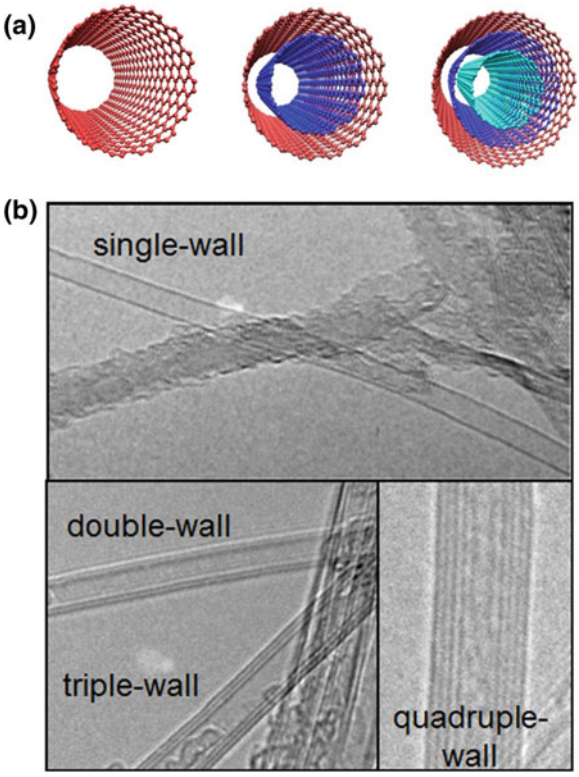

Fig. 10.1 **a** Schematics of single-, double- and triple-walled carbon nanotubes. **b** HRTEM images of single to quadruple-walled boron nitride nanotubes. (Reprinted with permission from [20, 21]. © 2012 Wiley-VCH Verlag GmbH & Co. KGaA, Weinheim and © 2012 IOP Publishing Ltd.)

networks. The rolling direction of graphene (or h-BN nanosheet) is denoted by the chirality vector (n, m). The indexes n and m denote the number of unit vectors along two directions in the honeycomb lattice. The nanotubes are called "*zig-zag*" if $m = 0$, while called "*arm-chair*" if $m = n$. Both CNT and BNNT can crystallize in single-walled and multi-walled nanophases. Multi-walled carbon nanotubes (MWCNTs) are simply composed of multiple concentric single-walled carbon nanotubes (SWCNTs), as illustrated in Fig. 10.1a. The interlayer distances are about 0.35 nm for CNT and 0.33 nm for BNNT, respectively.

Several synthesized methods have been demonstrated in growing both single- and multi-walled CNTs, such as arc discharge [8, 9], laser ablation [10], and chemical vapor deposition (CVD) [11] methods. Growth of directionally aligned CNTs has also been reported using CVD methods with the aid of external electrical fields [12]. Synthesis of high quality BNNT materials has been a major hurdle in BNNT research. BNNTs can be synthesized using catalyst based-CVD methods [13, 14], and laser heating methods [15–18]. High quality BNNTs of high crystalline, small diameters and long lengths have been synthesized using an innovative laser-based catalyst-free HTP (high-temperature/pressure) (also called PVC (pressurized vapor/condenser)) methods [19]. Figure 10.1b shows representative high-resolution

transmission electron microscopy (HRTEM) images of single- to quadruple-walled BNNTs synthesized using the HTP method [20, 21].

Both CNTs and BNNTs possess many extraordinary material properties and are promising for a number of applications. Both CNTs and BNNTs are light-weight materials and have excellent mechanical properties, thermal conductivity, and chemical stability [22]. The elastic modulus of individual CNTs is found to be ~1 TPa [23], while the elastic modulus of BNNTs as high as 1.3 TPa [24] has been reported. The reported thermal conductivity of SWCNTs is close to 3500 W m^{-1} K^{-1} [25], while the thermal conductivity of single-walled BNNTs (SWBNNTs) is predicted to be even higher than that of SWCNTs [26]. However, the electrical properties of CNTs and BNNTs are quite distinct. SWCNTs are either metallic or semi-conductive depending on their chirality vectors (n, m). SWCNTs are metallic only if $n-m$ is an integer of 3. MWCNTs typically possess metallic behaviors. In contrast, BNNTs possess a large bandgap (~5.5 eV) [7, 27–29] that is independent of their chirality vectors, and are considered as excellent electrical insulators. BNNTs have a strong resistant to oxidation at high temperature [30], and are inert to almost all harsh chemicals [31]. BNNT can survive up to 800–900 °C in air, much higher than the range of 300–400 °C reported for CNTs. CNTs hold tremendous potentials for a variety of applications, such as composites, electronics, sensors and biomedicines [32–35], while applications of BNNTs include composites [36], protective shields/capsules [37], and electrical insulators. Compared to the extensive studies and literature on the structural, material properties and applications of CNTs, the research on BNNTs is still in its very early stage, which is mainly ascribed to technical challenges in the synthesis of high quality BNNT materials [22].

Since the discovery of graphene in 2004 [38], research of 2D nanostructure has been exploding. Tremendous advances have been achieved in the study of their fundamental structure, material properties and applications. In addition to graphene and h-BN sheets, more heterogeneous van der Waals materials, such as molybdenum disulfide (MoS_2) and tungsten disulfide (WS_2), have been joining the family of 2D nanostructure. These innovative 2D nanomaterials provide platforms of studying new physical phenomena, such as quantum hall effect [39] and superlattice Dirac points [40], and enable a variety of applications, such as composites, electronics and renewable energy.

Graphene is a monolayer of carbon atoms arranged in a honeycomb network and can be considered as an un-rolled SWCNT [41–45]. Graphene has received a great deal of attention due to its exceptional mechanical, electrical and thermal properties. The Young's modulus and strength of monolayer graphene are reported to be ~1 TPa and 130 GPa, respectively [46]. Studies have shown that graphene exhibits thermal conductivity in the range of 3080–5150 W m^{-1} K^{-1} [47, 48], and possesses an exceptionally high specific surface area of 2630 m^2/g [49]. Due to its extraordinary structural and physical properties, graphene is promising for a large number of potential applications, including field-effect transistors [26, 50–52], electromechanical resonators [53], solar cells [4, 54–57], ultra-capacitors [58, 59], polymer composites [60–66], and biomedical devices [67–69].

Several production methods of graphene have been demonstrated, including bottom-up synthesis, CVD growth, and graphite exfoliation methods [70–76]. Because many applications of graphene are based on monolayer graphene sheets, production of monolayer graphene has been intensively studied and several synthesis methods have been reported. Exfoliation of graphite by using micromechanical cleavage or chemical intercalation methods is capable of producing monolayer graphene [41, 43, 77–87]. Bulk graphite flake can be first intercalated to graphite oxide in acids, and then exfoliated to graphene oxide sheets with the aid of ultrasonication or surfactant [43, 80, 81, 88, 89]. The produced graphene oxide can be reduced to graphene using treatments of hydrazine. Graphene nanosheets can be stabilized in the aqueous solution with the aid of surfactants [42, 57, 90]. To recover graphene conductivity, the chemical groups on the graphene surface can be removed by means of thermal annealing [42, 54]. It is reported that, through controlling temperature and pressure, monolayer graphene can be synthesized on the ethylene-deposited nickel surface using CVD methods [70, 71]. Production of large-size and uniform graphene on copper surface is also demonstrated [91]. Growth of wafer-size single-crystal monolayer graphene on silicon substrates is realized using CVD methods with the aid of a reusable hydrogen-terminated germanium buffer layer [92], a landmark advance toward the commercial success of graphene in electronics applications. It is also reported that narrow monolayer or few-layer graphene nanoribbons can be produced through unzipping MWCNTs using plasma etching [93] or oxidation [94] methods. Ultra-thin BN nanosheets can be produced from bulk h-BN materials using mechanical cleavage and chemical exfoliation approaches. Studies interestingly show that h-BN sheets are an ideal substrate material for graphene-based electronics [95]. Mobilities and carrier inhomogeneities for graphene electronics assembled on h-BN substrates are reported to be almost one order of magnitude better than devices on traditional SiO_2 substrates. The superior electronics performance is mostly attributed to the fact that h-BN has an atomically smooth surface and a lattice constant similar to that of graphene, and has large optical phonon modes and electrical bandgaps.

10.3 Overview of Nanoscale Adhesion Interactions

The mechanism of nanoscale adhesion interactions are generally based on two fundamental types of interface phenomena: (1) the physical adsorption based on non-bonded van der Waals interactions; (2) the chemical adsorption based on chemical bonding interactions. For pristine and defect-free carbon nanotube and graphene structures that are made of chemically stable covalent sp^2 C–C bonding networks, the van der Waals interaction-based physical adsorption accounts for the adhesion interactions between nanostructures themselves (e.g. nanotube-nanotube and graphene-graphene) and their adhesion interactions with other material surfaces (e.g. flat substrate surfaces or polymer matrices). It is noted that hybridized sp^3 bonds, which are chemically more active than sp^2 bonds, may be formed in the

structure of carbon nanotubes either by chemical treatments [96] or by introducing significant local mechanical strains [97, 98]. The existence of sp^3 bonds leads to the formation of chemical bonds on the interface between carbon nanotubes and other material surfaces (e.g. gold), resulting in substantially higher adhesion strength than the van der Waals interaction-based adsorption [99]. For nanotube- and nanosheet-based polymer nanocomposites, the interface between these nanofillers and polymer matrices is critical to their bulk mechanical properties, and thus their functionality and performance. Efficient load-transfer between nanofillers and polymer matrices requires adequate interfacial strength. The van der Waals interface is usually far from satisfying the interfacial strength requirement for a full utilization of the high-strength properties of nanofillers. To enhance the interfacial strength, the surfaces of nanotubes or nanosheets need to be chemically functionalized by introducing additional functional groups and forming strong covalent bonds on the nanofiller-polymer interface.

Due to their high-aspect-ratio characteristics, the surface-to-volume ratios for nanotubes are extremely high. Therefore, the surface effect has a significant impact on their properties and applications. For example, as-grown CNTs are typically in the form of bundles or entangled networks, rather than individually separated tubes, which is due to the van der Waals interaction among neighboring tubes in the bundle or network. Studies have shown that adhesion plays an important role in the catalyst-based nanotube synthesis [100–102]. The adhesion between catalyst particles and nanotubes needs to be strong enough in order to support the nucleation-based nanotube growth. The elastic modulus and yield strength of bundled CNTs are found to be much lower than those of individual tubes because the van der Waals interaction between neighboring tubes is much weaker than the covalent C–C bonds in the tube [103–105]. This phenomenon also occurs for BNNTs. BNNTs reportedly possess a higher surface adhesion energy compared to CNTs as a result of the strong electrostatic interaction from the permanent dipole interactions between boron and nitrogen atoms [106]. Therefore, interfacial interactions may play an even more critical role in the properties and applications of BNNTs, compared with CNTs. It is noted that the mechanical properties of MWCNTs and bundled SWCNTs can be significantly increased when nanotubes are exposed to moderate electron beam irradiation [107, 108]. The mechanical strength enhancement is attributed to the electron-beam induced cross-links between neighboring graphite layers, which significantly enhanced interfacial interactions in the bundled or concentrically nested nanotube structures.

The interfacial interaction between individual nanotubes and polymer matrices is of importance to the bulk mechanical properties of the nanotube-reinforced polymer nanocomposites. Studies on the polymerization dynamics in the presence of carbon nanotubes [109–111] suggest that these high-strength nanofillers are much more than passive contributors to the mechanical enhancement of polymers. Nanotubes not only just mix into polymers, but also initiate and participate in reactions that change polymer chains in the neighborhood of nanotubes.

Due to the important roles of the above-mentioned interfacial interactions in the synthesis, properties and applications of 1D and 2D nanostructure-based material

systems, nanoscale interfacial phenomena have been under intensive studies during the past decades by using a variety of theoretical and experimental techniques. The theoretical modeling techniques, either based on classical continuum mechanics (CM) or atomistic-level molecule dynamics (MD) and quantum mechanics (QM), usually predict the interfacial interaction based on nanostructures of either perfect structural configurations (i.e. defect-free) or pre-defined defects, such as Stone-Wales transformations. Stone-Wales transformations are a type of crystallographic defects as a result of chemical bond rotation, and may be created during either synthesis or post-synthesis deformation process of nanotubes and nanosheets [112]. Theoretical modeling and simulations are capable of providing many useful insights into the nature of interfacial adhesions, and their roles in the structural and physical properties and applications of 1D and 2D nanostructures. However, because interfacial interactions are greatly influenced by a number of factors, including inevitable and hard-to-quantify surface imperfections (e.g. defects and molecule contamination [51, 113–115]), experimental characterization of interfacial interactions is of great importance not only to the verification of the accuracy and reliability of theoretical models and predictions, but also to the development of future advanced predictive models. However, due to their nanoscale dimensions, it is technically difficult to manipulate and perform quantitative characterization of the interfacial interactions in 1D and 2D nanostructures, which demands precise positioning of nanostructure and concurrent measurements of both the applied load and the mechanical response of nanostructure with adequate force and spatial resolutions. In the following section, we review the recent advances in both theoretical studies and experimental characterization of nanoscale adhesion interactions. The review focuses on adhesion interactions in carbon nanotubes and graphene, while other nanostructures (e.g. boron nitride nanotubes and MoS_2 sheets) are also discussed.

10.4 Theoretical and Experimental Studies of Nanoscale Adhesion Interactions

10.4.1 Binding Interaction Between Nanostructures

For one pair of parallel SWCNTs, their binding interaction is based on the van der Waals interaction among all the carbon atoms on both nanotubes, and can be characterized using the Lennard-Jones potential [116]. The Lennard-Jones potential defines the interaction between two atoms as $u(r) = A/r^{12} - B/r^6$, where r is the atom distance, and A and B are material constants (for carbon-carbon interactions, $A = 15.2$ eVÅ^6 and $B = 24.1$ keVÅ^{12}) [103]. It is noted that the r^{-6} term represents attractive interactions, while the r^{-12} term represents repulsive interactions. The equilibrium distance between two atoms, r_0, corresponds to the minimum van der Waals energy and is given by $r_0 = (2A/B)^{1/6}$. By using a continuum model based

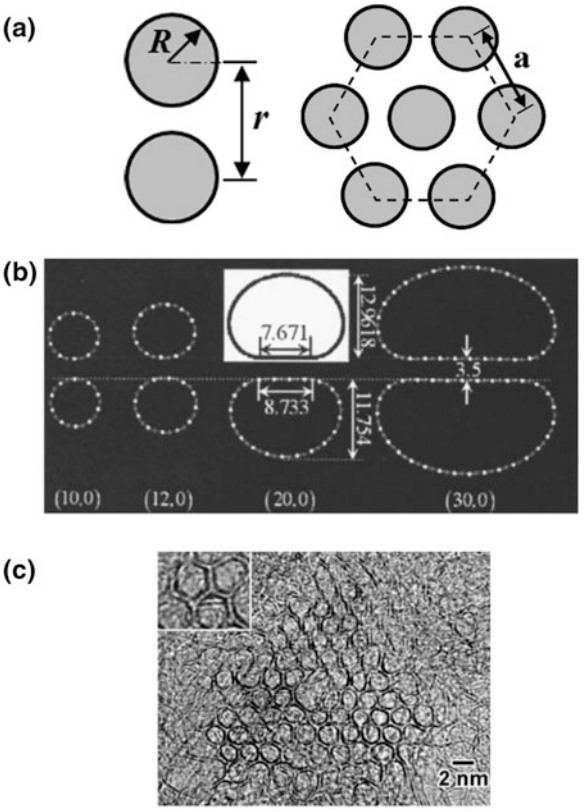

Fig. 10.2 **a** Schematics of the cross-sections of (*left*) one pair of contacting single-walled carbon nanotubes and (*right*) a bundle of single-walled carbon nanotubes in a hexagonal assembly configuration. **b** Deformed cross-sections of a series of one pair of (n, 0) carbon nanotubes. (Reprinted with permission from [117]. © 2005 American Institute of Physics Publishing LLC). **c** HRTEM image of a lattice of polygonized single-walled carbon nanotubes. (Reprinted with permission from [118]. © 2001 American Physical Society)

on the Lennard-Jones potential, the per-unit-length van der Waals energy between two identical, parallel, and undeformed SWCNTs, whose cross-sections are illustrated by the left drawing in Fig. 10.2a, is given as [103]

$$W(r) = \frac{3\pi n_\sigma^2}{8R^3}\left(-AI_A + \frac{21B}{32R^6}I_B\right), \tag{10.1}$$

in which R is the nanotube radius, r is the perpendicular distance between the tube centers, $n_\sigma = 38/\text{nm}^2$ is the graphene surface density of carbon atoms. I_A and I_B are two double integrals and are given as

$$I_A = \int_0^{2\pi}\int_0^{2\pi}\left[(\cos\theta_2 - \cos\theta_1)^2 + (\sin\theta_2 - \sin\theta_1 + r/R)^2\right]^{-5/2} \mathrm{d}\theta_1 \mathrm{d}\theta_2, \tag{10.2a}$$

$$I_B = \int_0^{2\pi}\int_0^{2\pi}\left[(\cos\theta_2 - \cos\theta_1)^2 + (\sin\theta_2 - \sin\theta_1 + r/R)^2\right]^{-11/2} \mathrm{d}\theta_1 \mathrm{d}\theta_2. \tag{10.2b}$$

The inter-tube van der Waals interaction reportedly has a substantial influence on the cross-section of nanotubes. Studies have shown that only nanotubes of small radii may preserve their circular cross-sections under the inter-tube binding interaction. By using a nonlinear elastic model, Tang et al. report that the cross-section of the nanotube remains intact if the nanotube radius $R \leq R_{cr} = \sqrt{Et^3/12W(1-v^2)}$, in which t, E and v are the effective wall thickness, Young's modulus and Poisson's ration of nanotubes, respectively [117]. For nanotubes of $R > R_{cr}$, a flat contact interface is formed as a result of the tube-tube adhesion interaction. The lateral deformation of one pair of identical nanotubes is demonstrated by MD simulations based on the Lennard-Jones potential. As shown in Fig. 10.2b, both (10, 0) and (12, 0) nanotubes are able to preserve their circular cross-sections when binding to another identical tube, while for (20, 20) and (40, 40) tubes, the binding interfaces are formed by two flat segments on the cross-sections of both tubes.

As a result of the inter-tube binding interaction, directly synthesized carbon nanotubes tend to self-organize into crystalline bundles of two dimensional triangular lattices on their cross-sections [9, 10], which are illustrated by the right drawing of Fig. 10.2a. Assuming that the nanotubes in the bundle remain undeformed, the equilibrium lattice constant is estimated to be a = 2r + 0.313 nm based on (10.1), which gives a = 1.67 nm for a bundle of (10, 10) tubes with a radius of 0.6785 nm [103]. For bundles consisting of tubes of large diameters, the inter-tube van der Waals force may induce significant tube deformations in the radial (transverse) direction, resulting in the formation of facets and hexagonal cross-sections. Figure 10.2c shows a high resolution transmission electron microscopy (HRTEM) image of single-walled carbon nanotubes in a bundle with hexagonal cross-sections (the original tube diameter is about 1.7 nm) [118].

The longitude deformation of nanotubes may be greatly affected by the adhesion interaction between the contact surfaces of different nanotubes or different segments of the same nanotube. MD simulations reveal the formation of racket-shape structures through the self-binding of a long carbon nanotube [119]. The intra-tube association and dissociation can be initiated and controlled through tuning the ambient temperature. Figure 10.3a shows a Y-shape branching junction formed by two partially bound double-walled carbon nanotubes (DWCNTs) [120]. The separation of the two tubes at the junction is considered as a result of a balanced equilibrium between the tube-tube binding interaction and the bending deformations of the tubes. The binding energy between two joined tubes at the junction point can be estimated based on the bending modulus of the tube (EI) and the separation angle 2θ. The schematic drawing in Fig. 10.3a illustrates a continuum model that considers the nanotubes as Euler beams. The binding energy per unit tube length is given as [120]

$$\gamma = \frac{4EI}{l^2}\left(\theta - 3\frac{\Delta}{l}\right)^2, \tag{10.3}$$

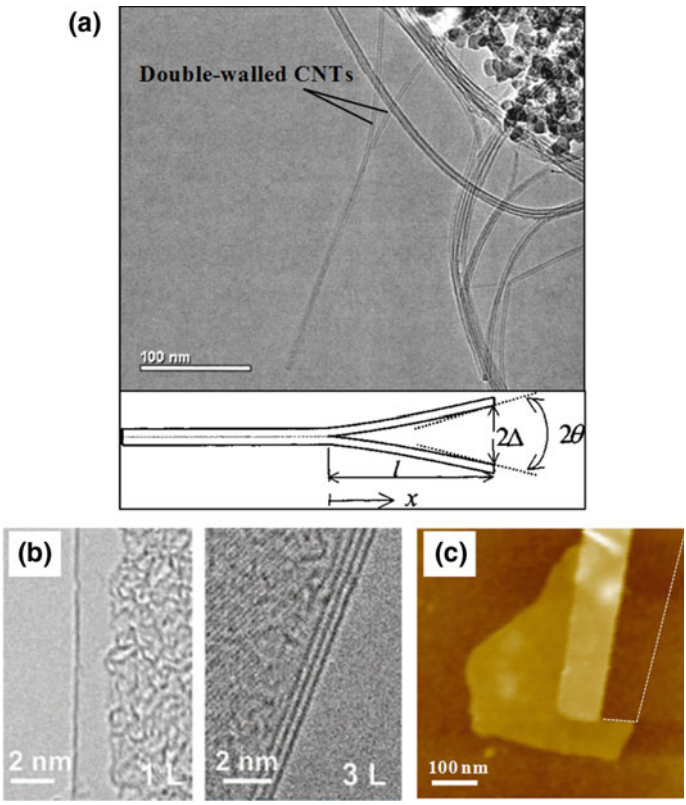

Fig. 10.3 **a** HRTEM image of double-walled carbon nanotubes synthesized by using CVD methods (*upper*); a double beam model for two adhered carbon nanotubes (*lower*). (Reprinted with permission from [120]. © 2003 American Institute of Physics Publishing LLC). **b** HRTEM images of the folding edges of graphene films with one (*left*) and three (*right*) graphite layers. (Reprinted with permission from [122]. © 2009 American Chemical Society). **c** AFM image of one partially self-folded graphene on a flat silicon oxide substrate. The *white dashed lines* mark the presumably original edge positions of the flipped graphene segment. (Reprinted with permission from [123]. © 2014 American Institute of Physics Publishing LLC)

where l is the separation length of the tube and Δ is one-half of the opening width. For the DWCNTs shown in Fig. 10.3a that have an estimated bending stiffness $EI = 1.07 \times 10^{-23}$ N m^2, γ is calculated to be 0.36 nJ/m using (10.3), which is close to the value obtained from atomistic modeling (0.32 nJ/m) [120].

Self-folding phenomenon also occurs in graphene. Compared to its high in-plane rigidity, the bending rigidity of graphene is small due to its ultra-small thickness. Therefore, it is often energetically favorable for graphene to stay in a self-folded conformation. Studies have shown that the graphene sheets can be folded by scratching using a scanning tip [85] or by high temperature annealing [121]. The two HRTEM images shown in Fig. 10.3b reveal the respective folding structures of

mono- and trilayer graphene, in particular the regions along their folding edges [122]. Figure 10.3c shows an atomic force microscopy (AFM) image of one partially self-folded trilayer graphene sheet on a flat silicon oxide substrate [123]. It can be seen from the AFM topography image that a portion of the graphene sheet ($\sim$100 nm in width) is torn and flipped on top of the flat segment on the substrate. The conformation of a self-folded graphene sheet results from a competition between its bending rigidity and adhesion interaction between graphene layers. Because graphene possesses a high Young's modulus, there is little or no in-plane stretching deformation in folded graphene. Therefore, it is a plausible venue to quantify the bending stiffness of graphene through measuring its folding conformation. For the self-folded trilayer graphene shown in Fig. 10.3c, analysis based on a nonlinear continuum mechanics model reveals that it possesses a bending stiffness of about 6.6 eV, which is about four times the reported values for monolayer graphene (1.4–1.6 eV) [124, 125].

For the experimental studies as exemplified in Fig. 10.3, the strength of the binding interaction between nanotubes or graphene can only be estimated at one single location (i.e. the separation or delamination point) due to the nature of their static equilibrium configurations. Quantification of the binding interaction at multiple positions on the interface requires nanomechanical peeling techniques. Figure 10.4a, b illustrate a nanomechanical peeling scheme that is used to study the binding interaction between two SWCNT bundles at various binding locations [126]. A selected scanning electron microscopy (SEM) snapshot of an actual peeling experiment is shown in Fig. 10.4c. The peeling measurements are performed on two partially bound nanotube bundles, including one fixed-fixed freestanding bundle. The floating-end of the other bundle is attached to the tip of a nanomanipulator probe, which is mounted to a 3D piezo-driven nanomanipulator stage. The nanomanipulator stage is incorporated with a closed-loop feedback controlled feature, and is capable of moving in XYZ axes at a resolution of 1 nm. By controlling the displacement of the probe, the grabbed nanotube bundle can be gradually peeled off from the other fixed-fixed bundle. The peeling process can be considered as a quasi-static process and the delamination of the bundle at the separation interface (i.e. the peel front) can be attributed to a balanced competition between the adhesion interaction between the nanotubes on the binding interface and the local bending deformation of the delaminated bundle. The peeling test is interpreted using a nonlinear elastica model that assumes the bundled nanotubes as an inextensible rod and is illustrated in Fig. 10.4b. The deformation profile of the peeled-off nanotube bundle can be divided into three segments: *OA*, *AB* and *BC*. Point *A* denotes the peel front. Segment *AB* is considered under pure bending, while segment *BC* is considered under pure stretching. The governing equation of the deformed rod segment *AB* is given as

$$EI\frac{\mathrm{d}^2\theta}{\mathrm{d}s^2} - P\sin(\alpha - \theta) = 0, \tag{10.4}$$

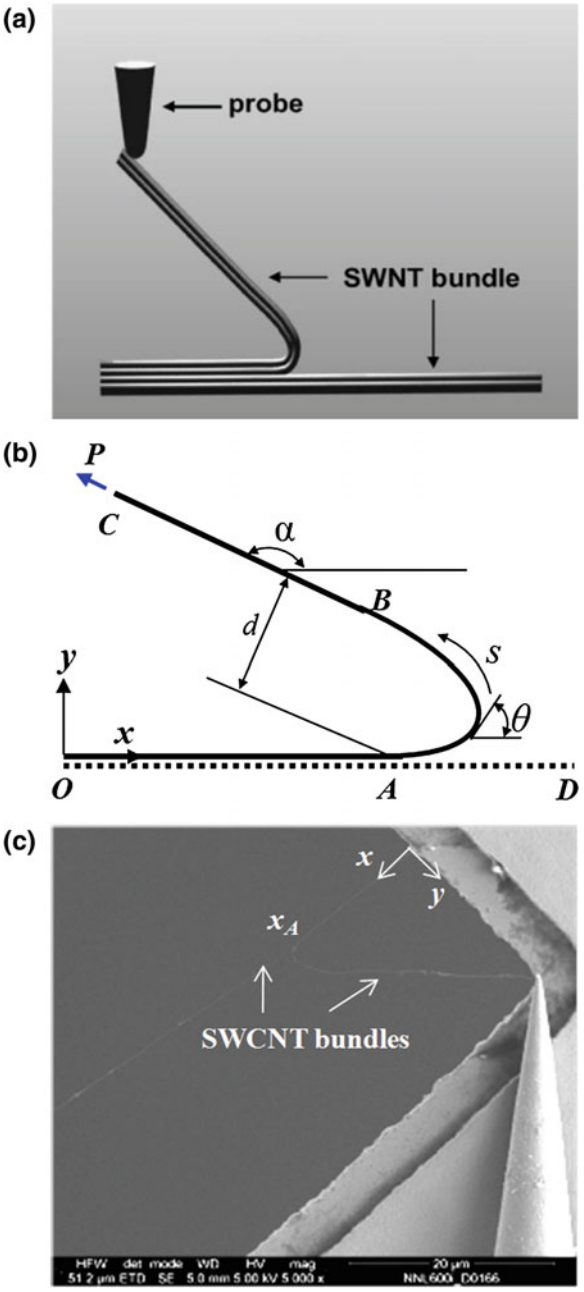

Fig. 10.4 **a** Schematic of peeling off one nanotube bundle from another free-standing nanotube bundle by means of nanomanipulation. **b** Schematic of the nonlinear elastica model for the nanomechanical peeling measurements illustrated in (**a**). **c** One representative SEM snapshot of peeling off a single-walled carbon nanotube bundle. (Reprinted with permission from [126]. © 2010 Wiley-VCH Verlag GmbH & Co. KGaA, Weinheim)

where EI is the flexural rigidity of the rod, s is the arc length along the deformed rod measured from the fixed end O, $\theta = \theta(s)$ is the slope angle of segment AB, and α is the peeling angle or slope angle of segment BC. In the Cartesian coordinate system, the corresponding governing equation for segment AB is given as [126]

$$x(\theta) = x_A + \frac{1}{\sqrt{P/EI}} \int_0^\theta \frac{\cos\theta}{\sqrt{2(1-\cos(\alpha-\theta))}} \mathrm{d}\theta \quad (0 \le \theta \le \alpha)\,, \tag{10.5a}$$

$$y(\theta) = \frac{1}{\sqrt{P/EI}} \int_0^\theta \frac{\sin\theta}{\sqrt{2(1-\cos(\alpha-\theta))}} \mathrm{d}\theta \quad (0 \le \theta \le \alpha)\,, \tag{10.5b}$$

where x_A is the x coordinate of the peel front. By fitting the measured deformation curvatures from the captured high-resolution SEM images as exemplified by Fig. 10.4c, the peeling force P, normalized by the bending stiffness of the delaminated nanotube bundle EI, can be obtained. The comparison between the measured deformation curvature for the peeled-off nanotube shown in Fig. 10.4c and the theoretical predictions based on (10.5a, 10.5b) is shown in Fig. 10.5a, which displays a good agreement with the normalized peeling force P/EI as the only fitting parameter in the theoretical prediction. The per-unit-length adhesion energy or energy release rate at the peel front is given by $G = P(1-\cos\alpha)$, in which the slope angle α is measured directly from the SEM images. Based on a series of peeling experiments at various peel front positions performed on the same nanotube sample, the corresponding peeling forces and the adhesion energies between two nanotube bundles are calculated and presented in Fig. 10.5b, c, respectively. The adhesion energy between two SWCNT bundles is found to be $G = EI(0.75 \pm 0.15)\mu\mathrm{m}^{-2}$, which indicates a 20 % fluctuation from the mean value of the predicted adhesion energy. Such variation in the adhesion energy may be attributed to several possible reasons, such as defects and/or surface contamination on the nanotube structure.

Nanomechanical peeling techniques can be also used to study the interfacial interaction in 2D nanomaterials. Tang et al. propose an in situ TEM peeling technique to investigate the initial stage in the cleavage of 2D nanostructure [127]. Figure 10.6a shows a schematic drawing of the in situ TEM peeling test of a MoS_2 crystal that is loaded in an edge-on orientation. A sharp tungsten (W) tip with a tip diameter as small as ~ 10 nm is mounted in a nanomanipulator, and is controlled to approach and contact the MoS_2 crystal. Because there are many pre-existing atomic steps on the crystal surface, it is feasible for the tungsten probe to contact the crystalline edges with a selected number of atomic layers, and then to cleave them from the crystal. The selected TEM snapshots shown in Fig. 10.6b–d demonstrate the processes of peeling single monolayer sheet from a MoS_2 crystal using the nanomechanical cleavage technique. Initially, the tungsten tip first contacts the outermost layer of MoS_2 crystal. After the contact, the probe is moved at an inclined angle, as indicated by the arrow in Fig. 10.6b. The single monolayer that is attached to the probe is gradually peeled off from the bulk crystal, as shown in

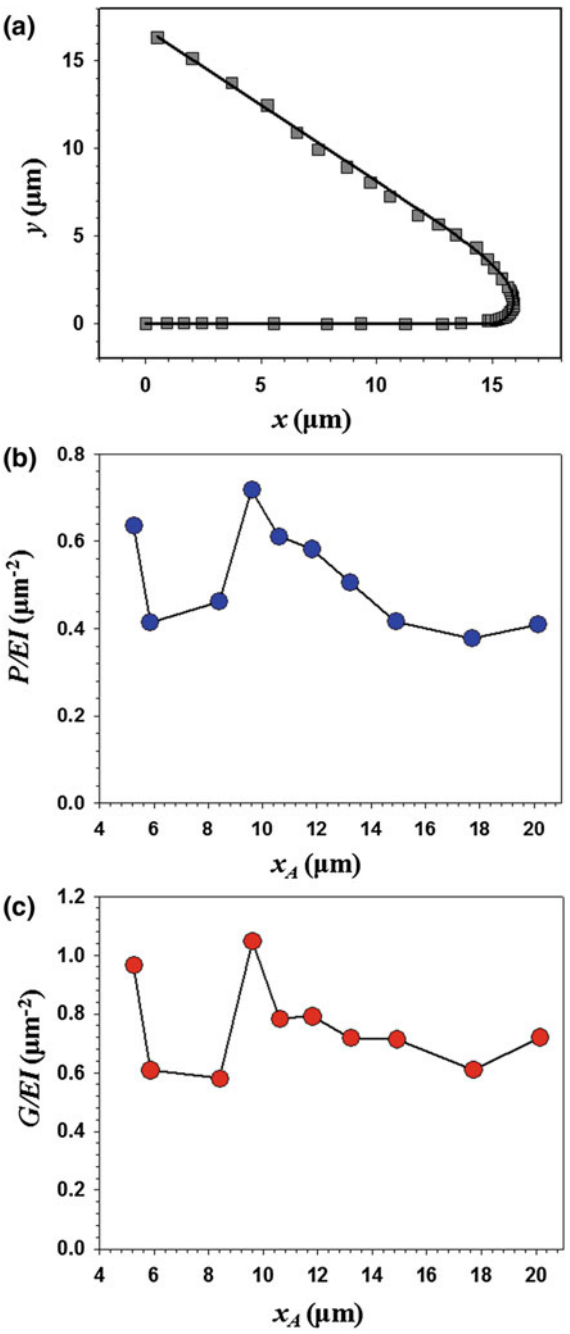

Fig. 10.5 **a** Comparison between experimental measurements (*squares*) and theoretical predictions (*solid curve*) of the deformation curve of the delaminated nanotube bundle shown in Fig. 10.4c. **b** The predicted peeling force for peeling measurements performed at a variety of peel front positions. **c** The predicted adhesion energy per unit length between the nanotube bundles at a variety of peel front positions. Both the peeling force and the adhesion energy are normalized by the bending rigidity of the delaminated bundle *EI*. (Reprinted with permission from [126]. © 2010 Wiley-VCH Verlag GmbH & Co. KGaA, Weinheim)

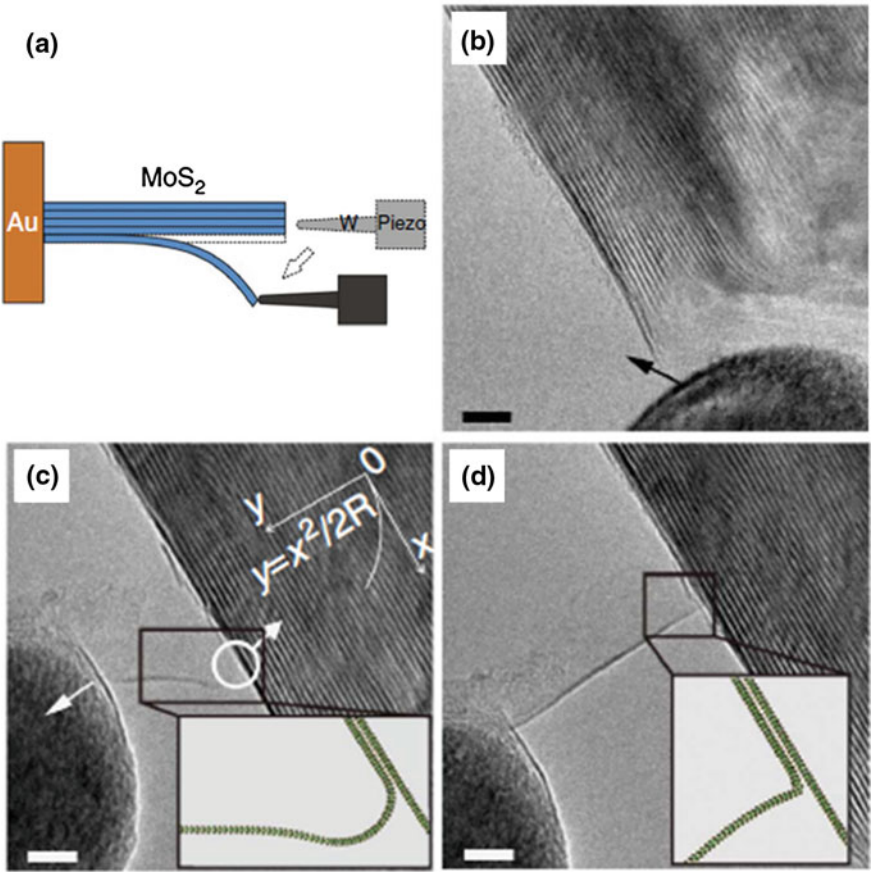

Fig. 10.6 **a** Schematic of the experimental setup for nanomechanical cleaving and peeling off individual layers from a MoS_2 crystal using a tungsten tip. **b–d** Selected HRTEM images showing nanomechanical cleavage of a monolayer MoS_2: the initial contact (**b**), intermediate peeled-off and bent (**c**), and stretched (**d**) states of a monolayer MoS_2 (*scale bars* 5 nm). The simulated atomic structures of the peeled-off monolayer MoS_2 are presented in the insets of (**c**) and (**d**). (Reprinted with permission from [127]. © 2014 Macmillan Publishers Ltd.)

Fig. 10.6c. By applying a peeling force through moving the tip, the monolayer MoS_2 sheet is stretched and ultimately separated from the bulk crystal (Fig. 10.6d). MD simulations of the cleavage of monolayer MoS_2 sheets are performed and displayed as insets in Fig. 10.6c, d for the corresponding experimental processes, which agree well with the experimental observation. The deformation profile of the monolayer MoS_2 sheet shown in Fig. 10.6c can be used to quantify the interlayer binding interaction in MoS_2 crystal. In equilibrium, the interlayer binding energy can be calculated by $\gamma = D/2R^2$, where $D = 27$ eV Å^2 atom^{-1} is the bending stiffness of monolayer MoS_2, R is the radius of curvature at the contact point and is

estimated to be ~1.5 nm through curve fitting of its measured deformation profile based on the recorded TEM image (Fig. 10.6c). The interlayer binding energy in single-crystal MoS_2 is calculated to ~0.11 N/m.

10.4.2 Adhesion Interaction Between Nanostructures and Flat Surfaces

The adhesion interactions between nanostructures and flat substrate surfaces may induce significant transverse (radial) and/or longitude structural deformation for 1D and 2D nanostructures. Hertel et al. report a molecular-mechanics study of the elastic deformation of SWCNTs and MWCNTs on flat silicon substrates [128]. The results show that the lateral deformation of the nanotube cross-section is dependent on both the outer diameter and the bending stiffness of the nanotube. As shown in Fig. 10.7a, both (5, 5) and (10, 10) tubes can keep their original circular cross-section configurations, while tubes of larger diameters, such as (20, 20) tubes, are under noticeable transverse deformations. The radial deformation of the nanotube becomes more prominent with the increase of its tube radius. A flat segment in the nanotube cross-section comes into being as a result of its binding interaction with the substrate. The radial deformation of the nanotube can decrease or even vanish by means of adding inner tube layers, thus forming double- or multi-walled carbon nanotubes as shown by the lower images in Fig. 10.7a. The increase of the inner walls effectively increases the tube's bending rigidity, while their contribution to the tube's adhesion interaction with the substrate is small. This is because the van der Waals interaction decreases rapidly with an increase of the distance. Figure 10.7b illustrates the deformations in two crossed (10, 10) carbon nanotubes on a graphite substrate that are obtained by MD simulations [128]. The upper nanotube deforms as a result of its adhesion interactions with both the lower tube and the substrate. The lower image in Fig. 10.7b reveals the atomistic level deformation of the nanotubes at the crossed tube junction. The contact between the two crossed tubes is reported to be about 5.5 nN. The cross-section heights of both tubes are reduced by 20 %. The MD simulation results demonstrate that the adhesion between the nanotube and the substrate plays an important role in the nanotube's radial deformation.

The mechanical deformations in crossed BNNT junctions are investigated by using AFM [129]. Figure 10.8a shows a representative AFM image of one crossed BNNT junction that is formed by a pair of double-walled BNNTs. From the topography image, in particular, the inset zoom-in image of the junction, it can be seen that one tube crosses over the other tube on the substrate with a cross angle of 83.7°. Figure 10.8b shows the cross-sectional profile of each tube at a position that is away from the junction as well as of the tube junction. The height of upper tube, lower tube and crossed tubes at the junction are measured to be 3.55, 3.61 and 5.5 nm, respectively. Therefore, the cross-sectional height reduction of the two

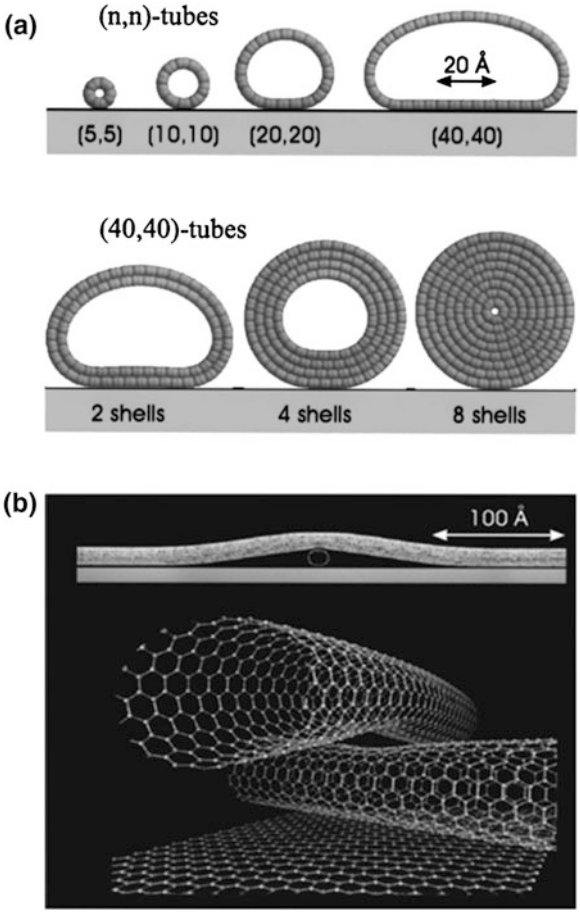

Fig. 10.7 **a** Molecular mechanics calculation of the radial deformation of carbon nanotubes on flat silicon substrates. The *upper images* show the radial compressions of single-walled carbon nanotubes of a variety of diameters. The *lower images* show the effect of the number of tube walls on the radial deformation of a (40, 40) tube. **b** Molecular mechanics calculation of the axial and radial deformations of two crossed (10, 10) carbon nanotubes. The lower image is a magnified view of the crossed nanotube junction. (Reprinted with permission from [128]. © 1998 American Physical Society)

crossed tubes is calculated to be 1.66 nm or about 23.2 % of the sum of their original tube heights. Data obtained on 12 crossed tubes junctions show that the total tube height reduction at the junction is in a nearly linear relationship with the summation of the outer diameters of the two tubes forming the junction. The contact force between the two tubes in the junction is estimated based on contact mechanics theories and is reported to be within the range of 4.2–7.6 nN. The bending deformation profile of the upper tube in the junction can be used to estimate the Young's modulus of BNNTs, which is reported to be 1.07 ± 0.11 TPa. Numerical simulations of the mechanical deformations of the crossed BNNT junctions are performed using finite element methods (FEM). Figure 10.8c shows the deformation of the crossed tube junction and the corresponding deformed finite element meshes for the junction shown in Fig. 10.8a. Detailed views of the local deformation in each tube close to the junction are displayed in Fig. 10.8d. The solid curves displayed next to the tube deformation snapshots are the respective central

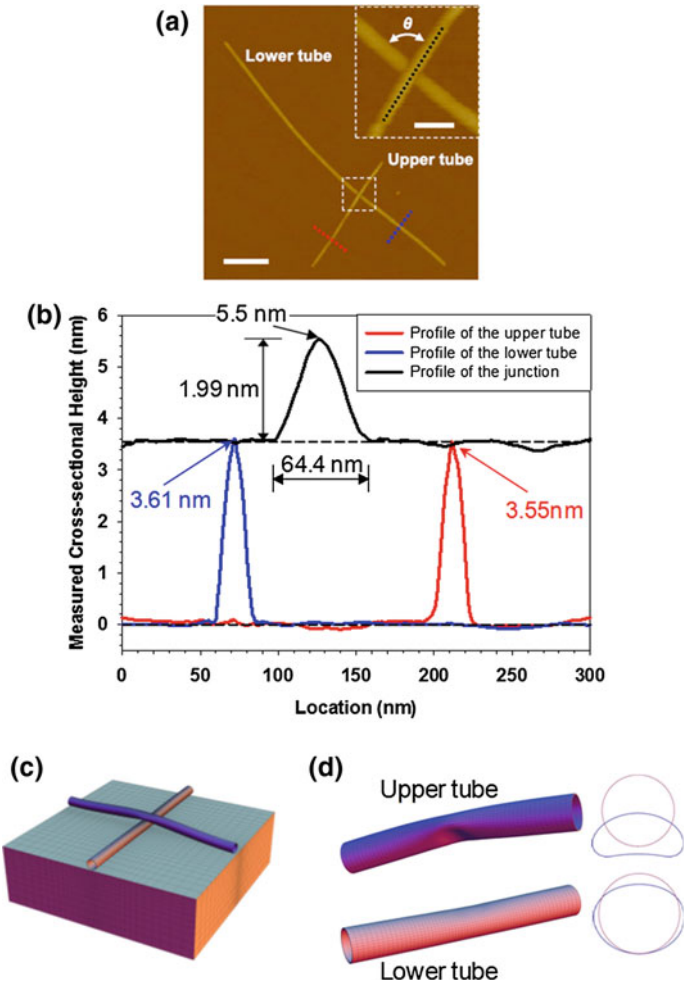

Fig. 10.8 **a** AFM image of a crossed boron nitride nanotube junction (*scale bar* 200 nm). The *inset* shows a zoom-in view of the tube junction (*scale bar* 50 nm). **b** AFM topographic profiles of the *upper* and the *lower* tubes and the tube junction along the respective *dotted lines* marked in the AFM image shown in (**a**). **c**, **d** The finite element simulation of the crossed tube junction shown in (**a**). The global view of the junction is displayed in (**c**). The local deformations of the *upper* and the *lower* tubes in the vicinity of the contact zone are displayed in (**d**). The *solid curves* shown next to the tube deformation snapshots in (**d**) are the respective central cross-sections of the deformed tubes, which are contrasted with their original undeformed shapes (*dotted curves*). (Reprinted with permission from [129]. © 2014 American Institute of Physics Publishing LLC)

cross-sections of the deformed tubes, while the dotted curves show their original undeformed cross-sections. The FEM simulation results show that the total tube height reduction at the junction is contributed mostly by the local deformation in the upper tube, which is quite substantial compared to its original shape.

The local transverse deformations of nanotubes have a substantial impact on their electrical properties. Both experiments and theoretical modeling demonstrate that the radial deformation of SWCNTs can greatly influence their electronic structures (e.g. bandgaps), and result in metal-to-semiconductor transitions or vice versa [130–132]. Radial deformations can reduce the bandgap of BNNTs from insulator to semiconductor or even conductor [133]. Tuning the bandgaps of these tubular nanostructures through engineering their transverse deformations will open new routes for many novel electronics applications, such as molecular switches [97].

Several methods have been proposed to engineer local radial deformations in nanotubes. AFM-based nanomanipulation method using sharp AFM probes is capable of inducing substantial local radial deformations in individual tubes [97, 134]. However, this method is a slow and sequential approach. The limitation indicates that the AFM-based nanomanipulation approach is only useful for processing a very small quantity of nanotubes, while not feasible for large-scale processing and integration. A simple and practical approach of engineering radial deformations in nanotubes based on a nanomembrane-covering scheme is proposed and demonstrated for both CNTs and BNNTs [135, 136]. The schematic of the membrane-covering scheme is shown in Fig. 10.9a. A covering membrane conforms to and transversely compresses an underlying nanotube as a result of its adhesion interaction with the substrate. Monolayer graphene oxide (MLGO) with a thickness of 0.7 nm is employed as covering membrane. Figure 10.9b shows one AFM image of three SWCNTs that are covered or partially covered by a MLGO membrane. The nanotube denoted with "1" in the AFM image has an original diameter or cross-sectional height of 2.36 nm, and is partially covered by the MLGO membrane with only one tube end sticking out. The two AFM line topography profiles displayed in Fig. 10.9c show the respective cross-section profiles of the uncovered and the membrane-covered portions of this tube. Its tube height of the covered portion is measured to be 1.72 nm. Therefore, the tube height reduction as a result of the MLGO covering is 0.64 nm, or 27.1 % of its original tube height. The CNT height profiles presented in Fig. 10.9c are also contrasted with the respective cross-section profiles for one selected SWBNNT of a similar original tube diameter. The measured cross-section height reduction for the BNNT is found to be 0.74 nm, which is noticeably higher than that of the SWCNT of the same tube diameter. The AFM measurements reveal that the engineered radial deformations for both types of tubes increase with the tube diameter, and are more for SWBNNTs compared with SWCNTs of the same tube diameter. The results displayed in Fig. 10.9d reveal net radial height reductions of up to 44.1 % for SWBNNTs and up to 29.7 % for SWCNTs. A similar scenario is also observed for double-walled BNNTs (DWBNNTs) and DWCNTs, with a difference of about 3–5 % in radial deformation strain within the measured tube diameter ranges. The observed difference in radial height reduction between BNNTs and CNTs is ascribed to the fact that the effective radial modulus of BNNTs is relatively smaller than that of comparable CNTs [20, 21]. The observed radial deformations for those double-walled tubes are found to be significantly lower than their respective

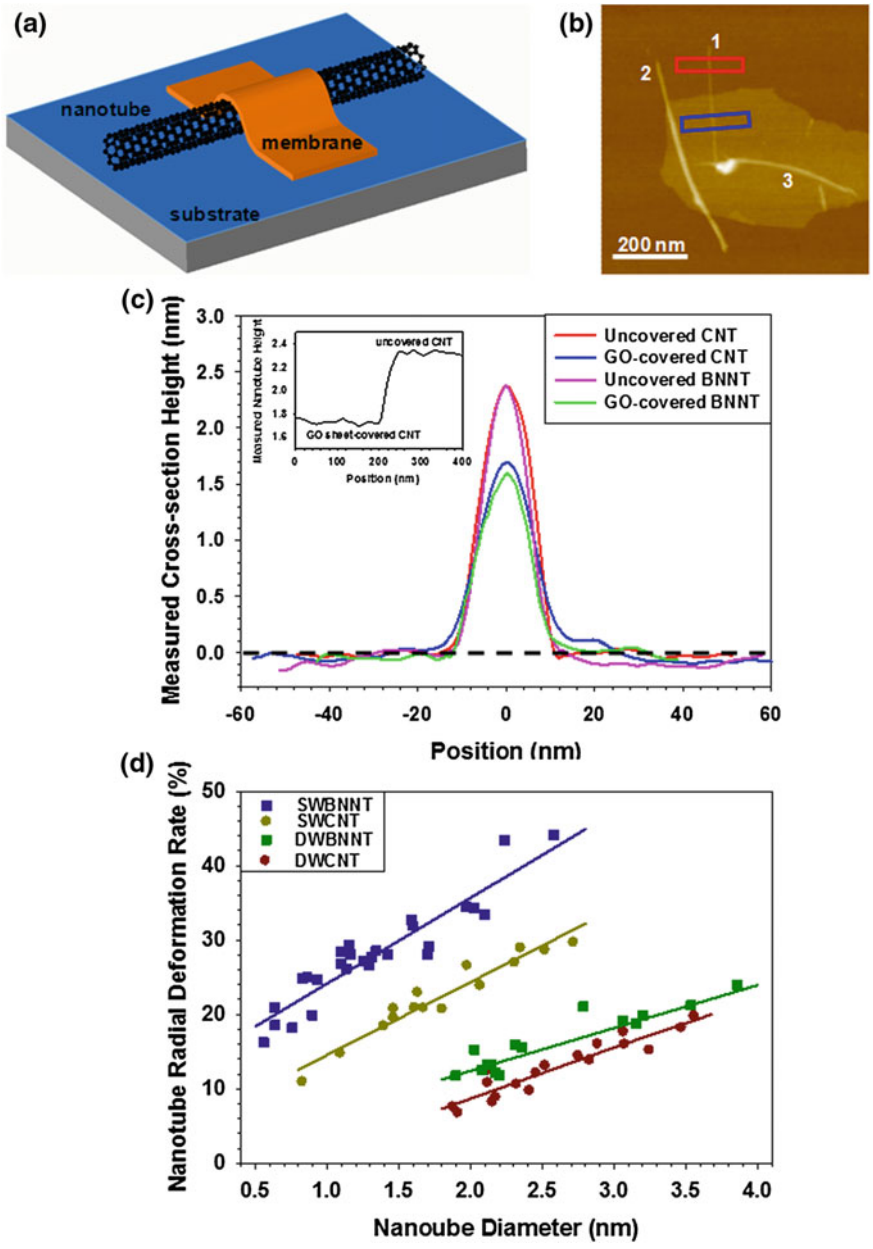
(a)
nanotube
membrane
substrate
(b)
1
2
3
200 nm
(c)
Measured Cross-section Height (nm)
Position (nm)
Uncovered CNT
GO-covered CNT
Uncovered BNNT
GO-covered BNNT
Measured Nanotube Height
uncovered CNT
GO sheet-covered CNT
Position (nm)
(d)
Nanotube Radial Deformation Rate (%)
Nanoube Diameter (nm)
SWBNNT
SWCNT
DWBNNT
DWCNT

◀ **Fig. 10.9** **a** Schematic of a nanotube on a flat substrate partially covered by a thin membrane. **b** AFM image of three dispersed carbon nanotube covered or partially covered by a monolayer graphene oxide membrane. **c** Comparison of the respective cross-section profiles of the uncovered portion and the membrane-covered portion of carbon nanotube #1 shown in (**b**), and the respective cross-section profiles for one single-walled boron nitride nanotube with a similar diameter. The *inset curve* shows the variation of the measured carbon tube height along the tube longitude axis around the edge of the covering graphene oxide membrane. (Reprinted with permission from [135]. © 2012 American Chemical Society). **d** The respective dependences of the monolayer graphene oxide membrane-covering induced actual nanotube radial strain on the nanotube outer diameters for both single- and double-walled carbon and boron nitride nanotubes. (Reprinted with permission from [136]. © 2012 American Institute of Physics Publishing LLC)

comparable single-walled counterparts. For tubes of 2 nm in outer diameter, the MLGO-covering induced radial strains in SWCNTs and SWBNNTs are reported to be 29.5 and 40.5 %, respectively, compared with 12 % for DWCNTs and 16 % for DWBNNTs. Therefore, the engineered radial deformation in nanotubes using the membrane-covering scheme decreases with the increase of the number of tube walls. The proposed approach of engineering radial deformations in nanotubes is compatible with existing micro/nano fabrication techniques and thus suitable for large-scale processing and integration.

Experimental characterization of the adhesion interaction between nanostructures and flat substrates has been documented in several studies [137–144]. The quantification of the adhesion interaction requires the delamination of the interface between the nanostructure and the substrate, either along the normal or tangent direction of the binding interface. The mechanical peeling test is a technique of separating the binding interface along its normal direction and has been widely employed to measure macroscopic adhesive strength [145] and microscopic bonding strength in thin films [146].

Strus et al. propose an AFM-based nanomechanical peeling scheme to measure the binding interaction between individual carbon nanotubes and flat substrates, as illustrated in Fig. 10.10a [140]. In this nanomechanical peeling scheme, one carbon nanotube, which is attached to a tipless AFM cantilever, is first brought into contact with a flat graphite substrate. Then the nanotube is gradually peeled off from the substrate by lifting the AFM cantilever. The vertical component of the applied peeling force on the nanotube at each peeling stage is quantified through measuring the deflection of the AFM cantilever using a laser reflection scheme. The peeling measurements are interpreted using a nonlinear elastica model. Figure 10.10b shows the theoretically predicted peeling process for both approaching (forming the nanotube-substrate interface) and retracting (separating the nanotube-substrate interface) processes based on representative parameters of the tested nanotubes [141]. The peeling force, the work needed to peel a nanotube off the substrate, and the energy release rate per unit tube length can be obtained from the recorded force-displacement distance curve. The solid curve in Fig. 10.10b illustrates all of the possible peeling forces as a function of the peeling point displacement. The dashed and solid arrowed curves represent the respective accessible forces during the processes of the nanotube approaching and retracting from the substrate. The

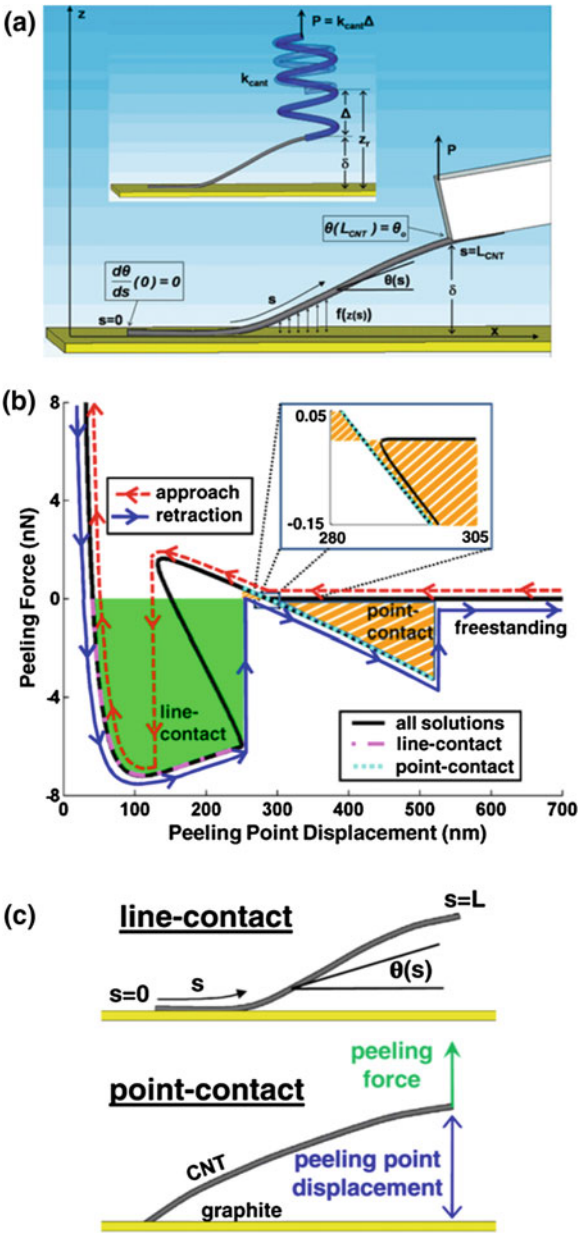

Fig. 10.10 **a** Schematic of peeling off one carbon nanotube from a flat substrate by using AFM. (Reprinted with permission from [140]. © 2008 American Chemical Society). **b** Theoretically predicted process of peeling a carbon nanotube from a graphite surface based on representative experimental parameters. **c** Schematics of the line-contact and point-contact configurations in the nanotube peeling off process. (Reprinted with permission from [141]. © 2009 Elsevier Ltd.)

contact between the nanotube and the substrate may exist in two distinct configurations: line contact (the nanotube is in an S-shape) and point contact (the nanotube is in an arc-shape), as illustrated in Fig. 10.10c, suggesting that substantial structural transitions exist for the deformed nanotube during the nanomechanical peeling

process. It is reported that the required peeling force to lift a MWCNT (1.5 μm in length, 10 and 41 nm for inner and outer diameters, respectively) from a highly order pyrolitic graphite (HOPG) substrate is 14 nN. By using this nanomechanical peeling scheme, the adhesion interactions between carbon nanotubes and a variety of material surfaces have been investigated. The per-unit-length CNT–substrate interfacial binding energies are reported to be 0.6 pJ/m for polyimide, 1.1 pJ/m for graphite, and 1.7 pJ/m for epoxy [141].

It is noted that the nanotube deformation during the nanomechanical peeling process is not directly measured in the above-mentioned AFM-based peeling scheme. The quantification of the adhesion interaction between a nanotube and a substrate has to rely on the postulated nanotube deformation curve obtained by theoretical modeling. Ishikawa et al. [147] perform nanomechanical peeling tests inside a high resolution scanning electron microscope. A self-detecting AFM cantilever is used to measure the peeling force at a resolution of 0.1 nN. The mechanical deformation of a nanotube during the peeling process is visualized and recorded by using high resolution electron beam. Their results confirm that the mechanical peeling of a nanotube from a flat substrate involves multi-stable states of the nanotube between the line and point contacts, as previously suggested by Strus et al. [140, 141]. By using this in situ SEM-AFM based nanomechanical peeling technique, the needed forces to peel off one and the same MWCNT from the substrates of graphite, mica and NaCl (001) are investigated and reported to be 2.2, 1.8, and 1.9 nN, respectively. Roenbeck et al. investigate the adhesion energy between MWCNTs and graphene using an approach combining in situ SEM peeling experiments and theoretical computations [143]. The adhesion energy at the MWCNT-graphene interface is obtained using a finite element analysis, and is reported to be 6.0 ± 2.6 nJ/m. The surface energy of graphene is analyzed using molecular mechanics simulations, and is reported to be within 0.20–0.36 J/m^2.

The AFM-based peeling technique is also employed to study chemical bonding-based adhesion interactions between CNTs and substrates. The chemical bonds on the nanotube-substrate interface are typically formed by the functional groups introduced to the surfaces of the nanotube and/or the substrate through chemical functionalization. Li et al. investigate the adhesion interaction between individual CNTs and a variety of polypeptides [148]. The adhesion interactions of the polypeptide chains coated-AFM tip to pristine CNTs and carboxylated CNTs are studied via the force-distance curve of the AFM, which operates in the force modulation mode. It is found that both the pH value of the solution and the degree of the CNT oxidation have a strong influence on the adhesion interaction. The measurements also reveal the existence of the π–π stacking interaction between aromatic moieties in the peptide chains and the nanotube surface.

Studies have suggested that the C–C bond of sp^2 hybridization in the pristine CNT can be converted to chemically more active sp^3 hybridization as a result of the local distortion strain induced by external forces [97, 98]. The hybridized sp^3 carbon atoms can form strong short-range chemical-bonding interactions with other material surfaces, such as gold. Gonzalez et al. investigate the chemical bonding force between the hybridized sp^3 C–C bond network in a SWCNT and a gold

surface inside an ultrahigh vacuum AFM [99]. A gold-coated AFM tip is controlled to first push against, and then pull from the surface of a SWCNT that is lying on a flat SiO_2 substrate. The adhesion force between the gold layer that is coated on the AFM tip and the nanotube is measured to be about 2 nN, which is consistent with density function theory (DFT)-based theoretical predictions.

The binding interaction between a nanotube in the closed circular ring configuration and a flat gold surface is investigated using a combined experimental-theoretical nanomechanical testing approach [142]. The nanomechanical testing scheme is illustrated in Fig. 10.11a, where a vertically placed CNT ring is pushed against (or pulled away from) the substrate by an external force *P*. Figure 10.11b

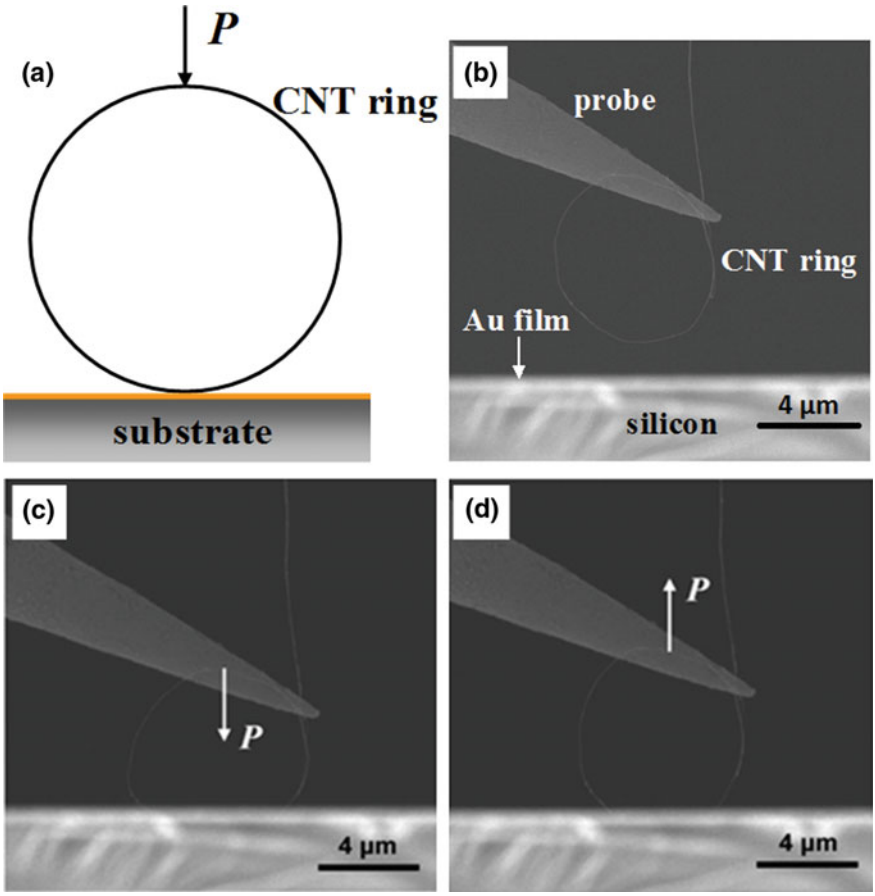

Fig. 10.11 **a** Schematic of a carbon nanotube ring on a flat substrate under a point load. **b** SEM image of a carbon nanotube ring attached to a manipulator probe being positioned close to a vertically placed flat silicon substrate with a deposited gold film on *top*. **c**, **d** SEM snapshots of the carbon nanotube ring in (**b**) being pushed against and pulled away from the substrate. (Reprinted with permission from [142]. © 2010 Wiley-VCH Verlag GmbH & Co. KGaA, Weinheim)

shows one tested CNT ring of 7 μ in diameter that is partially attached to a nanomanipulator probe. The CNT ring is formed by self-folding of a long and thin bundle of single walled carbon nanotubes through nanomanipulation inside a high resolution SEM. By adjusting the orientation of the manipulator probe, the CNT ring is placed horizontal, and its normal direction is parallel to the direction of the electron beam. The CNT ring is controlled to vertically push against or pull away from a gold film that is deposited on a flat silicon substrate. Figure 10.11c shows the compressive deformation of the CNT ring when it is pushed onto the substrate. Substantial tensile deformation occurs in the CNT ring when it is gradually pulled from the substrate. Figure 10.11d captures the tensile deformation of the CNT ring for the moment right before the CNT ring is released from the substrate. The measurements show that the deformation of the CNT ring is purely elastic and no permanent plastic deformation is observed after three repeated cycles of pushing and pulling. The mechanical deformations of the CNT ring in both compression and tension are interpreted using a nonlinear elastica model [142, 149]. Figure 10.12a, b show comparisons between experimental measurements (circle curves) and

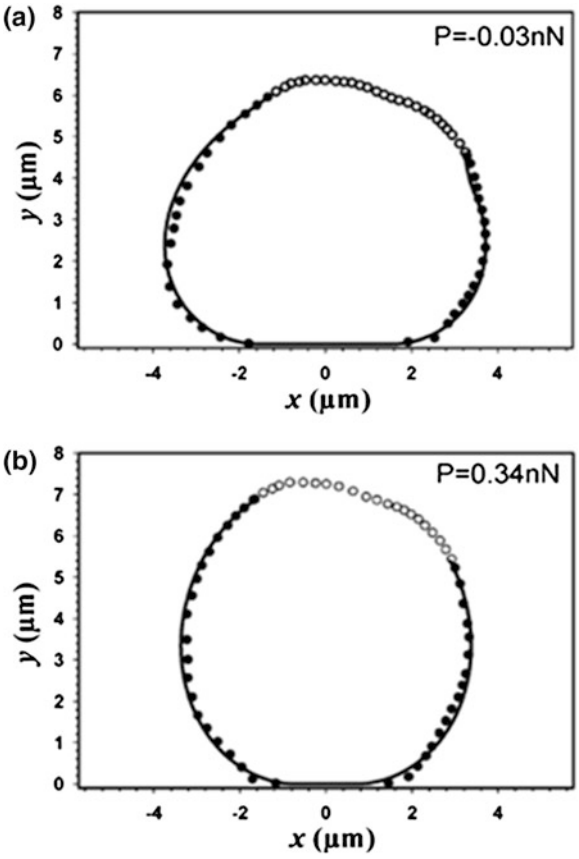

Fig. 10.12 **a**, **b** Comparison between experimental measurements (*circles*) and theoretical predictions (*solid curves*) for the deformed nanotube ring shown in Fig. 10.11c, d, respectively. The theoretically predicted applied force P is marked on each figure. (Reprinted with permission from [142]. © 2010 Wiley-VCH Verlag GmbH & Co. KGaA, Weinheim)

theoretical predictions (solid curves) on the deformation curvatures of the CNT ring in both compression and tension based on the respective SEM snapshots shown in Fig. 10.11c, d. The corresponding applied forces on the CNT ring are predicted based on the measured deformation curvatures of the CNT ring. The results show that the predicted compressive load on the CNT ring shown in Fig. 10.11c is 0.03 nN, while the predicted tensile load on the CNT ring shown in Fig. 10.11d is 0.34 nN. The measurements reveal that the van der Waals interaction between CNT ring and the substrate has a profound effect on the mechanical deformation of the CNT ring. Figure 10.13a shows the relationship between the applied force and the height of the deformed CNT ring, while Fig. 10.13b shows the relationship between the applied force and the contact length between the CNT ring and the substrate. The results show that the CNT ring of large ring diameter may experience significant deformation purely due to its adhesion interaction with the substrate. A linear relationship between the applied force and the CNT ring deformation is exhibited in Fig. 10.13a when the CNT ring is under compressive loads, suggesting that CNT nanorings can be pursued for a number of applications, such as ultrasensitive force

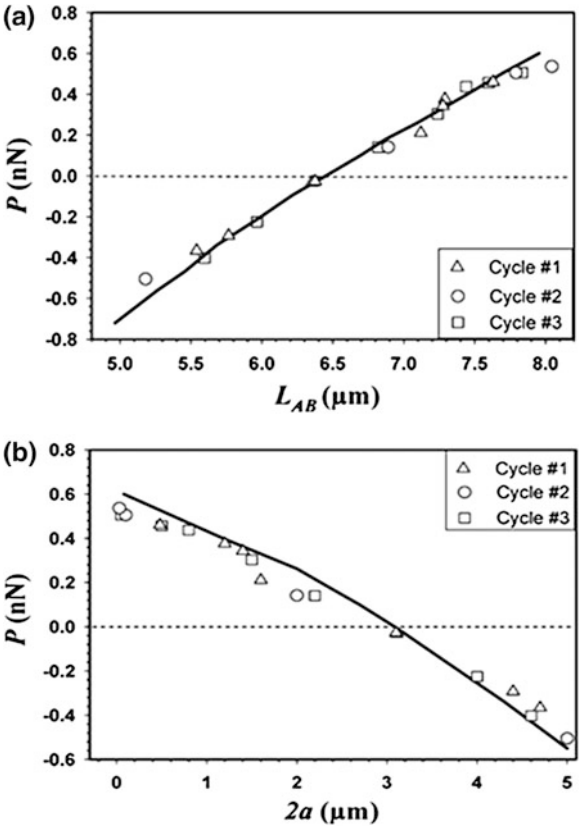

Fig. 10.13 **a** Relationship between experimentally measured ring height and theoretically predicted applied load for three repeated pushing/pulling cycles of the same nanotube ring. **b** Relationship between the theoretically predicted applied load and the contact length of the deformed ring for three repeated pushing/pulling cycles of the same carbon nanotube ring. (Reprinted with permission from [142]. © 2010 Wiley-VCH Verlag GmbH & Co. KGaA, Weinheim)

sensors and flexible and stretchable structural components in nanoscale mechanical and electromechanical systems.

Koenig et al. use a pressurized blister technique to directly measure the adhesion energy of graphene with a silicon oxide substrate [137]. The mechanically exfoliated graphene is deposited over a silicon oxide substrate patterned with pre-defined microcavities, as shown in Fig. 10.14a. The sample is then placed inside a pressurized nitrogen gas chamber until the internal pressure in the microcavity is larger than the external atmospheric pressure. The pressure difference across the graphene membrane forces the membrane to bulge upwards, resulting in an increase of the microcavity volume. The shape of the bulged graphene membrane is characterized

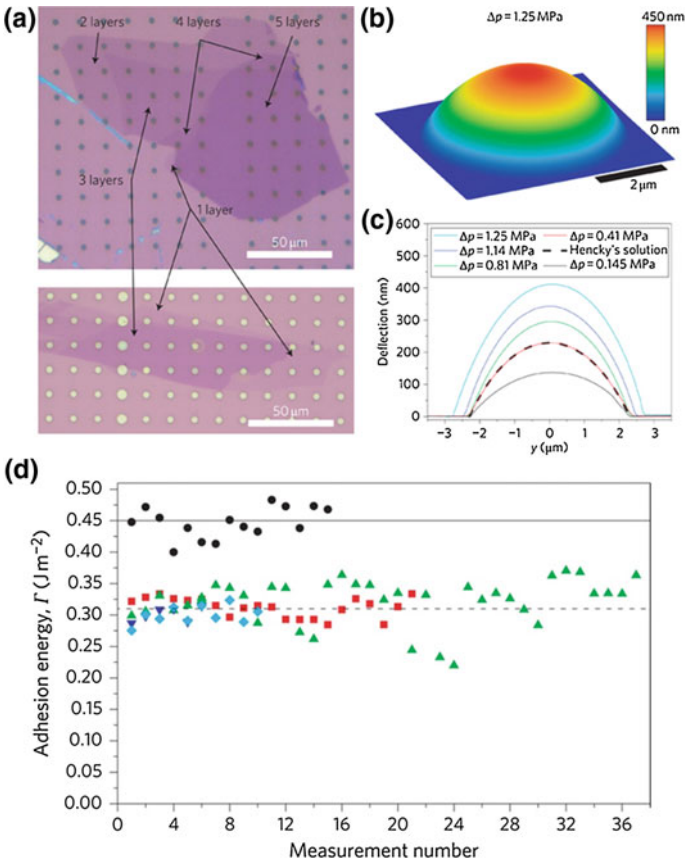

Fig. 10.14 Pressurized graphene membranes. **a** Two optical images showing graphene flakes with one to five suspended layers (*top*), and with one and three suspended layers (*bottom*). **b** AFM topography image of a pressurized graphene membrane. **c** AFM topography line profiles through the center of the pressurized graphene membrane in (**b**) under a variety of pressure differences. **d** Adhesion energy of graphene membranes with a SiOx substrate. (Reprinted with permission from [137]. © 2011 Macmillan Publishers Ltd.)

by using AFM, as shown in Fig. 10.14b. Figure 10.14c shows a series of AFM line topography profiles through the center of a pressurized graphene membrane under various pressure differences. The results indicate that the graphene membrane is either clamped to the substrate by the van der Waals force or delaminated from the substrate, and the membrane deflection increases with the internal pressure. The adhesion energy between graphene and silicon oxide substrates, as displayed in Fig. 10.14d, is reported to be 0.45 ± 0.02 J/m^2 for monolayer graphene and 0.31 ± 0.03 J/m^2 for multilayer graphene (2–5 layers). Zong et al. investigate graphene adhesion with a silicon surface by means of intercalation of nanoparticles [138]. The nanoparticles trapped at graphene-silicon interfaces act as point wedges to support axisymmetric blisters. By assuming graphene as a continuous linear elastic membrane, the local adhesion strength is calculated to be 0.151 ± 0.028 J/m^2 based on classical continuum mechanics models. Yoon et al. directly measure the adhesion energy between as-grown graphene and copper substrates using a double cantilever beam fracture mechanics testing method [144]. In the double beam test, both silicon beams with embedded graphene are loaded at a constant displacement rate, until the graphene film is delaminated from the copper substrate. The adhesion energy of graphene-copper interfaces is reported to be 0.72 ± 0.07 J/m^2, which is considerably higher than the values reported in prior two studies [137, 138]. The high adhesion energy is attributed to an increase of electronic density at the graphene-metal interface.

10.4.3 Interfacial Interaction Between Nanostructures and Polymer Matrices

For 1D and 2D nanostructure-based polymer nanocomposites, the interfacial interaction between nanostructures and supporting polymer matrices plays critical roles in the realization of the reinforcing effect of the high-strength additive nanofillers and in the bulk mechanical performance of nanocomposites. This is because the load transfer efficiency in nanocomposite materials depends on the interfacial shear strength between nanofibers and polymer matrices. A high interfacial shear stress allows the transfer of the applied load to nanofibers over a short distance. Understanding the interfacial shear stress is an essential step to the optimal design of the nanofiber-reinforced polymer nanocomposites. Because pristine nanostructures, such as CNTs and graphene, have very smooth and chemically stable surfaces, the mechanical strength of their interfaces with polymers based on pure van der Waals interactions is fairly weak, thus greatly downgrading theirs reinforcing effects. Therefore, surface functionalization of these nanofillers is of importance for increasing the mechanical performance of nanocomposites because the added functional groups on the nanostructure surface can significantly strengthen interfacial interactions, thus increasing the interfacial shear strength.

The interfacial interactions between nanofibers and polymers are usually investigated by performing single-fiber pull-out tests, in which the embedded nanofibers is stretched out of polymer matrices by an external force. The pull-out phenomenon is the prevalent failure mode observed in nanofiber-reinforced polymer nanocomposites. It is worth mentioning that a vast majority of the reported studies on nanofiber-reinforced polymers in the literature are carried out at a macroscopic level, and can at most be used to evaluate interfacial strength properties qualitatively and indirectly [150, 151]. Reports on direct, quantitative, and microscopic measurements of the interfaces formed by individual nanofibers with polymers remain quite limited [152–160]. The seemingly simple testing scheme of pulling out individual nanofibers from surrounding matrices actually poses many technical difficulties. For instance, the embedded portion of the nanofiber needs to stay in a planar and straight manner and the pulling force shall be well aligned with nanofiber axis to avoid any bending effect. It is a challenging task to grab the free end of a nanofiber and to apply and quantify the pulling load, while monitoring its mechanical response at adequate force and spatial resolutions. Some of the early-stage experimental and theoretical studies of nanotube-polymer interfaces are briefly summarized here. Figure 10.15a shows a fractured CNT–epoxy nanocomposites specimen, in which CNTs are pulled out of the polymer matrix [161]. Figure 10.15b shows an AFM-based pullout experiment to measure the fracture energy on the nanotube-polymer interface through stretching out one CNT from a polymer matrix [158]. One CNT, which is mounted to an AFM tip, is brought down to the surface of a liquid phase epoxy polymer until a substantial segment of the nanotube is embedded into the polymer. After curing, the nanotube is pulled out from the polymer by lifting off the AFM cantilever. The total interfacial fracture energy between the nanotube and the polymer is calculated based on the maximum pullout force and the embedded nanotube length. It is reported that strong interface, which corresponds to higher fracture energy, occurs for small diameter nanotubes and long embedded length. In addition, it is reported that the chemical modification of the nanotube surface provides a substantially higher interfacial strength, which is ascribed to the strong chemical bonding between the modified CNT and the polymer matrix.

The adhesion and interfacial interactions between CNTs and a variety of polymers such as polyethylene [162, 163], epoxy [164–166] and polystyrene [167] matrices have been investigated by using molecular modeling. Figure 10.15c illustrates the polyethylene cross-links on the interface of a nanotube and a bulk polyethylene polymer [162]. The single-tube pull-out tests based on MD simulations reveal that the interfacial strength is affected not only by the presence of the cross-links, but also by their locations. The cross-links on the interface may shift locations during nanotube pull-out process, thus affecting the potential energy of the whole system. Figure 10.15d shows the variation in total potential energy as a function of the pull-out displacement for interfaces with four polyethylene cross-links in upper and lower regions, which are defined based on their distances to the nanotube exposed end. It is reported that an interface with cross-links closer to the nanotube exposed end (“upper regions”) allows energy transfer along a longer pull-

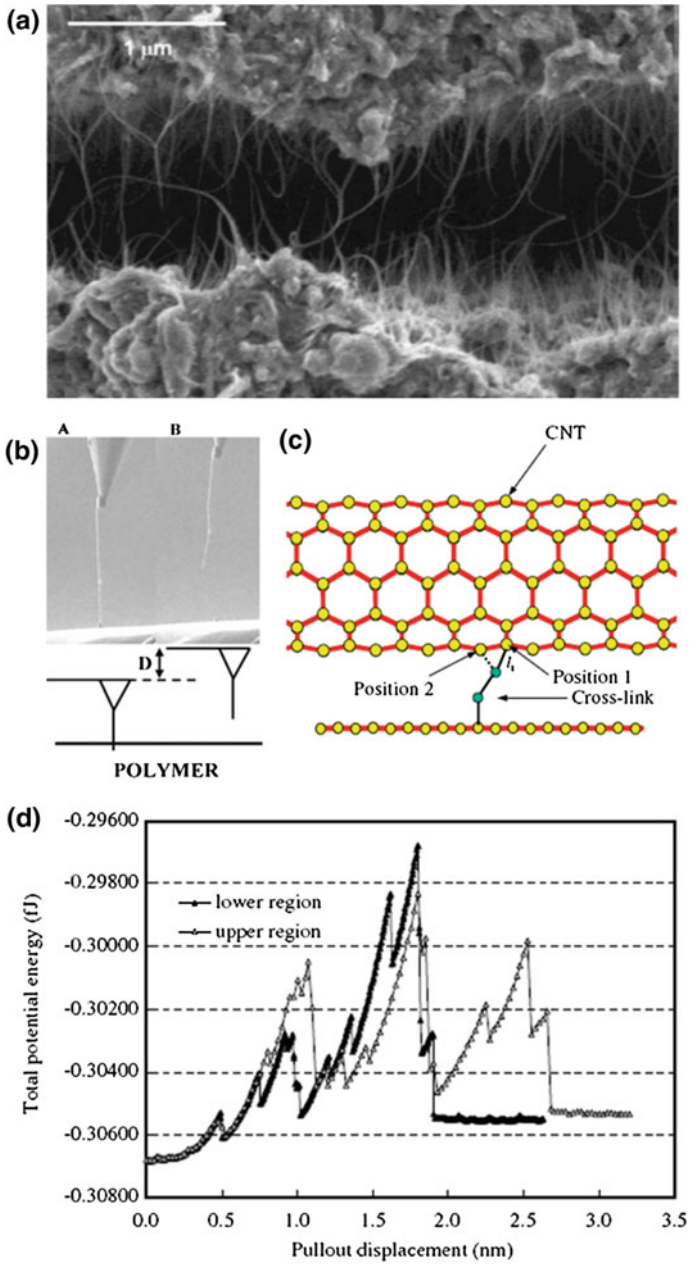

Fig. 10.15 **a** SEM image of a fractured carbon nanotube-epoxy nanocomposite specimen, showing nanotubes being pulled out of the polymer matrix. (Reprinted with permission from [161]. © 2000 Wiley-VCH Verlag GmbH, Weinheim). **b** SEM images of pulling out a single carbon nanotube from a polymer. The nanotube is mounted onto an AFM tip and partially embedded in the polymer matrix. The nanotube is pulled out from the polymer by lifting the AFM cantilever. (Reprinted with permission from [158]. © 2006 Wiley-VCH Verlag GmbH & Co. KGaA, Weinheim). **c** Schematic of position switching for cross-links on a carbon nanotube-polymer interface. **d** Energy variation during the pull-out of a carbon nanotube with four cross-links at the nanotube-polymer interface. (Reprinted with permission from [162] © 2007 Elsevier Ltd.)

out displacement because the cross-links have a longer traveling distance on the nanotube. The fluctuation in the total energy is caused by the switching of the cross-link bonds, while the interface with all cross-links in upper region has a smaller energy variation, compared to interfaces with all cross-links in the lower region. The calculated interfacial shear stress for interfaces having all cross-links in the lower region is higher compared to the case when the cross-links are all in the upper region.

In nanotube-reinforced polymer nanocomposites, the stress in the polymer is transferred to the outermost shell of the tube through the tube-polymer interface, while the inner tube shells contribute little to load bearing due to the weak inter-wall van der Waals interaction. Therefore, it is of advantage to use small-diameter tubes in exploring their polymer nanocomposites applications. Recently, an innovative single-tube pull-out testing scheme based on in situ electron microscopy nanomechanical characterization techniques is proposed to quantitatively characterize the mechanical strength of interfaces formed by individual DWCNTs (3.1 nm in median diameter) and poly(methyl methacrylate) (PMMA) and epoxy [168, 169]. Figure 10.16a illustrates the in situ nanomechanical single-tube pull-out testing scheme inside a SEM chamber. The nanotube-polymer interface is formed inside a polymer/nanotube/polymer sandwich structure, in which a free-standing cantilevered nanotube is partially embedded into a thin-film polymer. One pre-calibrated AFM cantilever that is mounted on a 3D piezo stage is used to first grip the free end of the protruding nanotube and then displaced to apply a tensile force to stretch the tube out of the polymer. With the aid of a high resolution electron beam, the mechanical deformation/displacement of both the nanotube and the AFM cantilever can be visualized in situ with resolutions of a few nanometers during the pull-out process.

Figure 10.16b, c shows two selected SEM snapshots of one representative single-tube pull-out test on a CNT–epoxy interface. The tip of an AFM force sensor is first controlled to approach the free end of a nanotube that is partially embedded into a thin film polymer, as shown in Fig. 10.16b. Then the free end of the tube is spot-welded to the tip of the AFM sensor by means of electron-beam-induced deposition (EBID) of platinum (Pt). Subsequently, the AFM force sensor is displaced incrementally to apply an increasing tensile stretching force until the embedded portion of the tube is fully pulled out of the polymer film (Fig. 10.16c). The whole tube, including the embedded segment, remains straight after pull-out, and is aligned nearly parallel to the stretching direction. A number of single-tube pull-out tests are performed on the CNT–PMMA and CNT–epoxy samples. Figure 10.17 shows the dependence of the pull-out load on the embedded tube length recorded in these measurements. The results show that the pull-out force first increases with the embedded length, and then fluctuates within a narrow band range even after a several-fold increase of the embedded length. The nanotube pull-out process can be considered as interfacial debonding process through crack propagation. The interface debonding process leads to an unchanged pull-out load when the embedded length exceeds a threshold value named as “critical embedded length”. The results shown in Fig. 10.17 reveal that an effective interfacial shear load transfer between the nanotube and the polymer occurs only within the critical

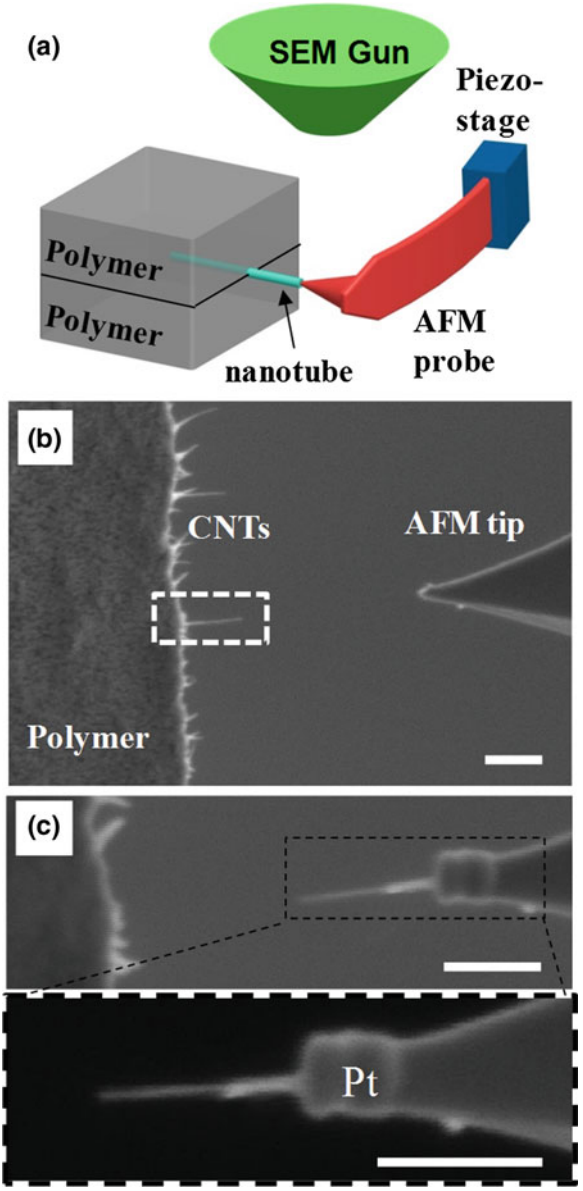

Fig. 10.16 **a** 3D illustration of an in situ nanomechanical single-tube pull-out measurement inside a scanning electron microscope. (Reprinted with permission from [168]. © 2013 Wiley-VCH Verlag GmbH & Co. KGaA, Weinheim). **b**, **c** Selected SEM snapshots of pulling out one double-walled carbon nanotube from an epoxy film. The *bottom* image in (**c**) is a zoom-in view of the pulled-out tube. The *scale bars* represent 500 nm. (Reprinted with permission from [169]. © 2015 Elsevier Ltd.)

embedded length range and any further increase of the embedded length does not lead to increase of the shear load on the nanotube-polymer interface. The observed dependence of the pull-out load on the embedded tube length is a clear indication of the shear lag effect on the failure of the CNT–epoxy and CNT–PMMA interfaces. Furthermore, the results show that the maximum pull-out load of CNT–epoxy interfaces is about 44 % higher than that of CNT–PMMA interfaces. The higher

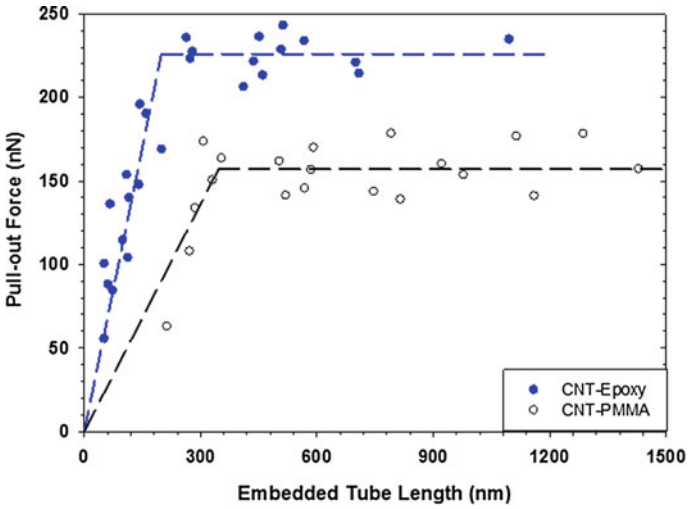

Fig. 10.17 The measured dependence of the pull-out load on the embedded tube length. The *solid dots* represent the data recorded on carbon nanotube-epoxy interface. The *empty circles* represent the data on carbon nanotube-PMMA interface. The *dashed lines* represent the respective linear fitting curves to the data set whose tube embedded lengths are below or above the critical embedded length. (Reprinted with permission from [169]. © 2015 Elsevier Ltd.)

interfacial strength of CNT–epoxy interfaces is partially attributed to the forced molecular deformations of aromatic moieties in epoxy chains in the vicinity of the binding interface, which is supported by molecular dynamics simulations of the CNT–polymer interfacial interactions [169].

The effect of the interfacial interaction between graphene and polymer on the graphene-based polymer nanocomposites has been investigated both experimentally and theoretically. In a study reported by Ramanathan et al. [83], the mechanical properties of reinforced PMMA polymer by 1 wt% functionalized graphene sheets (FGS) that are partially oxygenated substantially exceed the mechanical performance of pure PMMA as well as its composites with SWCNTs and expanded graphite (EG) plates, which is displayed in Fig. 10.18a. The superior mechanical performance of FGS-based PMMA composites is ascribed to fact that oxygen functionalities enhance the bonding interactions of graphene sheets with polymer matrices. Figure 10.18b shows an SEM image of the EG–PMMA interface. The thick protruding plates from the simple expanded graphite exhibits poor bonding to the polymer matrix. Figure 10.18c shows an SEM image of the FSG–PMMA interface. The small thickness and the wrinkled morphology features of the FGS as well as their surface chemistry lead to strong interfacial interactions with the polymer matrix, as illustrated by polymer adhesion to the pulled-out FGS. Goncalves et al. [170] investigate the mechanical properties of graphene oxide (GO)-PMMA nanocomposite films, which are prepared using different percentages of PMMA grafted GO (G-PMMA) and pristine GO. The mechanical analysis shows that G-PMMA is an effective reinforcing agent, and yields tougher films than both

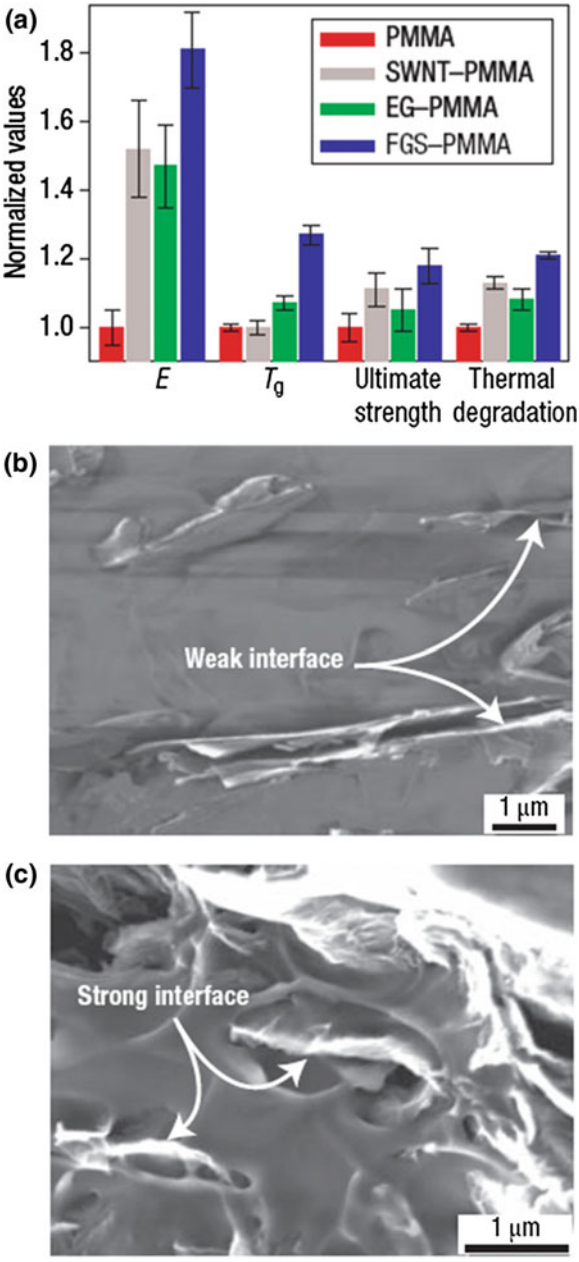

Fig. 10.18 **a** Summary of the thermo-mechanical property improvements for 1 wt% FGS–PMMA composites, compared to SWCNT–PMMA and EG–PMMA composites. All property values are normalized by the respective values for pure PMMA. **b** SEM image of EG–PMMA composites: the thick graphite plates exhibit poor bonding to the polymer matrix. **c** SEM image of FGS–PMMA composites: the graphene nanosheets exhibit strong bonding to the polymer matrix. (Reprinted with permission from [83]. © 2008 Macmillan Publishers Ltd.)

pure PMMA films and PMMA composite films with unmodified GO. Such mechanical improvement is attributed to the efficient load transfer between graphene sheets and PMMA matrices. Das et al. [171] employ the nanoindentation technique to evaluate the mechanical properties of polyvinyl alcohol (PVA) and PMMA composites reinforced by functionalized few-layer graphene. The results show a significant increase in elastic modulus, hardness and crystallinity with the addition of 0.6 wt% of graphene.

Shear lag effect on graphene-polymer interface is explored using Raman spectroscopy. Gong et al. use Raman spectroscopy to monitor stress transfer in a model composite consisting of a thin polymer film and a mechanically cleaved monolayer graphene [172]. An optical micrograph of the specimen is shown in Fig. 10.19a, which also display a schematic diagram of the specimen. Local strain mapping is performed to evaluate the adhesion strength between polymer and monolayer graphene using Raman spectroscopy. Figure 10.19b shows the local strain in the graphene monolayer at 0.4 % matrix tensile strain. The results show that the strain initially increases from the edges of graphene and keeps constant across the middle of the monolayer, which is a signature of the shear lag effect on graphene-PMMA interfaces [173]. A quite different strain distribution is observed when the matrix tensile strain is increased to 0.6 %. In this case, the strain increases linearly from the edges to the center of the graphene up to 0.6 % and decreases rapidly in the middle to around 0.4 %. This phenomenon is ascribed to a failure of the graphene-polymer interface, and the stress transfer occurs through interfacial friction. The interfacial shear strength of graphene-PMMA interfaces is reported to be about 2.3 MPa.

The van der Waals force-based interfacial binding interaction between graphene and polymer matrices [174, 175] and the role of the surface functionalization on the interfacial strength [176] are investigated using MD simulations. Figure 10.20a shows the results of the interfacial strength between graphene and polyethylene polymer by performing a peeling test to remove the graphene from the polymer surface through applying a force normal to the graphene-polymer binding interface [174]. Three cases are investigated for different boundary constraints imposed at the beginning of the simulations: *Case A*: a portion of the polymer at the top is fixed in space; *Case B*: a portion of the polymer near the graphene surface is fixed in space; *Case C*: all polymer atoms are fixed. Figure 10.20a also shows the comparison of the load–displacement response for three cases *A*, *B* and *C* in opening mode separation of the graphene sheet from the supportive polymer matrix. The required separation forces for cases *B* and *C* are comparable and significantly higher than that for case *A*. Figure 10.20b shows the effect of the surface functionalization on the graphene-polymer interfacial bonding strength [176]. The upper image in Fig. 10.20b illustrates a functionalized graphene with carboxyl groups randomly chemisorbed to 2.5 % of the carbon atoms, while the lower image shows the interaction energy during the pullout of the graphene sheet from a PMMA matrix as a function of the degree of the graphene surface functionalization. The MD simulations show that the chemical functionalization of graphene surface can dramatically increase the interfacial bonding strength between the graphene and the polymer matrix, which positively correlates with the degree of the graphene surface functionalization.

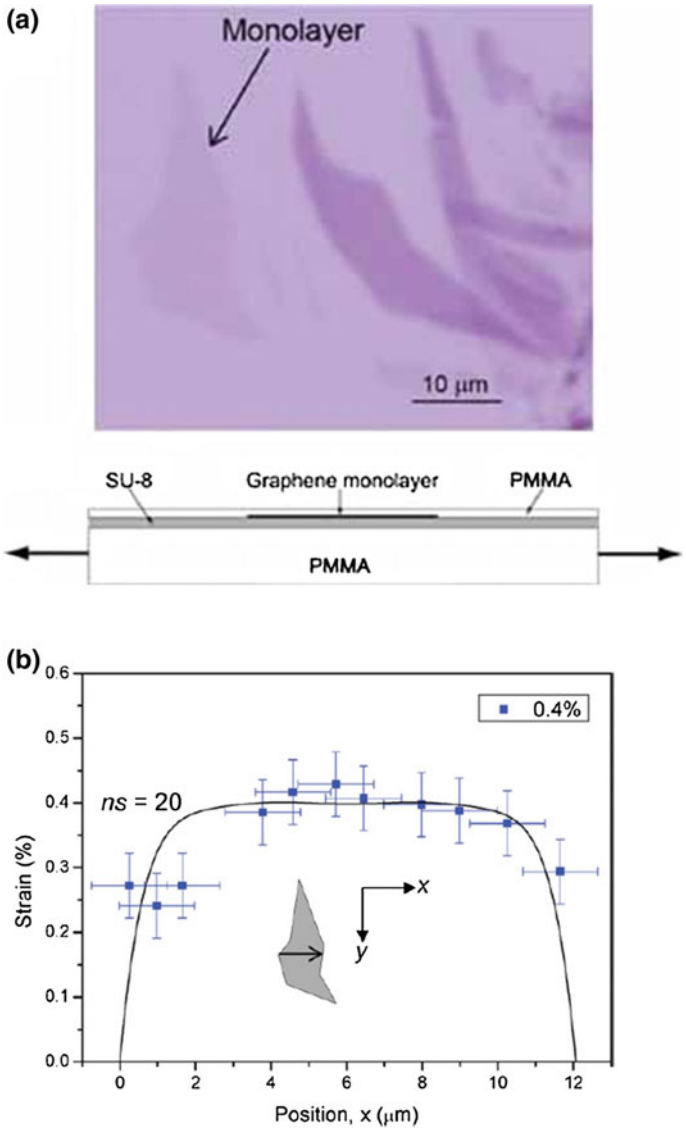

Fig. 10.19 Interfacial shear transfer at graphene-polymer interfaces. **a** *Upper* Optical micrograph showing the monolayer graphene flake investigated. *Lower* Schematic diagram of a section through the composite. **b** Variation of axial strain in the x-direction with positions across the monolayer graphene at matrix strains of 0.4 %. The *solid lines* are fitting curves based on the shear-lag theory. (Reprinted with permission from [172]. © 2010 Wiley-VCH Verlag GmbH & Co. KGaA, Weinheim)

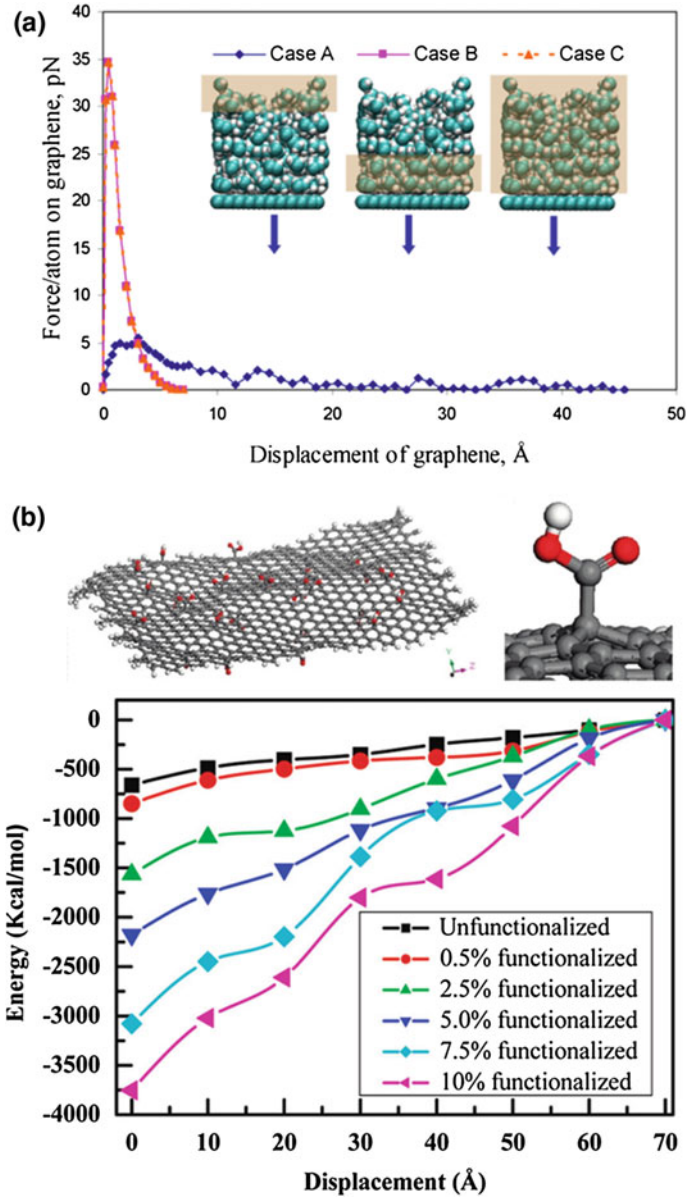

Fig. 10.20 **a** Comparison of the load-displacement responses for cases *A*, *B* and *C* in opening mode separation of the monolayer graphene from the supporting polymer matrix. (Reprinted with permission from [174]. © 2009 IOP Publishing Ltd.). **b** *Upper* Illustration of graphene with carboxyl groups randomly chemisorbed to 2.5 % of the carbon atoms. *Lower* Interfacial interaction energy in the pull-out of the graphene sheet from the PMMA matrix at various degrees of graphene functionalization. (Reprinted with permission from [176]. © 2010 American Chemical Society)

10.5 Conclusions and Outlook

Nanoscale adhesions play an important role in the properties and applications of 1D and 2D nanostructure-based materials systems, and have been an active and intensively researched area during the past decade. The recent fast growing interests on the scalable synthesis of innovative 1D and 2D materials as well as the rapid development of experimental and computational characterization instrumentation and infrastructure will continue to drive the future research on this area. In particular, non-carbon materials in the family of vdW nanostructures (e.g. boron nitride, molybdenum disulfide and tungsten disulfide) have been garnering increasing attention. Unlike the symmetric and non-polarized C–C bond, the chemical bonds in these non-carbon nanomaterials are formed by two or more chemical elements and generally polarized. The resulting non-uniformly distributed electron charges lead to strong electrostatic interactions. Therefore, the nanoscale adhesion in these non-carbon nanostructure-based material systems is more sophisticated and scientifically stimulating in nature. Computational modeling will likely play an even more important role in the nanoscale adhesion research thanks to the tremendous development of infrastructure for high-performance computing. In spite of the current attempts to use the computational simulations in studying nanoscale adhesions, we believe that there are more rooms for researchers to make contribution to the development of novel modeling and simulation tools that allow the simulations of nanoscale adhesion complementary to the experimental observations on both spatial and temporal scales. The complementary experimental and computational effort will help to decipher many of the complex and delicate nanoscale adhesion phenomena that are inaccessible by either experiments or modeling/simulations alone.

Acknowledgments The authors gratefully thank the financial support from State University of New York at Binghamton, American Chemical Society-Petroleum Research Fund, and US Air Force Office of Scientific Research. A special thanks is due to Dr. M. Zheng, co-author of a previous version of the chapter [177]. We freely used material from the previous version and thank him for his contribution.

References

1. T. Rueckes, K. Kim, E. Joselevich, G.Y. Tseng, C.L. Cheung, C.M. Lieber, Carbon nanotube-based nonvolatile random access memory for molecular computing. Science **289**, 94–97 (2000)
2. C.H. Ke, H.D. Espinosa, Feedback controlled nanocantilever device. Appl. Phys. Lett. **85**, 681–683 (2004)
3. C.H. Ke, H.D. Espinosa, In situ electron microscopy electromechanical characterization of a bistable NEMS device. Small **2**, 1484–1489 (2006)
4. J.E. Jang, S.N. Cha, Y. Choi, G.A.J. Amaratunga, D.J. Kang, D.G. Hasko, J.E. Jung, J.M. Kim, Nanoelectromechanical switches with vertically aligned carbon nanotubes. Appl. Phys. Lett. **87**, 163114 (2005)
5. S. Iijima, Helical microtubules of graphitic carbon. Nature **354**, 56–58 (1991)

6. N.G. Chopra, R.J. Luyken, K. Cherrey, V.H. Crespi, M.L. Cohen, S.G. Louie, A. Zettl, Boron-nitride nanotubes. Science **269**, 966–967 (1995)
7. A. Rubio, J.L. Corkill, M.L. Cohen, Theory of graphitic boron-nitride nanotubes. Phys. Rev. B **49**, 5081–5084 (1994)
8. T.W. Ebbesen, P.M. Ajayan, Large-scale synthesis of carbon nanotubes. Nature **358**, 220–222 (1992)
9. C. Journet, W.K. Maser, P. Bernier, A. Loiseau, M.L. de la Chapelle, S. Lefrant, P. Deniard, R. Lee, J.E. Fischer, Large-scale production of single-walled carbon nanotubes by the electric-arc technique. Nature **388**, 756–758 (1997)
10. A. Thess, R. Lee, P. Nikolaev, H. Dai, P. Petit, J. Robert, C. Xu, Y.H. Lee, S.G. Kim, A.G. Rinzler, D.T. Colbert, G.E. Scuseria, D. Tománek, J.E. Fischer, R.E. Smalley, Crystalline ropes of metallic carbon nanotubes. Science **273**, 483–487 (1996)
11. W.Z. Li, S.S. Xie, L.X. Qian, B.H. Chang, B.S. Zou, W.Y. Zhou, R.A. Zhao, G. Wang, Large-scale synthesis of aligned carbon nanotubes. Science **274**, 1701–1703 (1996)
12. Y. Zhang, A. Chang, J. Cao, Q. Wang, W. Kim, Y. Li, N. Morris, E. Yenilmez, J. Kong, H. Dai, Electric-field-directed growth of aligned single-walled carbon nanotubes. Appl. Phys. Lett. **79**, 3155–3157 (2001)
13. C.-Y. Su, Z.-Y. Juang, K.-F. Chen, B.-M. Cheng, F.-R. Chen, K.-C. Leou, C.-H. Tsai, Selective growth of boron nitride nanotubes by the plasma-assisted and iron-catalytic CVD eethods. J. Phys. Chem. C **113**, 14681–14688 (2009)
14. O.R. Lourie, C.R. Jones, B.M. Bartlett, P.C. Gibbons, R.S. Ruoff, W.E. Buhro, CVD growth of boron nitride nanotubes. Chem. Mater. **12**, 1808–1810 (2000)
15. D. Golberg, Y. Bando, M. Eremets, K. Takemura, K. Kurashima, H. Yusa, Nanotubes in boron nitride laser heated at high pressure. Appl. Phys. Lett. **69**, 2045–2047 (1996)
16. D.P. Yu, X.S. Sun, C.S. Lee, I. Bello, S.T. Lee, H.D. Gu, K.M. Leung, G.W. Zhou, Z.F. Dong, Z. Zhang, Synthesis of boron nitride nanotubes by means of excimer laser ablation at high temperature. Appl. Phys. Lett. **72**, 1966–1968 (1998)
17. T. Laude, Y. Matsui, A. Marraud, B. Jouffrey, Long ropes of boron nitride nanotubes grown by a continuous laser heating. Appl. Phys. Lett. **76**, 3239–3241 (2000)
18. R. Arenal, O. Stephan, J.-L. Cochon, A. Loiseau, Root-growth mechanism for single-walled boron nitride nanotubes in laser vaporization technique. J. Am. Chem. Soc. **129**, 16183–16189 (2007)
19. M.W. Smith, K.C. Jordan, C. Park, J.-W. Kim, P.T. Lillehei, R. Crooks, J.S. Harrison, Very long single- and few-walled boron nitride nanotubes via the pressurized vapor/condenser method. Nanotechnology **20**, 505604 (2009)
20. M. Zheng, X. Chen, I.-T. Bae, C. Ke, C. Park, M.W. Smith, K. Jordan, Radial mechanical properties of single-walled boron nitride nanotubes. Small **8**, 116–121 (2012)
21. M. Zheng, C. Ke, I.-T. Bae, C. Park, M.W. Smith, K. Jordan, Radial elasticity of multi-walled boron nitride nanotubes. Nanotechnology **23**, 095703 (2012)
22. D. Golberg, Y. Bando, Y. Huang, T. Terao, M. Mitome, C.C. Tang, C.Y. Zhi, Boron nitride nanotubes and nanosheets. ACS Nano **4**, 2979–2993 (2010)
23. M.S. Dresselhaus, *Carbon Nanotubes* (Springer, Berlin, 2001)
24. N.G. Chopra, A. Zettl, Measurement of the elastic modulus of a multi-wall boron nitride nanotube. Solid State Commun. **105**, 297–300 (1998)
25. E. Pop, D. Mann, Q. Wang, K. Goodson, H.J. Dai, Thermal conductance of an individual single-wall carbon nanotube above room temperature. Nano Lett. **6**, 96–100 (2006)
26. Y. Xiao, X.H. Yan, J.X. Cao, J.W. Ding, Y.L. Mao, J. Xiang, Specific heat and quantized thermal conductance of single-walled boron nitride nanotubes. Phys. Rev. B **69**, 205415 (2004)
27. X. Blase, A. Rubio, S.G. Louie, M.L. Cohen, Stability and band gap constancy of boron nitride nanotubes. EPL Europhys. Lett. **28**, 335 (1994)
28. C.H. Lee, M. Xie, V. Kayastha, J. Wang, Y.K. Yap, Patterned growth of boron nitride nanotubes by catalytic chemical vapor deposition. Chem. Mater. **22**, 1782–1787 (2010)

29. C.H. Lee, J. Wang, V.K. Kayatsha, J.Y. Huang, Y.K. Yap, Effective growth of boron nitride nanotubes by thermal chemical vapor deposition. Nanotechnology **19**, 455605 (2008)
30. Y. Chen, J. Zou, S.J. Campbell, G. Le Caer, Boron nitride nanotubes: pronounced resistance to oxidation. Appl. Phys. Lett. **84**, 2430–2432 (2004)
31. D. Golberg, Y. Bando, K. Kurashima, T. Sato, Synthesis and characterization of ropes made of BN multiwalled nanotubes. Scr. Mater. **44**, 1561–1565 (2001)
32. H.G. Craighead, Nanoelectromechanical systems. Science **290**, 1532–1535 (2000)
33. B. Mahar, C. Laslau, R. Yip, Y. Sun, Development of carbon nanotube-based sensors: a review. Sens. J. IEEE **7**, 266–284 (2007)
34. J.N. Coleman, U. Khan, Y.K. Gun'ko, Mechanical reinforcement of polymers using carbon nanotubes. Adv. Mater. **18**, 689–706 (2006)
35. Z. Liu, S. Tabakman, K. Welsher, H.J. Dai, Carbon nanotubes in biology and medicine: in vitro and in vivo detection, imaging and drug delivery. Nano Res. **2**, 85–120 (2009)
36. C. Zhi, Y. Bando, T. Terao, C. Tang, H. Kuwahara, D. Golberg, Towards thermoconductive, electrically insulating polymeric composites with boron nitride nanotubes as fillers. Adv. Funct. Mater. **19**, 1857–1862 (2009)
37. Y. Li, P.S. Dorozhkin, Y. Bando, D. Golberg, Controllable modification of SiC nanowires encapsulated in BN nanotubes. Adv. Mater. **17**, 545–549 (2005)
38. K.S. Novoselov, A.K. Geim, S.V. Morozov, D. Jiang, Y. Zhang, S.V. Dubonos, I.V. Grigorieva, A.A. Firsov, Electric field effect in atomically thin carbon films. Science **306**, 666–669 (2004)
39. Y. Zhang, Y.-W. Tan, H.L. Stormer, P. Kim, Experimental observation of the quantum Hall effect and Berry's phase in graphene. Nature **438**, 201–204 (2005)
40. M. Yankowitz, J. Xue, D. Cormode, J.D. Sanchez-Yamagishi, K. Watanabe, T. Taniguchi, P. Jarillo-Herrero, P. Jacquod, B.J. LeRoy, Emergence of superlattice Dirac points in graphene on hexagonal boron nitride. Nat. Phys. **8**, 382–386 (2012)
41. K.S. Novoselov, D. Jiang, F. Schedin, T.J. Booth, V.V. Khotkevich, S.V. Morozov, A.K. Geim, Two-dimensional atomic crystals. Proc. Natl. Acad. Sci. U.S.A. **102**, 10451–10453 (2005)
42. D. Li, M.B. Müller, S. Gilje, R.B. Kaner, G.G. Wallace, Processable aqueous dispersions of graphene nanosheets. Nat. Nanotechnol. **3**, 101–105 (2008)
43. S. Stankovich, D.A. Dikin, G.H.B. Dommett, K.M. Kohlhaas, E.J. Zimney, E.A. Stach, R.D. Piner, S.T. Nguyen, R.S. Ruoff, Graphene-based composite materials. Nature **442**, 282–286 (2006)
44. A.K. Geim, K.S. Novoselov, The rise of graphene. Nat. Mater. **6**, 183–191 (2007)
45. D. Li, R.B. Kaner, Graphene-based materials. Science **320**, 1170–1171 (2008)
46. C. Lee, X. Wei, J.W. Kysar, J. Hone, Measurement of the elastic properties and intrinsic strength of monolayer graphene. Science **321**, 385–388 (2008)
47. D. Teweldebrhan, A.A. Balandin, Modification of graphene properties due to electron-beam irradiation. Appl. Phys. Lett. **94**, 013101 (2009)
48. S. Ghosh, I. Calizo, D. Teweldebrhan, E.P. Pokatilov, D.L. Nika, A.A. Balandin, W. Bao, F. Miao, C.N. Lau, Extremely high thermal conductivity of graphene: prospects for thermal management applications in nanoelectronic circuits. Appl. Phys. Lett. **92**, 151911 (2008)
49. D.R. Dreyer, S. Park, C.W. Bielawski, R.S. Ruoff, The chemistry of graphene oxide. Chem. Soc. Rev. **39**, 228–240 (2009)
50. X. Li, X. Wang, L. Zhang, S. Lee, H. Dai, Chemically derived, ultrasmooth graphene nanoribbon semiconductors. Science **319**, 1229–1232 (2008)
51. G.D. Lee, C.Z. Wang, E. Yoon, N.M. Hwang, K.M. Ho, The formation of pentagon-heptagon pair defect by the reconstruction of vacancy defects in carbon nanotube. Appl. Phys. Lett. **92**, 043104 (2008)
52. C. Józsa, M. Popinciuc, N. Tombros, H.T. Jonkman, B.J. van Wees, Electronic spin drift in graphene field-effect transistors. Phys. Rev. Lett. **100**, 236603 (2008)

53. J.S. Bunch, A.M. van der Zande, S.S. Verbridge, I.W. Frank, D.M. Tanenbaum, J.M. Parpia, H.G. Craighead, P.L. McEuen, Electromechanical resonators from graphene sheets. Science **315**, 490–493 (2007)
54. X. Wang, L. Zhi, K. Müllen, Transparent, conductive graphene electrodes for dye-sensitized solar cells. Nano Lett. **8**, 323–327 (2008)
55. J. Zhou, P. Fei, Y.F. Gao, Y.D. Gu, J. Liu, G. Bao, Z.L. Wang, Mechanical-electrical triggers and sensors using piezoelectric micowires/nanowires. Nano Lett. **8**, 2725–2730 (2008)
56. W. Hong, Y. Xu, G. Lu, C. Li, G. Shi, Transparent graphene/PEDOT–PSS composite films as counter electrodes of dye-sensitized solar cells. Electrochem. Commun. **10**, 1555–1558 (2008)
57. J.B. Wu, H.A. Becerril, Z.N. Bao, Z.F. Liu, Y.S. Chen, P. Peumans, Organic solar cells with solution-processed graphene transparent electrodes. Appl. Phys. Lett. **92**, 263302 (2008)
58. M.D. Stoller, S. Park, Y. Zhu, J. An, R.S. Ruoff, Graphene-based ultracapacitors. Nano Lett. **8**, 3498–3502 (2008)
59. S.R.C. Vivekchand, C.S. Rout, K.S. Subrahmanyam, A. Govindaraj, C.N.R. Rao, Graphene-based electrochemical supercapacitors. J. Chem. Sci. **120**, 9–13 (2008)
60. S. Wang, M. Tambraparni, J. Qiu, J. Tipton, D. Dean, Thermal expansion of graphene composites. Macromolecules **42**, 5251–5255 (2009)
61. S. Ganguli, A.K. Roy, D.P. Anderson, Improved thermal conductivity for chemically functionalized exfoliated graphite/epoxy composites. Carbon **46**, 806–817 (2008)
62. Y. Sanchez-Paisal, D. Sanchez-Portal, N. Garmendia, R. Munoz, I. Obieta, J. Arbiol, L. Calvo-Barrio, A. Ayuela, Zr-metal adhesion on graphenic nanostructures. Appl. Phys. Lett. **93**, 053101 (2008)
63. S. Wang, Y. Zhang, N. Abidi, L. Cabrales, Wettability and surface free energy of graphene films. Langmuir **25**, 11078–11081 (2009)
64. K. Kalaitzidou, H. Fukushima, L.T. Drzal, Mechanical properties and morphological characterization of exfoliated graphite-polypropylene nanocomposites. Compos. Part -Appl. Sci. Manuf. **38**, 1675–1682 (2007)
65. D. Cho, S. Lee, G. Yang, H. Fukushima, L.T. Drzal, Dynamic mechanical and thermal properties of phenylethynyl-terminated polyimide composites reinforced with expanded graphite nanoplatelets. Macromol. Mater. Eng. **290**, 179–187 (2005)
66. S.H. Xie, Y.Y. Liu, J.Y. Li, Comparison of the effective conductivity between composites reinforced by graphene nanosheets and carbon nanotubes. Appl. Phys. Lett. **92**, 243121 (2008)
67. N. Mohanty, V. Berry, Graphene-based single-bacterium resolution biodevice and DNA transistor: interfacing graphene derivatives with nanoscale and microscale biocomponents. Nano Lett. **8**, 4469–4476 (2008)
68. M. Xu, D. Fujita, N. Hanagata, Perspectives and challenges of emerging single-molecule DNA sequencing technologies. Small **5**, 2638–2649 (2009)
69. W. Hu, C. Peng, W. Luo, M. Lv, X. Li, D. Li, Q. Huang, C. Fan, Graphene-based antibacterial paper. ACS Nano **4**, 4317–4323 (2010)
70. C. Berger, Z. Song, X. Li, X. Wu, N. Brown, C. Naud, D. Mayou, T. Li, J. Hass, A.N. Marchenkov, E.H. Conrad, P.N. First, W.A. de Heer, Electronic confinement and coherence in patterned epitaxial graphene. Science **312**, 1191–1196 (2006)
71. J. Hass, W.A. de Heer, E.H. Conrad, The growth and morphology of epitaxial multilayer graphene. J. Phys.: Condens. Matter. **20**, 323202 (2008)
72. K.V. Emtsev, F. Speck, T. Seyller, L. Ley, J.D. Riley, Interaction, growth, and ordering of epitaxial graphene on SiC{0001} surfaces: a comparative photoelectron spectroscopy study. Phys. Rev. B **77**, 155303 (2008)
73. P.W. Sutter, J.-I. Flege, E.A. Sutter, Epitaxial graphene on ruthenium. Nat. Mater. **7**, 406–411 (2008)
74. A.L. Vázquez de Parga, F. Calleja, B. Borca, M.C.G. Passeggi, J.J. Hinarejos, F. Guinea, R. Miranda, Periodically rippled graphene: growth and spatially resolved electronic structure. Phys. Rev. Lett. **100**, 056807 (2008)

75. W. Zhou, Y. Huang, B. Liu, J. Wu, K.C. Hwang, B.Q. Wei, Adhesion between carbon nanotubes and substrate: mimicking the gecko foothair. NANO **2**, 175–179 (2007)
76. L. Zhi, K. Müllen, A bottom-up approach from molecular nanographenes to unconventional carbon materials. J. Mater. Chem. **18**, 1472–1484 (2008)
77. U. Stöberl, U. Wurstbauer, W. Wegscheider, D. Weiss, J. Eroms, Morphology and flexibility of graphene and few-layer graphene on various substrates. Appl. Phys. Lett. **93**, 051906 (2008)
78. Q. Shao, G. Liu, D. Teweldebrhan, A.A. Balandin, High-temperature quenching of electrical resistance in graphene interconnects. Appl. Phys. Lett. **92**, 202108 (2008)
79. D. Dietzel, T. Mönninghoff, L. Jansen, H. Fuchs, C. Ritter, U.D. Schwarz, A. Schirmeisen, Interfacial friction obtained by lateral manipulation of nanoparticles using atomic force microscopy techniques. J. Appl. Phys. **102**, 084306 (2007)
80. H.E. Jeong, K.Y. Suh, Nanohairs and nanotubes: Efficient structural elements for gecko-inspired artificial dry adhesives. Nano Today **4**, 335–346 (2009)
81. Y. Kashiwase, T. Ikeda, T. Oya, T. Ogino, Manipulation and soldering of carbon nanotubes using atomic force microscope. Appl. Surf. Sci. **254**, 7897–7900 (2008)
82. G. Wang, X. Gou, J. Horvat, J. Park, Facile synthesis and characterization of iron oxide semiconductor nanowires for gas sensing application. J. Phys. Chem. C **112**, 15220–15225 (2008)
83. T. Ramanathan, A.A. Abdala, S. Stankovich, D.A. Dikin, M. Herrera-Alonso, R.D. Piner, D. H. Adamson, H.C. Schniepp, X. Chen, R.S. Ruoff, S.T. Nguyen, I.A. Aksay, R.K. Prud'Homme, L.C. Brinson, Functionalized graphene sheets for polymer nanocomposites. Nat. Nanotechnol. **3**, 327–331 (2008)
84. B.Z. Jang, A. Zhamu, Processing of nanographene platelets (NGPs) and NGP nanocomposites: a review. J. Mater. Sci. **43**, 5092–5101 (2008)
85. H.C. Schniepp, K.N. Kudin, J.-L. Li, R.K. Prud'homme, R. Car, D.A. Saville, I.A. Aksay, Bending properties of single functionalized graphene sheets probed by atomic force microscopy. ACS Nano **2**, 2577–2584 (2008)
86. T. Szabó, O. Berkesi, P. Forgó, K. Josepovits, Y. Sanakis, D. Petridis, I. Dékány, Evolution of surface functional groups in a series of progressively oxidized graphite oxides. Chem. Mater. **18**, 2740–2749 (2006)
87. C. Xu, X. Wu, J. Zhu, X. Wang, Synthesis of amphiphilic graphite oxide. Carbon **46**, 386–389 (2008)
88. M. Lotya, Y. Hernandez, P.J. King, R.J. Smith, V. Nicolosi, L.S. Karlsson, F.M. Blighe, S. De, Z. Wang, I.T. McGovern, G.S. Duesberg, J.N. Coleman, Liquid Phase production of graphene by exfoliation of graphite in surfactant/water solutions. J. Am. Chem. Soc. **131**, 3611–3620 (2009)
89. S. Vadukumpully, J. Paul, S. Valiyaveettil, Cationic surfactant mediated exfoliation of graphite into graphene flakes. Carbon **47**, 3288–3294 (2009)
90. D.A. Dikin, S. Stankovich, E.J. Zimney, R.D. Piner, G.H.B. Dommett, G. Evmenenko, S.T. Nguyen, R.S. Ruoff, Preparation and characterization of graphene oxide paper. Nature **448**, 457–460 (2007)
91. X. Li, W. Cai, J. An, S. Kim, J. Nah, D. Yang, R. Piner, A. Velamakanni, I. Jung, E. Tutuc, S.K. Banerjee, L. Colombo, R.S. Ruoff, Large-area synthesis of high-quality and uniform graphene films on copper foils. Science **324**, 1312–1314 (2009)
92. J.-H. Lee, E.K. Lee, W.-J. Joo, Y. Jang, B.-S. Kim, J.Y. Lim, S.-H. Choi, S.J. Ahn, J.R. Ahn, M.-H. Park, C.-W. Yang, B.L. Choi, S.-W. Hwang, D. Whang, Wafer-scale growth of single-crystal monolayer graphene on reusable hydrogen-terminated germanium. Science **344** (6181), 286–289 (2014)
93. L. Jiao, X. Xian, Z. Wu, J. Zhang, Z. Liu, Selective positioning and integration of individual single-walled carbon nanotubes. Nano Lett. **9**, 205–209 (2009)
94. D.V. Kosynkin, A.L. Higginbotham, A. Sinitskii, J.R. Lomeda, A. Dimiev, B.K. Price, J.M. Tour, Longitudinal unzipping of carbon nanotubes to form graphene nanoribbons. Nature **458**, 872–876 (2009)

95. C.R. Dean, A.F. Young, I. Meric, C. Lee, L. Wang, S. Sorgenfrei, K. Watanabe, T. Taniguchi, P. Kim, K.L. Shepard, J. Hone, Boron nitride substrates for high-quality graphene electronics. Nat. Nanotechnol. **5**, 722–726 (2010)
96. J.-L. Tsai, S.-H. Tzeng, Y.-J. Tzou, Characterizing the fracture parameters of a graphene sheet using atomistic simulation and continuum mechanics. Int. J. Solids Struct. **47**, 503–509 (2010)
97. T.W. Tombler, C. Zhou, L. Alexseyev, J. Kong, H. Dai, L. Liu, C.S. Jayanthi, M. Tang, S.-Y. Wu, Reversible electromechanical characteristics of carbon nanotubes under local-probe manipulation. Nature **405**, 769–772 (2000)
98. E.D. Minot, Y. Yaish, V. Sazonova, J.-Y. Park, M. Brink, P.L. McEuen, Tuning carbon nanotube band gaps with strain. Phys. Rev. Lett. **90**, 156401 (2003)
99. C. González, J. Ortega, F. Flores, D. Martínez-Martín, J. Gómez-Herrero, Initial stages of the contact between a metallic tip and carbon nanotubes. Phys. Rev. Lett. **102**, 106801 (2009)
100. F. Ding, P. Larsson, J.A. Larsson, R. Ahuja, H. Duan, A. Rosén, K. Bolton, The importance of strong carbon–metal adhesion for catalytic nucleation of single-walled carbon nanotubes. Nano Lett. **8**, 463–468 (2008)
101. M.A. Ribas, F. Ding, P.B. Balbuena, B.I. Yakobson, Nanotube nucleation versus carbon-catalyst adhesion–probed by molecular dynamics simulations. J. Chem. Phys. **131**, 224501 (2009)
102. P. Larsson, J.A. Larsson, R. Ahuja, F. Ding, B.I. Yakobson, H. Duan, A. Rosén, K. Bolton, Calculating carbon nanotube–catalyst adhesion strengths. Phys. Rev. B **75**, 115419 (2007)
103. L.A. Girifalco, M. Hodak, R.S. Lee, Carbon nanotubes, buckyballs, ropes, and a universal graphitic potential. Phys. Rev. B **62**, 13104–13110 (2000)
104. J.P. Lu, Elastic properties of carbon nanotubes and nanoropes. Phys. Rev. Lett. **79**, 1297–1300 (1997)
105. C. Ke, M. Zheng, I.-T. Bae, G. Zhou, Adhesion-driven buckling of single-walled carbon nanotube bundles. J. Appl. Phys. **107**, 104305 (2010)
106. J.H. Hsu, S.H. Chang, Surface adhesion between hexagonal boron nitride nanotubes and silicon based on lateral force microscopy. Appl. Surf. Sci. **256**, 1769–1773 (2010)
107. B. Peng, M. Locascio, P. Zapol, S. Li, S.L. Mielke, G.C. Schatz, H.D. Espinosa, Measurements of near-ultimate strength for multiwalled carbon nanotubes and irradiation-induced crosslinking improvements. Nat. Nanotechnol. **3**, 626–631 (2008)
108. A. Kis, G. Csanyi, J.P. Salvetat, T.N. Lee, E. Couteau, A.J. Kulik, W. Benoit, J. Brugger, L. Forro, Reinforcement of single-walled carbon nanotube bundles by intertube bridging. Nat. Mater. **3**, 153–157 (2004)
109. Z. Jia, Z. Wang, C. Xu, J. Liang, B. Wei, D. Wu, S. Zhu, Study on poly(methyl methacrylate)/carbon nanotube composites. Mater. Sci. Eng. A **271**, 395–400 (1999)
110. R. Haggenmueller, F. Du, J.E. Fischer, K.I. Winey, Interfacial in situ polymerization of single wall carbon nanotube/nylon 6,6 nanocomposites. Polymer **47**, 2381–2388 (2006)
111. W. Leelapornpisit, M.-T. Ton-That, F. Perrin-Sarazin, K.C. Cole, J. Denault, B. Simard, Effect of carbon nanotubes on the crystallization and properties of polypropylene. J. Polym. Sci., Part B: Polym. Phys. **43**, 2445–2453 (2005)
112. H. Jiang, X.Q. Feng, Y. Huang, K.C. Hwang, P.D. Wu, Defect nucleation in carbon nanotubes under tension and torsion: Stone-Wales transformation. Comput. Methods Appl. Mech. Eng. **193**, 3419–3429 (2004)
113. G.G. Samsonidze, G.G. Samsonidze, B.I. Yakobson, Energetics of Stone-Wales defects in deformations of monoatomic hexagonal layers. Comput. Mater. Sci. **23**, 62–72 (2002)
114. K.I. Tserpes, P. Papanikos, The effect of Stone-Wales defect on the tensile behavior and fracture of single-walled carbon nanotubes. Compos. Struct. **79**, 581–589 (2007)
115. H.S. Wong, C. Durkan, N. Chandrasekhar, Tailoring the local interaction between graphene layers in graphite at the atomic scale and above using scanning tunneling microscopy. ACS Nano **3**, 3455–3462 (2009)
116. J.E. Lennard-Jones, Perturbation problems in quantum mechanics. Proc. R. Soc. A **129**, 598–615 (1930)

117. T. Tang, A. Jagota, C.-Y. Hui, Adhesion between single-walled carbon nanotubes. J. Appl. Phys. **97**, 074304 (2005)
118. M.J. López, A. Rubio, J.A. Alonso, L.-C. Qin, S. Iijima, Novel polygonized single-wall carbon nanotube bundles. Phys. Rev. Lett. **86**, 3056–3059 (2001)
119. M.J. Buehler, Y. Kong, H. Gao, Y. Huang, Self-folding and unfolding of carbon nanotubes. J. Eng. Mater. Technol. **128**, 3–10 (2006)
120. B. Chen, M. Gao, J.M. Zuo, S. Qu, B. Liu, Y. Huang, Binding energy of parallel carbon nanotubes. Appl. Phys. Lett. **83**, 3570–3571 (2003)
121. Z. Liu, K. Suenaga, P.J.F. Harris, S. Iijima, Open and closed edges of graphene layers. Phys. Rev. Lett. **102**, 015501 (2009)
122. A. Reina, X. Jia, J. Ho, D. Nezich, H. Son, V. Bulovic, M.S. Dresselhaus, J. Kong, Large area, few-layer graphene films on arbitrary substrates by chemical vapor deposition. Nano Lett. **9**, 30–35 (2009)
123. X. Chen, L. Zhang, Y. Zhao, X. Wang, C. Ke, Graphene folding on flat substrates. J. Appl. Phys. **116**, 164301 (2014)
124. D.-B. Zhang, E. Akatyeva, T. Dumitrică, Bending ultrathin graphene at the margins of continuum mechanics. Phys. Rev. Lett. **106**, 255503 (2011)
125. N.G. Chopra, L.X. Benedict, V.H. Crespi, M.L. Cohen, S.G. Louie, A. Zettl, Fully collapsed carbon nanotubes. Nature **377**, 135–138 (1995)
126. C. Ke, M. Zheng, G. Zhou, W. Cui, N. Pugno, R.N. Miles, Mechanical peeling of free-standing single-walled carbon nanotube bundles. Small **6**, 438–445 (2010)
127. D.-M. Tang, D.G. Kvashnin, S. Najmaei, Y. Bando, K. Kimoto, P. Koskinen, P.M. Ajayan, B.I. Yakobson, P.B. Sorokin, J. Lou, D. Golberg, Nanomechanical cleavage of molybdenum disulphide atomic layers. Nat. Commun. **5**, 3631 (2014)
128. T. Hertel, R.E. Walkup, P. Avouris, Deformation of carbon nanotubes by surface van der Waals forces. Phys. Rev. B **58**, 13870–13873 (1998)
129. Y. Zhao, X. Chen, C. Park, C.C. Fay, S. Stupkiewicz, C. Ke, Mechanical deformations of boron nitride nanotubes in crossed junctions. J. Appl. Phys. **115**, 164305 (2014)
130. O. Gülseren, T. Yildirim, S. Ciraci, Ç. Kılıç, Reversible band-gap engineering in carbon nanotubes by radial deformation. Phys. Rev. B **65**, 155410 (2002)
131. B. Shan, G.W. Lakatos, S. Peng, K. Cho, First-principles study of band-gap change in deformed nanotubes. Appl. Phys. Lett. **87**, 173109 (2005)
132. A.P.M. Barboza, A.P. Gomes, B.S. Archanjo, P.T. Araujo, A. Jorio, A.S. Ferlauto, M.S.C. Mazzoni, H. Chacham, B.R.A. Neves, Deformation induced semiconductor-metal transition in single wall carbon nanotubes probed by electric force microscopy. Phys. Rev. Lett. **100**, 256804 (2008)
133. Y.-H. Kim, K.J. Chang, S.G. Louie, Electronic structure of radially deformed BN and BC3 nanotubes. Phys. Rev. B **63**, 205408 (2001)
134. H.W.C. Postma, A. Sellmeijer, C. Dekker, Manipulation and imaging of individual single-walled carbon nanotubes with an atomic force microscope. Adv. Mater. **12**, 1299–1302 (2000)
135. M. Zheng, L.-F. Zou, H. Wang, C. Park, C. Ke, Engineering radial deformations in single-walled carbon and boron nitride nanotubes using ultrathin nanomembranes. ACS Nano **6**, 1814–1822 (2012)
136. M. Zheng, L. Zou, H. Wang, C. Park, C. Ke, Quantifying the transverse deformability of double-walled carbon and boron nitride nanotubes using an ultrathin nanomembrane covering scheme. J. Appl. Phys. **112**, 104318 (2012)
137. S.P. Koenig, N.G. Boddeti, M.L. Dunn, J.S. Bunch, Ultrastrong adhesion of graphene membranes. Nat. Nanotechnol. **6**, 543–546 (2011)
138. Z. Zong, C.-L. Chen, M.R. Dokmeci, K. Wan, Direct measurement of graphene adhesion on silicon surface by intercalation of nanoparticles. J. Appl. Phys. **107**, 026104 (2010)
139. S. Akita, H. Nishijima, T. Kishida, Y. Nakayama, Influence of force acting on side face of carbon nanotube in atomic force microscopy. Jpn. J. Appl. Phys. **39**, 3724 (2000)

140. M.C. Strus, L. Zalamea, A. Raman, R.B. Pipes, C.V. Nguyen, E.A. Stach, Peeling force spectroscopy: exposing the adhesive nanomechanics of one-dimensional nanostructures. Nano Lett. **8**, 544–550 (2008)
141. M.C. Strus, C.I. Cano, R.B. Pipes, C.V. Nguyen, A. Raman, Interfacial energy between carbon nanotubes and polymers measured from nanoscale peel tests in the atomic force microscope. Compos. Sci. Technol. **69**, 1580–1586 (2009)
142. M. Zheng, C. Ke, Elastic deformation of carbon-nanotube nanorings. Small **6**, 1647–1655 (2010)
143. M.R. Roenbeck, X. Wei, A.M. Beese, M. Naraghi, A. Furmanchuk, J.T. Paci, G.C. Schatz, H.D. Espinosa, In situ scanning electron microscope peeling to quantify surface energy between multiwalled carbon nanotubes and graphene. ACS Nano **8**, 124–138 (2014)
144. T. Yoon, W.C. Shin, T.Y. Kim, J.H. Mun, T.-S. Kim, B.J. Cho, Direct measurement of adhesion energy of monolayer graphene as-grown on copper and its application to renewable transfer process. Nano Lett. **12**, 1448–1452 (2012)
145. J.W. Cook, S. Edge, D.E. Packham, The adhesion of natural rubber to steel and the use of the peel test to study its nature. Int. J. Adhes. Adhes. **17**, 333–337 (1997)
146. A. Bagchi, A.G. Evans, The mechanics and physics of thin film decohesion and its measurement. Interface Sci. **3**, 169–193 (1996)
147. M. Ishikawa, R. Harada, N. Sasaki, K. Miura, Adhesion and peeling forces of carbon nanotubes on a substrate. Phys. Rev. B **80**, 193406 (2009)
148. X. Li, W. Chen, Q. Zhan, L. Dai, L. Sowards, M. Pender, R.R. Naik, Direct measurements of interactions between polypeptides and carbon nanotubes. J. Phys. Chem. B **110**, 12621–12625 (2006)
149. M. Zheng, C. Ke, Mechanical deformation of carbon nanotube nano-rings on flat substrate. J. Appl. Phys. **109**, 074304 (2011)
150. B.A. Newcomb, H.G. Chae, P.V. Gulgunje, K. Gupta, Y. Liu, D.E. Tsentalovich, M. Pasquali, S. Kumar, Stress transfer in polyacrylonitrile/carbon nanotube composite fibers. Polymer **55**, 2734–2743 (2014)
151. D. Roy, S. Bhattacharyya, A. Rachamim, A. Plati, M.-L. Saboungi, Measurement of interfacial shear strength in single wall carbon nanotubes reinforced composite using Raman spectroscopy. J. Appl. Phys. **107**, 043501–043501–6 (2010)
152. T. Ozkan, Q. Chen, I. Chasiotis, Interfacial strength and fracture energy of individual carbon nanofibers in epoxy matrix as a function of surface conditions. Compos. Sci. Technol. **72**, 965–975 (2012)
153. M.P. Manoharan, A. Sharma, A.V. Desai, M.A. Haque, C.E. Bakis, K.W. Wang, The interfacial strength of carbon nanofiber epoxy composite using single fiber pullout experiments. Nanotechnology **20**, 295701 (2009)
154. T. Tsuda, T. Ogasawara, F. Deng, N. Takeda, Direct measurements of interfacial shear strength of multi-walled carbon nanotube/PEEK composite using a nano-pullout method. Compos. Sci. Technol. **71**, 1295–1300 (2011)
155. C.A. Cooper, S.R. Cohen, A.H. Barber, H.D. Wagner, Detachment of nanotubes from a polymer matrix. Appl. Phys. Lett. **81**, 3873–3875 (2002)
156. A.H. Barber, S.R. Cohen, H.D. Wagner, Measurement of carbon nanotube–polymer interfacial strength. Appl. Phys. Lett. **82**, 4140 (2003)
157. A.H. Barber, S.R. Cohen, S. Kenig, H.D. Wagner, Interfacial fracture energy measurements for multi-walled carbon nanotubes pulled from a polymer matrix. Compos. Sci. Technol. **64**, 2283–2289 (2004)
158. A.H. Barber, S.R. Cohen, A. Eitan, L.S. Schadler, H.D. Wagner, Fracture transitions at a carbon-nanotube/polymer interface. Adv. Mater. **18**, 83–87 (2006)
159. Y. Ganesan, C. Peng, Y. Lu, P.E. Loya, P. Moloney, E. Barrera, B.I. Yakobson, J.M. Tour, R. Ballarini, J. Lou, Interface toughness of carbon nanotube reinforced epoxy composites. ACS Appl. Mater. Interf. **3**, 129–134 (2011)

160. Y. Ganesan, H. Salahshoor, C. Peng, V. Khabashesku, J. Zhang, A. Cate, N. Rahbar, J. Lou, Fracture toughness of the sidewall fluorinated carbon nanotube-epoxy interface. J. Appl. Phys. **115**, 224305 (2014)
161. P.M. Ajayan, L.S. Schadler, C. Giannaris, A. Rubio, Single-walled carbon nanotube–polymer composites: strength and weakness. Adv. Mater. **12**, 750–753 (2000)
162. S.C. Chowdhury, T. Okabe, Computer simulation of carbon nanotube pull-out from polymer by the molecular dynamics method. Compos. Part -Appl. Sci. Manuf. **38**, 747–754 (2007)
163. C.Y. Wei, Adhesion and reinforcement in carbon nanotube polymer composite. Appl. Phys. Lett. **88**, 093108 (2006)
164. J.Q. Liu, T. Xiao, K. Liao, P. Wu, Interfacial design of carbon nanotube polymer composites: a hybrid system of noncovalent and covalent functionalizations. Nanotechnology **18**, 165701 (2007)
165. M. Wong, M. Paramsothy, X.J. Xu, Y. Ren, S. Li, K. Liao, Physical interactions at carbon nanotube-polymer interface. Polymer **44**, 7757–7764 (2003)
166. J. Gou, B. Minaie, B. Wang, Z. Liang, C. Zhang, Computational and experimental study of interfacial bonding of single-walled nanotube reinforced composites. Comput. Mater. Sci. **31**, 225–236 (2004)
167. K. Liao, S. Li, Interfacial characteristics of a carbon nanotube-polystyrene composite system. Appl. Phys. Lett. **79**, 4225–4227 (2001)
168. X. Chen, M. Zheng, C. Park, C. Ke, Direct measurements of the mechanical strength of carbon nanotube–poly(methyl methacrylate) interfaces. Small **9**, 3345–3351 (2013)
169. X. Chen, L. Zhang, M. Zheng, C. Park, X. Wang, C. Ke, Quantitative nanomechanical characterization of the van der Waals interfaces between carbon nanotubes and epoxy. Carbon **82**, 214–228 (2015)
170. G. Gonçalves, P.A.A.P. Marques, A. Barros-Timmons, I. Bdkin, M.K. Singh, N. Emami, J. Grácio, Graphene oxide modified with PMMA via ATRP as a reinforcement filler. J. Mater. Chem. **20**, 9927 (2010)
171. B. Das, K.E. Prasad, U. Ramamurty, C.N.R. Rao, Nano-indentation studies on polymer matrix composites reinforced by few-layer graphene. Nanotechnology **20**, 125705 (2009)
172. L. Gong, I.A. Kinloch, R.J. Young, I. Riaz, R. Jalil, K.S. Novoselov, Interfacial stress transfer in a graphene monolayer nanocomposite. Adv. Mater. **22**, 2694–2697 (2010)
173. H.L. Cox, The elasticity and strength of paper and other fibrous materials. Br. J. Appl. Phys. **3**, 72–79 (1952)
174. A.P. Awasthi, D.C. Lagoudas, D.C. Hammerand, Modeling of graphene-polymer interfacial mechanical behavior using molecular dynamics. Model. Simul. Mater. Sci. Eng. **17**, 015002 (2009)
175. H. Salahshoor, N. Rahbar, Nano-scale fracture toughness and behavior of graphene/epoxy interface. J. Appl. Phys. **112**, 023510 (2012)
176. C. Lv, Q. Xue, D. Xia, M. Ma, J. Xie, H. Chen, Effect of chemisorption on the interfacial bonding characteristics of graphene–polymer composites. J. Phys. Chem. C **114**, 6588–6594 (2010)
177. C.-H. Ke, M. Zheng, in *Simulations in Nanobiotechnology*, ed. by K. Eom. Nanoscale Adhesion Interactions in 1D and 2D Nanostructure-Based Material Systems (Elsevier, 2011)

Chapter 11
Mesoporous Carbon for Energy

Pengfei Zhang and Sheng Dai

Abstract Ordered mesoporous carbons (OMCs) are of great interest in energy-related research and applications, partly due to their high surface areas, uniform pore channels, and narrow pore size distributions. During the past decades, a number of breakthroughs for the synthesis of OMCs, including hard templating methods and soft templating strategies, have been made by carbon chemists. Thanks to unique properties, OMCs-based supercapacitors are attracting more and more attention around the world in recent years in view of their ultrafast charge-discharge rate, high power capability, low maintenance, and long cycle life. In this chapter, we wish to overview those representative pathways for OMC materials and their performance in supercapacitor application.

11.1 Introduction

In the past decades, porous carbon materials have manifested themselves in various applications, such as: development of new electrical energy storage and conversion devices, catalyst or catalyst support, gas storage systems, etc. [1]. The importance of these carbonaceous materials actually resides in their excellent physical and chemical properties tunable in a wide range, such as high surface area, large pore volumes, good electronic conductivity, designable chemical composition, chemical and thermal stability [2, 3]. Nowadays, carbon materials with various pore structures (e.g. micropore, mesopore) have been devised by different synthetic strategies [4, 5]. Being the most popular and frequently used carbons, activated

P. Zhang · S. Dai
Chemical Sciences Division, Oak Ridge National Laboratory, Oak Ridge, TN 37831, USA

S. Dai (✉)
Department of Chemistry, University of Tennessee, Knoxville, TN 37996, USA
e-mail: dais@ornl.gov

Q. Li (ed.), *Anisotropic Nanomaterials*, NanoScience and Technology,
DOI 10.1007/978-3-319-18293-3_11

carbons, dominated by micropores, are generally prepared from carbonization of biomass sources such as coconut, coal and further activations involving exposure in harsh oxidizing atmospheres (e.g. CO_2, steam) or chemical treatment with acids (e.g. phosphoric acid), bases (e.g. KOH, NaOH), or salts (e.g. $ZnCl_2$, $SnCl_2$) are necessary for directing porosity [6–8]. Meanwhile, carbon materials with well-defined mesopore have received significant attention owing to their large and tunable pore size and uniform pore channel, which would be beneficial to various fields, such as: carbon-based supercapacitor [9–11].

Nowadays, the fast growth of portable electronic devices and hybrid electric vehicles has promoted the urgent and increasing demand for high-power energy storages, such as supercapacitors. At present, activated carbons are widely used as the electric double layer capacitor (EDLC) electrode materials because of their low cost, scalable character and a variety of biomass precursors. Though conventionally activated carbons possess a large surface area, their EDLC performance can be somewhat limited because they actually contain an abundant proportion of micropores not always fully accessible to big ions [12, 13]. Therefore, only exposed outer surface are utilized for charge storage. In addition, even in the situation wherein the micropores are filled by the electrolyte, the ionic transfer in such small pores may be so slow that the high rate capability could not be reached. Both charge storage and rate capability are also limited by the randomly connected pores within activated carbon. In contrast, ordered mesoporous carbon materials at this stage could resolve above-mentioned questions for promising energy devices [14]. In this chapter, we wish to summarize recent advances on the preparation of ordered mesoporous carbons (OMCs) and their applications as supercapacitors. Ordered mesoporous carbons are generally fabricated by a hard or soft-templating approach, as shown in the following.

11.2 Ordered Mesoporous Carbons (OMCs) from Hard-Templating Method

Ryoo's groups for the first time introduced OMCs in 1999, where mesoporous MCM-48 derived from the surfactant self-assembly approach was used as the hard template and sucrose inside the pores of the MCM-48 was carbonized in N_2 [15]. The CMK-1 carbon was obtained after subsequent removal of the silica template with a hot ethanolic solution of NaOH (Fig. 11.1). X-ray powder diffraction (XRD) pattern of CMK-1 indicated the highly ordered pore arrangement and the CMK-1 carbon underwent a systematic transformation into new structural symmetry from that of the silica template. The nitrogen adsorption isotherm of CMK-1 featured a sharp adsorption step owing to the capillary condensation of N_2 molecules inside these uniform mesopores (Fig. 11.2).

Three months later, Hyeon et al. reported the synthesis of another OMC material by also employing mesoporous MCM-48 aluminosilicate with three-dimensional

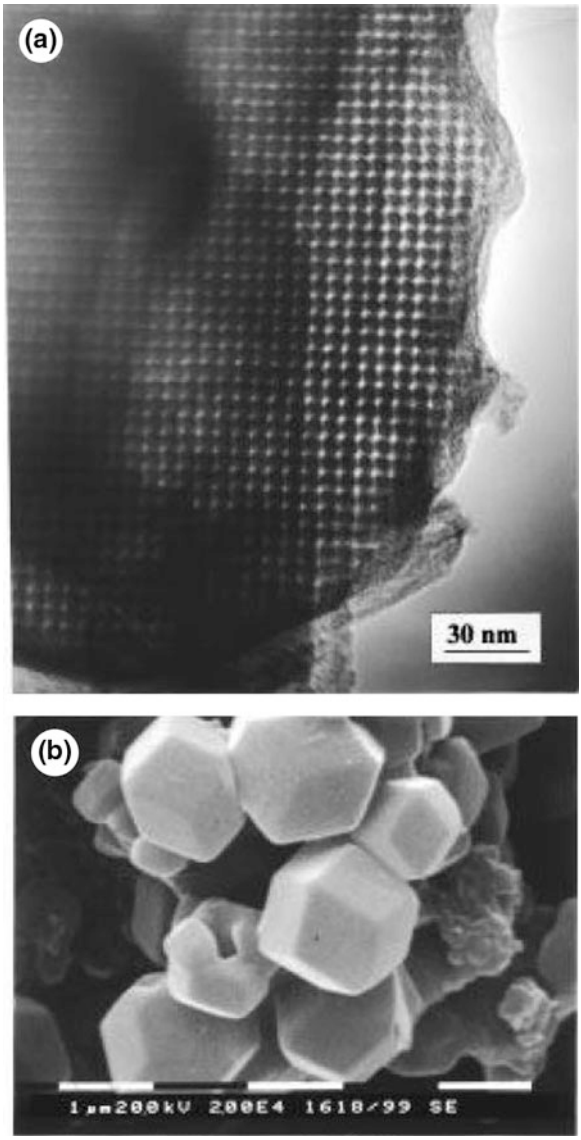

Fig. 11.1 **a** Representative transmission electron micrograph of the ordered carbon molecular sieve CMK-1, obtained by the template synthesis with the mesoporous silica molecular sieve MCM-48. This image was obtained with a Philips CM20 transmission electron microscope operated at 100 kV from thin edges of a particle supported on porous carbon grid. **b** Scanning electron micrograph of a CMK-1 sample. This image was obtained on a Philips SEM-535M microscope using an acceleration voltage of 20.0 kV. Reproduced with permission from [15]. Copyright 1999 American Chemical Society

channel structure as the template and with phenolic resin as the carbon source [16]. The dissolution of MCM-48 frameworks using 48 % aqueous hydrofluoric acid generated mesoporous carbon, designated SNU-1. The specific surface area of SNU-1 was found to be 1257 m^2/g from nitrogen BET adsorption measurements (Fig. 11.3). Nitrogen adsorption–desorption curves showed hysteresis at high relative pressure characteristic of mesopores. The pore size distribution data calculated from the adsorption branch of the nitrogen isotherm by the BJH (Barrett–Joyner–

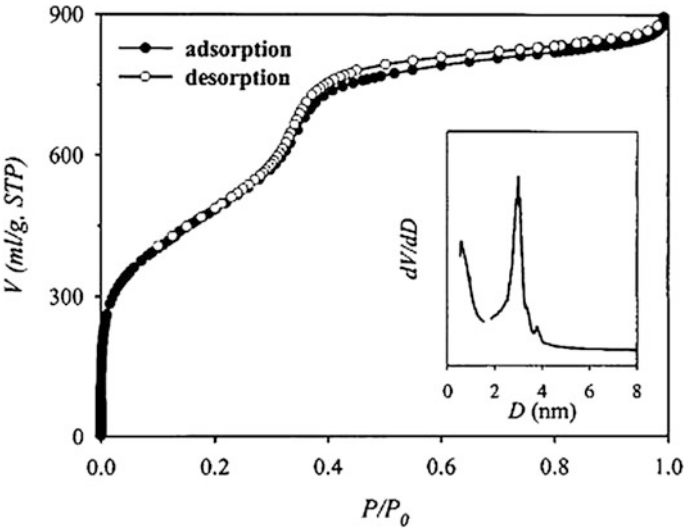

Fig. 11.2 Argon adsorption-desorption isotherms at 87 K for the carbon molecular sieve CMK-1. *Inset* The corresponding pore size distribution curves obtained from the desorption by the Barrett–Joyner–Halenda method (>1.7 nm), and the Horvath–Kawazoe analysis (0.5–1.7 nm). Reproduced with permission from [15]. Copyright 1999 American Chemical Society

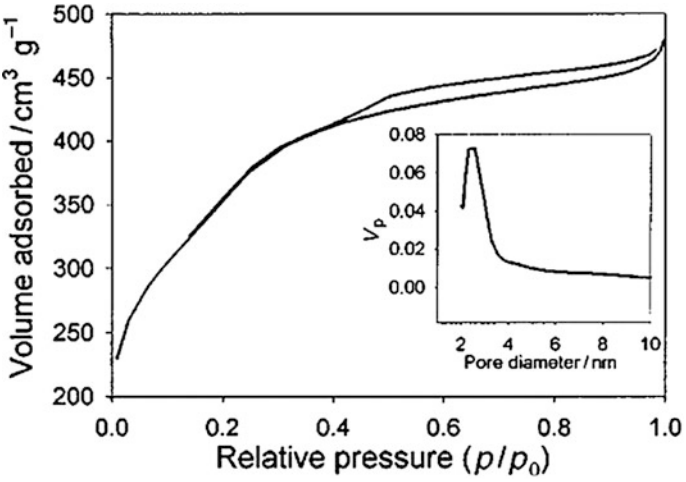

Fig. 11.3 N_2 adsorption and desorption isotherms of mesoporous SNU-1 carbon. *Inset* The corresponding pore size distribution curve calculated from the adsorption branch of the nitrogen isotherm by the BJH method. *V*p is the incremental pore volume. The isotherms were collected at 77 K on a Micrometrics ASAP2010 Gas Adsorption Analyzer after the carbon material was degassed at 250 °C at 30 mTorr for 5 h. Reproduced with permission from [16]. Copyright 1999 Royal Society of Chemistry

Halenda) method showed that pores are uniform with an average pore size of 2.3 nm. The performance of SNU-1 in an electrochemical double-layer capacitor was also evaluated by the same group. In this topic, our group introduced the mesoporous carbon "C48" using mesophase pitch as the carbon precursor and MCM-48 silica as a hard template. The C48 material exhibited XRD patterns similar to that of CMK-1 [17, 18]. The framework of the C48 carbon network was composed of carbon nanorods of 1.5–2 nm length interconnected in three-dimensions.

Besides MCM-48, the hexagonally structured SBA-15 mesoporous silica (SBA-15) was another frequently-investigated hard template for OMC synthesis. For example, a highly ordered, hexagonal OMC-CMK-3, was reported by Ryoo and co-workers with SBA-15 as the template. CMK-3 is composed of carbon nanorods arranged in a hexagonal pattern, with connecting bridges between them (Fig. 11.4) [19]. Actually, the specific surface area of CMK-3 was higher than calculated value for CMK-3 with nonporous pore wall, suggesting that pore wall of CMK-3 was rich in complementary micropores (Fig. 11.5). The pore size of OMC material synthesized with a hard template is primarily controlled by the pore wall thickness of the inorganic templates, which can be in principle tailored by the selection of template.

In addition, various carbon precursors, e.g., sucrose, furfuryl alcohol, naphthalene, C_2H_2, polyacrylonitrile, and phenolic resin, can be utilized for OMCs. For example, Schüth and Lu reported nitrogen-containing OMC with well-developed bimodal system by using SBA-15 as template and polyacrylonitrile as carbon source via a nanocasting pathway (Fig. 11.6) [20, 21]. However, those hard templating methods require the preparation of mesoporous silica, adding time and

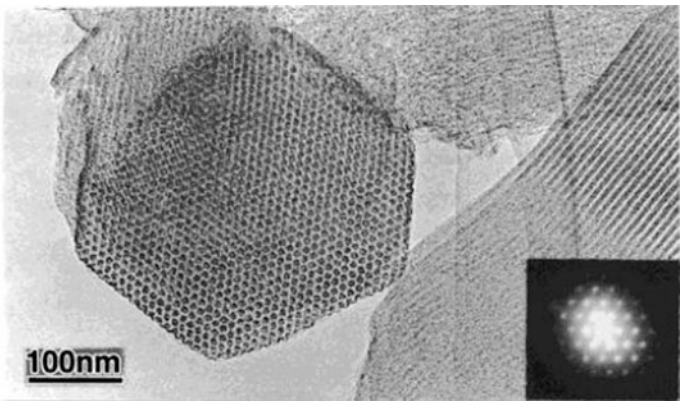

Fig. 11.4 Typical TEM images of the ordered mesoporous carbon molecular sieve, CMK-3. This carbon was synthesized using sucrose as a carbon source and SBA-15 silica as a template. The TEM images were obtained with a JEM-4000 EX operated at 400 kV from the carbon material after silica template was completely removed with HF solution. Reproduced with permission from [19]. Copyright 2000 American Chemical Society

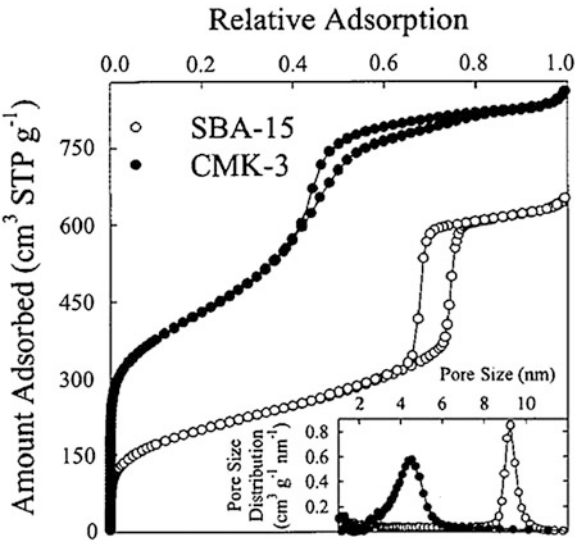

Fig. 11.5 N_2 adsorption–desorption isotherm at 77 K for CMK-3 and SBA-15. *Inset* The pore size distributions. Reproduced with permission from [19]. Copyright 2000 American Chemical Society

increased costs to the preparation of the final carbon materials and the use of concentrated sodium hydroxide or toxic hydrofluoric acid for removing templates makes this process difficult in industrial scale. Complementary to the hard-templating method, the soft-templating synthesis of mesoporous carbons by the organic–organic self-assembly offers several advantages in terms of cost and processing possibility [22].

11.3 Ordered Mesoporous Carbons from Soft-Templating Method

Somewhat like the self-assembly process for ordered mesoporous metal oxides developed earlier [23], soft templating construction of OMCs relies on the cooperative assembly between structure-directing templates and organic carbon sources during initial polymerization. In 2004, our group for the first time showed the synthesis of ordered mesoporous carbon films by a soft template route [24]. This methodology involves pre-organization of the resorcinol monomers and polystyrene-block poly(4-vinylpyridine) (PS-P4VP) into a nanostructured film with hydrogen bond induced self-assembly (Fig. 11.7). Formaldehyde gas was then vapored to the film for in situ cross-linking the resorcinol monomers. The resulting resorcinol-formaldehyde resin was transformed into a highly ordered mesoporous carbon film during carbonization process, while those PS-P4VP template decomposed into gaseous species. SEM and TEM images illustrated that the pore diameter is 33.7 ± 2.5 nm and the wall thickness is 9.0 ± 1.1 nm (Fig. 11.8). This soft-templating approach actually inspired rapid progresses in this topic.

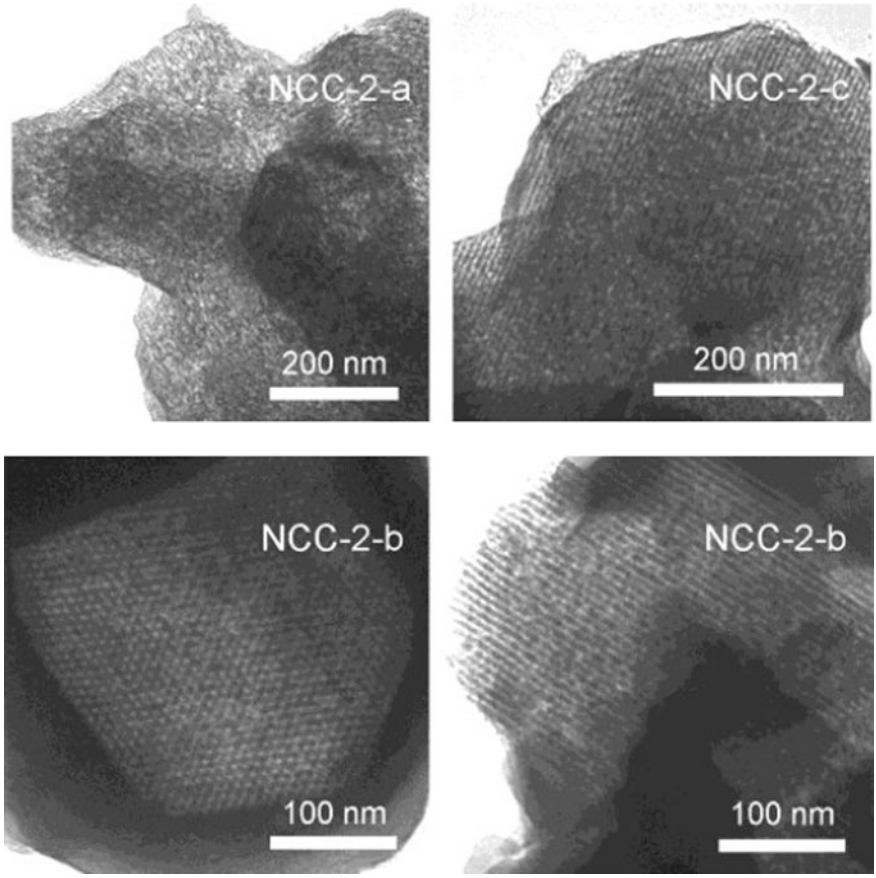

Fig. 11.6 TEM images of NCC-2-a, NCC-2-b, and NCC-2-c. Reproduced with permission from [21]. Copyright 2004 American Chemical Society

In addition to PS-P4VP, other block copolymers were also developed as soft templates for OMCs. Tanaka and co-workers showed the possibility of common Pluronic PEO-*b*-PPO-*b*-PEO as soft template. They carried out the resorcinol-formaldehyde polymerization in the presence of Pluronic F127 and triethyl orthoacetate as co-precursor (Fig. 11.9) [25]. The co-precursor triethyl orthoacetate here increased the ordering of the porous structure in some degree. Zhao's group completed a detailed investigation of OMCs prepared with different co-polymers, such as F127, F108 and P123 [26–28]. For example, the pore morphology of as-made OMCs could be controlled by the fraction of the hydrophobic block during polymerization, that is tuning the PEO content in the copolymer or changing the ratio of carbon precursor-to-template (Fig. 11.10). Different mesostructures of OMCs, including lamellar (La), bicontinuous (Ia3d), hexagonal (p6mm) and cubic globular (Im3m) could be obtained by increasing curvature at the micelle interface.

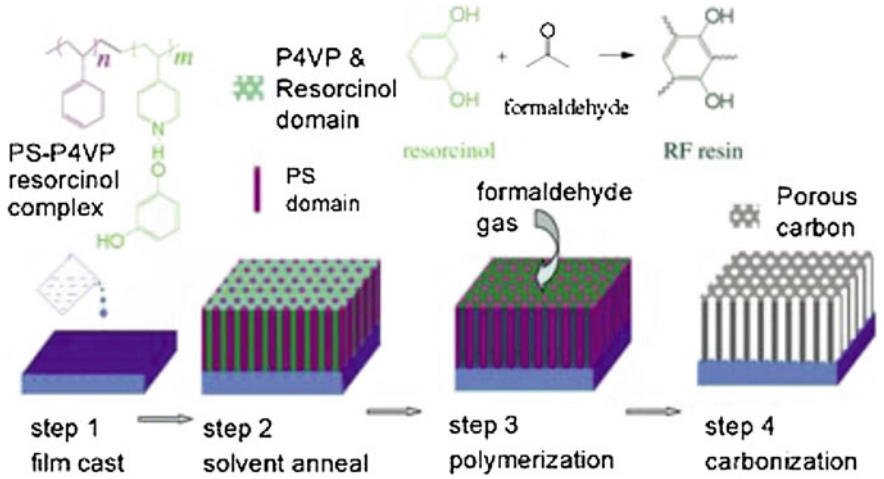

Fig. 11.7 Schematic representation of the synthesis protocol used to prepare well-defined carbon nanostructures. *Step 1* Film casting of PS-P4VP/resorcinol supramolecular assembly. *Step 2* Completion of microphase separation by solvent annealing at 80 °C in DMF/benzene mixed vapor. The resorcinol is organized in the well-defined P4VP domain. *Step 3* In situ polymerization of resorcinol and formaldehyde by exposing the film to formaldehyde gas. Highly cross-linked RFR is formed within the P4VP domain. *Step 4* Pyrolysis of the polymeric film in N_2. A hexagonal carbon-channel array is formed by sacrificing the block copolymer. Reproduced with permission from [24]. Copyright 2004 Wiley-VCH Verlag GmbH & Co. KGaA, Weinheim

Just recently, our group established a surfactant-free synthesis of mesoporous carbon materials through the polymerization of phloroglucinol-formaldehyde resins in the presence of polyethylene glycol (PEG) with acidic ethanol (Fig. 11.11) [29]. The essence of this strategy relies in the PEG-mediated spinodal decomposition for porosity control, instead of the traditional micellar self-assembly approaches. Mesoporous carbons with specific surface areas up to 392 m^2/g and pore size around 20 nm could be fabricated by this method (Fig. 11.12). In comparison with those triblock copolymers, utilization of linear PEG as a sacrificial soft-template provides a more sustainable alternative for OMCs.

In the past decade, a family of carbon precursors, such as phenol, resorcinol and phloroglucinol, were employed for the synthesis of soft-templated OMCs, most of which were based on chemistry of phenol-aldehyde polymerization. Those molecules forms hydrogen-bonded networks with block polymers and then are cross-linked by formaldehyde in the presence of acid or base catalyst. The hydroxy group on the substrate is a key point for interacting with soft template. For example, Dai and co-workers studied the polymerization processes by phenol-formaldehyde, resorcinol-formaldehyde and phloroglucinol-formaldehyde [30]. It was observed that phloroglucinol could complete the polymerization more rapid than resorcinol or phenol (40 min vs. 1–3 weeks, respectively). The authors considered that the high hydroxy density in the oligomers formed from phloroglucinol provides a greater

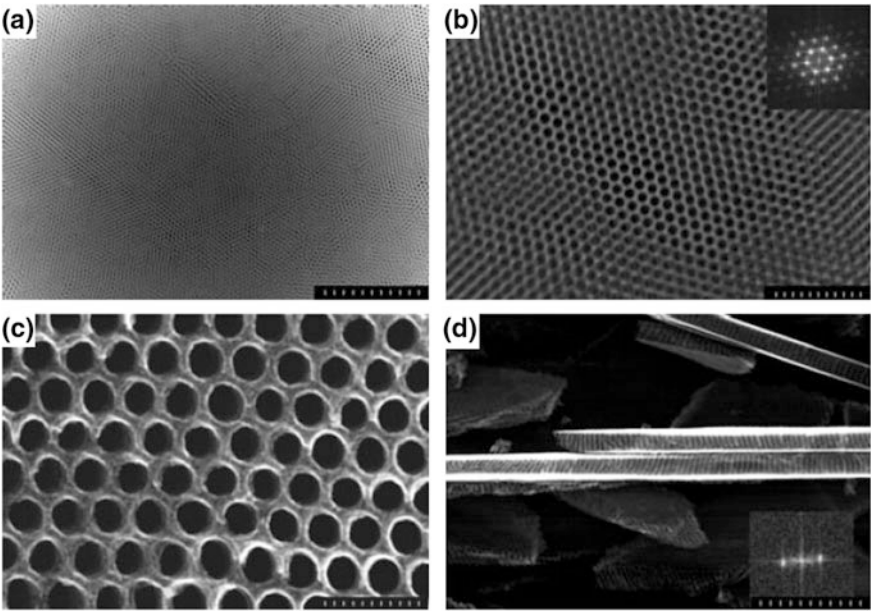

Fig. 11.8 Electron microscopy images of the carbon film. **a** Z-contrast image of the large-scale homogeneous carbon film in a 4 × 3 μm area. The scale bar is 1 μm. **b** Z-contrast image showing details of the highly ordered carbon structure. In the *inset*, a Fourier transform (FT) of the image shows a pattern with multiple reflections, which are characteristic of a highly ordered hexagonal array. The scale bar is 300 nm. **c** High-resolution SEM image of the surface of the carbon film with uniform hexagonal-pore array. The pore size is 33.7 ± 2.5 nm and the wall thickness is 9.0 ± 1.1 nm. The scale bar is 100 nm. **d** SEM image of the film cross section, which exhibits all parallel straight channels perpendicular to the film surface. The scale bar is 100 nm. The inset is the FT of the cross section image. The FT pattern shows the reflections of the periodic parallel channels. Reproduced with permission from [24]. Copyright 2004 Wiley-VCH Verlag GmbH & Co. KGaA, Weinheim

driving force for the self-assembly interaction with the PEO blocks, as compared with those provided by the oligomers from phenol and resorcinol (Fig. 11.13).

Considering environment and sustainability issues, above methods with fossil-based sources are restricted for long term development. It seems of great interest to develop renewable carbon sources for the synthesis of OMCs. Antonietti and co-workers recently illustrated another OMCs by hydrothermal carbonization (HTC) of fructose in the presence of block copolymer surfactant Pluronic F127 [31]. Since HTC of fructose can occur under relatively low temperature (e.g. 130 °C), fructose was selected for this micellar self-assembly. HTC of fructose with F127 additive can lead to composite material, presenting a well ordered structure with an F127 micelle diameter of ~10 nm and carbon wall thickness of ~6 nm (Fig. 11.14). Though corresponding carbon material after thermal treatment (550 °C) showed long-range regularly ordered pore structure with cubic Im3m symmetry (From HRTEM and SSAXS analysis), N_2 sorption analysis presented a non-reversible microporous type I

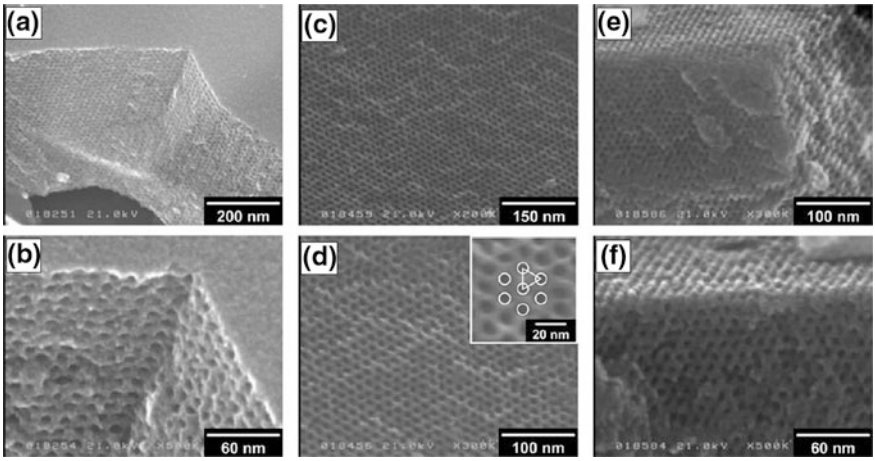

Fig. 11.9 FE-SEM images of carbonized COU-1. The carbonization temperatures were as follows: **a**, **b** 400 °C, **c**, **d** 600 °C and **e**, **f** 800 °C. Reproduced with permission from [25]. Copyright The Royal Society of Chemistry 2005

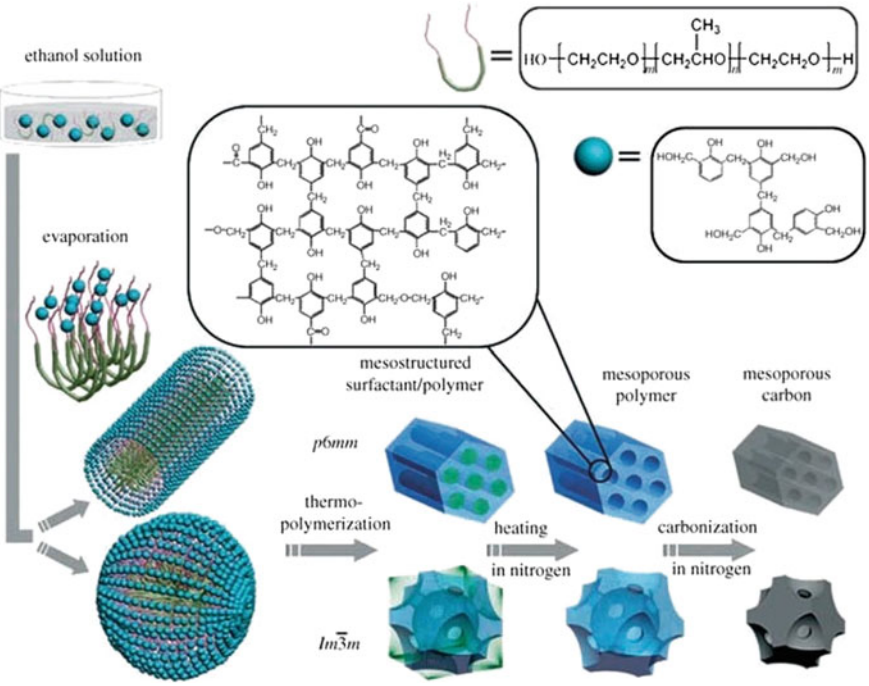

Fig. 11.10 Schematic representation of the procedure used to prepare mesoporous carbon frameworks. Reproduced with permission from [27]. Copyright 2005 Wiley-VCH Verlag GmbH & Co. KGaA, Weinheim

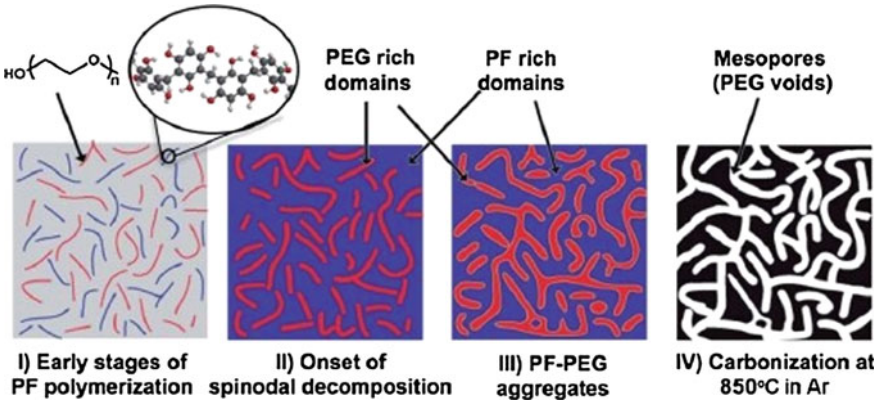

Fig. 11.11 Schematic illustration of spinodal decomposition (*I–III*) and subsequent formation of mesoporous carbon (*IV*) from PF–PEG adduct. Reproduced with permission from [29]. Copyright The Royal Society of Chemistry 2014

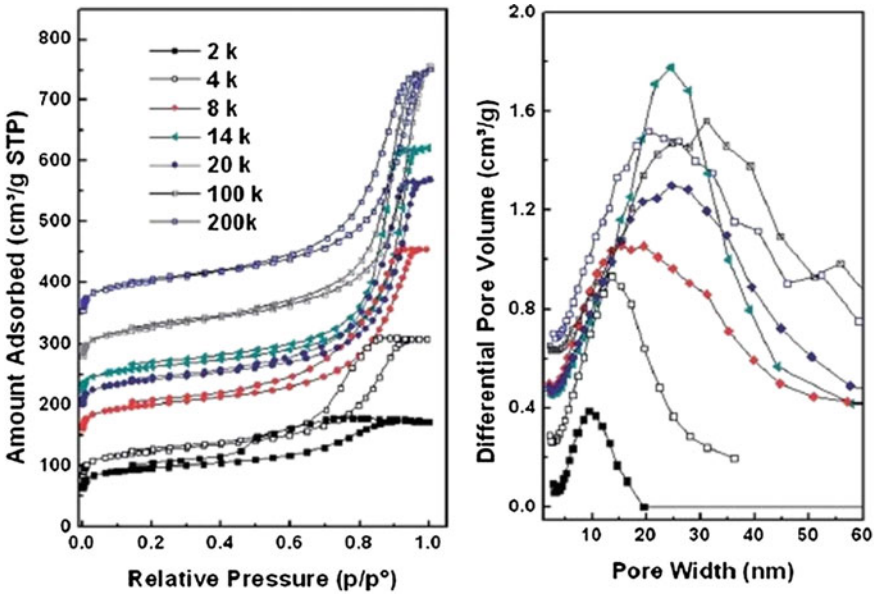

Fig. 11.12 Nitrogen −196 °C adsorption isotherms (*left*) and corresponding pore size distributions (*right*) calculated using KJS method of carbon samples with respective PEG (in Da). For clarity, the isotherms were offset by consecutive increments of 50 cm^3/g and pore size distributions offset in consecutive increments of 0.2 cm^3/g. Reproduced with permission from [29]. Copyright The Royal Society of Chemistry 2014

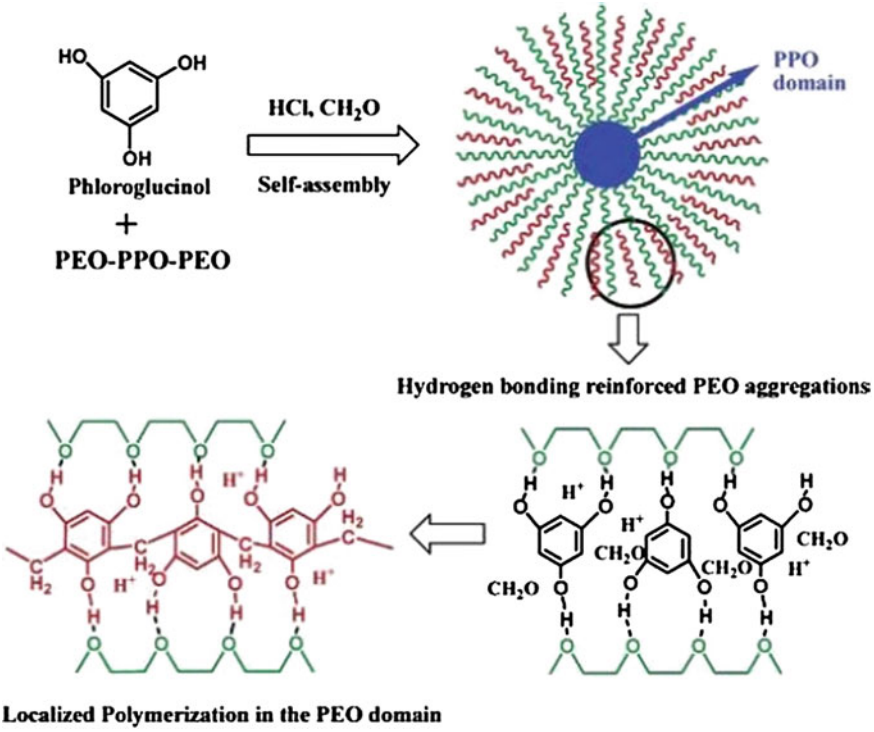

Fig. 11.13 Localized Polymerization. Reproduced with permission from [30]. Copyright 2006 American Chemical Society

isotherm with pore size distribution around 0.9 nm (Fig. 11.15). The authors attribute the narrowed pores during template removal to structural shrinkage or partial co-carbonization of the block copolymer inside channels. To shift pore structure into the mesoporous domain, the swelling agent trimethylbenzene was added to the F127/Fructose mixture for larger micelles. OMC material with a type IV N_2 sorption profile and capillary condensation feature at P/Po ≈ 0.45, was observed and the BET surface area is 116 m^2/g, giving another pathway for OMC family (Fig. 11.16). During suggested mechanism for this process, fructose is absorbed in the initial stages via H-bonding with the hydrophilic PEO moiety of F127 (or with TMB additive) and then proceeds dehydration/polycondensation to generate a polyfuran-like network for further thermal treatment (550 °C).

Another biomass product—tannin with multi phenolic hydroxyls were just recently explored for the synthesis of OMCs. Parmentier and co-workers synthesized OMC materials with tannin extracted from wattle barks as carbon source via the self-assembly process of an amphiphilic triblock copolymer [32]. Tannins are naturally present in plants and have well known and established processes for their extraction from wood materials. Tannins on their own are also able to self-condense

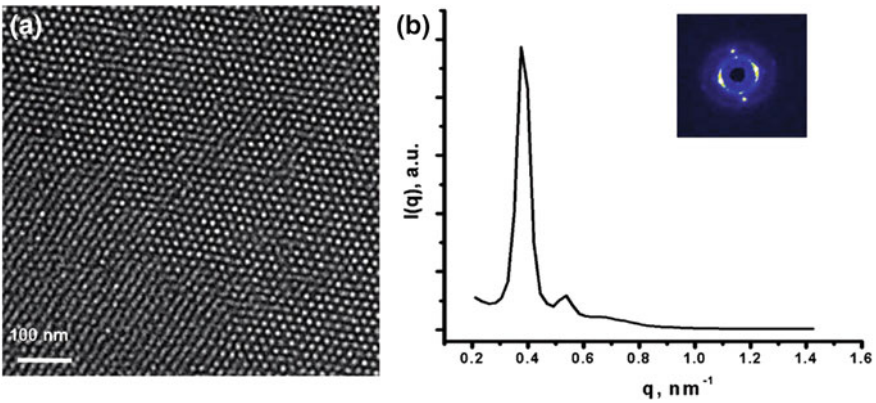

Fig. 11.14 **a** TEM micrograph and **b** Synchrotron SAXS pattern of C-MPG1-com (*inset* 2D scattering pattern). Reproduced with permission from [31]. Copyright 2011 American Chemical Society

to form a three-dimensional network by creating covalent bonds between the different flavonoid units and no cross-linker agents were needed in this process. In this process, the multiple adjacent hydroxyl groups of flavanoid unit probably play a key role for the self-assembly with PEO via hydrogen bonds (Fig. 11.17). OMC materials with specific surface area up to 545 m^2/g and pore size around 7–9 nm were obtained (Fig. 11.18). This tannin-based approach with cheap, renewable and non toxic precursor provides a greener way for OMC materials.

Recently, Wang and co-workers reported a self-transformation strategy to control the Fructose based HTC/soft templating. Insoluble melamine sulphates were introduced to direct the HTC/F127 procedure [33]. During this process, melamine sulphates were co-assembled and copolymerized with fructose, and further in situ transformed into OMC products with N-doping. HRTEM images exhibited ordered pores in the carbon flakes with pore diameter around 3 nm and wall thickness about 10 nm. The N_2 sorption analysis (S_{BET} = 761 m^2/g) presented a type IV isotherm and the pore size distribution showed a sharp peak at 3.3 nm and a broad shoulder less than 2 nm (Fig. 11.19).

11.4 Ordered Mesoporous Carbons for Supercapacitor

Hyeon and co-worker studied the EDLC performance of SNU-1 sample in 1999 [16]. Comparing with activated carbon, MSC-25, the SNU-1 sample showed a more ideal capacitor behavior with a more rectangular-shaped cyclic voltammogram (CV) curve. When the scan rates were enhanced from 5 to 50 mV s^{-1}, SNU-1 carbon retained a rectangular shape up to a scan rate of 20 mV s^{-1}. By contrast, MSC-25 carbon showed a deformed CV curve at a scan rate of 10 mV s^{-1} and a

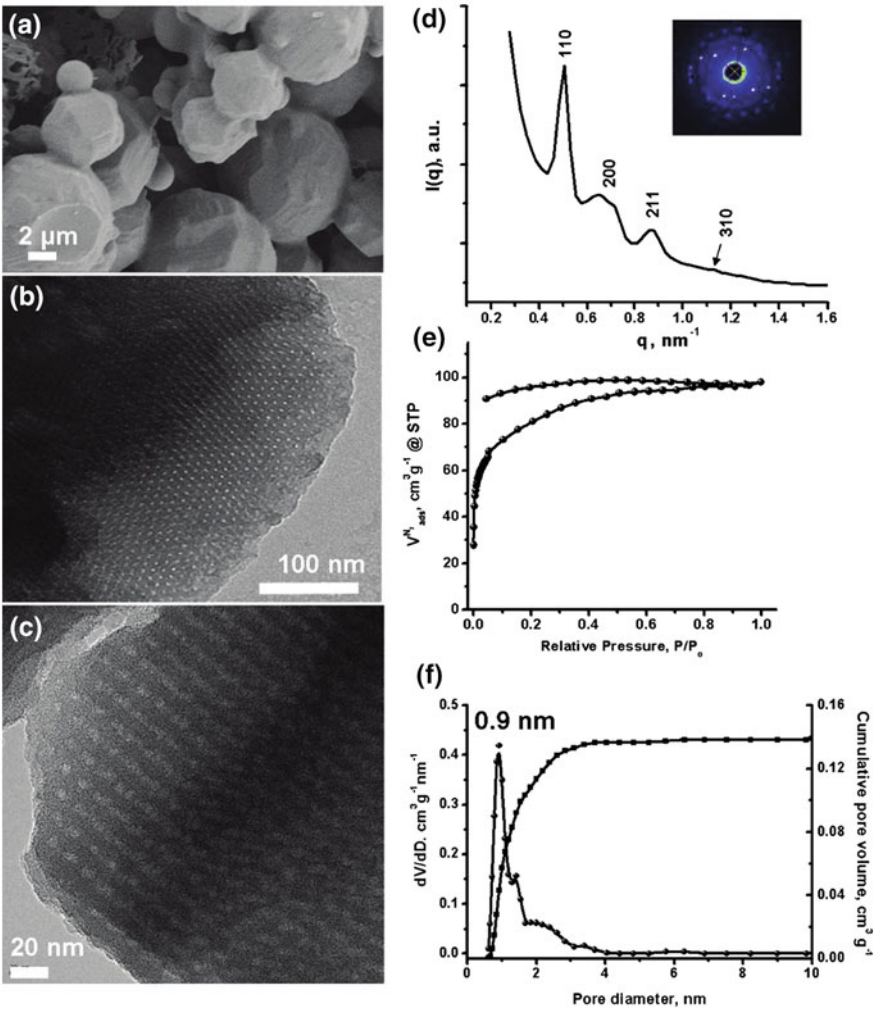

Fig. 11.15 **a** SEM, **b** TEM, **c** HRTEM micrographs, **d** synchrotron SAXS pattern (*inset* 2D scattering pattern), **e** N_2 sorption isotherm, and **f** QSDFT pore size distribution of C-MPG1-*micro*. Reproduced with permission from [31]. Copyright 2011 American Chemical Society

completely collapsed one at a scan rate of 20 mV s^{-1} (Fig. 11.20). Those results reflected the advantage of regular interconnected mesopores for fast electrolyte transfer.

Specific surface areas of OMC materials are generally considered as key factors for the EDLC performance, since EDLCs utilize the electric double layer formed at the electrode/electrolyte interface for charge storage. An activation process by heating a physical mixture of potassium hydroxide and soft-template OMC within

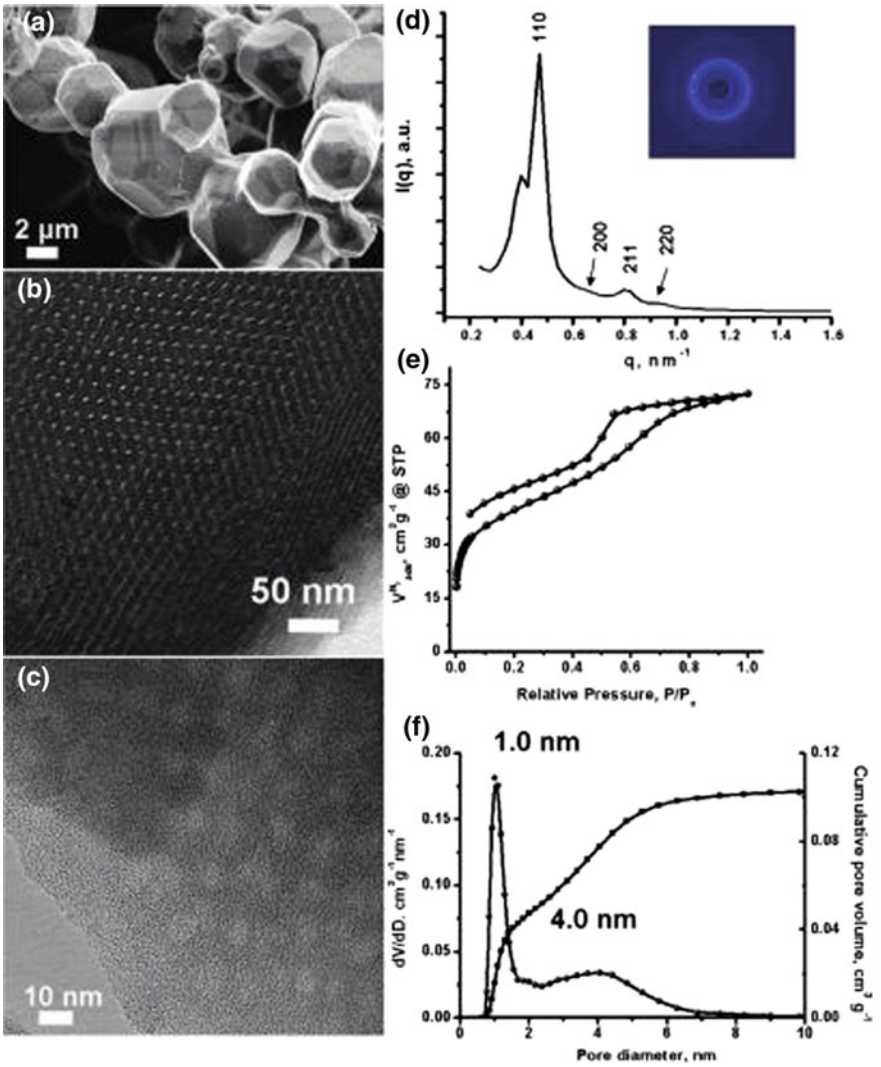

Fig. 11.16 **a** SEM, **b** TEM, and **c** HRTEM micrographs, **d** synchrotron SAXS pattern (*inset* 2D scattering pattern), **e** N_2 sorption isotherm, and **f** QSDFT pore size distribution of as-synthesized C-MPG1-*meso*. Reproduced with permission from [31]. Copyright 2011 American Chemical Society

N_2 at high temperatures (400–1000 °C), was introduced for higher surface areas [34]. The quantity of KOH and activation temperature affected the activation process, and the increased surface area was induced by activation-developed micropore. Around 70 % of the total surface area came from micropore. In addition, this activation process would increase carbon burn-off with lower carbon yield. Being as

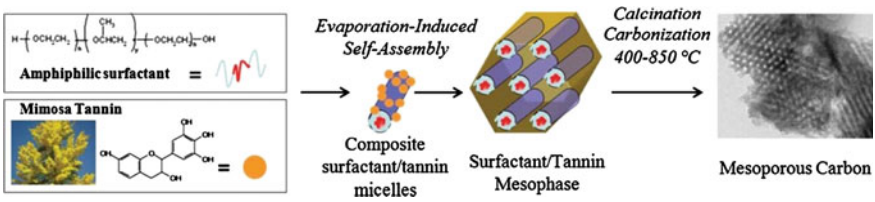

Fig. 11.17 Scheme for the synthesis of the ordered mesoporous polymer and carbon materials. Reproduced with permission from [32]. Copyright The Royal Society of Chemistry 2012

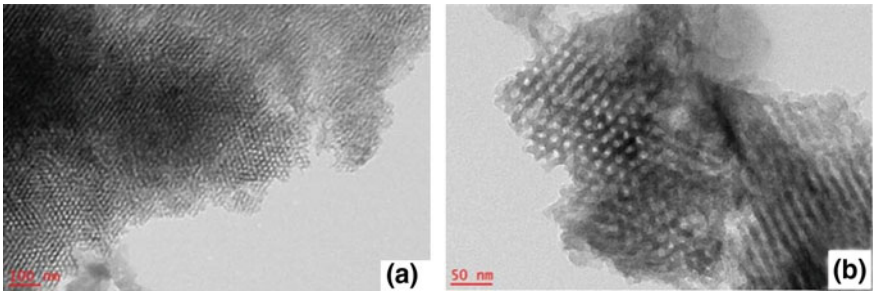

Fig. 11.18 TEM micrographs of the IS2M-1 phase (tannin-derived polymer) obtained by the evaporation self-assembly process and calcined at 400 °C. The low magnification (**a**) shows the limited size of the ordered domains (**b**). Reproduced with permission from [32]. Copyright The Royal Society of Chemistry 2012

EDLCs, activated OMC with surface area of 1940 m^2/g showed a specific capacitance of 188 F/g at a sweep scan rate of 1 mV/s in 0.1 M sodium chloride aqueous electrolyte, much higher than the capacitance (71.3 F/g) by only OMC sample from phenolic resin precursors (520 m^2/g). Liu and co-workers illustrated a silica-assisted co-assembly route to OMCs. In their strategy, the mixture of phenol-formaldehyde resol and tetraethyl orthosilicate were used to co-assembly in the presence of F127 by an EISA strategy. After triblock polymer removal, carbonization and HF acid etching of silica, OMC with pore size around 6.7 nm and extremely high surface area could be obtained [35]. When this sample was studied as EDLC electrode within organic electrolyte $[(C_2H_5)_4N][BF_4]$, a good capacitance of 112 F/g between 0 and 3 V was observed at a scan rate of 200 mV/s. Importantly, a outstanding stability with capacitance retention of 88 % was got by this sample after 1000 cycles [36].

In addition, increasing efforts have been recently devoted to the synthesis of element-doped mesoporous carbons, which could combine the high mesoporosity and unique characters of doped carbon frameworks, such as: enhanced mechanical, semiconducting, field-emission and electrical properties. Zhao and co-workers reported nitrogen-doped OMC material with a high N content by using evaporation-induced self-assembly of a low-molecular-weight soluble resol and dicyandiamide

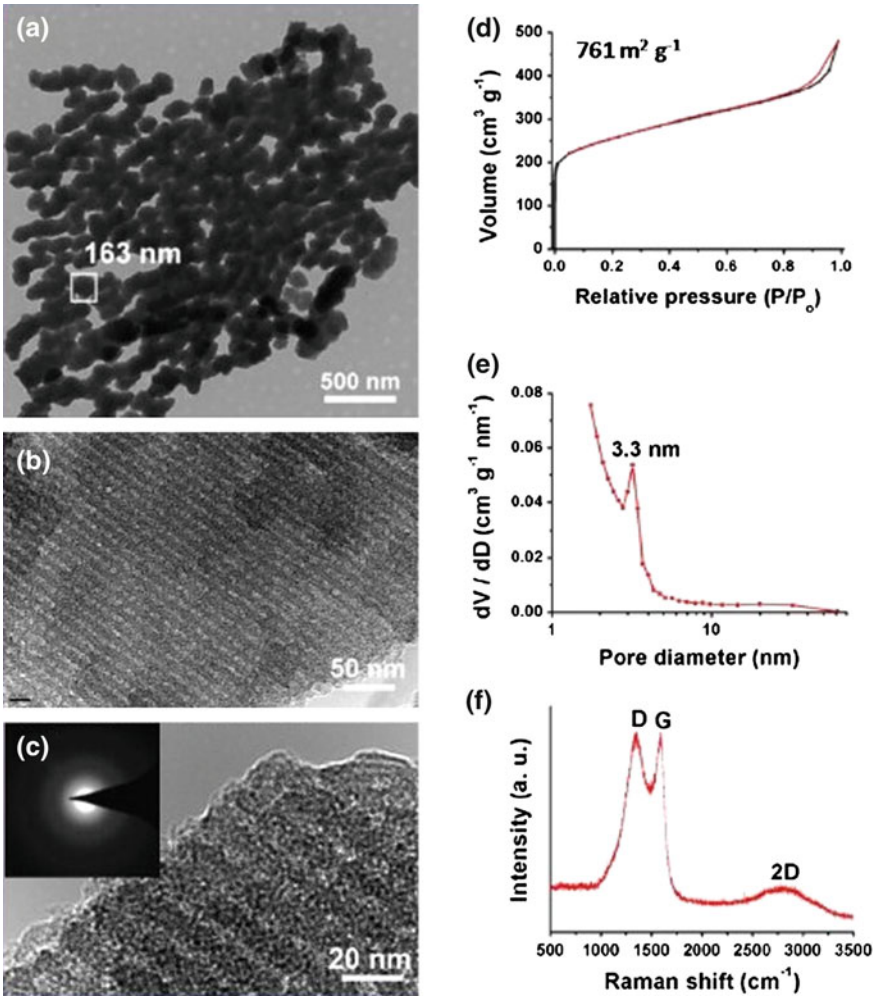

Fig. 11.19 Characterizations of sample OMCC-3-1 prepared at a DFructose/melamine molar ratio of 3 and a sulphuric acid/melamine molar ratio of 1: **a** TEM image; **b** and **c** HRTEM micrographs (*inset* the 2D scattering pattern); **d** N_2 sorption isotherm; **e** pore size distribution curve; **f** Raman spectra. Reproduced with permission from [33]. Copyright 2014 American Chemical Society

in the presence of F127 template (Fig. 11.21) [3]. The high nitrogen content (up to 13.1 %) was attributed to the introduction of DCDA, since it could form stable microdomains of carbon nitrides in the matrix of phenolic resin. The nitrogen-doped OMC sample exhibited good performance as supercapacitor electrodes, with specific capacitance of 262 F/g (1 M H_2SO_4) and 227 F/g (6 M KOH) at a current density of 0.2 A/g, better than that by the mesoporous FDU-15 carbon without nitrogen modification (Fig. 11.22).

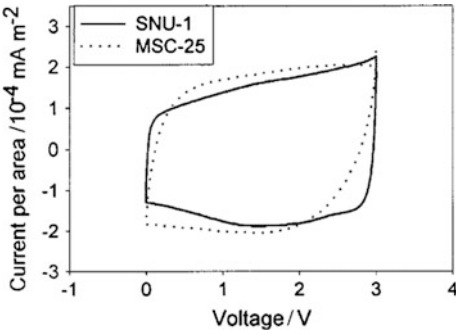

Fig. 11.20 Cyclic voltammograms of SNU-1 and MSC-25 activated carbon in organic electrolyte (1 M NEt_4BF_4 in propylene carbonate). A two-electrode system consisting of working and counter electrodes was used. These two electrodes were fabricated with equal amounts of the carbon materials. CV measurements were made in the potential range 0–3 V with a scan rate of 5 mV/s. Reproduced with permission from [16]. Copyright 1999 Royal Society of Chemistry

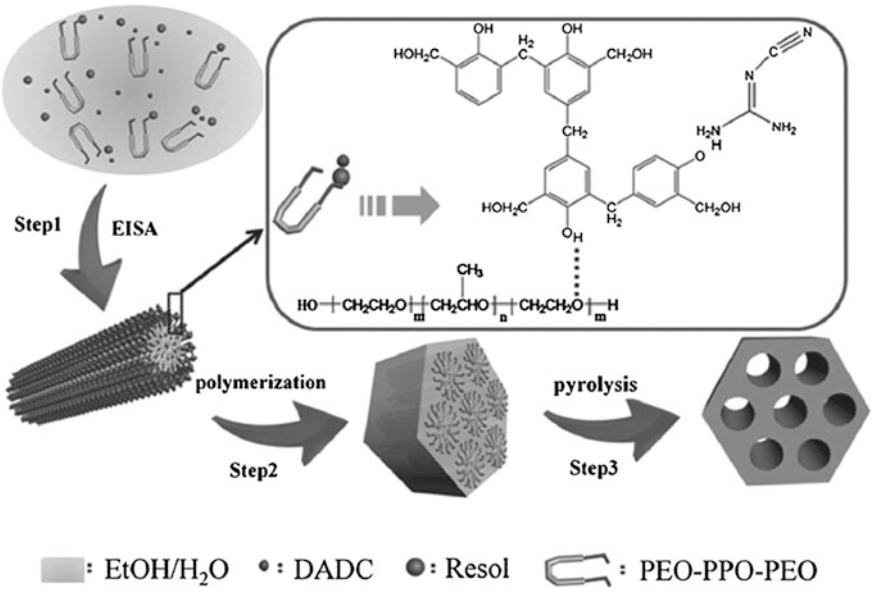

Fig. 11.21 The formation process of ordered N-doped mesoporous carbon from a one-pot assembly method using dicyandiamide (DCDA) as a nitrogen source. Reproduced with permission from [3]. Copyright 2013 Wiley-VCH Verlag GmbH & Co. KGaA, Weinheim

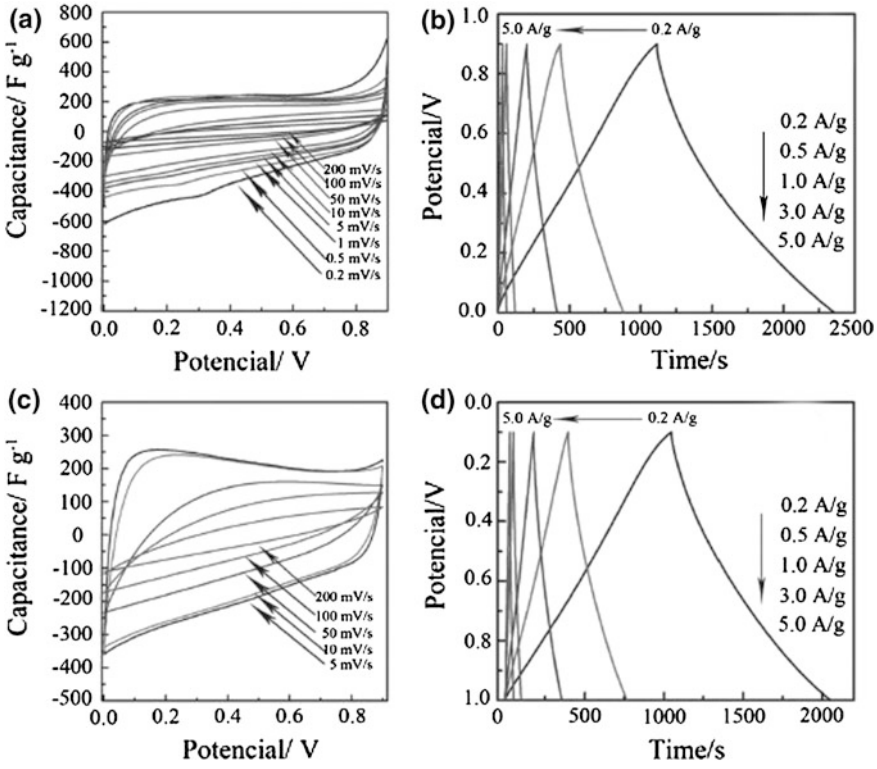

Fig. 11.22 Electrochemical performance of the sample H-NMC-2.5 using a three-electrode cell: cyclic voltammograms at different scan rates in 1 M H_2SO_4 (**a**) and 6 M KOH (**c**); and galvanostatic charge/discharge curves at different current densities in 1 M H_2SO_4 (**b**) and 6 M KOH (**d**). Reproduced with permission from [3]. Copyright 2013 Wiley-VCH Verlag GmbH & Co. KGaA, Weinheim

11.5 Summary

OMC science has progressed tremendously from the discovery with hard templating strategy in 1999. The ability to control pore sizes that cover all the mesopore range, while maintaining well-defined order motivates research on these materials at the starting time. The recent advances include tuning chemical composition, surface modification, search for sustainable carbon sources or greener synthetic routes. Continued study of OMC material is also focusing on the optimization of volumetric density with high surface area materials, towards high energy storage capacity, because further development of electrochemical capacitors is highly dependent on the development of new electrode materials. The increasing ability to

manipulate the OMC material on nanoscale, including precise control over surface area, pore size, pore structure and surface character, would in principle benefit carbon-based energy applications.

Acknowledgments P.F.Z. and S.D. were supported as part of the Fluid Interface Reactions, Structures, and Transport (FIRST) Center, an Energy Frontier Research Center funded by the U.S. Department of Energy, Office of Science, Office of Basic Energy Sciences.

References

1. M. Antonietti, K. Müllen, Carbon: the sixth element. Adv. Mater. **22**, 787 (2010)
2. H. Liang, Q. Guan, L. Chen, Z. Zhu, W. Zhang, S.-H. Yu, Macroscopic-scale template synthesis of robust carbonaceous nanofiber hydrogels and aerogels and their applications. Angew. Chem. Int. Ed. **51**, 5101–5105 (2012)
3. J. Wei, D. Zhou, Z. Sun, Y. Deng, Y. Xia, D.Y. Zhao, A controllable synthesis of rich nitrogen-doped ordered mesoporous carbon for CO_2 capture and supercapacitors. Adv. Funct. Mater. **23**, 2322–2328 (2013)
4. P.F. Zhang, J. Yuan, T. Fellinger, M. Antonietti, H.R. Li, Y. Wang, Improving hydrothermal carbonization by using poly(ionic liquid)s. Angew. Chem. Int. Ed. **52**, 6028–6032 (2013)
5. M. Titirici, M. Antonietti, Chemistry and materials options of sustainable carbon materials made by hydrothermal carbonization. Chem. Soc. Rev. **39**, 103–116 (2010)
6. N. Baccile, M. Antonietti, M.-M. Titirici, One-step hydrothermal synthesis of nitrogen-doped nanocarbons: albumine directing the carbonization of glucose. Chem. Sus. Chem. **3**, 246–253 (2010)
7. Q. Wang, H. Li, L.Q. Chen, X.J. Huang, Monodispersed hard carbon spherules with uniform nanopores. Carbon **39**, 2211–2214 (2001)
8. S. Joo, S. Choi, I. Oh, J. Kwak, Z. Liu, O. Terasaki, R. Ryoo, Ordered nanoporous arrays of carbon supporting high dispersions of platinum nanoparticles. Nature **412**, 169 (2001)
9. A.H. Lu, J. Nitz, M. Comotti, C. Weidenthaler, K. Schlichte, C. Lehmann, O. Terasaki, F. Schüth, Spatially and size selective synthesis of Fe-based nanoparticles on ordered mesoporous supports as highly active and stable catalysts for ammonia decomposition. J. Am. Chem. Soc. **132**, 14152–14162 (2010)
10. J. Liang, Y. Zheng, J. Chen, J. Liu, D. Hulicova-Jurcakova, M. Jaroniec, S.Z. Qiao, Facile oxygen reduction on a three-dimensionally ordered macroporous graphitic C_3N_4/Carbon composite electrocatalyst. Angew. Chem. Int. Ed. **51**, 3892–3896 (2012)
11. Y. Zhai, Y. Dou, D.Y. Zhao, P.F. Fulvio, R.T. Mayes, S. Dai, Carbon materials for chemical capacitive energy storage. Adv. Mater. **23**, 4828–4850 (2011)
12. A.B. Fuertes, G. Lota, T.A. Centeno, E. Frackowiak, Templated mesoporous carbons for supercapacitor application. Electrochim. Acta **50**, 2799–2805 (2005)
13. H. Liu, X. Wang, W. Cui, Y. Dou, D. Zhao, Y.Y. Xia, Highly ordered mesoporous carbon nanofiber arrays from a crab shell biological template and its application in supercapacitors and fuel cells. J. Mater. Chem. **20**, 4223–4230 (2010)
14. Z. Qiao, B. Guo, A.J. Binder, J. Chen, G.M. Veith, S. Dai, Controlled synthesis of mesoporous carbon nanostructures via a "silica-assisted" strategy. Nano Lett. **13**, 207–212 (2013)
15. R. Ryoo, S. Joo, S. Jun, Synthesis of highly ordered carbon molecular sieves via template-mediated structural transformation. J. Phys. Chem. B **103**, 7743–7746 (1999)
16. J. Lee, S. Yoon, T. Hyeon, S.M. Oh, K.B. Kim, Synthesis of a new mesoporous carbon and its application to electrochemical double-layer capacitors, Chem. Commun. **21**, 2177–2178 (1999)

17. Z.J. Li, W.F. Yan, S. Dai, Surface functionalization of ordered mesoporous carbons–a comparative study. Langmuir **21**, 11999–12006 (2005)
18. Z.J. Li, S. Dai, Surface functionalization and pore size manipulation for carbons of ordered structure. Chem. Mater. **17**, 1717–1721 (2005)
19. S. Jun, S.H. Joo, R. Ryoo, M. Kruk, M. Jaroniec, Z. Liu, T. Ohsuna, O. Terasaki, Synthesis of new, nanoporous carbon with hexagonally ordered mesostructure. J. Am. Chem. Soc. **122**, 10712–10713 (2000)
20. H. Darmstadt, C. Roy, S. Kaliaguine, S. Choi, R. Ryoo, Surface chemistry of ordered mesoporous carbons. Carbon **40**, 2673–2683 (2002)
21. A.H. Lu, A. Kiefer, W. Schmidt, F. Schüth, Synthesis of polyacrylonitrile-based ordered mesoporous carbon with tunable pore structures. Chem. Mater. **16**, 100–103 (2004)
22. Y. Wan, Y. Shi, D.Y. Zhao. Designed synthesis of mesoporous solids via nonionic-surfactant-templating approach. Chem. Commun. (9)897–926 (2007)
23. Y. Ren, Z. Ma, P.G. Bruce, Ordered mesoporous metal oxides: synthesis and applications. Chem. Soc. Rev. **41**, 4909–4927 (2012)
24. C. Liang, K. Hong, G.A. Guiochon, J.W. Mays, S. Dai, Synthesis of a large-scale highly ordered porous carbon film by self-assembly of block copolymers. Angew. Chem. Int. Ed. **43**, 5785–5789 (2004)
25. S. Tanaka, N. Nishiyama, Y. Egashira, K. Ueyama. Synthesis of ordered mesoporous carbons with channel structure from an organic–organic nanocomposite, Chem. Commun. 2125–2127 (2005)
26. Y. Wan, Y. Shi, D.Y. Zhao, Supramolecular aggregates as templates: ordered mesoporous polymers and carbons. Chem. Mater. **20**, 932–945 (2008)
27. Y. Meng, D. Gu, F. Zhang, Y. Shi, H. Yang, Z. Li, C. Yu, B. Tu, D.Y. Zhao, Ordered mesoporous polymers and homologous carbon frameworks: amphiphilic surfactant templating and direct transformation. Angew. Chem. Int. Ed. **44**, 7053–7059 (2005)
28. Y. Deng, T. Yu, Y. Wan, Y. Shi, Y. Meng, D. Gu, L. Zhang, Y. Huang, C. Liu, X. Wu, D.Y. Zhao, Ordered mesoporous silicas and carbons with large accessible pores templated from amphiphilic diblock copolymer poly(ethylene oxide)-b-polystyrene. J. Am. Chem. Soc. **129**, 1690–1697 (2007)
29. K.M. Nelson, Z. Qiao, S.M. Mahurin, R.T. Mayes, C.A. Bridges, S. Dai, A non-micellar synthesis of mesoporous carbon via spinodal decomposition. RSC Adv. **4**, 23703–23706 (2014)
30. C. Liang, S. Dai, Synthesis of mesoporous carbon materials via enhanced hydrogen-bonding interaction. J. Am. Chem. Soc. **128**, 5316–5317 (2006)
31. S. Kubo, R.J. White, N. Yoshizawa, M. Antonietti, M.-M. Titirici, Ordered carbohydrate-derived porous carbons. Chem. Mater. **23**, 4882–4885 (2011)
32. S. Schlienger, A. Graff, A. Celzard, J. Parmentier, Direct synthesis of ordered mesoporous polymer and carbon materials by a biosourced precursor. Green Chem. **14**, 313–316 (2012)
33. S. Wang, C. Han, J. Wang, J. Deng, M. Zhu, J. Yao, H. Li, Y. Wang, Controlled synthesis of ordered mesoporous carbohydrate-derived carbons with flower-like structure and N-doping by self-transformation. Chem. Mater. **26**, 6872–6877 (2014)
34. X. Wang, J. Lee, C. Tsouris, D.W. DePaoli, S. Dai, Preparation of activated mesoporous carbons for electrosorption of ions from aqueous solutions. J. Mater. Chem. **20**, 4602–4608 (2010)
35. R. Liu, Y. Shi, Y. Wan, Y. Meng, F. Zhang, D. Gu, Z. Chen, B. Tu, D.Y. Zhao, Triconstituent co-assembly to ordered mesostructured polymer–silica and carbon–silica nanocomposites and large-pore mesoporous carbons with high surface areas. J. Am. Chem. Soc. **128**, 11652–11662 (2006)
36. H. Li, R. Liu, D.Y. Zhao, Y.-Y. Xia, Electrochemical properties of an ordered mesoporous carbon prepared by direct tri-constituent co-assembly. Carbon **45**, 2628–2635 (2007)

Chapter 12
Hyperbolic Metamaterials: Design, Fabrication, and Applications of Ultra-Anisotropic Nanomaterials

Kandammathe Valiyaveedu Sreekanth, Antonio De Luca and Giuseppe Strangi

Abstract Hyperbolic metamaterial (HMM) is a non-magnetic extremely anisotropic nanostructure that cannot be found in nature at optical frequencies having an open hyperboloid iso-frequency surface. Interestingly, these anisotropic media support highly confined wavevector modes (high-k modes) in addition to surface plasmon modes within the structure due to hyperbolic dispersion. The high-k modes in an anisotropic hyperbolic metamaterials are conventionally refereed to as volume plasmon polaritons (VPPs) or bulk Bloch plasmon polaritons (BPPs). Since BPPs are highly confined within the entire structure, the excitation, collection and control those modes at optical frequencies are very challenging. Here, the focus will be on the excitation and collection of bulk plasmon polaritons from anisotropic hyperbolic metamaterials at optical frequencies using the grating coupling principle. In this chapter, the basic properties of hyperbolic metamaterials are first introduced. Then we give a comprehensive overview, describing on design, fabrication and characterization of grating coupled anisotropic hyperbolic metamaterials (GCAHMs) in a wide wavelength range, from visible to near infrared. Numerical simulation results supporting the obtained experimental data are also presented. Finally, we describe potential applications of GCAHMs in photonics and biomedical research with concluding remarks.

K.V. Sreekanth · G. Strangi (✉)
Department of Physics, Case Western Reserve University,
10600 Euclid Avenue, Cleveland, OH 44106, USA
e-mail: giuseppe.strangi@case.edu

A. De Luca · G. Strangi
Department of Physics and CNR-NANOTEC UOS di Cosenza,
University of Calabria, 87036 Rende, Italy

Q. Li (ed.), *Anisotropic Nanomaterials*, NanoScience and Technology,
DOI 10.1007/978-3-319-18293-3_12

12.1 Introduction

Recently, metamaterials research has received tremendous significance in many potential applications for higher performances. The main core in all metamaterials comprises of fabricating a medium composed of unit cells of size far below the excitation wavelength. In contrast to existing optical metastructures in the visible and near-infrared wavelength regions, hyperbolic metamaterials (HMMs) are distinguished as promising class of metamaterials [1]. In the recent past, there have been considerable efforts in the development of metastructures with hyperbolic dispersion at optical and infrared frequencies. The emerging field of hyperbolic metamaterials promises a variety of applications such as spontaneous emission enhancement [2, 3], nano-imaging [4, 5], negative refraction [6, 7], biosensing [8] and Dyakonov plasmonics [9]. HMMs are bulk three-dimensional sub-wavelength structures, which are non-magnetic and anisotropic in permittivity. This advanced quantum nanophotonic system has facilitated the development of optical hyperbolic iso-frequency surfaces with a diagonal form of the permittivity tensor ($\varepsilon = diag(\varepsilon_x, \varepsilon_y, \varepsilon_z)$) in which diagonal elements have different signs ($\varepsilon_x = \varepsilon_y$ and $\varepsilon_x \cdot \varepsilon_z < 0$) leading to a hyperbolic dispersion $\omega^2/c^2 = (k_x^2 + k_y^2)/\varepsilon_z + k_z^2/\varepsilon_x$. This shows that HMMs have dielectric properties ($\varepsilon > 0$) in one direction and metallic properties in another direction ($\varepsilon < 0$). Interestingly, due to hyperbolic dispersion, HMM supports high-wavevector propagating waves. Also this type of dispersion leads to the existence of high photonic density of states, which can be investigated by understanding the modifications in spontaneous emission of emitters placed in the vicinity of HMM [10]. As shown in Fig. 12.1, two approaches have been proposed for the practical realization of hyperbolic metamaterials: (i) alternating layers of metal and dielectric that are much narrower than the wavelength, and (ii) metal nanorods in a dielectric host such as porous anodic alumina (AAO). According to Maxwell-Garnett effective medium theory (EMT), both of these approaches achieve the desired extremely anisotropic response in a broad spectral bandwidth because of its non-resonant nature. By choosing appropriate metal (Ag or Au) and dielectric (TiO_2, SiO_2, Al_2O_3, Si) layers, the hyperbolic dispersion properties of the above mentioned two configurations can be tuned to function in a wide wavelength range from visible to near-infrared.

Being characterized by hyperbolic dispersion, HMMs support surface plasmon polaritons (SPPs) as well as highly confined bulk plasmon polaritons (BPPs). A periodic metal/dielectric stack (HMM) supports bulk plasmon modes, which are the entire family gap plasmon modes of the multilayer. These high-k modes are conventionally known as volume plasmon polaritons (VPPs) or bulk Bloch plasmon polaritons (BPPs). BPPs are propagating waves inside the multilayer whereas decay exponentially outside the structure. The absolute values of modal indices of BPP modes are larger than those of SPPs, varying from positive to negative. However, well known SPPs are electromagnetic waves that propagate along the interface between two media having different sign of permittivity (metal and dielectric), and decay exponentially into both media. The existence of high-k modes is the reason

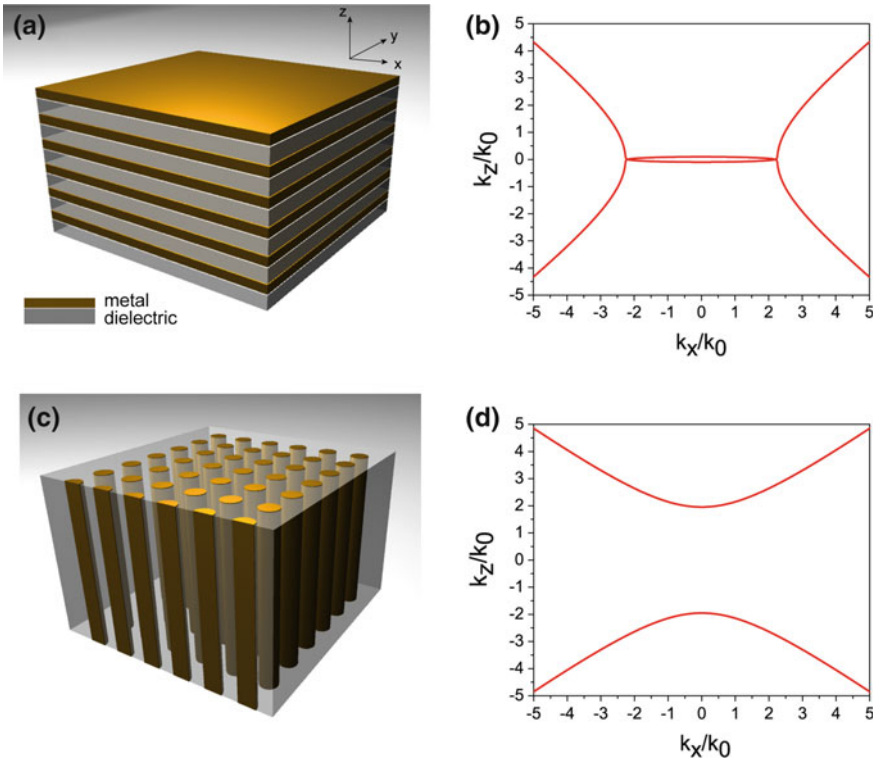

Fig. 12.1 Schematic diagram of **a** 1D metal/dielectric planar HMM, and **c** 2D metal nanorod HMM. Iso-frequency diagram of **b** 1D HMM and **d** 2D HMM

for many promising applications of HMMs. This concept was theoretically and numerically investigated by many research groups [11, 12]. According to Avrutsky et al., BPPs represent the entire family gap plasmon modes (modes with symmetric field distribution) of a metal-dielectric subwavelength structure [13]. Recently, Zhukovsky et al. have theoretically demonstrated that the coupling of short range surface plasmon polaritons (SRSPPs) is responsible for the existence of VPPs in a multilayer system [14]. However, the experimental verification of their existence in a multilayer is extremely challenging because of the large optical loss due to very high modal indices and deep sub-wavelength confinement. Since BPPs are highly confined within the entire structure, it is very challenging to excite, collect and control those modes at optical frequencies. The existence of SPPs and BPPs in periodic subwavelength metallo-dielectric structures at infrared frequencies has been previously experimentally demonstrated [13, 15]. The attenuated total reflection (ATR) method has been used to excite both SPPs and BPPs at infrared frequencies. However, it is a challenging issue to excite BPPs in the optical region using ATR method because of the unavailability of high refractive index prisms for matching the momentum between incident light and the high-k modes. Recently,

subwavelength interference pattern from a hyperbolic medium has been experimentally demonstrated by fabricating a diffraction grating on top of the hyperbolic medium [16].

In this context, we have proposed a novel hypergrating configuration [17] to design optical HMMs and experimentally demonstrate that it is possible to excite SPP and BPP modes at optical frequencies using a grating coupling technique based on surface plasmon excitation. Nanofabrication and nanophotonics strongly interplayed during the design and fabrication processes to create the artificial metal-dielectric superlattice with subwavelength layer thickness (almost λ/20), and to implement a proper grating to couple and simultaneously probe SPP and BPP modes.

In this chapter, we will discuss the design and fabrication of HMMs based on metal/dielectric multilayers and experimentally shows the presence of high-k modes inside the metastructure. Then SPPs and BPPs will be excited and probed up through the grating coupling technique, by fabricating a properly designed one- and two-dimensional metallic diffraction grating on top of the HMM. Our proposed grating coupled anisotropic hyperbolic metamaterials (GCAHMs) demonstrate an extraordinary potential to open new routes towards a wide range of breakthrough applications including bio-chemical sensing, spontaneous emission enhancement and optical sub-wavelength resolution imaging.

12.2 Design and Fabrication of Grating Coupled Anisotropic Hyperbolic Metamaterials

Since the HMM belongs to effective medium approximations [18], we have used effective medium theory (EMT) to design the planar metal/dielectric metastructure. More specifically, the unit cell of metamaterial must be much smaller than the excitation wavelength to achieve an overall homogeneity. Here, the designed HMM is an anisotropic medium with uniaxial dielectric tensor components, $\varepsilon_{xx} = \varepsilon_{yy} = \varepsilon_{ll}$ and $\varepsilon_{zz} = \varepsilon_{\perp}$, which are approximated as follows:

$$\varepsilon_{ll} = \frac{t_m \varepsilon_m + t_d \varepsilon_d}{t_m + t_d} \tag{12.1}$$

$$\varepsilon_{\perp} = \frac{\varepsilon_m \varepsilon_d (t_m + t_d)}{t_m \varepsilon_d + t_d \varepsilon_m} \tag{12.2}$$

In (12.1) and (12.2), (t_d, ε_d) and (t_m, ε_m) are the thickness and dielectric permittivity of dielectric and metal, respectively. The schematic of the designed hyperbolic metastructure is shown in Fig. 12.2a, consisting of 12 alternating layers of gold (Au) and titanium dioxide (TiO_2) thin films. The HMM was realized by sequential deposition of TiO_2 and Au layers on a glass substrate (Micro slides from Corning) using RF sputtering technique (TiO_2 target from Stanford Materials Corporation) and thermal evaporation of Au pellets (from Kurt J. Lesker

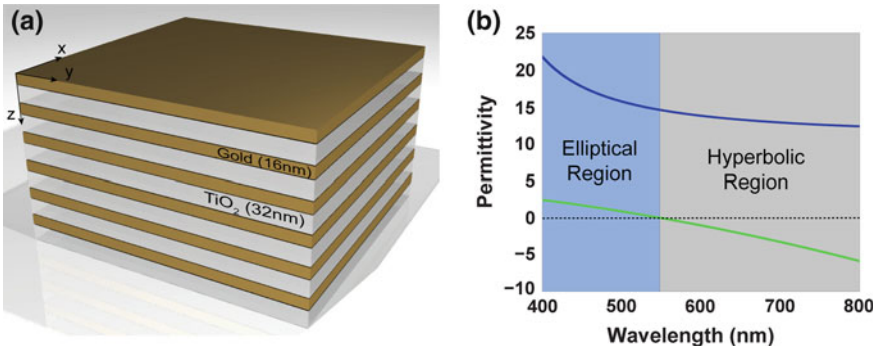

Fig. 12.2 **a** Schematic diagram of fabricated HMM, which consists of 6 bilayers of Au/TiO_2 and **b** real parts of effective permittivity of HMM determined with effective media theory and confirmed using spectroscopic ellipsometry

Company), respectively. Variable Angle Spectroscopic Ellipsometry (J.A. Woollam Co., Inc, V-VASE) was used to measure the thicknesses of both layers and obtained thicknesses are 32 and 16 nm for TiO_2 and Au, respectively. Hence the calculated fill fraction of metal is 33 %. The EMT derived dielectric permittivity tensor components of the entire structure is shown in Fig. 12.2b. In the calculation, the optical constants of Au are calculated starting from Drude free-electron theory, $\varepsilon_m = 1 - \left(\frac{\omega_p^2}{\omega(\omega + i/\tau)}\right)$, where ω_p is the plasma frequency of Au, ω is the excitation frequency and τ is the relaxation time. The dielectric constant of TiO_2 is set to be 7.3 [19]. Then, we performed spectroscopic ellipsometry measurements to confirm the behavior of dielectric tensor components. According to Fig. 12.2b, the fabricated structure is a type II HMM with dielectric permittivity tensor components, $\varepsilon_{ll} < 0$ and $\varepsilon_{\perp} > 0$, confirming the designed hyperbolic dispersion at optical frequencies, above 548 nm wavelength.

According to the grating coupling technique of surface plasmon excitation, the surface plasmon modes can be excited when the wavevector of the grating diffraction orders are greater than those of the incident light. Under this condition, diffraction orders are no longer propagating waves, but evanescent field and the enhanced wavevector of evanescent field is responsible for the coupling of incident light to the surface plasmon modes according to the coupling condition given by $k_{spp}^2 = n_0^2 k_0^2 \sin^2\theta \pm 2n_0 m k_g k_0 \sin\theta \cos\phi + (mk_g)^2$. Being θ the incident grazing angle, ϕ is the azimuthal angle (the angle between the plane of incidence and the grating wavevector), n_0 is the refractive index of incident medium, $k_0 = 2\pi/\lambda$ is the vacuum wavevector, m is the grating diffraction order and $k_g = 2\pi/\Lambda$ is the grating wavevector, with Λ being the grating period. When $\phi = 0$, $k_{spp} = n_0 k_0 \sin\theta \pm mk_g$. On the other hand, by introducing a diffraction grating on top of the HMM, it is possible to diffract light and produce a wide range of wave vectors into the HMM. Due to the existence of impedance mismatch at the various openings, the generated wave vectors can couple through the surface modes [20].

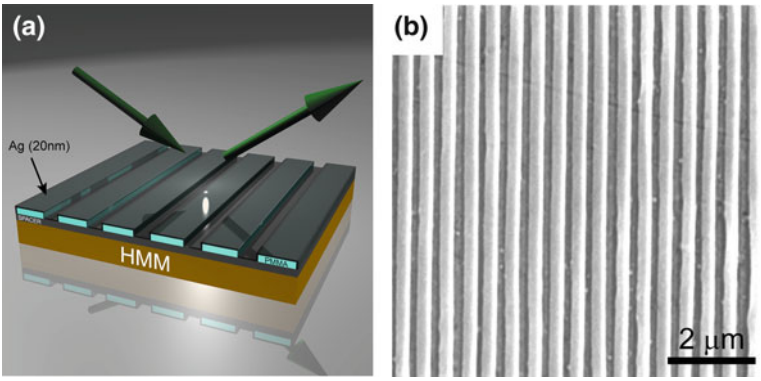

Fig. 12.3 **a** Schematic diagram of fabricated GCAHM in reflection geometry and **b** SEM image of fabricated Ag diffraction grating on top of the HMM

In order to excite both surface and bulk plasmon modes inside the HMM, we designed and fabricated a GCAHM as shown in Fig. 12.3a. GCAHM is a combined structure of metallic diffraction grating (1D or 2D) and HMM. We used Electron-beam lithography to pattern diffraction grating on top of the HMM. Then we directly deposited a silver (Ag) layer of 20 nm thickness on the PMMA grating. Ag has been selected as metal, because it is well known that it has a lower optical loss level compared to Au and hence it has higher plasmonic coupling efficiency. Note that there are no problems existing in evaporating Ag directly onto photoresist and we ensured that the over layer contamination is negligible. The SEM image of as prepared grating lines is shown in Fig. 12.3b. From the image, it is clear that the Ag is uniformly distributed on the sample. Note that the total area successfully patterned on the HMM is around 5 mm × 5 mm.

The fabricated gratings have an average period of 500 nm, average slit width of 160 nm and height around 120 nm. In order to avoid the direct contact of grating with HMM, a TiO_2 spacer layer of 10 nm thick was deposited between them.

12.3 Experimental Results and Discussion

In this section, we discuss the characterization and opto-plasmonic properties of GCAHMs. For this purpose, we used techniques such as variable angle spectroscopic ellipsometry (190–3300 nm) and ultra-fast time-resolved photoluminescence (time resolution about 5 ps).

To show the existence of both SPP and BPP modes in HMM, six different samples have been fabricated and analyzed. The reflectance spectra of these six samples as a function of excitation wavelength were acquired using a J.A.Woollam Co. Inc V-VASE ellipsometer. Here the incident grazing angle is set to be 50^{o} and the incident light is TM-polarized. In order to compare the results, we first analyzed

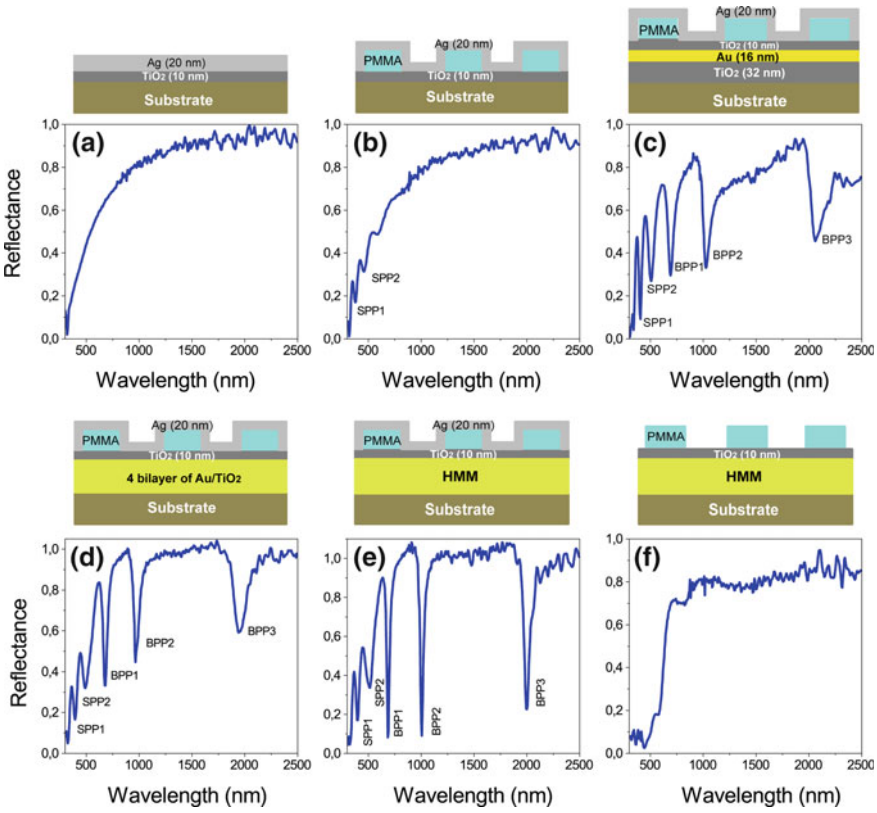

Fig. 12.4 Reflectance spectra as a function of excitation wavelength. Studied structure is shown above the each graph: **a** Uniform Ag layer of 20 nm thickness on a TiO_2/glass substrate, **b** reference sample **c** control sample, **d** Ag grating on a 4 bilayers of Au/TiO2, **e** GCAHM (Ag grating on a 6 bilayers of Au/TiO2), and **f** GCAHM without Ag layer on top of the grating

the reflectance spectrum of a uniform Ag layer (20 nm) on a TiO_2/glass substrate (Fig. 12.4a) by using variable angle spectroscopic ellipsometry. It is well known, that it is not possible to excite surface plasmons for this sample because there is no plasmonic coupling. Then we studied the reflectance spectrum of a reference sample (Ag grating on a TiO_2/glass substrate). Two reflectance minima are observed for visible wavelength (from 350 to 450 nm), which shows the existence of SPPs in the sample (Fig. 12.4b). The reflectance spectrum of a control sample (Ag grating on a single bilayer of Au/TiO_2) was shown in Fig. 12.4c. In contrast to Fig. 12.4b, the control sample shows three extra reflectance minima at wavelengths such as 700, 1000 and 2000 nm in addition to other two reflectance minima of SPP. These minima at higher wavelengths show the existence of gap plasmon (or bulk plasmon) modes in the control sample. Further, we have studied the reflectance spectrum in samples which consist of Ag grating on a 4 bilayers of Au/TiO_2 and observed almost same behavior as that of the control sample (Fig. 12.4d). However,

both surface plasmon and bulk plasmon bands are slightly modified. Figure 12.4e shows the reflectance spectrum of a GCAHM. According to Fig. 12.4e, the reflectance minima at wavelength such as 700, 1000 and 2000 nm are very narrow and deeper as compared to Fig. 12.4c, d. The very deep and narrow modes in the reflectance spectrum represent the existence of highly confined bulk plasmon polaritons (super modes) in the GCAHM. Due to the coupling of individual gap plasmon modes, the reflectance minima of bulk plasmon modes are slightly shifted when the number of bilayer is increased from 1 to 6. In order to validate these results, we have analyzed the reflectance spectrum of a GCAHM without Ag layer on top of the grating and result is shown in Fig. 12.4f. It is evident from the figure that no reflectance minima are obtained for that sample because there is no surface plasmon excitation, similar to Fig. 12.4a. Since both surface and bulk plasmon mode excitation depends on incident angle, we have measured the reflectance of GCAHM for different angles of incidence [17]. We have observed a blue shift in reflectance minima for both surface and bulk plasmon modes as the incident angle increases. This is attributed to the variation in modal indices (effective indices) of modes with incident angles. However, the shift decreases when the excitation wavelengths decrease and the reflectance dip became deeper and narrow for higher incident angles. In order to validate the experimental results with theory, the dispersion relations of both SPP and BPP modes are investigated. The dispersion plot of SPP and BPP modes are shown in Fig. 12.5. It is clear from the figure that dispersions of both modes are well beyond the air light line and the wavevector of SPP modes are higher at shorter wavelengths ($\lambda < 440$ nm). However, the wavevector of BPP modes are higher than that of SPP modes at higher wavelengths. Hence, it is confirmed that the experimentally observed reflectance minima at shorter wavelengths (350–450 nm) are due to SPP modes and at higher wavelengths (700, 1000 and 2000 nm) are due to BPP modes.

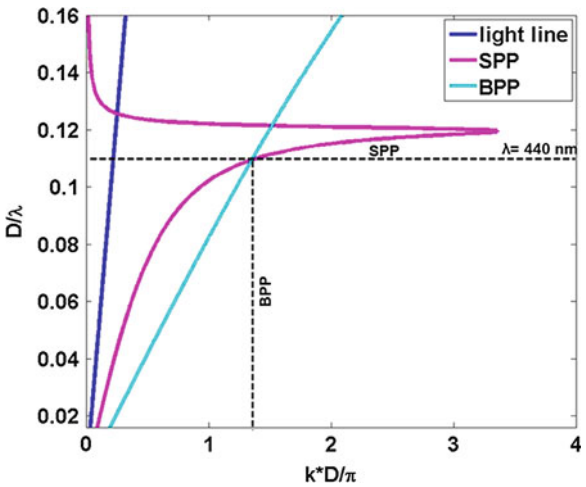

Fig. 12.5 Dispersion relations of SPP and BPP modes. Both X and Y axes are normalized with respect to period (D) of the HMM

As mentioned above, HMM supports BPPs and SPPs at each metal/dielectric interfaces. Both modes can be experimentally probed by studying the reflectance spectra as a function of incident angle and frequency. The excitation of SPP modes in the samples such as reference, control and GCAHM is shown in Fig. 12.6a, b. Here, the coupling angle of all samples is increased when the excitation light wavelength is increased from 350 to 400 nm. According to the grating coupling technique, the modal index of the mode is given as, $n_{\text{modal}} = ((\lambda/\Lambda) + n_0 \sin\theta)$. Hence the experimentally calculated modal indices of the GCAHM for the wavelengths 350 and 400 nm are 1.315 and 1.66, respectively. Also, the theoretically calculated modal indices of the SPP modes for the wavelength region 300–400 nm are shown in Fig. 12.7a. It is evident from the figure that the SPP modal index increases with increasing wavelength for shorter wavelength region. It shows that the experimental results are well correlated with the theoretical results. In addition, the control and GCAHM samples show deeper and narrower reflection minima as compared to the reference sample, since a multilayer structure also supports various plasmonic modes such as long- and short-range surface plasmons at each metal/dielectric interfaces.

The excitation of bulk plasmon modes at different excitation wavelengths are shown in Fig. 12.6c–f. We investigated the bulk plasmon mode excitation at three bulk plasmon bands such as 650–750, 1000–1100 and 2000–2100 nm. One can see that very narrow and deep reflectance minima are obtained for GCAHM as compared to control sample. This shows the excitation of bulk plasmon modes in the GCAHM structure. The shift in coupling angle from control to GCAHM is more relevant at higher wavelengths. This large shift in coupling angle could be due to the strong mode confinement of bulk modes at higher wavelengths. Also, the decrease in resonance angle is observed when the excitation wavelength is increased in each bulk plasmon bands, which shows the decrease in modal indices

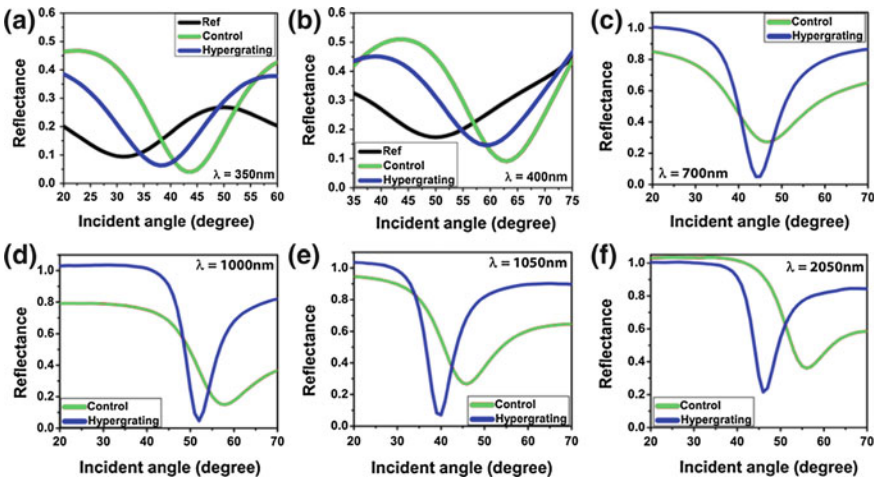

Fig. 12.6 Excitation of SPP modes (**a** and **b**) and BPP modes (**c–f**) as a function of incident angle

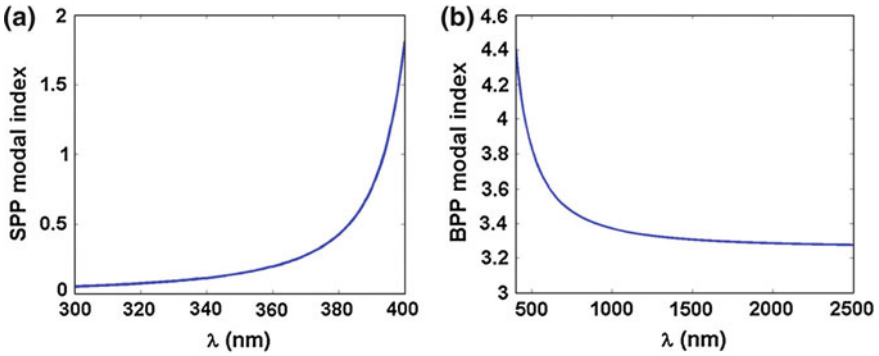

Fig. 12.7 **a** SPP and **b** BPP modal index variation with wavelength

Table 12.1 Modal indices of BPP modes

Wavelength (nm)	Coupling angle (°)	Modal index
Wavelength band: 650–750 nm (Fundamental mode)		
650	64	2.2
700	44	2.09
730	34	2.02
750	22	1.87
Wavelength band: 1000–1100 nm (1st order mode)		
1000	52	2.8
1050	40	2.74
1080	32	2.7
1100	25	2.62
Wavelength band: 2000–2100 nm (2nd order mode)		
2000	50	4.77
2030	46	4.78
2050	44	4.79
2100	38	4.81

of bulk modes with an increase of excitation wavelength. The modal indices of BPP modes of three bulk plasmon bands are calculated and tabulated in Table 12.1. Then the modal indices of BPP modes are theoretically calculated [13] and shown in Fig. 12.7b. From the theoretical and experimental data, it is confirmed that the modal index of BPP modes are decreasing with increasing wavelength for shorter wavelength band (650–750 and 1000–1100 nm). However, the modal index values are almost constant at higher wavelength band (2000–2100 nm). In particular, we obtained very large coupling angle shift for visible wavelength band (650–750 nm) as compared to higher wavelength band (2000–2100 nm). This large shift is due to the large modal index variation of BPP modes at shorter wavelength region. From the modal index analysis of BPP modes, it is found that the modal index of BPP modes increases when the wavelength range of the BPP band is increased from

visible to near infrared. Therefore, the modes at first BPP band (650–700 nm) represent the fundamental modes and modes at other two bands represent the higher order modes (i.e. 1000–1100 nm are the first order modes and 2000–2100 nm are the second order modes).

In addition, we have investigated the influence of metallic diffraction grating dimension on the excitation of BPPs. The schematics of 1D and 2D GCAHMs are shown in Fig. 12.8a. Au/SiO_2 HMMs have been fabricated by the sequential deposition of SiO_2 (28 nm) and Au (15 nm) on a glass substrate. Then 1D and 2D diffraction gratings were patterned on top of a SiO_2 spacer layer using electron-beam lithography. A 20-nm Ag layer was then deposited directly on top of the sample. Scanning electron microscope (SEM) images of both 1D and 2D Ag diffraction gratings on top of a Au/SiO_2 HMM are also shown in Fig. 12.8a. The reflectance spectra as a function of the incident angle for grating-coupled 1D and 2D Au/SiO_2 HMMs were compared, as shown in Fig. 12.8b.

In order to show the existence of bulk plasmon modes in the Au/SiO_2 HMM, the reflectance spectra were obtained at wavelengths from 500 to 2000 nm. As shown in Fig. 12.8b, the reflectance spectra of HMMs are shifted when the modes are excited using 1D or 2D gratings. The 2D gratings provide narrower and deeper reflectance spectra compared to 1D grating for all the wavelengths. The very narrow and deep modes in the reflectance spectra for 2D grating-coupled Au/SiO_2 stacks confirm strong plasmonic coupling [21]. The strong mode confinement and higher plasmonic coupling for the 2D grating reflects the larger modal index values of 2D GCAHM, hence the diffraction grating dimension is a key parameter to improve the radiation coupling within the structure.

Time-resolved photoluminescence measurements were performed to study the fluorescence lifetime and decay rate of excitonic molecules (emitters) coupled with the plasmon modes of the GCAHMs. In this case, we have considered Ag/Al_2O_3 GCAHM that shows a hyperbolic dispersion above 430 nm wavelength [22]. Since the emitter is placed inside the GCAHM, it is very difficult to couple the incident radiation to the emitter because of the impedance mismatch between air and HMM. However, the grating coupling out-couples the highly confined modes from the structure to the far field. In order to study the decay rate enhancement, Coumarin 500 dye molecules were dissolved in PMMA. The dye doped PMMA layer was introduced between the 2D metallic diffraction grating and HMM. An ultrafast time resolved spectroscopy (TCSPC) setup has been used to investigate the fluorescence lifetime of the dye molecules and how they are affected from the plasmon field. The time resolution of the TCSPC experimental setup is $\tau_{res} \leq 5$ ps. The Coumarin molecules were excited by using pulsed laser light at 380 nm with a pulse width of about 120 fs and a repetition rate of 4 MHz. The maximum emission wavelength of Coumarin 500 dye dissolved PMMA was observed at 470 nm for 380 nm excitation wavelength [22]. In order to show the transition from elliptical to hyperbolic dispersion, the investigated emission wavelengths were varied. The short-living excitonic states of the emitters placed in the vicinity of the HMM and the measured fluorescent lifetime as a function of emission wavelength, would represent a clear signature of the transition from elliptical to hyperbolic dispersion. The fluorescence

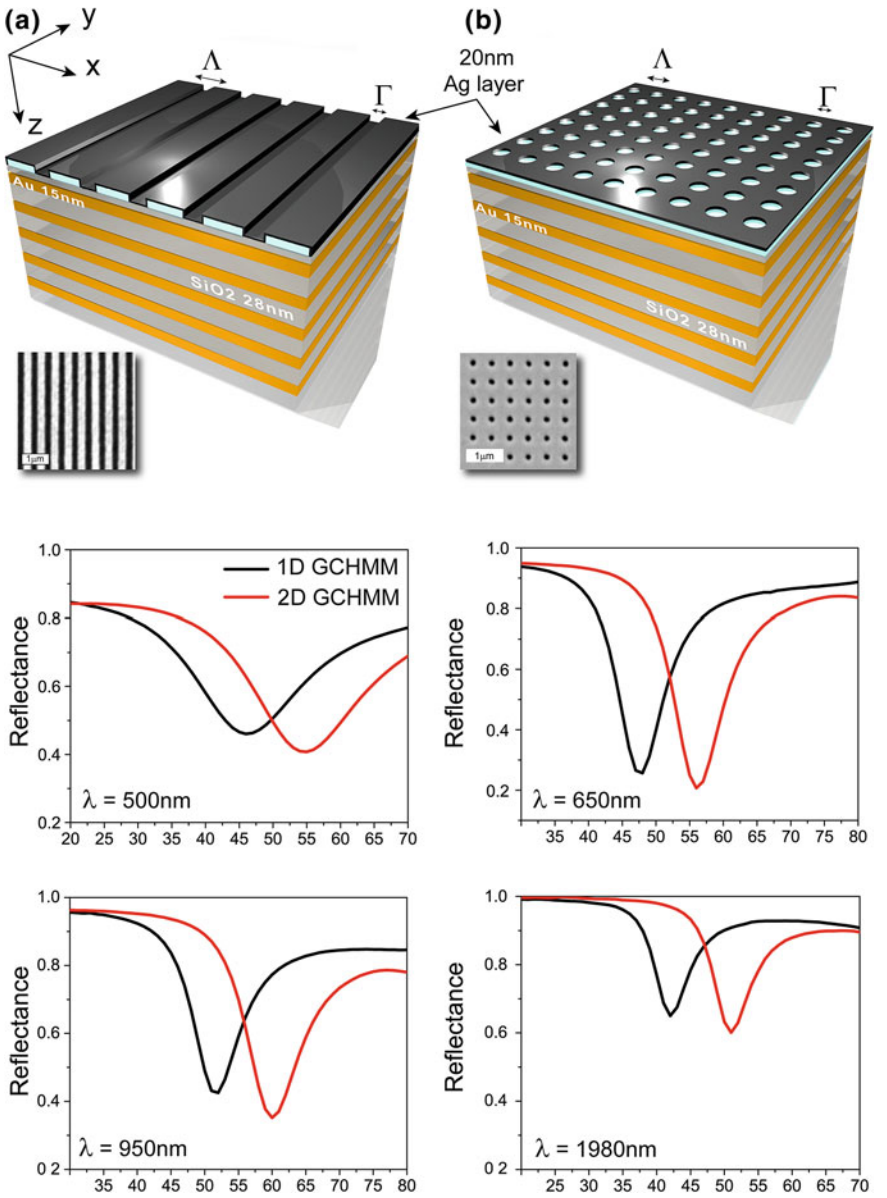

Fig. 12.8 **a** Schematics of 1D and 2D GCAHMs. SEM image of 1D and 2D Ag diffraction gratings on top of the HMM, and **b** reflectance spectra as a function of the incident angle of 1D and 2D Au/SiO_2 GCAHMs for different excitation wavelengths

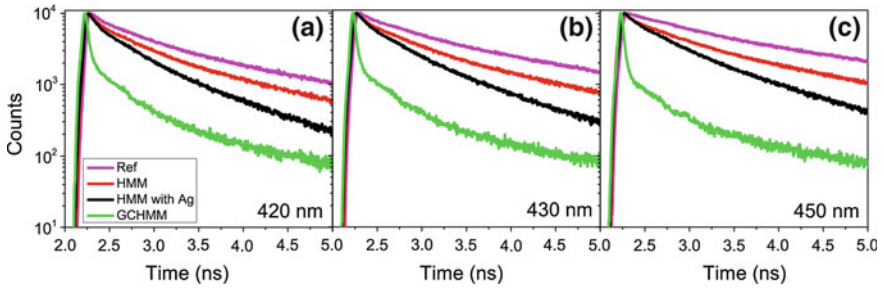

Fig. 12.9 Time-resolved photoluminescence measurements of Coumarin dye on various samples, Ref (*pink*), HMM (*red*), HMM with Ag (*black*), and GCAHM (*green*) with emission wavelength: **a** in elliptical region (λ_e = 420 nm), **b** at critical wavelength (λ_c = 430 nm), and **c** in hyperbolic region (λ_h = 450 nm)

time decay curves of four samples at spectral regions such as elliptical dispersion (420 nm), the critical wavelength (430 nm), and the hyperbolic dispersion (450 nm) are shown in Fig. 12.9. Four different samples such as reference (pink curve), HMM (red curve), Ag film deposited HMM (black curve) and GCAHM (green curve) were investigated for comparison. The data have been fitted using three exponential functions, $R(t) = B_1 e^{-t/\tau_1} + B_2 e^{-t/\tau_2} + B_3 e^{-t/\tau_3}$ with τ_i being the decay times. Since longer time (τ_3) is attributed to uncoupled dye molecules, located above the coupling distance from the HMM, we have used shorter decay times (τ_1 and τ_2) to predict the decay rate enhancement, since shorter decay times are related to molecules strongly coupled with HMM. The transition from elliptical to hyperbolic dispersion is evident from the obtained curves, showing a large variation in time decay for HMM compared to reference sample when the emission wavelength is varied from elliptical to hyperbolic region. The coupling of the high-k metamaterial states is responsible for the observed behaviour of HMM [2]. The observed response of HMM definitely supports the existence of high k-modes in the fabricated Ag/Al_2O_3 HMM.

The decay rate enhancement is defined as the inverse of decay time. To verify the large decay rate enhancement of GCAHM, the sample is compared with HMM and Ag film deposited HMM samples. Throughout the wavelength spectral range of the HMM, one can see that the GCAHM (green curve) shows a large decay rate variation with respect to HMM (red curve) and Ag film deposited HMM (black curve). In addition, the decay rate variation increases when the emission wavelength is varied from the elliptical to hyperbolic spectral region of the HMM. The maximum decay rate is obtained for GCAHM for all wavelengths, which are 1/0.035, 1/0.030, and 1/0.031 ns^{-1} for 420, 480 and 510 nm, respectively. The corresponding decay rates at the respective wavelengths are 1/0.220, 1/0.491, and 1/0.575 ns^{-1} for HMM and 1/0.071, 1/0.353 and 1/0.534 ns^{-1} for Ag film deposited HMM. Note that the first decay time (τ_1) is considered here for comparison. This large decay rate of GCAHM is attributed to the strong coupling of emitters to HMM via metallic diffraction grating. Specifically, the metallic grating excites the plasmonic Bloch modes (high-k modes) as well as surface plasmon polaritons of HMM

and there is a strong overlap between these modes with the quantum emitters, which leads to a broadband enhancement of photonic density of states (PDOS). In addition, 2D diffraction grating scatters the high-k modes of HMM into well-defined free space modes. The sub-wavelength confinement of the emitter inside the GCAHM structure also enhances the decay rate. Furthermore, improved decay rate is observed for Ag film deposited HMM at certain emission wavelengths as compared to HMM. It is attributed to the presence of Ag scatterers intermixed at the interface with dye doped PMMA layer and to the non-radiative contributions.

In order to emphasize the improved plasmon-exciton coupling in GCAHM, normalized lifetimes of GCAHM and Ag film deposited HMM are compared. The first (τ_1) and second (τ_2) decay times of both samples, normalized with respect to HMM as a function of emission wavelength, are shown in Fig. 12.10a, b, respectively. It is evident from those figures that same decay rate variation is obtained for both decay times. For GCAHM, lifetime values are higher in elliptical region and smaller in hyperbolic region. This behaviour represents the preferential emission of high-k modes from GCAHM. However, the lifetimes of Ag film deposited HMM are randomly varying along the spectral range showing that the presence of Ag film does not support the preferential emission of high-k modes. The shorter lifetime values of GCAHM in the hyperbolic region are due to the hyperbolic dispersion. It should be noted that the lifetime values of GCAHM behave non-monotonically as function of the wavelength; they decrease by reaching a minimum value at 510 nm, then in the same hyperbolic region show a change of slope towards higher lifetime values. The observed behaviour is a clear signature of the out-coupling ability of GCAHM. According to τ_1, a maximum of 18-fold decay rate enhancement is obtained for GCAHM at 510 nm emission wavelength, whereas fivefold decay rate enhancement is obtained for τ_2. In comparison to Ag film deposited HMM, the maximum decay rate enhancement for GCAHM is observed at 510 nm, which is

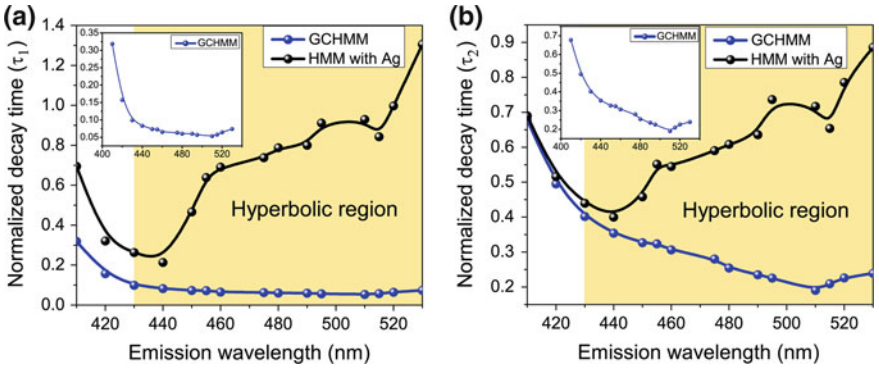

Fig. 12.10 Lifetimes of dye on GCAHM and Ag film deposited HMM normalized with respect to HMM sample: for **a** first decay time (τ_1) and **b** second decay time (τ_2). The *solid lines* are for eye guide. Enlarged plot of normalized decay time of GCAHM is shown in the *inset* of (**a**) and (**b**)

around 17 times and 4 times higher for τ_1 and τ_2, respectively. The observed large spontaneous emission rate enhancement of GCAHM is mainly due to radiative recombination rate, whereas non-radiative recombination rate is negligible in GCAHM. Thus the observed behaviour of GCAHM strongly supports the influence of diffraction grating on the spontaneous emission rate enhancement. The advantage of GCAHM is the ability to outcouple the high wavevector plasmonic modes from HMM structure to far-field. In the case of HMM, the field inside the multilayer is highly confined and cannot be detected at far field due to the evanescent nature of the confined field at the top surface of HMM. However, the grating coupler transforms the evanescent field in a propagating field for far-field detection [23]. This is evident from the time-resolved photoluminescence measurements.

12.4 Numerical Simulation

A numerical simulation has been implemented to obtain a complete analysis of the enhanced emission rates observed in the previous section. In order to study the decay rate enhancement analytically, we have used a semi-classical approach in which quantum emitters have been considered as radiating point dipoles [24]. According to this method, the decay rate enhancement with respect to vacuum of a point dipole with dipole moment 'μ', placed at a distance 'd' from a HMM is given by [25],

$$\beta = \frac{\Gamma}{\Gamma_0} = (1-\eta) + \frac{3\eta}{2k_0^3}\mathrm{Re}\int_0^\infty \exp(2ik_z d)\,\frac{k_{ll}dk}{k_z|\mu^2|} \left\{\frac{1}{2}\mu_{ll}^2[(1+r_s)k_0^2 - (1-r_p)k_z^2] + \mu_\perp^2(1+r_p)k_{ll}^2\right\} \tag{12.3}$$

where η is the intrinsic quantum yield of the emitter, k_0 is the vacuum wavevector of the medium where the emitter resides, k_{ll} is the wavevector parallel to the interface of the HMM, $k_z = \sqrt{k_0^2 - k_{ll}^2}$ and r_s, r_p are the Fresnel reflection coefficients for s- and p-polarization, respectively. Here the Fresnel reflection coefficients of the HMM are obtained by means of the transfer matrix method [18]. In our simulation, the relative permittivity of Ag is obtained from Drude model, $\varepsilon_{Ag}(\omega) = 1 - \left(\omega_p^2/(\omega^2 + iv\omega)\right)$ with $\omega_p = 11.5\ \mathrm{fs}^{-1}$ and $v = 0.083\ \mathrm{fs}^{-1}$ [26]. Note that the point dipole (emitter) resides in PMMA and refractive index of PMMA is set to be 1.49 for wavelengths in the range of 400–800 nm [19]. Here the separation distance (emitter-plasmon) and intrinsic quantum yield of Coumarin dye is taken as 12 nm and 0.98 [27], respectively.

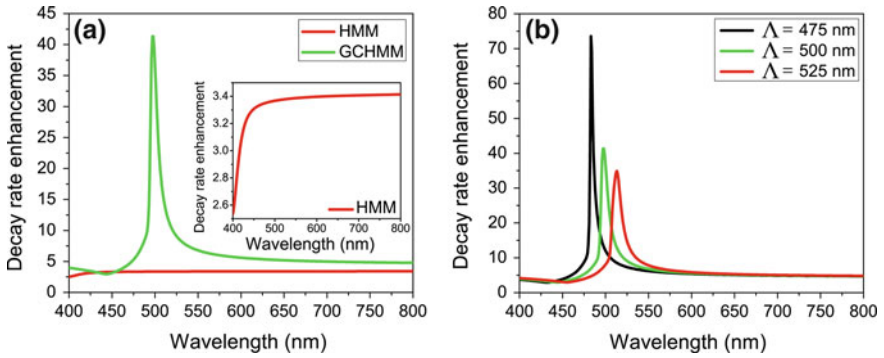

Fig. 12.11 **a** Calculated decay rate enhancement of GCAHM with period 500 nm and HMM. Enlarged plot of decay rate enhancement of HMM is shown in the *inset* of (**a**). **b** Tuning of the decay rate enhancement of GCAHM with grating period

The decay rate enhancement of HMM and GCAHM is shown in Fig. 12.11. As shown in the inset of Fig. 12.11a, an improved decay rate enhancement is observed for HMM in the hyperbolic spectral region (above 430 nm). Due to the strong coupling between the emitter and the high-k modes in HMM, the decay rate enhancement monotonically increases in hyperbolic region. In particular, this coupling strength increases for shorter interaction distances (d/λ). In comparison to HMM, GCAHM shows improved decay rate enhancement for all wavelengths. However, for a particular wavelength band, GCAHM provides very large enhancement of β with respect to HMM. For 500 nm grating period, the maximum β is obtained at 497 nm wavelength that is 12 times higher than HMM. It shows that the simulation results are in good agreement with experiments. However, there is a slight discrepancy in wavelength at which maximum emission rate was observed. This can be attributed to the non-uniform periodicity (average period = 500 nm) of fabricated diffraction grating as compared to uniform periodicity (500 nm) considered in the simulation. According to the simulation model, the maximum value of β in GCAHM depends on the periodicity of the diffraction grating. Note that the periodicity of the grating is introduced in the calculation of Fresnel reflection coefficients for s- and p-polarization, i.e., $k_x = n_0 k_0 \sin\theta \pm m(2\pi/\Lambda_x) \pm n(2\pi/\Lambda_y)$ with $\Lambda_x = \Lambda_y = \Lambda$ for grating with square lattice symmetry. The decay rate enhancement of GCAHM with different grating periods is shown in Fig. 12.11b. It shows the possibility of tuning the spectral position of the maximum β and broadband enhancement of β by varying the grating period. According to Fig. 12.11b, the larger enhancement of β is observed for smaller period (Λ = 475 nm) that is due to the fact that smaller periods provide better momentum match and outcouple most of the high-k modes from HMM. Since HMM provides broadband decay rate enhancement in hyperbolic region, a single period diffraction grating can outcouple a single wavelength as observed in our simulation. However, by designing a proper chirped grating a broadband outcoupling of plasmonic modes is possible [28]. Therefore the broadband outcoupling of single photon as well as

outcoupling of greater number of high-k modes can be achieved by engineering modified diffraction grating geometry.

We further performed finite difference time domain (FDTD) numerical simulation to show the influence of grating coupling in GCAHM. In order to compare the obtained results, the electromagnetic field distribution along the HMM and GCAHM is simulated by assuming that the quantum emitter (point dipole) with a specified emission wavelength resides in PMMA above the multilayer. In hyperbolic region, the electric field (EF) cross-sectional map (xz-plane) of both HMM and GCAHM as a function of emission wavelength are shown in Fig. 12.12. According to Fig. 12.12a, c, the magnitude of EF for HMM increases when the emission wavelength is varied from 480 to 510 nm. This is due to the monotonic increase of the fluorescence decay rate of HMM in the hyperbolic region. In comparison to HMM, GCAHM provides enhanced EF on the substrate as well as above the grating (in air), which evidently shows the outcoupling effect of GCAHM. It is clearly visible that the EF distribution on GCAHM extensively varies with emission wavelength. The maximum EF distribution for GCAHM along the multilayer and the strong coupling between grating, and point dipole is observed for 497 nm emission wavelength. This behaviour of GCAHM definitely supports the maximum decay rate enhancement observed at 497 nm in Fig. 12.11a. Note that the enhanced EF distribution is observed close to the surface of the HMM in which higher plasmonic density of states can be outcoupled. In the case of GCAHM, the

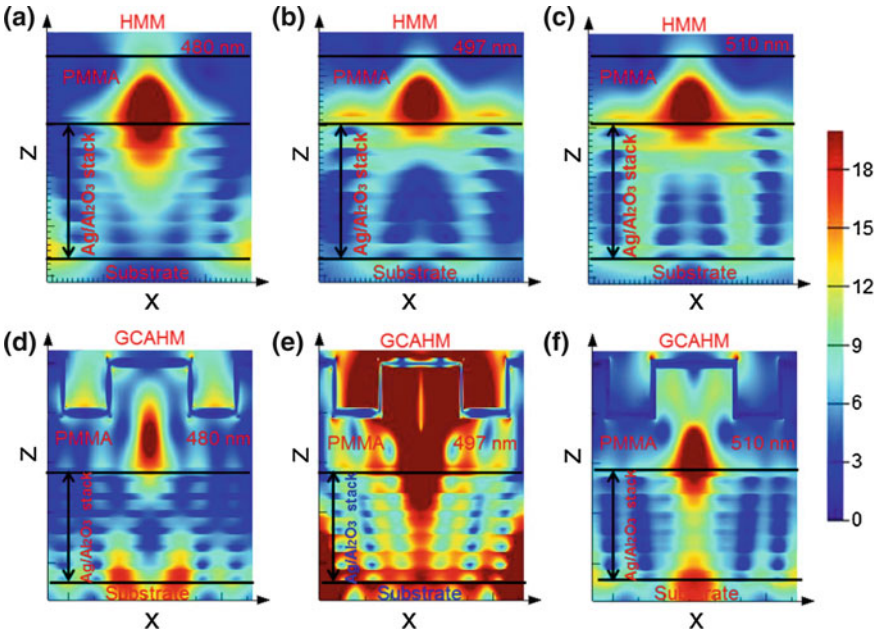

Fig. 12.12 Cross-sectional map of the electric field distribution in the hyperbolic region with emission wavelength such as 480, 497, and 510 nm: **a–c** for HMM and **d–f** for GCAHM

enhanced field distribution observed at 497 nm definitely supports a strong overlap between the excited high-k modes and quantum emitter, which can provide a broadband enhancement of photonic density of states, in addition to an outcoupling effect from GCAHM. As mentioned before, the outcoupling strength depends on the periodicity and the geometry of the diffraction grating. In short, the outcoupling of non-radiative plasmonic modes as well as strong plasmon-exciton coupling through the diffraction grating is responsible for the observed large spontaneous emission decay rate enhancement in GCAHM.

12.5 Applications

The proposed GCAHMs are expected to find a multitude of applications from imaging and sensing to quantum optics. Recently, nanograting based SPR biochemical sensors have received an increasing attention due their advantages to effect the miniaturization and to make the size of the chips even smaller for commercial applications including antigen-antibody, protein, and chemicals detection [29]. The sensitivity of such sensors can be remarkably improved by using a GCAHM based sensor configuration.

To demonstrate the suitability of our structure for sensing applications, a proof-of-concept experiment was carried out using a flow cell-based 1D GCAHM. Microfluidic techniques have been used to construct the microchannel on top of the sensor [30]. The aqueous solutions of glycerol with different weight ratios have been pumped into the sensor flow channel using a syringe pump allowing interactions with the GCAHM surface. The corresponding refractive index range of pure distilled water (DI) water and 0.5 % glycerol in DI water is 1.333–1.3336 [31]. It is possible to calibrate and determine the detection limit of the system by knowing the difference in refractive index between DI water and glycerol. As shown in Fig. 12.13, the

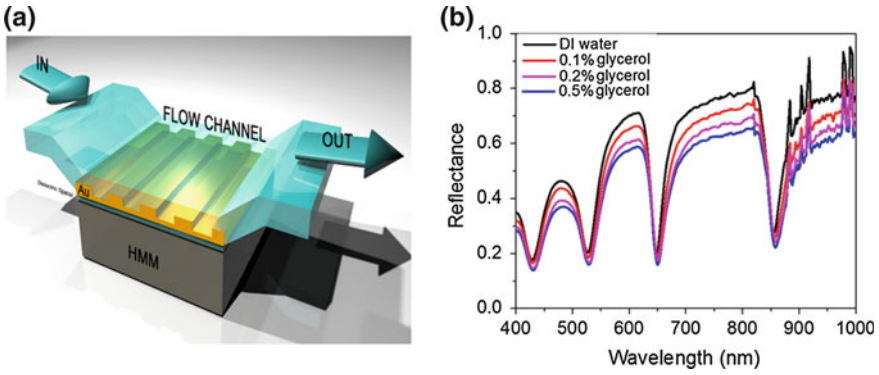

Fig. 12.13 **a** Schematic of proposed flow cell-based GCAHM and **b** reflectance spectra of a 1D GCAHM with different weight ratios of glycerol in DI water

GCAHM supports four plasmonic modes in the wavelength range from visible to near IR. There is a red shift in resonance wavelength when the weight ratio of glycerol changes and the quality factor of the resonance clearly declines when the glycerol concentration increases. These results demonstrate the sensing ability of the 1D GCAHM. The wavelength shift and calculated sensitivity at 30^{o} angle of incidence for NIR wavelength mode (around 850 nm) is 12 and 20,000 nm per RIU. The corresponding wavelength shift and calculated sensitivity for visible wavelength modes are: 8 and 13,333 nm per RIU for the second and third mode ($\sim$540 and 660 nm), and 6 and 10,000 nm per RIU for the first mode ($\sim$440 nm). The sensitivity of the device can also be tuned by varying the spectral wavelength range and angle of incidence. The maximum sensitivity (20,000 nm per RIU) is higher than the sensitivity of all known conventional plasmonic sensors. This preliminary experiment determined whether the 1D GCAHM was suitable for sensing applications. The sensitivity of the device can be improved further using 2D or 3D grating-coupled HMMs, by selecting exact angles of incidence, by narrowing the quality factor of the resonance by using proper metal and dielectric combinations for HMMs, by concentrating the molecules within a small region using super-hydrophobic surfaces, by hydrogenation of graphene with super-hydrophobic surfaces, and by chemical functionalization of the hydrophobic grating. A distinct advantage of this geometry is that the spectral position of the resonance can be tuned from visible to NIR by changing both the HMM and the diffraction grating parameters.

The proposed configuration can also be expected to find important applications in optical sub-wavelength resolution imaging in cancer research. In addition, this configuration can offer the possibility of engineering the photonic density of states for Purcell factor enhancement for potential applications including biosensing [32], surface-enhanced Raman spectroscopy [33] and single photon sources [34].

12.6 Summary

In this chapter we have discussed various GCAHM configurations recently proposed in different papers. We designed, fabricated and characterized optical GCAHMs for the excitation of both surface and bulk plasmon modes in a hyperbolic metamaterial. Nanofabrication and nanophotonic techniques have been synergistically combined to create the designed metal-dielectric multilayer lattice coupled with a subwavelength silver grating to excite and probe SPP and BPP modes. The excitation of those tailored modes was experimentally demonstrated in a wide wavelength region from visible to near infrared using TM-polarized light. The experimental results were then validated with theoretical models. HMMs are considered to be among the most promising optical metamaterials, since they represent a very advanced quantum nanophotonic system having unique opto-plasmonic features. In addition, we designed and fabricated a GCAHM based on Ag/Al_2O_3 multilayers to show the outcoupling effect and large spontaneous emission rate enhancement of fluorescent molecules. In comparison to Ag/Al_2O_3

HMM without diffraction grating, we obtained 18-fold spontaneous emission rate enhancement of dye molecules placed in the close proximity of GCAHM.

Simulations based on a semi-classical approach to show the decay rate enhancement analytically have been reported. Futhermore, we have carried out FDTD numerical simulation to show the enhanced field distribution and outcoupling effect in GCAHM. A good agreement between experiments and simulations was obtained, which confirms that the observed enhancement of GCAHM is due to the outcoupling of non-radiative plasmonic modes as well as strong plasmon-exciton coupling in HMM via diffracting grating. Finally, we have demonstrated the biosensing applications of GCAHM. A maximum refractive index sensitivity of 20,000 nm per RIU was observed in our experiments.

Acknowledgments We acknowledge support of the Ohio Third Frontier Project "Research Cluster on Surfaces in Advanced Materials (RC-SAM) at Case Western Reserve University". The research leading to these results has received funding partially from the Italian Project "NanoLase"–PRIN 2012, protocol number 2012JHFYMC.

References

1. A. Poddubny, I. Iorsh, P. Belov, Y. Kivshar, Hyperbolic metamaterials. Nat. Photon. **7**, 948–957 (2013)
2. H.N.S. Krishnamoorthy, Z. Jacob, E. Narimanov, I. Kretzschmar, V.M. Menon, Topological transitions in metamaterials. Science **336**, 205–209 (2012)
3. K.V. Sreekanth, T. Biaglow, G. Strangi, Directional spontaneous emission enhancement in hyperbolic metamaterials. J. Appl. Phys. **114**, 134306 (2013)
4. A. Ono, J.I. Kato, S. Kawat, Subwavelength optical imaging through a metallic nanorod array. Phys. Rev. Lett. **95**, 267407 (2005)
5. Z. Liu, H. Lee, Y. Xiong, C. Sun, X. Zhang, Far-field optical hyperlens magnifying sub-diffraction-limited objects. Science **315**, 1686 (2007)
6. A.J. Hoffman et al., Negative refraction in semiconductor metamaterials. Nat. Mater. **6**, 946–950 (2007)
7. K.V. Sreekanth, A. De Luca, G. Strangi, Negative refraction in graphene-based hyperbolic metamaterials. Appl. Phys. Lett. **103**, 023107 (2013)
8. A.V. Kabashin et al., Plasmonic nanorod metamaterials for biosensing. Nat. Mater. **8**, 867–871 (2009)
9. D. Artigas, L. Torner, Dyakonov surface waves in photonic metamaterials. Phys. Rev. Lett. **94**, 013901 (2005)
10. Z. Jacob, I.I. Smolyaninov, E.E. Narimanov, Broadband purcell effect: radiative decay engineering with metamaterials. Appl. Phys. Lett. **100**, 181105 (2012)
11. J. Schilling, Uniaxial metallo-dielectric metamaterials with scalar positive permeability. Phys. Rev. E **74**, 046618 (2006)
12. X. Ni, S. Ishii, M.D. Thoreson, V.M. Shalaev, S. Han, S. Lee, A.V. Kildishev, Loss-compensated and active hyperbolic metamaterials. Opt. Exp. **19**, 25242–25254 (2011)
13. I. Avrutsky, I. Salakhutdinov, J. Elser, V. Podolskiy, Highly confined optical modes in nanoscale metal-dielectric multilayers. Phys. Rev. B **75**, 241402 (2007)
14. S.V. Zhukovsky, O. Kidwai, J.E. Sipe, Physical nature of volume plasmon polaritons in hyperbolic metamaterials. Opt. Exp. **21**, 14982–14987 (2013)

15. Z. Shi, G. Piredda, A.C. Liapis, M.A. Nelson, L. Novotny, R.W. Boyd, Surface-plasmon polaritons on metal-dielectric nanocomposite films. Opt. Lett. **34**, 3535–3537 (2009)
16. S. Ishil, A.V. Kildishev, E. Narimanov, V.M. Shalaev, V.P. Drachev, Sub-wavelength interference pattern from volume plasmon polaritons in a hyperbolic medium. Laser Photonics Rev. **7**, 265–271 (2013)
17. K.V. Sreekanth, A. De Luca, G. Strangi, Experimental demonstration of surface and bulk plasmon polaritons in hypergratings. Sci. Rep. **3**, 3291 (2013)
18. C.L. Cortes, W. Newman, S. Molesky, Z. Jacob, Quantum nanophotonics using hyperbolic metamaterials. J. Opt. **14**, 063001 (2013)
19. E.D. Palik, *Handbook of Optical Constants of Solids, Orlando* (Academic, Orlando, 1985)
20. W. Yan, L. Shen, L. Ran, J.A. Kong, Surface modes at the interfaces between isotropic media and indefinite media. J. Opt. Soc. Am. A: **24**, 530–535 (2007)
21. K.V. Sreekanth, A. De Luca, G. Strangi, Excitation of volume plasmon polaritons in metal-dielectric metamaterials using 1D and 2D diffraction gratings. J. Opt. **16**, 105103 (2014)
22. K.V. Sreekanth, K.K. Hari, A. De Luca, G. Strangi, Large spontaneous emission rate enhancement in grating coupled hyperbolic metamaterials. Sci. Rep. **3**, 3291 (2014)
23. D. Lu, J.J. Kan, E.E. Fullerton, Z. Liu, Enhancing spontaneous emission rates of molecules using nanopatterned multilayer hyperbolic metamaterials. Nat. Nanotech. **9**, 48–53 (2014)
24. G.W. Ford, W.H. Weber, Electromagnetic interactions of molecules with metal surfaces. Phys. Rep. **105**, 227403 (1984)
25. W.D. Newman, C.L. Cortes, Z. Jacob, Enhanced and directional single-photon emission in hyperbolic metamaterials. J. Opt. Soc. Am. B **30**, 766–775 (2013)
26. A. Husakou, J. Herrmann, Steplike transmission of light through a metal dielectric multilayer structure due to an intensity-dependent sign of the effective dielectric constant. Phys. Rev. Lett. **99**, 127402 (2007)
27. J.M. Drake, M.L. Lesiecki, J. Sansregret, W.R.L. Thomas, Organic dyes in PMMA in a planar luminescent solar collector: a performance evaluation. Appl. Opt. **21**, 2945 (1982)
28. J.S. Bouillard, S. Vilain, W. Dickson, G.A. Wurtz, A.V. Zayats, Broadband and broadangle SPP antennas based on plasmonic crystals with linear chirp. Sci. Rep. **2**, 829 (2012)
29. S. Zeng, D. Baillargeat, H.P. Hod, K.T. Yong, Nanomaterials enhanced surface plasmon resonance for biological and chemical sensing applications. Chem. Soc. Rev. **43**, 3426–3452 (2014)
30. U.A. Gurkan et al., Controlled viable release of selectively captured label-free cells in microchannels. Lab Chip **11**, 3979 (2011)
31. R.C. Weast, *CRC Handbook of Chemistry and Physics* (CRC Press, Boca Raton, 1987)
32. J. Homola, S.S. Yee, G. Gauglitz, Surface plasmon resonance sensors: review. Sens. Actuators B **54**, 3 (1999)
33. P.L. Stiles, J.A. Dieringer, N.C. Shah, R.P. Van Duyne, Surface-enhanced raman spectroscopy. Annu. Rev. Anal. Chem. **1**, 601–626 (2008)
34. B. Lounis, M. Orrit, Single-photon sources. Rep. Prog. Phys. **68**, 1129–1179 (2005)

Chapter 13
Printed Anisotropic Molecular Alignments

Munehiro Kimura

Abstract The fabrication of ordered organic molecular layers is of fundamental interest in many opto-electronic applications. Needless to say, the performance of liquid crystal displays, organic light emitting devices, organic field effect transistors and organic photovoltaic cells all depends on achieving a required degree of molecular alignment. To date, several processes have been developed to achieve the alignments, including the rubbing, Langmuir-Blodgett, alignment transcription, flow coating, gravure coating, and slit coating methods. In this chapter, these fabrication methods will be introduced and discussed and future technologies will be considered.

13.1 Necessity of Controlling Molecular Alignment and Demand for Printing Techniques

At present, liquid crystal displays (LCDs) are among the most successful organic electronic devices [1, 2]. The basic operation of LCDs is made possible by the reorientation of liquid crystal (LC) molecules that are initially aligned in a certain direction using a so-called alignment film. One of the most important performance indices associated with LCDs is the so-called contrast ratio, defined as the ratio of maximum to minimum luminance. Light leakage in the extinction state (equal to the minimum luminance) resulting from imperfect alignment of the liquid crystal molecules deteriorates this contrast ratio, meaning that the initial molecular alignment is the most vital factor affecting LCD quality. Molecular alignments near boundary surfaces have been widely studied on the basis of both experimental and theoretical aspects and there have been many reports on LCDs that discuss the nature of their molecular alignment and means of controlling this alignment [3, 4].

M. Kimura (✉)
Department of Electric Engineering, Nagaoka University of Technology, 1603-1 Kamitomioka, Nagaoka 940-2188, Japan
e-mail: nutkim@nagaokaut.ac.jp

Q. Li (ed.), *Anisotropic Nanomaterials*, NanoScience and Technology,
DOI 10.1007/978-3-319-18293-3_13

The mechanical rubbing method is still widely used for industrial purposes, since it is readily applicable to mass-production. Recently, however, the patterned photo-alignment technique has been put into practical use. In general, all LC alignment techniques are in many ways similar since the LC must in all cases exhibit orientational order and the capacity for self-assembly. The role of the alignment film when fabricating LC devices is to promote the initial alignment of the LC molecules.

The alignment of organic semiconductors in optoelectronic and electronic devices can be considered analogous to the alignment of LC molecules in LCDs. In the case of an organic semiconductor, charge transport can be attributed to π-bonding orbitals and quantum mechanical wavefunction overlaps, and so a molecular order that enhances the π-bonding overlap between molecules is important [5, 6]. It has been reported that the carrier mobility in field-effect transistor devices consisting of pentacene nanolayers is remarkably improved by inserting a self-assembled monolayer (SAM) at the semiconductor/gate dielectric interface [7]. This enhanced mobility can be explained by the formation of large, highly π-conjugated crystal grains in the pentacene nanolayers formed at the SAM surface. That is, the SAM assists in the molecular alignment of the pentacene.

The requirements for future applications of organic electronic devices such as LCDs and organic semiconductor devices, including organic thin film transistors (OTFTs), organic light emitting diodes (OLEDs) and organic photo voltaic (OPV) devices, are similar: bendability (or flexibility) and printability. These applications, sometimes referred to by the general term printed electronics, have significant potential to allow new innovations in electronic devices [8]. To promote the practical applications of these organic electronic devices, the development of molecular alignment techniques is quite important. In the following sections, molecular alignment techniques with applications to the formation of LCDs are reviewed, including a brief discussion of conventional techniques such as rubbing, for which it should be emphasized that an alignment film is required. In addition, novel alternative techniques such as gravure printing and slit coating that do not require preparation of an alignment film are introduced.

13.2 LC Alignment by Means of an Alignment Film

In general, LC molecular alignment is accomplished by means of a polymeric alignment film, which is first applied to a substrate and then treated in some manner. In industrial applications, polyimide derivatives are widely used for this purpose and may be treated using the gravure coating method, as shown in Fig. 13.1. Following this treatment, the film functions as an alignment film.

The mechanical rubbing method, first reported by Mauguin in 1911, is one of the most common means of processing the polymeric alignment film [9]. Figure 13.2 presents an illustration of a typical rubbing machine. As its name suggests, the surface of a polymeric film previously applied to the substrate is mechanically

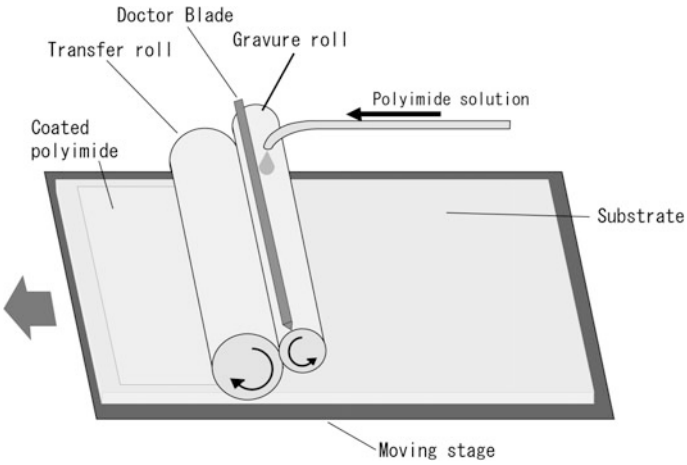

Fig. 13.1 Gravure coater for coating polyimide alignment film

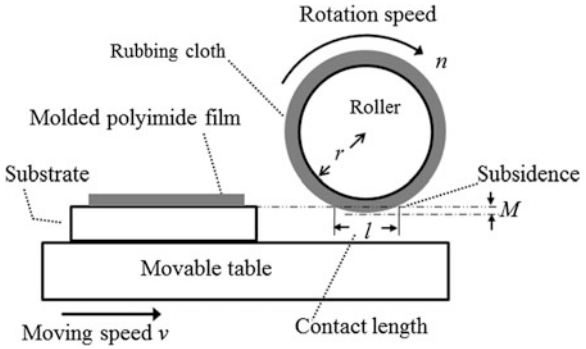

Fig. 13.2 Schematic illustration of a rubbing machine

rubbed by a cloth wrapped around a drum. The untreated polymer film has no alignment capability but is capable of inducing LC alignment following the rubbing process. The rubbing process is fairly practical, although the associated mechanism by which rubbing enhances the film and the action that the rubbed polymer film exerts to generate LC molecular alignment are not perfectly understood. It can be said, however, that mechanically-induced anisotropy on the alignment film surface induces an anisotropic interaction with the LC molecules [10–12].

As noted, the anisotropy in the treated alignment film results in LC alignment and, to date, several alternative methods for introducing anisotropy in the film have been proposed. In 1987, Kakimoto et al. reported that Langmuir-Blodgett (LB) films of polyimides deposited on a substrate exhibited a fair degree of orientation relative to the transfer direction of the substrate [13]. Figure 13.3 illustrates the LB method, also known as the vertical dipping method. These deposited LB films

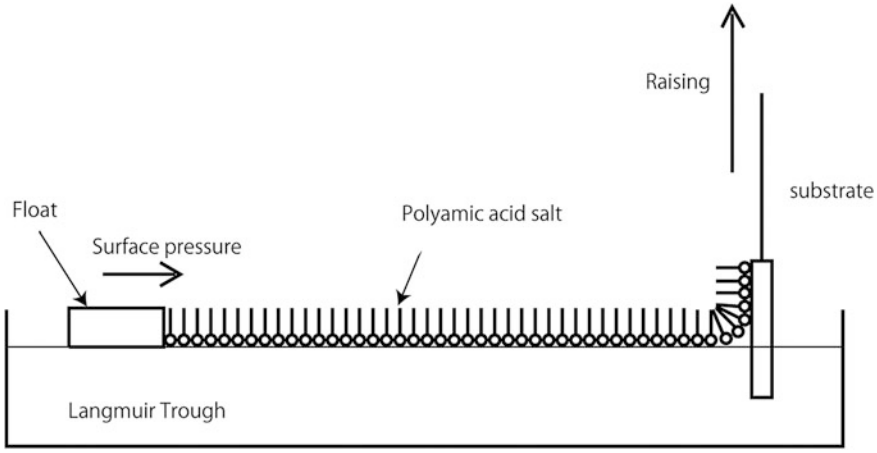

Fig. 13.3 Schematic illustration of Langmuir-Blodgett method. Substrate is moving upward and downward in order to move the monomolecular polyamic acid salt film from the water surface. This method is also called vertical dipping method

exhibit the ability to induce planar LC alignment without rubbing. A mechanism by which LC alignment is induced by LB films has been suggested [14], in which a polymeric LB film transferred onto a substrate by upwards pulling perpendicular to the water surface is stretched uniaxially, generating anisotropy. Mechanical stretching, however, is not the only external influence that induces anisotropy; the photo alignment method is one of the promising techniques from an industrial standpoint [15].

13.3 Surface Memory Effect

It is important to note that, in the abovementioned LCD preparation methods, the polymeric film must be preprocessed by external stimuli before applying the LC molecules. Some unique experiments have demonstrated that alignment may also be accomplished by taking advantage of the memory effect [16–18], by which "LCs align LCs" [19] thus maintaining orientational order. In the case of organic field effect transistors (OFETs), it is important to develop deposition techniques capable of simultaneously aligning the crystal axes, so as to induce enhanced mobility, and increasing the crystalline grain size, such that it is larger than the channel length of the OFET. Many methods have been proposed for producing organic semiconductor molecules, including flow coating [20], zone casting [21], drop casting on tilted substrates [22], hollow-pen writing [23], solution-sheared deposition [24], sustaining of a semiconductor solution on a tilted substrate [25], dip coating [26] and droplet drying under a directional gas flow [27]. In these methods, the

directional movement of the air-solution-substrate contact line (i.e. the shear flow force) is usually the driving force aligning the organic molecules. Once an external force is applied to the molecules, the molecular alignment is sustained through their recrystallization from that starting structure, especially near the substrate surface. Of these methods, we will examine the alignment transcription, reactive mesogen polymerization and flow-coating methods, since these lead to the development of the alignment printing methods described further on.

13.3.1 Alignment Transcription Method

Toko et al. proposed a non-rubbing technique known as the alignment transcription (AT) method [28], involving the fabrication processes shown in Fig. 13.4. Here the original substrates are coated with pre-rubbed polyimide films while the counter

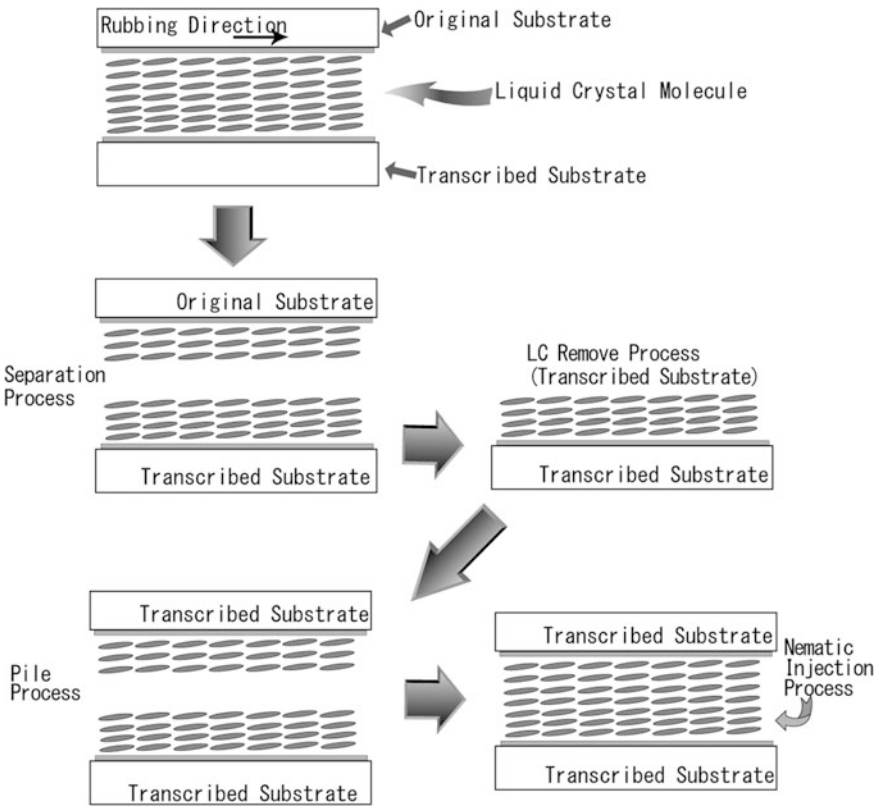

Fig. 13.4 Fabrication processes of the Alignment transcription method. Reproduction by permission from [28]

substrates are coated with non-rubbed polyimide films. An original substrate is placed upon a transcribed substrate, leaving an appropriately-spaced gap, to make the transcription cell, and then heated to the temperature at which the LC exhibits its isotropic phase, to allow for LC injection. The cell is subsequently cooled to ambient temperature, whereupon the LC transitions to the nematic phase and LC molecules are aligned along the rubbing direction of the original substrate. The original substrate is then separated from the transcribed substrate, removing all the LC molecules except for those situated in the vicinity of the surface of the transcribed substrate. Finally, the transcribed substrate is placed over another transcribed substrate to form an AT-LC cell and the LC in the nematic phase is injected into this cell. The azimuthal anchoring strength of the AT-LCD process has been reported to be comparable to that obtained by the rubbing process, suggesting that the LC molecular order propagated from the bulk orientation can be memorized by the polyimide surface. Unfortunately, due to the labor-intensive repetitive cell fabrication process involved with this technique, the AT method has not been put into practical use.

13.3.2 Polymerization of a UV-Curable Reactive Mesogen Monomer at the Surface

To obtain high image quality with LCDs, the patterned vertical alignment (PVA) mode is typically used [29]. In a PVA panel, the pixel and common electrodes are situated in an alternating pattern and thus an oblique field having vertical and horizontal components is generated, with a biased applied voltage that rotates the LC molecules downwards in four different diagonal directions. Challenges associated with the real-applications of LCDs to the PVA mode included unexpected disinclination and insufficient response time, especially when the applied electric voltage is kept low so as to maintain a low gray level. Furthermore, additional structures such as protrusions are required. Kim et al. has proposed a relatively simple technique to solve these problems that requires neither the rubbing process nor protrusion structuring [30]. In this method, a UV-curable reactive mesogen (RM) monomer and a photoinitiator are doped into the nematic LC mixture in advance. The mixture is placed in the PVA cell, the inner surfaces of which have a vertical alignment layer with patterned electrodes, as shown in Fig. 13.5. Immediately following LC injection, the RM monomer and the LC molecules are vertically aligned. Subsequently, a voltage higher than the Freedericksz transition voltage (V_{th}) is applied to the cell such that the RM monomer as well as the LC reorient at a slight tilt angle from the vertical alignment in response to an electric field. In this state, the PVA cell is exposed to UV light, during which the RM monomers are polymerized at a constant tilt angle on the surface of the substrate and thus a pretilt layer is formed in the cell and remains in this state even after removing the voltage. Using this process, the pretilt angle can be controlled on the

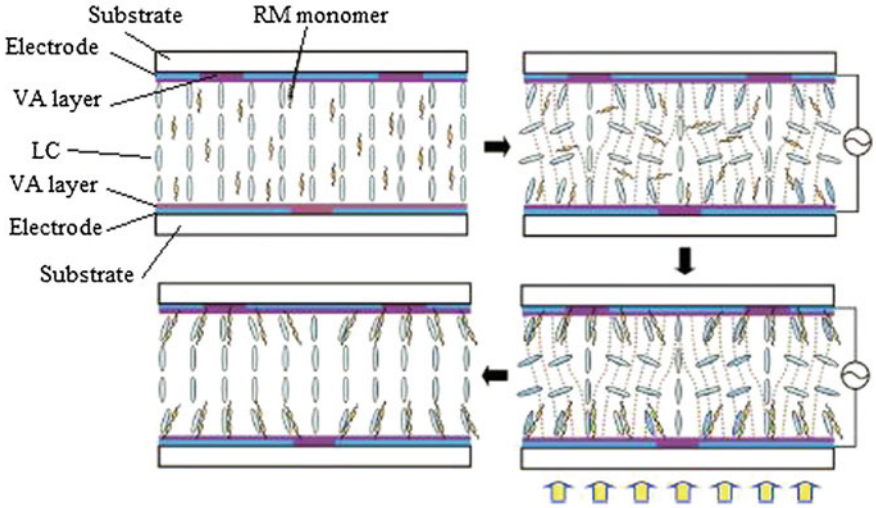

Fig. 13.5 Schematic illustration of the patterned vertical alignment (PVA) cell exhibiting how the pretilt angle is formed using reactive mesogen (RM) monomer. Reproduction by permission from [30]

surface of a vertical alignment film and, as a result, the necessary driving voltage and response time are both reduced. Recently, a technique of this sort not requiring a polyimide film has been proposed [31]. This is possible because the polyimide film is no longer necessary if the RM brings about surface segregation and polymerization in the vicinity of the glass surface, meaning that the polymerized RM film can take the place of the polyimide, such that the surface memory effect acts as a surface anchoring effect.

13.3.3 Flow-Coating Method

It has been reported that a flow-coating method [32] may be useful as a means of forming highly oriented and fairly uniform organic semiconductor material films from materials such as 6,13-bis(triisopropylsilylethynyl) pentacene (TIPSPEN), even on OFET device substrates with pre-deposited source/drain electrodes [20]. This method is understood by considering the work of Sakamoto et al. [20], and Fig. 13.6 shows a schematic illustration of the flow-coating technique. Here the flow coater consists of a movable blade composed of a 13 mm-wide, 2 mm-thick fluorine-coated glass plate, together with a stationary sample stage. The movable blade is inclined at an angle of approximately 1.5° from the substrate surface plane, and the gap height between the blade and the substrate surface is set to 200 μm. After placing the leading edge of the movable blade above the coating start line, 16 μl of a 0.6 wt% solution of TIPSPEN in chloroform is transferred into the blade/substrate gap by

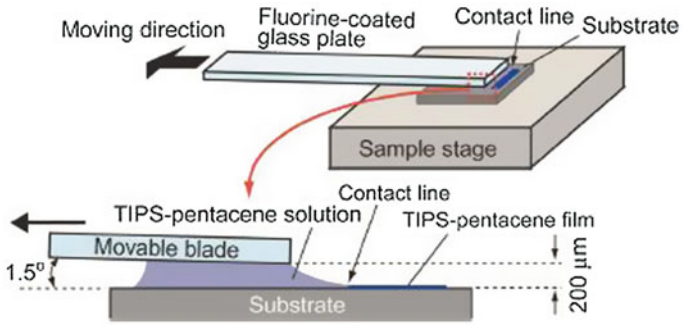

Fig. 13.6 Schematic illustration of the flow-coating method. Reproduction by permission from [20]

capillary action and the flow-coating is immediately initiated at a constant blade speed of 200 μm/s. The flow-coated films thus formed are composed of arrays of needle-shaped crystals whose long axes are aligned along the flow-coating direction. It has been reported that the contact resistance, as well as the field-effect mobility, of bottom-contact/bottom-gate (BC/BG) type TIPSPEN OFETs vary with the channel current direction with respect to the flow-coating direction.

13.4 Printing Methods

All of the methods described above require an auxiliary polymeric film to align the LC molecules, such as a polyimide acting as an alignment film. Such films, however, are no longer necessary if the LC molecules are able to align themselves autonomously. This is advantageous since it obviates the need for the thermal curing step, allows the manufacturing processes to be performed at room temperature and permits plastic rather than glass substrates, all of which reduce production costs. Below, two methods aimed at introducing a printing process are introduced, in particular the slit coating method, which will be described in detail. If and when these coating methods are put to practical use, it is expected that injection-free processes will be possible and productivity will consequently be improved. As noted, these methods are also advantageous since they lower the cost of LCD fabrication by removing the need for an alignment film.

13.4.1 Gravure-Coating Method

As discussed, the standard industrial LCD manufacturing process employs a polyimide alignment film. Such films are commonly treated using the gravure

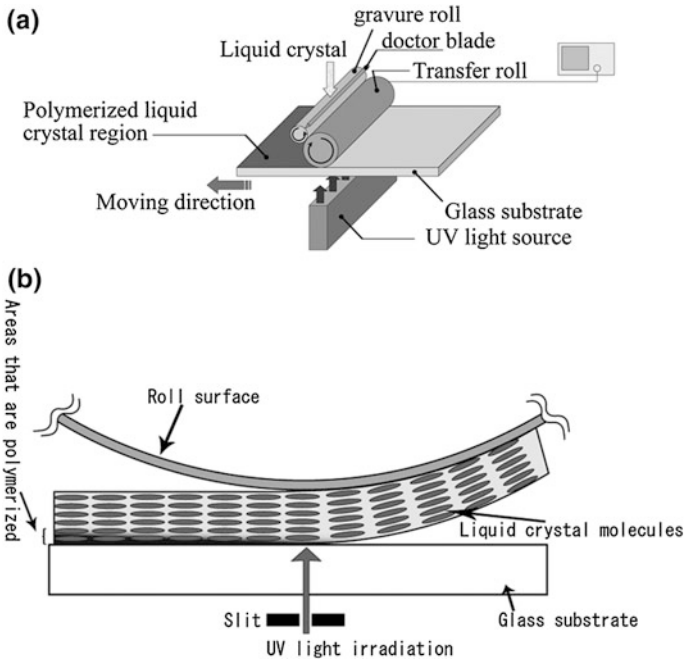

Fig. 13.7 LC gravure printing method. **a** Schematic illustration of the instrument. **b** Model of the LC alignment transfer

coating method and, based on this technique, a novel means of transferring LC molecules that have been aligned in advance has been devised. This process takes advantage of the observation that the substrate need not be flat if sufficient transferring time is allowed. Figure 13.7 illustrates an example of the gravure printing method [33, 34], in which the host LC (ZLI-2293) is doped with a guest UV-curable LC (UCL-011-K1, DIC) acting as the RM. Here the LC molecules are placed between the gravure roll and the doctor blade, following which an LC layer of the desired thickness is formed on the transfer roll. Throughout this process, the linear velocity of the substrate and the rotational speed of the transfer roll are synchronized. The LC molecules are pre-aligned on the transfer roll since the roll is equipped with interdigitated electrodes capable of inducing planar alignment. In the case of vertical alignment, a planar electrode is employed to generate a vertical electric field between the transfer roll and the substrate. The aligned LC molecular layer is subsequently transferred to the glass substrate while maintaining molecular alignment and, immediately following this transfer, the added RM is polymerized by UV irradiation, since otherwise the LC alignment on the glass substrate will be rapidly disrupted by thermally induced motion. It has been reported that UV polymerization of the RM tends to induce surface segregation [35]. That is, the RM is found in higher concentrations in the vicinity of the glass-LC layer interface. It is also important to emphasize that the LC molecules near the air-LC layer interface

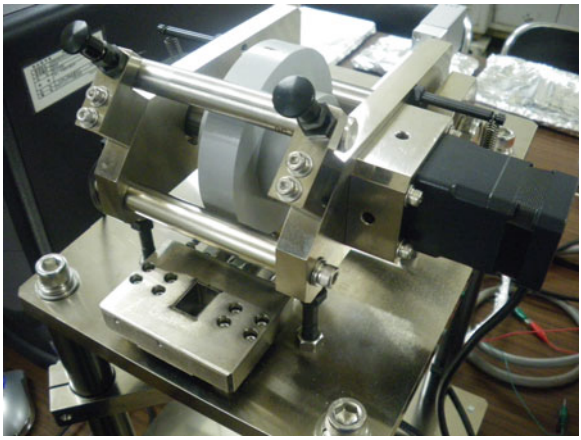

Fig. 13.8 Photograph of the prototype LC gravure coating machine

are not polymerized and remain in the nematic phase because the radical polymerization of the RM is disturbed by atmospheric oxygen. Finally, the LC layer transferred to the substrate is laminated against another LC-transferred substrate to form a sandwich-type LC cell. Figure 13.8 presents a photograph of a prototype LC gravure coating machine. The size of the layer and the LC alignment depend on the printing plate, and therefore multi-domain pattern alignment is also possible with such devices.

13.4.2 Slit-Coater Method

A slit coater, also known as a dye coater or a lip coater, is widely used for painting or spreading a fluid with uniform thickness. Recently, we reported that the slit-coater method is also applicable to LCD fabrication. The slit coater does not merely take the place of the one-drop fill (ODF) process in LCD fabrication; it has been demonstrated that LC layers formed by a slit coater exhibit uniaxial alignment and that this alignment is maintained following UV polymerization, suggesting the possibility of a molecular alignment technique incorporating a non-thermal curing process. In such a process, locally polymerized LC regions would replace the (typically polyimide) molecular alignment film. As a result, a slit coater can potentially serve as both an LC filling process and a molecular alignment process, thus reducing the required quantity of LCD fabrication steps.

Figure 13.9 shows a slit-coater system and a schematic diagram of such a system, including the slit nozzle and UV light source. In this process, the substrate —positioned on the carrier stage—is moved such that it is coated on one side with LC molecules. During this coating, the LC molecules undergo self-organized alignment resulting from the shear-flow force. UV irradiation from the bottom side of the substrate is performed simultaneously to polymerize a thin LC layer adjacent

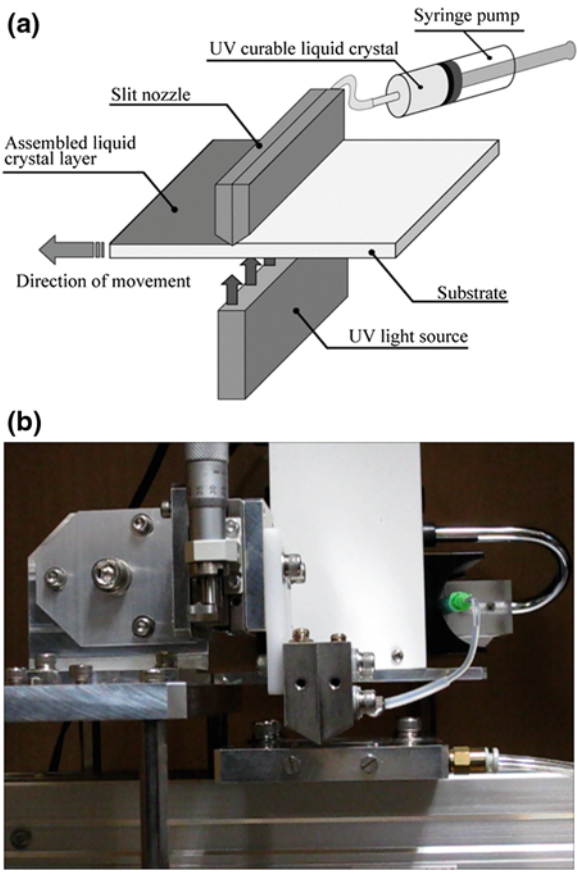

Fig. 13.9 **a** Schematic illustrations of the slit coater method. **b** Photograph of the experimental instrument

to the substrate, as illustrated in Fig. 13.10. This locally polymerized LC region, with a typical thickness of several tens of nanometers, acts as a molecular alignment film. Consequently, the slit coater can be used to achieve both LC filling and molecular alignment. Following the LC coating and UV irradiation, the top surface of the LC layer remains in the nematic phase. Therefore, by combining two such substrates coated in this manner with LC layers, an LCD panel can be fabricated without the LC injection process. As noted, the LC alignment is brought about by the shear flow between the slit nozzle and the substrate. The process parameters that control the LC alignment are therefore the slit width, slit length, coating gap, delivery rate of LC materials from the slit nozzle, stage movement velocity and UV irradiation intensity. In our own experimental trials, the slit width was fixed at 20 μm, the slit length at 13 mm and the coating gap at approximately 100 μm. The LC host molecule was a nematic cyanobiphenyl compound (ZLI-2293, Merck) exhibiting positive dielectric anisotropy, while the guest UV-curable LC was UCL-011-K1 (DIC), added at a concentration of 5 wt%. The LC mixture was delivered to the slit nozzle at a fixed rate using a syringe pump and the stage

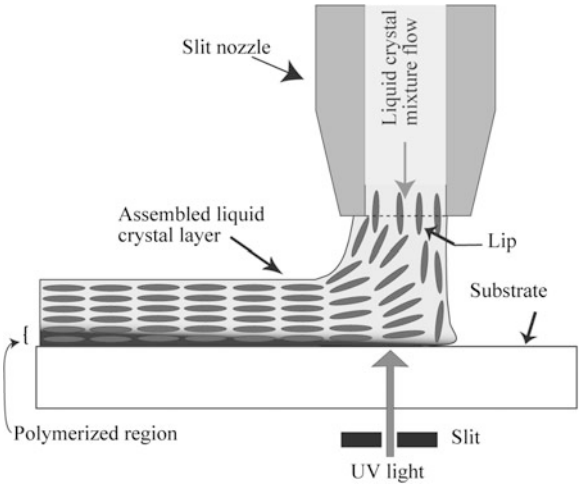

Fig. 13.10 Schematic model of shear flow molecular alignment during the slit coating process

was moved at a fixed rate using a stepper motor. A high pressure Ushio SP9-250DB mercury lamp with a central wavelength of 365 nm was employed as the light source. The stage was moved at 0.50 mm/s and the UV irradiation intensity was 100 mW/cm^2. It is expected that such polymerized thin LC layers will function as well as conventional alignment films.

Figure 13.11a, b present photographs of the coated LC films, in which the coating direction is parallel to the crossed polarizer (a) and at 45° with respect to the polarization axis of one polarizer (b). These images show uniform and uniaxial alignment of the layers. Figure 13.12a, b show enlarged images of these same samples obtained by polarized optical microscopy (POM). It is evident that the extinction direction is parallel to the coating direction of the LC layer, suggesting a uniaxial planar alignment of the LC direction. It is also obvious that numerous streak-like defects are present, almost parallel to the LC coating direction. These appear to represent damage to either the LC layer or the substrate, possibly generated mechanically by contact between the slit nozzle and the substrate. To reduce the number of these defects, precise control of the gap between the slit nozzle and the substrate is required. Unfortunately, relatively large gaps on the order of 200 μm generate few defects but also allow for insufficient LC alignment. In Fig. 13.12b, scale-like defects are also found, possibly caused by the movement of the stage. In order to reduce the number of these defects, it was necessary to construct an LC coating system with very precise mechanical movements. For this purpose, a prototype slit coater specially designed for LC alignment was manufactured, as shown in Fig. 13.13 (produced by the Toray Engineering Co., Ltd., Japan). Figure 13.14 presents a photograph of a coated LC film obtained by means of this prototype slit coater, using a slit length of 100 mm, a slit width of 20 μm and a coating gap of approximately 100 μm. The thickness of the coated LC layer is approximately 1 μm. It can be seen that the initial portion of the LC coating, where the slit nozzle first approaches the substrate, is not well aligned, since the molecular

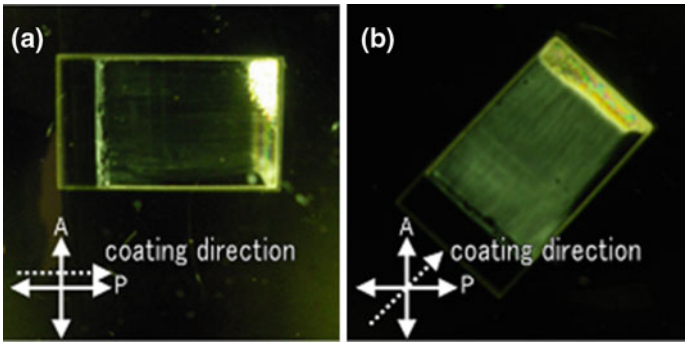

Fig. 13.11 Photographs of the LC films fabricated using the slit coater and simultaneous UV irradiation. **a** The coating direction is parallel to the polarizer under the crossed-nicols. **b** The coating direction is 45° with respect to the polarizer under the crossed-nicols

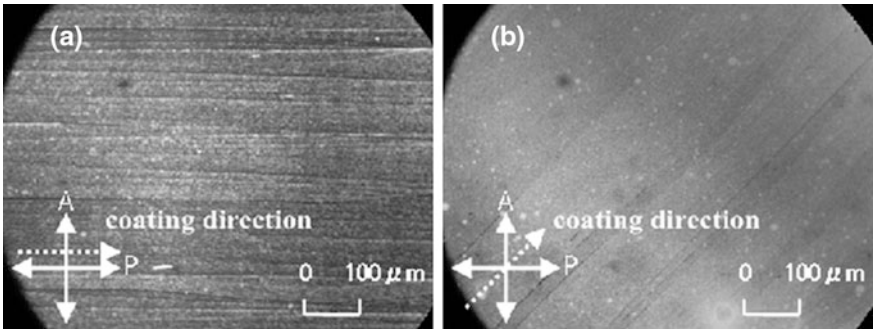

Fig. 13.12 Microphotographs of the LC films fabricated by the slit coater. **a** The coating direction is parallel to the polarizer under the crossed-nicols. **b** The coating direction is 45° with respect to the polarizer under the crossed-nicols

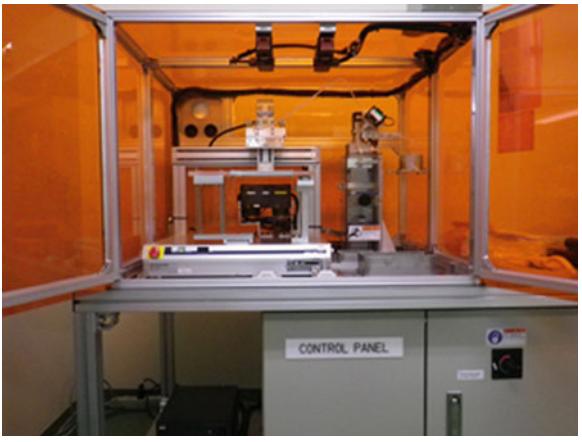

Fig. 13.13 Photograph of the prototype slit coater specialized for LC alignment

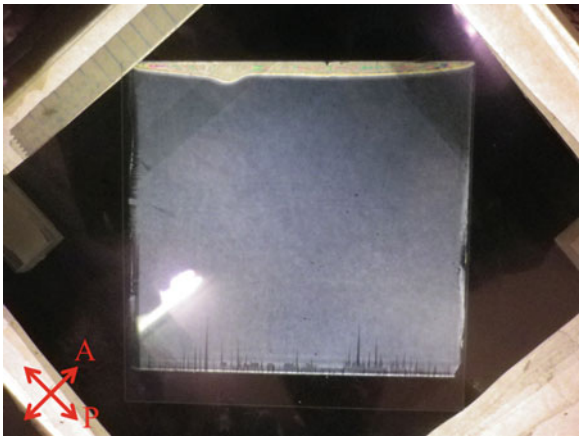

Fig. 13.14 Photograph of the LC alignment fabricated by prototype slit coater. The size of the glass substrate is 100 × 100 mm. The coating direction is 45° with respect to the polarizer under the crossed-polarizers

alignment is difficult to control during the initial discharge from the lip of the nozzle. This effect is currently unavoidable and, in fact, the same defect is seen at the terminal region of the film because no shear flow force is generated around the initial and terminal portions. However, this is not an insurmountable problem; for example, in the case of a roll-to-roll process, the initial and terminal portions of the substrate film could simply be cut off.

As noted, it is assumed that the LC alignment is brought about by the shear flow between the slit nozzle and the substrate. Figure 13.15 presents a numerical simulation of liquid flow based on the Navier–Stokes equation [36], as obtained using commercially available software (ANSYS Fluent, ANSYS Inc.) [37]. In computational fluid dynamics, the semi-implicit method for pressure linked equations (SIMPLE) algorithm is a widely used numerical procedure to solve the Navier–Stokes equation [38]. Here the Navier–Stokes equation was discretized using the finite volume method and, to simplify the calculations, an isotopic liquid with a viscosity of 160 mPa s was assumed, even though the LC is actually an anisotropic fluid. The calculation parameters were as follows: an LC layer thickness of 2 μm, a gap between the lip and the substrate of 100 μm, a contact angle between the substrate and the fluid of 30°, a contact angle between the lip and the fluid of 60°, a surface tension of 30 mN m and a substrate velocity of 10 mm/min. Figure 13.15a shows the shape of the fluid bead between the slit coater lip and the substrate, from which it can be determined that the meniscus front and back radii are approximately 0.2 and 0.3 mm, respectively. Figure 13.15b pictures the fluid pathways, indicating the movement of the fluid over a certain duration of the reduced time. The pathline along the nozzle depicts the fluid flow of the upper LC layer, representing the LC molecules that reach the surface of the bead (the interface between the air and fluid) and that have a relatively low flow velocity. In contrast, the line running directly toward the substrate depicts the fluid flow of the lower LC layer, for which the flow velocity is relatively high. It is evident that there is a distribution of flow velocities between the lip and substrate, and this distribution induces the shear flow.

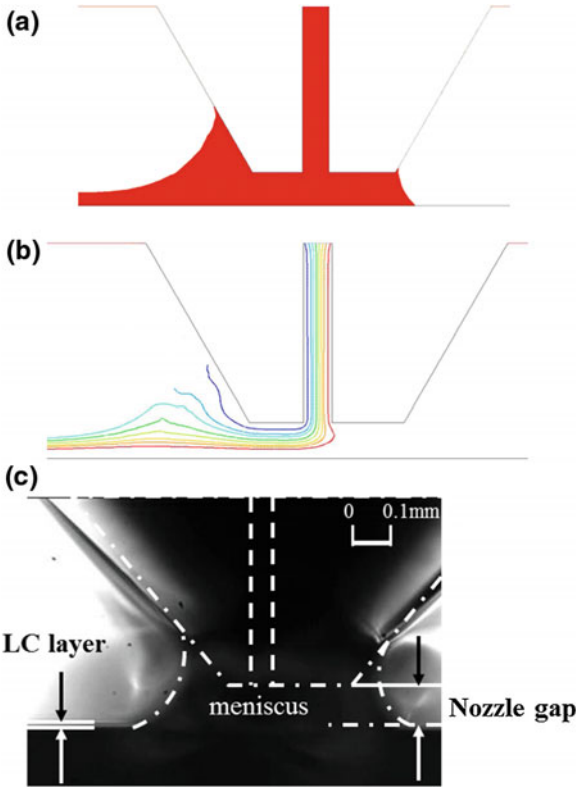

Fig. 13.15 The aspect of the shear flow. **a** Simple numerical simulation of a liquid flow based on the continuity equation and Navier–Stokes equation. **b** Pathlines of the fluid, which represents the trace of the fluid in certain duration of the reduced time. The line color represents the reduced position. **c** High-speed camera snapshot around the lip of slit coater

Figure 13.15c shows a photographic image of the lip of the slit coater obtained with a high-speed camera (Fastcam MC2.1, Photron) during a trial in which a nematic mixture composed of a fluorinated derivative was used. Comparing Figs. 13.15a, c, it is clear that the shape of the bead as captured by the high-speed camera is similar to that depicted by the numerical simulation. Although the dynamics of an anisotropic fluid such as a nematic LC are complex, the gradient of the flow velocity in the numerical simulation suggests the existence of shear flow near the substrate, which induces the LC molecular alignment.

Various investigations were performed with regard to UV irradiation of these layers. In those cases in which the LC alignment is fixed by UV irradiation after the LC coating process is complete, as in Fig. 13.16, it is not necessary to situate the UV source immediately below the slit nozzle and so the LC coating and UV irradiation may be carried out separately. This is beneficial since it prevents the slit nozzle from being covered by the polymerization agent. Furthermore, it is not necessary to synchronize the stage velocity and UV irradiation duration. In trials performed by our group, the UV irradiation intensity was 10 mW/cm^2, the irradiation time was 300 s and the UV light impinged on the sample vertically, coming from the underside of the substrate. Figure 13.17 provides photographic images of

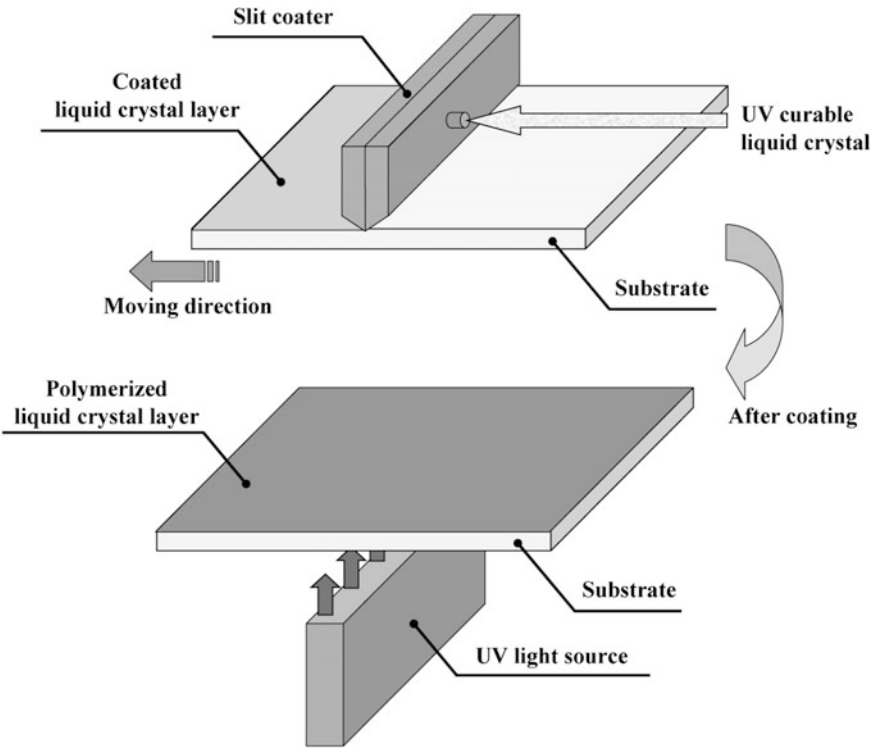

Fig. 13.16 Schematic illustration of the UV irradiation after LC coating using slit coater

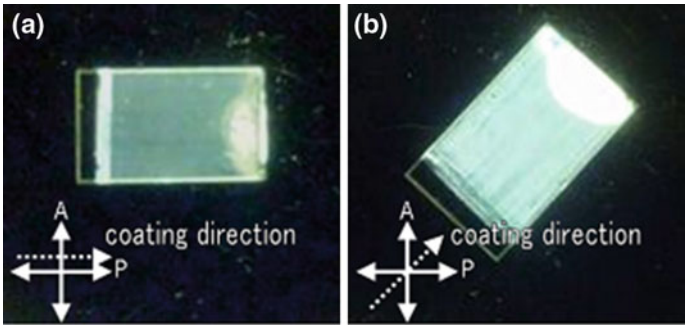

Fig. 13.17 Photographs of LC-coated films consist of ZLI-2293 and UCL-011-K1 before UV irradiation. **a** The coating direction is parallel to the polarizer under the crossed-nicols. **b** The coating direction is 45° with respect to the polarizer under the crossed-nicols

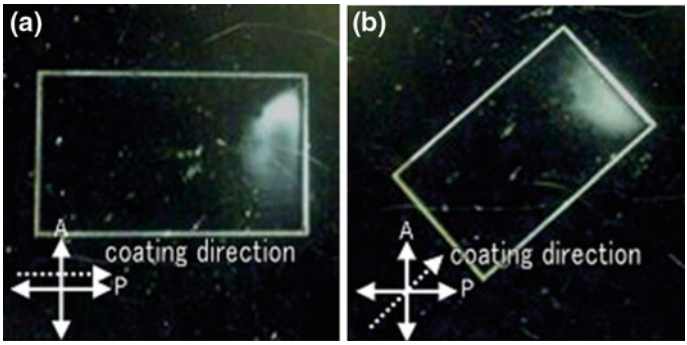

Fig. 13.18 Photographs of LC-coated films consisting of ZLI-2293 and UCL-011-K1 after UV irradiation with high-pressure mercury lamp under crossed polarizer. **a** The coating direction is parallel to the polarizer under the crossed-nicols. **b** The coating direction is 45° with respect to the polarizer under the crossed-nicols

coated LC films under crossed nicols immediately after the coating process and prior to UV irradiation, where the guest material is UCL-011-K1 (DIC). These photographs show that uniform and uniaxial LC alignment was obtained. Figure 13.18 shows photographs of these same coated LC films after UV irradiation. The transmittance under crossed nicols is not changed by rotating the LC-coated film, implying that the planar alignment of the LC changes the vertical alignment. It was also confirmed that this alignment transition behavior was affected by the duration of the UV irradiation, which was typically 40 s. One possible cause of such an effect could be thermal fluctuations induced by the irradiation. To verify this hypothesis, a UV band-pass filter was inserted between the UV light source and the substrate in order to filter out the vis-light. However, the alignment transition behavior was still observed. Subsequently, a He–Cd laser (λ = 325 nm, 10 mW) was introduced in place of the high-pressure mercury lamp, whereupon it was found that this alignment transition behavior was observed regardless of the laser intensity. In order to examine the effect of the RM material, LC-coated films in which the guest material was a mixture of RM257 (Merck), C12A and DMPAP (Aldrich) were fabricated, following which UV irradiation was performed using the He–Cd laser. In this case, the alignment transition behavior was not observed regardless of the extent of UV irradiation. From these experimental results, it is believed that the alignment transition behavior results from anisotropic polymerization, which in turn is dependent on the guest material [39].

To allow practical application of the slit coater, it is necessary to consider the structure of the moving stage that acts as the substrate carrier. The motion of the moving stage has to be precise so as to maintain the gap between the substrate and slit nozzle. As shown in Fig. 13.19a, the UV irradiation is carried out through the moving stage and so the stage must transmit UV light and cannot be constructed of metal plate. In our case, the glass substrate was carried on a square frame. Although this is sufficient to carry a small substrate, a larger, thin substrate would likely warp

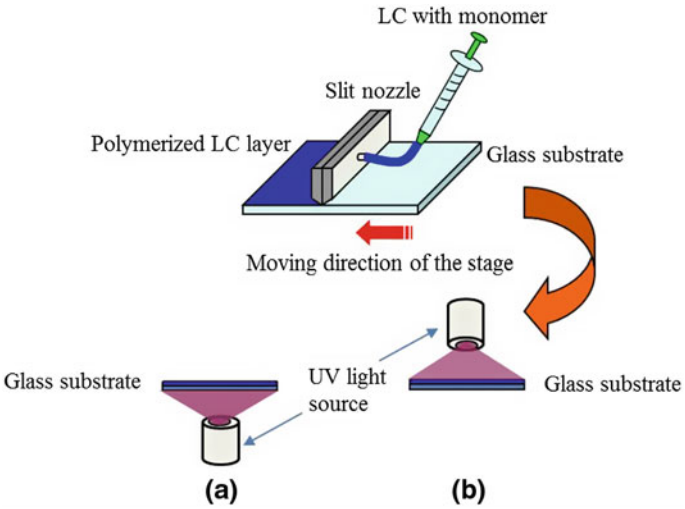

Fig. 13.19 Schematic diagram of the slit coater and UV irradiation. **a** UV irradiation from the side of a glass substrate (exposure type 1), **b** UV irradiation from the side of the air-LC interface (exposure type 2)

under such conditions. Thus, to coat LCs with uniform thicknesses, it is recommended that the moving stage be made of a flat, solid plate with UV light projected downwards onto the LC layer. To assess other potential scenarios, LC layers were polymerized under two UV irradiation conditions; irradiation from the side of the glass substrate (exposure type 1) and irradiation from the side of the air-LC interface (exposure type 2). The effects of UV dosage on the electro-optical (EO) characteristics of LC sample cells fabricated under the two proposed conditions were then assessed. A host nematic LC material (Merck ZLI-2293), a liquid crystalline diacrylate monomer (1.0 wt%, Merck RM257) and a photoinitiator (0.1 wt%, 2,2-dimethoxy-2-phenyl acetophenone, DMPAP, Aldrich) were used in this study. The UV irradiation times were 30 or 90 s and the UV irradiation intensity was set to 5 mW/cm^2, using a deep UV Ushio Spot Cure SP9-250DB lamp at 365 nm. It is known that, even during the early stages of polymerization, the formation of the polymer network is accompanied by the phase separation of the reaction mixture into two regions: polymer-rich and LC-rich [40]. This phase separation results in a solidified polymer film in the region of the substrate closest to the UV source. Therefore, the polymer-rich region will be formed in the vicinity of the substrate in the case of exposure type 1 while, for exposure type 2, the polymer-rich region will be formed near the air-LC interface. These different boundary conditions will have an impact on the voltage-dependent transmittance (V–T) and hysteresis characteristics of the slit-coated twisted-nematic (TN) LC cells. Figure 13.20 presents the V–T curves and hysteresis characteristics of slit-coated TN LC cells fabricated under exposure types 1 and 2 at room temperature. The V–T curves show that, for both types of UV exposure conditions, the average threshold

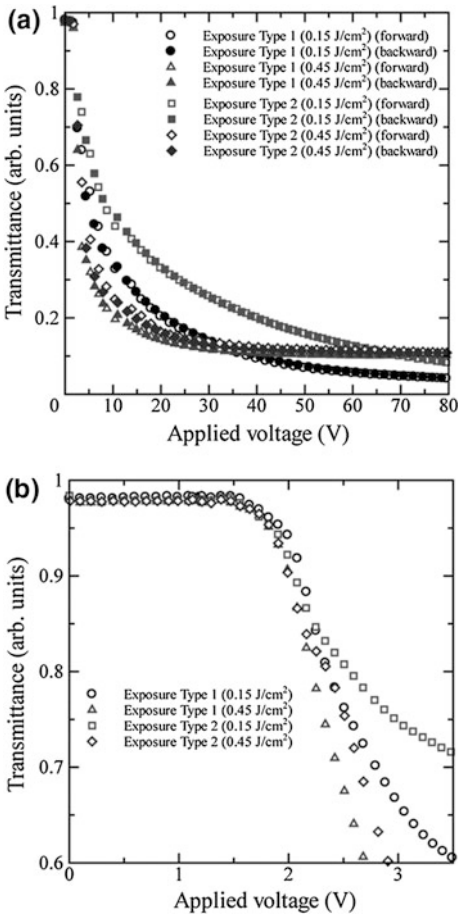

Fig. 13.20 **a** V–T curves and hysteresis characteristics of slit-coated TN LC cells fabricated under exposure types 1 and 2 at UV exposure dosages of 0.15 and 0.45 J/cm^2 at room temperature and **b** V–T curves near the threshold voltages

voltage was ∼1.5 V and the slit-coated TN LC cells could be switched to the black state at rather high voltages. From the V–T curves it is also evident that there was almost no hysteresis behavior. However, effects of the UV exposure type and exposure dosage on the steepness of the V–T curves were observed. These steepness parameter characteristics indicate that exposure type 1 gives steeper V–T curves and that longer exposure times produce steeper curves. The curve steepness for these slit-coated TN LC cells was also found to be greater than those for conventional TN LC cells. It was concluded that the V–T characteristics of cells made using exposure type 2 were inferior to those produced using exposure type 1 [41]. In accordance with these experimental results, plate-like quartz glass was subsequently adopted as a moving carrier stage, as shown in Fig. 13.13.

Figure 13.21 summarizes the dependence of the pretilt angle on the UV exposure dosage [42]. Here higher UV exposures are seen to generate larger pretilt angles on the slit-coated substrate surface. It is believed that increasing UV exposures form a

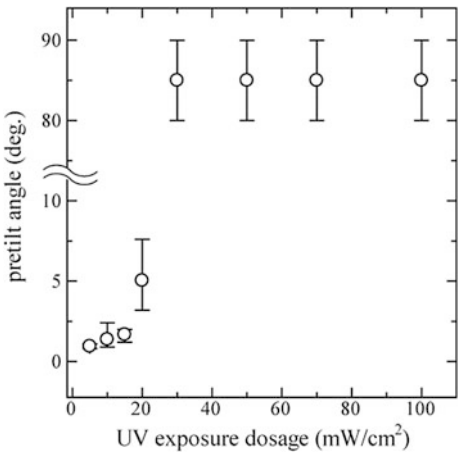

Fig. 13.21 Dependence of the pretilt angle on the UV exposure dosage

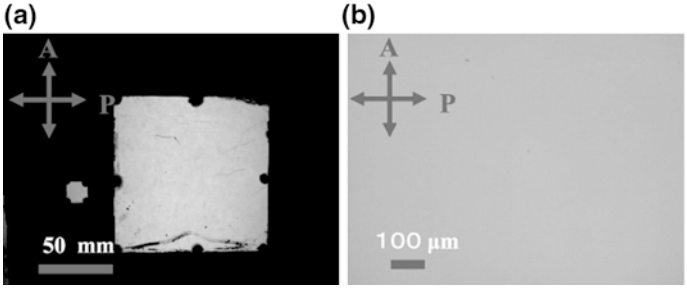

Fig. 13.22 Photographs of the TN-LCD **a** Fabricated by experimental instrument (*left*) and prototype instrument (*right*). **b** Microphotograph of TN-LCD fabricated by prototype instrument

denser polymer network, resulting in a stronger anchoring force sustaining the pretilt of the LC molecules on the substrate surface [43]. These higher pretilt angles are likely due to the surface hydrophobicity of the substrate, as has been reported previously in the literature [44]. The resulting pretilt angle will also depend on the structure and concentration of the RM as well as on the process conditions [45–49].

Figure 13.22 shows photographs of TN LCDs fabricated using the slit-coater method, acquired using the transmission mode (or say normally white mode). As can be seen from these images, sufficiently uniform alignment was realized. Figure 13.23 presents the experimental results for the EO properties of TN LCDs formed using the UV curable additive RM257 at concentrations of 2.1 and 1.1 wt% [37]. For comparison purposes, the same TN LCD was made using the conventional rubbing method, employing a polyimide alignment film. Compared with the reference TN-LCD, similar EO properties were obtained at UV intensities of 5 mW/cm^2, and no hysteresis characteristics are observed in the EO response in Fig. 13.23b.

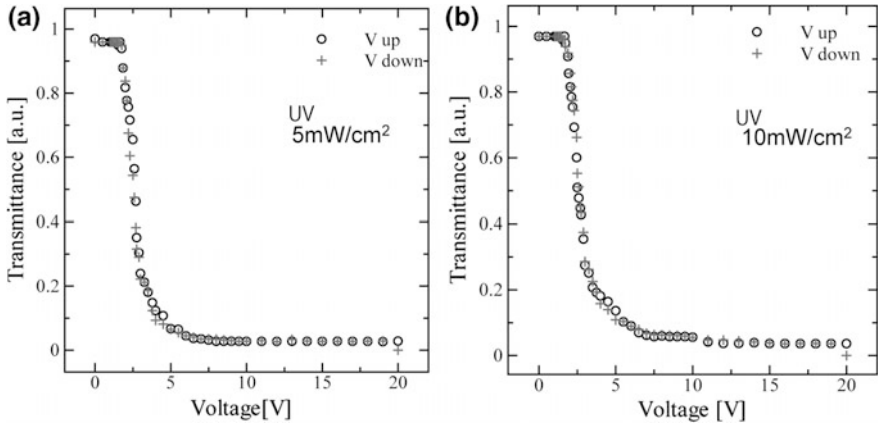

Fig. 13.23 Electro-optical properties of the TN-LCD fabricated by slit coater method. **a** The dosage of RM257 was 2.1 wt%. **b** The dosage of RM257 was 1.1 wt%

Regardless of the UV intensity, the threshold voltage was 1.9 V, which coincides with that for the reference TN LCD fabricated by the rubbing method. The contrast ratio is approximately 84.3, which again is not inferior to that of the LCD made by the conventional rubbing method (approximately 90.4) under laboratory conditions. However, when applying the UV curable additive at 2.1 wt% and/or UV intensities of 10 mW/cm^2, the EO properties below 5 V and above 12 V were different to those of the reference TN LCD. This difference appears to result from variations in the polymer network formation process.

In the revised fabrication process, it is quite beneficial that the production time is only a few minutes from the first substrate washing to the substrate lamination, since the baking process for the alignment film (which typically takes several tens of minutes) is not required. Furthermore, the performance of the TN LCD made using the slit coater method is equal to that of the TN LCD made by the rubbing method. By way of a trial, an in-plane switching (IPS) mode LCD was fabricated on a film substrate. It should be noted that the fabricated IPS-LCD was not a conventional sandwich type LCD but rather a single substrate type LCD not incorporating a counterpart substrate, as shown in Fig. 13.24b. Figure 13.24c shows the appearance of the IPS LCD, for which the driving area was 10 × 10 mm^2. As shown in Fig. 13.24c, a bendable IPS LCD film was obtained, and exhibited completely satisfactory switching operation (white region in the figure). Figure 13.25 presents the experimental results for the EO properties of an IPS LCD fabricated by the slit-coater method, employing UV-reactive mesogens at concentrations of 0.02 wt% (DMPAP) and 0.1 wt% (RM257). This figure demonstrates that the device produced a normal response with minimal hysteresis. In this case, a counterpart substrate was not included and, as a result, the air-LC interface had no anchoring function, which in turned caused the hysteresis in the EO response. In a real LCD,

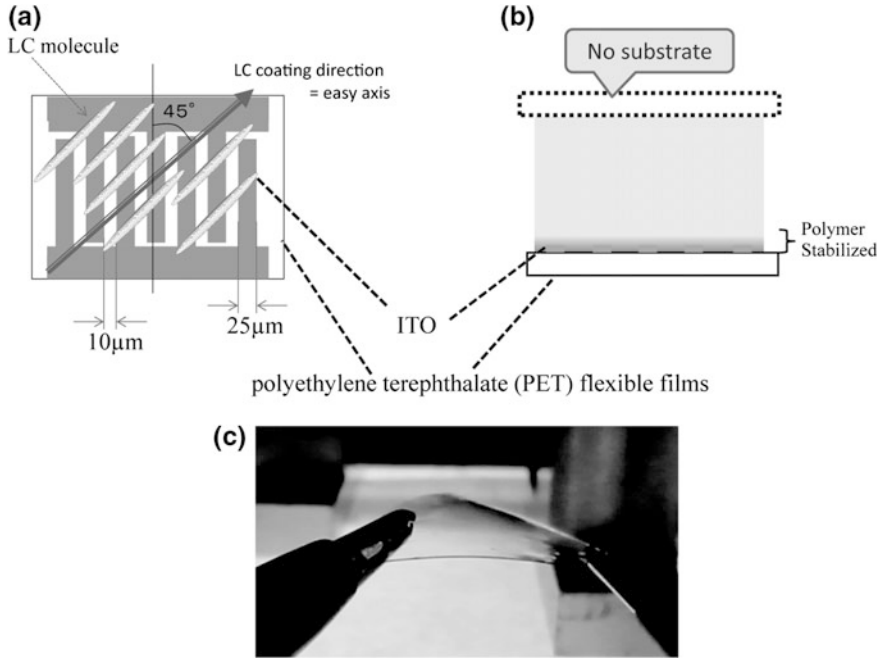

Fig. 13.24 Schematic model of single film substrate IPS-LCD. **a** Top view model. **b** Side view model. **c** Appearance of the IPS-LCD fabricated by experimental instrument

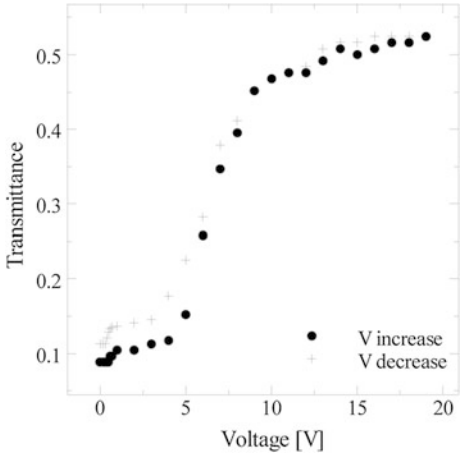

Fig. 13.25 Electro-optical properties of the IPS-LCD fabricated on single substrate

because of the fluidity of the LC, a counterpart substrate would be required. Figure 13.26 shows a sandwich-type, bendable TN-LCD fabricated using a prototype slit coater with polycarbonate films.

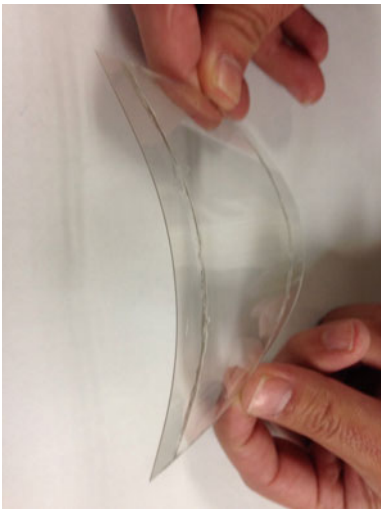

Fig. 13.26 Appearance of the bendable TN-LCD made by polycarbonate films

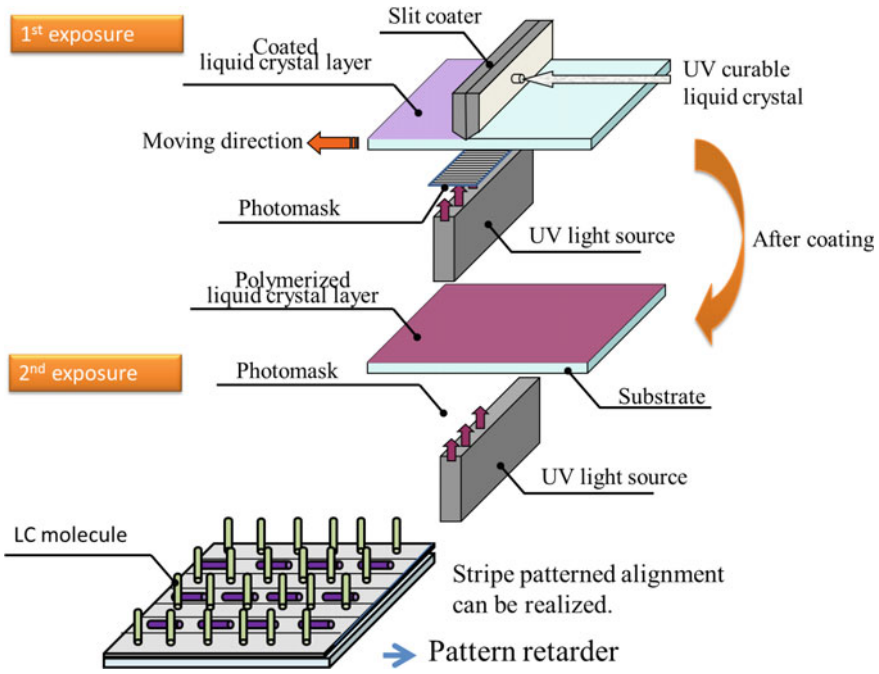

Fig. 13.27 Model of the vertical/planar striped alignment. Firstly, UV irradiation through a grid photomask is carried out in order to polymerize the planarly aligned regions. Then whole the substrate was UV irradiated to reveal the vertical alignment

13.5 Future Applications of the Printing Method

Rather than high quality, so-called "printed electronics" are more often expected to offer flexibility, bendability, robustness and low cost. With regard to reducing the manufacturing cost, plastic films have higher potential than advanced glass substrates [50]. In addition, the slit-coater method is adaptable for use with roll-to-roll technology as a continuous production process for LCDs. In the case of nano-imprint lithography, a master mold is required [51] and large master molds are costly and tend to wear away with use. A further advantage of the slit-coater method is therefore the lack of a master mold, since patterned alignment in which the vertical and planar alignments are arranged in an alternating fashion can be realized by inserting a grid photomask, as shown in Fig. 13.27. Useful products that may result from this process are pattern retarders and patterned polarizer films and, in the near future, the use of plastic substrates in conjunction with roll-to-roll processing should allow commercial scale production of leaflet-type, disposable LCDs. The slit-coater method may also be extended beyond the alignment of LCs and applied to the alignment of nano-rods. In addition, certain RM materials may be anisotropically polarized following polarized UV irradiation. Thus a rich variety of commercial products can be predicted to result from these novel technologies.

References

1. E. Lueder, *Liquid Crystal Displays* (John Wiley & Sons, Chichester, 2001)
2. D.-K. Yang, S.-T. Wu, *Fundamentals of Liquid Crystals* (John Wiley & Sons, Chichester, 2006)
3. T. Uchida, H. Seki, Surface alignment of liquid crystals, in *Liquid Crystals-Applications and Uses*, vol. 3, ed. by B. Bahadur (World Scientific, 1990)
4. K. Takatoh, M. Hasegawa, M. Koden, N. Itoh, R. Hasegawa, M. Sakamoto, *Alignment Technologies and Applications of Liquid Crystal Devices* (Taylor & Francis, London, 2005)
5. V. Coropceanu, J. Cornil, D.A. da Silva Filho, Y. Olivier, R. Silbey, J.L. Brédas, Charge transport in organic semiconductors. Chem. Rev. **107**, 926–952 (2007)
6. H. Ishii, K. Kudo, T. Nakayama, N. Ueno (eds.), *Electronic Processes in Organic Electronics* (Springer, Japan, 2015)
7. C.D. Dimitrakopoulos, P.R.L. Malenfant, Organic thin film transistors for large area electronics. Adv. Mater. **14**, 99–117 (2002)
8. K. Suganuma. *Introduction to Printed Electronics*, Springer, 2014
9. C. Mauguin, Sur les cristaux liquides de Lehmann. Bull. Soc. fr. Miner. **34**, 71–76 (1911)
10. J.M. Geary, J.W. Goodby, A.R. Kmetz, J.S. Patel, The mechanism of polymer alignment of liquid crystal materials. J. Appl. Phys. **62**, 4100–4108 (1987)
11. H. Kikuchi, J.A. Logan, D.Y. Yoon, Study of local stress, morphology, and liquid crystal alignment on buffed polyimide surfaces. J. Appl. Phys. **79**, 6811–6817 (1996)
12. I. Hirosawa, Method of characterizing rubbed polyimide film for liquid crystal display devices using reflection ellipsometry. Jpn. J. Appl. Phys. **35**, 5873–5875 (1996)
13. Y. Nishikata, A. Morikawa, Y. Takiguchi, A. Kanamoto, M. Suzuki, M. Kakimoto, Y. Imai, Orientation of polymer chain of polyimide LB films, and alignment of liquid crystals on the LB films. Nippon Kagaku Kaishi **11**, 2174–2179 (1987), Electrooptic bistability and threshold

characteristics of ferroelectric liquid crystal cell possessing polyimide Langmuir-Blodgett film as an aligning layer. Jpn. J. Appl. Phys. **27**, L1163–L1164 (1988)
14. M. Sugi, N. Minari, K. Ikegami, S. Kuroda, K. Saito, M. Saito, Vertical dipping method as a means of controlling the in-plane molecular orientation in Langmuir-Blodgett films. Thin Solid Films **178**, 157–164 (1989)
15. O. Yaroshchuk, Y. Reznikov, Photoalignment of liquid crystals: basics and current trends. J. Mater. Chem. **22**, 286–300 (2012)
16. N.A. Clark, Surface memory effects in liquid crystals: influence of surface composition. Phys. Rev. Lett. **55**, 292–295 (1985)
17. Y. Ouchi, M.B. Feller, T. Moses, Y.R. Shen, Surface memory effect at the liquid-crystal-polymer interface. Phys. Rev. Lett. **68**, 3040–3043 (1992)
18. B.O. Myrvold, A weak surface memory effect in liquid crystal cells with rubbed polyimide layers. Liq. Cryst. **18**, 287–290 (1995)
19. T. Shioda, Y. Okada, D.-H. Chung, Y. Takanishi, K. Ishikawa, B. Park, H. Takezoe, Liquid crystals align liquid crystals. Jpn. J. Appl. Phys. **41**, L266–L268 (2002)
20. K. Sakamoto, J. Ueno, K. Bulgarevich, K. Miki, Anisotropic charge transport and contact resistance of 6,13-bis(triisopropylsilylethynyl) pentacene field-effect transistors fabricated by a modified flow-coating method. Appl. Phys. Lett. **100**, 123301 (2012)
21. A. Tracz, J.K. Jeszka, M.D. Watson, W. Pisula, K. Müllen, T. Pakula, Uniaxial alignment of the columnar super-structure of a hexa (alkyl) hexa-*peri*-hexabenzocoronene on untreated glass by simple solution processing. J. Am. Chem. Soc. **125**, 1682–1683 (2003)
22. W.H. Lee, D.H. Kim, Y. Jang, J.H. Cho, M. Hwang, Y.D. Park, Y.H. Kim, J.I. Han, K. Cho, Solution-processable pentacene microcrystal arrays for high performance organic field-effect transistors. Appl. Phys. Lett. **90**, 132106 (2007)
23. R.L. Headrick, S. Wo, F. Sansoz, J.E. Anthony, Anisotropic mobility in large grain size solution processed organic semiconductor thin films. Appl. Phys. Lett. **92**, 063302 (2008)
24. H.A. Becerril, M.E. Roberts, Z. Liu, J. Locklin, Z. Bao, High-performance organic thin-film transistors through solution-sheared deposition of small-molecule organic semiconductors. Adv. Mater. **20**, 2588–2594 (2008)
25. T. Uemura, Y. Hirose, M. Uno, K. Takimiya, J. Takeya, Very high mobility in solution-processed organic thin-film transistors of highly ordered [1]benzothieno[3,2-b]benzothiophene derivatives. Appl. Phys. Exp. **2**, 111501 (2009)
26. C.W. Sele, B.K.C. Kjellander, B. Niesen, M.J. Thornton, J.B.P.H. van der Putten, K. Myny, H. J. Wondergem, A. Moser, R. Resel, A.J.J.M. van Breemen, N. van Aerle, P. Heremans, J.E. Anthony, G.H. Gelinck, Controlled deposition of highly ordered soluble acene thin films: effect of morphology and crystal orientation on transistor performance. Adv. Mater. **21**, 4926–4931 (2009)
27. M.J. Kim, H.W. Heo, Y.K. Suh, C.K. Song, Morphology control of TIPS-pentacene grains with inert gas injection and effects on the performance of OTFTs. Org. Electron. **12**, 1170–1176 (2011)
28. Y. Toko, B.Y. Zhang, T. Sugiyama, K. Katoh, T. Akahane, Characteristics of liquid crystal display fabricated by alignment transcription method. Mol. Cryst. Liq. Cryst. **304**, 107–112 (1997)
29. K. Sueoka, H. Nakamura, Y. Taira, Improving the moving-image quality of TFT-LCDs, Digest of SID Symposium, pp. 203–206 (1997)
30. S.G. Kim, S.M. Kim, Y.S. Kim, H.K. Lee, S.H. Lee, G.-D. Lee, J.-J. Lyu, K.H. Kim, Stabilization of the liquid crystal director in the patterned vertical alignment mode through formation of pretilt angle by reactive mesogen. Appl. Phys. Lett. **90**, 261910 (2007)
31. Y. Momoi, M. Kwak, D. Choi, Y. Choi, K. Jeong, T.i Koda, O. Haba, K. Yonetake. Polyimide-free LCD by dissolving dendrimers. J. SID **20**(9), 486–492 (2012)
32. J.C. Meredith, A.P. Smith, A. Karim, E.J. Amis, Combinatorial materials science for polymer thin-film dewetting. Macromolecules **33**, 9747–9756 (2000)
33. M. Kimura, Japan Patent Unexam. Publ. No.2009-175247

34. M. Kimura, Progress of rubbing and non-rubbing techniques, in *Proceedings of the IMID'10*, pp. 185–186 (2010)
35. S.H. Lee, S.M. Kim, S.-T. Wu, Emerging vertical-alignment liquid-crystal technology associated with surface modification using UV-curable monomer. J. SID **17**, 551–559 (2009)
36. L.D. Landau, E.M. Lifshitz, *Fluid Mechanics* (Pergamon Press, New York, 1987)
37. M. Kimura, K. Honda, S. Yodogawa, K. Ohtsuka, T.N. Oo, K. Miyashita, H. Hirata, T. Akahane, Flexible LCDs fabricated with a slit coater: not requiring an alignment film. J. SID **20**, 633–639 (2012)
38. S.V. Patankar, *Numerical Heat Transfer and Fluid Flow* (Hemisphere, New York, 1980)
39. H. Sato, K. Miyashita, M. Kimura, T. Akahane Study of liquid crystal alignment formed using slit coater. Jpn J. Appl. Phys. **50**, 01BC16 (2011)
40. A.S. Sonin, N.A. Churochkina, Liquid crystals stabilized by polymer networks. Polym. Sci. A. **52**, 463 (2010)
41. K. Ohtsuka, Y. Nagataki, K. Goda, T.N. Oo, K. Miyashita, H. Hirata, M. Kimura, T. Akahane, Study of liquid crystal display fabricated using slit coater under two ultraviolet irradiation conditions. Jpn. J. Appl. Phys. **52**, 05DB04 (2013)
42. Y. Nagataki, T.N. Oo, T. Yamamoto, K. Miyashita, H. Hirata, M. Kimura, T. Akahane, Study of electro-optical properties of liquid crystal/reactive mesogen-coated liquid crystal display fabricated by slit coater. Liq. Cryst. **41**, 667–672 (2013)
43. T.J. Chen, K.L. Chu, Pretilt angle control for single-cellgap transflective liquid crystal cells. Appl. Phys. Lett. **92**, 091102 (2008)
44. B.Y. Liu, L.J. Chen, Role of surface hydrophobicity in pretilt angle control of polymer-stabilized liquid crystal alignment systems. J. Phys. Chem. C **117**, 13474–13478 (2013)
45. A. Goetz, M.K. Memmer, M. Bremer, A. Taugerbeck, K. Tarumi, D. Pauluth. Advanced liquid crystal materials for fast switching display modes, in *Proceedings of the IDW'08*, LCT6—3 (2008)
46. A. Goetz, A. Taugerbeck, G. Bernatz, K. Tarumi, Advanced liquid-crystal materials for the polymersustained vertically aligned (PS-VA) mode. Digest SID Symp. **41**, 718–720 (2010)
47. E.Y. Jeon, K.H. Kim, J.H. Lee, T.H. Yoon, Single cellgap transflective liquid crystal device created by controlling the pretilt angle using a liquid crystalline reactive monomer. Opt. Express **19**, 25617–25622 (2011)
48. R.A.M. Hikmet, C.D. Witz, Gel layers for inducing adjustable pretilt angles in liquid crystal systems. J. Appl. Phys. **70**, 1265–1269 (1991)
49. D.K. Yang. Polymer-stabilized liquid crystal displays, in *Progress in Liquid Crystal Science and Technology in Honor of Shunsuke Kobayashi's 80th Birthday,* ed. by H.S. Kwok, S. Naemura, H.L. Ong (World Scientific, 2013), pp. 597–628
50. A. Koike, M. Nishizawa, H. Tokunaga, J. Akiyama, T. Tsujimura, K. Hayashi, Novel non-alkaline glass substrate with ultra-low thermal shrinkage for higher resolution active matrix displays, in *Proceedings of the IDW'13*, FMC4-2 (2013)
51. N. Kooy, K. Mohamed, L.T. Pin, O.S. Guan, A review of roll-to-roll nanoimprint lithography. Nanoscale Res. Lett. **9**, 320–332 (2014)

Index

Q. Li (ed.), *Anisotropic Nanomaterials*, NanoScience and Technology,
DOI 10.1007/978-3-319-18293-3